LITHOSPHERIC-SCALE TECTONICS OF THE INDIA-ASIA COLLISIONAL SYSTEM

by

Sean Kelly

Submitted in partial fulfillment of the Requirements for the
Degree of Doctor of Philosophy

at

Dalhousie University
Halifax, Nova Scotia
March 2024

TABLE OF CONTENTS

Page

LIST OF TABLES ..... **vii**

LIST OF FIGURES ..... **viii**

ABSTRACT ..... **xi**

LIST OF ABBREVIATIONS AND SYMBOLS USED ..... **xii**

ACKNOWLEDGEMENTS ..... **xvi**

CHAPTER 1. INTRODUCTION **1**

1.1 The Himalayan-Tibetan and Pamir-Hindu Kush Systems 2

1.1.1 Topography and Geology of the HT-HKP Orogen *3*

1.1.2 India-Asia Mantle-Scale Conditions and Properties of the Lithosphere *5*

1.1.3 Interpretations Regarding Current Seismically Imaged Subsurface Features *6*

1.1.4 Interpretations of the Magmatic Record Involving Lower Lithosphere Processes *8*

1.2 Motivation and Goals of the Research Undertaken in the Thesis 8

1.2.1 Observations and Inferences from the Pamir-Hindu Kush System that Require Explanation *9*

1.2.2 Observations and Inferences from the Central Himalayan-Tibetan System that Require Explanation *10*

1.2.3 Observations and Inferences from the Early Eohimalayan phase of the Central H-T System *13*

1.3 Benchmark Geodynamical Models of the Himalayan-Tibetan System 14

1.3.1 Analogue Plasticine Models *14*

1.3.2 Rayleigh Taylor (dripping) Instabilities and Delamination Models *15*

1.3.3 Horizontal Plane-strain and Plane-stress Analytic and Numerical Models *16*

1.3.4 Multi-Terrane 2D Geodynamical Models *17*

1.3.5 3D Geodynamical Models *20*

1.4 Research Objectives and Outline of Thesis Content 21

1.4.1 Geodynamical Modelling Approach *22*

1.4.2 Choice and Justification of Model Parameters *22*

1.4.3 Organization of the Thesis *25*

1.5 References for Chapter 1 27

CHAPTER 2. BALANCED CROSS-SECTIONS AND NUMERICAL MODELING OF THE LITHOSPHERIC-SCALE EVOLUTION OF THE HINDU KUSH AND PAMIR 42

2.1 Abstract 42

2.2 Introduction 43

2.3 Geological and Geophysical Constraints 45

2.3.1 Estimates of the Timing of Collision, Total India-Asia Convergence, and Convergence Velocity 46

2.3.2 Constraints from Upper-Mantle-Scale Seismic Interpretations 48

2.4 Constraints on the Evolution of the Hindu Kush and Pamir Systems 49

2.4.1 Partitioning Accommodation of Convergence in the Hindu Kush and Pamir Lithospheres 50

2.4.2 Crustal Structure and Shortening Estimates in the Hindu Kush and Pamir 51

2.4.3 Timing of Shortening 55

2.4.4 Nature of the Indian Margin 56

2.5 Geometrical Balanced Cross-Sections for the Interpreted Evolution of the Hindu Kush and Pamir 56

2.5.1 Crustal Erosion Estimates Based on Changes in Cross-Sectional Area During Shortening 57

2.5.2 Interpretations Based on Geometrical Balanced Sections and Possible Explanations 58

2.6 Hindu Kush and Pamir Characteristics to be Explained by Numerical Model Experiments 60

2.7 Design of the Numerical Models 61

2.7.1 Experimental Parameters 65

2.8 Model Results and Comparison with Observations 67

2.8.1 MHA (Hindu Kush) 67

2.8.2 MPA (Pamir) 73

2.9 Supporting Models (Sensitivity Tests) 79

2.9.1 Double Subduction in Pamir Models: Sensitivity to Strong Alai Terrane CLM 79

2.9.2 Double Subduction in Hindu Kush Models: Sensitivity to NH-CLM Properties 80

2.9.3 Pamir Domes: the Effect of Buoyant Melted Crust 80

2.9.4 Vanj Magmatism; Pamir Model Sensitivity to Weaker Alai Terrane CLM 81

2.9.5 Hindu Kush FI Slab Breakoff; Sensitivity of Subducted Fringe India to Density Variations *81*

2.10 Discussion: Comparison of Models MHA and MPA and the Three-Dimensional Nature of the Hindu Kush and Pamir System 84

2.11 Conclusions 87

2.12 Supporting Information for Chapter 2 90

2.13 References for Chapter 2 90

2.14 References for Chapter 2 Supporting Information 104

CHAPTER 3. INHERITED TERRANE PROPERTIES EXPLAIN ENIGMATIC POST-COLLISIONAL HIMALAYAN-TIBETAN EVOLUTION 107

3.1 Abstract 107

3.2 Introduction 108

3.3 Methods 108

3.4 Results and Comparison with Observations 112

3.5 Conclusions 119

3.6 Acknowledgements 121

3.7 Supporting Information for Chapter 3 121

3.8 References for Chapter 3 121

CHAPTER 4. EOHIMALAYAN METAMORPHISM AND SUBSEQUENT TECTONIC QUIESCENCE EXPLAINED 132

4.1 Abstract 132

4.2 Introduction 133

4.3 Methods 136

4.4 MEA Results: Limited Opening of the Subduction Channel 136

4.5 Eohimalayan Metamorphism: MEA Predictions and Model-data Comparisons 143

4.5.1 MEA Results *143*

4.5.2 Model – data Comparisons *145*

4.6 Supplementary Models 151

4.6.1 No Opening of the Subduction Channel: Model MEB *151*

4.6.2 Wide Opening of the Subduction Channel: Model MEC *152*

4.7 Tectonic Quiescence between Eohimalayan and Neohimalayan Orogenesis? 155

4.7.1 Evidence for Tectonic Quiescence *155*

4.7.2 Apparent Indentation of Asia by India: Model MEA *158*

4.7.3 Effect of Continued Subduction of Indian Continental Mantle Lithosphere: Model MED *158*

4.8 Discussion and Conclusions 161

4.9 Supplementary Information 164

4.10 References for Chapter 4 166

CHAPTER 5. A MACHINE-LEARNING BASED METHOD FOR DISCRIMINATING TECTONIC ENVIRONMENTS FROM GEOCHEMICAL DATA 174

5.1 Abstract 174

5.2 Introduction 174

5.3 Glossary of Terms 177

5.4 Outline of the Method 180

5.4.1 Supervised Learning for Group Identification *180*

5.4.2 Linear Support Vector Machine *185*

5.4.3 SVM Comparison with Pearce Discrimination Diagrams and Traditional Tectonic Discrimination Diagrams *189*

5.4.4 Measuring Performance *190*

5.4.5 SVM Regularization and Feature Extraction *192*

5.4.6 Group Proposal Schemes *198*

5.4.7 Summary of the Workflow *204*

5.5 Evaluating the Method: Group Identification Using Mid-Ocean Ridge and Continental Arc Data 206

5.5.1 Longitudinal Group Proposal Scheme *206*

5.5.2 General Spatial Group Proposal Scheme *210*

5.6 Applying the method to the Himalayan-Tibetan System 214

5.6.1 Himalayan-Tibetan System *214*

5.6.2 Tibetan Magmatic Record *215*

5.6.3 Methodology and Data Preparation *218*

5.6.4 Group Identification *219*

5.6.5 Feature Extraction *224*

5.6.6 Discussion of HT Groups *227*

5.7 Conclusions and Future Research 234
5.8 References for Chapter 5 236
CHAPTER 6. DISCUSSION 244
6.1 Mantle-Scale Tectonics of the Himalayan-Tibetan and Pamir-Hindu Kush Systems 244
6.2 Comparison of Model Processes with Observations from the HT-HKP Systems 245
6.3 The Asian Shortening Deficit: An Enduring Problem 247
6.4 Future directions 252
6.5 References for Discussion Section 253
CHAPTER 7. CONCLUSIONS 258
MASTER REFERENCE LIST 260

LIST OF APPENDICES

Appendix A: Chapter 2 Appendices 305
Appendix B: Chapter 3 Appendices 319
Appendix C: Chapter 4 Appendices 342
Appendix D: Chapter 5 Appendices 375
Appendix E: Permissions 386

LIST OF TABLES

Table 4.1. Model Mechanical and Thermal parameters.....142

Table 5.1. Comparison of the differences between the identified groups based on some conventional geochemical discriminants and those identified using SVM 230

LIST OF FIGURES

Figure 1.1. Terrane map of the HT-HKP system 3

Figure 1.2. North-south seismic velocity cross-sections showing Vp anomalies (modified from Replumaz et al., 2014) along the Hindu Kush section 7

Figure 1.3. Example of a Type 1 model. 18

Figure 1.4. Example of a Type 2 model 19

Figure 2.1. Map of the western region of the India-Asia collision zone 44

Figure 2.2. Seismic velocity cross-section showing Vp anomalies 48

Figure 2.3. Geometrically interpreted evolution of the Hindu Kush, balanced at the mid-upper crustal and lower lithospheric scale. 52

Figure 2.4. Geometrically interpreted evolution of the Pamir, corresponding to that of the Hindu Kush 53

Figure 2.5. Schematic cross-sections of the Pamir and the Hindu Kush 61

Figure 2.6. Initial model geometry for the H and P models 66

Figure 2.7. Evolution of MHA (Hindu Kush model). 72

Figure 2.8. Evolution of MPA (Pamir model). 78

Figure 2.9. Key results from supporting P models and H models. 83

Figure 3.1. Complexities in the evolution of the Himalayan-Tibetan orogen 109

Figure 3.2. Initial geometry and properties of model A (MA), cross-sectional geodynamical model. 111

Figure 3.3. Evolution of model A (MA) supplemented with model B 114

Figure 3.4. Comparison of models B and A with tomographic observations 119

Figure 4.1. Initial geometry and properties of model MEA, cross-sectional geodynamical model. 137

Figure 4.2. Evolution of MEA 140

Figure 4.3. Close-ups of MEA in the vicinity of the suture showing formation and exhumation of UHP rocks (50.5-46 Ma; a-e) and widening of the subduction channel accompanied by asthenosphere upwelling 144

Figure.4.4. P-T-t results from Model MEA-C2 compared with P-T-t data from Eohimalayan MP-MT metamorphic complexes 149

Figure 4.5. Evolution of MEB, showing effect of no subduction channel opening. 153

Figure 4.6. Evolution of MEC, showing effect of wide subduction channel opening. 154

Figure 4.7. Evolution of MEA compared with MED, showing effect of continuous underthrusting of Indian continental lithosphere beneath Asia 160

Figure 4.8. Summary of the early evolution of the Himalayan-Tibetan orogen showing the proposed explanation for Early Eohimalayan metamorphism and magmatism, followed by Late Eohimalayan tectonic quiescence, as precursors to Neohimalayan evolution.....165

Figure 5.1. Supervised ML model using data from known tectonic environments.....183

Figure 5.2. Supervised learning applied to data from unknown tectonic environments..184

Figure 5.3. Example of SVM with two classes of data (solid and open circles), and two features (parameters X_1 and X_2).....187

Figure 5.4. Two clearly separable groups of data in feature space.....189

Figure 5.5. Unscaled accuracy with decreasing value of regularization.....194

Figure 5.7. Histogram of data frequency for ϕ-values of the MOR and CA classes 198

Figure 5.8. Two hypothetical distributions of distinguishable classes 201

Figure 5.9. A hypothetical oblique group proposal scheme informed by hypothetical results from Figure 5.8 202

Figure 5.10. Two hypothetical examples of a curve separating data geographically, a) based simply on longitude, and b) a more complicated geometry.....202

Figure 5.11. Two hypothetical examples of a curve separating data geographically, a) based simply on longitude, which is equivalent to b) a dipping plane intersecting a horizontal green plane, and b) a more complicated geometry, which is equivalent to d) a curved surface intersecting a horizontal plane. 203

Figure 5.12. Graphical overview of the method workflow used here.....205

Figure 5.13. Performance curve for CA and MOR data 208

Figure 5.14. Performance curve with longitude where MOR and CA clusters overlap. .209

Figure 5.15. Performance curve with longitude where MOR and CA overlap completely.....210

Figure 5.16. Results of the general group proposal scheme. 213

Figure 5.17. Map of the main Himalayan and Tibetan terranes and the distribution of magmatic units.....215

Figure 5.18. Performance curves for the HT dataset 221

Figure 5.19. Performance curves for the North Group and the South Group.....223

Figure 5.20. The best performing grouping of samples from the south of the Bangong suture and younger than 45 Ma 224

Figure 5.21. Bar chart representation of the unitless decision vector values separating the pre-collisional (N1+N2) and post-collisional (N3+N4) samples (a) and N3 from N4 (b) for each element used in the analysis. 226

Figure 5.22. Bar chart representation of the unitless decision vector values separating Groups S1 from S3a+S3b (a), and S3a from S3b (b), for each element used in the analysis 227

Figure 5.23. Element and element ratios commonly used to characterize the HT magmatic rocks with time 231

Figure 5.24. K_2O concentrations plotted against N_2O concentrations. Data is colored by group. 232

Figure 5.25. Element concentrations identified as important for distinguishing the groups based on the SVM decision vectors (Subsection 5.6.5) plotted with time 233

Figure 6.1. A simplified schematic depiction of planform distributed eastward flow of Tibet 250

ABSTRACT

The India-Asia orogenic system is the largest and among the most well studied orogens on Earth. Despite its status as an archetype for large hot orogens, there remain many unknowns regarding the first-order evolution of this system. Part of this uncertainty concerns the behavior of the continental lithospheric mantle (CLM).

This thesis uses 2D mantle-scale geodynamical models to investigate how behavior of the CLM has influenced the evolution of the India-Asia collisional system. By incorporating diverse sets of geological observations, the focus of this research is to show that these diverse, often enigmatic observations of the system, can be explained self-consistently with geodynamical models.

For the Himalayan-Tibetan orogen, model results show that early CLM delamination of a weak central Qiangtang terrane, followed by delamination of the southern Lhasa CLM, can produce far-field crustal deformation and magmatism which later migrates south, contrary to expectations of continent-continent collision. Qiangtang delamination in the models drives opening of the subduction channel resulting in upwelling hot asthenosphere under the Himalayan crust, explaining early Eohimalayan metamorphism and predicting tectonic quiescence in Himalayan growth. Tectonic quiescence predicts significantly more shortened Asian crust than Indian crust, which may explain the relative narrow width of the Himalaya as compared to the Tibetan plateau.

For the Hindu Kush and Pamir, seismic evidence shows opposing slabs, with a steeply north-dipping slab inferred to be Indian CLM under the Hindu Kush, and a shallowly south-dipping slab, inferred to be Asian CLM under the Pamir. Models show that if the western-most part of the indenting India plate comprised thin, marginal lithosphere, this can lead to steep subduction of Indian lithosphere as observed for the Hindu Kush. In contrast, full thickness Indian lithosphere can indent Asia, leading to forced delamination of Asian CLM producing the observed south-dipping slab under the Pamir and the Pamir orocline.

Given the usefulness of geochemical data for understanding lithospheric processes, a secondary goal of this research was to develop novel machine learning techniques for studying geochemical data. Results of this research show that unrecognized geochemical features reflecting tectonic processes can be discovered using these methods.

LIST OF ABBREVIATIONS AND SYMBOLS USED

ALE	Arbitrary Lagrangian Eulerian
ATF	Altyn Tagh Fault
BS	Bangong Suture
C	Regularization Parameter
CLM	Continental Lithospheric Mantle
DMD	Dry Maryland Diabase
HK	Hindu Kush
HK-P	Hindu Kush and Pamir
HP	High Pressure (Metamorphism)
HREE	Heavy Rare Earth Elements
H-T	Himalaya and Tibet
HT-HKP	Himalaya-Tibet, Hindu Kush, and Pamir
IYS	Indus-Yarlung Suture
IYSZ	Indus-Yarlung Suture Zone
JS	Jinsha Suture
KF	Karakoram Fault
KS	Kunlan Suture
LC	Lower Crust
LDA	Linear Discriminant Analysis
LREE	Light Rare Earth Elements
LS	Large-Scale (Computational Grid)
LT	Lhasa Terrane
Ma	Megaannum ‘Million Years Ago
MFT	Main Frontal Thrust
ML	Machine Learning
m.y.	Millions of Years
Myr	Millions of Years
Myr-pc	Millions of Years Post-Collision
OC	Oceanic Crust

OIB	Ocean Island Basalt
OLM	Oceanic Lithospheric Mantle
p	Unscaled Accuracy
PC	Procontinent
p_s	Scaled Accuracy
P–T	Pressure–Temperature
P–T–t	Pressure–Temperature–Time
QT	Qiangtang Terrane
RC	Retrocontinent
REE	Rare Earth Element
SGT	Songpan Ganze Terrane
STP	Standard Pressure and Temperature
S-point	Subduction Point
Sp	Subduction Point
Su	Suture
SVM	Support Vector Machine
UHP	Ultra-High Pressure (Metamorphism)
(U)HP	(Ultra)-High Pressure (Metamorphism)
WOL	Wet Olivine
WQ	Wet Quartzite

List of Symbols (units where applicable)

A_r	Volumetric Radioactive Heat Production (μWm^{-3})
A	Pre-exponential Factor for Power-Law Flow ($MPa\text{-}n\ s^{-1}$)
c_p	Specific heat ($J\ g^{-1}\ K^{-1}$)
C	Cohesion (Pa)
d	mantle depletion (kg/m^3)
E	Surface Erosion Rate ($cm\ yr^{-1}$)
f	Viscosity Scaling Factor
g	Gravitational Acceleration ($m\ s^{-2}$)

$\dot{I}_2'$	Second Invariant of Deviatoric Strain Rate
K	Thermal Conductivity ($Wm^{-1}K^{-1}$)
n	Stress Exponent for Power-Law Flow
P	Pressure (Pa)
P_{max}	Maximum Recorded Pressure (GPa)
Q	Activation Energy for Power-Law Flow (kJ mol^{-1})
R	Gas Constant (J mol-1 K^{-1})
T_k	Absolute Temperature (K)
T	Temperature (C or K)
t	Time (s)
$T@P_{max}$	Temperature at Maximum Pressure (°C)
u	Velocity (m s^{-1})
V_p	(Pro-) Convergence Velocity (cm yr^{-1})
V	Activation Volume for Power-Law Flow (m^{-3} mol^{-1})
v	Velocity (m s^{-1})
W_s	Viscosity Strain-Weakening Factor
x	Spatial Coordinate (km)
Δx	Amount of Convergence (km)

List of Greek Symbols (units where applicable)

α	Thermal Expansivity (K^{-1})
α	Parameter Describing the Shape of Eastward Tibetan Parabolic Extrusion
β	Viscous Bulk Modulus (Pa s)
ε	Strain
$\dot{\varepsilon}$	Strain Rate (s^{-1})
η_{eff}^{v}	Effective viscosity (Pa s)
ρ	Density (kg m^{-3})
σ_{ij}	Deviatoric Stress Tensor (Pa)
σ_y	Yield Stress (Pa)

ϕ	Angle of Internal Friction

ACKNOWLEDGEMENTS

I would like to thank my supervisor Chris Beaumont for his guidance and supervision throughout my academic career. Additionally, I would like to thank my supervisory committee for their guidance (Rebecca A Jamieson, Jared Butler, and James Brenan). I am grateful to Ana Corbalán Castejón, for her continued encouragement throughout my PhD. I am particularly thankful for the unwavering support of my partner, Tanya Cooper.

CHAPTER 1. INTRODUCTION

Continental orogens are key aspects of plate-tectonics. In large hot orogens (Jamieson and Beaumont, 2013) it is well recognized that the behavior of the underlying continental lithospheric mantle (CLM) is important to the first-order evolution of these systems (Ghazian and Buiter, 2013; Houseman et al., 1981; Jamieson and Beaumont, 2013; Kay and Kay, 1993; Molnar et al., 1993; Willett et al., 1993), yet CLM behavior remains a major unsolved problem in our understanding of continental orogenesis (Avouac, 2007; Ghazian and Buiter, 2013; Jamieson and Beaumont, 2013; Molnar, 1988; Molnar and Bendick, 2019; Toussaint et al., 2004). This is because direct evidence of the lower lithosphere processes is typically not preserved in the rock record (Chen, M., et al., 2017; Guo et al., 2018; Heintz et al., 2009; Klemperer et al., 2013), or remains unrecognized.

The Himalayan-Tibetan (H-T) orogen, including its western extension the Hindu Kush and Pamir (HK-P; which together with the H-T part is referred to here as HT-HKP), offers an excellent opportunity to study CLM behavior owing to observations of this system which deviate from our expectations of simple models of continent-continent collision between uniform continental lithospheres, where crustal deformation is expected to initiate near the suture between the continents and propagate uniformly outwards. These observations not only challenge our understanding of the HT-HKP system, but also offer a diverse set of constraints for geodynamical models regarding its evolution. These deviations from simple uniform continent-continent collision are inferred to reflect deformation and removal of CLM during orogenesis which is controlled by inherited lithosphere heterogeneities.

This thesis explores geodynamical models of the western HK-P and the central H-T part of the system to investigate whether CLM processes such as mantle removal, delamination, and subduction can explain many poorly understood observations of this system. Additionally, a machine-learning approach for identifying previously unrecognized geochemical signatures which may reflect these CLM processes is presented.

1.1 The Himalayan-Tibetan and Pamir-Hindu Kush Systems

The HT-HKP orogenic system was produced as a consequence of the collision of the Indian subcontinent with Asia following the subduction of the ancient Neotethys ocean, and ~61-62 Ma contact between the Indian and Asian distal margins (An et al., 2021). The ensuing ~54 Ma collision between full-thickness Indian and Asian crusts (Hu et al., 2016; Najman et al., 2017) and ~4000 km of total post-contact convergence (van Hinsbergen et al., 2012; Ingalls et al., 2016; Yuan et al., 2021) produced significant crustal thickening in both Asian and Indian crusts, resulting in the largest currently active orogenic system on Earth. This system, which is ~3000 km wide along-strike, includes the Tibetan plateau and the Himalayan mountain range in the central part of the system, the Pamir and Hindu Kush in the west, and the rejuvenated Tian Shan range further north (e.g., Yin and Harrison, 2000).

Owing in part to its size and the fact that it is modern and continues to be active, this system, and the H-T orogen in particular, is among the most well-studied orogenic systems, and in many ways is regarded as an archetype for large hot orogens. However, uncertainties regarding the first-order evolution of this system, many of which concern the behavior of the lower lithosphere (Avouac, 2007; Ghazian and Buiter, 2013; Jamieson and Beaumont, 2013; Molnar, 1988; Molnar and Bendick, 2019; Toussaint et al., 2004), challenge its usefulness as an archetype. Owing to its interest among the geological community and status as an archetype, explaining these uncertainties is particularly important.

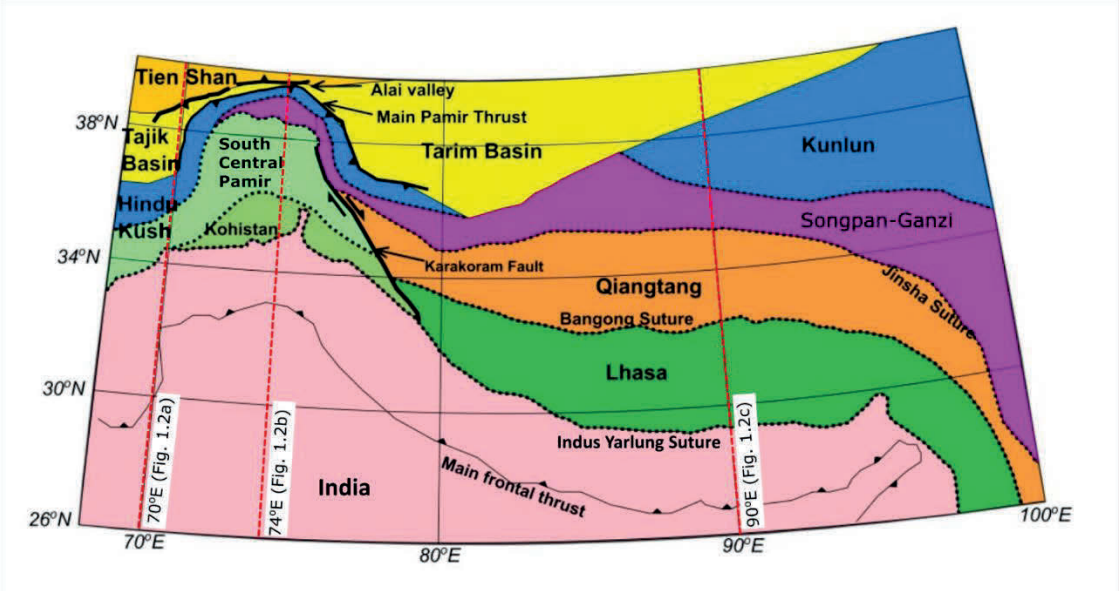

Figure 1.1. Terrane map of the HT-HKP system, showing the main accreted Asian terranes and northern India. The locations of the seismic sections shown in Figure 1.2 are shown as dashed red lines.

1.1.1 Topography and Geology of the HT-HKP Orogen

The HT-HKP orogen is the largest elevated topographic feature on Earth (Spicer et al., 2021). The central part of the system is dominated by the high-elevation, low-relief Tibetan plateau (Fielding et al., 1994). This plateau is bounded by the Himalayan mountain range to the south, by the Longman Shan range in the east, and to the north by the Kunlun range, which separates it from the Tarim basin further north. North of the Tarim basin, the Tian Shan mountain range was rejuvenated and uplifted after the India-Asia collision (Avouac et al., 1993).

In the western part of the system, the Pamir, a high-relief plateau, is separated from Tibet further east by the Karakoram range. The Pamir is bounded to the south-east by the Hindu Kush range, the westernmost part of the HT-HKP orogenic system, to the north-east by the Tajik basin, to the south by the Pakistan Himalaya, to the north by the Alai valley, and by the Tien Shan further north. The northern front of the Pamir forms an arcuate range known as the Pamir orocline.

The Tibetan plateau comprises a series of elongated terranes – from south to north the Lhasa, Qiangtang, Songpan-Ganzi, and Kunlun terranes – which were accreted to Asia during the Paleozoic and Mesozoic (Kapp and DeCelles, 2019; Yin and Harrison, 2000) prior to the India-Asian collision. In the western part of the system, the Pamir comprises from south to north the Kohistan terrane, a composite southern and central Pamir terrane, and a northern Pamir terrane. The northern terrane and the central/southern Pamir terrane correlate with the Tibetan Songpan-Ganzi and Qiangtang terranes respectively, and the Kohistan terrane is possibly a geographic extension of the Tibetan Lhasa terrane (Schwab et al., 2004).

In contrast, the Himalayan mountain range consists primarily of deformed crust of Indian provenance and is separated from Asian crust by the Indus-Yarlung suture zone (IYSZ) (Yin and Harrison, 2000). The Himalaya expose predominantly metasedimentary rocks ranging from low to high-grade (Yin and Harrison, 2000). The Himalaya sit on a basal detachment, the Main Himalayan Thrust, which is currently exposed along the Main Frontal Thrust. This active thrust fault accommodates much of the current India-Asia convergence and separates the Himalaya from the relatively undeformed Indian crust further south (Burgess et al., 2012). High- to ultrahigh-pressure rocks are exposed in the IYSZ, notably near Khagan and Tso Morari (O'Brien 2019). Further west, near the Hindu Kush, the region of India crustal deformation, the Sulaiman Range, is notably smaller compared with its Himalayan counterpart. Overall, there is a significant asymmetry in across-orogen widths of thickened Indian and Asian crusts, with the Himalaya being relatively narrow (~300 km) compared to Tibet (~1000 km; Yin and Harrison, 2000).

There are several Cenozoic magmatic and volcanic suites throughout Tibet and the Pamir. Most notable is the widespread Gangdese arc in southern Lhasa terrane, which records the protracted (~237–38 Ma) history of Neotethyan subduction (Kapp and DeCelles, 2019; Wang, C., et al., 2016; Yin and Harrison, 2000). Syn-collisional (~45 Ma) magmatic activity and coeval crustal deformation was underway in the central Qiangtang terrane (Spicer et al., 2021), then migrated outwards, first into the Lhasa terrane ~29 Ma,

followed by recent (~18 Ma to present) magmatic activity in northern Tibet (Kapp and DeCelles, 2019).

In the southern Pamir, the Cretaceous Rushan-Pshart and Karakoram arcs record southward subduction and accretion of the Pamir terranes (Chapman et al., 2018). After collision the Vanj magmatic complex (42–36 Ma) was emplaced in central Pamir, which may have a similar tectonic cause as the ~45 Ma magmatism in the Qiangtang terrane in Tibet (Chapman et al., 2018). Later ~12 to 10 Ma magmas were emplaced throughout central/southern Pamir (Ducea et al., 2003; Robinson et al., 2007).

Large crustal domes expose rocks exhumed from 1.3 GPa (~50 km depth) within the Pamir. These domes were exhumed between ~20 and 2 Ma (Hacker et al., 2017; Stübner et al., 2013; Worthington et al., 2020) and are associated with coeval ~24 to 10 Ma magmatism (Chapman et al., 2018). These domes are north-south oriented extensional structures (Stübner et al., 2013) which formed during continuous northward India-Asia convergence.

1.1.2 India-Asia Mantle-Scale Conditions and Properties of the Lithosphere

Seismic imaging has revealed aspects of the lithospheric structure under India and Tibet, as well as several anomalies imaged in the upper and lower mantle below the system. In the west, the most notable imaged features of the lithosphere are oppositely dipping slabs with a steeply north-dipping slab under the Hindu Kush and a shallowly south-dipping slab under the Pamir (Kufner et al., 2016; Replumaz et al., 2014). Kufner et al. (2016) interpreted these slabs as reflecting steeply subducting Indian lithospheres under the Hindu Kush and subducting Asian CLM under the Pamir. Figure 1.2 shows seismic p-wave velocity anomalies (V_p) under the Hindu Kush, Pamir and central H-T sections (Figs 1.2a-c) and corresponding interpretations (Figs 1.2d-f) based on Replumaz et al. (2014). The steeply dipping inferred Indian and Asian lithospheres under the Hindu Kush and Pamir are labeled anomalies 1 and 2 respectively in Figures 1.2d and 1.2e.

Under the central H-T part of the system, the imaged lithospheric structure reveals thickened lithosphere under the Lhasa terrane, and thinned lithosphere (or anomalously hot lithosphere) under the central part of Tibet under the Qiangtang terrane (Chen and Niu et al., 2017; Nunn et al., 2014; Owens and Zandt 1997; Replumaz et al., 2014; see Figs 1.2c and f), although there are some disagreements regarding the thicknesses of the lithosphere (see Chen M., et al., 2017 for details). In addition, there are several seismic anomalies imaged in the mantle below India and Tibet. The largest of these (anomaly 3) is a continuously imaged northwest/southeast anomaly that spans the entire system along-strike (Van der Voo et al., 1999).

1.1.3 Interpretations Regarding Current Seismically Imaged Subsurface Features

The seismic tomographic images of this system have led to various interpretations regarding its lithospheric-scale evolution.

In the west, Kufner et al. (2016) hypothesized that the oppositely dipping slabs under the Hindu Kush and Pamir could be explained by along-strike differences in the nature of the indenting Indian lithosphere. They suggested that thin, north/south oriented marginal Indian lithosphere in the westernmost part of India could have led to steep subduction as imaged below the Hindu Kush, while full thickness continental Indian lithosphere could have underthrust Asia to the east, leading to forced delamination and shallow subduction of Asian CLM as imaged below the Pamir.

In the central H-T part of the system, the thickened lithosphere under southern Tibet and thinned lithosphere under central Tibet have been interpreted as reflecting shallow subduction of Indian lithosphere under Asia, together with removal (or thinning) of Asian CLM under central Tibet (e.g., Nunn et al., 2014; Owens and Zandt, 1997; Replumaz et al., 2014).

The large continuous anomaly (anomaly 3 in Fig 1.2) imaged across the system is generally interpreted to be a remnant of the Neotethys subducted slab – the implication

being that the Neotethys slab detached from India near the time of contact with Asia and sank into the mantle (Replumaz et al., 2014; Van der Voo et al., 1999). Several smaller anomalies imaged under the Hindu Kush-Pamir and central H-T parts of the system (anomalies 4 and 5 in Fig 1.2) have been variably interpreted as remnant parts of Asian or Indian CLM which detached from the lithosphere and sank into the upper mantle during the evolution of this system (Replumaz et al., 2014).

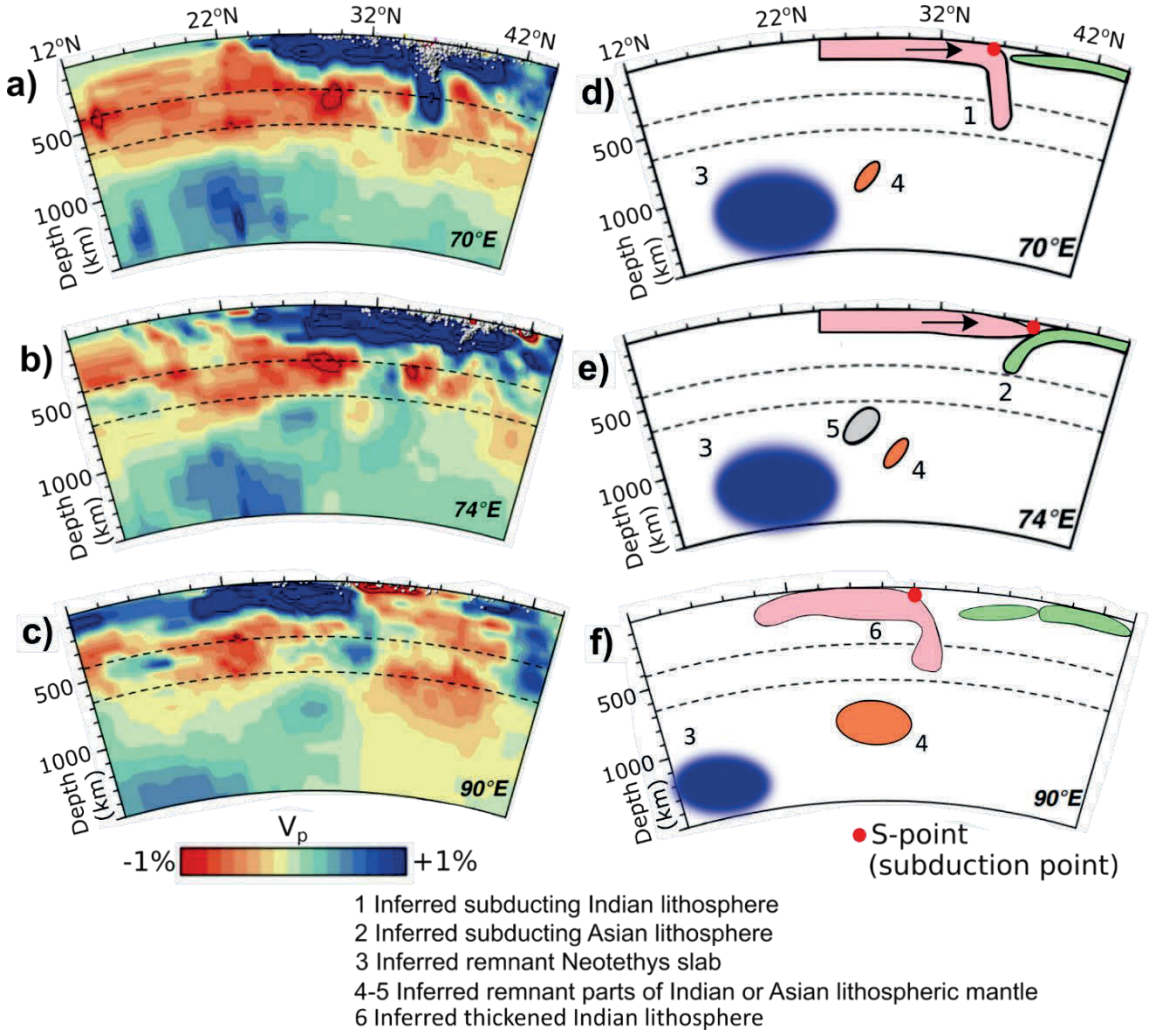

Figure 1.2. North-south seismic velocity cross-sections showing Vp anomalies (modified from Replumaz et al., 2014) along the Hindu Kush section (a), Pamir section (b) and central Himalayan-Tibetan section (c). Fast velocities (blue) are interpreted as cold regions, reflecting either lithosphere or subducted remnant parts of lithosphere, and white dots are earthquake locations. d) - f) are the corresponding interpretations from Replumaz et al. (2014). See text for details. The locations of the inferred S-points, defined as the point where lower Indian lithosphere subducts, are marked by a red dot.

1.1.4 Interpretations of the Magmatic Record Involving Lower Lithosphere Processes

Magmatic activity in Tibet and Pamir has been interpreted as reflecting removal of parts of the Asian CLM. For example, some authors (e.g., Chen 2013; Ding et al., 2007) have interpreted early post-collisional ultra-potassic magmatism in the Qiantang terrane as being caused by removal of Qiangtang CLM at ~46 Ma leading to upwelling hot asthenosphere, while others (e.g., Chung et al., 2005) have attributed this magmatism instead to thinned CLM under these regions. Similarly, later post-collisional magmatism in Lhasa terrane from ~29 Ma has been interpreted as reflecting removal of Lhasa terrane CLM (e.g., Chung et al., 2005), while others (e.g., Guo et al., 2015), have attributed this to break-off or roll-back of subducted Indian lower lithosphere. Likewise in the west, Chapman et al. (2018) have interpreted the Vanj magmatic suite as reflecting removal of Asian CLM under the Pamir ~42 Ma.

While these interpretations are conceptual, and sometimes contradictory, they illustrate the historical importance that inferred CLM processes have played in interpreting the styles of magmatism in this system.

1.2 Motivation and Goals of the Research Undertaken in the Thesis

There are several enigmatic observations about the HT-HKP system requiring explanation. Many of these observations concern the poorly understood evolution of the CLM, and the diversity of these disparate observations offers an opportunity to use geodynamical models to test whether CLM processes can offer explanations for these observations. The main goal of the research reported in this thesis (Chapters 2–4) is to use 2D numerical geodynamical models at the mantle-scale to explore whether the behavior of the lower lithosphere, in particular styles of subduction and CLM removal mechanisms, can offer novel explanations for many of the unexplained aspects of the HT-HKP system. The models presented in this thesis explore both the central (H-T), and the western (HK-P) parts of the system. Observations requiring explanation are presented separately below for both the HK-P and central H-T parts of the system.

1.2.1 Observations and Inferences from the Pamir-Hindu Kush System that Require Explanation

1) Rocks buried to ultra-high pressures (UHP) were exhumed shortly after collision (46-47 Ma) in the Kaghan region of the western part of the H-T system near the IYSZ (Hu et al., 2016; O'Brien, 2019).

2) The IYSZ has advanced northwards significantly (1700 km in the Hindu Kush and 1800 km in the Pamir) since the time of contact, based on the location of the imaged latitude of the NT slab (anomaly 3 Fig. 1.2), assuming that NT slab break-off occurred near the location of India-Asia contact and that the slab sank vertically. Similarly, seismic evidence implies that the Indian CLM has underthrust Asia and advanced north 200 km under the Hindu Kush and 350 km under the Pamir (Kufner et al., 2016). First-order geometric arguments, discussed in detail in Chapter 2, imply that a significant amount of Indian and Asian lithosphere was removed from the system since contact, however the mechanism and timing for this removal requires explanation.

3) There was a pulse of magmatic activity, referred to as the Vanj complex, within the northern Pamir between 42 and 37 Ma (Chapman et al., 2018).

4) High temperature crustal xenoliths exhumed during 37-11 Ma volcanism within the southern Pamir record high temperatures (~1100^{o}C) in the lower crust, suggesting partial melting of the Asian lower crust during this interval (Ducea et al., 2003).

5) From 21 Ma to 2 Ma gneiss domes exhumed mid- to lower-crustal rocks within the Pamir (Stübner et al., 2013; Worthington et al., 2020). Notably, these extensional structures, bounded by approximately east/west striking normal faults, (Stübner et al., 2013) formed during continuous India-Asia convergence. This

may seem unexpected in a shortening environment, but is also observed in the H-T system (north Himalayan gneiss domes, e.g., Lee et al., 2004).

6) The northern margin of the Pamir formed the Pamir orocline, which suggests that Pamir crust overthrust the Alai terrane crust (Burtman and Molnar, 1993), implying it was initially much wider, leaving only the current vestigial Alai Valley. However, further west, the Tajik basin, possibly a lateral equivalent of the Alai/Tarim terranes, remains relatively intact (Chapman et al., 2017; Schneider et al., 2019).

7) South of the Hindu Kush, the region of deformed Indian crust equivalent to the Himalaya-(the Sulaiman fold belt), is diminished in magnitude relative to both the Pakistan Himalaya further east and the Himalaya elsewhere in the system.

8) Seismic observations show oppositely dipping slabs under the Hindu Kush and Pamir with a steeply north-dipping slab under the Hindu Kush and the shallowly south-dipping slab under the Pamir. It remains to be explained how and why these contrasting styles of subduction/underthrusting developed.

1.2.2 Observations and Inferences from the Central Himalayan-Tibetan System that Require Explanation

1) The Gangdese arc, active during the subduction of the Neotethys oceanic lithosphere, experienced extensive magmatism between ~65 Ma and 45 Ma (Ma et al., 2022), with peak in magmatic intensity (52-51 Ma) about the time of collision of India with Asia (Lee et al., 2009; Zhu et al., 2015, Ma et al., 2022). Waning magmatism continued in the Gangdese Arc until 38 Ma.

2) Rocks buried to UHP conditions were exhumed shortly after collision (50–47 Ma) near Tso Morari in southwestern Tibet (Donaldson et al., 2013; Leech et al., 2005; O'Brien 2019). However, this timing is subject to confirmation.

3) Metamorphism and magmatism began in the Himalaya during the Eocene (O'Brien, 2019; Wang et al., 2019), with contemporaneous magmatism in south Lhasa terrane which continued until ~38 Ma (Kapp and DeCelles, 2019). This was followed by a magmatic lull (Aikman et al., 2008; Ding et al., 2016; Kapp and DeCelles, 2019; Ji et al., 2016; Zeng et al., 2011). Notably, the heat source for this early metamorphism remains unknown, as metamorphic observations show that high temperatures in the Himalaya were reached faster than would be expected from crustal thickening and radioactive heating alone (Ryan and Dewey, 2019).

4) Paleomagnetic data taken at face value show that the IYSZ and the Lhasa terrane, in particular, both migrated north shortly after the H-T contact (Tong et al., 2017; Yi et al. 2011; Zhu et al., 2017). If correct, this indicates that Asian lithosphere began shortening early and absorbed much of the early contact to post-collisional convergence.

5) There was crustal shortening and thickening in the central Qiantang terrane at ~50 Ma shortly after Indian-Asian collision (Kapp and DeCelles, 2019; Li et al., 2018; Spurlin et al., 2005; Staisch et al., 2014; Staisch et al., 2016; Wang et al., 2014), followed by magmatism in the northern Qiangtang terrane starting ~45 Ma (Chen et al., 2013; Ding et al., 2007; Guo et al., 2006; Ou et al., 2017), ~400 km north of the current IYSZ location (although this distance was likely larger at the time of emplacement prior to subsequent Asian shortening). This deviates from simple models of continent-continent collision where crustal thickening and magmatism are expected to initiate near the suture and migrate outwards into both continents.

6) After initiating in the central Qiangtang terrane, thickening and plateau uplift subsequently migrated outwards (after ~39 Ma) into the southern and northern Tibetan terranes (Kapp and DeCelles, 2019; Sundell et al., 2023).

7) Between 27-21 Ma magmatic activity migrated from the Qiangtang terrane into the Lhasa terrane further south (Chung et al., 2003; Kapp and DeCelles, 2019; Liu

et al., 2014). However, the reason for this sweep or jump in magmatism, notably following the Lhasa magmatic lull, remains unexplained.

8) Following the southward sweep or jump of magmatism there was continued (20-10 Ma) widespread, low-volume magmatism in the Lhasa terrane, with progressive northward termination over time (Chung et al., 2005; Kapp and DeCelles, 2019; Liu et al., 2014).

9) There is recent magmatic activity in northern Tibet, starting at 18 Ma (Chung et al., 2005; Kapp and DeCelles, 2019). Additionally, there is evidence from xenoliths, exhumed at ~3 Ma, of high (1000°C) crustal temperatures (Hacker et al. 2000, see observation 11 below). Evidence for late-stage igneous activity in the northern terranes, taken together with observed magmatism in the Qiantang terrane (observation 5), and later Lhasa terrane igneous activity (observation 7), show that magmatism, crustal deformation and metamorphism migrated through the system over time in a seemingly sporadic way.

10) Seismic images indicate thickened lithosphere under the Lhasa terrane and northern India up to the Bangong suture zone, and a region of thinned lithosphere immediately north of this thickened region under the Qiangtang terrane (Chen M., et al., 2017; Owens and Zandt, 1997). As noted above (Subsection 1.2.4; Fig 1.2c, 1.2f), this is commonly interpreted to reflect underthrust Indian lithosphere beneath the Lhasa terrane and a region under central Tibet with missing or thinned CLM.

11) Evidence from xenoliths entrained in recently emplaced (3 Ma) igneous rocks in the Qiangtang terrane indicates that the modern crust under central Tibet is hot (800–1000°C) (Hacker, 2000) at depths of 30 – 50 km. This, together with evidence from seismic tomography, suggests that the modern Qiangtang crust, now thickened to ~70 km, is exposed directly to hot asthenosphere below. However, the mechanism and timing of CLM removal remains unexplained.

1.2.3 Observations and Inferences from the Early Eohimalayan phase of the Central H-T System

1) Early ~57–45 Ma gabbroic magmas with primitive isotopic signatures were emplaced in the Tethyan Himalaya (TH) and the Gangdese arc, suggesting a mantle melt source and limited crustal contamination (Ji et al., 2016; Wang et al., 2019).

2) In the western Himalaya near Kaghan, rocks reaching UHP conditions at ~48–46 Ma were partially exhumed and overprinted by hotter amphibolite facies (~1 GPa and 700°C) metamorphism between ~45–40 Ma (O'Brien, 2019). Reheating during exhumation is not expected in typical models of UHP exhumation (e.g., Butler et al., 2013; Butler et al., 2014).

3) Metamorphism of Himalayan crustal rocks started near the time of collision (~54 Ma; e.g., Smit et al., 2014) and reached peak PT conditions (~0.6–0.8 GPa and ~650–750°C) between ~40–35 Ma in some locations exposed in the north Himalayan gneiss domes and Greater Himalayan Sequence (e.g., Ding et al., 2016; Carosi et al., 2019). The heat source for this metamorphism shortly after collision remains to be explained.

4) Granites emplaced between ~40–35 Ma have geochemical signatures indicating a crustal melt source (Aikman et al., 2008; Zeng et al., 2011; Regus et al., 2014). This, combined with melting conditions indicated by Eohimalyan migmatites in some localities (Imayama et al., 2018), indicate that the THS reached melting conditions during the mid-Eocene.

5) Deformation and thickening of the TH were underway by at least ~45 Ma, based on the ages of metamorphic fabrics (Wiesmayr and Grasemann 2002), and the ages of undeformed intrusions cross-cutting deformed TH rocks (Aikman et al., 2008). Additionally, sediments deposited in the Indian foreland basin during the

Paleocene–Eocene are inferred to be derived from the TH (DeCelles et al., 2014). Together, these observations suggest that the TH was deformed, uplifted, and eroded during this interval.

6) The relatively small cross-sectional area of the Himalayan crust and modest shortening estimates (350–650 km, e.g., Yin and Harrison; Long et al., 2012) suggest that Indian crust cannot have continuously accreted to a growing Himalaya since contact at ~61 Ma. It remains to be explained how the Himalaya evolved between the early Eohimalayan and the later Neohimalayan growth phases.

1.3 Benchmark Geodynamical Models of the Himalayan-Tibetan System

Geodynamical models have been used previously to explain various aspects of the H-T system. Some of these key studies are discussed below, highlighting their limitations and the need for further geodynamical modelling.

1.3.1 Analogue Plasticine Models

Tapponnier et al. (1982) used plasticine models to investigate the lateral extrusion of Asian lithosphere owing to post-collisional India-Asia convergence. In their models, a rigid indenter representing the Indian lithosphere was pressed into a plasticine block representing the Asian lithosphere.

These models, in which the upper and lower model surfaces (equivalent to the Earth's surface and the lithospheric base) are bounded by plates, were limited to horizontal plane strain, which only allows for lateral/horizontal deformation/motion of the analogue Asian lithosphere. Owing to this, thickening or removal of mantle materials (i.e., vertical motions of mantle materials), which is expected to play a crucial role in the evolution of the India-Asia system, could not be modelled with this approach.

1.3.2 Rayleigh Taylor (dripping) Instabilities and Delamination Models

Rayleigh-Taylor (RT or dripping) instabilities of the lower lithosphere have been investigated both analytically (e.g., Conrad and Molnar, 1997; Turcotte and Schubert, 2002) and numerically (e.g., Houseman et al., 1981; Houseman and Molnar, 1997). In these models a dense, gravitationally unstable lower lithosphere forms a sinusoidal perturbation which initially grows slowly, followed by an exponential increase in growth-rate until a critical "instability time" (Houseman and Molnar, 1997). For typical CLM, the timeframe for such instabilities is expected to be ~10 My (Houseman and Molnar, 1997), which may be slower than, and therefore dominated by, tectonically driven folding of the CLM during delamination. An initial phase of tectonically driven folding is expected to lead to more rapid removal of CLM as compared to purely gravitationally driven CLM.

In contrast to dripping instabilities, delamination models involve a channelized flow of weak rock in a layer between the upper and lower lithosphere. Bird (1979) envisioned asthenosphere upwelling into a vertical conduit through the CLM up to the base of the crust. This upwelled asthenosphere is assumed to be less dense than the CLM and exerts lateral pressure which induces a horizontal channelized flow in the lower crust resulting in asthenosphere progressively displacing the lower crust. In this model, as the lower crust is replaced by asthenosphere, the dense CLM progressively peels away from the upper/mid-crust. While Bird (1979) envisioned detachment by channelized flow in the lower crust, the layer accommodating the flow could be at other depths in the lithosphere provided the layer was suitably weak and thick, and the lithosphere below it was suitably dense. Delamination in Bird's model leads to progressive crustal deformation, uplift, and heating owing to exposure from hot upwelling upper mantle, which may result in a sweep of magmatic and deformational activity as the CLM progressively peels away from the mantle.

While both models predict crustal uplift following mantle removal (Bird, 1979; Conrad and Molnar, 1997) there are key differences between these styles of mantle removal. RT instabilities are symmetric, expected to be limited to the lower lithosphere, and are

unlikely to result in significant crustal deformation owing to their relatively long wavelengths (Conrad and Molnar, 1997; Turcotte and Schubert, 1982). In contrast, peeling delamination, as envisioned by Bird (1979), is expected to progress asymmetrically and removes the lower crust and CLM, thus exposing the residual mid- and upper crust to hot upwelling asthenosphere, which would likely result in magmatism, crustal uplift, and possibly deformation of the overlying crust (Bird, 1979).

However, both models have simplifications which limit their applicability to the India-Asia system. Neither model accounts for the effects of simultaneous tectonically-driven horizontal strains, whereas India-Asia convergence has been continuous since contact and collision. Additionally, the RT instability models described above assume laterally homogenous lithosphere, whereas Asia comprises accreted terranes whose inherited properties may have played an important role in explaining the complexities discussed in Subsections 1.2.1 and 1.2.2. Finally, the delamination model does not explain how the vertical conduit in the CLM which facilitates delamination initially forms.

1.3.3 Horizontal Plane-strain and Plane-stress Analytic and Numerical Models

Analytical and numerical models in 2D planform have been investigated for both plane-strain and plane-stress (or "thin-sheet") scenarios. In the plane-strain case, materials are limited to horizontal displacements, like the analogue models described in 1.3.1, whereas in the plane-stress cases, vertical motions are allowed but the models assume constant strain vertically. Vilotte et al. (1982) compared plane-strain and plane-stress models of the H-T system, where India acts as a rigid indenter into Asia, to investigate how Asia accommodates Indian convergence through lateral escape and/or crustal thickening. Other authors (e.g., England and Mackenzie, 1982; Houseman and England, 1986, and its companion paper England and Houseman, 1986) have also used plane-stress models in which India acts as a rigid indenter into Asia to investigate uplift of the Tibetan plateau.

Additionally, plane-stress models which include terrane heterogeneities, and incorporate the effects of mantle removal in a simple way, have been investigated by Neil and

Houseman (1997). Neil and Houseman's models consider a strong Tarim terrane and/or a weak Tien Shan terrane, to investigate strain transfer from the relatively undeformed Tarim Basin to the uplifted Tien Shan. Their models also consider mantle removal in a simple way, by instantaneously increasing the ratio of buoyancy forces to viscous forces (the "Argand number") in regions of the model where the lithospheric thickness has exceeded some threshold.

Like the analogue models discussed in Subsection 1.3.1, because plane-strain models do not consider vertical motions, they cannot capture thickening or removal of the CLM which are anticipated to play an important role in the H-T evolution. While plane-stress models can account for thickening of the lithosphere, and consider terrane heterogeneity and the effect of mantle removal in a simple way (e.g., Neil and Houseman, 1997), they cannot explicitly model processes involving CLM removal because these processes require decoupling of the CLM from the crust which violates the assumption of uniform strain with depth.

1.3.4 Multi-Terrane 2D Geodynamical Models

2D vertical cross-section numerical geodynamical models applied to the India-Asia system have investigated the effects that both terrane heterogeneity and continuous convergence have played in CLM deformation and removal, in addition to the distribution of crustal shortening with time.

Kelly et al. (2016) used 2D cross-sectional geodynamical models of continent-continent collision where the retro-lithosphere has a single accreted terrane (representing Lhasa) which is weak and dense. These terrane models, in which the pro-lithosphere (the lower plate) continuously converges on the retro-lithosphere (the upper plate), reveal modes of CLM removal that are different from the simple analytic models described above.

In one mode (their Type 1 models), convergence leads to pro-lithosphere indentation, which is accommodated by rapid, localized CLM folding in the weak accreted terrane. In

Type 1 models initial folding of the lithosphere eventually becomes gravitationally unstable and the lower crust and mantle lithosphere detaches/delaminates from the upper lithosphere and sinks. While this style of removal resembles an RT instability, the initial growth phase is driven by indentation rather than gravity alone, and the delamination results from channel flow in the low viscosity mid-crust, not an RT instability in the CLM itself. As a result, the rate of initial folding is significantly faster, and the entire lower lithosphere is folded and subsequently removed. Since the entire lower lithosphere (lower crust and CLM) are removed in Type 1 models, the middle and upper crust are exposed to upwelling hot asthenosphere, which is expected to produce magmatism either by asthenospheric decompression melting or conductive heating and melting of the crust following mantle removal, or both.

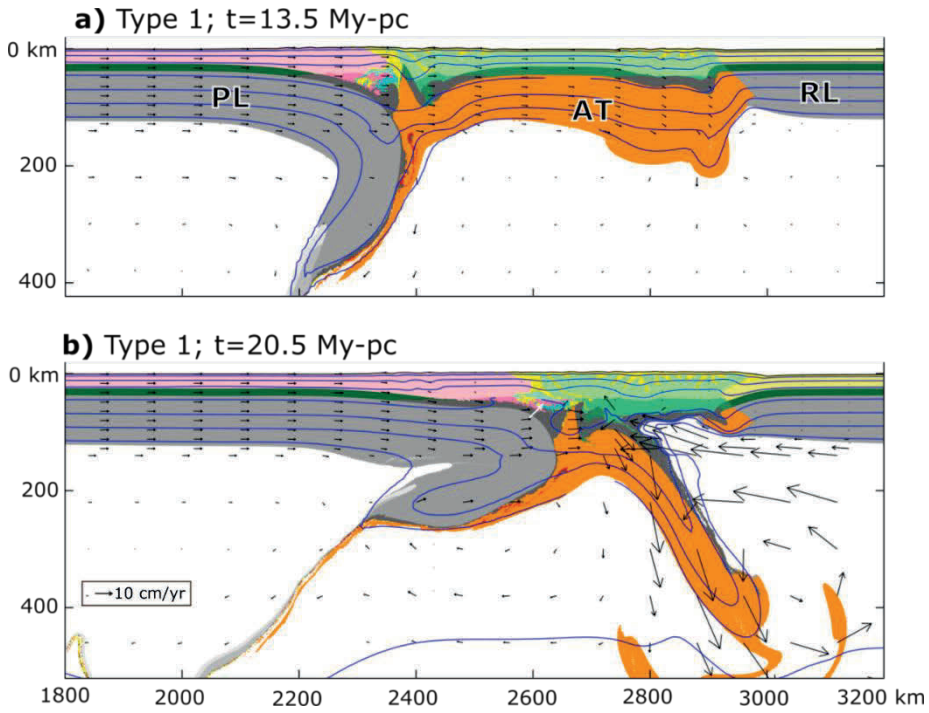

Figure 1.3. Example of a Type 1 model. The pro-lithosphere (PL) advances to the right at 5 cm/yr causing deformation of the retro-lithosphere (RL), which is focused on the weak and dense accreted terrane (AT). **a)** The accreted terrane initially deforms by folding, which **b)** eventually delaminates by peeling away from the mid-crust. CLM is colored grey or orange, lower crust is dark green or dark grey, and the mid- and upper crust is colored pink, light green and yellow. Model time (t) is in millions of years post PL-RL collision (My-pc). Modified from Kelly et al. (2016).

Another mode of mantle removal (their Type 2) involves entrainment of the subducting pro-lithosphere CLM and the retro-lithosphere CLM, a form of double subduction eventually leading to tearing of the retro-lithosphere CLM and removal of the composite entrained pro- and retro-lithosphere CLMs. Notably, in Types 1 and 2, CLM removal arises owing to the combined effects of lateral differences between the terrane properties and simultaneous convergence.

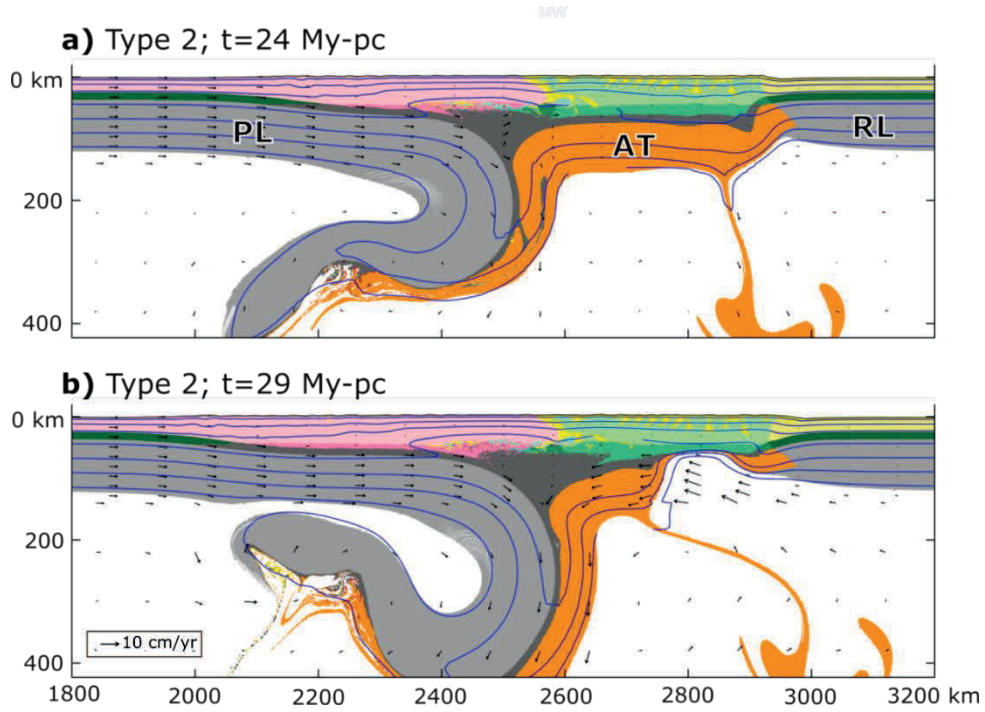

Figure 1.4. Example of a Type 2 model. **a)** The accreted terrane CLM is entrained by the subducting PL CLM, which **b)** eventually tears away from the rest of the RL CLM and subducts. Labeling as in Fig 1.3. Modified from Kelly et al. (2016).

Huangfu et al. (2018) used 2D cross-sectional geodynamical models to investigate the central H-T system by considering models with two accreted terranes - a southern strong terrane, and a northern weak terrane. The southern strong terrane in their models is considered a composite Lhasa/Qiangtang terrane. They explored differences in the relative widths of these two terranes and identified two modes of mantle removal: complete removal of both accreted terranes (their Mode I) and removal of the weak terrane (their Mode II).

Both the Kelly et al. (2016) and Huangfu et al. (2018) models fail to reproduce many of the observations of the H-T system (Subsection 1.2.2), in particular, early deformation and magmatism in the central Qiangtang terrane, which later migrates into the southern Lhasa terrane. This is likely because these authors considered only a single accreted terrane (Kelly et al., 2016) or grouped the Lhasa and Qiangtang terranes together (Huangfu et al., 2018). Since many of the observations of the H-T system (Subsection 1.2.1) concern differences in the evolution of the Lhasa and Qiangtang terranes, differences in the properties of these terranes are expected to play an important role in explaining the evolution of this system.

1.3.5 3D Geodynamical Models

3D numerical geodynamical models have also been investigated for the HT-HKP system. Capitanio and Replumaz (2013) used 3D geodynamical models to investigate whether tearing of a subducting Indian slab could explain the curvature of the IYSZ. While not necessarily the focus of their study, their model results do not offer explanations for many of the observations listed in section 1.2, for example the enigmatic migration of magmatic activity within Tibet, or explanations for the Eohimalayan metamorphic record. This is likely because their models considered Asia as a single homogenous continent, and their models did not calculate the temperature field, which is necessary to explain the Eohimalayan metamorphic record. Additionally, their models may not have had the necessary computational resolution to capture processes such as mantle delamination. Their models have 64 elements vertically over 1000 km model depth, corresponding to ~15 km vertical resolution, although the authors do not specify if the elements are distributed uniformly with depth.

Chen L., et al. (2017) used 3D numerical models to explore whether along-strike variations in the strength of the lower crust could explain the differences in the width of the Tibetan plateau, however their models do not explain many of the observations listed in Subsection 1.2. For example, these models do not explain how magmatic activity initiated in central Tibet and subsequently migrated south. This is likely because they

only considered along-strike heterogeneities, rather than across-strike differences in terrane properties. Additionally, their model domains are likely too small (1000 km × 1000 km horizontally by 200 km vertically) and the model run-times too short (~18 My) to capture many aspects of the post-contact evolution of the H-T system, because this evolution occurred over a ~59 My interval, was distributed over larger geographic distances than 1000 km (even in its current state, both along and across strike) and likely involved important mantle processes (e.g., subduction of India lithosphere) at depths greater than 200 km.

Chen et al. (2020) used 3D numerical models to investigate the role that weak zones, representing terrane sutures, could play in the evolution of the H-T system. Their model results show that deformation focuses along the weak sutures early in the evolution of the models. While their model results show that far field uplift of the central Tibetan plateau can be explained by weak suture zones, their results do not explain the Tibetan magmatic record (Subsection 1.2.2), or Eohimalayan metamorphic record (1.2.3), likely, in part, because their model domains (1000 km × 1000 km horizontally by 200 km vertically) and run times (~20 My) are insufficient to fully explain the post-contact H-T evolution.

Many of the limitations of previous 3D geodynamical models for the H-T system may be owing to insufficient model resolution (e.g., Capitanio and Replumaz, 2013), or model domain sizes and run times (e.g., Chen and Capitanio et al., 2017; Chen et al., 2020), which all likely reflect the significant increase in computational demand for 3D models compared to 2D models.

1.4 Research Objectives and Outline of Thesis Content

The main research objectives of this thesis are to develop and use 2D numerical geodynamical models for the Hindu Kush, Pamir, and central Himalayan-Tibetan systems, to explain the observations listed in Subsections 1.2.1 and 1.2.2.

Given the usefulness of magmatic geochemistry for constraining tectonic processes, a secondary objective of this research is to explore machine learning methods for interpreting geochemical data.

1.4.1 Geodynamical Modelling Approach

The numerical models explored in this thesis are upper-mantle-scale 2D cross-sectional geodynamical models computed using the nested version of the Sopale finite element software (Beaumont et al., 2009; Fullsack 1995). The design of the models takes a parsimonious approach, emphasizing the simplest model designs capable of capturing the diverse range of complexities discussed in Subsections 1.2.1, 1.2.2. and 1.2.3. The key model design elements explored in this thesis are the geometry and inherited CLM properties of the Asian terranes, and the nature of the Indian lithosphere and Indian rifted margin.

Since terrane heterogeneity is expected to play a key role in explaining the enigmatic and differing ways that the Asian terranes evolved, the model designs include each major terrane separately. For the Hindu Kush, model designs also explore the hypothesis raised by Kufner et al. (2016) regarding thinned marginal Indian lithosphere along this section.

The geometries of Asian terranes and Indian lithosphere prior to the India-Asia collision were hypothesized using simple geometric arguments and balanced cross-sectional restoration techniques, based on the timing and location of contact, and the present geometry and locations of terrane boundaries constrained by geological and geophysical data. This approach is discussed in detail in Chapter 2 for the HK-P systems, and a similar approach was used for each of the subsequent modelling chapters. Each modelling chapter has a methods section outlining the specific modelling details.

1.4.2 Choice and Justification of Model Parameters

Here I introduce the most important model parameters, with a more detailed discussion of others in the individual chapters. The behavior of the CLM is primarily controlled by the

dimensionless Archimedes number (Kelly et al., 2016; note that both the separately defined Argand number and Archimedes number are often labeled Ar). The Archimedes number is defined as the ratio of gravitational forces to viscous forces, namely,

1.1 $$Ar^{1/2} = \frac{\rho_{eff} g L^3}{\eta V L}$$

For the CLM, the effective density ρ_{eff} in the gravitational force is the difference between the density of the underlying or surrounding asthenosphere and the CLM (i.e., $\rho_{eff} = \rho_m - \rho_l$), and η, L, and V are characteristic viscosity, length, and velocity scales respectively. In the numerical models the effect of thermal expansion is taken into account in ρ_{eff}.

The viscosity of mantle peridotite used in the numerical models is based on a power-law flow described by,

1.2 $$\eta_{eff}^{v} = \frac{f}{W_s} A^{-1/2} \dot{I}_2^{\prime(1-n)/2n} \exp\left(\frac{Q + PV^*}{nRT_k}\right)$$

where η_{eff}^{v} is, the effective viscosity, W_s is the strain-dependent weakening factor, A is a pre-exponential factor, $\dot{I}_2'$ is the second invariant of the deviatoric strain rate, Q is the activation energy, P is the pressure, V^* is the activation volume, n is the stress exponent, R is the universal gas constant, and T_k is temperature in Kelvin. The factor f is a linear scaling factor. Butler, et al. (2014) showed that, within experimental uncertainties, stronger/weaker materials can be represented in a predictable way by exploring values of this linear scaling parameter. For model mantle materials, values of these constants (excepting f which is varied) are taken from experimentally derived flow laws based on olivine (Karato and Wu, 1993).

The strength of peridotite is strongly controlled by its water content, with ‘dry’ peridotite being strong, and ‘damp’ or ‘hydrous/wet’ peridotite being relatively weak (Karato and

Wu, 1993). CLM peridotite, which is typically thought to be dry and refractory, can become hydrated through reaction with hydrous or metasomatic fluids or melts (Griffin et al., 2009). Therefore, ranges of f-values for the CLM materials are explored in the models to investigate the effects of CLM water content.

Besides the viscosity of the CLM, the other first-order control on CLM behavior is its density. Peridotite density is strongly controlled by chemical depletion, typically expressed by the Mg number, Mg# = 100×Mg/[Mg+Fe], with highly depleted (high Mg#) peridotite being relatively less dense than fertile (low Mg#) peridotite (Lee, 2003). Most CLM is thought to be depleted, owing to partitioning of Fe into melts during partial melting of mantle during formation of lithosphere. CLM materials can become fertilized (less depleted) through melt metasomatism (Griffin et al., 2009; Lee, 2003). Ranges of CLM depletion below standard peridotite ($\rho_m = 3370\ kg/m^3$) are measured by the parameter d, where the density of depleted CLM is $\rho_l = 3370\ kg/m^3 - d$. Values of terrane CLM depletions explored in the models range from $d = 50$ representing highly depleted (buoyant) peridotite to $d = 0$, representing undepleted (neutrally buoyant) peridotite.

Model materials are subject to thermal expansion. The densities of model materials are calculated as:

$$\rho(T) = \rho_r[1 - \alpha(T - T_r)] \tag{1.3}$$

where ρ_r is the material reference density at standard ("reference") pressure and temperature, T is the model-calculated temperature, T_r is the reference temperature, and α is the thermal expansion coefficient. For some materials α is temperature dependent and varies linearly from α_1 to α_2 as the temperature varies between T_1 and T_2

CLM materials with $d = 0$, while neutrally buoyant relative to the asthenosphere at standard temperatures, can become negatively buoyant because for typical geotherms they are cold relative to the underlying upper mantle. In general, CLM materials with $d \lesssim$

30 are negatively buoyant for typical geotherms and may sink into the upper mantle, however, upon heating at depth may subsequently buoy back up towards the surface.

While the viscosity and density of the CLM are the first-order controls on CLM behavior, the effect that CLM deformation and/or removal has on the overlying crust is expected to be controlled by crustal strength. Therefore, crustal strength is also explored as a secondary factor, by varying the f-values of the terrane crusts. Details regarding the material properties are described in each modelling chapter.

1.4.3 Organization of the Thesis

The main body of this thesis is organized into four chapters (Chapters 2-5), followed by a discussion and conclusions section in Chapter 6.

Chapter 2 explores the Hindu Kush and Pamir in the westernmost part of the HT-HKP orogen. This chapter first describes lithospheric-scale constraints on the evolution of the Hindu Kush and Pamir using evidence from the locations of seismically imaged anomalies in the mantle, the timing of contact and collision, the rate of convergence with time, and observations regarding crustal deformation and magmatism. These constraints are summarized by lithospheric scale restored balanced cross-sections, which are subsequently used to inform the design of 2D numerical geodynamical models along representative cross-sections along both the Hindu Kush and Pamir regions. The results of these models are shown to explain many features of the Hindu Kush and Pamir regions described above in Subsection 1.2.1.

Following a similar approach to the Hindu Kush and Pamir models, Chapter 3 explores 2D geodynamical models of the central H-T part of the system. These model results, bracketed by two models (Models MA and MB), show that the observations of the H-T system described in Subsection 1.2.2 can be explained as emergent phases in the evolution of these models.

Chapter 4 expands on the results of models MA and MB (Chapter 3), to explore the early Eocene (Eohimalayan) metamorphism of the Himalaya. In a model similar in evolution to MA (MEA) pressure-temperature-time (P-T-t) paths for tracked model particles are calculated and compared with metamorphic P-T-t data from the central H-T system. The results show that the early Eocene metamorphic record of the Himalaya can be explained by subduction zone widening driven by removal of the Qiangtang CLM shortly after India-Asia collision. In these models, the subduction zone gap remains open, and convergence between India and Asia is almost entirely accommodated by Asia for the interval ~45 Ma –30 Ma, after which the subduction zone closes and Himalayan growth commences, marking the onset of the "Neohimalayan" phase. Based on these model results, it is hypothesized that the Himalaya was tectonically quiescent during the interval ~45 Ma – 30 Ma, between early Eohimalayan metamorphism and later Himalayan growth during the Neohimalayan phase.

Chapter 5 presents a machine learning-based method for investigating geochemical datasets. One of the themes of this research is the need for diverse observations to constrain CLM behavior, owing to the lack of direct evidence, or a single unambiguously fingerprinting indirect observation, for these processes. Given the usefulness of geochemical data for interpreting mantle processes, expanding on traditional approaches to geochemical interpretation may be beneficial for understanding the behavior of the lower lithosphere. The method outlined in this chapter seeks spatio-temporal clusters of samples which are geochemically distinguishable. The goal of the method is to find unrecognized geochemical signatures which may reflect tectonic processes associated with the spatial regions and time intervals coinciding with these discovered clusters.

In Chapter 6, a discussion of the main research outcomes is presented, including suggestions for future research, and concluding remarks. Also included is a discussion of the estimates of the amount of Asian tectonic shortening during H-T orogenesis.

1.5 References for Chapter 1

Aikman, A.B., Harrison, T.M., and Lin, D. (2008). Evidence for early (> 44 Ma) Himalayan crustal thickening, Tethyan Himalaya, southeastern Tibet. *Earth and Planetary Science Letters, 274,* 14–23. https://doi.org/10.1016/j.epsl.2008.06.038

An, W., Hu, X., Garzanti, E., Wang, J.G., and Liu, Q. (2021). New precise dating of the India-Asia collision in the Tibetan Himalaya at 61 Ma. *Geophysical Research Letters*, *48*, p.e2020GL090641. https://doi.org/10.1029/2020GL090641

Avouac, J. P. (2007). Dynamic processes in extensional and compressional settings - mountain building: From earthquakes to geological deformation. Gerald Schubert (Ed.), *Treatise on geophysics*, *6*, 377–439. Elsevier. https://doi.org/10.1016/B978-044452748-6.00112-7

Avouac, J.-P., Tapponnier, P., Bai, M., You, H., and Wang, G. (1993). Active thrusting and folding along the northern Tien Shan and late Cenozoic rotation of the Tarim relative to Dzungaria and Kazakhstan. *Journal of Geophysical Research: Solid Earth, 98,* 6755–6804. https://doi.org/10.1029/92JB01963

Beaumont, C., Jamieson, R.A., Butler, J.P., and Warren, C.J. (2009). Crustal structure: A key constraint on the mechanism of ultra-high-pressure rock exhumation. *Earth and Planetary Science Letters, 287,* 116–129. https://doi.org/10.1016/j.epsl.2009.08.001

Bird, P. (1979). Continental delamination and the Colorado Plateau. *Journal of Geophysical Research: Solid Earth*, *84*, 7561–7571. https://doi.org/10.1029/JB084iB13p07561

Burgess, W.P., Yin, A., Dubey, C.S., Shen, Z.K., and Kelty, T.K. (2012). Holocene shortening across the Main Frontal Thrust zone in the eastern Himalaya. *Earth and Planetary Science Letters*, *357*, 152–167. https://doi-org.ezproxy.library.dal.ca/10.1016/j.epsl.2012.09.040

Burtman, V.S. and Molnar, P. (1993). Geological and geophysical evidence for deep subduction of continental crust beneath the Pamir. *Geological Society of America Bulletin, 281,* 1–76. https://doi.org/10.1130/SPE281-p1

Butler, J. P., Beaumont, C., and Jamieson, R. A. (2013). The Alps 1: A working geodynamic model for burial and exhumation of (ultra)high pressure rocks in Alpine-type orogens. *Earth and Planetary Science Letters, 377-378*, 114-131. https://doi.org/10.1016/j.epsl.2013.06.039

Butler, J.P., Beaumont, C., and Jamieson, R.A. (2014). The Alps 2: Controls on crustal subduction and (ultra) high-pressure rock exhumation in Alpine-type orogens. *Journal of Geophysical Research: Solid Earth, 119,* 5987–6022. https://doi.org/10.1002/2013JB010799

Capitanio, F.A. and Replumaz, A. (2013). Subduction and slab breakoff controls on Asian indentation tectonics and Himalayan western syntaxis formation. *Geochemistry, Geophysics, Geosystems*, *14*, 3515–3531. https://doi.org/10.1002/ggge.20171

Carosi, R., Montomoli, C., Iaccarino, S., and Visona, D. (2019). Structural evolution, meta-morphism and melting in the greater Himalayan sequence in central-western Nepal. In: Treloar, P.J., Searle, M.P. (Eds.), Himalayan Tectonics: A Modern Synthesis. *Geological Society, London, Special Publications, 483*, 305–323. https://doi.org/10.1144/SP483.3

Chapman, J.B., Carrapa, B., Ballato, P., DeCelles, P.G., Worthington, J., Oimahmadov, I., et al. (2017). Intracontinental subduction beneath the Pamir Mountains: Constraints from thermokinematic modeling of shortening in the Tajik fold-and-thrust belt. *Geological Society of America Bulletin, 129,* 1450–1471. https://doi.org/10.1130/B31730.1

Chapman, J.B., Scoggin, S.H., Kapp, P., Carrapa, B., Ducea, M.N., Worthington, J. et al. (2018). Mesozoic to Cenozoic magmatic history of the Pamir. *Earth and Planetary Science Letters*, *482*, 181-192. https://doi.org/10.1016/j.epsl.2017.10.041

Chen, J., Wu, J., Xu, J., Dong, Y., Wang, B., and Kang, Z. (2013). Geochemistry of Eocene high-Mg# adakitic rocks in the northern Qiangtang terrane, central Tibet: Implications for early uplift of the plateau. *Geological Society of America Bulletin*, *125*, 1800–1819. https://doi.org/10.1130/B30755.1

Chen, L., Capitanio, F.A., Liu, L., and Gerya, T.V. (2017). Crustal rheology controls on the Tibetan plateau formation during India-Asia convergence. *Nature Communications*, *8*, 5992. https://doi.org/10.1038/ncomms15992

Chen, L., Liu, L., Capitanio, F.A., Gerya, T.V., and Li, Y. (2020). The role of pre-existing weak zones in the formation of the Himalaya and Tibetan plateau: 3-D thermomechanical modelling. *Geophysical Journal International*, *221*, 1971–1983. https://doi.org/10.1093/gji/ggaa125

Chen, M., Niu, F., Tromp, J., Lenardic, A., Lee, C.T.A., Cao, W., and Ribeiro, J. (2017). Lithospheric foundering and underthrusting imaged beneath Tibet. *Nature Communications, 8,* 15659. https://doi.org/10.1038/ncomms15659

Chung, S.L., Chu, M.F., Zhang, Y., Xie, Y., Lo, C.H., Lee, T.Y., et al. (2005). Tibetan tectonic evolution inferred from spatial and temporal variations in post-collisional magmatism. *Earth-Science Reviews*, *68*, 173–196. https://doi.org/10.1016/j.earscirev.2004.05.001

Chung, S.-L., Liu, D., Ji, J., Chu, M.-F., Lee, H.-Y., Wen, D.-J., et al. (2003). Adakites from continental collision zones: Melting of thickened lower crust beneath southern Tibet. *Geology*, *31*, 1021–1024. https://doi.org/10.1130/G19796.1

Conrad, C.P. and Molnar, P. (1997). The growth of Rayleigh—Taylor-type instabilities in the lithosphere for various rheological and density structures. *Geophysical Journal International*, *129*, 95-112. https://doi.org/10.1111/j.1365-246X.1997.tb00939.x

DeCelles, P.G., Kapp, P., Gehrels, G.E., and Ding, L. (2014). Paleocene-Eocene foreland basin evolution in the Himalaya of southern Tibet and Nepal: Implications for the age of initial India-Asia collision. *Tectonics*, *33*, 824–849. https://doi.org/10.1002/2014TC003522

Ding, L., Kapp, P., Yue, Y., and Lai, Q. (2007). Postcollisional calc-alkaline lavas and xenoliths from the southern Qiangtang terrane, central Tibet. *Earth and Planetary Science Letters, 254*, 28–38. https://doi.org/10.1016/j.epsl.2006.11.019

Ding, L., Qasim, M., Jadoon, I.A., Khan, M.A., Xu, Q., and Cai, F. (2016). The India–Asia collision in north Pakistan: Insight from the U–Pb detrital zircon provenance of Cenozoic foreland basin. *Earth and Planetary Science Letters, 455,* 49–61 https://doi.org/10.1016/j.epsl.2016.09.003

Donaldson, D.G., Webb, A.A.G., Menold, C.A., Kylander-Clark, A.R., and Hacker, B.R. (2013). Petrochronology of Himalayan ultrahigh-pressure eclogite. *Geology*, *41*, 835–838. https://doi.org/10.1130/G33699.1

Ducea, M.N., Lutkov, V., Minaev, V.T., Hacker, B., Ratschbacher, L., and Luffi, P. (2003). Building the Pamirs: The view from the underside. *Geology, 31*, 849–852. https://doi.org/10.1130/G19707.1

England, P. and Houseman, G. (1986). Finite strain calculations of continental deformation: 2. Comparison with the India-Asia collision zone. *Journal of Geophysical Research: Solid Earth*, *91*, 3664–3676. https://doi.org/10.1029/JB091iB03p03664

England, P. and McKenzie, D. (1982). A thin viscous sheet model for continental deformation. *Geophysical Journal International*, *70*, 295–321. https://doi.org/10.1111/j.1365-246X.1982.tb04969.x

Fielding, E., Isacks, B., Barazangi, M., and Duncan, C. (1994). How flat is Tibet? *Geology*, *22*, 63-167. https://doi.org/10.1130/0091-7613(1994)022%3C0163:HFIT%3E2.3.CO;2

Fullsack, P. (1995). An arbitrary Lagrangian-Eulerian formulation for creeping flows and its application in tectonic models. *Geophysical Journal International, 120*, 1–23. https://doi.org/10.1111/j.1365-246X.1995.tb05908.x

Ghazian, R.K. and Buiter, S.J. (2013). A numerical investigation of continental collision styles. *Geophysical Journal International*, *193*, 1133–1152. https://doi.org/10.1093/gji/ggt068

Griffin, W.L., O'reilly, S.Y., Afonso, J.C., and Begg, G.C. (2009). The composition and evolution of lithospheric mantle: A re-evaluation and its tectonic implications. *Journal of Petrology, 50,* 1185–1204. https://doi.org/10.1093/petrology/egn033

Guo, X., Gao, R., Zhao, J., Xu, X., Lu, Z., Klemperer, S.L., and Liu, H. (2018). Deep-seated lithospheric geometry in revealing collapse of the Tibetan Plateau. *Earth-Science Reviews*, *185*, 751–762. https://doi.org/10.1016/j.earscirev.2018.07.013

Guo, Z., Wilson, M., Liu, J., and Mao, Q. (2006). Post-collisional, potassic and ultrapotassic magmatism of the northern Tibetan Plateau: Constraints on characteristics of the mantle source, geodynamic setting and uplift mechanisms. *Journal of Petrology*, *47*, 1177–1220. https://doi.org/10.1093/ petrology/egl007

Guo, Z., Wilson, M., Zhang, M., Cheng, Z., and Zhang, L. (2015). Post-collisional ultrapotassic mafic magmatism in South Tibet: Products of partial melting of pyroxenite in the mantle wedge induced by roll-back and delamination of the subducted Indian continental lithosphere slab. *Journal of Petrology*, *56*, 1365–1406. https://doi.org/10.1093/petrology/egv040

Hacker, B.R., Gnos, E., Ratschbacher, L., Grove, M., McWilliams, M., Sobolev, S.V., et al. (2000). Hot and dry deep crustal xenoliths from Tibet: *Science*, *287*, 2463–2466. https://doi.org/10.1126/science.287.5462.2463

Hacker, B.R., Ratschbacher, L., Rutte, D., Stearns, M.A., Malz, N., Stübner, K., et al. (2017). Building the Pamir–Tibet Plateau—Crustal stacking, extensional collapse, and lateral extrusion in the Pamir: 3. Thermobarometry and Petrochronology of Deep Asian Crust. *Tectonics, 36,* 1743–1766. https://doi.org/10.1002/2017TC004488

Heintz, M., Kumar, V.P., Gaur, V.K., Priestley, K., Rai, S.S., and Prakasam, K.S. (2009). Anisotropy of the Indian continental lithospheric mantle. *Geophysical Journal International, 179,* 1341–1360. https://doi.org/10.1111/j.1365-246X.2009.04395.x

Houseman, G.A., McKenzie, D.P., and Molnar, P. (1981). Convective instability of a thickened boundary layer and its relevance for the thermal evolution of continental convergent belts. *Journal of Geophysical Research: Solid Earth*, *86,* 6115–6132. https://doi.org/10.1029/JB086iB07p06115

Houseman, G. and England, P. (1986). Finite strain calculations of continental deformation: 1. Method and general results for convergent zones. *Journal of Geophysical Research: Solid Earth*, *91*, 3651–3663. https://doi.org/10.1029/JB091iB03p03664

Houseman, G.A. and Molnar, P. (1997). Gravitational (Rayleigh–Taylor) instability of a layer with non-linear viscosity and convective thinning of continental lithosphere. *Geophysical Journal International*, *128*, 125–150. https://doi.org/10.1111/j.1365-246X.1997.tb04075.x

Hu, X., Garzanti, E., Wang, J., Huang, W., An, W., and Webb, A. (2016). The timing of India-Asia collision onset–Facts, theories, controversies. *Earth-Science Reviews, 160,* 264–299. https://doi.org/10.1016/j.earscirev.2016.07.014

Huangfu, P., Li, Z.H., Gerya, T., Fan, W., Zhang, K.J., Zhang, H., and Shi, Y. (2018). Multi-terrane structure controls the contrasting lithospheric evolution beneath the western and central–eastern Tibetan plateau. *Nature Communications, 9,* 3780. https://doi.org/10.1038/s41467-018-06233-x

Imayama, T., Takeshita, T., Yi, K., and Fukuyama, M. (2018). Early Oligocene partial melting via biotite dehydration melting and prolonged low-pressure–low-temperature metamorphism of the upper High Himalaya Crystalline Sequence in the far east of Nepal. In: Sharma, R., Villa, I.M., Kumar, S. (Eds.), Crustal Architecture and Evolution of the Himalaya–Karakoram–Tibet Orogen. *Geological Society, London, Special Publications*, *481*, 147-173. https://doi.org/10.1144/SP481.2

Ingalls, M., Rowley, D.B., Currie, B., and Colman, A.S. (2016). Large-scale subduction of continental crust implied by India-Asia mass-balance calculation. *Nature Geoscience, 9,* 848–853. https://doi.org/10.1038/ngeo2806

Jamieson, R. A. and Beaumont, C. (2013). On the origin of orogens. *Geological Society of America Bulletin, 125,* 1671–1702. https://doi.org/10.1130/B30855.1

Ji, W.Q., Wu, F.Y., Chung, S.L., Wang, X.C., Liu, C.Z., Li, Q.L., et al (2016). Eocene Neo-Tethyan slab breakoff constrained by 45 Ma oceanic island basalt–type magmatism in southern Tibet. *Geology*, *44,* 283–286. https://doi.org/10.1130/G37612.1

Kapp, P. and DeCelles, P.G. (2019). Mesozoic–Cenozoic geological evolution of the Himalayan-Tibetan orogen and working tectonic hypotheses. *American Journal of Science*, *319*, 159–254. https://doi.org/10.2475/03.2019.01

Karato, S. and Wu, P. (1993). Rheology of the upper mantle: A synthesis. *Science, 260,* 771–778. https://doi.org/10.1126/science.260.5109.771

Kay, R.W. and Kay, S.M. (1993). Delamination and delamination magmatism. *Tectonophysics, 219,* 177–189. https://doi.org/10.1016/0040-1951(93)90295-U

Kelly, S., Butler, J.P., and Beaumont, C. (2016). Continental collision with a sandwiched accreted terrane: Insights into Himalayan–Tibetan lithospheric mantle tectonics? *Earth and Planetary Science Letters, 455,* 176–195. https://doi.org/10.1016/j.epsl.2016.08.039

Klemperer, S.L., Kennedy, B.M., Sastry, S.R., Makovsky, Y., Harinarayana, T., and Leech, M.L. (2013). Mantle fluids in the Karakoram fault: Helium isotope evidence. *Earth and Planetary Science Letters*, *366*, 59–70. https://doi.org/10.1016/j.epsl.2013.01.013

Kufner, S.-K., Schurr, B., Sippl, C., Yuan, X., Ratschbacher, L., Ischuk, A., et al. (2016). Deep India meets deep Asia: Lithospheric indentation, delamination and break-off under Pamir and Hindu Kush (Central Asia). *Earth and Planetary Science Letters, 435,* 171–184. https://doi.org/10.1016/j.epsl.2015.11.046

Lee, C.-T. A. (2003). Compositional variation of density and seismic velocities in natural peridotites at STP conditions: Implications for seismic imaging of compositional heterogeneities in the upper mantle. *Journal of Geophysical Research: Solid Earth, 108,* https://doi.org/10.1029/2003JB002413

Lee, H.-Y., Chung, S.-L., Lo, C.-H., Ji, J., Lee, T.-Y., Qian, Q., and Zhang, Q. (2009). Eocene Neotethyan slab breakoff in southern Tibet inferred from the Linzizong volcanic record. *Tectonophysics*, *477*, 20–35. https://doi.org/10.1016/j.tecto.2009.02.031

Lee, J., Hacker, B., and Wang, Y. (2004). Evolution of North Himalayan gneiss domes: Structural and metamorphic studies in Mabja Dome, southern Tibet. *Journal of Structural Geology*, *26*, 2297–2316. https://doi.org/10.1016/j.jsg.2004.02.013

Leech, M.L., Singh, T.S., Jain, A.K., Klemperer, S.L., and Manickavasagam, R.M. (2005). The onset of India–Asia continental collision: Early, steep subduction required by the timing of UHP metamorphism in the western Himalaya. *Earth and Planetary Science Letters*, *234*, 83–97. https://doi.org/10.1016/j.epsl.2005.02.038

Li, L., Garzione, C.N., Pullen, A., Zhang, P., and Li, Y. (2018). Late Cretaceous–Cenozoic basin evolution and topographic growth of the Hoh Xil Basin, central Tibetan Plateau. *Geological Society of America Bulletin*, *130*, 499–521. https://doi.org/10.1130/B31769.1

Liu, D., et al. (2014). Postcollisional potassic and ultrapotassic rocks in southern Tibet: Mantle and crustal origins in response to India–Asia collision and convergence. *Geochimica et Cosmochimica Acta*, *143*, 207–231. https://doi.org/10.1016/j.gca.2014.03.031

Long, S.P., McQuarrie, N., Tobgay, T., Coutand, I., Cooper, F.J., Reiners, P.W., et al. (2012). Variable shortening rates in the eastern Himalayan thrust belt, Bhutan: Insights from multiple thermochronologic and geochronologic data sets tied to kinematic reconstructions. *Tectonics*, *31,* TC5004. https://doi.org/10.1029/2012TC003155

Ma, X., Attia, S., Cawood, T., Cao, W., Xu, Z., and Li, H. (2022). Arc tempos of the Gangdese batholith, southern Tibet. *Journal of Geodynamics*, *149*, 101897. https://doi.org/10.1016/j.jog.2022.101897

Molnar, P. (1988). Continental tectonics in the aftermath of plate tectonics. *Nature, 335,* 131–137. https://doi.org/10.1038/335131a0

Molnar, P. and Bendick, R. (2019). Seismic moments of Intermediate-depth earthquakes beneath the Hindu Kush: Active stretching of a Blob of sinking thickened mantle lithosphere? *Tectonics*, *38*, 1651–1665. https://doi.org/10.1029/2018TC005336

Molnar, P., England, P., and Martinod, J. (1993). Mantle dynamics, uplift of the Tibetan Plateau, and the Indian monsoon. *Reviews of Geophysics, 31,* 357–396. https://doi.org/10.1029/93RG02030

Najman, Y., Jenks, D., Godin, L., Boudagher-Fadel, M., Millar, I., Garzanti, E., et al. (2017). The Tethyan Himalayan detrital record shows that India–Asia terminal collision occurred by 54 Ma in the Western Himalaya. *Earth and Planetary Science Letters, 459,* 301–310. https://doi.org/10.1016/j.epsl.2016.11.036

Neil, E.A. and Houseman, G.A. (1997). Geodynamics of the Tarim Basin and the Tian Shan in central Asia. *Tectonics*, *16*, 571–584. https://doi.org/10.1029/97TC01413

Nunn, C., Roecker, S.W., Tilmann, F.J., Priestley, K.F., Heyburn, R., Sandvol, E.A., et al. (2014). Imaging the lithosphere beneath NE Tibet: Teleseismic P and S body wave tomography incorporating surface wave starting models. *Geophysical Journal International, 196,* 1724–1741. https://doi.org/10.1093/gji/ggt476

O'Brien, P.J. (2019). Eclogites and other high-pressure rocks in the Himalaya: A review. P. J. Teloar, and M. P. Searle (Eds.), Himalayan Tectonics: A Modern Synthesis, *Geological Society, London, Special Publications*, *483*, 183–213. https://doi.org/10.1144/SP483.13

Ou, Q., Wang, Q., Wyman, D.A., Zhang, H.-X., Yang, J.-H., Zeng, J.-P., et al. (2017). Eocene adakitic porphyries in the central-northern Qiangtang Block, central Tibet: Partial melting of thickened lower crust and implications for initial surface uplifting of the plateau. *Journal of Geophysical Research: Solid Earth*, *122*, 1025–1053. https://doi.org/10.1002/2016JB013259

Owens, T.J. and Zandt, G. (1997). Implications of crustal property variations for models of Tibetan plateau evolution. *Nature, 387,* 37-43. https://doi.org/10.1038/387037a0

Replumaz, A., Capitanio, F.A., Guillot, S., Negredo, A.M., and Villaseñor, A. (2014). The coupling of Indian subduction and Asian continental tectonics. *Gondwana Research, 26,* 608–626. https://doi.org/10.1016/j.gr.2014.04.003

Robinson, A.C., Yin, A., Manning, C.E., Harrison, T.M., Zhang, S.H., and Wang, X.F. (2007). Cenozoic evolution of the eastern Pamir: implications for strain-accommodation mechanisms at the western end of the Himalayan–Tibetan orogen. *Geological Society of America Bulletin*, *119*, 882–896. https://doi.org/10.1130/B25981.1

Ryan, P.D. and Dewey, J.F. (2019). The sources of metamorphic heat during collisional orogeny: The Barrovian enigma. *Canadian Journal of Earth Sciences*, *56*, 1309–1317. https://doi.org/10.1139/cjes-2018-0182

Schneider, F. M., Yuan, X., Schurr, B., Mechie, J., Sippl, C., and Kufner, S.-K, et al. (2019). The crust in the Pamir: Insights from receiver functions. *Journal of Geophysical Research: Solid Earth*, *124*, 9313-9331. https://doi.org/10.1029/2019JB017765

Schwab, M., Ratschbacher, L., Siebel, W., McWilliams, M., Minaev, V., Lutkov, V., et al. (2004). Assembly of the Pamirs: Age and origin of magmatic belts from the southern Tien Shan to the southern Pamirs and their relation to Tibet. *Tectonics*, *23,* TC4002. https://doi.org/10.1029/2003TC001583

Smit, M.A., Hacker, B.R., and Lee, J. (2014). Tibetan garnet records early Eocene initiation of thickening in the Himalaya. *Geology, 42*, 591–594. https://doi.org/10.1130/G35524.1

Spicer, R.A., Su, T., Valdes, P.J., Farnsworth, A., Wu, F.X., Shi, G., et al. (2021). Why 'the uplift of the Tibetan Plateau' is a myth. *National Science Review*, *8*, nwaa091. https://doi.org/10.1093/nsr/nwaa091

Spicer, R.A., Su, T., Valdes, P.J., Farnsworth, A., Wu, F.X., Shi, G. et al. (2021). The topographic evolution of the Tibetan Region as revealed by palaeontology. *Palaeobiodiversity and Palaeoenvironments*, *101*, 213-243. https://doi.org/10.1007/s12549-020-00452-1

Spurlin, M.S., Yin, A., Horton, B.K., Zhou, J., and Wang, J. (2005). Structural evolution of the Yushu-Nangqian region and its relationship to syncollisional igneous activity, east-central Tibet. *Geological Society of America Bulletin*, *117*, 1293–1317. https://doi.org/10.1130/B25572.1

Staisch, L.M., Niemi, N.A., Hong, C., Clark, M.K., Rowley, D.B., and Currie, B. (2014). Cretaceous- Eocene depositional age for the Fenghuoshan Group, Hoh Xil Basin: Implications for the tectonic evolution of the northern Tibet Plateau. *Tectonics*, *33*, 281–301, https://doi.org/10.1002/2013TC003367

Staisch, L.M., Niemi, N.A., Clark, M.K., and Chang, H. (2016). Eocene to late Oligocene history of crustal shortening within the Hoh Xil Basin and implications for the uplift history of the northern Tibetan plateau. *Tectonics*, *35*, 862–895. https://doi.org/10.1002/2015TC003972

Stübner, K., Ratschbacher, L., Weise, C., Chow, J., Hofmann, J., Khan, J., et al. (2013). The giant Shakhdara migmatitic gneiss dome, Pamir, India-Asia collision zone: 2. Timing of dome formation. *Tectonics, 32,* 1404–1431. https://doi.org/10.1002/tect.20059

Sundell, K.E., Laskowski, A.K., Howlett, C., Kapp, P., Ducea, M., Chapman, J.B. and Ding, L. (2023). Episodic Late Cretaceous to Neogene crustal thickness variation in southern Tibet. *Terra Nova*, *36,* 45-52. https://doi.org/10.1111/ter.12689

Tapponnier, P., Peltzer, G., Le Dain, A.Y., Armijo, R., and Cobbold, P. (1982). Propagating extrusion tectonics in Asia: New insights from simple experiments with plasticine. *Geology*, *10*, 611–616. https://doi.org/10.1130/0091-7613(1982)10%3C611:PETIAN%3E2.0.CO;2

Tong, Y., Yang, Z., Mao, C., Pei, J., Pu, Z., and Xu, Y. (2017). Paleomagnetism of Eocene red-beds in the eastern part of the Qiangtang Terrane and its implications for uplift and southward crustal extrusion in the southeastern edge of the Tibetan Plateau. *Earth and Planetary Science Letters*, *475*, 1–14. https://doi.org/10.1016/ j.epsl.2017.07.026

Toussaint, G., Burov, E., and Jolivet, L. (2004). Continental plate collision: Unstable vs. stable slab dynamics. *Geology*, *32*, 33–36. https://doi.org/10.1130/G19883.1

Turcotte, D.L. and Schubert, G., (2002). *Geodynamics (2nd ed)*. Cambridge University press. Cambridge. 492–499.

Van der Voo, R., Spakman, W., and Bijwaard, H. (1999). Tethyan subducted slabs under India. *Earth and Planetary Science Letters, 171*, 7–20. https://doi.org/10.1016/S0012-821X(99)00131-4

van Hinsbergen, D.J., Lippert, P.C., Dupont-Nivet, G., McQuarrie, N., Doubrovine, P.V., Spakman, and W., Torsvik, T.H. (2012). Greater India Basin hypothesis and a two-stage Cenozoic collision between India and Asia. *Proceedings of the National Academy of Science, 109,* 7659–7664. https://doi.org/10.1073/pnas.1117262109

Wang, C., Dai, J., Zhao, X., Li, Y., Graham, S.A., He, D., et al. (2014). Outward-growth of the Tibetan Plateau during the Cenozoic: A review. *Tectonophysics*, *621*, 1–43. https://doi.org/10.1016/j.tecto.2014.01.036

Wang, C., Ding, L., Zhang, L.Y., Kapp, P., Pullen, A., and Yue, Y.H. (2016). Petrogenesis of Middle–Late Triassic volcanic rocks from the Gangdese belt, southern Lhasa terrane: Implications for early subduction of Neo-Tethyan oceanic lithosphere. *Lithos*, *262*, 320–333. https://doi.org/10.1016/j.lithos.2016.07.021

Wang, Y. F., Zeng, L., Gao, J., Zhao, L., Gao, L. E., and Shang, Z. (2019). Along-arc variations in isotope and trace element compositions of Paleogene gabbroic rocks in the Gangdese batholith, southern Tibet. *Lithos*, *324*, 877-892. https://doi.org/10.1016/j.lithos.2018.11.036

Wiesmayr, G. and Grasemann, B. (2002). Eohimalayan fold and thrust belt: Implications for the geodynamic evolution of the NW-Himalaya (India). *Tectonics*, *21*, 8–1. https://doi.org/10.1029/2002TC001363

Willett, S., Beaumont, C., and Fullsack, P. (1993). Mechanical model for the tectonics of doubly vergent compressional orogens. *Geology, 21,* 371–374. https:/doi.org/10.1130/00917613(1993)021<0371:MMFTTO>2.3.CO;2

Worthington, J. R., Ratschbacher, L., Stübner, K., Khan, J., Malz, N., Schneider, S., et al. (2020). The Alichur dome, South Pamir, western India–Asia collisional zone: Detailing the Neogene Shakhdara–Alichur syn-collisional gneiss-dome complex and connection to lithospheric processes. *Tectonics*, *39,* https://doi.org/10.1029/2019TC005735

Yi, Z., Huang, B., Chen, J., Chen, L., and Wang, H. (2011). Paleomagnetism of early Paleogene marine sediments in southern Tibet, China: Implications to onset of the India–Asia collision and size of Greater India. *Earth and Planetary Science Letters*, *309*, 153–165. https://doi.org/10.1016/j.epsl.2011.07.001

Yin, A. and Harrison, T.M. (2000). Geologic evolution of the Himalayan-Tibetan orogen. *Annual Review of Earth Planetary Sciences, 28,* 211–280. https://doi.org/10.1146/annurev.earth.28.1.211

Yuan, J., Yang, Z., Deng, C., Krijgsman, W., Hu, X., Li, S., et al. (2021). Rapid drift of the Tethyan Himalaya terrane before two-stage India-Asia collision. *National Science Review*, *8*, nwaa173. https://doi.org/10.1093/nsr/nwaa173

Zeng, L., Gao, L.E., Xie, K., and Liu-Zeng, J. (2011). Mid-Eocene high Sr/Y granites in the Northern Himalayan gneiss domes: Melting thickened lower continental crust. *Earth and Planetary Science Letters*, *303*, 251–266. https://doi.org/10.1016/j.epsl.2011.01.005

Zhu, D., Wang, Q., and Zhao, Z. (2017). Constraining quantitatively the timing and process of continent-continent collision using magmatic record: Method and examples. *Science China Earth Sciences, 60,* 1040–1056. https://doi.org/10.1007/s11430-016-9041-x

Zhu, D.-C., Wang, Q., Zhao, Z.-D., Chung, S.-L., Cawood, P.A., Niu, Y., et al. (2015). Magmatic record of India-Asia collision. *Scientific Reports*, *5*, 14289. https://doi.org/10.1038/srep14289

CHAPTER 2. BALANCED CROSS-SECTIONS AND NUMERICAL MODELING OF THE LITHOSPHERIC-SCALE EVOLUTION OF THE HINDU KUSH AND PAMIR

This chapter is a modified version of the article 'Balanced Cross-Sections and Numerical Modeling of the Lithospheric-Scale Evolution of the Hindu Kush and Pamir' by S. Kelly and C. Beaumont, published in the *Journal of Geophysical Research: Solid Earth* (Kelly et al., 2021).

2.1 Abstract

The role of deformation and removal of continental lithospheric mantle (CLM) during continent-continent collision, while recognized as fundamental to the evolution of orogenic systems, often remains speculative as direct evidence for these processes is typically absent. Nevertheless, these poorly understood deep lithospheric processes are expected to produce first-order controls on the style of crustal shortening, magmatism, and metamorphism in large-scale orogens. The Hindu Kush and Pamir offer an excellent opportunity to constrain these deep processes, as high-quality seismic images reveal oppositely dipping slabs under the Hindu Kush and Pamir, inferred to be subducting Indian and Asian lithospheres, respectively. Using two-dimensional mantle-scale geodynamical models, we show that these along-strike differences can be explained by the nature of the indenting Indian plate; thinner fringe Indian crust beneath the Hindu Kush, and full-thickness Indian crust beneath the Pamir. In the Hindu Kush models, steep subduction of India follows early delamination of the Asian lithospheric mantle, whereas in the Pamir models, Asian delamination is followed by flat-slab underthrusting of Indian CLM and forced subduction of northern Asian terranes. These styles of mantle delamination and subduction have key implications for the ensuing styles of magmatism, metamorphism, and crustal-scale evolution of these systems. In the Hindu Kush, subduction of fringe India leads to burial of Indian crust under Asia, limiting both Himalayan growth and deformation of the Tajik Basin. In contrast, in the Pamir, forced

subduction of the Alai terrane leads to Alai crust underthrusting the Pamir, forming the Pamir orocline.

2.2 Introduction

The behavior of continental lithospheric mantle (CLM) during continent-continent collision remains an unresolved problem in plate tectonics (e.g., Avouac, 2007; Ghazian and Buiter, 2013; Jamieson and Beaumont, 2013; Molnar, 1988; Molnar and Bendick, 2019; Toussaint et al., 2004), because direct evidence for deep processes involving the CLM is typically absent or ambiguous (e.g., Chen et al., 2017; Guo et al., 2018; Heintz et al., 2009; Klemperer et al., 2013). Nonetheless, it is recognized that these processes are profoundly important to the evolution of orogens (Ghazian and Buiter, 2013; Houseman et al., 1981; Jamieson and Beaumont, 2013; Kay and Kay, 1993; Molnar et al., 1993; Willett et al., 1993). For many small, cold collisional orogens, as defined by Beaumont et al. (2006), evidence suggests that CLM follows the oceanic lithosphere and continues to subduct (Jamieson and Beaumont, 2013; Lippitsch et al., 2003), but for large, hot orogens, there are multiple possibilities for deformation, modification and/or removal of CLM (Kelly et al., 2016; Li, Liu et al., 2016b; Molnar and Bendick, 2019). For example, for the Himalayan-Tibetan (H-T) orogen, delamination or convective removal of CLM under Tibet has been inferred (e.g., Chung et al., 2005; England and Houseman, 1988; Molnar et al., 1993; Nunn et al., 2014; Owens and Zandt, 1997), and has been used to explain uplift of the Tibetan Plateau (e.g., Dewey et al., 1988; England and Houseman, 1989). However, formulation of realistic geodynamical models of the behavior of CLM in collisional orogens is often hindered by a lack of agreement in interpretations of upper-mantle-scale processes from seismic and other geophysical and geological data (e.g., Chen et al., 2017).

The Hindu Kush and Pamir, the westernmost parts of the India-Asian collisional zone (Figure 2.1), offer an opportunity to explore geodynamical models of continental subduction and CLM behavior during collisional orogenesis. Their advantage is that they are two of the most seismically active intercontinental regions on Earth, and experience

significant seismicity up to intermediate upper-mantle depths (Billington et al., 1977; Kufner et al., 2016; Kufner et al., 2017; Pegler and Das, 1998; Sippl, Schurr, Yuan, et al., 2013b). High-quality earthquake mechanism and location data and tomographic images of the CLM under this region offer a rare opportunity to constrain geodynamical models. These images reveal dipping slabs, mostly interpreted to have opposing orientations – a steep, north-dipping slab under the Hindu Kush and a shallow south-dipping slab subducting under the Pamir (Bai and Zhang, 2015; Koulakov and Sobolev, 2006; Kufner et al., 2016; Lister et al., 2008; Replumaz et al., 2014; Sippl, Schurr, Tympel et al., 2013a; Sippl, Schurr, Yuan et al., 2013b). The slabs are generally interpreted to be respectively subducting Indian and Asian CLMs under the Hindu Kush and Pamir (Kufner et al., 2016; Replumaz et al., 2014).

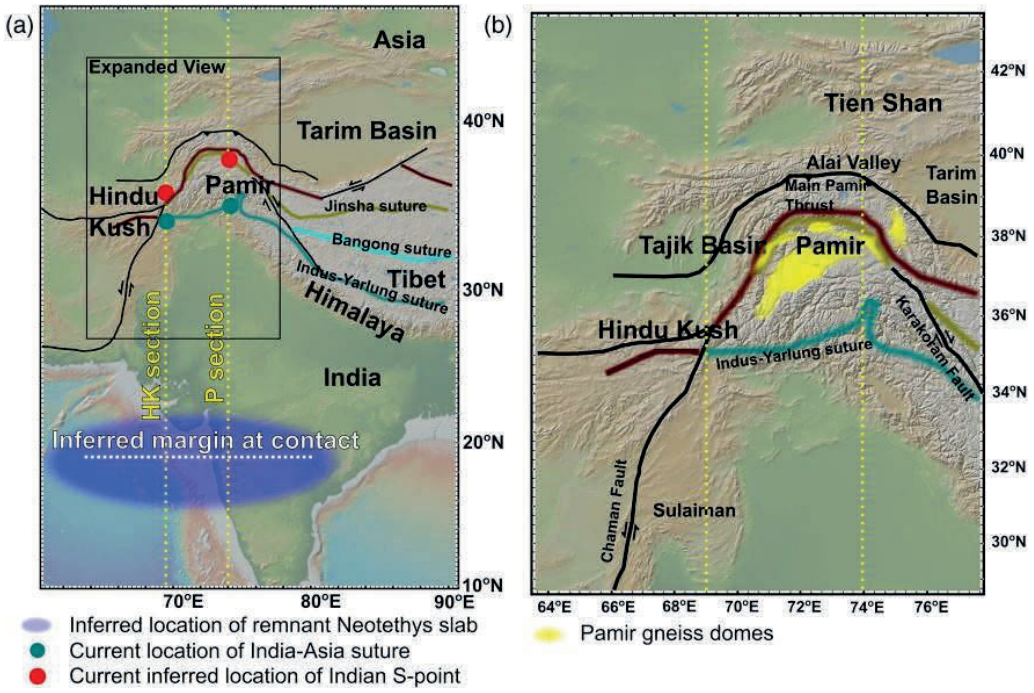

Figure 2.1. (a) Map of the western region of the India-Asia collision zone. The location of the seismically imaged Neotethyan slab (blue oval), S-point (red dots), and Indus-Yarlung sutures (teal blue dots) are shown for the Hindu Kush and Pamir sections. Also shown are locations of the reconstructed precollisional Asian margin (dashed white line); major sutures (modified from Replumaz et al., 2014) including Indus-Yarlung suture (teal blue), Bangong suture (cyan blue) and Jinsha suture (brown); and faults (thin black lines-modified from Yin, 2006). (b) Smaller-scale map of the Hindu Kush and Pamir (location shown in a), showing the major regions described in the text, and the approximate locations of the Pamir gneiss domes (yellow). Topographic base maps from http://www.geomapapp.org.

The focus of our research is twofold. First, we present lithospheric-scale constraints on the evolution of the Hindu Kush and Pamir systems by using geometric arguments to balance first-order lithospheric cross-sections. Second, we present geodynamical models, constrained by these geometric arguments, which provide possible explanations for simplified versions of the lithospheric-scale evolution of the Hindu Kush and Pamir systems. We aim to answer two key questions: (1) what along-strike differences across the Hindu Kush and Pamir gave rise to these particular contrasting styles of CLM deformation? and more broadly: (2) does continental subduction, or other processes such as CLM delamination, explain the styles of crustal shortening, magmatism, and metamorphism in these regions?

2.3 Geological and Geophysical Constraints

The Hindu Kush and the Pamir (Figure 2.1) are parts of the India-Asia collision zone, produced by collision of India with Asia following closure of the Neotethys (e.g., Burtman and Molnar, 1993; Yin, 2006; Yin and Harrison, 2000). The Hindu Kush is a narrow, ~250–300 km north-to-south, east-west trending mountain range which joins the Pamir along its eastern margin, and is bounded to the north by the Tajik Basin and to the south by the Sulaiman Range. Significant postcollisional convergence in the Kohistan-Pamir region produced a much wider (~500 km) north-to-south oroclinal region of thickened crust with an arcuate northern Pamir range front (Figure 2.1). The Pamir plateau contains the enigmatic Pamir gneiss domes, extensional structures formed within this contractional tectonic setting. The Pamir is bounded by the narrow Alai Valley to the north, Tarim Basin and Tibet to the east, the Pakistan Himalaya to the south, and the Hindu Kush and Tajik Basin to the west (Figure 2.1). Further north, the Tien Shan paleo-orogen was also reactivated following collision (Avouac et al., 1993).

The Hindu Kush and Pamir regions comprise a series of ribbon terranes accreted to Asia prior to the India-Asia collision (Yin and Harrison, 2000). Very broadly, these terranes can be divided into a southernmost Kohistan arc terrane, and a central-northern composite

terrane which is approximately correlative with the Qiangtang, Songpan, and possibly Lhasa, terranes in the Himalayan-Tibetan region to the east (Schwab et al., 2004).

2.3.1 Estimates of the Timing of Collision, Total India-Asia Convergence, and Convergence Velocity

Estimates of the timing of the initial collision between India and Asia vary according to the method used, with onset of overlapping sedimentation derived from the opposing margins dating the earliest "contact" at ~56–60 Ma (Hu et al., 2016; Rowley, 1996). Moreover, different plate configurations for collision have been proposed (Hu et al., 2016, and refs. therein). The simplest configuration involves the collision of the passive margin of Greater India with Asia during the final closure of the Neotethys, following accretion and suturing of all terranes north of the Himalaya with Asia. An alternative is the "Greater India Basin" hypothesis (van Hinsbergen et al., 2012) which proposes that the Tethyan Himalaya was a microcontinent, rifted off and separated from India by a >2,000 km wide oceanic basin. In this interpretation, collision occurred first between the Tethyan Himalaya and Asia, and then between India and the Tethyan Himalaya following closure of this basin. To date, no geological evidence, for example, a suture, supports this hypothesis (see Hu et al., 2016 and Searle and Treloar, 2019 for reviews). Moreover, paleomagnetic interpretations for the position of the Tethyan Himalaya are now in question (Huang et al., 2017). Finally, the interpretation that collision between India and the Kohistan-Ladakh arc terrane occurred first, followed by collision between the Kohistan-Ladakh arc with Asia, has also been debated in recent literature (Borneman et al., 2015; Bouilhol et al., 2013; Rehman et al., 2011).

We follow Hu et al. (2016) in using "collision" to mean collision between full-thickness Indian crust (i.e., proximal margin) with Asia, and "contact" to refer to the contact between the distal Greater Indian margin and southernmost Asia. For the western India-Asia collision zone (Ladakh region), a robust collision age, 54 Ma, is based on the first arrival of Asian detritus on the proximal (neritic to nonmarine) Greater Indian margin (Najman et al., 2017). The inferred provenance of this sediment, from north of the Kohistan-Ladakh arc indicates Asia has sutured with the arc prior to the 54 Ma collision

with India (Najman et al., 2017). For the central India-Asia collision zone, “contact” is at 59 ± 1 Ma based on the first arrival of Asian-derived sediment on the distal portion of the Indian margin (Hu et al., 2015).

The convergence between India and Asia is generally estimated from paleomagnetic data and plate circuit motions. We rely on a recent estimate of ~3,150 km of India-Asia convergence along the western syntaxis since 56 Ma, which we assume to be the time of contact (Ingalls et al., 2016, their Figure 2.2b). This compares with the van Hinsbergen et al. (2011) equivalent estimate of ~3,500 km from their preferred Model A. Provenance analysis from the Pakistan Himalaya confirm India-Asia contact and formation of a foreland basin by 56–55 Ma (Ding et al., 2016; Qasim et al., 2018).

Estimates of the rate of India-Asia convergence since collision carry significant uncertainties. It is, however, generally accepted (Hu et al., 2016, and references therein; van Hinsbergen et al., 2011) that the convergence rate close to the time of collision was ~14 ± 2 cm/year and that it decreased rapidly soon after collision. There is closer agreement among convergence rate estimates since ~20 Ma (e.g., Ingalls et al., 2016; van Hinsbergen et al., 2011), with a current rate of ~3.6 cm/year (van Hinsbergen et al., 2011).

Here we adopt a 19°N position for the southern margin of Asia (Figure 2.1a) in the western syntaxis at 56 Ma, similar to the Ingalls et al. (2016) estimate, recognizing that the paleomagnetic constraints on this position are subject to uncertainty, >60 Ma at 5°N versus 50–55 Ma at ~20°N (D. Zhu et al., 2017, Figure 2).

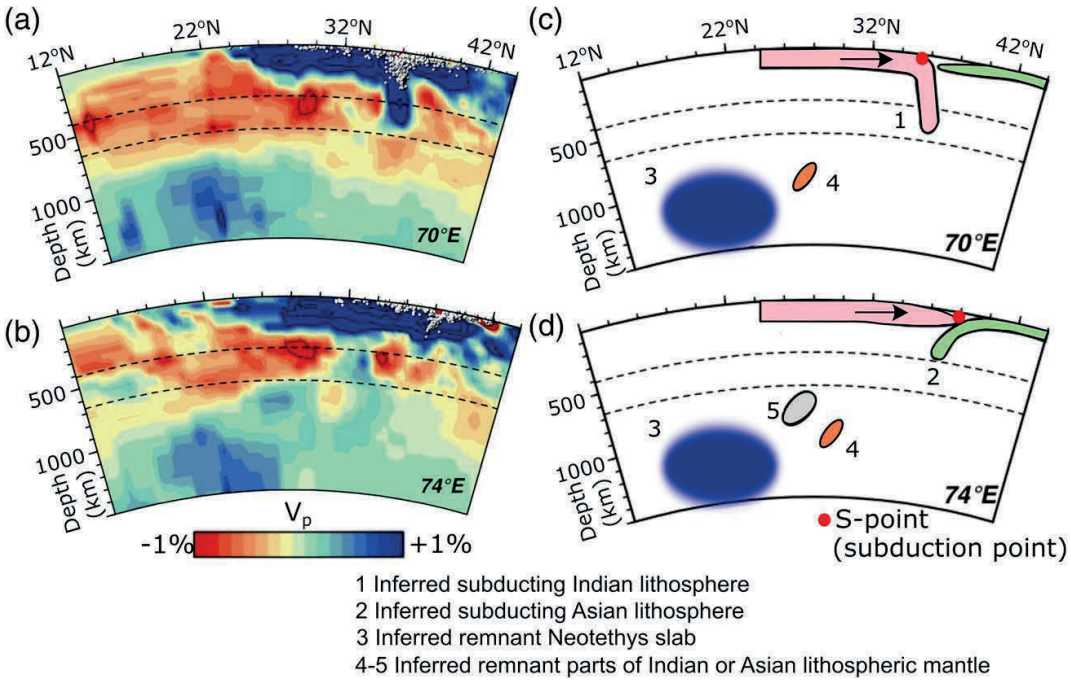

Figure 2.2. Seismic velocity cross-section showing Vp anomalies (modified from Replumaz et al., 2014) along the Hindu Kush section (a) and Pamir section (b**).** Fast velocities (blue) are interpreted as cold, subducted parts of lithosphere, and white dots are earthquake locations. (c) and (d) are the corresponding interpretations from Replumaz et al. (2014). See text for details. The locations of the inferred S-points are marked by a red dot.

2.3.2 Constraints from Upper-Mantle-Scale Seismic Interpretations

Figure 2.2a shows a representative interpretation (Replumaz et al., 2014) of the seismic anomalies and earthquake locations (labeled 1–4, Figure 2.2c) at longitude 70°E (adjacent to our Hindu Kush section at 69.5°E, Figure 2.1). Anomaly 1 is interpreted as Indian lithosphere which is steeply subducting to 600 km (blue region, Figure 2.1). Recent seismic analysis (Kufner et al., 2016, 2017) gives a more detailed interpretation indicating that the slab is currently extended and thinned as it breaks off, and therefore the amount of Indian lithosphere underthrusting is less than the apparent 600 km. The current S-point (subduction point), defined as the location where Indian CLM detaches and subducts, is located at latitude ~36°N (red dot, Figure 2.2c). Anomaly 3 is interpreted as a remnant part of the detached Neotethyan slab (Replumaz et al., 2014). Anomaly 4 is poorly imaged but has been interpreted as a detached part of Asian CLM (Replumaz et al., 2014).

Figure 2.2b shows anomalies under the Pamir section along longitude 74°E (Pamir section, Figure 2.1a) as interpreted by Replumaz et al. (2014). Anomaly 2 (Figure 2.2d) is interpreted to be Asian CLM subducting at a shallow angle to 400 km. Indian CLM is interpreted to underthrust Asian crust as a flat slab to latitude~38.5°N, close to the Asian CLM S-point. Anomaly 3 and the poorly imaged Anomaly 4 are interpreted to represent detached parts of Neotethyan and Asian slabs, respectively (Replumaz et al., 2014). Finally, the poorly imaged Anomaly 5 has been tentatively interpreted as detached Indian CLM.

When constructing the balanced cross-sections (Section 2.5), we accept the interpretation that Anomaly 3 is the Neotethyan oceanic lithosphere and that Anomaly 4 may be delaminated Asian CLM, and in addition that the 42–37 Ma Vanj magmatism may reflect early removal of Asian CLM within the Pamir (Chapman et al., 2018).

2.4 Constraints on the Evolution of the Hindu Kush and Pamir Systems

To first order, reconstructions of the evolution of the Hindu Kush and Pamir can be produced by considering simple geometric arguments coupled to the constraints from Section 2.3. We consider the two N-S cross-sections (Figure 2.1). The starting configurations are at the time of contact between the distal rifted margin of Greater India and the southern margin of Asia. Total convergence since contact is defined by the relative motion between an undeformed point within India and an equivalent stable point in Asia. We use “convergence” to mean reduction in distance between two locations and “shortening” to mean reduction in length balanced by thickening such that cross-sectional area is conserved (e.g., uniform thickening). These are not equivalent because convergence includes not only uniform shortening, but depth-dependent shortening, subduction/delamination, crustal erosion via surface processes, and lateral escape (the last not considered here).

In addition, the accommodation of convergence may be different in the upper and lower parts of the lithosphere, owing to horizontal decoupling/detachment, thereby requiring the two layers to be considered separately. For the upper part, our middle and upper crust, the

amount of convergence accommodated within Asian crust is equal to the northward motion of the Indus-Yarlung suture since slab break-off at 19°N (Table A1). In the lower part, our lower crust and CLM, convergence within Asia corresponds to the total amount of S-point advance (i.e., advance of the location where oceanic lithosphere or CLM subducts) since slab break-off (Table A1). Once the amount of convergence within Asia has been estimated, the amount of Indian convergence is equal to the remainder of the 3,150 km total convergence (Ingalls et al., 2016) since Neotethyan oceanic slab break-off, assuming that the crustal suture and the S-point were at the same location at the time of slab break-off. This remainder includes the amount of convergence between contact and collision. We also assume that slab break-off took place at nearly the same latitude as initial contact, 19°N (Figures 2.1 and 2.2). We base this on the inferred near-stable paleomagnetic latitude of southernmost Asia 100–50 Ma (Bian et al., 2017; Li, Ding et al., 2016a) and the lack of S-point advance during subduction of the Indian rifted margin in a large range of numerical models of the type we describe later.

In order to minimize the effect of northwestward flow of Pamir crust into the Tajik Basin region of the Hindu Kush (Abdulhameed et al., 2020; Burtman, 2000; Chapman et al., 2017) on our crustal shortening estimates, we focus on the Hindu Kush section along longitude 69.5°E (Figure 2.1).

2.4.1 Partitioning Accommodation of Convergence in the Hindu Kush and Pamir Lithospheres

The seismic section at 70°E, adjacent to the Hindu Kush section, shows the crustal suture is currently ~1,700 km north of the detached Neotethyan slab (Anomaly 3, Figure 2.2c), thereby requiring that the balance of ~1,450 (3,150 − 1,700) km of convergence was accommodated by the Greater Indian margin and Indian crusts since contact, probably largely by subduction. In the Pamir section (74°E, Figure 2.2b), the crustal suture is ~1,800 km north of the Neotethyan slab (Anomaly 3, Figure 2.2d). The corresponding convergence accommodated by removal of the Greater Indian margin and Indian crusts since contact is therefore ~1,350 (3,150−1,800) km, also probably largely by subduction.

Under the Pamir cross-section, Indian lithosphere is interpreted to underlie the Asian crust as far north as the subducting Asian slab. This location, marking the Indian S-point, is ~2,150 km north of the Neotethyan slab (Anomaly 3, Figure 2.2d). Under the Hindu Kush, a steeply north-dipping slab, interpreted to be subducting Indian lithosphere (Anomaly 1, Figure 2c), marks the S-point ~1,900 km north of the Neotethyan slab. These distances require that the Asian lower lithosphere has accommodated ~2,150 km of convergence under the Pamir and ~1,800 km under the Hindu Kush, with the balance of ~1,000 (3,150–2,150) km and ~1,250 (3,150–1,900) km of Indian lower lithosphere convergence accommodated by subduction or other mechanisms under the Pamir and Hindu Kush, respectively, since contact.

The assumptions and methods used in making these convergence estimates and the associated estimates explained in the next two sections are listed in Table A1. The implied cumulative geometrical evolutions are shown in Figures 2.3 and 2.4.

2.4.2 Crustal Structure and Shortening Estimates in the Hindu Kush and Pamir

Within the Pakistan Himalaya, ~300 km of structural shortening has been measured (Dipietro and Pogue, 2004; Schmidt et al., 2011, and references therein) but this does not include crustal erosion by surface processes or subduction.

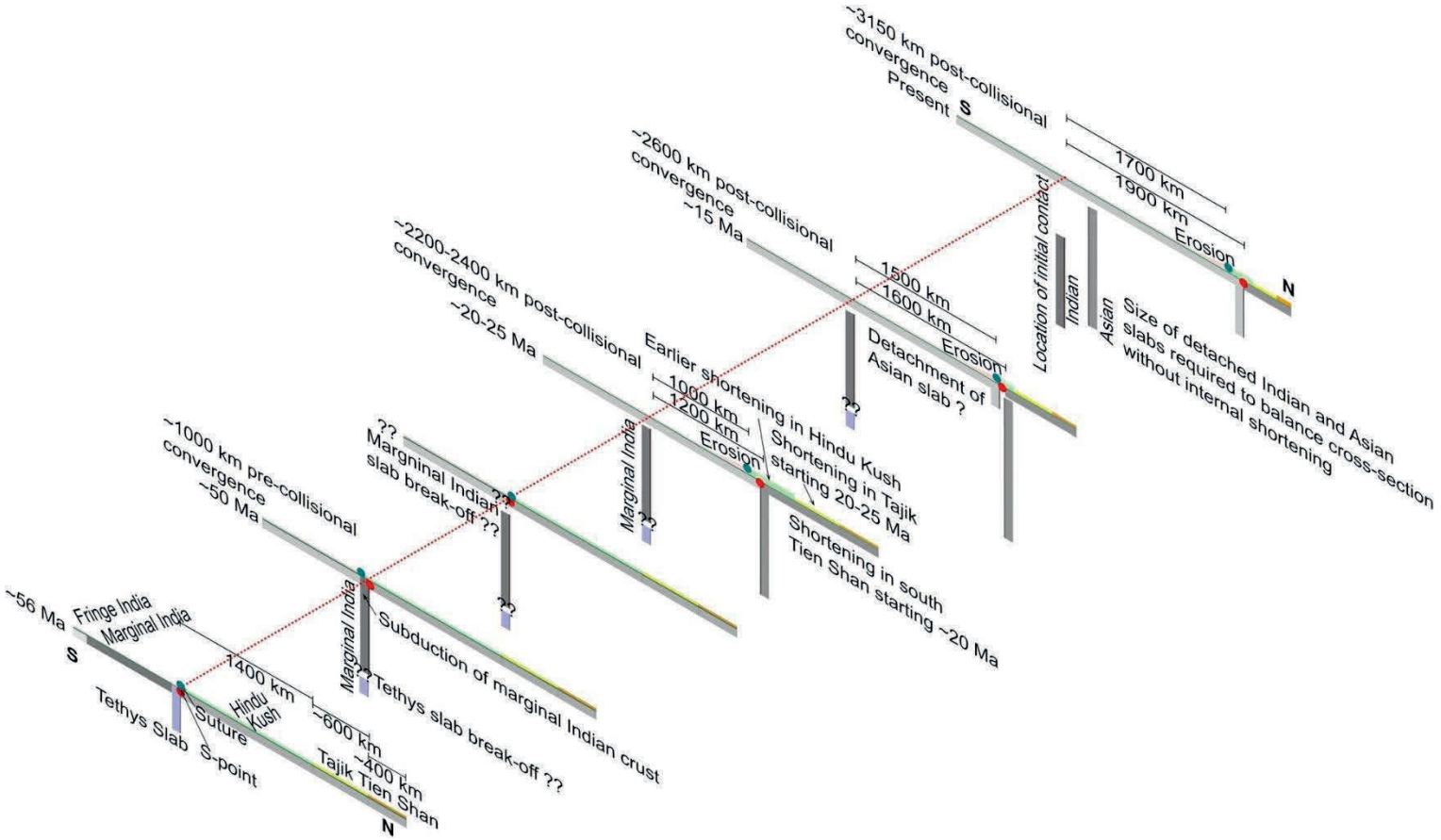

Figure 2.3. Geometrically interpreted evolution of the Hindu Kush, balanced at the mid-upper crustal and lower lithospheric scale, from bottom left (initial contact) to the top right (current geometry). The dotted red line indicates the location of initial contact, while the red dot and teal blue dot indicate the evolving locations of the S-point and Indus-Yarlung suture, respectively. These locations initially coincide, but S-point and suture are progressively displaced from the site of initial collision and from each other during convergence. The vertical gray bars in the last section represent the cumulative volume of lower lithosphere required to balance the sections without internal shortening. They provide a measure of the lower lithosphere that has been removed, but only an approximate lateral position where this lithosphere may be located.

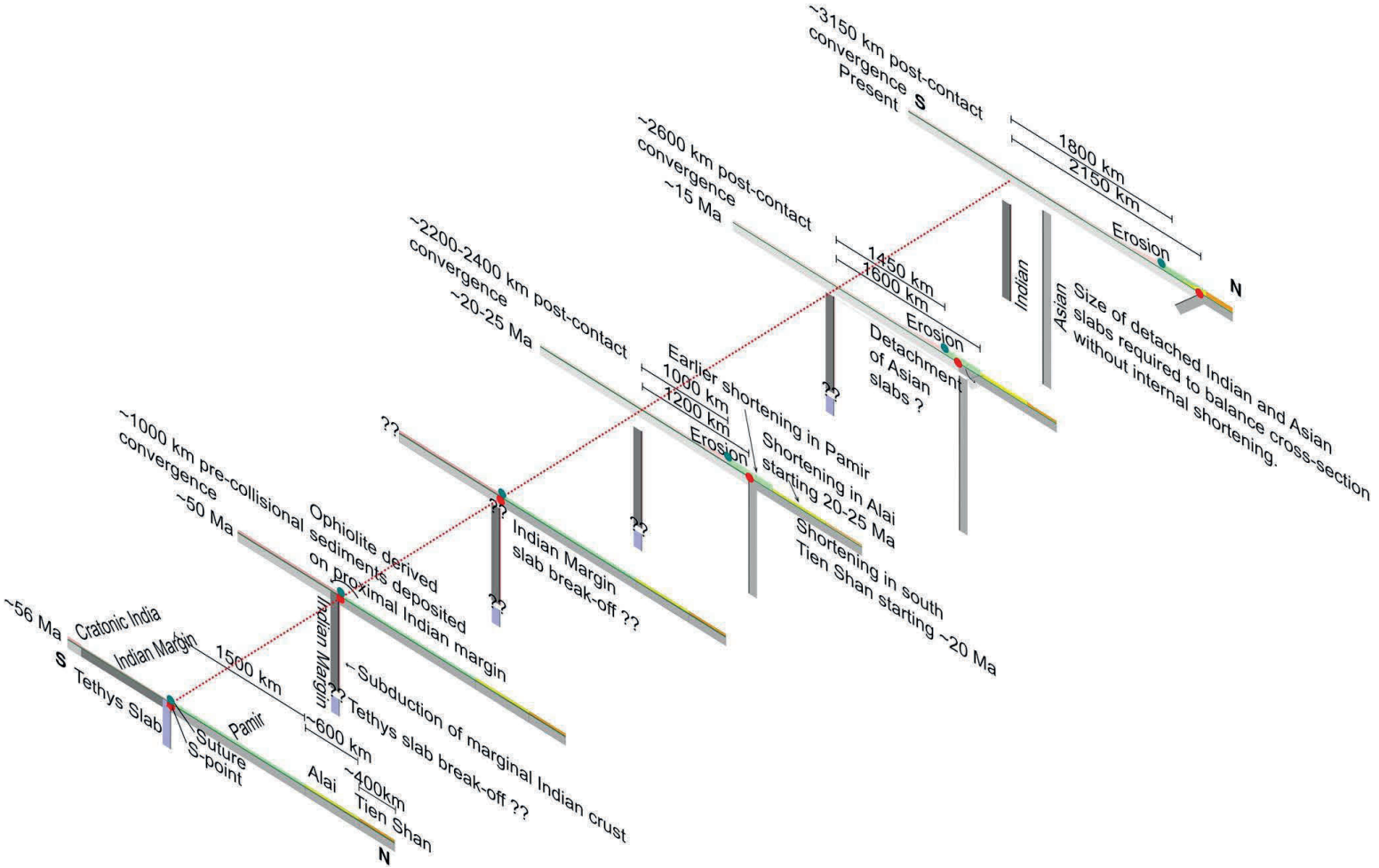

Figure 2.4. Geometrically interpreted evolution of the Pamir, corresponding to that of the Hindu Kush (Figure 2.3, caption).

Geophysical, sedimentological, and structural measurements are interpreted to suggest that the formerly larger Alai Valley/Alai terrane region has been overthrust by at least 200–~300 km by the Pamir orocline (Burtman and Molnar, 1993). Correspondingly, to the west, the Tajik Basin has experienced overthrusting from the Pamir by a thin-skinned fold-thrust belt with an evaporite detachment. N-S shortening is estimated at >35–40 km, and E-W shortening is <30 km (Chapman et al., 2017). Other estimates of overthrusting (Gągała et al., 2020) are larger with 22–148 km of ~E-W shortening. However, the underlying main crustal layer is estimated to be 35–45 km thick (Schneider et al., 2019) indicating little shortening of the crust, which is our focus. From another perspective, if the crusts of the Alai and Tajik Basin terranes are lateral equivalents of the Tarim Basin to the east and had equal initial north to south widths (~600 km), the implied reduction in width within the Alai terrane crust is ~600 km and that in the Hindu Kush and Tajik terrane crust is up to ~350 km depending on the longitude, but crustal-scale shortening does not extend into the present Tajik Basin along our 69.5°E cross section (Schneider et al., 2019). In addition, an estimated 200 ± 50 km of late Cenozoic shortening has been inferred within the Tien Shan (Avouac et al., 1993).

When these shortening estimates are subtracted from the within-Asia postcontact convergence, this leaves ~1,150 (1700 − [200 + 350]) km for the Hindu Kush section to be partitioned between the Indus-Yarlung suture and the Tajik Basin. Correspondingly, for the Pamir section subtracting the Tien Shan and Alai terrane shortening leaves ~1,000 (1,800 − [200 + 600]) km of crustal convergence to be absorbed between the Main Pamir Thrust and the Indus-Yarlung suture (Figure 2.1).

The original widths of the undeformed Hindu Kush and Pamir regions are equal to their current widths plus the amount of crustal convergence partitioned within these regions. Currently, the Hindu Kush orogen is ~250 km wide which implies that the precollisional crust was ~1,400 (250 + 1,150) km wide, greatly at odds with its current size. Likewise, the Pamir-Kohistan region is ~500 km wide, which implies that the precollisional crust in this region was ~1,500 (500 + 1,000) km wide. Note that these original widths are upper bounds based on contact and collision at 19°N.

2.4.3 Timing of Shortening

Evidence from the age of prograde metamorphic monazite from deep crustal xenoliths erupted within Miocene volcanics indicates that the Pamir region crust was thickened early in the Cenozoic (Ducea et al., 2003), and more specifically between 37 and 27 Ma (Smit et al., 2014). Later, rapid exhumation of the Pamir gneiss domes by ~17 Ma implies that the region experienced periods of Miocene and more recent (7–2 Ma) localized crustal extension (Hacker et al., 2017; Stübner et al., 2013; Worthington et al., 2020).

Within the Alai region, structural and sedimentological evidence shows that the Alai Valley experienced internal shortening at ~20–25 Ma, and later at ~15 Ma, which resulted in underthrusting of Alai crust under the Pamir (Coutand et al., 2002). This is supported by marine sedimentological evidence which indicates that the Tarim Basin was submerged and connected westward to the Neotethys Ocean through the Alai Valley until the early Oligocene (Sun and Jiang, 2013), implying little Alai crustal thickening at that time.

Extrapolating modern strain rates in the Tien Shan backwards in time predicts that shortening beginning as late as ~10 Ma would have produced the total ~200 km of present-day shortening (Abdrakhmatov et al., 1996; England and Molnar, 2015), which is supported by sedimentological evidence in the northern Tien Shan (Bullen et al., 2001). However, sedimentological evidence from the southern Tien Shan indicates uplift starting at ~20 Ma (Heermance et al., 2007). Either the strain rate varied with time, or deformation in the Tien Shan propagated from south to north, or both.

Taken together, these results give a general indication that deformation in the Hindu Kush and Pamir cross-section crusts progressed from south to north with early thickening and development of a plateau in the Pamir. This was followed by later (~20–25 Ma and ~15 Ma) thickening/overthrusting of the Alai terrane to the Alai Valley but little thickening of crust beneath the Tajik Basin. Tien Shan shortening commenced at about 20 Ma.

Within the Himalayan Pamir section, ultra-high-pressure (UHP) metamorphic rocks from the Kaghan region indicate that Indian crust reached UHP conditions between 47 and 43 Ma (Hu et al., 2016; O'Brien, 2019), probably as a result of subduction.

2.4.4 Nature of the Indian Margin

Our estimate of the respective ~1,350 and ~1,450 km convergence required to have been accommodated by Indian crust in the Pamir and Hindu Kush (Section 2.4.1) is at odds with the measured amount of shortening observed within India (~300 km), as well as the current width and thickness of the Himalaya, a problem that cannot be explained by erosion alone. Although the shortening deficit could be explained by total subduction of the Greater Indian Basin (van Hinsbergen et al., 2011) or a backarc basin (Kapp and DeCelles, 2019), there is currently no evidence to support these hypotheses. Here we adopt a simple solution in which the Greater India margin was ~1,000 km wide, and that most of its crust subducted between contact and collision. This solution is compatible with the time lag between contact at the distal margin (56 Ma) and collision within the proximal margin (~51 Ma) during which 700 km of Indian margin would have been subducted at a convergence rate of 14 cm/year.

2.5 Geometrical Balanced Cross-Sections for the Interpreted Evolution of the Hindu Kush and Pamir

Figures 2.3 and 2.4 are lithosphere-scale geometrical cross-sections of the Hindu Kush and Pamir (69.5°E and 74°E, respectively), showing the interpreted evolution of these systems based on the arguments made above, assuming ~56 Ma contact, and assuming all of the convergence was accommodated south of the northern margin of the Tien Shan (Figure 2.1). They are independently balanced at the upper and lower lithospheric scale, with a detachment level at the top of the lower crust.

2.5.1 Crustal Erosion Estimates Based on Changes in Cross-Sectional Area During Shortening

Erosion of crust and removal of the sediment from the cross-sections plays an important role in their balancing, as we illustrate here. The purpose is to demonstrate the large effect of lower crustal subduction, as indicated for the Hindu Kush and Pamir (Kufner et al., 2017; Sippl, Schurr, Tympel et al., 2013a). The actual erosion estimates are, however, approximations because they depend on the assumptions we make. Additionally, we consider only the total amounts but not the timing of erosion.

In addition to balancing the upper and lower lithosphere, we assume ~36 km normal precollisional thickness continental crusts and that the 12 km thick lower crust subducts as part of the lower lithosphere. The cumulative decrease in the cross-sectional area of the upper lithosphere results from erosion, whereas that of the lower crust is from subduction and delamination.

Assuming that the average current crustal thickness in the Hindu Kush is ~60–65 km (Jadoon and Khurshid, 1996; Schneider et al., 2019) the corresponding thickening factor is ~1.7 from the assumed initial 36 km. Assuming pure shear shortening reduces the width of the Hindu Kush from 1,400 km to 825 km, 575 km wider than its current width, leaving the equivalent of ~35,000 km^2 (575 × 60 km of thickened crust, or 975 × 36 km) of normal thickness crust to be removed from the cross-section by erosion, a very large amount. If, however, the lower crust has been removed by subduction, achieving a 60 km total crustal thickness requires a thickening factor of 2.5 for the upper lithosphere (upper and mid-crust), thereby producing a smaller, 550 km, width after shortening from 1,400 km. This leaves the requirement for erosion at ~18,000 km^2 (300 × 60 km), or the equivalent of an erosion rate of 0.37 mm/year over a time averaged width of 825 km, totaling 21.8 km over ~60 Myr. Although this rate is relatively high, it is still within the realm of estimated erosion rates and amounts to 3 mm/year where the erosion focused on a 100 km width of the southern orogenic front.

The Himalaya experienced significant erosion along most of the India-Asia collision zone (Hodges, 2000), and shielded southern Asian crust from strong erosion. However, in the Hindu Kush region, where the equivalent of the Himalaya is greatly reduced, Asian crust, possibly a terrane equivalent to the Kohistan Arc, was removed partly by erosion. This is consistent with the estimate above, in which the Hindu Kush experienced significantly more erosion than Asian crust elsewhere in the collision zone. At least part of this can be explained by early, 55–43 Ma, erosion of Asian crust immediately west of our Pamir section in north Pakistan, inferred from the provenance of Indus foreland basin sediments (Ding et al., 2016).

Correspondingly, in the Pamir cross-section, doubling full-thickness crust by pure shear shortening to ~72 km (Schneider et al., 2019) will reduce the combined width of the Pamir and Kohistan terranes from 1,500 km to 750 km (250 km greater than their current width) leaving the equivalent of 18,000 km^2 of crust (250 × 72 km of thickened crust or 500 × 36 km of normal thickness crust) to be eroded if there was no loss of lower crust by other processes. However, the same 72 km total thickness crust can be produced by shortening the 24 km thick upper/mid crust by a factor of 3 and subducting the lower crust. This reduces the width of the Pamir and Kohistan crusts to 500 km from their initial 1,500 km width, in approximate agreement with their current width, but requiring much more shortening than observed. In summary, both cross-sections experienced significant erosion, focused in the "missing" Asian terrane for the Hindu Kush and in the Himalaya for the Pamir.

2.5.2 Interpretations Based on Geometrical Balanced Sections and Possible Explanations

Some key inferences can be made from the reconstructed sections (Figures 2.3 and 2.4) while taking the assumptions (Table A1) into account.

1) Both the Hindu Kush and Pamir systems evolved to produce at least ~1,900 km of S-point advance. It is unrealistic that this S-point advance was accommodated by internal shortening of Asian CLM alone, and we therefore infer that a significant

amount of Asian CLM was removed, possibly delaminated or subducted. The amounts removed are represented, without implication for the removal mechanism, by the vertical gray bars in Figures 2.3 and 2.4. Sippl et al. (2013a) modeled flat-slab underthrusting of Indian CLM beneath Asia, resulting in shallow southward subduction of the remaining intact Asian CLM. However, they assumed that further to the south Asian CLM was already missing, and there was therefore no attempt to explain how it was removed. Kelly et al. (2016) and Li et al. (2016b) showed how CLM can be removed during postcollisional advancing subduction by a number of different mechanisms depending on the strength and density of the CLM.

2) Upwelling of asthenosphere to <60 km depth following delamination of CLM is expected to generate voluminous magmatism by decompression melting (McKenzie and Bickle, 1988; White and McKenzie, 1989). We therefore speculate that the lack of evidence for such magmatism within the Indian crust in the Hindu Kush and Pamir regions implies that either the CLM under Indian crust remained intact, or that CLM was removed under Indian crust that had already thickened to >60 km, thereby minimizing decompression melting. By contrast, within the Asian crust, evidence from ultrapotassic volcanism and associated erupted xenoliths from the southern Pamir indicates that the Asian lower crust likely partially melted from ~35 Ma to ~11 Ma (Ducea et al., 2003). This may have been accomplished by exposing the crust to hot, upwelling asthenosphere following delamination of Asian CLM.

3) While both the Hindu Kush and Pamir sections have experienced significant S-point advance, the Hindu Kush S-point advanced ~250 km less than that of the Pamir (Figures 2.3 and 2.4). It can also be inferred that the Indian CLM has recently underthrust/subducted as a flat slab under the Pamir, whereas the Indian CLM under the Hindu Kush subducted at a steep angle and advanced less, and is currently breaking off as noted earlier. Kufner et al. (2016) hypothesized that the steeply subducting Indian CLM under the Hindu Kush indicates that the

westernmost part of the Indian continent comprised a fringe of thinned and dense rifted continental margin lithosphere. While this Indian fringe lithosphere may have been less buoyant, thereby promoting subduction, the large amount of S-point advance along this section precludes cases where the western Indian CLM was sufficiently dense that it subducted in place or with S-point retreat. However, the part of Indian CLM that is currently subducting is evidently dense enough to induce slab break-off.

4) The balanced cross-sections also show that significant parts of the Indian CLM (represented by vertical gray bar, Figures 2.3 and 2.4, where the dark gray represents the portion accommodated by a wide Indian margin) have been removed from both the Hindu Kush and Pamir regions. If our hypothesis of a wide Indian margin is correct, complete subduction of this margin accounts for most of the Indian CLM to be removed.

2.6 Hindu Kush and Pamir Characteristics to be Explained by Numerical Model Experiments

Having proposed geometrical balanced cross sections for the lithospheric-scale evolution of the Hindu Kush and Pamir systems based on observations and geometrical estimates, we now list both observed and inferred key characteristics of each system that require explanation (Figure 2.5, labeled h and p, respectively). These include: (p1) UHP exhumation near Indus-Yarlung suture; (p2/h1) removal of a significant part of Indian CLM; (p3/h2) removal of a significant part of Asian CLM; (p4) Vanj magmatism; (p5) high temperature crustal xenoliths; (p6) formation of Pamir gneiss domes; (p7/h3) advance of the Pamir orocline over the Alai terrane crust contrasted with the relatively intact Tajik Basin; (h4) diminished size of the Hindu Kush fold-and-thrust belt compared with the Himalaya to the east; (p8/h5) south-dipping Asian lithosphere under the Pamir, and steeply north-dipping Indian lithosphere under the Hindu Kush; (p9/h6) significant northward advance of the S-point under the Pamir (~2,150 km) and the Hindu Kush (~1,900 km) sections; (p10/h7) significant northward advance of the Indus-Yarlung suture along the Pamir (~1,800 km) and Hindu Kush sections (~1,700 km).

We focus on numerical models which explore the roles of two processes in the development of the characteristics listed above, namely: (1) the effects that Asian CLM properties have on the styles of Asian delamination/removal and the style of Indian CLM subduction, and; (2) for Hindu Kush models, we investigate "fringe" models designed to represent thinner Indian crust along the subducting western fringe of the Indian plate.

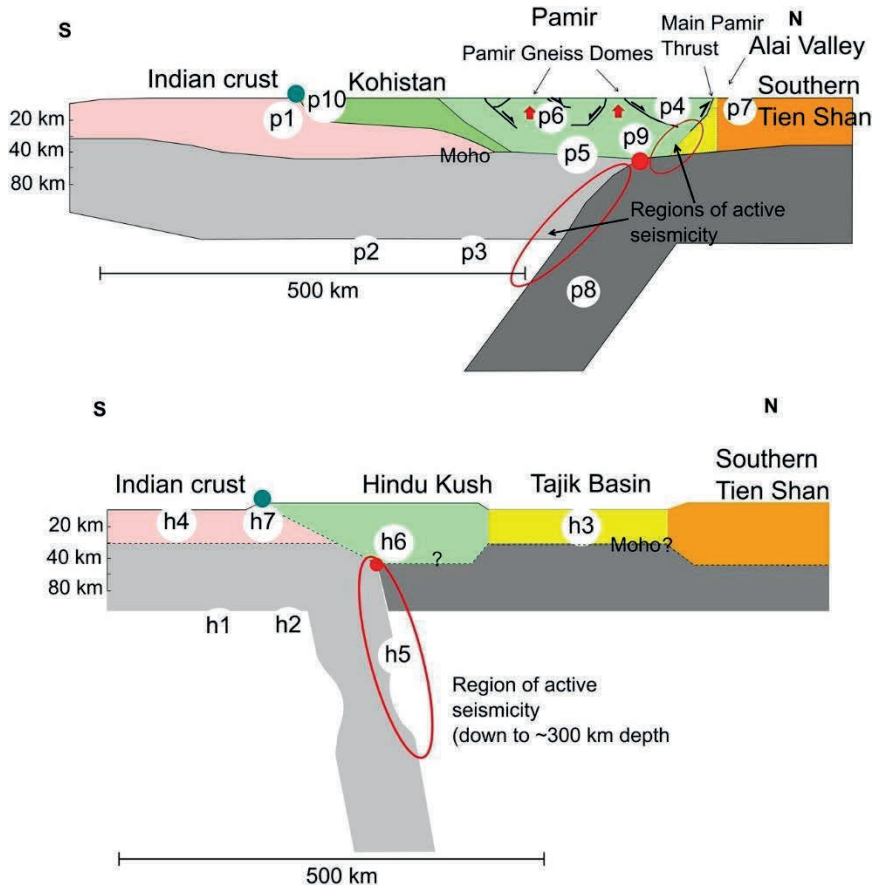

Figure 2.5. Schematic cross-sections of (top) the Pamir (modified from Mechie et al., 2012), and (bottom) the Hindu Kush, showing a list of key features for the Pamir (p1–p10) and Hindu Kush (h1–h7) that require explanation. See text for further details. V ≈ H.

2.7 Design of the Numerical Models

The numerical geodynamical models were computed using the two-dimensional thermomechanical finite element software SOPALE-nested (Beaumont et al., 2009; Fullsack, 1995; see modeling methods in supporting information), which calculates

deformation of earth materials at the mantle scale as either frictional-plastic or creeping viscous flow and solves an energy balance equation for the temperature field (equations A1–A3). The geometries of the H (Hindu Kush) and P (Pamir) model types (Figure 2.6) are simplifications of the natural equivalents but contain Asian accreted terranes restored to their initial widths as estimated above. Model regions are labeled with an acronym derived from the natural setting, which distinguishes models from observations while allowing easy comparison. The modeling methodology is similar to our earlier publications (e.g., Kelly et al., 2016, 2020).

The models have standard uniform layering for all continental regions (except "fringe" continents, described below; Table A2), comprising 24, 12, and 84 km thick continental upper/middle crust, lower crust and CLM (with total lithospheric thickness 120 km). The range of chemical densities of the retrolithosphere CLMs (Figure 2.6) should be interpreted to reflect differing amounts of chemical depletion (e.g., Mg#, Lee, 2003) and these variations are investigated in the model experiments (Table A2, Figure 2.6). The I-CLM and IR (Indian rifted margin)-CLM of the prolithosphere have constant chemical depletion such that their density is 50 kg/m^3 less than the sublithospheric mantle, corresponding to a close-to-cratonic CLM with an Mg# ~92–93 (Lee, 2003), appropriate for India. Initial models demonstrated that prolithosphere CLM with higher density prevents advancing S-point subduction, which fails a basic requirement of models for the Hindu Kush and Pamir systems. Oceanic, NT, lithosphere comprises 2, 6, and 92 km thick layers of sediment, oceanic crust, and oceanic mantle lithosphere in which the upper 60 km of the latter is chemically depleted and 30 kg/m^3 less dense than the oceanic lower lithosphere and sublithospheric mantle.

Our Hindu Kush section aligns with the western edge of the Indian continent which is thought to comprise a north-south rifted margin with thin crust. Models with 24–36 km thick crusts were tested. The 30 km crustal model is the one presented here in which the "fringe" margin comprises respectively, 22, 8, and 70 km thick upper crust, lower crust and lithospheric mantle, considered to have been inherited from the rifting. In the models this lithosphere is further thickened by accretion of cooling sublithospheric mantle with

the thickness increment determined by the initial steady-state temperature field of the model. At depths less than 60 km, the accreted lithospheric mantle is depleted by 30 kg/m^3 to represent the effects of decompression melting.

Model materials deform by frictional-plastic flow or viscous creeping flow (equations A4 and A5, Table A2). The Drucker-Prager (frictional-plastic) yield stress (equation A4) depends on the calculated dynamical pressure, and the effective internal angle of friction, ϕ_{eff} which takes into account the effect of near-hydrostatic pore pressure (supporting information). The friction angle of materials is decreased linearly from $\phi_{eff} = 15°$ (initial friction angle) to 2° (strain-softened friction angle) as the effective strain increases from 0.5 to 1.5 (Table A2). Oceanic sediment, which is considered to be weaker, has ϕ_{eff} 8°–2°.

When viscous, materials deform by power-law flow (equation A5) based on reliable laboratory measurements of wet quartzite, dry Maryland diabase, and wet olivine (supporting information for references). Viscous flow also involves linear strain-weakening determined by W_s, the strain-weakening factor (equation A5), which varies from 1 to 3 as the effective strain increases from 5 to 10 (supporting information). We model stronger and weaker materials than the laboratory-derived flow laws using the scaling factor f (equation A5). This scaling represents variations between dehydrated or hydrated rock types, and/or differences in composition (see Beaumont et al., 2006; Butler et al., 2014; supporting information).

High stress in colder regions of the lithospheric mantle is limited to be close to but not less than the Peierls threshold stress, σ_p(Table A2). This is achieved by rescaling the effective viscosity in high stress regions by a Peierls weakening factor. This approach approximates the rapid decrease in material viscosity experienced under an exponential flow law beyond the Peierls threshold stress (supporting information).

The upper surface of models is a stress-free boundary, and the base and sides are respectively free-slip and no-slip boundaries. The left lithospheric boundary velocity

decreases with time, $V_p(t)$ = 14–3.6 cm/year (Figure 2.6b), to represent slowing of the Indian plate after collision, while the right lithospheric boundary condition is $V_r(t) = 0$. Total convergence is 3,150 km in 56 Myr. Sublithospheric velocity boundary conditions act to ensure the model is volume and isostatically balanced.

Continental crust has laterally uniform radioactive heat production (A_R 2.0 and 0.4 $\mu W/m^3$) for the upper/ middle, and lower levels, respectively. Coupled with the thermal boundary conditions, no-flux side boundaries, and 21 mW/m^2 basal heat flux, the resulting initial steady-state surface heat flow and Moho temperatures on the continents are 74 mW/m^2 and ~650°C, but lower for the Indian fringe margin. The initial temperature at the base of the lithosphere throughout the model is ~1,370°C. Material thermal expansivity (α) and conductivity (K) are temperature-dependent, with their values linearly varying (e.g., from K_1 *to* K_2) over a range of temperatures (e.g., T_1 to T_2; Table A2). Other thermal properties are given in Table A2.

Sediment and upper/middle continental crust undergo melt-weakening as in Butler et al. (2015) except that we use a different solidus (supporting information). The viscosity decreases linearly from the calculated power-law value to a fixed linear value of 10^{19} Pa s from the pressure-dependent dry solidus to the solidus temperature plus 50°C. This represents the effect of a small amount (4%–7%) of partial melt.

Crustal materials undergo reversible pressure- and temperature-dependent density changes corresponding to the eclogite and coesite-eclogite phase transitions, following Warren et al. (2008) (see Table A2 for density changes). In addition, upper/middle crust coesite-eclogite materials which reach pressures and temperatures 100°C above the dry solidus undergo an increase in power-law viscosity (f = 1.25–10), and may subsequently revert to high-pressure eclogite densities, but do not further retrograde to normal crustal density. This is designed to model, in a simple way, the formation of restite after extraction of a small amount of melt at these pressures and temperatures (Massonne and Fockenberg, 2012). Mantle materials undergo a reversible olivine-perovskite phase change at the upper-lower mantle boundary (~660 km depth) by a reaction with a

Clapeyron slope of −2.0 MPa/K, resulting in a density increase (proportional for all mantle materials) of ∼8% (for a discussion of these parameters, see Billen, 2010). Crustal materials undergo equivalent phase changes at the upper-lower mantle boundary.

Models have an upper free surface, and the model topography is a product of the model calculation without any imposed constraints except for water loading where the surface is below sea level. Slope-dependent surface erosion acts on the local subaerial topography. It varies according to the local slope of the model surface, where it is defined by a maximum erosion rate *E(x)* that operates on a slope of 45°, scaled down linearly to the local slope of the surface. The erosion rate is also modulated by a spatial climate function (Figure 2.6d) designed to reproduce humid (moderate erosion) conditions on the left (south)-facing orogenic front and relatively arid (lower erosion) conditions over the interior plateau region. The climate function moves to follow the development and movement of the orogen. Maximum erosion rates are ∼0.5 cm/year on the orogenic front.

2.7.1 Experimental Parameters

As noted above, we suspect that both the Hindu Kush and the Pamir sections evolved to produce delamination of a region of CLM under Asia. Following our previous work (Kelly et al., 2016, 2020) we focus on cases where some of the Asian terranes have weak and dense (less depleted) CLM, which is therefore prone to delamination.

Cases of weak CLM are tested by scaling the *f*-factor of the olivine-based mantle material (Karato and Wu, 1993) to represent the hydration level of mantle peridotite (Hirth and Kohlstedt, 1996), with $f = 5$ for "dry" peridotite and $f = 1$ for moderately hydrated "wet" peridotite (see Butler et al., 2014, Figure 1b for the close agreement of this *f*-scaling of viscosity with the effect of water content on experimental flow laws for olivine). Model sublithospheric upper mantle has $f = 2$.

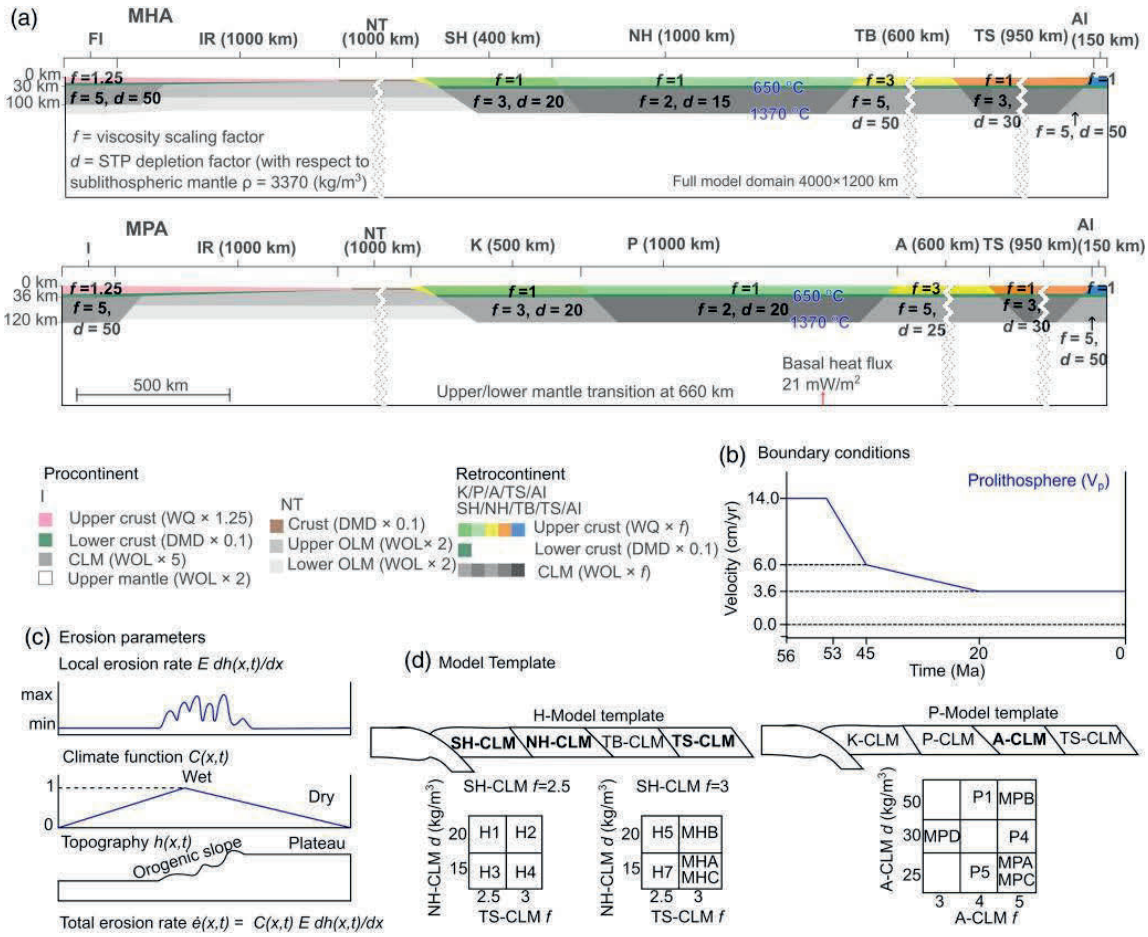

Figure 2.6. a) Initial model geometry for the H and P models (MHA and MPA), comprising at left an Indian continent, FI, "Fringe India" (representing the west Indian rifted margin) which has thin (30 km) crust for H models and normal thickness crust (36 km) for P models; IR, their northern rifted margins with a depth-dependent extension geometry; NT (Neotethys), oceanic Neotethys lithosphere overlying upper mantle to 660 km deep and then lower mantle to 1,200 km; and at right a retrocontinent (Asia). The H-model retrocontinent contains SH (South Hindu Kush), NH (North Hindu Kush), TB (Tajik Basin), and TS (Tien Shan) terranes and an AI terrane (Asian Interior), a strong lithosphere region representing undeformed interior Asia to the north. Correspondingly, P-model retrocontinent contains K (Kohistan), P (Pamir), A (Alai), TS (Tien Shan) terranes and also an AI (Asian Interior) terrane. The *f*-values for the crust and *f* and *d* CLM values of each terrane used in models MPA and MHA are shown. (b) Variation in convergence velocity with time applied to the left lithosphere boundary. (c) Spatially variable, climate and slope-dependent erosion model in which the horizontal axes represent the x-axis of the model, that is, horizontal position. (d) Shows a template of the range of models that were tested. In these models the *f* and *d* values for the MH models (NH, SH, and TS- CLMs) and MP (A-CLM) were varied with respect to those shown in (a), which are those for MHA and MPA. CLM, continental lithospheric mantle.

CLM is also expected to be chemically depleted (exhibited by the Mg#) from partial melting (Griffin et al., 2009; Lee, 2003). In the models CLM chemical depletion, d (0–50 kg/m^3), represents the decrease in mantle lithosphere density with respect to undepleted sublithospheric upper mantle (ρ = 3,370 kg/m^3). Dense model CLM may either be interpreted to represent low levels of initial chemical depletion or refertilization of depleted peridotite through melt metasomatism. The effects of melt metasomatism (dense CLM) and rehydration (weak CLM) may be present individually, or together both in nature and in the models.

Model parameters have also been chosen to explore how they affect processes responsible for observations outlined in Section 2.6, and the S-point advance and style of Indian CLM subduction.

2.8 Model Results and Comparison with Observations

An initial wider parameter search allowed us to focus on sets of eight and six models for the H and P sections (Figure 2.6). All of these models are geometrically the same as those shown in Figure 6 but have variations in the depletion densities (*d*) and viscosities (*f*) of the SH (Southern Hindu Kush), NH (Northern Hindu Kush) and TB (Tajik Basin) CLMs (H models) and of the A (Alai) CLM (P models) (Figure 6 and supporting information). We present here successful models, MHA and MPA, for the Hindu Kush and Pamir sections, complemented by other models that illustrate the effects of small variations in model properties (Section 2.9, Supporting Models). Model time is given in Ma (million years before present) assuming that contact of Indian and Asian lithospheres was at 56 Ma. This choice enables direct comparison with observed ages.

2.8.1 MHA (Hindu Kush)

Model HA (MHA; Figure 2.7 and Animation MHA) is a case where the CLMs of SH and NH (South and North Hindu Kush) are weaker and denser (*f* = 3, *d* = 20; *f* = 2, *d* = 15, respectively), than the strong and depleted TB-CLM (Tajik Basin) (*f* = 5, *d* = 50) to the

north, which represents cratonic-like CLM. For the same reason, the TB-terrane upper/middle crust is also strong ($f = 3$; Figure 2.6). The TS-CLM (Tien Shan) has ($f = 3$, $d = 30$). MHA achieves each of the required features of a successful model as outlined in Section 2.6 (h1–h7, Figure 2.5b).

MHA is shown starting with contact of the distal IR (Indian rifted margin) and SH terrane at 56 Ma (Figure 2.7a). Break-off of IR at 48.5 Ma (Figure 2.7b) follows shortly after complete IR subduction. Subduction and break-off of the 1,000 km wide IR can explain the amount of fringe Indian CLM that is required to be removed (h1) as implied by the Hindu Kush balanced sections (Section 2.5). The break-off also occurs before northward advance of the S-point in MHA. If correct, this implies that the imaged slab (Figure 2.2), inferred to be Neotethys, represents both the Neotethys and the Indian margin.

At 48.5 Ma, subducted UHP crust is shown at and below the base of the lithosphere (Figure 7b, red). Its exhumation is not synchronous with slab break-off but is delayed by 4 Myr to 44.5 Ma (Figure 2.7b inset, light blue). This timing coincides with that of the observed Kaghan UHP exhumation (e.g., O'Brien, 2019) further to the east on the Pamir section. No UHP crust has been reported from the Hindu Kush section; this is also consistent with MHA, which later reburies the UHP rocks by underthrusting, as discussed below. Absence of exhumed UHP crust in the Hindu Kush does not prove exhumation and reburial, but MHA does indicate that both the Hindu Kush and Pamir regions could have had similar early evolutions, including UHP exhumation.

Following break-off of IR, the Asian side of the system becomes highly contractional, with the FI-SH (Fringe India-South Hindu Kush suture, i.e., Indus-Yarlung equivalent) and S-point migrating northward at approximately the convergence velocity. Contraction caused by FI-terrane indentation is accommodated by thickening of the NH-crust and thickening and folding of the NH-CLM by 39.5 Ma (Figure 2.7c, inset), the weakest CLM in the system. At 38.5 Ma NH-CLM delaminates and sinks into the mantle (Figure 2.7c).

Observations of the last Neotethys marine invasion of the Tajik Basin and western Tarim Basin (Wang et al., 2019) at 40 Ma and its final withdrawal at 37 Ma are consistent with the delamination of the NH-CLM in MHA. The thickening of the NH-crust and the downward pull of the delaminating NH-CLM can explain the flexural subsidence leading to the marine invasion, and the subsequent rebound following NH-CLM delamination can explain the final withdrawal (Figure 2.7c and inset).

Delamination of NH-CLM exposes NH-crust to upwelling sublithospheric mantle (Figure 2.7c) which may produce decompression melting, yielding basalts that intrude and/or underplate the crust. Exposure of the NH-crust to hot asthenosphere heats its base to 1,100°C. By 37 Ma the SH-CLM begins to peel away from the crust and delaminate from north to south (Figure 2.7d, inset) while the overlying SH-crust shortens. By 34 Ma most of the SH-CLM delaminates and sinks into the mantle (Figure 2.7d). The combined NH- and SH- CLM delamination in MHA accounts for the amount of Asian CLM to be removed (h2) that is implied by the Hindu Kush balanced sections (Section 2.5). Following SH-CLM delamination a small part of it remains intact below the shortened, now 200 km wide, SH-crust (Figure 2.7e).

By 29.5 Ma FI-CLM and residual SH-CLM begin to subduct (Figure 2.7e). Thin, 30 km, FI crust is colder than standard 36 km thick crust and therefore remains more strongly coupled to the FI-CLM during subduction. As a result, most of the FI-crust and previously exhumed UHP material is underthrust beneath SH-crust (Figures 2.7d and 2.7e) leaving only a small Himalaya mountain belt. Later, FI-crust is thrust northward and underplates all of the remaining NH crust at a depth of 75 km (Figure 2.7e). Underthrusting of FI-crust contrasts with decoupling and accretion of hotter I-mid and upper crust seen in H-T models with standard thickness crust (Kelly et al., 2020). The underthrusting potentially explains the lack of a significant Himalayan thrust belt in the Hindu Kush region (h4, Figure 2.1) in contrast with that elsewhere in the H-T orogen. If correct, this implies that Indian crust now resides under the Hindu Kush.

FI-CLM begins to subduct at a steep angle and by 22.5 Ma reaches ~400 km depth (Figure 2.7e, inset). Beginning at 15.5 Ma the relatively buoyant FI-CLM slab folds back and floats up under the FI continent (Figure 7e, inset) while FI-CLM underthrusting continues.

Since FI-CLM is depleted and therefore buoyant, the system remains compressive during continued FI-subduction, resulting in advancing subduction and continued shortening of the Asian terranes, and closing of the gap between the FI-CLM and the TB-CLM by 15.5 Ma (Figure 2.7e, inset). Starting at 9 Ma the now doubly thickened SH- and NH-crusts, as well as the strong TB terrane, resist further deformation, and the distant TS terrane begins to shorten (Figure 2.7f, inset).

At 0 Ma (Figure 2.7f) the FI-CLM has subducted to 400 km. The S-point has advanced by ~1,600 km, while the FI-SH suture (Indus-Yarlung equivalent) has advanced by ~1,500 km. Overall, there has been a remarkable shortening and destruction of the SH- and NH-crusts which have shortened to just 350 km wide. SH-crust has almost completely disappeared by underthrusting and erosion. 38.5–~25 Ma SH-crustal shortening is coupled to relatively strong erosion (max 0.5 mm/year) of its southern end because, in the absence of a significant Himalaya, this region now forms the main eroding orogenic front. This is in contrast to the rest of the H-T system where the main orogenic front comprises Himalayan Indian crust.

The configuration described above is consistent with the observed contact between India and a narrow Hindu Kush (h4), which raises the question of our hypothesized existence of the model SH terrane. This terrane, correlative to the Kohistan arc, is required to balance the initial width of the Asian lithosphere in the Hindu Kush region if its Indus-Yarlung suture was at 19–22°N at collision. MHA evolves such that SH-crust is no longer exposed which is entirely consistent with, and partly explains, the narrow Hindu Kush (h4) and the missing equivalent of the Kohistant arc.

The stronger TB-crust has only shortened by 250 km, leaving it 350 km wide at 0 Ma, and preserves 300 km of undeformed northern TB-crust, consistent with observations of the thickness of the main crustal layer (Schneider et al., 2019). While shortening skips over the northern TB main crustal layer, the TS-crust experiences ~250 km of shortening in MHA (Figure 2.7f), which is also consistent with observations.

The final MHA geometry agrees well with the observed ~1,700 km and ~1,900 km of Indus-Yarlung suture and S-point advance respectively, based on the assumed 19°N slab break-off position, and with the narrow Hindu Kush orogen (h6–h7).

The final mantle-scale configuration of MHA shows a steeply dipping 400-km-long limb of subducted, largely FI-CLM beneath the Hindu Kush orogen. This style of steep subduction is broadly in agreement with seismic tomographic images (Kufner et al., 2016; Replumaz et al., 2014), but does not exhibit the extension to 600 km owing to current slab break-off (Kufner et al., 2016), an aspect discussed in Section 2.9.

As noted in Section 2.7, we specifically tested MH models with a range of FI crustal thicknesses, 24–36 km, following the Kufner et al. (2016) proposal that thin crust, Fringe India, subducted under the Hindu Kush and may account for present configuration of subducted Indian lithosphere. Models with 24 km crust are too cold to detach efficiently at the base of the mid-crust and were therefore unsuccessful. Lithosphere with full, 36 km, crust is hotter, owing to a thicker layer of radioactive heating, and detaches easily at the base of the mid-crust, which leads to accretion of a large Himalaya and not the inferred underthrusting of Indian crust beneath the Hindu Kush. MHA, with 30 km crust, gave the best results, probably because the intermediate lithospheric temperature both required crustal underthrusting before detachment, and facilitated subduction of the less buoyant FI-CLM. Although we tested FI crustal thickness, the more general conclusion is that models with a thinner and/or colder lithosphere will probably satisfy observational constraints from the Hindu Kush.

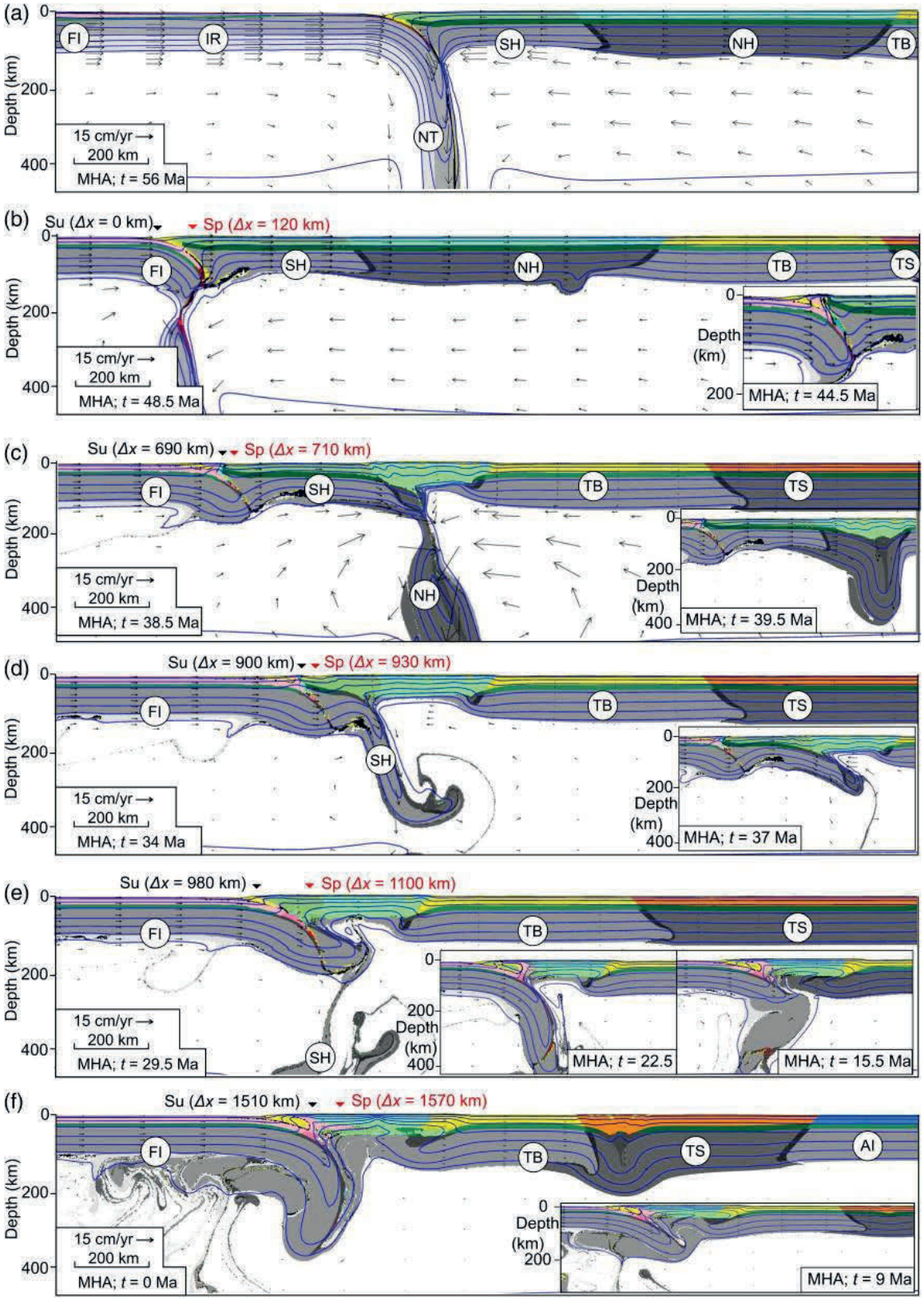

Figure 2.7. Evolution of MHA (Hindu Kush model). Times (*t*) are measured backward from the present assuming continental contact at 56 Ma, and isotherms are shown every

200°C starting at 100°C. Note that panels show different regions of the model, progressively stepping to the right. Crustal suture, Su (equivalent of the Indus- Yarlung suture), and S-point, Sp, are shown with the distance (Δx) they have been translated to the right (north) since the IR (India rifted margin) slab break-off. Arrows are velocity vectors. Dark-gray passive marker regions between continental lithospheric mantles (CLMs) have the same properties as adjacent CLM to the right/north. See Figure 2.6a and Section 2.8.1 for MHA model properties. Model regions are given acronyms corresponding to the natural system; FI (Fringe India), IR (Indian rifted margin), SH (Southern Hindu Kush), NH (Northern Hindu Kush), TB (Tajik Basin), TS (Tien Shan), and AI (Asian Interior). CLM, continental lithospheric mantle.

2.8.2 MPA (Pamir)

MPA (Figure 2.8, Animation MPA) is a case where the CLMs of the Pamir cross-section terranes, K (Kohistan) and P (Pamir), are weaker and denser ($f = 3$, $d = 20$; $f = 2$, $d = 20$, respectively), than the A-CLM (Alai) ($f = 5$, $d = 25$) to the north. The TS-CLM (Tien Shan) has ($f = 3$, $d = 30$). As with MHA, the A-terrane (TB equivalent) upper/middle crust in MPA is strong ($f = 3$). A-CLM, while as strong as the TB-CLM, is less depleted ($f = 5$, $d = 25$). For comparison, supporting model MPC (Section 2.9) has A-CLM as strong and depleted as the TB-CLM in MHA.

MPA reproduces most of the required features of a successful model as outlined in Section 2.6 (p1–p10, Figure 2.5b). Supporting models (Section 2.9) show how the remaining observed features may emerge.

MPA evolution is shown starting with contact of the distal IR (Indian rifted margin) and K-terrane at 56 Ma (Figure 2.8a) following subduction of the NT (Neotethys) oceanic lithosphere. The NT slab breaks off at 48.5 Ma at a shallow depth (Figure 2.8b) following subduction of IR and as the full thickness I-lithosphere (India) collides with the K-terrane. I-crust, subducted to near the base of the lithosphere and subject to UHP metamorphism (red), exhumes (blue) to the surface near the I-K (Indus-Yarlung) crustal suture at 47 Ma, delayed by 1.5 Myr with respect to slab break-off (Figure 2.8b, inset).

Subduction and break-off of the wide IR may explain p1, removal of the required amount of Indian lower lithosphere inferred from the balanced lithospheric-scale sections (Figure

2.4). The IR break-off is at the same location as the NT slab. As with MHA, this implies that the tomographically located slab (19–22˚N), interpreted to be Neotethys, likely represents a composite of Neotethys and Indian lithospheres. Exhumation of I-crustal UHP rocks near the I-K suture at 47 Ma in MPA (Figure 2.8b, inset) is in agreement with p2, exhumed 47 ± 1 Ma Indian UHP rocks at Kaghan, near the Indus-Yarlung suture (Hu et al., 2016; O'Brien, 2019).

After IR break-off, I-lithosphere indents the retrolithosphere, leading to rapid I-K crustal suture, S-point advance, and shortening of the retrolithosphere. Shortening focuses in the weakest terrane, P, near the P- to A-terrane boundary, owing to the contrast in CLM strength across this boundary. Shortening of P-CLM (Figure 2.8c, inset) is therefore accommodated in a remote part of the system, not adjacent to the I-K suture where the indenter acts. By 37 Ma the I-K suture has advanced 630 km at essentially the I-lithosphere convergence velocity (Figure 2.8c). P-CLM first folds, then delaminates by northward subduction (Figure 8c, 37 Ma), and breaks off and sinks by 34.5 Ma.

Delamination leaves a limited region of P-crust exposed to hot upwelling asthenosphere (Figure 2.8d). This region is much narrower than the original width of the P-terrane because some P-CLM remains and the P-crust has shortened and thickened during delamination. The upwelling hot asthenosphere may explain the heat source for, and origin of p4, 42–37 Ma Vanj magmatism, by decompression melting. Upwelling is late with respect to Vanj magmatism in MPA, but supplementary model MPD (Section 2.9.4) is in better agreement with the timing of Vanj magmatism. In particular, this decompression explanation is in general agreement with the Chapman et al. (2018) interpretation that Vanj magmatism was derived from the asthenosphere and emplaced into the Central/South Pamir where it assimilated crustal material. The limited spatial extent of the upwelling in MPA (Figure 2.8d) is also consistent with that of the Vanj magmatism.

Following removal of P-CLM, continued indentation of the retrocontinent shunts the K-CLM and residual P-CLM northward under the exposed P-crust, eventually contacting the

A-CLM, and by 25 Ma forcing double subduction of the composite K/P-CLM and the A-CLM (Figure 2.8d, inset). Subduction of the K-CLM produces progressive north to south shortening of the southern P-crust and K-crust. During forced subduction of the A-CLM, the strong overlying A-crust resists shallow detachment and is subsequently underthrust southward beneath P-crust (Figures 2.8d and 2.8e and insets).

By 20 Ma, continued subduction of the composite K/P-CLM causes K-CLM to rupture, leading to its nearly complete removal, and exposing most of the now thickened P-crust to hot, upwelling asthenosphere, thereby heating its base to 1,100°C (Figure 2.8e).

Basal heating of the P-crust to ~1,100°C by 20 Ma (Figures 2.8d and 2.8e) may explain the timing and mechanism of metamorphism of p5, crustal xenoliths found within the Dunkeldik volcanics, which reached ~1,100°C at 2.4–2.7 GPa sometime between 57 Ma and ~11 Ma (the time of volcanism; Ducea et al., 2003). The large range of metamorphic ages interpreted for these xenoliths may reflect the two stages of CLM delamination and crustal heating seen in MPA, namely; P-CLM delamination at 34.5 Ma and more pervasive long-lived heating following K-CLM delamination at 20 Ma. In particular, time of heating following the earlier P-CLM delamination agrees well with the Ducea et al. (2003) interpretation that crustal materials under the Pamir reached partial melting conditions starting at 34 Ma. It is also consistent with the additional heating and burial of the already hot xenoliths starting at ~20 Ma (Kooijman et al., 2017) which may have been caused by the second K-CLM delamination.

During indentation of the retrocontinent and subsequent P and K delamination, both the I-K suture and the S-point advance northward nearly equally (Figure 2.8e), and therefore, little I-crust is detached and accreted to the model Himalaya.

It is worth emphasizing that between IR slab break-off and removal of the K-CLM, the I-K suture advance totals 1,160 km. During this time convergence has been almost entirely accommodated within the retro-CLM (ultimately by delamination and removal) and retrocrust (by shortening and thickening) resulting in a quiescence in model Himalaya

development because there is little accretion of detached I-crust. However, during the K-CLM delamination and break-off, I-CLM starts to underthrust and the I-upper crust detaches, shortens and thickens, and the model Himalaya grows. Correspondingly, the S-point advance now outpaces that of the I-K suture (compare Figures 2.8d–f, inset). The quiescence in model Himalaya development is from the early slab break-off (~48.5 Ma) to the onset of I-CLM underthrusting (~22 Ma), spanning 26.5 Myr.

By 10.5 Ma the underthrusting I-CLM has closed the asthenospheric window under the central orogen (Figure 2.8e, inset) but the overlying crust remains hot, >900°C at its base. Contact of I- and A-CLMs at 10.5 Ma (Figure 2.8e, inset) causes the equally strong but less depleted A-CLM to delaminate slowly from south to north. As the A-CLM delaminates, A-crust continues to underthrust beneath P-crust (Figures 2.8f and 2.8e, inset).

By 8.5 Ma, hot, deep P-crust begins to upwell, forming a small dome in the P terrane (Figure 2.8e, inset). While late and limited in MPA, diapirism of hot Pamir crust may explain the Pamir gneiss domes, p6. In MPA only thermal expansion contributes to the buoyancy of hot crust driving diapirism, which is hence limited. Supporting model MPD (Section 2.9) with more buoyant crust has more fully developed domes.

The I-CLM progressively underthrusts the retrocrust (Figure 2.8f, and inset) such that at 2.5 Ma the S-point is located under the residual A-crust, resulting in 1,980 km of S-point advance, while the I-K suture has advanced by 1,560 km.

The 2.5 Ma geometry of MPA (Figure 2.8f) agrees well with the current maximum combined N-S width of the Kohistan and Pamir terranes (550 km in MPA and 500 km observed), a south-dipping Asian slab (Kufner et al., 2016; p8), ~2,150 km and ~1,800 km of S-point (p9) and Indus-Yarlung suture advance (p10), respectively, which are both subject to error estimates in the position of the subducted Neotethys. With $d = 25$, the A-CLM is negatively buoyant and subject to failure and necking (Figure 2.8, inset). The exact timing of this failure is not particularly important, but MPA clearly shows both

intact A-CLM at 2.5 Ma and necked A-CLM at 0 Ma, both well within the error estimates of the total convergence and the convergence velocity distribution.

Peeling away of the A-CLM in front of the advancing I-CLM results in significant shortening and underthrusting of A-crust (Figure 8f), with only 150 km of the previously 600 km wide A-crust exposed at the surface. This mechanism can explain the large advance of the Pamir over the Alai terrane along the Main Pamir Thrust, p7 (Burtman and Molnar, 1993), leaving only residual exposure of Alai-crust in the Alai valley, and is further developed in MPD (Section 2.9).

Initially, the combined widths of the K and P crusts in MPA were 1,500 km, but by the end (Figure 2.8f, inset) they have shortened to ~550 km and are 60–70 km thick. The combined A- and TS-CLMs delaminate and dip to the south ahead of the advancing I-CLM.

Deformation has also propagated into the TS-crust with 280 km of shortening since 10 Ma (Figure 2.8f, Animation MPA). Removal of a total width of 1,500 km of K- and P-CLMs, combined with the 600 km of subducted A- and TS-CLMs, provides a suitable explanation for p3, the required amount of removed Asian-CLM (2,150 km) inferred from the balanced sections.

In summary, Model PA evolves through several emergent phases, namely: early subduction and removal of a wide IR; removal of Asian lithosphere by rapid S-point advance and delamination; and finally, underthrusting of Indian CLM beneath the retrocrust, leading to “hard collision” of the CLMs and delamination of the A-CLM. These emergent behaviors of the lower lithosphere in turn strongly influence the style of crustal thickening, producing far-field thickening of the P-crust initially far from the suture zone, delayed thickening of the I-crust during the quiescent period, and finally shortening or overthrusting of the A-crust by the P-crust. Moreover, CLM delamination provides mechanisms to explain the observed magmatism, the presence of hot crustal

xenoliths, and gneiss doming. This emergent MPA evolution obviates the need to invoke precursor removal of CLM beneath the Asian terranes as in Sippl et al. (2013a).

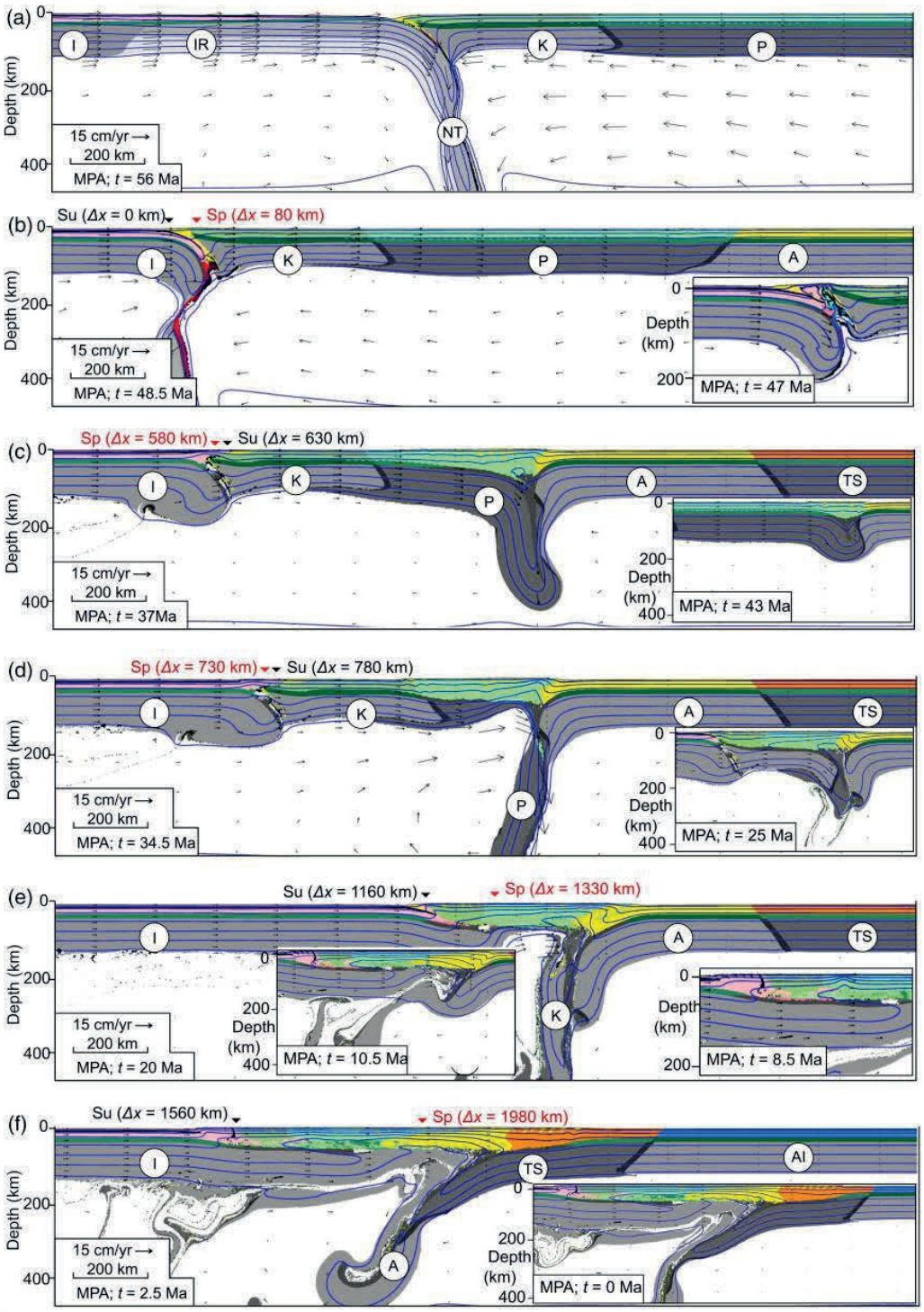

Figure 2.8. Evolution of MPA (Pamir model). Times (t) are measured backward from the present assuming continental contact at 56 Ma, and isotherms are shown every 200°C starting at 100°C. Note that panels show different regions of the model, progressively

stepping to the right. Crustal suture, Su (equivalent of the Indus-Yarlung suture), and S-point, Sp, are shown with the distance (Δx) they have been translated to the right (north) since the IR (India rifted margin) slab break-off. Arrows are velocity vectors. Dark-gray passive marker regions between continental lithospheric mantles (CLMs) have the same properties as adjacent CLM to the right/north. See Figure2.6a and Section 2.8.2 for MPA model properties. Model regions are given acronyms corresponding to the natural system; I (India), IR (Indian rifted margin), K (Kohistan), P (Pamir), A (Alai), TS (Tien Shan), and AI (Asian Interior). CLM, continental lithospheric mantle.

2.9 Supporting Models (Sensitivity Tests)

Models MHA and MPA were chosen from a larger set of sensitivity models. Figure 2.9 shows how small variations in the model properties lead to different emergent behaviors.

2.9.1 Double Subduction in Pamir Models: Sensitivity to Strong Alai Terrane CLM

Model PB (MPB; Figure 2.9a) illustrates a Pamir model in which the A-CLM (Alai) has the same properties as TB-CLM (Tajik Basin) in MHA, which makes the A-CLM buoyant and more resistant to forced delamination. Both MPA and MPB have A-CLM f = 5. The increased depletion density, d = 50 versus d = 25, in MPB means that I-CLM and A-CLM have the same properties and it is therefore not surprising that the later stages of the evolution lead to incipient double subduction, with neither CLM capable of dominating (Figure 2.9a). There is correspondingly much less delamination of A-CLM and advance of the P-crust over the A-crust than in MPA. The earlier evolution of MPB is the same as MPA.

Double subduction in MPB indicates that adopting the same CLM properties for the A and TB terranes (f = 5, d = 50) does not reproduce the inferred single-sided delamination/subduction of the Asian lithosphere beneath the Pamir. Earlier we suggested that both the Tajik Basin and Alai terranes may be westward continuations of the Tarim Basin cratonic-like lithosphere, which is expected to be strong and highly depleted (f = 5, d = 50). MHA shows this is acceptable for the Tajik Basin, explaining the resistance to delamination of its CLM and resistance to deformation of the overlying Tajik Basin crust.

The apparently less depleted Alai-CLM may result from metasomatism of an originally cratonic-like mantle.

2.9.2 Double Subduction in Hindu Kush Models: Sensitivity to NH-CLM Properties

Model HB (MHB) illustrates that Hindu Kush models may also develop double subduction. MHB is the same as MHA except the NH-CLM (North Hindu Kush) has d = 20 versus d = 15. The small increase in depletion density makes the NH-CLM more resistant to delamination and therefore subduction advance is enhanced with respect to MHA. This advance is further exploited during underthrusting of FI-CLM (Figure 2.9b, inset, 15.5 Ma) which shows the early stage of FI-CLM and TB-CLM collision leading to the onset of delamination of TB-CLM. At a similar time in MHA (Figure 2.7f, inset, 16.5 Ma) the two CLMs have just made contact. Between 16 and 0 Ma further subduction advance in MHB leads to double subduction (Figure 2.9b).

MHB demonstrates that strong, depleted TB-CLM is vulnerable to delamination if there is enough subduction advance of FI-CLM. Taken together, the MPB and MHB results can be interpreted to suggest that the current configurations of both the subducting Hindu Kush and Pamir CLMs may be transient, with the potential that one or both could evolve into double subduction.

2.9.3 Pamir Domes: the Effect of Buoyant Melted Crust

Model MPC (Figure 2.9c) is identical to MPA, except that the buoyancy of the P-crust (Pamir) is enhanced by a density decrease of 100 kg/m3 where the temperature is above 750°C. This reduced density represents simulated melting to produce hot migmatitic crust and corresponds to the bulk density decrease when 20% by volume of melt is retained (Zhu et al., 2011). Following delamination of the P-CLM in MPC (Figure 2.9c, 35.5 Ma), the base of the P-crust heats up to >900°C by exposure to the hot upwelling asthenosphere, and subsequently undergoes density reduction owing to simulated melting. Hot buoyant crust rises diapirically into the overlying upper crust, forming a fully

developed dome in the northern P-terrane with approximately 30 km of exhumation, in agreement with the 30–40 km of exhumation inferred for the Shakdara dome, p6 (Stübner et al., 2013). Doming in the northern P-terrane in MPC enhances underthrusting of A-crust as hot, buoyant P-crust within the dome is thrust over the A-crust.

Following subsequent delamination of the K-CLM starting at 26 Ma (Figure 2.9c, inset), and re-exposure of P-crust to hot upwelling asthenosphere, another dome is formed in the central P-crust. The timing of the second doming event is in reasonable agreement with the 21–2 Ma uplift of the Shakdara dome (Stübner et al., 2013) and the ∼20–4 Ma uplift of the Alichir dome (Worthington et al., 2020). Doming events in MPC follow soon after delamination of the P-and later K-CLMs. This connection between delamination and doming may explain the emergence of multiple domes observed in the Pamir if delamination is diachronous and piecemeal, for example, P-CLM followed by K-CLM.

2.9.4 Vanj Magmatism; Pamir Model Sensitivity to Weaker Alai Terrane CLM

Model MPD (Figure 2.9d) is an example where the A-CLM (Alai) is weaker and slightly more depleted than in MPA ($f = 3$, $d = 30$ in MPD vs. $f = 5$, $d = 25$ in MPA); all other properties are unchanged. The weaker retrocontinent in MPD compared with MPA encourages indentation of the retrolithosphere and leads to P-CLM delamination and subsequent upwelling asthenosphere and heating of P-crust by 36.5 Ma (Figure 2.9d), 2 Myr earlier than in MPA. P-CLM delamination may explain the heat source and origin of (p4) Vanj magmatism, and the timing of P-CLM delamination in MPD agrees with that of Vanj magmatism, 42–36 Ma (Chapman et al., 2018). MPA and MPD illustrate the sensitivity of the timing of P-CLM delamination to model CLM properties.

2.9.5 Hindu Kush FI Slab Breakoff; Sensitivity of Subducted Fringe India to Density Variations

As noted earlier, the subducted lithosphere under the Hindu Kush is breaking off (e.g., Kufner et al., 2017) which is not replicated in MHA. In MHC, we have tested changing

the eclogite-facies density of the lower crust to 3,400 kg/m^3, representing a mafic protolith composition, and decreasing the amount of CLM depletion to 25 kg/m^3, separately and in combination, during the last few million years of MHA evolution. This represents a preliminary sensitivity analysis for potential causes of slab break-off. The combined density changes cause slab break-off to be well underway 2 Myr after the changes, shown at 0 Ma (Figure 2.9e). The depth and style of the break-off is similar to that proposed by Kufner et al. (2017) (Figure 10 P2) with a simple shear zone at an approximate depth of 200 km (Figure 2.9e, inset). This style of break-off of a subducted slab is an alternative to the "sinking blob" (Molnar and Bendick, 2019), or mantle drip (Koulakov, 2011), but more modeling, and probably more detailed observations, are required to distinguish which mechanism operates.

MHA requires buoyant FI lithosphere in order to produce advancing subduction/indentation earlier in its evolution. If this is true for Fringe India, the negatively buoyant lithosphere causing the observed slab break-off is probably a localized denser region. That Fringe India may have variations in its lithospheric properties is not surprising if it is actually along-strike subduction of a rifted margin. Rifted margins commonly have promontories (more depleted and possibly stronger CLM) and re-entrants (basalt underplated lower crust and less depleted/metasomatized CLM), which would cause local negatively buoyant regions of the type we tested.

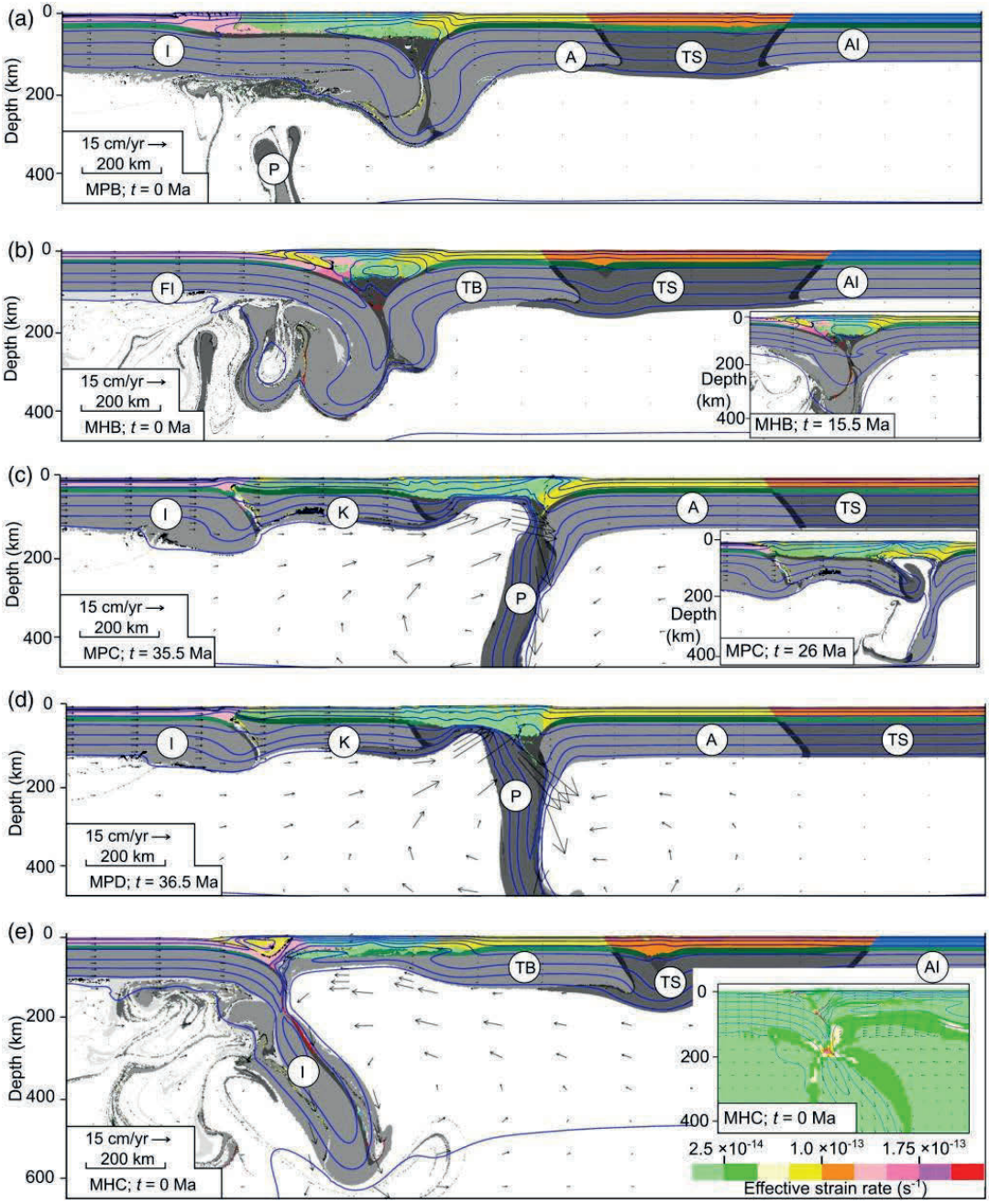

Figure 2.9. Key results from supporting P models (a, c, and d) and H models (b and e). See text (Section 2.9) for more details on the model results. Times (*t*) are measured backward from the present assuming continental contact at 56 Ma, and isotherms are shown every 200°C starting at 100°C. Note that panels show different regions of the model. Dark-gray passive marker regions between continental lithospheric mantles (CLMs) have the same properties as adjacent CLM to the right/north. Model regions are given acronyms corresponding to the natural system; For H-type models (MHB) FI (Fringe India), IR (Indian rifted margin), SH (Southern Hindu Kush), NH (Northern Hindu Kush), TB (Tajik Basin), TS (Tien Shan), AI (Asian Interior); for P-type models I (India), IR (Indian rifted margin), K (Kohistan), P (Pamir), A (Alai), TS (Tien Shan), and AI (Asian Interior). CLM, continental lithospheric mantle.

2.10 Discussion: Comparison of Models MHA and MPA and the Three-Dimensional Nature of the Hindu Kush and Pamir System

Interpretations of the tomographic seismic data and seismicity of the Hindu Kush and Pamir (e.g., Kufner et al., 2016; Kufner et al., 2017; Sippl, Schurr, Yuan et al., 2013b), as well as structural evidence from the Pamir and Tajik Basin (e.g., Abdulhameed et al., 2020), indicate that the two systems are coupled along strike and are unlikely to have evolved independently. The overall system is three dimensional. None of our two-dimensional models can address this coupling, but given their limited longitudinal separation, a parsimonious interpretation would not advocate major differences in their evolution. Here we compare MHA and MPA to see where their evolution is similar and where they differ, best viewed using the Animations (Animation MHA and MPA; see Kelly at al., 2021).

The initial geometries of both the balanced cross-sections and dynamical models assume that contact, collision, and slab break-off between India and Asia were close to 19°N, based on the tomographic images of interpreted subducted Neotethys lithosphere (Figure 2.2). Both MHA and MPA have similar restored initial Asian geometries with four previously accreted terranes south of AI, the Asian interior (Figure 2.6). The NT (Neotethys), IR (Indian rifted margin), and I (India) properties are almost the same; the only significant difference is the thickness of the Indian crust, 30 km for FI (Fringe India) and 36 km for I. In other respects, the models differ only in the strength and depletion properties of some of the Asian accreted terranes.

The early evolution of both models is the same, with subduction of NT and IR with no significant motion of the S-point or suture. Following simultaneous slab break-off, exhumation of UHP crust is 2.5 Myr later in MHA than in MPA. FI and I then indent the Asian terranes causing folding and delamination of the weakest Asian terranes CLM, NH-CLM (North Hindu Kush) and P-CLM (Pamir). P-CLM delamination in MPA (Figure 2.8) is well advanced and aligned with MHA at the time of NH-CLM break-off (Figure 2.7), but P-CLM remains attached while it is transported 150–200 km to the north before

break-off 4 Myr later. In nature, three-dimensional strike-coupling may have induced simultaneous delamination at an intermediate position. However, the potential differences between nature and models are regarded as minor, and both the Hindu Kush and Pamir can be regarded to have evolved together until and through the first delamination.

The model evolutions then diverge, with SH-CLM (South Hindu Kush) delaminating progressively from north to south, thereby shortening the SH-crust (Figure 2.7), whereas K-CLM (Kohistan) advances northward to contact A-CLM (Alai), with delamination following double subduction and with less shortening of the overlying K-crust (Figure 2.8). The opposite senses of delamination of SH-CLM, and K- and A-CLM, respectively to the south and north, sets the framework for the final stages of the model evolutions in which FI-CLM subducts to the north beneath the Hindu Kush (Figure 2.7) and TS-CLM (Tien Shan) delaminates/ peels back to the north beneath the Pamir.

In addition, unlike in MPA, the thinner, more strongly coupled FI-CLM in MHA subducts after delamination of Asian CLM (SH/NH-CLM). The partly subducted FI-crust underthrusts the retrocrust, detaches at depth and underplates the SH-crust. As a result, in contrast to I-crust in MPA, little FI detached crust remains south of the I-SH suture in MHA. This difference can account for the lack of a significant Himalaya and the demise of the SH-crust in the Hindu Kush region.

We therefore propose that the Kufner et al. (2016) hypothesis of a thinner fringe Indian lithosphere, in addition to contributing to the contrasting styles of Pamir and Hindu Kush subduction, may also explain why the Hindu Kush region lacks an analog to the large Himalayan mountain belt, owing to its stronger coupling to the down-going Indian plate. Furthermore, in the absence of a Himalayan equivalent, the southern margin of the evolving mountain belt may have been within Asia, as in MHA, thereby exposing the Asian crust to higher denudation rates, and possibly explaining why the Hindu Kush is relatively narrow compared with the Pamir.

Primary controls on the evolution of both MHA and MPA are the properties of the adjacent TB and A terranes. These need to be stronger (*f*-crust = 3 and *f*-CLM = 5) than the other Asian terranes in order to restrict the I-indentation. Higher strengths are consistent with these terranes being the westward continuation of the Tarim terrane, which is also interpreted to be strong, depleted, and cratonic-like. High strength and high depletion (*d* = 50) of TB inhibits TB-CLM delamination, thereby explaining preservation of the Tajik Basin. In contrast, the less depleted A-CLM (*d* = 25) does delaminate slowly from south to north to produce the southward-dipping, subducted Pamir slab. Attributing the different behaviors of the Tajik and Alai CLMs to small differences in density yields models results consistent with the observations, but other explanations involving different properties of the Indian lithosphere in these two regions are also possible.

Subduction/delamination of the Alai-terrane also explains underthrusting of Alai crust beneath the northward-advancing, thick, weak Pamir crust, thereby allowing the Pamir orocline to develop. The contrasting styles of deformation of the model TB- and A-CLMs necessitates that the three-dimensional evolution of the system involved some strike coupling, requiring tearing or warping of the CLM.

The current lithospheric configuration inferred from deeper seismicity and tomography (Kufner et al., 2016, their Figure 8) strongly suggests a two-slab model. The Hindu Kush (Indian) slab is subducting from the Indian side, detaching and abutting against the western edge of the arcuate Asian (probably Alai) slab at depth. The north-to-south Pamir deep seismicity arc, at a depth of 200 km (Kufner et al., 2016, their Figures 1 and 2) suggests the two slabs are not separated by a clean north-south strike-slip zone or tear. Instead, the Pamir-CLM has delaminated as a warped arc that is a deeper southward expression of the north and west sides of the Pamir crustal orocline. There may be some tearing of this inclined CLM sheet but the two slabs are interpreted to interact (Kufner et al., 2016). Whether this configuration implies significant coupling between the two slabs depends on the buoyancy of Pamir-CLM. A negatively buoyant, inclined CLM sheet will assist delamination, whereas a buoyant one will impede it. The MPA model results can be interpreted to indicate a negatively buoyant Alai-CLM.

2.11 Conclusions

We have used the Hindu Kush and Pamir regions as examples to study the influence of the mantle lithosphere on continent-continent collision.

Our approach is two-fold. First, we have constructed simple lithospheric-scale balanced sections based on first-order geometric arguments to infer the geometry of these regions prior to the India-Asian collision and to estimate the amounts and timing of removed Asian and Indian lithospheric mantle. Additionally, we have summarized a list of enigmatic features of these systems which require explanation (Figure 2.5). Second, based on these inferences, we developed and presented mantle-scale two-dimensional geodynamical models (MHA, MPA, and supporting models) for cross-sections through the Pamir and Hindu Kush. These models evolve self-consistently through a number of emergent styles of lithospheric mantle deformation, subduction/delamination, and crustal deformation, and provide a self-consistent explanation for the enigmatic features. The final geometry of these models is in broad agreement with the inferred current state of the lithosphere as revealed from seismic tomography and seismicity.

The primary controls on the model evolutions are the strength (viscosity) and density of the Asian CLMs characterized by the *f* and *d* parameters. These effects are best seen in the animations (Kelly et al., 2021). *f* scales the CLM wet olivine-based flow law such that the variation from one to five represents the range from "wet" to "dry" olivine. Note that the density variations in the model CLMs are very small, representing only 15–50 kg/m^3 reductions with respect to undepleted mantle with density 3,370 kg/m^3. The *f* and *d* values of the CLMs determine the ease and rate of their delamination. Weak, *f*2, and dense, *d*10, CLMs delaminate and sink very rapidly. The weakest relatively high density CLMs (*f*2-*d*15) and (*f*2-*d*20) beneath the NH (North Hindu Kush) and P (Pamir) terranes respectively, are destabilized and delaminate soon after the onset of indentation of Asia. The requirement that these CLMs delaminate first means that all other CLMs must be stronger and/or less dense. The choice of *f*3-*d*20 for the SH- and K-CLMs (South Hindu Kush and Kohistan) ensures later delamination and that the rate of delamination is slow.

That the TB (Tajik Basin) main crustal layer remains relatively undeformed requires that the underlying CLM is strong and buoyant, *f*5-*d*50, and resists delamination. All weaker, denser CLM delaminates. The adjacent A-CLM (Alai) is also strong and resists delamination. However, the observed final configuration with Asian CLM delaminating to the north requires it, and the more northerly TS-CLM (Tien Shan), delaminate slowly, which is achieved with *f*5-*d*25, the same strength as TB-CLM but slightly higher density. That later stage deformation propagates into the Tien Shan crust implies its CLM delaminates from the crust but has not had time to sink. This behavior is achieved with CLM f3-d30. The AI (Asian Interior) terranes are not deformed in the models, therefore the value of their *f* and *d* controls is not strongly constrained.

Based on the results of our models, we conclude that the evolutions of the Hindu Kush and Pamir are controlled by the inherited strength (viscosity) and density of the CLMs of terranes accreted to Asia before the India-Asia collision, with weak, higher density CLM, southern terranes (Pamir and Hindu Kush) delaminating first. The Tajik Basin and Alai terrane CLMs are the strongest and most buoyant, consistent with being westward continuations of the cratonic-type lithosphere of the Tarim Basin, and therefore resist delamination. The difference in the final configurations, with Indian CLM subducting to the north under the Hindu Kush and Asian (Alai and Tien Shan) CLM delaminated to the south under the Pamir, can be attributed to two differences in the MHA and MPA model properties – namely, slightly denser CLM under the Pamir than beneath the Hindu Kush, and thinner (30 vs. 36 km) and therefore colder, Indian "fringe" crust which assists subduction of Indian lithosphere beneath the Hindu Kush.

We derive the following testable predictions and relationships from the balanced cross-sections, MHA, MPA and supporting model results, and comparison with observations. Times listed in Ma are approximate.

1) Contact, collision, and slab break-off of the Greater Indian rifted margin with Asia is consistent with the tomographic image of the inferred Neotethys oceanic

lithosphere at ~19°N for both the Hindu Kush and Pamir. Based on the model results the image also includes the Greater Indian rifted margin.

2) The rifted margin of Greater India was ~1,000 km wide, and was subducted northward between 56 and 51 Ma, followed by slab break-off in the Greater Indian margin at ~48.5 Ma.

3) Greater Indian margin middle and upper crust buried to UHP conditions during margin subduction was exhumed several million years after slab break-off, at 47 and 44.5 Ma for the Pamir and Hindu Kush, respectively.

4) After Greater Indian margin slab break-off, Indian lithosphere primarily indented Asia equally for both the Hindu Kush and Pamir sections, resulting in limited growth of the Himalaya by accretion from India during the interval ~50–30 Ma and 50–20 Ma, as indicated by MHA and MPA, respectively.

5) Indian indentation leads to rapid northward translation of both the IYS suture and the adjacent terranes north of the suture and is accommodated primarily by shortening and delamination of the weak North Hindu Kush and Pamir CLMs (at 38.5 and 34.5 Ma, respectively) followed by heating of the overlying crust by upwelling sublithospheric mantle and associated decompression melting (e.g., Vanj magmatism).

6) The thin cold Indian fringe margin can also account for the small Hindu Kush Himalayan mountain belt because the crust remains attached to the subducting Indian lithosphere and consequently is underthrust beneath the Asian terranes. By contrast, thicker, hotter Pamir Indian crust detaches and is accreted to form a large Himalayan mountain belt.

7) Thermal expansion of the thickened crust alone does not explain formation of Pamir domes. However, Pamir-like domes form in the models if there is a crustal

density decrease of 100 kg/m3, owing to melt retention following CLM delamination and crustal heating and melting by upwelling sublithospheric mantle.

8) The total northward translation of the model sutures and S-points is in reasonable agreement with the corresponding estimates from the Hindu Kush and Pamir based on the inferred 19°N collision and slab break-off.

2.12 Supporting Information for Chapter 2

Supporting information for Chapter 2 is provided in Appendix A.

2.13 References for Chapter 2

Abdrakhmatov, K. Y., Aldazhanov, S. A., Hager, B. H., and Hamburger, M. W. (1996). Relatively recent construction of the Tien Shan inferred from GPS measurements of present-day crustal deformation rates. *Nature, 384*, 450–453. https://doi.org/10.1038/384450a0

Abdulhameed, S., Ratschbacher, L., Jonckheere, R., Gągała, Ł., Enkelmann, E., Käßner, A., et al. (2020). Tajik Basin and southwestern Tian Shan, northwestern India-Asia collision zone: 2. Timing of basin inversion, Tian Shan mountain building, and relation to Pamir-Plateau advance and deep India-Asia indentation. *Tectonics, 39*, e2019TC00587. https://doi.org/10.1029/2019TC005873

Avouac, J. P. (2007). Dynamic processes in extensional and compressional settings - mountain building: From earthquakes to geological deformation. In: Schubert, G. (Ed.), *Treatise on Geophysics*, *6*, 377–439. Elsevier. https://doi.org/10.1016/B978-044452748-6.00112-7

Avouac, J. P., Tapponnier, P., Bai, M., You, H., and Wang, G. (1993). Active thrusting and folding along the northern Tien Shan and late Cenozoic rotation of the Tarim relative to Dzungaria and Kazakhstan. *Journal of Geophysical Research, 98*, 6755–6804. https://doi.org/10.1029/92JB01963

Bai, L., and Zhang, T. (2015). Complex deformation pattern of the Pamir-Hindu Kush region inferred from multi-scale double-difference earthquake relocations. *Tectonophysics, 638*, 177–184. https://doi.org/10.1016/j.tecto.2014.11.006

Beaumont, C., Jamieson, R. A., Butler, J. P., and Warren, C. J. (2009). Crustal structure: A key constraint on the mechanism of ultra-high-pressure rock exhumation. *Earth and Planetary Science Letters, 287*, 116–129. https://doi.org/10.1016/j.epsl.2009.08.001

Beaumont, C., Nguyen, M. H., Jamieson, R. A., and Ellis, S. (2006). Crustal flow modes in large hot orogens. R. D. Law, M. P. Searle, and L. Godin (Eds.), Channel Flow, Ductile Extrusion and Exhumation in Continental Collision Zones. *Geological Society, London, Special Publications*, 91–145. https://doi.org/10.1144/GSL.SP.2006.268.01.05

Bian, W., Yang, T., Ma, Y., Jin, J., Gao, F., and Zhang, S. (2017). New Early Cretaceous paleomagnetic and geochronological results from the far western Lhasa terrane: Contributions to the Lhasa-Qiangtang collision. *Scientific Reports, 7*, 1–14. https://doi.org/10.1038/ s41598-017-16482-3

Billen, M. I. (2010). Slab dynamics in the transition zone. *Physics of the Earth and Planetary Interiors, 183*, 296–308. https://doi.org/10.1016/j.pepi.2010.05.005.2010

Billington, S., Isacks, B. L., and Barazangi, M. (1977). Spatial distribution and focal mechanisms of mantle earthquakes in the Hindu Kush–Pamir region: A contorted Benioff zone. *Geology, 5*, 699–704. https://doi.org/10.1130/0091-7613(1977)5<699:SDAFMO>2.0.CO;2

Borneman, N. L., Hodges, K. V., Soest, M. C., Bohon, W., Wartho, J. A., Cronk, S. S., et al. (2015). Age and structure of the Shyok suture in the Ladakh region of northwestern India: implications for slip on the Karakoram fault system. *Tectonics, 34*, 2011–2033. https://doi.org/10.1002/2015TC003933

Bouilhol, P., Jagoutz, O., Hanchar, J. M., and Dudas, F. O. (2013). Dating the India–Eurasia collision through arc magmatic records. *Earth and Planetary Science Letters, 366*, 163–175. https://doi.org/10.1016/j.epsl.2013.01.023

Bullen, M. E., Burbank, D. W., Garver, J. I., and Abdrakhmatov, K. Y. (2001). Late Cenozoic tectonic evolution of the northwestern Tien Shan: New age estimates for the initiation of mountain building. *Geological Society of America Bulletin, 113*, 1544–1559. https://doi.org/10.1130/0016-7606(2001)113%3C1544:LCTEOT%3E2.0.CO;2

Burtman, V.S. (2000). Cenozoic crustal shortening between the Pamir and Tien Shan and a reconstruction of the Pamir–Tien Shan transition zone for the Cretaceous and Palaeogene. *Tectonophysics, 319*, 69–92. https://doi.org/10.1016/s0040-1951(00)00022-6

Burtman, V. S., and Molnar, P. (1993). Geological and geophysical evidence for deep subduction of continental crust beneath the Pamir. *Geological Society of America Special Paper, 281*, 1–76. https://doi.org/10.1130/SPE281-p1

Butler, J. P., Beaumont, C., and Jamieson, R. A. (2014). The Alps 2: Controls on crustal subduction and (ultra) high-pressure rock exhumation in Alpine-type orogens. *Journal of Geophysical Research: Solid Earth, 119*, 5987–6022. https://doi.org/10.1002/2013JB010799

Butler, J. P., Beaumont, C., and Jamieson, R. A. (2015). Paradigm lost: Buoyancy thwarted by the strength of the Western Gneiss Region (ultra) high-pressure terrane, Norway. *Lithosphere, 7*, 379–407. https://doi.org/10.1130/L426.1

Chapman, J. B., Carrapa, B., Ballato, P., DeCelles, P. G., Worthington, J., and Oimahmadov, I., (2017). Intracontinental subduction beneath the Pamir Mountains: Constraints from thermokinematic modeling of shortening in the Tajik fold-and-thrust belt. *Geological Society of America Bulletin, 129*, 1450–1471. https://doi.org/10.1130/B31730.1

Chapman, J. B., Scoggin, S. H., Kapp, P., Carrapa, B., Ducea, M. N., Worthington, J., et al. (2018). Mesozoic to Cenozoic magmatic history of the Pamir. *Earth and Planetary Science Letters, 482*, 181–192. https://doi.org/10.1016/j.epsl.2017.10.041

Chen, M., Niu, F., Tromp, J., Lenardic, A., Lee, C. T. A., Cao, W., et al. (2017). Lithospheric foundering and underthrusting imaged beneath Tibet. *Nature Communications, 8*, 15659. https://doi.org/10.1038/ncomms15659

Chung, S. L., Chu, M. F., Zhang, Y., Xie, Y., Lo, C. H., Lee, T. Y., et al. (2005). Tibetan tectonic evolution inferred from spatial and temporal variations in post-collisional magmatism. *Earth-Science Reviews, 68*, 173–196. https://doi.org/10.1016/j.earscirev.2004.05.001

Coutand, I., Strecker, M. R., Arrowsmith, J. R., Hilley, G., Thiede, R. C., Korjenkov, A., et al. (2002). Late Cenozoic tectonic development of the intramontane Alai Valley, (Pamir-Tien Shan region, central Asia): An example of intracontinental deformation due to the Indo-Eurasia collision. *Tectonics, 21*, 3-1–3-19. https://doi.org/10.1029/2002TC001358

Dewey, J. F., Shackleton, R. M., Chengfa, C., and Yiyin, S. (1988). The tectonic evolution of the Tibetan Plateau. *Philosophical Transactions of the Royal Society of London – Series A: Mathematical and Physical Sciences, 327*, 379–413. https://doi.org/10.1098/rsta.1988.0135

Ding, L., Qasim, M., Jadoon, I. A., Khan, M. A., Xu, Q., Cai, F., et. al. (2016). The India-Asia collision in north Pakistan: Insight from the U-Pb detrital zircon provenance of Cenozoic foreland basin. *Earth and Planetary Science Letters, 455*, 49–61. https://doi.org/10.1016/j.epsl.2016.09.003

Dipietro, J. A., and Pogue, K. R. (2004). Tectonostratigraphic subdivisions of the Himalaya: A view from the west. *Tectonics, 23*, TC5001. https://doi.org/10.1029/2003TC001554

Ducea, M. N., Lutkov, V., Minaev, V. T., Hacker, B., Ratschbacher, L., Luffi, P., et al. (2003). Building the Pamirs: The view from the underside. *Geology, 31*, 849–852. https://doi.org/10.1130/G19707.1

England, P. C., and Houseman, G. A. (1988). The mechanics of the Tibetan Plateau. *Philosophical Transactions of the Royal Society of London – Series A: Mathematical and Physical Sciences, 326*, 301–320. https://doi.org/10.1098/rsta.1988.0089

England, P. C., and Houseman, G. A. (1989). Extension during continental convergence, with application to the Tibetan Plateau. *Journal of Geophysical Research, 94*, 17561–17579. https://doi.org/10.1029/JB094iB12p17561

England, P., and Molnar, P. (2015). Rheology of the lithosphere beneath the central and western Tien Shan. *Journal of Geophysical Research: Solid Earth, 120*, 3803–3823. https://doi.org/10.1002/2014JB011733

Fullsack, P. (1995). An arbitrary Lagrangian-Eulerian formulation for creeping flows and its application in tectonic models. *Geophysical Journal International, 120*, 1–23. https://doi.org/10.1111/j.1365-246X.1995.tb05908.x

Gągała, Ł., Ratschbacher, L., Ringenbach, J.-C., Kufner, S.-K., Schurr, B., Dedow, R., et al. (2020). Tajik Basin and Southwestern Tian Shan, Northwestern India-Asia Collision Zone: 1. Structure, Kinematics, and Salt Tectonics in the Tajik Fold-and-Thrust Belt of the Western Foreland of the Pamir. *Tectonics, 39*, e2019TC005871. https://doi.org/10.1029/2019tc005871

Ghazian, R. K., and Buiter, S. J. (2013). A numerical investigation of continental collision styles. *Geophysical Journal International, 193*, 1133–1152. https://doi.org/10.1093/gji/ggt068

Griffin, W. L., O'Reilly, S. Y., Afonso, J. C., and Begg, G. C. (2009). The composition and evolution of lithospheric mantle: a re-evaluation and its tectonic implications. *Journal of Petrology, 50*, 1185–1204. https://doi.org/10.1093/petrology/egn033

Guo, X., Gao, R., Zhao, J., Xu, X., Lu, Z., Klemperer, S. L., et al. (2018). Deep-seated lithospheric geometry in revealing collapse of the Tibetan Plateau. *Earth-Science Reviews, 185*, 751–762. https://doi.org/10.1016/j.earscirev.2018.07.013

Hacker, B. R., Ratschbacher, L., Rutte, D., Stearns, M. A., Malz, N., Stübner, K., et al. (2017). Building the Pamir-Tibet Plateau – Crustal stacking, extensional collapse, and lateral extrusion in the Pamir: 3. Thermobarometry and petrochronology of deep Asian crust. *Tectonics, 36,* 1743–1766. https://doi.org/10.1002/2017TC004488

Heermance, R. V., Chen, J., Burbank, D. W., and Wang, C. (2007). Chronology and tectonic controls of Late Tertiary deposition in the southwestern Tian Shan foreland, NW China. *Basin Research, 19*, 599–632. https://doi.org/10.1111/j.1365-2117.2007.00339.x

Heintz, M., Kumar, V. P., Gaur, V. K., Priestley, K., Rai, S. S., and Prakasam, K. S. (2009). Anisotropy of the Indian continental lithospheric mantle. *Geophysical Journal International, 179*, 1341–1360. https://doi.org/10.1111/j.1365-246X.2009.04395.x

Hirth, G., and Kohlstedt, D. L. (1996). Water in the oceanic upper mantle: implications for rheology, melt extraction and the evolution of the lithosphere. *Earth and Planetary Science Letters, 144*, 93–108. https://doi.org/10.1016/0012-821X(96)00154-9

Hodges, K. V. (2000). Tectonics of the Himalaya and southern Tibet from two perspectives. *Geological Society of America Bulletin, 112*, 324–350. https://doi.org/10.1130/0016-7606(2000)112<324:TOTHAS>2.0.CO;2

Houseman, G. A., McKenzie, D. P., and Molnar, P. (1981). Convective instability of a thickened boundary layer and its relevance for the thermal evolution of continental convergent belts. *Journal of Geophysical Research, 86*, 6115–6132. https://doi.org/10.1029/JB086iB07p06115

Huang, W., Lippert, P. C., Zhang, Y., Jackson, M. J., Dekkers, M. J., Li, J., et al. (2017). Remagnetization of carbonate rocks in southern Tibet: Perspectives from rock magnetic and petrographic investigations. *Journal of Geophysical Research: Solid Earth, 122*, 2434–2456. https://doi.org/10.1002/2017JB013987

Hu, X., Garzanti, E., Moore, T., and Raffi, I. (2015). Direct stratigraphic dating of India-Asia collision onset at the Selandian (middle Paleocene, 59 ± 1 Ma). *Geology, 43*, 859–862. https://doi.org/10.1130/G36872.1

Hu, X., Garzanti, E., Wang, J., Huang, W., An, W., and Webb, A. (2016). The timing of India-Asia collision onset–Facts, theories, controversies. *Earth-Science Reviews, 160*, 264–299. https://doi.org/10.1016/j.earscirev.2016.07.014

Ingalls, M., Rowley, D. B., Currie, B., and Colman, A. S. (2016). Large-scale subduction of continental crust implied by India-Asia mass-balance calculation. *Nature Geoscience, 9*, 848–853. https://doi.org/10.1038/ngeo2806

Jadoon, I. A., and Khurshid, A. (1996). Gravity and tectonic model across the Sulaiman fold belt and the Chaman fault zone in western Pakistan and eastern Afghanistan. *Tectonophysics, 254*, 89–109. https://doi.org/10.1016/0040-1951(95)00078-X

Jamieson, R. A., and Beaumont, C. (2013). On the origin of orogens. *Geological Society of America Bulletin, 125*, 1671–1702. https://doi. org/10.1130/B30855.1

Kapp, P., and DeCelles, P. G. (2019). Mesozoic–Cenozoic geological evolution of the Himalayan-Tibetan orogen and working tectonic hypotheses. *American Journal of Science, 319*, 159–254. https://doi.org/10.2475/03.2019.01

Karato, S. and Wu, P. (1993). Rheology of the upper mantle: A synthesis. *Science, 260*, 771–778. https://doi.org/10.1126/science.260.5109.771

Kay, R. W., and Kay, S. M. (1993). Delamination and delamination magmatism. *Tectonophysics, 219*, 177–189. https://doi.org/10.1016/0040-1951(93)90295-U

Kelly, S., Beaumont, C., and Butler, J. P. (2020). Inherited terrane properties explain enigmatic post-collisional Himalayan-Tibetan evolution. *Geology, 48*, 8–14. https://doi.org/10.1130/g46701.1

Kelly, S., Butler, J. P., and Beaumont, C. (2016). Continental collision with a sandwiched accreted terrane: Insights into Himalayan-Tibetan lithospheric mantle tectonics? *Earth and Planetary Science Letters, 455*, 176–195. https://doi.org/10.1016/j.epsl.2016.08.039

Klemperer, S. L., Kennedy, B. M., Sastry, S. R., Makovsky, Y., Harinarayana, T., and Leech, M. L. (2013). Mantle fluids in the Karakoram fault: Helium isotope evidence. *Earth and Planetary Science Letters, 366*, 59–70. https://doi.org/10.1016/j.epsl.2013.01.013

Kooijman, E., Smit, M. A., Ratschbacher, L., and Kylander-Clark, A. R. (2017). A view into crustal evolution at mantle depths. *Earth and Planetary Science Letters, 465*, 59–69. https://doi.org/10.1016/j.epsl.2017.02.032

Koulakov, I. (2011). High-frequency P and S velocity anomalies in the upper mantle beneath Asia from inversion of worldwide traveltime data. *Journal of Geophysical Research, 116*, B04301. https://doi.org/10.1029/2010JB007938

Koulakov, I., and Sobolev, S. V. (2006). A tomographic image of Indian lithosphere break-off beneath the Pamir–Hindukush region. *Geophysical Journal International, 164*, 425–440. https://doi.org/10.1111/j.1365-246X.2005.02841.x

Kufner, S.-K., Schurr, B., Haberland, C., Zhang, Y., Saul, J., Ischuk, A., et al. (2017). Zooming into the Hindu Kush slab break-off: A rare glimpse on the terminal stage of subduction. *Earth and Planetary Science Letters, 461*, 127–140. https://doi.org/10.1016/j.epsl.2016.12.043

Kufner, S.-K., Schurr, B., Sippl, C., Yuan, X., Ratschbacher, L., Ischuk, A., et al. (2016). Deep India meets deep Asia: Lithospheric indentation, delamination and break-off under Pamir and Hindu Kush (Central Asia). *Earth and Planetary Science Letters, 435*, 171–184. https://doi.org/10.1016/j.epsl.2015.11.046

Lee, C.-T. A. (2003). Compositional variation of density and seismic velocities in natural peridotites at STP conditions: Implications for seismic imaging of compositional heterogeneities in the upper mantle. *Journal of Geophysical Research, 108,* 2441. https://doi.org/10.1029/2003JB002413

Li, Z., Ding, L., Lippert, P. C., Song, P., Yue, Y., and van Hinsbergen, D. J. (2016a). Paleomagnetic constraints on the Mesozoic drift of the Lhasa terrane (Tibet) from Gondwana to Eurasia. *Geology, 44*, 727–730. https://doi.org/10.1130/G38030.1

Li, Z. H., Liu, M., and Gerya, T. (2016b). Lithosphere delamination in continental collisional orogens: A systematic numerical study. *Journal of Geophysical Research: Solid Earth, 121*, 5186–5211. https://doi.org/10.1002/2016JB013106

Lippitsch, R., Kissling, E., and Ansorge, J. (2003). Upper mantle structure beneath the Alpine orogen from high-resolution teleseismic tomography. *Journal of Geophysical Research, 108*, 2376. https://doi.org/10.1029/2002JB002016

Lister, G., Kennett, B., Richards, S., and Forster, M. (2008). Boudinage of a stretching slablet implicated in earthquakes beneath the Hindu Kush. *Nature Geoscience, 1*, 196–201. https://doi.org/10.1038/ngeo132

Massonne, H. J., and Fockenberg, T. (2012). Melting of metasedimentary rocks at ultrahigh pressure - Insights from experiments and thermodynamic calculations. *Lithosphere, 4*, 269–285. https://doi.org/10.1130/L185.1

Mckenzie, D. A. N., and Bickle, M. J. (1988). The volume and composition of melt generated by extension of the lithosphere. *Journal of Petrology, 29*, 625–679. https://doi.org/10.1093/petrology/29.3.625

Mechie, J., Yuan, X., Schurr, B., Schneider, F., Sippl, C., Ratschbacher, L., et al. (2012). Crustal and uppermost mantle velocity structure along a profile across the Pamir and southern Tien Shan as derived from project TIPAGE wide-angle seismic data. *Geophysical Journal International, 188*, 385–407. https://doi.org/10.1111/j.1365-246X.2011.05278.x

Molnar, P. (1988). Continental tectonics in the aftermath of plate tectonics. *Nature, 335*, 131–137. https://doi.org/10.1038/335131a0

Molnar, P. and Bendick, R. (2019). Seismic moments of intermediate-depth earthquakes beneath the Hindu Kush: Active stretching of a blob of sinking thickened mantle lithosphere? *Tectonics, 38*, 1651–1665. https://doi.org/10.1029/2018TC005336

Molnar, P., England, P., and Martinod, J. (1993). Mantle dynamics, uplift of the Tibetan Plateau, and the Indian monsoon. *Reviews of Geophysics, 31*, 357–396. https://doi.org/10.1029/93RG02030

Najman, Y., Jenks, D., Godin, L., Boudagher-Fadel, M., Millar, I., Garzanti, E., et al. (2017). The Tethyan Himalayan detrital record shows that India–Asia terminal collision occurred by 54 Ma in the Western Himalaya. *Earth and Planetary Science Letters, 459*, 301–310. https://doi.org/10.1016/j.epsl.2016.11.036

Nunn, C., Roecker, S. W., Tilmann, F. J., Priestley, K. F., Heyburn, R., Sandvol, E. A., et al. (2014). Imaging the lithosphere beneath NE Tibet: Teleseismic P and S body wave tomography incorporating surface wave starting models. *Geophysical Journal International, 196*, 1724–1741. https://doi.org/10.1093/gji/ggt476

Owens, T. J., and Zandt, G. (1997). Implications of crustal property variations for models of Tibetan plateau evolution. *Nature, 387*, 37–43. https://doi.org/10.1038/387037a0

O'Brien, P. J. (2019). Eclogites and other high-pressure rocks in the Himalaya: A review. Treloar, P.J., Searle, M.P. (Eds.), Himalayan Tectonics: A Modern Synthesis. *Geological Society, London, Special Publications, 483,* 183–213. https://doi.org/10.1144/SP483.13

Pegler, G., and Das, S. (1998). An enhanced image of the Pamir-Hindu Kush seismic zone from relocated earthquake hypocenters. *Geophysical Journal International*, *134*, 573–595. https://doi.org/10.1046/j.1365-246x.1998.00582.x

Qasim, M., Ding, L., Khan, M. A., Jadoon, I. A., Haneef, M., Baral, U., et al. (2018). Tectonic implications of detrital zircon ages from lesser Himalayan Mesozoic-Cenozoic strata, Pakistan. *Geochemistry, Geophysics, Geosystems, 19*, 1636–1659. https://doi.org/10.1002/2017GC006895

Rehman, H. U., Seno, T., Yamamoto, H., and Khan, T. (2011). Timing of collision of the Kohistan-Ladakh Arc with India and Asia: Debate. *Island Arc, 20*, 308–328. https://doi.org/10.1111/j.1440-1738.2011.00774.x

Replumaz, A., Capitanio, F. A., Guillot, S., Negredo, A. M., and Villaseñor, A. (2014). The coupling of Indian subduction and Asian continental tectonics. *Gondwana Research, 26*, 608–626. https://doi.org/10.1016/j.gr.2014.04.003

Rowley, D. B. (1996). Age of initiation of collision between India and Asia: A review of stratigraphic data. *Earth and Planetary Science Letters, 145*, 1–13. https://doi.org/10.1016/S0012-821X(96)00201-4

Schmidt, J., Hacker, B. R., Ratschbacher, L., Stübner, K., Stearns, M., Kylander-Clark, A., et al. (2011). Cenozoic deep crust in the Pamir. *Earth and Planetary Science Letters, 312*, 411–421. https://doi.org/10.1016/j.epsl.2011.10.034

Schneider, F. M., Yuan, X., Schurr, B., Mechie, J., Sippl, C., Kufner, S. K., et al. (2019). The crust in the Pamir: Insights from receiver functions. *Journal of Geophysical Research: Solid Earth, 124*, 9313–9331. https://doi.org/10.1029/2019JB017765

Schwab, M., Ratschbacher, L., Siebel, W., McWilliams, M., Minaev, V., Lutkov, V., et al. (2004). Assembly of the Pamirs: Age and origin of magmatic belts from the southern Tien Shan to the southern Pamirs and their relation to Tibet. *Tectonics, 23*, TC4002. https://doi.org/10.1029/2003TC001583

Searle, M. P., and Treloar, P. J. (2019). Introduction to Himalayan tectonics: A modern synthesis. Treloar, P. J. and Searle, M. P. (Eds.) Himalyan tectonics: A modern synthesis. *Geological Society, London, Special Publications, 483*, 1–17. https://doi.org/10.1144/SP483-2019-20

Sippl, C., Schurr, B., Tympel, J., Angiboust, S., Mechie, J., Yuan, X., et al. (2013a). Deep burial of Asian continental crust beneath the Pamir imaged with local earthquake tomography. *Earth and Planetary Science Letters, 384*, 165–177. https://doi.org/10.1016/j.epsl.2013.10.013

Sippl, C., Schurr, B., Yuan, X., Mechie, J., Schneider, F. M., Gadoev, M., et al. (2013b). Geometry of the Pamir-Hindu Kush intermediate-depth earthquake zone from local seismic data. *Journal of Geophysical Research: Solid Earth, 118*, 1438–1457. https://doi.org/10.1002/jgrb.50128

Smit, M. A., Ratschbacher, L., Kooijman, E., and Stearns, M. A. (2014). Early evolution of the Pamir deep crust from Lu-Hf and U-Pb geochronology and garnet thermometry. *Geology, 42*, 1047–1050. https://doi.org/10.1130/G35878.1

Stübner, K., Ratschbacher, L., Weise, C., Chow, J., Hofmann, J., Khan, J., et al. (2013). The giant Shakhdara migmatitic gneiss dome, Pamir, India-Asia collision zone: 2. Timing of dome formation. *Tectonics, 32*, 1404–1431. https://doi.org/10.1002/tect.20059

Sun, J., and Jiang, M. (2013). Eocene seawater retreat from the southwest Tarim Basin and implications for early Cenozoic tectonic evolution in the Pamir Plateau. *Tectonophysics, 588*, 27–38. https://doi.org/10.1016/j.tecto.2012.11.031

Toussaint, G., Burov, E., and Jolivet, L. (2004). Continental plate collision: Unstable vs. stable slab dynamics. *Geology, 32*, 33–36. https://doi.org/10.1130/G19883.1

van Hinsbergen, D. J., Lippert, P. C., Dupont-Nivet, G., McQuarrie, N., Doubrovine, P. V., Spakman, W., et al. (2012). Greater India Basin hypothesis and a two-stage Cenozoic collision between India and Asia. *Proceedings of the National Academy of Sciences, 109*, 7659–7664. https://doi.org/10.1073/pnas.1117262109

van Hinsbergen, D. J., Steinberger, B., Doubrovine, P. V., and Gassmöller, R. (2011). Acceleration and deceleration of India-Asia convergence since the Cretaceous: Roles of mantle plumes and continental collision. *Journal of Geophysical Research, 116*, B06101. https://doi.org/10.1029/2010JB008051

Wang, Y. F., Zeng, L., Gao, J., Zhao, L., Gao, L. E., and Shang, Z. (2019). Along-arc variations in isotope and trace element compositions of Paleogene gabbroic rocks in the Gangdese batholith, southern Tibet. *Lithos, 324*, 877–892. https://doi.org/10.1016/j.lithos.2018.11.036

Warren, C. J., Beaumont, C., and Jamieson, R. A. (2008). Modeling tectonic styles and ultra-high pressure (UHP) rock exhumation during the transition from oceanic subduction to continental collision. *Earth and Planetary Science Letters, 267*, 129–145. https://doi.org/10.1016/j. epsl.2007.11.025

White, R., and McKenzie, D. (1989). Magmatism at rift zones: The generation of volcanic continental margins and flood basalts. *Journal of Geophysical Research, 94*, 7685–7729. https://doi.org/10.1029/JB094iB06p07685

Willett, S., Beaumont, C., and Fullsack, P. (1993). Mechanical model for the tectonics of doubly vergent compressional orogens. *Geology, 21*, 371–374. https://doi.org/10.1130/00917613(1993)021<0371:MMFTTO>2.3.CO;2

Worthington, J. R., Ratschbacher, L., Stübner, K., Khan, J., Malz, N., Schneider, S., et al. (2020). The Alichur dome, South Pamir, western India-Asia collisional zone: Detailing the Neogene Shakhdara–Alichur syn-collisional gneiss-dome complex and connection to litho- spheric processes. *Tectonics, 39*, e2019TC005735. https://doi.org/10.1029/2019TC005735

Yin, A. (2006). Cenozoic tectonic evolution of the Himalayan orogen as constrained by along-strike variation of structural geometry, exhumation history, and foreland sedimentation. *Earth-Science Reviews, 76*, 1–131. https://doi.org/10.1016/j.earscirev.2005.05.004

Yin, A., and Harrison, T. M. (2000). Geologic evolution of the Himalayan-Tibetan orogen. *Annual Review of Earth and Planetary Sciences, 28*, 211–280. https://doi.org/10.1146/annurev.earth.28.1.211

Zhu, D., Wang, Q., and Zhao, Z. (2017). Constraining quantitatively the timing and process of continent-continent collision using magmatic record: Method and examples. *Science China Earth Sciences, 60*, 1040–1056. https://doi.org/10.1007/s11430-016-9041-x

Zhu, G., Gerya, T. V., Honda, S., Tackley, P. J. and Yuen, D. A. (2011). Influences of the buoyancy of partially molten rock on three-dimensional plume patterns and melt productivity above retreating slabs. *Physics of the Earth and Planetary Interiors*, *185*, 112–121. https://doi.org/10.1016/j.pepi.2011.02.005

2.14 References for Chapter 2 Supporting Information

Andrews, E. R., and Billen, M. I. (2009). Rheologic controls on the dynamics of slab detachment. *Tectonophysics, 464*, 60–69. https://doi.org/10.1016/j.tecto.2007.09.004

Beaumont, C., Jamieson, R. A., Nguyen, M. H., and Lee, B. (2001). Himalayan tectonics explained by extrusion of a low-viscosity crustal channel coupled to focused surface denudation. *Nature, 414*, 738-742. https://doi.org/10.1038/414738a

Butler, J. P., Beaumont, C., and Jamieson, R. A. (2013). The Alps 1: A working geodynamic model for burial and exhumation of (ultra)high pressure rocks in Alpine-type orogens. *Earth and Planetary Science Letters, 377-378*, 114-131. https://doi.org/10.1016/j.epsl.2013.06.039

Dipietro, J. A., Hussain, A., Ahmad, I., and Khan, M. A. (2000). The Main Mantle Thrust in Pakistan: Its character and extent. Asif Khan, M., Treloar, P. J., Searle, M. P., Qasim Jan M. (Eds.), Tectonics of the Nanga Parbat Syntaxis and the Western Himalaya. *Geological Society, London, Special Publications, 170*, 375-393. https://doi.org/10.1144/GSL.SP.2000.170.01.20

Gleason, G. C., and Tullis, J. (1995). A flow law for dislocation creep of quartz aggregates determined with the molten salt cell. *Tectonophysics, 247*, 1-23. https://doi.org/10.1016/0040-1951(95)00011-B

Huismans, R., and Beaumont, C. (2011). Depth-dependent extension, two-stage breakup and cratonic underplating at rifted margins. *Nature, 473*, 74-78. https://doi.org/10.1038/nature09988

Kameyama, M., Yuen, D. A., and Karato, S. I. (1999). Thermal-mechanical effects of low-temperature plasticity (the Peierls mechanism) on the deformation of a viscoelastic shear zone. *Earth and Planetary Science Letters, 168*, 159–172. https://doi.org/10.1016/S0012-821X(99)00040-0

Katayama, I., and Karato, S. I. (2008). Low-temperature, high-stress deformation of olivine under water-saturated conditions. *Physics of the Earth and Planetary Interiors, 168*, 125-133. https://doi.org/10.1016/j.pepi.2008.05.019

Mackwell, S. J., Zimmerman, M. E., and Kohlstedt, D. L. (1998). High-temperature deformation of dry diabase with application to tectonics on Venus. *Journal of Geophysical Research, 103*, 975-984. https://doi.org/10.1029/97JB02671

Mei, S., Suzuki, A. M., Kohlstedt, D. L., Dixon, N. A., and Durham, W. B. (2010). Experimental constraints on the strength of the lithospheric mantle. *Journal of Geophysical Research, 115*, B08204. https://doi.org/10.1029/2009JB006873

Negredo, A. M., Replumaz, A., Villaseñor, A., and Guillot, S. (2007). Modeling the evolution of continental subduction processes in the Pamir-Hindu Kush region. *Earth and Planetary Science Letters, 259*, 212–225. https://doi.org/10.1016/j.epsl.2007.04.043

Rosenberg, C. L., and Handy, M. R. (2005). Experimental deformation of partially melted granite revisited: Implications for the continental crust. *Journal of Metamorphic Geology, 23*, 19-28. https://doi.org/10.1111/j.1525-1314.2005.00555.x

Zheng, Y.-F., Xia, Q.-X., Chen, R.-X., and Gao, X.-Y. (2011). Partial melting, fluid supercriticality, and element mobility in ultrahigh-pressure metamorphic rocks during continental collision. *Earth-Science Reviews, 107*, 342-374. https://doi.org/10.1016/j.earscirev.2011.04.004

CHAPTER 3. INHERITED TERRANE PROPERTIES EXPLAIN ENIGMATIC POST-COLLISIONAL HIMALAYAN-TIBETAN EVOLUTION

This chapter is a modified version of the article 'Inherited Terrane Properties Explain Enigmatic Post-Collisional Himalayan-Tibetan Evolution' by S. Kelly, C. Beaumont, and J. P. Butler, published in the journal *Geology* (Kelly et al., 2020).

3.1 Abstract

Observations highlight the complex tectonic, magmatic, and geodynamic phases of the Cenozoic post-collisional evolution of the Himalayan-Tibetan orogen and show that these phases migrate erratically among terranes accreted to Asia prior to the Indian collision. This behavior contrasts sharply with the expected evolution of large, hot orogens formed by collision of lithospheres with laterally uniform properties. Motivated by this problem, we use two-dimensional numerical geodynamical model experiments to show that the enigmatic behavior of the Himalayan-Tibetan orogeny can result from crust-mantle decoupling, transport of crust relative to the mantle lithosphere, and diverse styles of lithospheric mantle delamination, which emerge self-consistently as phases in the evolution of the system. These model styles are explained by contrasting inherited mantle lithosphere properties of the Asian upper-plate accreted terranes. Deformation and lithospheric delamination preferentially localize in terranes with the most dense and weak mantle lithosphere, first in the Qiangtang and then in the Lhasa mantle lithospheres. The model results are shown to be consistent with 11 observed complexities in the evolution of the Himalayan-Tibetan orogen. The broad implication is that all large orogens containing previously accreted terranes are expected to have an idiosyncratic evolution determined by the properties of these terranes, and will be shown to deviate from predictions of uniform lithosphere models.

3.2 Introduction

Twelve observed complexities in the evolution of the central Himalayan-Tibetan orogen require explanation (Figure 3.1) (summarized from Yin and Harrison, 2000; Chung et al., 2005; Yin, 2006; Chen et al., 2012; Wang et al., 2014; Hu at al., 2016; Chapman and Kapp, 2017; Martin, 2017; van Hinsbergen et al., 2019; Kapp and DeCelles, 2019). These complexities show an erratic evolution in which deformation and magmatism migrate among Tibetan terranes in a manner that is not understood. We seek a solution in the form of an integrated model for the post-collisional evolution of the orogen. Our study shows that emergent features of parsimonious mantle-scale two-dimensional (2-D) geodynamical models involving a single continental collision explain many of these seemingly disparate observations when properties of previously accreted Asian terranes are considered. We note that there are along-strike variations in the observed evolution and anticipate that small changes to the model properties would reproduce these variations. In addition, there are divergent interpretations of the paleogeographic, tectonic, metamorphic, and magmatic processes responsible for these complex observations, so that models can only be consistent with a subset of interpretations. We outline the model design and methods, then compare two model results with observations.

3.3 Methods

Our mantle-scale 2-D finite element model computations used sopale-nested software (http://geodynamics.oceanography.dal.ca/sopale_nested.html) (see the Methods section in the GSA Data Repository, Appendix B) (Beaumont et al., 2009; Fullsack, 1995), which calculates frictional-plastic and creeping viscous flows and the evolving temperature. The models (Figure 3.2) represent the restored natural system at ~90°E, particularly the Asian accreted terranes. Regions (Figure 3.2A) are labeled with an abbreviation based on the natural setting.

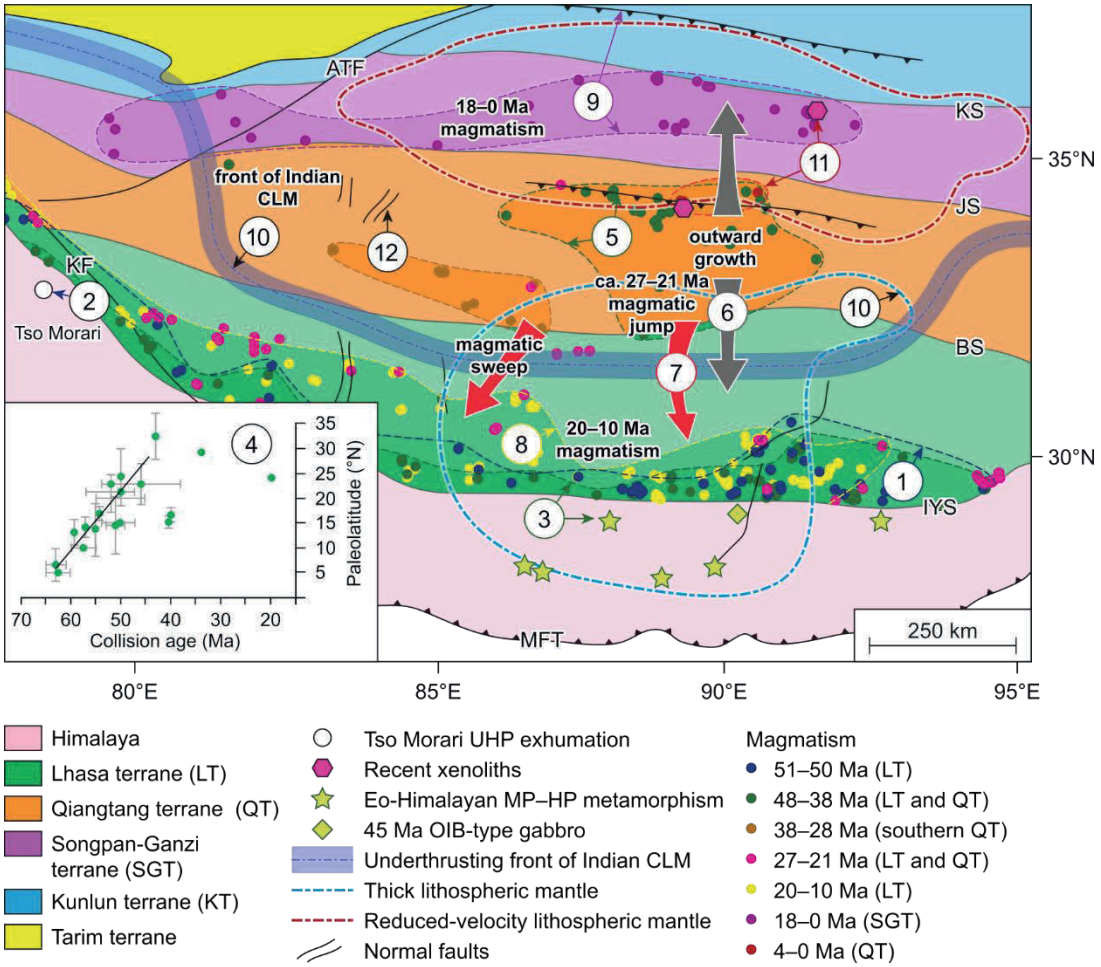

Figure 3.1. Complexities in the evolution of the Himalayan-Tibetan orogen**.** Important aspects requiring explanation include: 1—Gangdese arc magmatic flareup (Lee et al., 2009; Zhu et al., 2015) ca. 51 Ma; 2—Tso Morari exhumation of ultrahigh-pressure (UHP) rocks (Leech et al., 2005; Donaldson et al., 2013; O'Brien 2019); 3—Eohimalayan metamorphism and magmatism, and contemporary magmatism in the southern Lhasa terrane, that continues to ca. 38 Ma followed by magmatic lull (Ding et al., 2016; Kapp and DeCelles, 2019; Ji et al., 2016; Zeng et al., 2011; Aikman et al., 2008); 4— Early northward motion of the Indus-Yarlung suture (IYS) and Lhasa terrane shown by a general trend of paleomagnetic data for the "collision" to be farther north at younger ages (Zhu et al., 2017, their figure 2b and explanation of error bars; Yi et al., 2011; Tong et al., 2017; [see also DeCelles et al., 2002, their figure 9]; and Najman et al., 2010); 5—Early (50–45 Ma) crustal shortening and thickening in central Tibet (Spurlin et al., 2005; Staisch et al., 2014, 2016; Li et al., 2018; Kapp and DeCelles, 2019; Wang et al., 2014) (north Qiangtang terrane) rather than near the suture, followed by magmatism in the northern Qiangtang terrane (Guo et al., 2006; Ding et al., 2007; Chen et al., 2013; Ou et al., 2017); 6—Outward growth of the Tibetan Plateau from the Qiangtang terrane (Kapp and DeCelles, 2019); 7—27–21 Ma southward "sweep" and/or "jump" in magmatism from the Qiangtang to Lhasa terranes (Chung et al., 2003; Liu et al., 2014; Kapp and DeCelles, 2019); 8—Widespread southern Lhasa terrane 20–10 Ma small-volume magmatism and progressive northward termination (Chung et al., 2005; Liu et al., 2014, Kapp and DeCelles 2019); 9—Recent (since 18 Ma) magmatism in northern Tibet

(Songpan-Ganzi, western Qiangtang, and Kunlun terranes) (Chung et al., 2005; Kapp and DeCelles, 2019) and contemporaneous high-temperature, lower-crustal metamorphism, and crustal shortening and thickening mainly restricted to the Kunlun terrane; 10—Seismic interpretations indicating northward underthrusting of Indian lithosphere to the Bangong suture beneath the western Himalayan-Tibetan orogen, and accumulated mantle lithosphere beneath the Lhasa terrane and India in the central Himalayan-Tibetan orogen (90°E) (Owens and Zandt, 1997; Chen et al., 2017); 11—Recent (3 Ma) Qiangtang crustal magmatism with entrained hot xenoliths (Hacker et al., 2000); 12—15 Ma onset of east-west extension in the Himalaya and the Tibetan Plateau (Kapp and DeCelles, 2019). Model-derived explanations for numbered complexities are discussed later. Structures: KF—Karakoram fault; ATF—Altyn Tagh fault; KS—Kunlan suture; JS—Jinsha suture; BS—Bangong suture; IYS—Indus-Yarlung suture; MFT—Main Frontal thrust. Other abbreviations: MP—medium-pressure; HP—high-pressure; OIB—ocean island basalt; CLM—continental lithospheric mantle.

Depletion density, d (Figure 3.2), measures chemical depletion of the continental lithospheric mantle (CLM) (e.g., as in the Mg# = 100 × Mg/(Mg + Fe); Lee, 2003) with respect to sublithospheric mantle. The viscosity scaling factor, f, measures dehydration effects ($f = 2$, hydrated; $f \geq 5$, dehydrated) on CLM viscosity. Viscous flow laws are based on laboratory measurements of wet quartzite, dry Maryland diabase, and wet olivine, and include strain softening and weakening. The left lithospheric (prolithospheric) boundary velocity, $V_p(t)$, varies with time (t) between 15 and 4.5 cm/yr (Figure 3.2B), reproducing slowing of the Indian plate, while the right (retrolithospheric) boundary has $V_r(t) = 0$, except in the last 15 m.y. Sublithospheric side-boundary velocities ensure that the model is volume and isostatically balanced. Convergence totals 4000 km over 58 m.y.

Sediment and upper to middle continental crust undergo viscosity reduction corresponding to melt weakening by 4%–7% melt (see the Data Repository). Crustal materials undergo reversible density changes corresponding to eclogite and coesite-eclogite phase changes (Table DR1 in the Data Repository). Reversible phase changes at the 660 km depth boundary correspond to the olivine-perovskite transformation.

The models have a free upper surface. Slope-dependent erosion, with a maximum of 0.5 cm/yr, acts on the local topography and is modulated by a climate function representing the wet-arid transition across the orogen (Figure 3.2C).

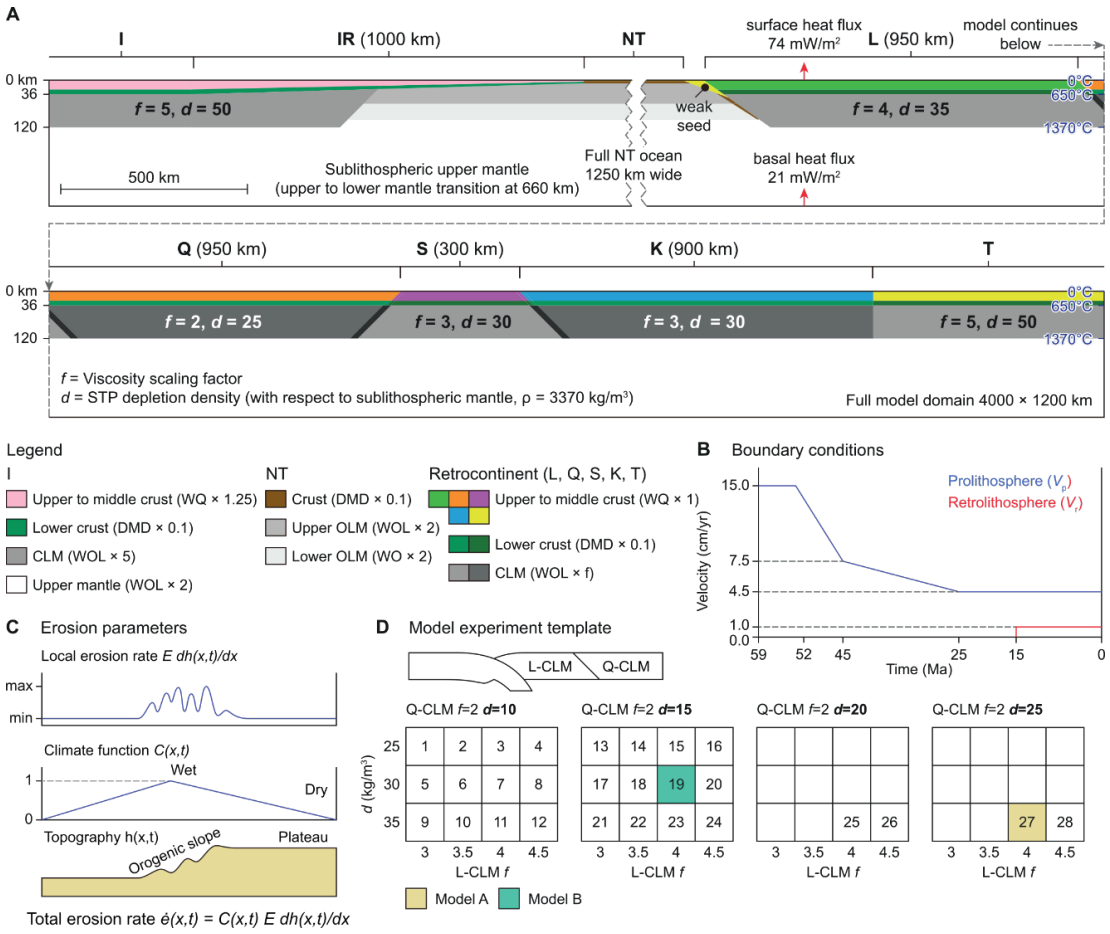

Figure 3.2. (A) Initial geometry and properties of model A (MA), cross-sectional geodynamical model**.** It comprises (left to right): Indian continent (I), its rifted margin (IR), Neotethys ocean (NT), and composite retrocontinent, overlying the upper mantle to 660 km depth and lower mantle to 1200 km. The retrocontinent comprises (from left to right): Lhasa terrane (L), Qiangtang terrane (Q), Songpan-Ganzi (Garze) terrane (S), composite Kunlun terrane (K), and Tarim terrane (T). Width of the retrocontinent is restored based on assumed NT breakoff at 11°N at 90°E. This implies an increase in the width of the retrocontinent of ~2200 km with respect to the current configuration, which is achieved in the model design by proportional increases in the lengths of Asian terranes south of the Tarim terrane. 1000-km-wide IR (Greater India rifted margin) has depth-dependent stretching geometry (Huismans and Beaumont, 2011). All continental regions have uniform-thickness layering (Table DR1 [see footnote 1]): 24 km upper to middle crust, 12 km lower crust, and 84 km continental lithospheric mantle (CLM) (extending to 120 km deep). Oceanic lithosphere layers comprise 2 km of sediment, 6 km of oceanic crust, and 92 km of oceanic mantle lithosphere. f is the viscosity scaling factor for power-law flow (see the Data Repository [footnote 1] in Appendix B). CLM densities are quoted as density depletion (in kg/m3) with respect to sublithospheric mantle density (3370 kg/m3) (see Table DR1 in Appendix B for other model properties). Continents have laterally uniform crustal radioactive heat production for upper–middle and lower continental crust of 2.0 and 0.4 μW/m3, respectively. Initial Moho and base lithosphere temperatures on continents are ~650 °C and ~1370 °C, respectively. Dips of sutures are

based on inferred accretion polarity. STP—standard temperature and pressure; WQ—wet quartzite; DMD—dry Maryland diabase; CLM—continental lithospheric mantle; WOL—wet olivine; OLM—oceanic lithospheric mantle. (B) Convergent velocity boundary conditions based on Ingalls et al. (2016). (C) Erosion model properties. Climate function is similar to that of Wang et al. (2014). (D) Model property template for L-CLM and Q-CLM. Numbers are model numbers: we refer to models by their L-CLM and Q-CLM *f* and *d* properties, using notation MA (L_*f*4-*d*35, Q_*f*2-*d*25) for MA, for example. Other properties do not vary.

3.4 Results and Comparison with Observations

Following a wider model parameter search, we investigated a set of 28 models (Figure 3.2D) by varying only the depletion densities and viscosities of the CLMs of the L (Lhasa) and Q (Qiangtang) terranes (see the Data Repository in Appendix B). Among these models, we focus on model A (MA) (we refer to models by their L-CLM and Q-CLM *f* and *d* properties, using notation MA (L_*f*4-d35, Q_*f*2-*d*25) for model MA) and model B (MB) (L_*f*4-*d*30, Q_*f*2-*d*15) (Figures 3.2 and 3.3; Table DR1; Figures DR1 and DR2; Videos DR1 and DR2 in Kelly et al., 2020). MA and MB differ only in that the L- and Q-CLMs are more depleted, i.e., less dense, in MA. The models are self-consistent, and stages in their evolution are emergent features of the overall system, not outcomes from model components acting individually. We show that MA corresponds to many observations from the central (86°–91°E) Himalayan-Tibetan orogen (Figure 3.1) (Chung et al., 2005; Kapp and DeCelles, 2019). MA and MB were chosen because they bracket the observations.

Initial NT (Neotethys) oceanic subduction in MA and MB at model location x = 1300 km equates with late-stage northward Neotethys subduction at 11°N (at 90°E), the interpreted position of the Neotethyan slab in the lower mantle (Van der Voo et al., 1999; Replumaz et al., 2013). This links the model and natural reference frames (x = 1300 km ≡ 11°N). The models also agree with Lhasa terrane calc-alkaline Gangdese-Linzizong magmatism during Neotethyan oceanic subduction (e.g., Zhu et al., 2019). Contact of the model distal margins corresponds to initial 58 Ma India-Asia sediment overlap (Najman et al., 2010; DeCelles et al., 2014; Hu et al., 2015) and is used to initialize the model time scale at 58 Ma. Contact is followed by India rifted margin (IR) subduction and full Indian continent

–Lhasa terrane (I-L) collision at 52 Ma (also at x ~1300 km, Figure 3.3), corresponding to 54–50 Ma Himalayan-Tibetan collision based on shallow-water sedimentation (Najman et al., 2010, 2017) and magmatic ε_{Hf} isotopic evidence (Chu et al., 2011).

Collision of I and L in MA and MB is followed by 52 Ma high-level slab breakoff (Figure 3.3A), consistent with ca. 51 Ma Gangdese arc peak magmatic flareup (observed complexity 1 shown in (Figure 3.1) (Lee et al., 2009; Zhu et al., 2015). Subsequent exhumation of ultrahigh-pressure (UHP) rocks in MA and MB at 50 Ma (Figure 3.3A, I) agrees with Tso Morari UHP exhumation (complexity 2) (50–47 Ma) (Leech et al., 2005; Donaldson et al., 2013; O'Brien, 2019) and is followed by lithospheric decoupling, subduction channel widening, and asthenospheric upwelling (Figure 3.3A, I). Upwelling can account for shallow decompression melting evidenced in 45 Ma ocean island basalt (OIB)–like gabbros intruded into the eastern Tethyan Himalaya (Ji et al., 2016) and magma contamination by Indian sediments. It may also explain the Gangdese magmatic flareup (complexity 1) (albeit slightly late) better than oft-invoked slab breakoff (Garzanti et al., 2018). Upwelled asthenosphere changes the subduction channel from cold to hot (Figure 3.3A, I), heats the overlying crust, and can also explain prograde Tethyan Eohimalayan metamorphism (ca. 48–45 Ma, temperature [T] ~650 °C, pressure [P] ~700 MPa) (Ding et al., 2016; Kapp and DeCelles, 2019) and accompanying crustal melting (Zeng et al., 2011; Aikman et al., 2008) (complexity 3). The upwelled asthenosphere in MA and MB remains hot (Figures 3.3A, and 3.3C) until the opening closes at ca. 36 Ma, potentially accounting for south Lhasa low-volume magmatism until 38 Ma (Kapp and DeCelles, 2019) and for lower-crustal temperatures >700 °C (complexity 3) (Smit et al., 2014) (Fig. 3.3A, I).

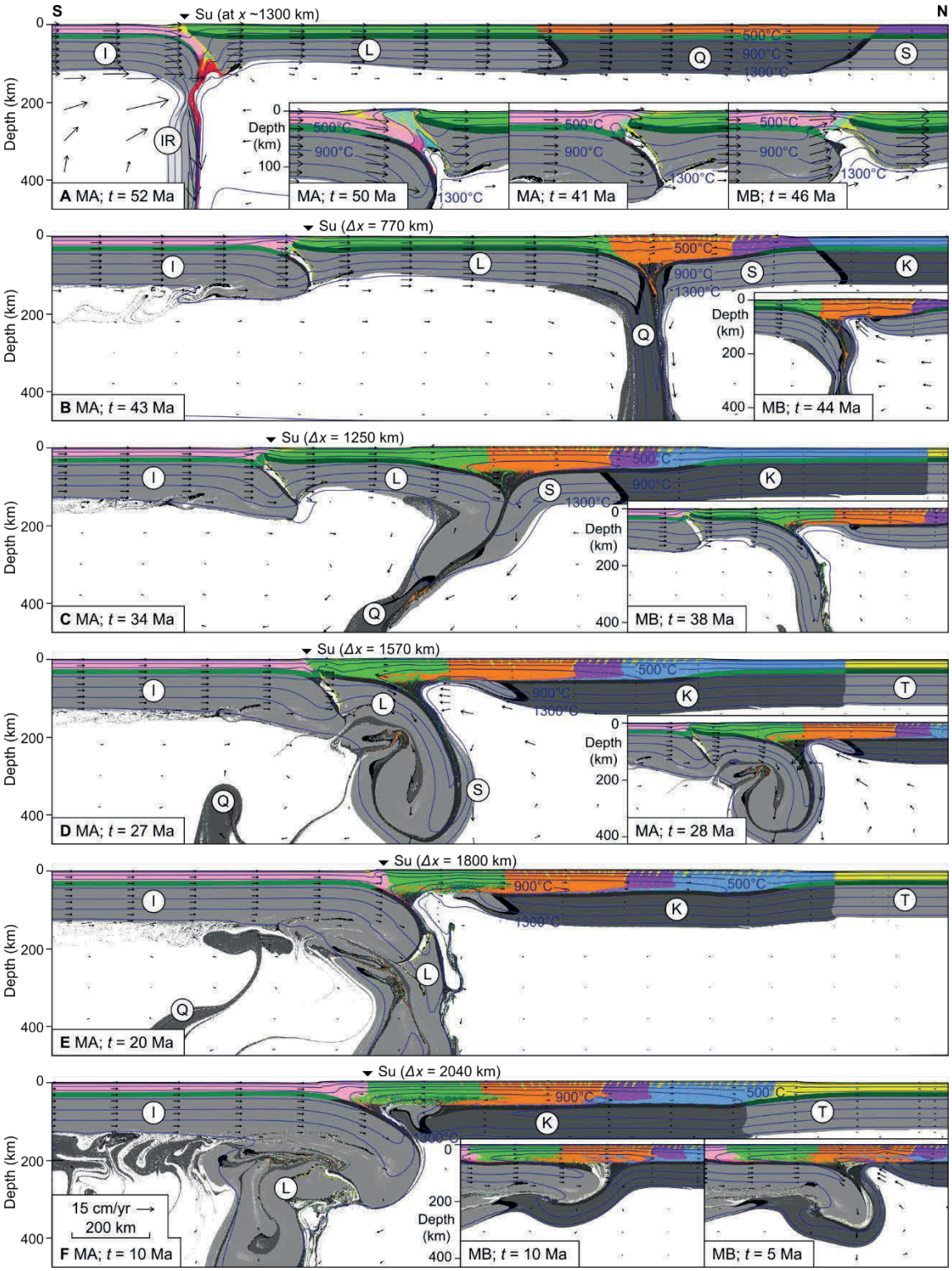

Figure 3.3. Evolution of model A (MA) supplemented with model B (MB**).** Times (t) are measured backward from the present assuming continental contact at 58 Ma, and isotherms are shown every 200 °C starting at 100 °C. Note that panels show different regions of the model, progressively stepping to the right. Crustal suture Su (equivalent of the Indus-Yarlung suture), is shown with the distance it has been translated to the right

(north) since the IR (India rifted margin) slab breakoff. x is the horizontal location of the suture at the time of slab breakoff in the Eulerian model reference frame relative to the left boundary, x = 0. Arrows are velocity vectors (scale in F). Dark-gray marker regions between continental lithospheric mantles (CLMs) have the same properties as adjacent CLM to the right/ north. (A) Breakoff of IR lithosphere following Neotethys and IR subduction, exhumation of ultrahigh-pressure (UHP) rocks (UHP IR crust in red, retrogressed UHP in blue, sediment in yellow), decoupling and widening of the subduction channel, and upwelling of the asthenosphere which becomes underplated mantle lithosphere when the temperature is <1350 °C. (B) Indentation of the retrolithosphere by I (Indian continent) lithosphere following slab breakoff, leading to shortening and thickening of the crust focused in the northern Q (Qiangtang terrane) coeval with Q-CLM folding and delamination, and decompression melting in MB. (C) Subduction of the L (Lhasa terrane) CLM either entrained with S (Songpan-Ganzi [Garze] terrane) CLM in MA or by retreating subduction in MB, and accompanied by crustal thickening spreading outward from Q. (D) Retreating subduction of L-CLM with entrained S-CLM, thereby exposing thickened Q and L crust to upwelled asthenosphere resulting in southward-propagating magmatism. (E) Limit of retreating subduction exposing southern L crust to magmatism. (F) Advancing subduction with significant Indian mantle lithosphere underthrusting, accompanied by shortening and thickening of the detached S and composite K (Kunlun terrane) crusts. T—Tarim terrane.

Subduction of I (Indian) lithosphere in MA and MB ceases at ca. 50 Ma following collision, slab breakoff, and accretion of the Tethyan Himalaya. Indian lithosphere then indents the Asian terranes, translating the model Indus-Yarlung suture (IYS) (Su in Figure 3.3) from x = 1300 km (Figure 3.3A) a distance of 750 km northward (to ≡18°N) by 43 Ma (complexity 4) (Figure 3.3B) and an additional distance of 670 km by 30 Ma, consistent with DeCelles et al. (2002, their figure 9). Some paleomagnetic compilations support this amount of translation (e.g., Yi et al., 2011; Tong et al., 2017; Zhu et al., 2017), but others place southern Lhasa at ~20°N at 58 Ma (e.g., van Hinsbergen et al., 2019), which may be appropriate for 80°–85°E. Little I-CLM subduction during indentation is, however, consistent with only minor Himalayan growth by accretion of Indian crust during this interval and with the widespread Eocene-Oligocene Indian unconformity (Yin, 2006; DeCelles et al., 2014; Hu et al., 2016; van Hinsbergen et al., 2019; Garzanti, 2019).

Indentation in MA and MB shortens the weak and dense (f = 2, d = 25 and f = 2, d = 15, respectively) Q-CLM between the stronger L-CLM and S-CLM (S—Songpan-Ganzi terrane) (Figure 3.3B; Table DR1 in Appendix B; Videos DR1 and DR2 in Kelly et al.,

2020). Coeval deformation of the overlying crust agrees with observed shortening of northern Qiangtang and adjacent Songpan-Ganzi crusts (complexity 5) (Spurlin et al., 2005; Staisch et al., 2014, 2016; Li et al., 2018; Kapp and DeCelles, 2019; Wang et al., 2014) and lack of coeval Lhasa crust shortening (Kapp and DeCelles, 2019). Q-CLM delaminates at 43 Ma (MA) and 44 Ma (MB) (Figure 3.3B), leading to upwelling of asthenosphere and heating of basal Qiangtang crust in MB (900–1100 °C), consistent with (ultra) potassic magmatism owing to melting of Qiangtang crust and mantle lithosphere (complexity 5) (Guo et al., 2006; Ding et al., 2007; Chen et al., 2013; Ou et al., 2017), notably after most crustal shortening (Kapp and DeCelles, 2019). Delaminated Q-CLM in MA and MB (at x ~3000 km, 26.3°N) matches the ~1000-km-deep tomographic anomaly "AS" at 90°E and 27°N interpreted to be Asian (Replumaz et al., 2013). The Q-CLM is also 1700 km (15°) north of the NT subducted slab, in agreement with the interpretation of Replumaz et al. (2013). If correct, this supports rapid northward translation within Tibet seen in MA and MB and Figure 3.1 (complexity 4).

Delamination of Q-CLM is followed in MA by L-CLM northward intracontinental subduction at ca. 44 Ma and closure of the subduction channel opening at 36 Ma (Figure 3.3C), consistent with diminished southern Lhasa magmatism ca. 38–25 Ma (complexity 3) (Chung et al., 2005; Ma et al., 2017; Kapp and DeCelles, 2019). As L-CLM subducts, Lhasa crust thickens, starting in the north, corresponding to widening of the proto–Tibetan Plateau to include the Lhasa terrane (complexity 6) (Kapp and DeCelles, 2019). At 34 Ma, L-CLM in MA has entrained S-CLM, producing double subduction (Figure 3.3C), whereas the less-depleted L-CLM in MB undergoes earlier retreat as it subducts (Figure 3.3C, I). In MA, detachment of L- and S-CLMs at 28 Ma initiates retreat and exposes Qiangtang crust to upwelling asthenosphere (Figure 3.3D).

Subsequent 27–22 Ma southward CLM retreat in MA (Figures 3.3D and 3.3E) explains the observed southward "sweep" and/or "jump" of magmatism from the Qiangtang terrane to the south Lhasa terrane from ca. 30 to 21 Ma (complexity 7) (Chung et al., 2003; Nomade et al., 2004; Liu et al., 2014; Kapp and DeCelles, 2019) and Indian input to negative $\varepsilon_{Hf}(t)$ from 26 Ma (Liu et al., 2017). Composite "Asian" subducted CLM sinks

but does not detach. Exposure of Qiangtang crust to hot asthenosphere in MA and MB (Figures 3.3B–3.3D) can also explain hot Oligocene-age xenoliths (>1000°C) in 28 Ma lavas in the southern Qiangtang crust (Ding et al., 2007). Contrasting MA versus MB subduction styles of L-CLM (Figure 3.3C; Videos DR1 and DR2 in Kelly et al., 2020) demonstrates the sensitivity to L-CLM depletion (d = 35 versus 30 kg/m^3).

Following 27–22 Ma L-CLM and S-CLM retreat in MA (Figures 3.3D and 3.3E), the southern Lhasa crust remains exposed to hot asthenosphere until 10 Ma (Figure 3.3F) when underthrusting I-CLM contacts vestigial S-CLM. This exposure is consistent with widespread coeval magmatism in the southern Lhasa terrane and its progressive northward termination (complexity 8) (Chung et al., 2005; Liu et al., 2014; Kapp and DeCelles, 2019).

Onset of northern Tibetan magmatism at ca. 18 Ma (Chung et al., 2005; Kapp and DeCelles, 2019) is partly explained by radioactive self-heating of thickened crust, reaching 700–900°C in S (Songpan-Ganzi) terrane and K (Kunlu) terrane and 1000–1100°C in Qiangtang lower crusts in MA by 10 Ma (complexity 9) (Figure 3.3F). In particular, recent (3 Ma) northern Qiangtang magmatism at 90°E with entrained xenoliths (Hacker et al., 2000) demonstrates in situ temperatures of 800–1000°C, depths of 30–50 km, and additional magmatic heating of ~200 °C (complexity 11). These P-T conditions and data (Wang et al., 2016) are similarly compatible with 5–0 Ma crustal temperatures in MB, which reach ~1200 °C in the Qiangtang terrane where CLM has been removed (Figures 3.3F and 3.4), and 900–1100°C in S and southern K crusts (Figures 3.4A and 3.4B). 18–0 Ma mantle-derived magmas (Turner et al., 1993, 1996; Hacker et al., 2000; Guo et al., 2006) may be explained by delamination of K-CLM under the S, not seen in MA or MB but seen in equivalent models with less-depleted K-CLM.

Terminal evolutions in MA and MB are similar (Figures 3.4A and 3.4B). In both, the slightly buoyant composite I-CLMs underthrust then curl under as they detach, with MB producing a more northerly thickened CLM lump. Their final configurations (Figures 3.4A and 3.4B) appear like tomographic images at ~90°E, many of which (e.g., Owens

and Zandt, 1997; Kosarev et al., 1999) (but not all; see explanation in Chen et al. [2017]) show fast upper-mantle velocity anomalies beneath the Lhasa terrane (complexity 10) and slow ones farther north, suggestive of the MB configuration. MB has ~500 km of I-CLM underthrusting since 23 Ma, implying equal shortening of detaching Indian crust, which agrees with 400–670 km of post–23 Ma Himalayan shortening (Long et al., 2012). The translated, 30.7°N suture (Su in Figure 3.4) in MB also generally agrees with the observed Indus-Yarlung suture, 29.3°N.

MB and MA topography (Figure 3.4; Figures DR1 and DR2 in Appendix B) show a 1000-km-wide plateau with up to 70-km-thick crust and limited thickening of northern Kunlun crust, in general agreement with observations. Crust in MB is allochthonous, with Lhasa crust underlain by I-CLM, no CLM below central Qiangtang crust, and K-CLM beneath northern Qiangtang and Songpan-Ganzi crusts. 1000 km of IR-CLM and 500 km of I-CLM subducted plus ~2600 km of L-, Q-, S-, and K-CLMs were removed. The convergence within Asia in both models is significantly larger than geologically measured post-collisional shortening. MA and MB require Q-CLM to be weaker than L-CLM to explain initial deformation in the Qiangtang terrane. This is consistent with their independently interpreted properties: Lhasa terrane has an Archean central core (Zhu et al., 2011), and the evolution of Qiangtang suggests that it should be weak (Kapp et al., 2000, 2003; Pullen et al., 2011; Pullen and Kapp, 2014).

Our models can be compared with those of Li et al. (2016) and Kelly et al. (2016). Both present “one accreted terrane” prototype models that are too simple for the Himalayan-Tibetan system. Huangfu et al. (2018) considered models with two accreted terranes, but their modes I and II results do not account for many of the 12 complexities (Figure 3.1), probably because their Lhasa and Qiangtang terranes were amalgamated into a single strong model terrane. Also see the Data Repository (in Appendix B) for other recent numerical models relevant to the Himalayan-Tibetan orogeny.

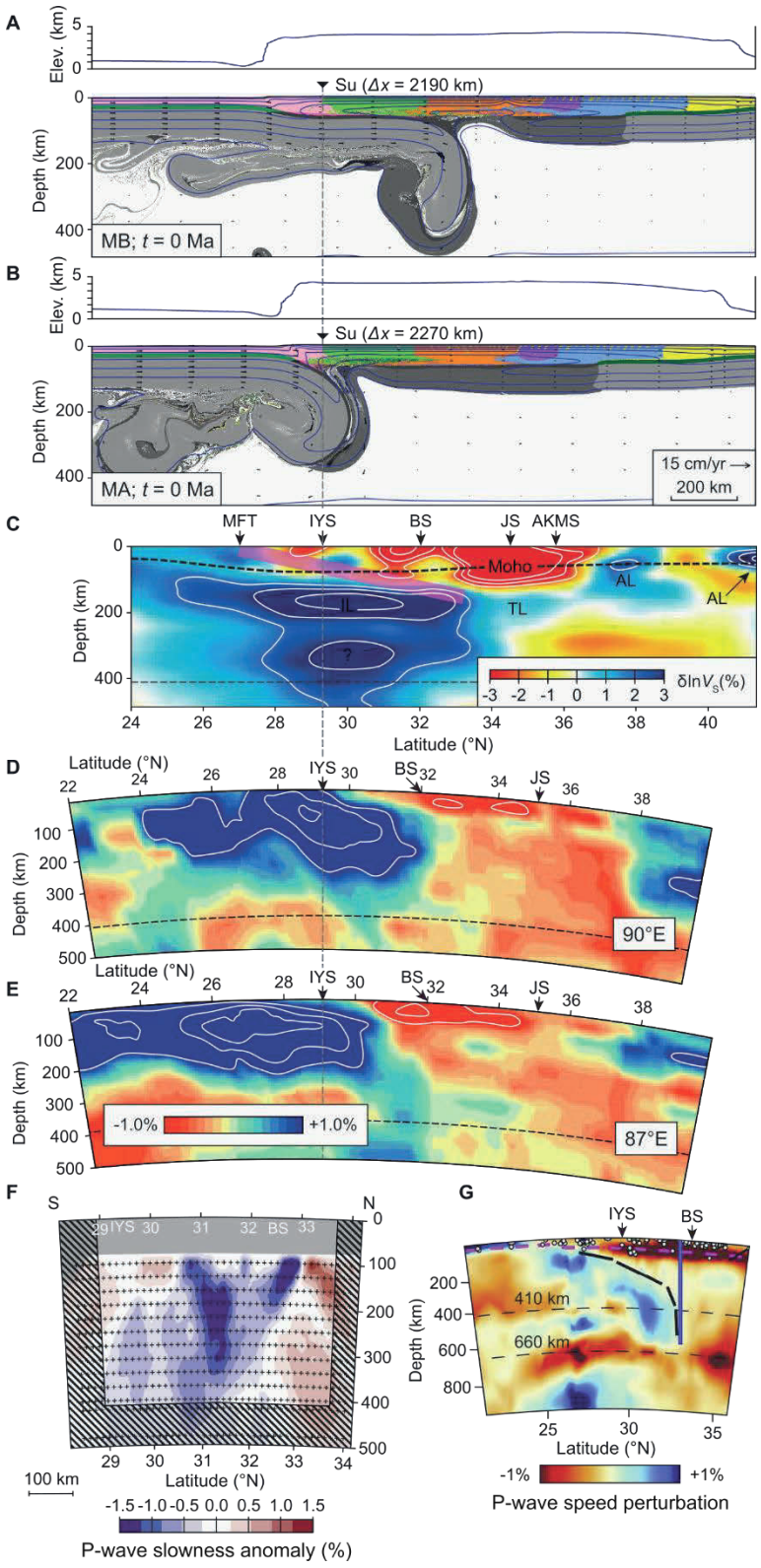

Figure 3.4. Comparison of models B (MB) and A (MA) with tomographic observations. (A,B) Topographic elevation (Elev.) and final configuration for MB (A) and MA (B)

(t—time). In both cases, advancing subduction with significant I-CLM (India continental lithospheric mantle) underthrusting leads to detachment and subsequent curling under. Su is model Indus-Yarlung suture (IYS) Δx is relative to the suture position at the time of slab breakoff. Arrows are velocity vectors (scale in B). (C) Tomographic image of shear wave speed anomalies ($\delta \ln V_s$) from Chen et al. (2017) at ~90°E. IL—Indian lithosphere; TL—Tibetan lithosphere; AL—Asian lithosphere. (D,E) Tomographic image of P-wave speed anomalies from Replumaz et al. (2014) at 90°E and 87°E, respectively (color scale for both shown in E). (F) Tomographic image of P-wave speed anomalies from Tilmann et al. (2003) at ~90°E. (G) Tomographic image of P-wave speed anomalies from Li et al. (2008) at ~87–90°E. IYS—Indus-Yarlung suture; BS—Bangong suture; JS—Jinsha suture; AKMS—Anymaqen - Kunlun-Muztagh suture; MFT—Main Frontal thrust. Images in C–G show what is interpreted to be thick lithosphere in a similar location to that in MB and MA. The style of thick lithosphere deviates strongly from that of normal lithospheric subduction. Dashed lines (C, D, E, G) mark the top of the upper mantle transition zones and the upper to lower mantle boundary.

3.5 Conclusions

We infer from MA and MB results that the complex and enigmatic space-time evolution of the Himalayan-Tibetan system (Figure 3.1) resulted from localized deformation of the CLMs of accreted Asian terranes, owing to high density and low viscosity. We regard MA and MB as working quantitative hypotheses for the Himalayan-Tibetan system. They exhibit emergent orogenic phases (Figure 3.3; Videos DR1 and DR2 in Kelly et al., 2020) consistent with observations and provide novel explanations. Key steps in the model evolution are IR slab breakoff, then I-indentation of Tibet, with deformation and delamination of weak Q-CLM. Once destabilized, more Tibetan CLM is removed by northward subduction of stronger L-CLM coupled to entrainment of S-CLM, followed by retreat. Removal of CLM exposes crust to upwelling asthenosphere and explains mantle-derived magmas, whereas independent or superimposed radioactive self-heating of thickened crust produces crustal melts and hot xenoliths. Testable predictions and relationships derived from the models are given in the Data Repository (in Appendix B).

MB and MA and Himalayan-Tibetan behaviors deviate fundamentally from large-hot orogens formed from uniform lithospheres. By implication, all large-hot orogens containing accreted terranes will develop unique styles governed by the strength and density of these terranes.

3.6 Acknowledgements

In its initial phase, this project was generously supported by the U.S. National Science Foundation Continental Dynamics project EAR-1008527; Paul Kapp and others' "Collaborative Research: The Suturing Process: Insight from the India–Asia Collision Zone" project through a subcontract, and by Natural Sciences and Engineering Research Council of Canada (NSERC) Discovery Grant 48-2012 to Beaumont. Beaumont also acknowledges support from the Canada Research Chair in Geodynamics. Kelly acknowledges an NSERC Scholarship. Numerical models used the software sopale-nested developed from SOPALE by D. Guptill, B. Lee, and members of the Dalhousie Geodynamics Group (Dalhousie University, Halifax, Nova Scotia, Canada). SOPALE was originally developed at Dalhousie University by P. Fullsack. We thank members of the Paul Kapp "suture" team and Becky Jamieson and James Brenan for discussions critical to the success of this research. We also thank Becky Jamieson, Glen Stockmal, and reviewers Alex Webb, Taras Gerya, and Paul Kapp for thoughtful comments that improved the manuscript.

3.7 Supporting Information for Chapter 3

Supporting information for Chapter 3 is provided in Appendix B.

3.8 References for Chapter 3

Aikman, A.B., Harrison, T.M., and Lin, D. (2008). Evidence for early (>44 Ma) Himalayan crustal thickening, Tethyan Himalaya, southeastern Tibet. *Earth and Planetary Science Letters, 274*, 14–23. https://doi.org/10.1016/j.epsl.2008.06.038

Beaumont, C., Jamieson, R.A., Butler, J.P., and Warren, C.J. (2009). Crustal structure: A key constraint on the mechanism of ultra-high-pressure rock exhumation. *Earth and Planetary Science Letters, 287*, 116–129. https://doi.org/10.1016/j.epsl.2009.08.001

Chapman, J.B., and Kapp, P. (2017). Tibetan magmatism database. *Geochemistry, Geophysics, Geosystems, 18*, 4229–4234. https://doi.org/10.1002/2017GC007217

Chen, J.-L., Xu, J.-F., Wang, B.-D., and Kang, Z.-Q. (2012). Cenozoic Mg-rich potassic rocks in the Tibetan Plateau: Geochemical variations, heterogeneity of subcontinental lithospheric mantle and tectonic implications. *Journal of Asian Earth Sciences, 53*, 115–130. https://doi.org/10.1016/j.jseaes.2012.03.003

Chen, J.-L., Wu, J.-B., Xu, J.-F., Dong, Y.-H., Wang, B.-D., and Kang, Z.-Q. (2013). Geochemistry of Eocene high-Mg# adakitic rocks in the northern Qiangtang terrane, central Tibet: Implications for early uplift of the plateau. *Geological Society of America Bulletin, 125*. 1800–1819, https://doi.org/10.1130/B30755.1

Chen, M., Niu, F., Tromp, J., Lenardic, A., Lee, C.- T.A., Cao, W., and Ribeiro, J. (2017). Lithospheric foundering and underthrusting imaged beneath Tibet. *Nature Communications*, *8*, 15659. https://doi.org/10.1038/ncomms15659

Chu, M.-F., Chung, S.-L., O'Reilly, S.Y., Pearson, N.J., Wu, F.-Y., Li, X.-H., et al. (2011). India's hidden inputs to Tibetan orogeny revealed by Hf isotopes of Transhimalayan zircons and host rocks. *Earth and Planetary Science Letters, 307*, 479–486. https://doi.org/10.1016/j.epsl.2011.05.020

Chung, S.-L., Liu, D., Ji, J., Chu, M.-F., Lee, H.-Y., Wen, D.-J., et al. (2003), Adakites from continental collision zones: Melting of thickened lower crust beneath southern Tibet. *Geology, 31.* 1021– 1024, https://doi.org/10.1130/G19796.1

Chung, S.-L., Chu, M.-F., Zhang, Y., Xie, Y., Lo, C.- H., Lee, T.-Y., et al. (2005), Tibetan tectonic evolution inferred from spatial and temporal variations in post-collisional magmatism: *Earth-Science Reviews, 68.* 173–196. https://doi.org/10.1016/j.earscirev.2004.05.001

DeCelles, P.G., Robinson, D.M., and Zandt, G. (2002). Implications of shortening in the Himalayan fold-thrust belt for uplift of the Tibetan Plateau. *Tectonics, 21*, 1062, 12-1–12-25. https://doi.org/10.1029/2001TC001322

DeCelles, P.G., Kapp, P., Gehrels, G.E., and Ding, L. (2014). Paleocene-Eocene foreland basin evolution in the Himalaya of southern Tibet and Nepal: Implications for the age of initial India-Asia collision. *Tectonics, 33*, 824–849. https://doi.org/10.1002/2014TC003522

Ding, H., Zhang, Z., Dong, X., Tian, Z., Xiang, H., Mu, H., et al. (2016). Early Eocene (c. 50 Ma) collision of the Indian and Asian continents: Constraints from the North Himalayan metamorphic rocks, southeastern Tibet. *Earth and Planetary Science Letters, 435*, 64–73. https://doi.org/10.1016/j.epsl.2015.12.006

Ding, L., Kapp, P., Yue, Y., and Lai, Q. (2007). Postcollisional calc-alkaline lavas and xenoliths from the southern Qiangtang terrane, central Tibet. *Earth and Planetary Science Letters, 254*, 28–38. https://doi.org/10.1016/j.epsl.2006.11.019

Donaldson, D.G., Webb, A.A.G., Menold, C.A., Kylander-Clark, A.R., and Hacker, B.R. (2013). Petrochronology of Himalayan ultrahigh-pressure eclogite. *Geology, 41*, 835–838. https://doi.org/10.1130/G33699.1

Fullsack, P. (1995). An arbitrary Lagrangian-Eulerian formulation for creeping flows and its application in tectonic models. *Geophysical Journal International, 120*, l–23. https://doi.org/10.1111/j.1365-246X.1995.tb05908.x

Garzanti, E. (2019). The Himalayan Foreland Basin from collision onset to the present: A sedimentary–petrology perspective. In: Treloar, P.J., and Searle, M.P. (Eds.), Himalayan Tectonics: A Modern Synthesis. *Geological Society, London, Special Publications, 483*. https://doi.org/10.1144/SP483.17

Garzanti, E., Radeff, G., and Malusà, M.G. (2018), Slab breakoff: A critical appraisal of a geological theory as applied in space and time. *Earth- Science Reviews*, *177*, 303–319. https://doi.org/10.1016/j.earscirev.2017.11.012

Guo, Z., Wilson, M., Liu, J., and Mao, Q. (2006). Post-collisional, potassic and ultrapotassic magmatism of the northern Tibetan Plateau: Constraints on characteristics of the mantle source, geodynamic setting and uplift mechanisms. *Journal of Petrology, 47*, 1177–1220. https://doi.org/10.1093/petrology/egl007

Hacker, B.R., Gnos, E., Ratschbacher, L., Grove, M., McWilliams, M., Sobolev, S.V., et al. (2000). Hot and dry deep crustal xenoliths from Tibet. *Science, 287*, 2463–2466. https://doi.org/10.1126/science.287.5462.2463

Hu, X., Garzanti, E., Moore, T., and Raffi, I. (2015). Direct stratigraphic dating of India-Asia collision onset at the Selandian (middle Paleocene, 59 ± 1 Ma). *Geology, 43*, 859–862. https://doi.org/10.1130/G36872.1

Hu, X., Garzanti, E., Wang, J., Huang, W., An, W., and Webb, A. (2016). The timing of India Asia collision onset—Facts, theories, controversies. *Earth-Science Reviews, 160*, 264–299, https://doi.org/10.1016/j.earscirev.2016.07.014

Huangfu, P., Li, Z.-H., Gerya, T., Fan, W., Zhang, K.-J., Zhang, H., and Shi, Y. (2018). Multi-terrane structure controls the contrasting lithospheric evolution beneath the western and central-eastern Tibetan plateau. *Nature Communications, 9*, 3780. https://doi.org/10.1038/s41467-018-06233-x

Huismans, R., and Beaumont, C. (2011), Depth-dependent extension, two-stage breakup and cratonic underplating at rifted margins. *Nature, 473*, 74–78. https://doi.org/10.1038/nature09988

Ingalls, M., Rowley, D.B., Currie, B., and Colman, A.S. (2016). Large-scale subduction of continental crust implied by India–Asia mass-balance calculation. *Nature Geoscience, 9*, 848–853. https://doi.org/10.1038/ngeo2806

Ji, W.-Q., Wu, F.-Y., Chung, S.-L., Wang, X.-C., Liu, C.-Z., Li, Q.-L., et al. (2016). Eocene Neo-Tethyan slab breakoff constrained by 45 Ma oceanic island basalt–type magmatism in southern Tibet. *Geology, 44*, 283–286. https://doi.org/10.1130/G37612.1

Kapp, P., and DeCelles, P.G. (2019). Mesozoic–Cenozoic geological evolution of the Himalayan- Tibetan orogen and working tectonic hypotheses. *American Journal of Science, 319*, 159–254. https://doi.org/10.2475/03.2019.01

Kapp, P., Yin, A., Manning, C.E., Murphy, M., Harrison, T.M., Spurlin, M., et al. (2000). Blueschist-bearing metamorphic core complexes in the Qiangtang block reveal deep crustal structure of northern Tibet. *Geology, 28*, 19–22. https://doi.org/10.1130/0091-7613(2000)28<19:BMCCIT>2.0.CO;2

Kapp, P., Yin, A., Manning, C.E., Harrison, T.M., Taylor, M.H., and Ding, L. (2003). Tectonic evolution of the early Mesozoic blueschist-bearing Qiangtang metamorphic belt, central Tibet. *Tectonics, 22*, 1043–1054. https://doi.org/10.1029/2002TC001383

Kelly, S., Butler, J.P., and Beaumont, C. (2016). Continental collision with a sandwiched accreted terrane: Insights into Himalayan–Tibetan lithospheric mantle tectonics? *Earth and Planetary Science Letters, 455*, 176–195. https://doi.org/10.1016/j.epsl.2016.08.039

Kosarev, G., Kind, R., Sobolev, S.V., Yuan, X., Hanka, W., and Oreshin, S. (1999). Seismic evidence for a detached Indian lithospheric mantle beneath Tibet. *Science, 283*, 1306–1309. https://doi.org/10.1126/science.283.5406.1306

Lee, C.-T. A. (2003). Compositional variation of density and seismic velocities in natural peridotites at STP conditions: Implications for seismic imaging of compositional heterogeneities in the upper mantle. *Journal of Geophysical Research, 108*, 2441. https://doi.org/10.1029/2003JB002413

Lee, H.-Y., Chung, S.-L., Lo, C.-H., Ji, J., Lee, T.-Y., Qian, Q., and Zhang, Q. (2009), Eocene Neotethyan slab breakoff in southern Tibet inferred from the Linzizong volcanic record: *Tectonophysics, 477*, 20–35. https://doi.org/10.1016/j.tec-to.2009.02.031

Leech, M.L., Singh, T.S., Jain, A.K., Klemperer, S.L., and Manickavasagam, R.M. (2005). The onset of India–Asia continental collision: Early, steep subduction required by the timing of UHP metamorphism in the western Himalaya. *Earth and Planetary Science Letters, 234*, 83–97. https://doi.org/10.1016/j.epsl.2005.02.038

Li, C., van der Hilst, R.D., Meltzer, A.S., and Engdahl, R.E. (2008). Subduction of the Indian lithosphere beneath the Tibetan Plateau and Burma. *Earth and Planetary Science Letters, 274*, 157–168. https://doi.org/10.1016/j.epsl.2008.07.016

Li, L., Garzione, C.N., Pullen, A., Zhang, P., and Li, Y. (2018). Late Cretaceous–Cenozoic basin evolution and topographic growth of the Hoh Xil Basin, central Tibetan Plateau. *Geological Society of America Bulletin, 130*, 499–521. https://doi.org/10.1130/B31769.1

Li, Z.-H., Liu, M., and Gerya, T. (2016). Lithosphere delamination in continental collisional orogens: A systematic numerical study. *Journal of Geophysical Research: Solid Earth, 121*, 5186–5211. https://doi.org/10.1002/2016JB013106

Liu, D., Zhao, Z., Zhu, D.C., Niu, Y., DePaolo, D.J., Harrison, T.M., et al. (2014). Postcollisional potassic and ultrapotassic rocks in southern Tibet: Mantle and crustal origins in response to India–Asia collision and convergence. *Geochimica et Cosmochimica Acta*, *143*, 207–231. https://doi.org/10.1016/j.gca.2014.03.031

Liu, D., Zhao, Z., DePaolo, D.J., Zhu, D.-C., Meng, F.- Y., Shi, Q., and Wang, Q. (2017). Potassic volcanic rocks and adakitic intrusions in southern Tibet: Insights into mantle-crust interaction and mass transfer from Indian plate. *Lithos, 268*, 48– 64. https://doi.org/10.1016/j.lithos.2016.10.034

Long, S.P., McQuarrie, N., Tobgay, T., Coutand, I., Cooper, F.J., Reiners, P.W., et al. (2012). Variable shortening rates in the eastern Himalayan thrust belt, Bhutan: Insights from multiple thermochronologic and geochronologic data sets tied to kinematic reconstructions. *Tectonics, 31*, TC5004. https://doi.org/10.1029/2012TC003155

Ma, L., Wang, Q., Li, Z.-X., Wyman, D.A., Yang, J.-H., Jiang, Z.-Q., et al. (2017). Subduction of Indian continent beneath southern Tibet in the latest Eocene (~35 Ma): Insights from the Quguosha gabbros in southern Lhasa block. *Gondwana Research, 41*, 77–92. https://doi.org/10.1016/j.gr.2016.02.005

Martin, A.J. (2017). A review of Himalayan stratigraphy, magmatism, and structure. *Gondwana Research, 49*, 42–80. https://doi.org/10.1016/j.gr.2017.04.031

Najman, Y., Appel, E., Boudagher-Fadel, M., Bown, P., Carter, A., Garzanti, E., et al. (2010). Timing of India-Asia collision: Geological, biostratigraphic, and palaeomagnetic constraints. *Journal of Geophysical Research*, *115*, B12416. https://doi.org/10.1029/2010JB007673

Najman, Y., Jenks, D., Godin, L., Boudagher-Fadel, M., Millar, I., Garzanti, E., et al. (2017). The Tethyan Himalayan detrital record shows that India–Asia terminal collision occurred by 54 Ma in the Western Himalaya. *Earth and Planetary Science Letters, 459*, 301–310, https://doi.org/10.1016/j.epsl.2016.11.036

Nomade, S., Renne, P.R., Mo, X., Zhao, Z., and Zhou, S. (2004). Miocene volcanism in the Lhasa block, Tibet: Spatial trends and geodynamic implications. *Earth and Planetary Science Letters, 221*, 227–243. https://doi.org/10.1016/S0012-821X(04)00072-X

O'Brien, P.J. (2019). Eclogites and other high-pressure rocks in the Himalaya: A review. Teloar, P. J. and Searle, M. P. (Eds.), Himalayan Tectonics: A Modern Synthesis, *Geological Society, London, Special Publications*, *483*, 183–213. https://doi.org/10.1144/SP483.13

Ou, Q., Wang, Q., Wyman, D.A., Zhang, H.-X., Yang, J.-H., Zeng, J.-P., et al. (2017), Eocene adakitic porphyries in the central-northern Qiangtang Block, central Tibet: Partial melting of thickened lower crust and implications for initial surface uplifting of the plateau. *Journal of Geophysical Research: Solid Earth, 122*, 1025–1053. https://doi.org/10.1002/2016JB013259

Owens, T.J., and Zandt, G. (1997), Implications of crustal property variations for models of Tibetan plateau evolution. *Nature, 387*, 37–43. https://doi.org/10.1038/387037a0

Pullen, A., and Kapp, P. (2014), Mesozoic tectonic history and lithospheric structure of the Qiangtang terrane: Insights from the Qiangtang metamorphic belt, central Tibet. Nie, J., et al., (Eds.), Toward an Improved Understanding of Uplift Mechanisms and the Elevation History of the Tibetan Plateau. G*eological Society of America Special Papers, 507,* 71–87. https://doi.org/10.1130/2014.2507(04)

Pullen, A., Kapp, P., Gehrels, G.E., Ding, L., and Zhang, Q. (2011). Metamorphic rocks in central Tibet: Lateral variations and implications for crustal structure. *Geological Society of America Bulletin, 123*, 585–600. https://doi.org/10.1130/B30154.1

Replumaz, A., Guillot, S., Villaseñor, A., and Negredo, A.M. (2013). Amount of Asian lithospheric mantle subducted during the India/Asia collision. *Gondwana Research, 24*, 936–945. https://doi.org/10.1016/j.gr.2012.07.019

Replumaz, A., Capitanio, F.A., Guillot, S., Negredo, A.M., and Villaseñor, A. (2014). The coupling of Indian subduction and Asian continental tectonics. *Gondwana Research, 26*, 608–626. https://doi.org/10.1016/j.gr.2014.04.003

Smit, M.A., Hacker, B.R., and Lee, J. (2014). Tibetan garnet records early Eocene initiation of thickening in the Himalaya. *Geology, 42*, 591–594. https://doi.org/10.1130/G35524.1

Spurlin, M.S., Yin, A., Horton, B.K., Zhou, J., and Wang, J. (2005). Structural evolution of the Yushu-Nangqian region and its relationship to syncollisional igneous activity, east-central Tibet. *Geological Society of America Bulletin, 117*, 1293–1317. https://doi.org/10.1130/B25572.1

Staisch, L.M., Niemi, N.A., Hong, C., Clark, M.K., Rowley, D.B., and Currie, B. (2014). Cretaceous-Eocene depositional age for the Fenghuoshan Group, Hoh Xil Basin: Implications for the tectonic evolution of the northern Tibet Plateau. *Tectonics, 33,* 281–301. https://doi.org/10.1002/2013TC003367

Staisch, L.M., Niemi, N.A., Clark, M.K., and Chang, H. (2016). Eocene to late Oligocene history of crustal shortening within the Hoh Xil Basin and implications for the uplift history of the northern Tibetan plateau. *Tectonics, 35*, 862–895. https://doi.org/10.1002/2015TC003972

Tilmann, F., and Ni, J., and INDEPTH III Seismic Team (2003). Seismic imaging of the downwelling Indian lithosphere beneath central Tibet. *Science, 300*, 1424–1427. https://doi.org/10.1126/science.1082777

Tong, Y., Yang, Z., Mao, C., Pei, J., Pu, Z., and Xu, Y. (2017). Paleomagnetism of Eocene red-beds in the eastern part of the Qiangtang Terrane and its implications for uplift and southward crustal extrusion in the southeastern edge of the Tibetan Plateau. *Earth and Planetary Science Letters, 475*, 1–14. https://doi.org/10.1016/j.epsl.2017.07.026

Turner, S., Hawkesworth, C., Liu, J., Rogers, N., Kelley, S., and van Calsteren, P. (1993). Timing of Tibetan uplift constrained by analysis of volcanic rocks. *Nature, 364*, 50–54. https://doi.org/10.1038/364050a0

Turner, S., Arnaud, N., Liu, J., Rogers, N., Hawkesworth, C., Harris, N., et al. (1996). Post-collision, shoshonitic volcanism on the Tibetan plateau: Implications for convective thinning of the lithosphere and the source of ocean island basalts. *Journal of Petrology, 37*, 45–71. https://doi.org/10.1093/petrology/37.1.45

Van der Voo, R., Spakman, W., and Bijwaard, H. (1999). Tethyan subducted slabs under India. *Earth and Planetary Science Letters, 171*, 7–20. https://doi.org/10.1016/S0012-821X(99)00131-4

van Hinsbergen, D.J.J., Lippert, P.C., Li, S., Huang, W., Advokaat, E.L., and Spakman, W. (2019). Reconstructing Greater India: Paleogeographic, kinematic, and geodynamic perspectives. *Tectonophysics, 760*, 69–94. https://doi.org/10.1016/j.tecto.2018.04.006

Wang, C., Dai, J., Zhao, X., Li, Y., Graham, S.A., He, D., et al. (2014). Outward-growth of the Tibetan Plateau during the Cenozoic: A review. *Tectonophysics, 621*, 1–43. https://doi.org/10.1016/j.tecto.2014.01.036

Wang, Q., Hawkesworth, C.J., Wyman, D., Chung, S.-L., Wu, F.-Y., Li, X.-H., Li, et al., (2016). Pliocene-Quaternary crustal melting in central and northern Tibet and insights into crustal flow. Nature communications, *7*, 11888. https://doi.org/10.1038/ncomms11888

Yi, Z., Huang, B., Chen, J., Chen, L., and Wang, H. (2011). Paleomagnetism of early Paleogene marine sediments in southern Tibet, China: Implications to onset of the India–Asia collision and size of Greater India. *Earth and Planetary Science Letters, 309*, 153–165. https://doi.org/10.1016/j.epsl.2011.07.001

Yin, A. (2006). Cenozoic tectonic evolution of the Himalayan orogen as constrained by along-strike variation of structural geometry, exhumation history, and foreland sedimentation. *Earth-Science Reviews, 76*, 1–131. https://doi.org/10.1016/j.earscirev.2005.05.004

Yin, A., and Harrison, T.M. (2000). Geologic evolution of the Himalayan-Tibetan orogeny. *Annual Review of Earth and Planetary Sciences, 28*, 211–280. https://doi.org/10.1146/annurev.earth.28.1.211

Zeng, L., Gao, L.-E., Xie, K., and Jing, L.-Z. (2011). Mid-Eocene high Sr/Y granites in the Northern Himalayan Gneiss Domes: Melting thickened lower continental crust. *Earth and Planetary Science Letters, 303*, 251–266. https://doi.org/10.1016/j.epsl.2011.01.005

Zhu, D.-C., Zhao, Z.-D., Niu, Y., Mo, X.-X., Chung, S.-L., Hou, Z.-Q., et al. (2011). The Lhasa Terrane: Record of a microcontinent and its histories of drift and growth. *Earth and Planetary Science Letters, 301*, 241–255. https://doi.org/10.1016/j.epsl.2010.11.005

Zhu, D.-C., Wang, Q., Zhao, Z.-D., Chung, S.-L., Cawood, P.A., Niu, Y., et al. (2015). Magmatic record of India-Asia collision. *Scientific Reports, 5*, 14289. https://doi.org/10.1038/srep14289

Zhu, D.C., Wang, Q., and Zhao, Z.D. (2017). Constraining quantitatively the timing and process of continent-continent collision using magmatic record: Method and examples. *Science China Earth Sciences, 60*, 1040–1056. https://doi.org/10.1007/s11430-016-9041-x

Zhu, D.-C., Wang, Q., Chung, S.-L., Cawood, P.A., and Zhao, Z.-D. (2019). Gangdese magmatism in southern Tibet and India–Asia convergence since 120 Ma. Treloar, P.J., and Searle, M.P. (Eds.), Himalayan Tectonics: A Modern Synthesis. *Geological Society, London, Special Publications, 483*. https://doi.org/10.1144/SP483.14

CHAPTER 4. EOHIMALAYAN METAMORPHISM AND SUBSEQUENT TECTONIC QUIESCENCE EXPLAINED

This chapter is a modified version of the article 'Eohimalayan Metamorphism and Subsequent Tectonic Quiescence Explained' by S. Kelly, C. Beaumont, and R. A. Jamieson, published in the journal *Earth and Planetary Science Letters* (Kelly et al., 2022).

4.1 Abstract

The early evolution of the Himalayan-Tibetan orogen remains enigmatic. A wide range of observations can be interpreted to suggest that two distinct Eohimalayan and Neohimalayan episodes of development were separated by a ~10-15 Myr interval of limited growth, or possible tectonic quiescence, apparently at odds with the continuous continental collision implied by plate tectonic convergence of India with respect to Asia. We present a numerical geodynamical model, MEA, which provides an internally self-consistent explanation for two apparently unrelated but persistent problems in early Himalayan evolution – the nature of Eohimalayan metamorphism, and the hiatus between Eo-and Neo-himalayan tectonism.

In MEA, Early Eohimalayan medium pressure-medium temperature (MP-MT) metamorphism can be explained by opening of the Neotethys subduction channel adjacent to the Indus-Yarlung-Tsangpo suture shortly after India and Asia collided. Subduction channel opening, driven by Qiangtang lithosphere delamination, results in asthenospheric upwelling into the subduction channel. Upwelling provides heat for prograde metamorphism of the Tethyan Himalaya, consistent with natural and model P-T-t paths, and could have produced basaltic magmatism. In MEA, gravitationally-driven delamination of Qiangtang mantle lithosphere after ~45 Ma pulls Lhasa terrane lithosphere to the north, causing shortening of the overlying Asian crust, and resulting in apparent indentation of Asia by India. During this Late Eohimalayan phase, MEA predicts that India and the southern part of Tibet advance northward at about the same

rate, resulting in little or no growth of the Tethyan Himalaya. High temperatures persist in Indian crust owing to the increasing role of radioactive self-heating. Renewed accretion and growth of the Himalaya following subduction channel closing at ~33 Ma lead to Neohimalayan deformation and metamorphism. We propose that the early history of the Himalaya is best explained in terms of two contrasting regimes – Early Eohimalayan accretion and metamorphism from ~55-45 Ma, and Late Eohimalayan tectonic quiesence and continuing MP-MT metamorphism from ~45-30 Ma.

4.2 Introduction

The Himalayan-Tibetan (H-T) system, the most extensively and intensively studied large-hot orogen (e.g., Jamieson et al., 2004) on Earth, is widely regarded as the archetype of large-scale collisional orogenesis (e.g., Yin and Harrison, 2000; Hodges, 2000; Hu et al., 2016; Searle, 2019). Tectonic inferences based on the wealth of H-T structural, metamorphic, and magmatic data commonly serve as a guide for understanding large-scale orogenesis in general (e.g., Yin, 2006; St-Onge et al., 2006). Despite its archetypal status, unanswered questions remain regarding fundamental aspects of H-T evolution (e.g., Aitchison et al., 2007; van Hinsbergen et al., 2019; Searle, 2019; Parsons et al., 2020; Kelly et al., 2020), including the processes and timing of Himalayan crustal accretion and thickening, the resultant metamorphism, magmatism, and erosion, and the lithosphere-scale geodynamical evolution of the H-T system. These uncertainties challenge not only our understanding of the H-T orogen but limit its usefulness as an archetype.

Among the uncertainties surrounding Himalayan tectonic evolution, none is more enigmatic than the nature of its early development. The stratigraphic record indicates that the India-Asia collision was progressive (e.g., DeCelles et al., 2014; Hu et al., 2016), starting with initial contact of distal margins at ~59±1 Ma (hereafter “contact”), with full-thickness Indian crust involved in the collision by ~54 Ma (hereafter “collision”). Observations from metamorphic and igneous rocks distinguish two distinct phases of Himalayan evolution – a mainly Eocene Eohimalayan phase (~59-30 Ma) and a mainly

Miocene to present (~30-0 Ma) Neohimalayan phase (e.g., Hodges and Silverberg, 1988; Le Fort, 1996; Hodges, 2000; Aikman et al., 2008). While Neohimalayan metamorphism and magmatism can be explained by 20 Myr of radioactive self-heating following crustal thickening (e.g., Jamieson et al., 2004, and references therein), the heat source for Eohimalayan medium pressure-medium temperature (MP-MT) metamorphism and crustal melting has not yet been identified (e.g., Aikman et al., 2012; Ryan and Dewey, 2019). In particular, data indicating that metamorphic conditions reached ~650◦C and 0.7-0.9 GPa as early as 45 Ma are incompatible with models in which thickening of radioactive crustal material is the dominant heat source (e.g., Jamieson et al., 2004; Beaumont et al., 2004) because the time lapse since collision (≤10 Myr) is too short.

Another source of uncertainty centers on the nature and duration of Himalayan crustal accretion and growth. Evidence from plate circuits and paleomagnetic data imply continuous convergence of India relative to Asia from ~59 Ma to the present, with India absorbing >2000 km of the total convergence (e.g., Ingalls et al., 2016; van Hinsbergen et al., 2011). However, the relatively narrow Himalaya and its small accreted crustal cross-sectional area, coupled with modest shortening estimates (minimum ~300-650 km; e.g., Yin and Harrison, 2000; DeCelles et al., 2011; Long et al., 2012), are inconsistent with the full >2000 km of convergence being accommodated by continuous detachment and accretion of Indian crust since initial contact or later collision. Given that structural and metamorphic data demonstrate that the Tethyan Himalaya accreted during early H-T orogenesis, it remains to be convincingly explained why the overall accretion and growth of the Himalaya accounts for only a small fraction of the total India-Asia convergence.

The following observations, listed in approximately chronological order, require explanation in any model addressing Eohimalayan orogenesis (Appendix C1 for details).

1) Early Eohimalayan diorites, gabbros, and basaltic dykes in the eastern Tethyan Himalaya and central and eastern Gangdese batholith, with ages ranging from 57-45 Ma, suggest that sublithospheric magmas intruded the crust without significant contamination (e.g., Ji et al., 2016; Wang et al., 2019).

2) In the western Himalaya, Eohimalayan ultra-high-pressure (UHP) metamorphism at 48-46 Ma (O'Brien, 2019, and references therein) was followed by partial exhumation and overprinting by amphibolite-facies assemblages (~1.0 GPa, 700◦C) at ~45-40 Ma. While the UHP metamorphism itself does not require a special explanation, the reheating is not readily explained by existing models.

3) Eohimalayan prograde metamorphism was underway by ~54 Ma (e.g., Smit etal., 2014), with peak P-T conditions (~0.6-0.8 GPa, 650-750°C) recorded at ~40-35 Ma in many localities in the north Himalayan gneiss domes and upper Greater Himalayan Sequence (GHS) (e.g., Ding et al., 2016; Carosi et al., 2019). As noted above, the heat source for this metamorphism remains enigmatic.

4) Eohimalayan granitic intrusions ranging from 45-35 Ma, with crustal geochemical signatures, have been documented in some north Himalayan gneiss domes (e.g., Aikman et al., 2008; Zeng et al., 2011; Regis et al., 2014). In combination with migmatites associated with some Eohimalayan metamorphic rocks (e.g., Imayama et al., 2018), this implies that Tethyan Himalayan crust was hot enough to melt by the mid-Eocene.

5) Tethyan Himalayan rocks were deformed and thickened (Ratschbacher et al., 1994) by at least ~45 Ma based on ages of THS fabrics (Wiesmayr and Grasemann, 2002) and undeformed granitoids cutting deformed TH rocks (Aikman et al., 2008). Paleocene-Eocene deposition of inferred TH-derived sediments into the Indian foreland basin in south-central Tibet (DeCelles et al., 1998, 2014) indicates TH uplift and erosion were underway at this time.

6) Finally, the small size of the Himalaya provides evidence that detachment and accretion of Indian crust to form the Himalaya cannot have continued unabated from contact at ~59 Ma to the present, suggesting that something is missing in our current understanding of the transition from Eohimalayan to Neohimalayan tectonics.

The purpose of this paper is to provide explanations for the poorly understood Eohimalayan orogenic phase and the transition from Eohimalayan to Neohimalayan tectonics. We start by addressing the problem of the heat source for Eohimalayan crustal magmatism and MT-MP metamorphism. In the second part of the paper we test the hypothesis that Early Eohimalayan tectonic growth, from contact through collision at ~59 Ma to ~45 Ma, was followed by 10-15 Myr of Late Eohimalayan tectonic quiescence. Renewed Neohimalayan crustal accretion and growth after ~30 Ma led to the development of the present-day Himalayan orogen. We first present the results of numerical Model EA (MEA; Eohimalayan (E) refinement of MA and MB, Kelly et al., 2020), and compare model predictions with observations from Eohimalayan metamorphic rocks. We then compare MEA results with those from supplementary models MEB, MEC, and MED. We show that enigmatic Eohimalayan evolution can be explained by the emergent, self-consistent properties of MEA, and offer this as a testable model for Eohimalayan tectonic development.

4.3 Methods

The models presented below (Figure 4.1) are variations on models MA and MB of Kelly et al. (2020) with additional tracking of model particles for pressure-temperature-time (P-T-t) evolution (Methods in Appendix C2). The mantle-scale 2-D finite element model computations used SOPALE-nested software (http://geodynamics.oceanography.dal.ca/sopale_nested.html) which calculates frictional-plastic and creeping viscous flows and the evolving temperature and pressure fields. Appendix C2a presents an abbreviated version of the numerical methods discussed in detail in Appendix C2b.

4.4 MEA Results: Limited Opening of the Subduction Channel

Model EA (MEA *f* 4-*d*35_*f* 2-*d*25_*f* 3-*d*30_ *f* 3-*d*30) (Figures 4.3-4.5 and Animation MEA from Kelly et al., 2022) has a weak and moderately dense Q-CLM (Qiangtang) (*f*= 2, *d*= 25) and the L, S and K terrane CLMs are stronger and moderately buoyant (*f*= 4, *d*=35 for L and *f*= 3, *d*= 30 for S and K). The cratonic T-CLM (Tarim) is strong and

buoyant (*f*= 5, *d*= 50). Model time is given in Ma (million years before present) assuming contact of Indian and Asian lithospheres was at 58 Ma. This choice enables direct comparison with geological ages.

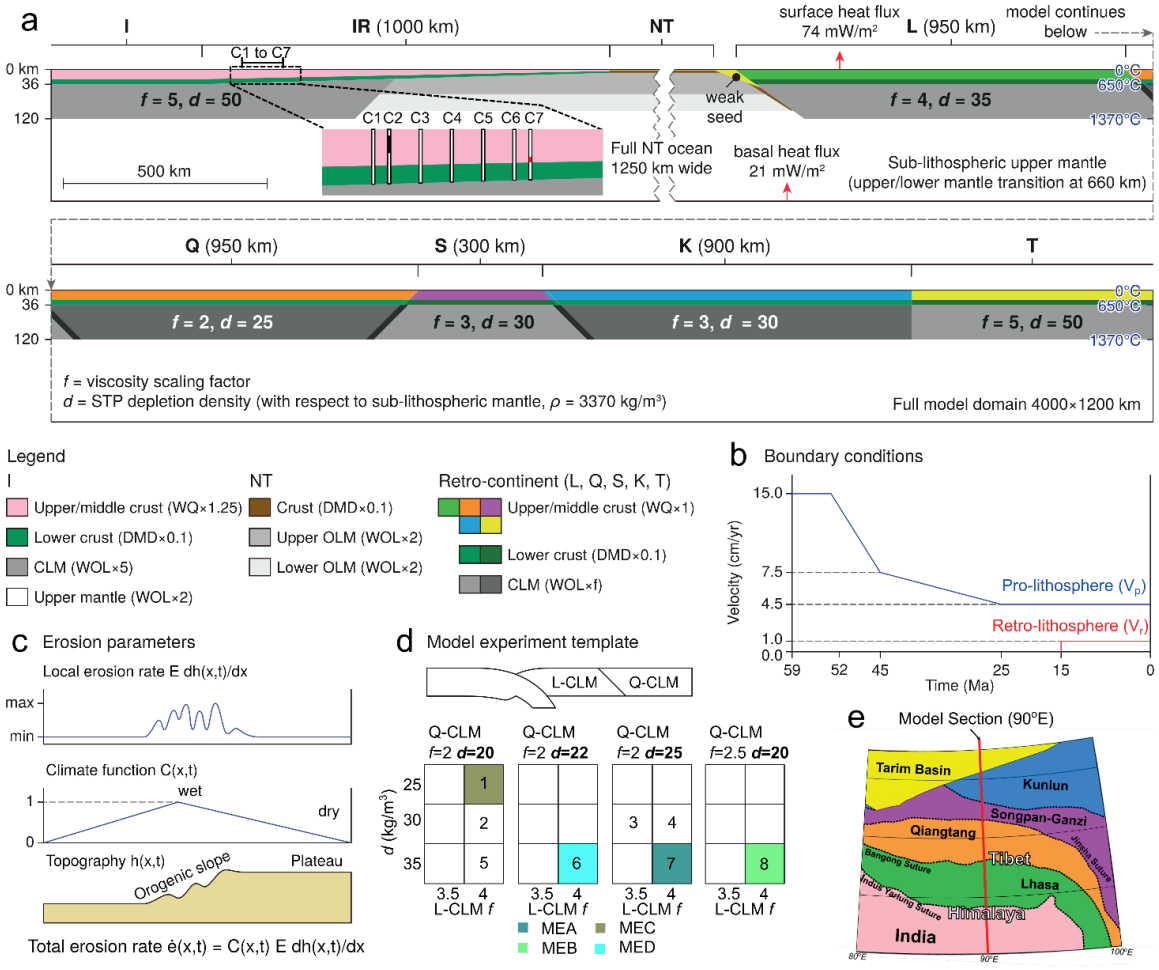

Figure 4.1. (a) Initial geometry and properties of model MEA, cross-sectional geodynamical model. It comprises (left to right): Indian continent (I), its rifted margin (IR), Neotethys ocean (NT), and composite retrocontinent; underlying upper mantle extends to 660 km depth and lower mantle to 1200 km. The retrocontinent comprises (from left to right): Lhasa terrane (L), Qiangtang terrane (Q), Songpan-Ganzi terrane (S), composite Kunlun terrane (K), and Tarim terrane (T). Inset: Initial locations of columns of tracked particles, C1 to C7, located within the proximal IR margin crust. Black zone in C2 and red zone in C7 show depth ranges of particles recording MP-MT and UHP conditions, respectively. Width of the retrocontinent is restored based on assumed NT breakoff at 11°N at 90°E. This implies an increase in the width of the retrocontinent of ~2200 km with respect to the current configuration, which is achieved in the model design by proportional increases in the lengths of Asian terranes south of the Tarim terrane. 1000-km-wide IR (Greater India rifted margin) has depth-dependent stretching geometry (Huismans and Beaumont, 2011). All continental regions start with uniform-

thickness layering (Table 4.1, footnote 1): 24 km upper to middle crust, 12 km lower crust, and 84 km continental lithospheric mantle (CLM), extending to 120 km depth. Oceanic lithosphere layers comprise 2 km of sediment, 6 km of oceanic crust, and 92 km of oceanic mantle lithosphere. f is the viscosity scaling factor for power-law flow (Appendices B1 and B2; Table 4,1, footnote 1). CLM densities are quoted as density depletion (d, in kg/m^3) with respect to sublithospheric mantle density (3370 kg/m^3) (see Table 4.1 for other model properties). Dark-gray passive marker regions between continental lithospheric mantles (CLMs) have the same properties as adjacent CLM to the right/north. Continents have laterally uniform crustal radioactive heat production for upper–middle and lower continental crust of 2.0 and 0.4 μW/m^3, respectively. Initial Moho and base lithosphere temperatures on continents are ∼650°C and ∼1370°C, respectively. The bases of the NT and IR lithospheres are also at ∼1370°C and the tapering IR crust has the same heat production values as the continental crusts. Dips of sutures are based on inferred accretion polarity. STP = standard temperature and pressure; WQ = wet quartzite; DMD = dry Maryland diabase; CLM = continental lithospheric mantle; WOL= wet olivine; OLM = oceanic lithospheric mantle. (b) Post-59 Ma convergent velocity boundary conditions based on Ingalls et al. (2016). (c) Erosion model properties. Climate function is similar to that of Wang et al. (2014). (d) Model property template for L-CLM and Q-CLM. Numbers are model numbers: we refer to models by their L-CLM and Q-CLM f and d properties, using notation MEA (L_*f* 4-*d*35, Q_*f* 2-*d*25) for MEA, for example. Other properties do not vary. (e) Terrane map of Himalaya and Tibet showing the location of the model section at 90°E.

MEA is shown starting with contact of the distal IR (India rifted margin) and L-terrane (Lhasa) at 58 Ma (Figure 4.2a) following NT (Neotethys) oceanic lithosphere subduction. The NT slab and IR breakoff at 52 Ma at a shallow depth (Figure 4.2b) as full thickness I-lithosphere underthrusts the L-terrane. I-crust, subducted to the base of the lithosphere and beyond, is subject to UHP metamorphism (Figure 4.2b, red).

By 50 Ma UHP crust starts to exhume and retrogresses as the NT subduction channel begins to open (Figure 4.2c, blue). MEA exhumation of UHP material at 50-46 Ma (Figures 4.2, 4.3) is in reasonable agreement with the timing of Tso Morari and Kaghan UHP exhumation by ∼44 Ma.

Following breakoff of the IR margin, the system becomes highly contractional with I-lithosphere apparently indenting the retrolithosphere (velocity vectors, Figure 4.2b-d). Asian terrane shortening is largely accommodated by deformation in the weakest and densest terrane, Q, producing Q-CLM folding and thickening of the overlying Q-crust (Figure 4.2d), consistent with observations (Kapp et al., 2005). Initial folding of the dense

Q-CLM by compressive forces (Figure 4.2j) leads to a self-sustaining, gravitationally-driven instability and progressive delamination removal of the Q-CLM. The Q-CLM delamination drives shortening within the Q-crust and progressively pulls the L-terrane north at a rate which outpaces the I-continent convergence rate. This process results in India-Asia separation localized at the suture and opening of the subduction channel (Figure 4.2d, e). This interpretation is confirmed by the tectonic boundary forces (Figure 4.2j) which show the force required to drive 'indentation' (red) actually decreases as Q-CLM delamination develops and Q-terrane shortening becomes largely self-driven. Bird (1978) proposed that delamination would allow sublithospheric mantle to upwell to the base of the crust, and Sizova et al. (2019) modelled subduction channel opening produced by slab rollback. In the H-T case we suggest slab rollback is unlikely owing to the fast convergence of India on Asia at collision. Subduction channel opening by self-driven delamination, as in MEA, is a viable alternative, particularly if slab breakoff preceded opening.

The progressive opening of the subduction zone is rapid from 48 to 42 Ma (Figure 4.2c-g), after which Q-CLM is completely delaminated (Figure 4.2f), leaving a 50 km wide subduction channel gap. Opening of the subduction channel produces upwelling of hot asthenosphere (Figure 4.2g), which converts to mantle lithosphere as it cools. Heating of I-crust by upwelling asthenosphere at ~40 km depth is shown by the upwarping of the 700°C isotherm by comparison with its position in the adjacent lithosphere (Figure 4.2g). In the next section we propose that this heating provides an explanation for Early Eohimalayan metamorphism. Opening of the subduction channel would be expected to produce extension of the overlying I-crust. However, in MEA, crust previously carried into the subduction channel rebounds, contracts, and fills the gap as it opens. The result is that shortened, not stretched, crust occupies the gap (Figure 4.2b-e).

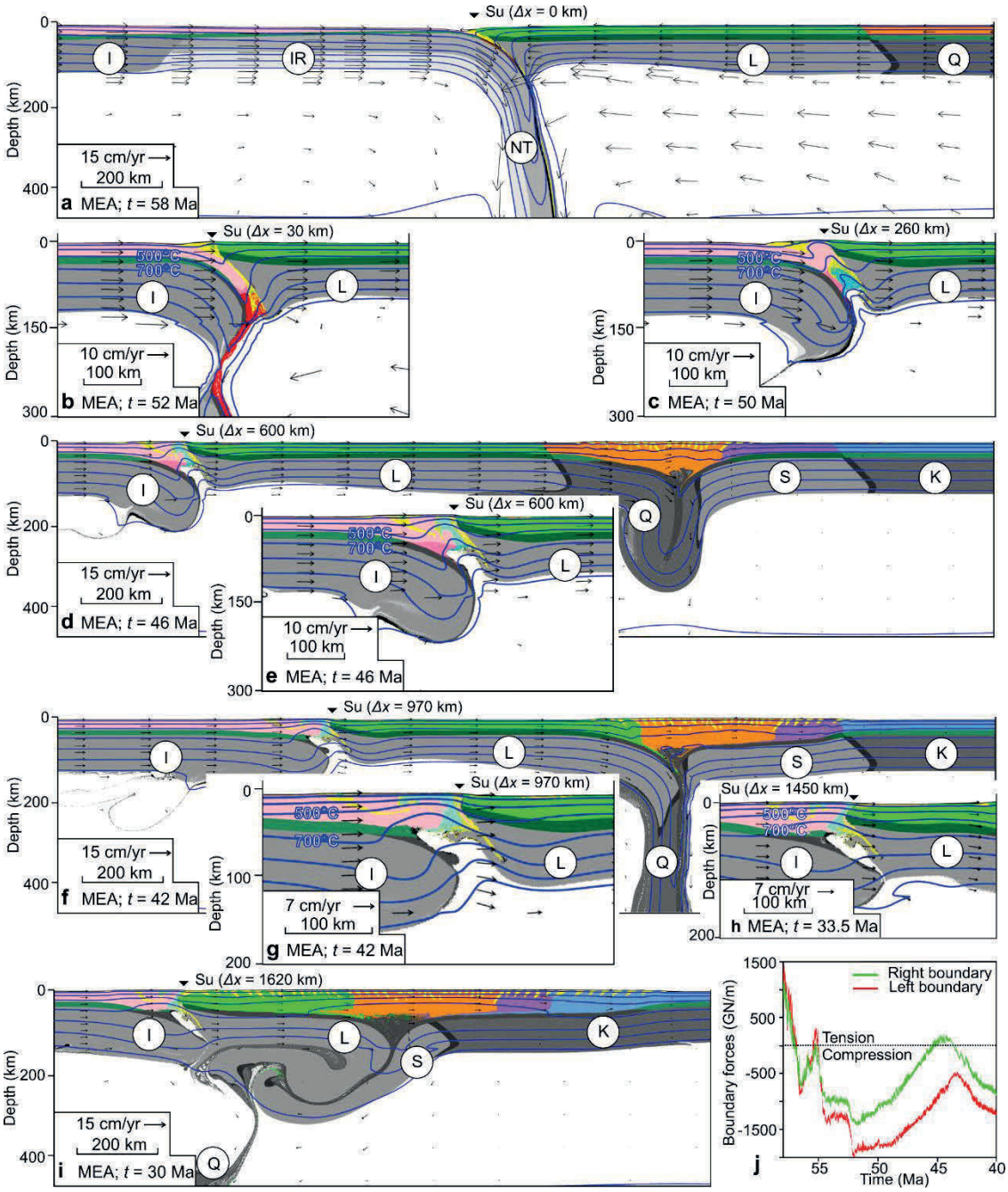

Figure 4.2. (a-i) Evolution of MEA. Times (t) are measured backward from the present assuming India-Asia contact at 58 Ma. Isotherms (blue lines) are shown every 200° C starting at 100° C. Panels show different regions of the model, progressively stepping to the right. Crustal suture, Su (equivalent of the Indus-Yarlung-Tsangpo suture), is labelled with the distance (Δx) it has been translated to the right (north) since the IR (India rifted margin) slab break-off. Arrows are velocity vectors. Convergent lithospheric velocities are imposed only at the left (pro-) boundary. Oppositely directed retro-lithospheric velocities (panel a) reflect a short interval of extension owing to NT retreating subduction and associated large-scale circulation in the retro-sublithospheric mantle (see MEA Animation). See Fig. 4.1 and Table 4.1 for MEA model properties. Model region

lithospheres are labeled with acronyms corresponding to the natural system; I (India), IR (Indian rifted margin), L (Lhasa), Q (Qiangtang), S (Songpan-Ganzi), K (Kunlun). I-crust is colored dark-pink and red as it is buried to high-pressure (HP) and ultra-HP (UHP) conditions respectively. UHP materials are subsequently colored dark-blue and light-blue during retrogression to HP and MP-MT conditions respectively. j) Evolution of model lithospheric tectonic forces at the pro-(left, red) and retro-(right, green) boundaries.

Following Q-CLM delamination, L-CLM (Lhasa) begins to peel back and delaminate from north to south while entraining S-CLM (Songpan-Ganzi) to the north (MEA Animation). At this time the delamination gravitational pull is reduced, such that I-convergence is now faster than the northward motion of the L-terrane, leading to progressive closure of the subduction channel gap by 33.5 Ma (Figure 4.2h). The crust above the subduction channel remains hot.

In summary, MEA shows that I, the suture, and the L-terrane all advance northward between 52 and 33.5 Ma at approximately the same rate as the I-convergence rate (Figure 4.2, Su, and velocity field). Small changes in the relative velocities across the suture are responsible for both the early opening of the subduction channel and its later closure. During this whole interval there is no accretion of I-crust and the model Himalaya does not grow. Later (Figure 4.2i), following closure of the subduction channel, I-CLM begins to underthrust L leading to renewed detachment and accretion of I-crust to the model Himalaya, signaling the onset of Neohimalayan orogenesis. In simple terms MEA predicts that Eohimalayan tectonics and metamorphism can be explained by the near-equal rate northward advance of the Tethyan Himalaya and the Indus-Yarlung-Tsangpo suture with no further accretion/shortening of Indian crust. A small variation in their relative velocity accounts for Eohimalayan metamorphism and magmatism in response to subduction channel opening.

Table 4.1. Model Mechanical and Thermal parameters. The Table lists reference (constant) properties for oceanic, and pro- and retro-continental model regions (labelled PC and RC). The densities and *f*-scaling factors are for the reference properties. The density for pro-CLM, 3320 kg m^{-3}, corresponds to a depletion density of 50 kg m^{-3} with respect to sublithospheric upper mantle. These properties are varied for the retrolithospheric terranes in the model experiments as shown in Figure 4.1 where densities are given in terms of depletion density with respect to the sublithospheric upper mantle.

	Units	Oceanic Sediment Cover	Upper and Mid- Crust (PC and RC)	Lower Crust (PC and RC)	Oceanic Crust	Continental Lithospheric Mantle (PC and RC)	Oceanic Lithospheric Mantle	Sub-Lithospheric Upper Mantle	Lower Mantle
Thickness (max)	km	2	24	12	6	84	92	Base lithosphere to 660 km depth	660 to 1200 km depth
Reference density (0ºC)	kg m^{-3}	2700	2700	2900	2950	Varies, see Fig. 2	3370† and 3355	3370	3630
Reference density HP (0ºC)§	kg m^{-3}	2800	2950	3300	3400	No change	No change	No change	No change
Reference density UHP (0ºC) §	kg m^{-3}	2900	3200	No change	No change	Increases from reference density by 260 below 660 km depth	Changes to 3630 below 660 km depth	Changes to 3630 below 660 km depth	No change
Effective angle of internal friction (휙)	deg	8-2#	15-2#	15-2#	15-2#	15-2#	15-2#	15-2#	15-2#
Cohesion	MPa	2	2	2	0	0	0	0	0
Flow law	-	WQ	WQ	DMD	DMD	WOL	WOL	WOL	Constant viscosity 1×10^{21} Pa s
Viscosity scaling factor (*f*)	-	1	Varies, see Fig. 2	0.1	0.1	Varies, see Fig. 2	2	2	-
Strain weakening factor (W_s)	-	3	3	3	3	1	1	1	-
n	-	4	4	4.7	4.7	3	3	3	-
***A*††**	Pa^{-n} s^{-1}	8.57×10^{-28}	8.57×10^{-28}	5.78×10^{-27}	5.78×10^{-27}	1.76×10^{-14}	1.76×10^{-14}	1.76×10^{-14}	-
Q	kJ mol^{-1}	223	223	485	485	430	430	430	-
V*	m^3 mol^{-1}	0	0	0	0	11×10^{-6}	11×10^{-6}	0	-
Peierls stress	MPa	-	-	-	-	100 (PC), 350 (RC)	150	-	-
Peierls weakening factor	-	-	-	-	-	1×10^{-5}	1×10^{-5}	-	-
Specific heat	m^2 s^{-2} K^{-1}	750	750	750	750	1250	1250	1250	1250
Thermal conductivity	W m^{-1} K^{-1}	2.25	2.25	2.25	2.25	5-2.4§§	5-2.4§§	2.4-52.5§§,##	2.4-52.5§§,##
Thermal diffusivity	m^2 s^{-1}	1×10^{-6}	1×10^{-6}	1×10^{-6}	1×10^{-6}	$1.3\text{-}0.64\times10^{-6}$ §§	$1.3\text{-}0.64\times10^{-6}$ §§	$0.64\text{-}14\times10^{-6}$ §§	$0.64\text{-}14\times10^{-6}$ †††
Thermal expansion coefficient	K^{-1}	3×10^{-5}	3×10^{-5}	3×10^{-5}	3×10^{-5}	$3.2\text{-}3.9\times10^{-5}$ †††	$3.2\text{-}3.9\times10^{-5}$ †††	$3.2\text{-}3.9\times10^{-5}$ †††	$3.2\text{-}3.9\times10^{-5}$ †††
Radioactive heat production	μW m^{-3}	1	2	0.4	0	0	0	0	0

† Oceanic lithospheric mantle is depleted by 15 kg m^{-3} above a depth of 60 km.
§ High-pressure (HP) and ultrahigh-pressure (UHP) densities.
# Includes the effect of strain softening. ϕ_{eff} varies from 15 to 2, or 8 to 2, as the accumulated effective strain increases from 0.5 to 1.5.

[††] Experimental pre-exponential factor has been converted from laboratory value to a corresponding one written in terms of the second invariants of deviatoric stress and strain rate. This is required to ensure that the flow law is coordinate invariant.
[§§] Thermal conductivity and diffusivity for lithospheric mantles vary linearly over the temperature range 273-1050 K.
[##] Enhanced thermal conductivity and diffusivity required to maintain adiabatic temperature gradient of 0.4 K km^{-1}.
[†††] Thermal expansion coefficient increases linearly over the temperature range 500-2000 K. See text for definition of the flow laws
Strain weakening varies linearly between the values given above as the second invariant of strain increases from 5 to 10

4.5 Eohimalayan Metamorphism: MEA Predictions and Model-data Comparisons

4.5.1 MEA Results

Evolving metamorphic conditions in MEA were tracked for sets of particles lying at depths of 2-34 km in originally vertical columns (MEA-C1-C7) spaced at 10-20 km intervals 800-900 km from the IR distal margin edge (Figure 4.1a). Particle positions and changes in pressure (P) and temperature (T) with time (t) were tracked from 58-30 Ma, and the output expressed as P-T-t, P-t, and T-t paths (Figures 4.3 and 4.4). Contrasts in model P-T-t paths across IR reflect proximity to the suture and consequent differences in the amount and timing of burial, heating, and exhumation.

As IR is subducted beneath the suture, columns MEA-C6-C7, initially 810-800 km from the outer IR edge, record ultra-high-pressure (UHP) metamorphism beginning at ~52 Ma. Exhumation of a UHP plume from the subduction channel beginning at ~50 Ma forces expulsion of overlying crust, forming a 10-20 km thick nappe emplaced over IR (Figure 4.3a-f). Particles originally at lower mid-crustal depths record peak P-T conditions (P_{max}, T@P_{max}) of 2-3 GPa and 700-900°C at ~48 Ma. Opening of the subduction channel after 49 Ma (Fig. 4.3c-e) leads to reheating of exhumed UHP material at mid-crustal levels.

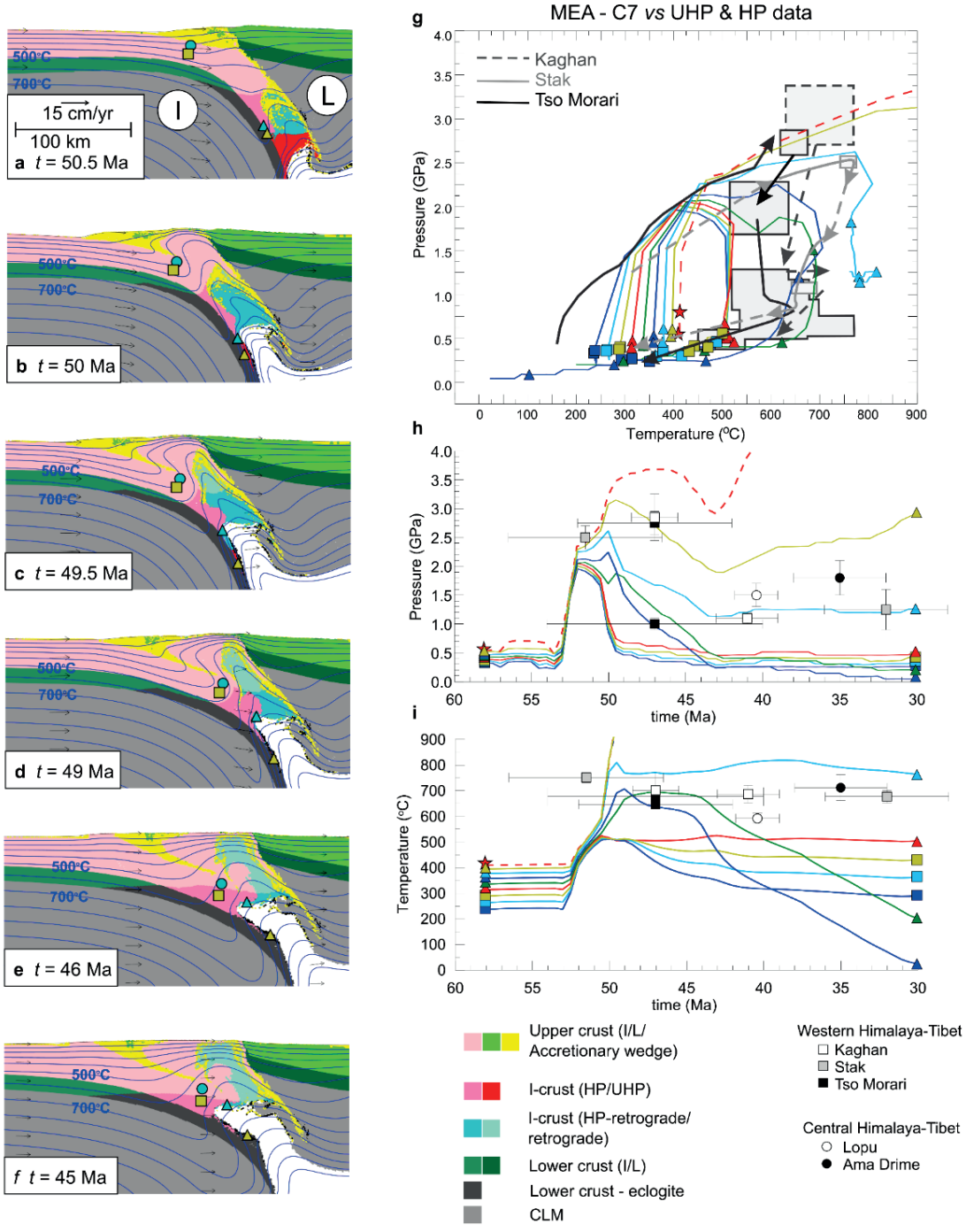

Figure 4.3. (a-f): Close-ups of MEA in the vicinity of the suture showing formation and exhumation of UHP rocks (50.5-46 Ma; a-e) and widening of the subduction channel accompanied by asthenosphere upwelling (50-45 Ma; b-f); equivalent lithosphere-scale results shown in Figure 4.2c-g; V=H. I-crust is colored dark-pink and red as it is buried to high-pressure (HP) and ultra-high-pressure (UHP) conditions respectively. UHP materials are subsequently colored dark-blue and light-blue during retrogression back to HP and

MP-MT conditions respectively. Symbols show positions of tracked particles in MEA-C7 (triangles) and MEA-C2 (circle and square) respectively. MEA-C7 triangles correspond to particles, originally at 19 and 21 km depth, that bracket UHP conditions (panels g-i); MEA-C2 symbols correspond to representative particles, originally at 7 and 15 km depth, that record MP-MT conditions (Figure 4.4). Isotherms at 100°C intervals. Note elevated isotherms in vicinity of opened subduction channel (a-f) and emplacement of crustal nappe driven by UHP exhumation (~50-46 Ma; b-e). (g-i) P-T-t, P-t and T-t results from MEA-C7 (column 7; Fig.4.1a) compared with equivalent Eohimalayan data from UHP and HP rocks in the western and central Himalaya and southern Tibet (gray, black, and white outlines, symbols, and lines). Data sources: Kaghan (O'Brien et al., 2001; Parrish et al., 2006; O'Brien, 2019); Stak (Lanari et al., 2013; Kouketsu et al., 2016); Tso Morari (Guillot et al., 1997; de Sigoyer et al., 1997; Donaldson et al., 2013; Palin et al., 2017); Lopu (Laskowski et al., 2017); Ama Drime (Groppo et al., 2007; Kellett et al., 2014). Data locations and full references given in Appendix C1.

In contrast, MEA-C1-C2-C3 (columns 1-3), initially 900-870 km from the outer IR edge, record an early high-pressure pulse at 50-45 Ma, reflecting emplacement of the thick crustal nappe driven by UHP exhumation (Figure 4.3a-f). Continued deformation of IR leads to thinning of the nappe by 45 Ma; pressures therefore decline from 45-40 Ma and remain approximately constant until 30 Ma. Temperature increases rapidly from 50-40 Ma and remains nearly constant or declines slightly from 40-30 Ma. The corresponding P-T-t paths display steep prograde segments to about 45 Ma followed by near-isothermal decompression, with relatively little change in P or T after 40 Ma (MEA-C2, Figure 4.4). P_{max} and T_{max} lie in the range 0.9-1.5 GPa and 600-750°C, depending on the depths of the tracked particles. Equivalent pressures and prograde P-T-t paths (gray shading, Figure 4.4) for the case where a thick crustal nappe is not emplaced can be predicted from the model cross-sections; temperature is not significantly affected. In this case, MP-MT conditions are recorded by particles in the upper and middle crust (Figure 4.4).

4.5.2 Model – data Comparisons

Data on the P-T-t conditions of Eohimalayan metamorphism were compiled for comparison with P-T-t, P-t, and T-t paths from MEA and its variants (data sources and localities in Appendix C1, Figure C.2). In many cases, peak P-T conditions and ages are well defined; in contrast, prograde P-T paths and ages rely on relatively broad constraints. Data indicating prograde to peak metamorphism in the range 58-30 Ma were included

where dates could be reliably tied to specific P-T estimates - e.g., monazite dates linked to mineral assemblages in pelitic rocks using trace element chemistry and/or petrographic setting. As the observations suggest that high temperature conditions were maintained from ~45-30 Ma, no distinction between Early and Late Eohimalayan metamorphism can be made on the basis of the P-T-t data. Ages and P-T conditions of Neohimalayan (post-30 Ma) metamorphism, exhumation, and cooling were not included.

(U)HP metamorphism: Rocks recording Eohimalayan metamorphism in the coesite-eclogite (UHP) stability field are largely confined to the western Himalaya and southwestern Tibet (O'Brien, 2019, and references therein). High-pressure (HP) eclogite facies conditions are documented locally in the west-central Himalaya and southern Tibet, with variably overprinted eclogites reported from many other localities (O'Brien, 2019). In the western Himalaya, (U)HP rocks typically record P_{max} and $T@P_{max}$ conditions of ~2.5-3.0 GPa and 600-750°C at ~52-48 Ma (Fig. 3g-i), followed by decompression and reheating at 1.0-1.2 GPa by 45-40 Ma. In the central Himalaya, HP rocks record peak P-T conditions of 1.5-2.0 GPa and 600-700°C at 40-35 Ma, with exhumation after 30 Ma (Figure 4.3g-i).

Results from particles near the middle-lower crust boundary of MEA-C7 (column 7) produce P-T-t paths similar to those observed in (U)HP rocks from the western Himalaya (Figure 4.3g). While no single tracked particle fully reproduces the complete P-T-t data array, particles originally at 19-21 km depth bracket the observations, with P_{max} of 2.0-3.0 GPa at 53-49 Ma and T_{max} of 600-800°C at 50-45 Ma, with the 19 km particle reheated to ~825°C at 40-38 Ma (Figure 4.3g). The same particles record P-T conditions similar to those from central Himalayan HP rocks at 40-30 Ma. Deeper particles are subducted and shallower particles exhumed.

Western Himalaya MT-MP metamorphism: In most western Himalayan examples, Eohimalayan peak P (0.6-0.9 GPa) is inferred to have approximately coincided with peak T (600-700°C) at ~30 Ma, with prograde metamorphism in the range ~45-30 Ma followed by near-isothermal decompression associated with Neohimalayan ages of 30-20

Ma (Figure 4.4a). In contrast, data from the Gumburanjun dome suggest peak conditions of 0.9-1.0 GPa and 700-750°C at 37-39 Ma, with substantial decompression before 30 Ma (Figure 4.4a; St20).

Results from MEA-C2 particles originally at 7-15 km depth produce P-T-t paths similar to those observed in MP-MT metamorphic complexes from the western Himalaya (Figure 4.4a). While there is no evidence in the observations for the HP pulse associated with pre-45 Ma nappe emplacement in the model, the corresponding pre-45 Ma pressure range for the case without nappe emplacement (gray shading, Figure 4.4a) is compatible with inferred prograde P-T paths from the region. After 45 Ma, model P-t and T-t paths show very good correspondence with the observations, with P of 0.6-0.8 GPa and T of 550-750°C maintained from 45-30 Ma (Figure 4.4a).

Central Himalaya: In the central Himalaya, observations suggest a wider range of P-T-t path styles and peak P conditions than those reported further west (Figure 4.4b; e.g., Carosi et al., 2019, and references therein). Data from a few localities suggest peak P of 1.0-1.2 GPa was reached by 45-35 Ma, coinciding with, or some-what earlier than, peak T (Figure 4.4b; K21, I15, Sh20), with other data suggesting P-T conditions more like those in the western Himalaya. Although Vannay and Hodges (1996) interpreted data from the vicinity of the Kalopani Shear Zone as indicating decompression after ~30 Ma, Carosi et al. (2016) have interpreted more recent data to indicate that exhumation from peak Eohimalayan P ~0.8 GPa started as early as 41 Ma, with subsequent Neohimalayan overprinting.

Comparison of these observations with results from MEA-C2 shows broad agreement (Fig.4b), although none of the observations show the 50-45 Ma high-pressure pulse predicted by model MEA. Model results corrected for the case without nappe emplacement (gray shading, Figure 4.4b) are compatible with most observations; higher P (1.0-1.2 GPa) at 45-35 Ma reported from some localities may reflect deeper particles not shown on Figure 4.4. Model T-t predictions (T_{max}600-750°C at ~45-40 Ma; Figure 4.4b) agree well with Eohimalayan peak T-t estimates.

Eastern Himalaya: In the eastern Himalaya, Eohimalayan peak P (0.6-0.9 GPa) approximately coincided with peak T (650-750°C), with exhumation beginning after ~30 Ma (Figure 4.4c). Data from migmatitic rocks in the Ghunsa region suggest peak T ~800°C at P > 1.0 GPa with some decompression before 33 Ma (Figure 4.4c; Imayama et al., 2018), although elsewhere in the same region peak conditions were reached only after ~30 Ma.

Comparison of the data with MEA-C2 shows broad agreement with model results corrected for the case without nappe emplacement (gray shading, Figure 4.4c). Exceptions include later high-temperature migmatites in the upper GHS (Imayama et al., 2018) and earlier prograde metamorphism in the Mabja dome (Smit et al., 2014; Figure 4.4c). In the latter case, we note that conversion from model time to geological time is based on the assumption that initial India-Asia contact was at 58 Ma. Since this may have varied along-strike, somewhat earlier or later contact along any given transect would require corresponding adjustments to the model time.

In summary, the model-data comparisons suggest that subduction channel opening in MEA can account for Eohimalayan metamorphism by exposing the base of the crust to heat from upwelling asthenosphere. The same process also accounts for Eohimalayan mafic magmatism, since decompression melting of hydrated sublithospheric mantle would have accompanied subduction channel opening and asthenospheric upwelling. Mid-crustal peak temperatures in MEA overlap with partial melting conditions, indicating that felsic magmas could have been produced in the middle to lower crust after ~45 Ma. We do not imply that Eohimalayan intrusions caused the metamorphism; rather, both metamorphism and melting resulted from the same process – crustal heating in response to asthenospheric upwelling. Following subduction channel closing after 35 Ma, crustal temperatures ≥700°C were maintained by radioactive heating of the thickened crust (Appendix C3).

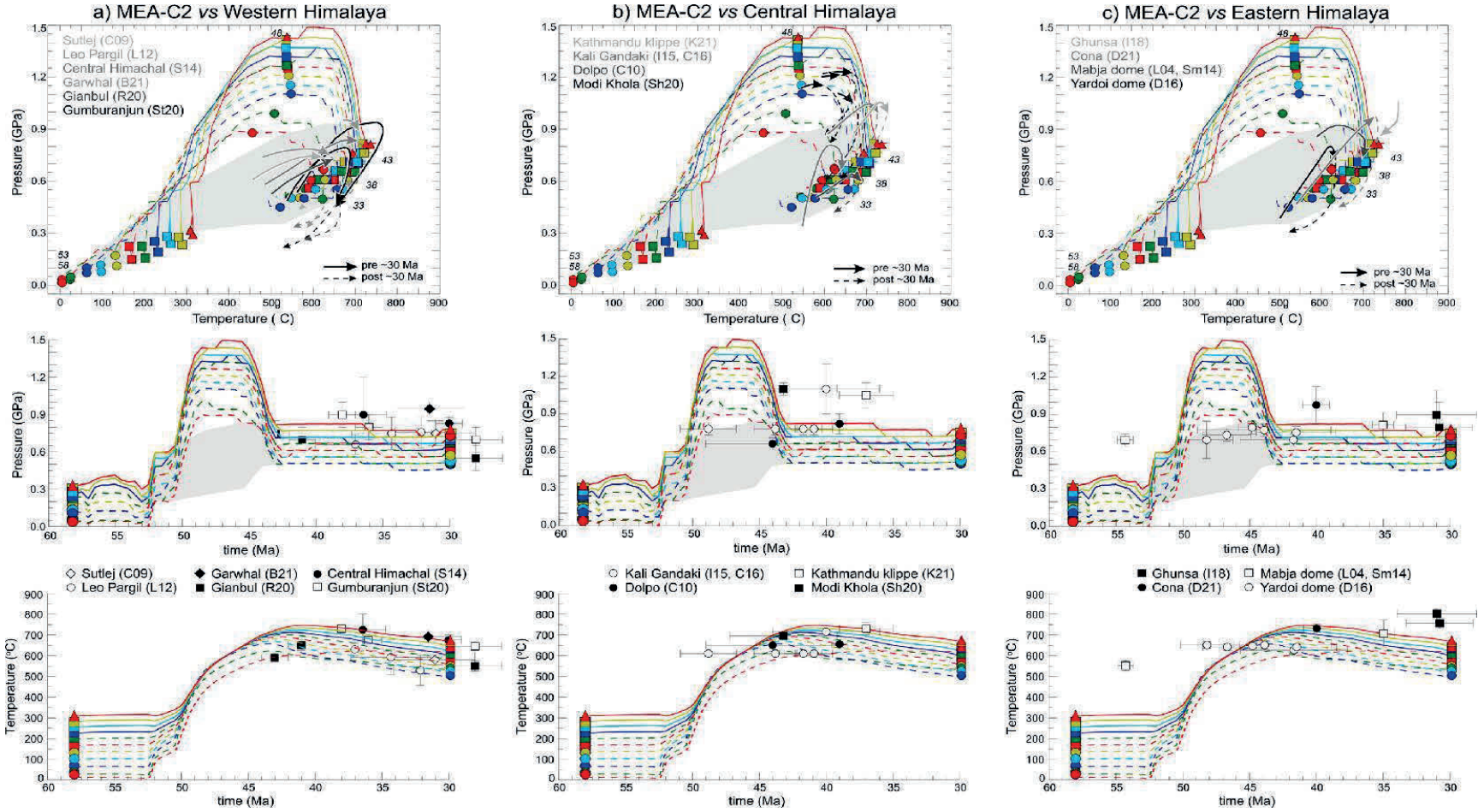

Figure.4.4. P-T-t results from Model MEA-C2 (column 2) compared with P-T-t data from Eohimalayan MP-MT metamorphic complexes; C2 location shown in Figure 4.1a. Model results (colored symbols and lines) from tracked particles at original depths ca. 2-20 km (upper and middle crust); model P-T-t paths with P_{max} > 1.5 GPa not shown. Symbols at 5 Myr intervals; overlapping symbols indicate little or no change in P-T conditions in that interval. Gray shading shows equivalent model results for case where no UHP nappe is exhumed (Figure 4.3c-e). Distinction between pre-and post-30 Ma observed P-T-t path segments (solid vs dashed arrows,

upper panels) and uncertainties in P-t and T-t data (middle and lower panels) from information in source papers. a) Western Himalaya: C09 = Chambers et al. (2009); L12 = Langille et al. (2012); B21 = Benetti et al. (2021); R20 = Robyr and Lanari (2020); S14 = Stübner et al. (2014); St20 = Stipska et al. (2020). b) Central Himalaya: I15 = Iaccarino et al. (2015); C16= Carosi etal. (2016); C10 = Carosi et al. (2010); K21 = Khanal et al. (2021); Sh20 = Shresta et al. (2020). c) Eastern Himalaya: I18 = Imayama et al. (2012, 2018); D21 = Ding et al. (2021); L04 = Lee et al. (2004), Lee and Whitehouse (2007); Sm14 = Smit et al. (2014); D16 = Ding et al. (2016). Data locations and full references given in Appendix C1.

4.6 Supplementary Models

4.6.1 No Opening of the Subduction Channel: Model MEB

Model EB (MEB *f* 4-*d* 35_*f* 25-*d* 20_*f* 3-*d* 30_*f* 3-*d* 30_5mm/yr max erosion) (Figure 4.5) is the same as MEA except that Q-CLM (Qiangtang) has *d*= 20 as opposed to *d* = 25, i.e. slightly more dense, *f* = 2.5 as opposed to *f* = 2, and the maximum surface erosion rate is 5 mm/yr, not 1 mm/yr.

MEB evolution is the same as MEA up to and including shallow slab breakoff at 52 Ma, followed by underthrusting of full thickness I-lithosphere beneath the L-terrane. I-crust subducted to near the base of the lithosphere is subject to UHP metamorphism. UHP exhumation and retrogression (Figure 4.5a-d, blue) are rapid, spanning 50 to 46 Ma. By 46 Ma (Figure 4.5c) the Q-CLM has shortened and folded, and delamination is finishing by 42 Ma (Figure 4.5e). During this time the suture (Su, Figure 4.5) has advanced northward by 880 km, producing the same apparent indention of the Asian terranes as in MEA. As in MEA, Asian shortening is mainly self-driven by the negative buoyancy force of Q-CLM delamination. MEB is therefore similar to MEA, with the important difference that Q-CLM delamination pulls the L-terrane north at the same rate as I-continent convergence. The subduction channel therefore does not open during or after delamination (Figure 4.5e, f). The temperature field is perturbed only by exhuming UHP material which raises the 500°C isotherm (Figure 4.5). The 700°C isotherm remains at depth in the closed subduction channel and the 600°C isotherm remains in the lower crust even at 30 Ma.

MEB therefore demonstrates that without subduction channel opening, heating of I-crust is insufficient to explain Early Eohimalayan magmatism and metamorphism. The significantly cooler I-crust in MEB is reflected in the model P-T-t and T-t paths (Figure 4.5g, i). MEB paths display steep prograde and decompression trajectories, with T_{max}<700°C for mid-crustal particles (Figure 4.5g, i). Neither P-t nor T-t paths match

observed P-T conditions after ~40 Ma, and the high temperatures required for Eohimalayan metamorphism are not sustained.

4.6.2 Wide Opening of the Subduction Channel: Model MEC

Model EC (MEC *f* 4-*d* 25_*f*2-*d* 20_*f* 3-*d* 30_*f* 3-*d* 30) (Figure 4.6) is exactly the same as MEA except that the CLM of the L and Q terranes is less depleted and they are therefore denser than MEA (L-CLM $d = 25$ vs. $d = 35$; Q-CLM $d = 20$ vs. $d = 25$).

MEC evolution is the same as MEA and MEB until the onset of UHP exhumation and retrogression which starts 0.5 Myr earlier than in MEA at 50.5 Ma (Figure 4.6a) and is largely complete by 48 Ma (Figure 4.6b), by which time there is significant opening of the subduction channel. Delamination of Q-CLM (Figure 4.6c, d) at 45 Ma is 3 Myr earlier than in MEA and the width of the subduction zone opening is 100 km roughly double that of MEA, both owing to the higher density of the delaminating Q-CLM. There is also significant extension and thinning of the crust above the subduction channel, placing the 700°C isotherm in the mid-crust at a depth of 20 km with the 900°C isotherm not much deeper (Figure 4.6d). The subduction channel remains open until 38 Ma, with similar temperature conditions, and then slowly closes by 33.5 Ma (Figure 4.6e) with some crustal thickening and burial of the 700°C isotherm.

Although both MEA and MEC produce upwelling of hot asthenosphere into the opened subduction channel, wider MEC opening also leads to substantial crustal extension and thinning after 45 Ma. As a result, MEC P-t paths predict $P < 0.6$ GPa after 45 Ma, and mid-crustal particles cool between 45 and 35 Ma (Figure 4.6g). After 35 Ma, closing of the subduction channel produces a second increase in both P and T. The P-T-t paths therefore display a double loop not observed in the natural system.

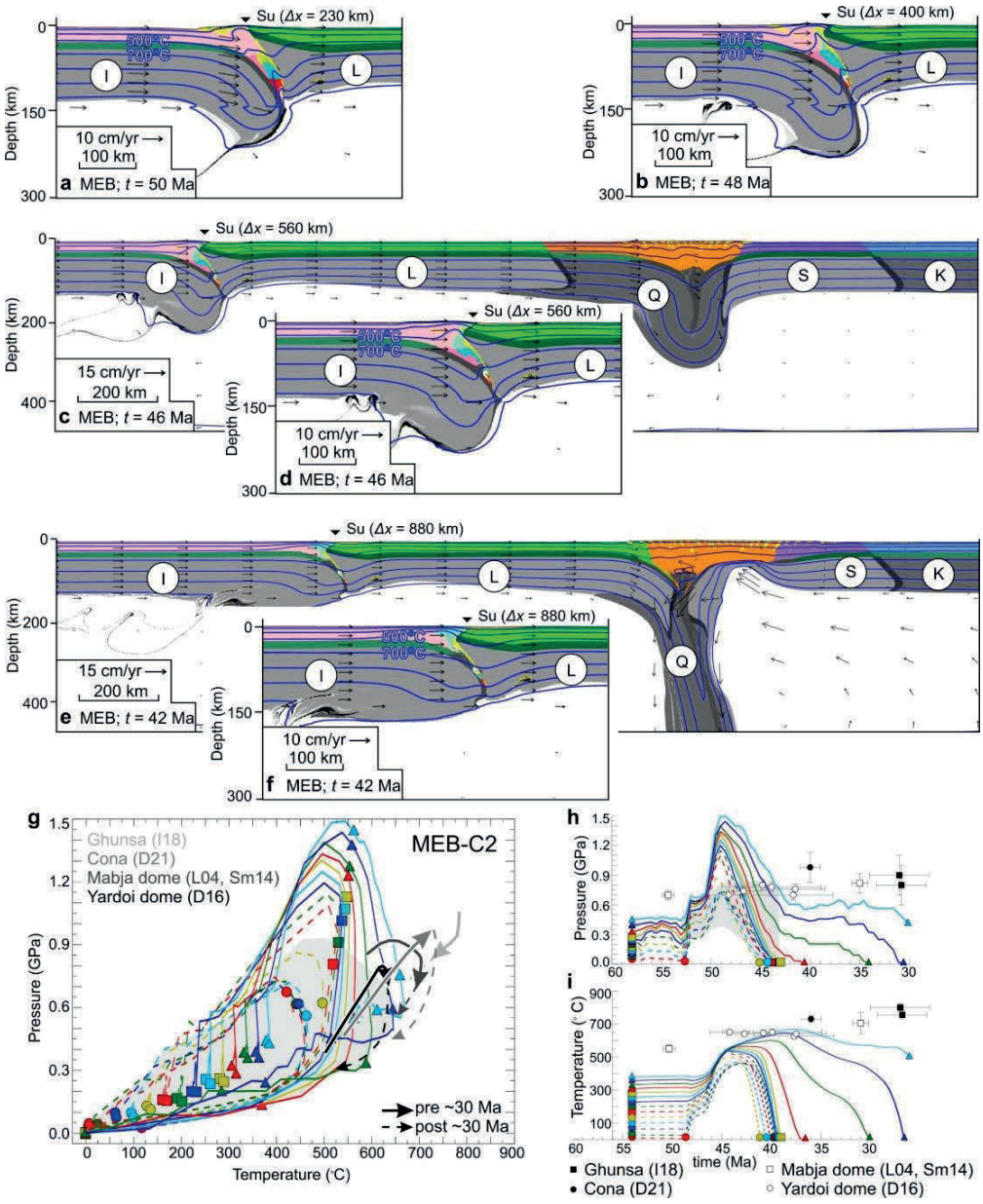

Figure 4.5. (a-f) Evolution of MEB, showing effect of no subduction channel opening. Times (t) are measured backward from the present assuming India-Asia contact at 58 Ma**.** Panels show different regions of the model, progressively stepping to the right. Crustal suture, Su (equivalent to the Indus-Yarlung-Tsangpo suture) is shown with the distance (Δx) it has been translated to the right (north) since the IR (India rifted margin) slab break-off. Isotherms (blue lines) are shown every 200°C starting at 100°C. Arrows are velocity vectors. (g-i) P-T-t, P-t and T-t results from MEB-C2 (colored symbols and lines), compared with equivalent data from rocks in the Eastern Himalaya (gray, black, and white outlines, symbols, and lines). Gray shading shows equivalent model results for case where no UHP nappe is exhumed (Fig.3c-e). Data sources: Ghunsa (Imayama et al., 2012, 2018); Cona (Ding et al., 2021); Mabja dome (Lee et al., 2004; Lee and Whitehouse, 2007; Smit et al., 2014); Yardoi dome (Ding et al., 2016). Full references and locations are given in Appendix C1.

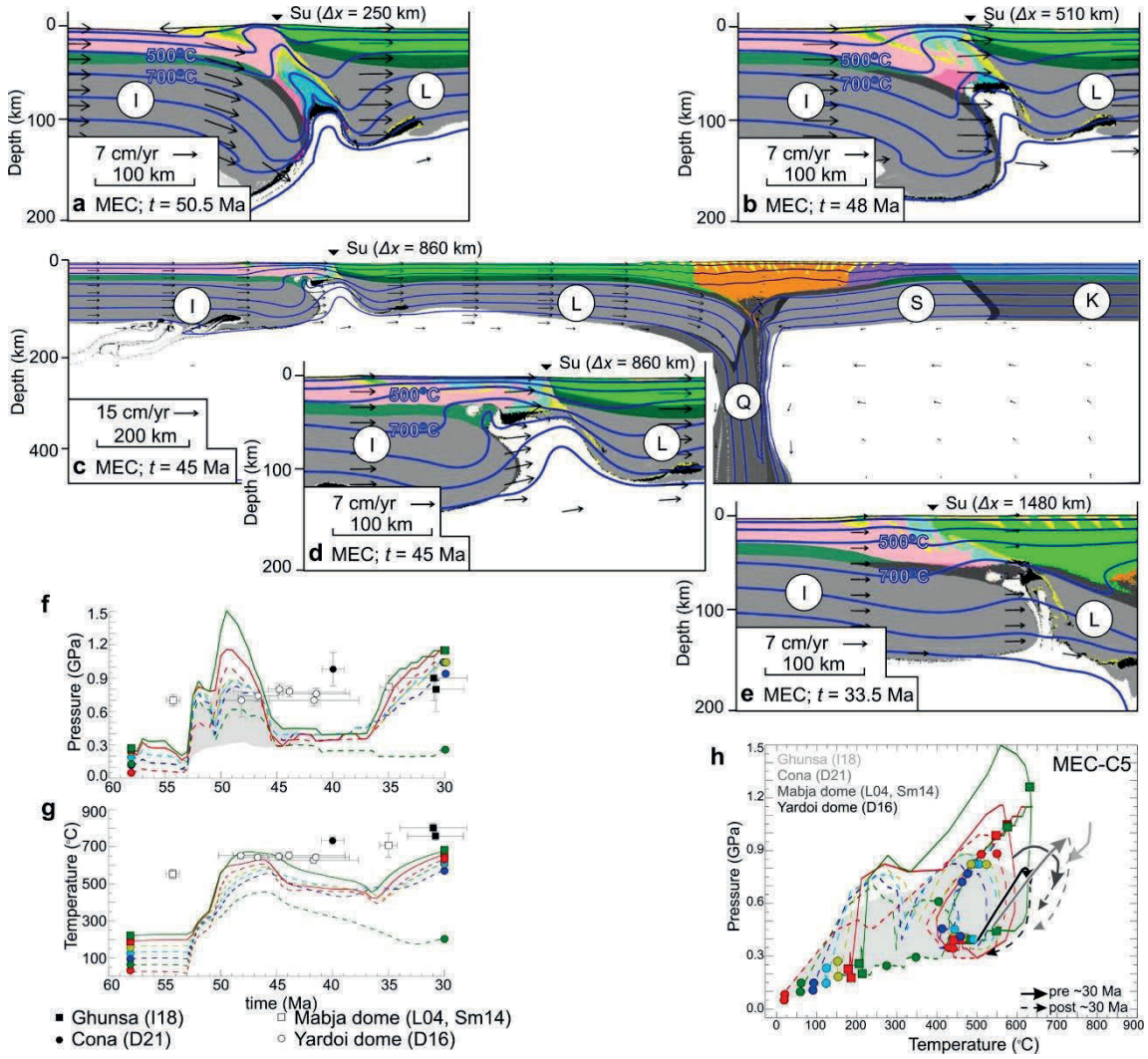

Figure 4.6. (a-e) Evolution of MEC, showing effect of wide subduction channel opening. Times (t) are measured backward from the present assuming India-Asia contact at 58 Ma. Panels show different regions of the model, progressively stepping to the right. Crustal suture, Su (equivalent of the Indus-Yarlung-Tsangpo suture) is shown with the distance (Δx) it has been translated to the right (north) since the IR (India rifted margin) slab break-off. Isotherms (blue lines) are shown every 200°C starting at 100°C. Arrows are velocity vectors. Labelling of model lithosphere domains and material colors as in Figure 4.2 (f-h) P-t, T-t and P-T-t results from MEC-C5 (column 5; Figure 1a), compared with equivalent data from rocks in the Eastern Himalaya (gray, black, and white outlines, symbols, and lines). Gray shading shows equivalent model results for case where no UHP nappe is exhumed (Figure 4.3c-e). Data sources as in Figure 4.5; locations and full references in Appendix C1.

4.7 Tectonic Quiescence between Eohimalayan and Neohimalayan Orogenesis?

4.7.1 Evidence for Tectonic Quiescence

The possibility of a hiatus in the tectonic growth of the Himalaya following Early Eohimalayan metamorphism has been suggested by Hodges and Silverberg (1988), Aikman et al. (2008) and Kelly et al. (2020), among others. Van Hinsbergen et al. (2019) noted that throughout the 50–30 Ma period, "Whatever the nature of the lithosphere that underthrusted the Himalaya in this time period, it left no observed accretionary record in the Himalayan geology. From about ~30–25 Ma onward, forward propagating accretion of continent-derived rock started again and accreted the deeper structural levels of the Greater Himalaya...".

Here we demonstrate that Late Eohimalayan (~43-30 Ma) tectonic quiescence in the Himalaya is compatible with what we term "passive northward motion of the Tethyan Himalaya" as seen in MEA. Finally, we use MED to demonstrate an alternative in which India continued to underthrust Asia after the Early Eohimalayan collision. We first list additional evidence for quiescence.

1) The enduring interpretation that the Himalayan orogeny has two stages, early and late, is supported by data from igneous and metamorphic rocks along the entire belt. Evidence for growth/accretion in the interval between them is limited. As noted by Aitchison et al. (2007), "... Eocene through mid-Oligocene sediments in the area, where preserved, are mostly carbonates and reflect tectonic quiescence". They also referred to "a hiatus in collision related events" and showed that seawater $^{87/86}Sr$ only increased from the beginning of the Oligocene (their Figure 7). The latter is commonly interpreted to signal surface/tectonic uplift and climate change.

2) Prograde metamorphism, with both P and T increasing, is documented from ~55-40 Ma. While high T was maintained after 40 Ma, there is no clear

evidence for a corresponding P increase (Figure 4.4). Thrusting related to detachment and thickening of Himalayan crust should have buried upper crust in the footwall, resulting in new or accentuated prograde metamorphism with P increasing. Near-constant or slightly declining P after ~45-40 Ma suggests no further thickening of Himalayan crust.

3) The reconstructed development and southward advance of the Himalayan foreland basins suggests little shortening of Indian crust or advance of the Himalayan thrust front in the intervals 45-40 Ma and 40-25 Ma (Figure 12B, C of DeCelles et al., 2014), much less than the estimated India-Asia convergence during these time intervals.

4) The persistence of marine sedimentation into the Late Eohimalayan (<44 Ma) in the vicinity of the IYTS provides evidence that these locations were not tectonically uplifted above sea level as would be expected if the Himalaya continued to accrete Indian crust after the Early Eohimalayan. Wang et al. (2020, and references therein) compiled new and existing evidence (their Figures. 8, 9) interpreted to show that marine sedimentation persisted until ~38 Ma, about the same time that the onset of widespread clastic sedimentation indicates filling of the marine basins (Garzanti, 2019).

5) The inferred near-stationary flexural bulge within India (DeCelles et al., 2014) offers additional evidence of limited under-thrusting of Indian lithosphere beneath the Himalaya. Limited advance of the thrust belt is also consistent with the widespread un/disconformity (Garzanti, 2019, and references therein) attributed to erosion/no deposition on the foreland flexural bulge. Aitchison et al. (2007) concluded that "... problems exist with the suggestion (implicit in the work by DeCelles et al., 1998) that the location of the forebulge essentially remained static as it should have migrated through the area. If estimates of the rate of India's northern motion (motion absorbed by underthrusting/subduction) at the time in question (Acton, 1999) are correct, then over 16.5 Myr the

forebulge would have migrated ~1550 km southward rather than remaining in the same place".

6) That much of the surface exposure in the Tethyan Himalaya consists of low-grade rocks (e.g. anchizone, Wiesmayr and Grasemann, 2002) indicates that total erosion, including Neohimalayan erosion, is relatively low, except where deeper levels are tectonically exposed as in the North Himalaya domes. By implication the erosion rate in low-grade areas during the 44-30 Ma Late Eohimalayan interval was low, suggesting limited tectonic crustal thickening and associated surface uplift.

7) There is no strong evidence of deformation and uplift in the vicinity of the IYTS zone between the initial India-Asia collision and the onset of Oligocene thrusting (~30 Ma) on the Gangdese thrust in southern Tibet and subsequent (20-10 Ma) development of the Great Counterthrust system (Yin et al., 1999; Laskowski et al., 2018). The 20-25 Myr time lag reinforces the puzzle (Le Fort, 1996) of why crustal thickening of the suture zone lagged by so long. There is no record of sedimentation in the Xigaze forearc basin after 51 Ma, but the basin remained buried, possibly under a wedge-top basin and/or thrusting on the Gangdese thrust (Yin et al., 1999), until exhumation and rapid cooling at 21-15 Ma (Orme, 2019). If the Himalaya had continued to grow by accretion after 45 Ma, deformation and exhumation of the suture and forearc would be expected long before 30 and 21 Ma, respectively.

8) The relatively narrow Himalaya and small cross-sectional area of its accreted crust, coupled with modest shortening estimates (minimum ~300-650 km; e.g., Yin and Harrison, 2000; DeCelles et al., 2011; Long et al., 2012), indicate that much of the total 4000 km India-Asia convergence did not result in accretion of detached upper and middle Indian crust to the Himalaya.

While these points taken individually can be explained in a variety of ways, when taken together they can all be explained by a single consistent proposition, namely quiescence.

4.7.2 Apparent Indentation of Asia by India: Model MEA

As discussed earlier, MEA explains Eohimalayan metamorphism, but we show here that it also explains the subsequent putative Late Eohimalayan quiescence. The model Himalaya in MEA from 45-30 Ma (i.e., end Early Eohimalayan orogenesis, through quiescence, to the end of Late Eohimalayan development) (Figure 4.7b-e, MEA Animation; see Kelly et al., 2022) shows very little change in its configuration and size because there is no accretion to, or shortening within, the model Himalayan crust. Instead, the convergence of India on Asia is absorbed by shortening in the interior of Asia, particularly in the Q-terrane and later the L-terrane (Figure 4.2a, d, f, i and MEA Animation; see Kelly et al., 2022), during which time the IYTS suture has advanced northward by 920 km. In fact, in MEA there is very little convergence between India and the IYTS from the time of Neotethys slab breakoff at 52 Ma (Figure 4.7a) throughout Early and Late Eohimalayan orogenesis. Early Eohimalayan metamorphism in MEA coincides with opening of the subduction channel - i.e., implied extension, not shortening - in the vicinity of the suture (Figure 4.7b-d). However, extension is not seen in MEA owing to upwelling and shortening of underthrust I-crust. In contrast, MEC does exhibit equivalent crustal extension/stretching. By implication, mappable extension may or may not be observed at the IYTS. As noted earlier, the MEA model result implies that indentation of Asia by India may be largely apparent.

4.7.3 Effect of Continued Subduction of Indian Continental Mantle Lithosphere: Model MED

Additional model MED (Figure 4.7) contrasts with MEA by showing how the model Himalaya continues to grow throughout Eohimalayan orogeneis as a consequence of

continued subduction of Indian lithosphere. This behavior is in stark contrast to many of the observations of Eohimalayan development listed above.

MED (*f* 4-*d*35_*f* 2-*d*22_*f* 3-*d*30_*f* 3-*d*30) is the same as MEA except that the depletion of the Q-CLM is slightly less (*d*= 22 vs *d*= 25). In contrast to MEA, there is an aborted slab breakoff at 52 Ma (Figure 4.7f) followed by continued underthusting of the I-CLM (India) and detachment and accretion of the overlying crust to the model Himalaya. The accretion of I-crust leads to a model Himalayan orogen that is 200 km wide and up to 75 km thick by 50 Ma, and 400 km wide and 70 km thick by 45 Ma (Figure 4.7g, h). The subduction channel does not open and most of the mid-and upper crust remains at T <700°C. Only the exhuming retrogressed UHP material achieves T > 700°C before ~35 Ma, when radioactive heating becomes significant (Appendix C3). By 30 Ma, the MED orogen is 600 km wide (wider than the modern Himalaya), showing that continued accretion of India crust (i.e. no quiescence) produces an unreasonably large Himalayan orogen. In other regards MED is similar to MEA. Slab breakoff occurs at 45.5 Ma, 7 Myr later than in MEA (Figure 4.7h), and delamination of Q-CLM at 38 Ma, 4 Myr later than in MEA.

In summary, models MEA and MED are similar except that MED shows accretion and growth of the Himalaya throughout the Eohimalayan phase because I-CLM continues to underthrust Asia. There is no Late Eohimalayan quiescence. MEA shows how quiescence is possible while India and Tibet translate northward after the initial Eohimalayan collision.

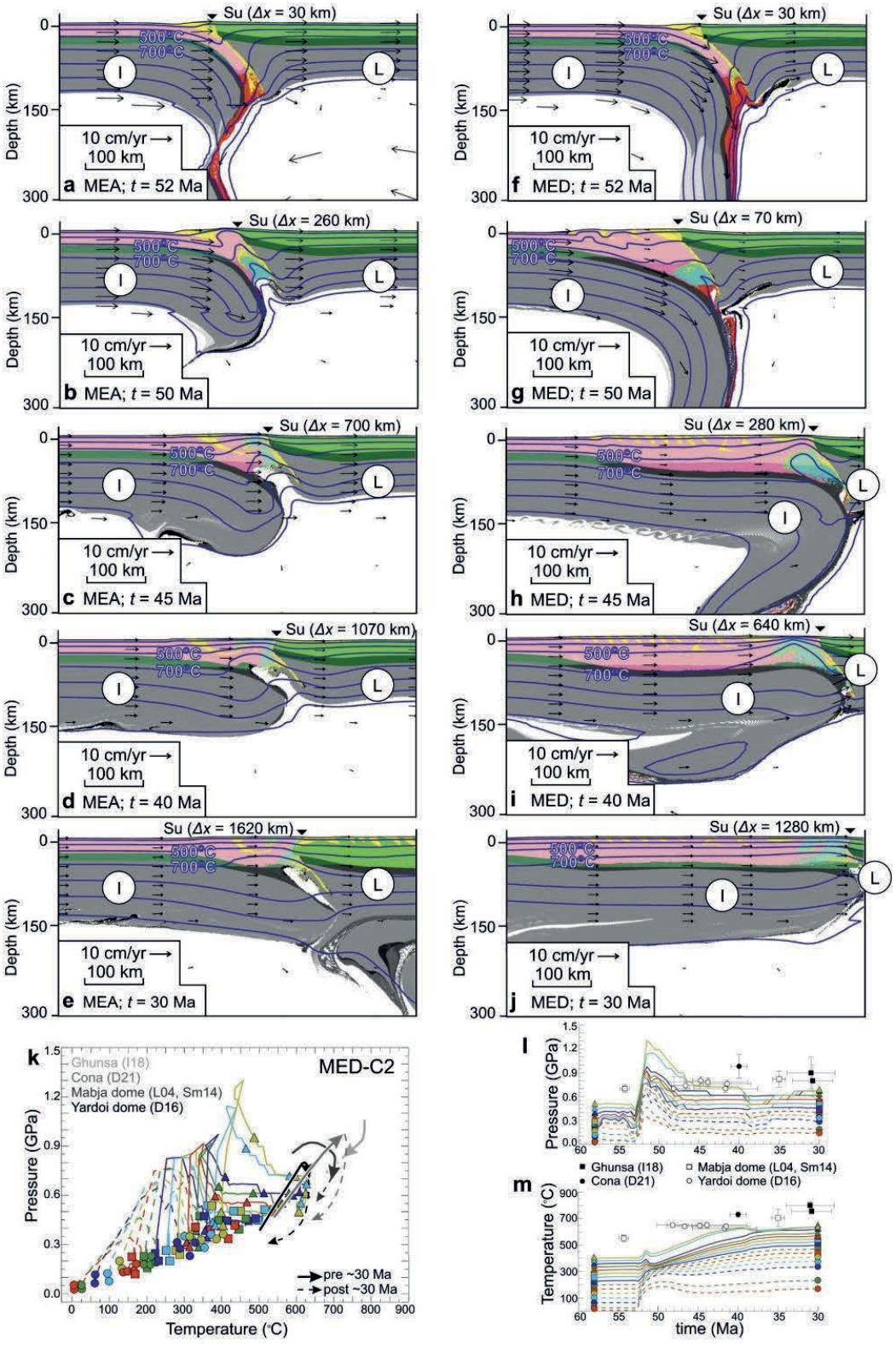

Figure 4.7. (a-j) Evolution of MEA (a-e) compared with MED (f-j), showing effect of continuous underthrusting of Indian continental lithosphere beneath Asia. Times (*t*) are measured backward from the present assuming India-Asia contact at 58 Ma. Panels show

model results in the vicinity of the suture (Su), which is labelled with the distance (Δx) it has been translated to the right (north) since the IR (India rifted margin) slab break-off. I = India, L = Lhasa terrane. Isotherms (blue lines) are shown every 200°C starting at 100°C. Arrows are velocity vectors. Material colors as in Figure 4.2. (k-m) P-T-t, P-t and T-t results from MED-C2 compared with equivalent data from rocks in the Eastern Himalaya (gray, black, and white outlines, symbols, and lines). Data sources as in Figure 4.5; locations and full references in Appendix C1.

4.8 Discussion and Conclusions

We have presented a testable explanation of the Eohimalayan evolution of Himalayan-Tibetan orogenesis, spanning the time of contact (~58 Ma) through what we term Early and Late Eohimalayan evolution, and ending at ~30 Ma, just before the onset of Neohimalayan evolution. This proposed explanation is based on numerical model MEA (Figure 4.2), a refined version of models MA and MB (Kelly et al., 2020), and is summarized diagrammatically in Figure 4.8. This explanation is a significant departure from previous proposals but is self-consistent, involving several emergent phases. The key to the explanation is remarkably simple and involves small changes in the relative northward velocities of India and Tibetan terranes after the India-Asia collision and slab breakoff. We have compared and contrasted MEA with closely related models (MEB, MEC, MED) that bracket the explanation provided by MEA but fail to explain the full range of observations.

Our inferences concerning the evolution of Eohimalayan orogenesis based on MEA lead us to the conclusions listed below.

1) The subducted Neotethys and Indian Rifted margin slab broke off at 52 Ma, after initial India-Asia contact at ~58 Ma and subduction of the Indian Rifted margin from 58 to 52 Ma.

2) In the western part of the H-T orogen UHP crust exhumed and retrogressed from 50 to 46 Ma. Similar UHP exhumation may have occurred elsewhere in the orogen and may yet be discovered.

3) Sections 4.4 and 4.5 demonstrate that within the context of MEA, the key to Early Eohimalayan crustal metamorphism and melting is heating of Tethyan Himalayan crust by upwelling of hot sublithospheric mantle into the Neotethyan subduction channel which opens between 50 and 46 Ma and closes at about 34 Ma. This style of heating is more efficient than radioactive self-heating of thickened crust and can explain >700°C temperatures in the mid-crust soon after the onset of upwelling. Moreover, the enhanced temperature is sustained through 30 Ma by crustal radioactive self-heating (Appendix C3). Mafic magmatism can be explained by limited decompression melting during upwelling in the subduction channel.

4) The subduction channel in MEA opens during rapid convergence of India and Tibet on Asia during Early Eohimalayan orogenesis. We contend that the subduction channel opened owing to the self-driven shortening of Tibetan lithosphere during delamination of the Qiangtang continental mantle lithosphere, which in MEA produced a northward-directed tectonic force (Figure 4.2) sufficient to shorten the Qiangtang crust and those of Tibetan terranes to the north and south. The rate of the self-driven advance of the IYTS in MEA from 46 to ~40 Ma is slightly larger than the convergence rate of India on the suture, which explains the limited opening of the subduction channel (Section 4.4). This differs from models in which a subduction channel opens during retreating subduction or slab rollback (e.g., Sizova et al., 2019). While retreat/rollback can account for early high-temperature metamorphism, the evidence for continuous, rapid India-Asia convergence suggests that slab rollback or retreat is unlikely to have operated in the H-T system.

5) MEA has the further property that, after the Early Eohimalayan Tethyan India collision with Asia (~52-46 Ma), there is little or no additional accretion of Indian crust to the Himalaya during the Late Eohimalyan interval (~43-30 Ma) until the onset of renewed underthrusting of Indian mantle lithosphere beneath the Lhasa terrane starting between 30 and 25 Ma. During Late Eohimalayan evolution, India and the southern part of Tibet in MEA both advance northward at the same rate,

with limited shortening and growth of the Tethyan Himalaya. This explanation of Late Eohimalayan quiescence (Section 4.7) is internally self-consistent, and also consistent with the subduction channel remaining open during delamination of the Qiangtang and Lhasa CLMs, which drove shortening within Asia. We note that even today GPS data show that most of the convergence of India on Asia is transferred across the Himalaya to Tibet.

6) Neither the MEA results nor the observations show a clear distinction between Early and Late Eohimalayan metamorphic P-T conditions despite the contrasting tectonic settings. In MEA, peak P-T conditions in the partial melting range are achieved by ~45 Ma in response to heating by upwelling sublithospheric mantle, with high temperatures sustained during the quiescent phase by the increasing effect of radioactive self-heating. Metamorphic assemblages and mineral chronometers could therefore have continued to re-equilibrate from 45 Ma until Neohimalayan crustal thickening, metamorphism, and exhumation began after 30 Ma. The change from Early Eohimalayan accretion to Late Eohimalayan quiescence is therefore not evident in the metamorphic record.

7) MED results (Section 4.7) demonstrate that continued underthrusting/subduction of Indian mantle lithosphere beneath the Lhasa terrane during Late Eohimalayan orogenesis has the potential to grow an Eohimalayan Himalaya that significantly exceeds the size of the modern Himalaya (Figure 4.7). This strengthens arguments in favor of a two-phase Himalayan-Tibetan orogeny separated by Late Eohimalayan quiescence, even though this is cryptic in regard to metamorphism. By contrast, MEA satisfies the evidence for quiescence noted in Section 4.7.

8) The tectonic conditions that led to subduction channel opening and early heating in MEA are unlikely to have been unique to the H-T orogen. We suggest similar processes could have operated in other orogens where peak Barrovian (MP-MT) conditions were reached less than 20 Myr after collision (e.g., Viete and Lister, 2017; Ryan and Dewey, 2019). By illuminating some aspects of Eohimalayan

tectonics, the results of this study may therefore extend the applicability of the Himalayan archetype to other orogenic systems.

Our proposition of a tectonically quiescent Late Eohimalayan interval, owing to shortening within Asian terranes but not the Himalaya, needs to be tested. Evidence that would falsify the hypothesis includes: 1) paleomagnetic data showing little or no northward motion of India, particularly the northern Tethyan Himalaya, relative to stable Asia during the proposed quiescence; 2) tomographic evidence of a ~1000 km long slab unambiguously attributed to Indian lithosphere subducted during 44 -30 Ma; 3) structural evidence of significant (>100 km) shortening within the Himalaya during the proposed quiescence, and; 4) metamorphic evidence of significant pressure increases reflecting crustal shortening during the proposed quiescent interval; constant or increasing temperature has been shown to be compatible with quiescence. If the proposed quiescent interval is verified, we suggest naming it the Mesohimalayan phase.

4.9 Supplementary Information

Supplementary material (Appendix C) related to this article can be found on-line at https://doi.org/10.1016 /j.epsl.2021.117350

Further supporting information is also provided in Appendix C.

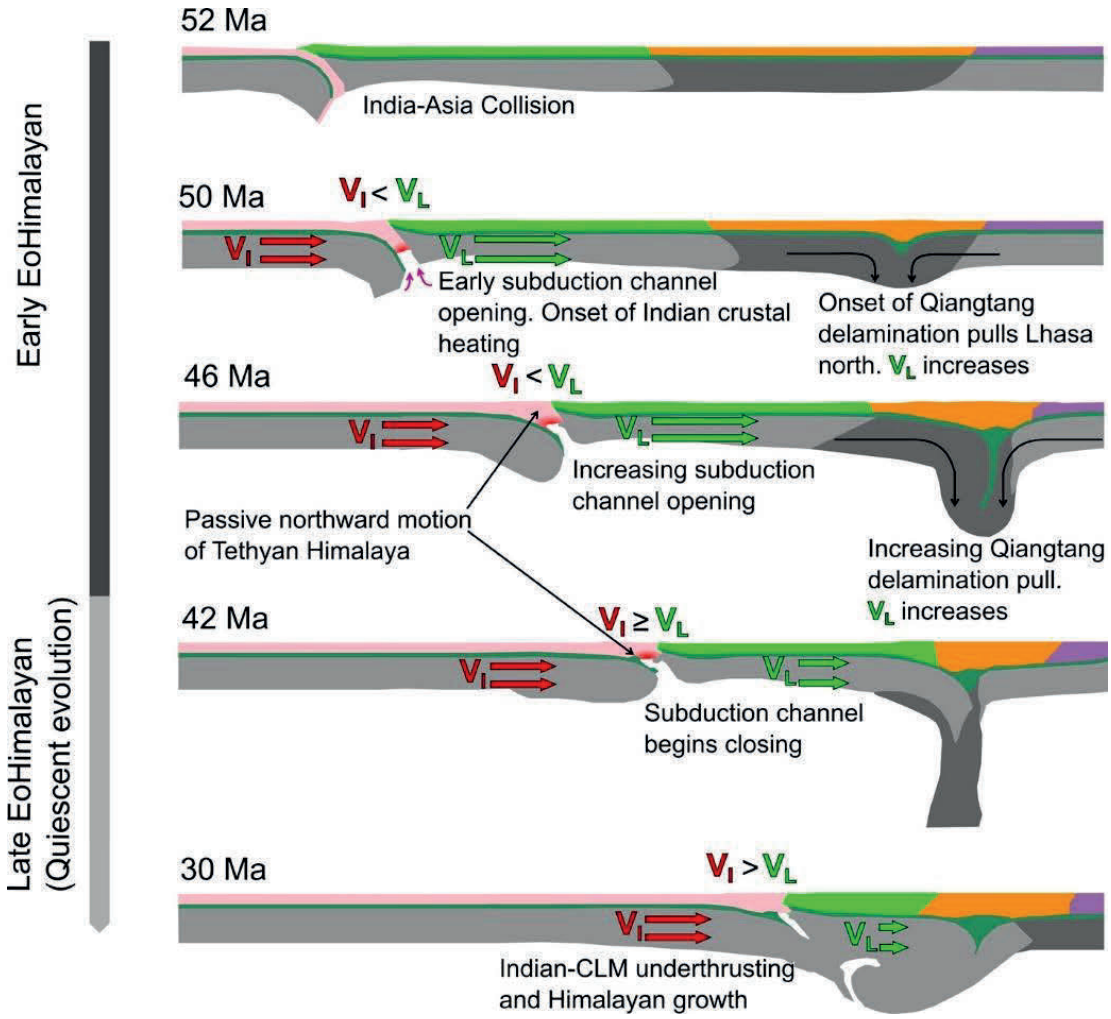

Figure 4.8. Summary of the early evolution of the Himalayan-Tibetan orogen showing the proposed explanation for Early Eohimalayan metamorphism and magmatism, followed by Late Eohimalayan tectonic quiescence, as precursors to Neohimalayan evolution. The explanation is simple and involves only small changes in the relative northward velocities of India (I, V_I) and the Lhasa terrane (L, V_L). During the Early Eohimalayan (~55-45 Ma), $V_I < V_L$, the Neothethys subduction channel opens, asthenosphere upwells and heats the Indian crust causing metamorphism and magmatism; hot colors correspond broadly to Indian crust heated to >700°C during Early Eohimalayan metamorphism. During the Late Eohimalayan (~45-30 Ma), $V_I \geq V_L$, the subduction channel closes slowly but there is little to no underthrusting of India beneath the Lhasa terrane and no accretion of offscraped Indian crust. The Tethyan Himalaya therefore experiences tectonic quiescence. Resumption of Indian underthrusting at 30-25 Ma causes Neohimalayan orogenesis. Regions in figure correspond to, from left to right (south to north): India (pink), Lhasa (green), Qiangtang (orange), Songpan-Ganzi (purple). Further discussion in text.

4.10 References for Chapter 4

Acton, G.D. (1999). Apparent polar wander of India since the Cretaceous with implications for regional tectonics and true polar wander. *Memoir of the Geological Society of India 44,* 129–175.

Aikman, A.B., Harrison, T.M., and Hermann, J. (2012). Age and thermal history of Eo- and Neohimalayan granitoids, eastern Himalaya. *Journal of Asian Earth Sciences, 51*, 85–97. https://doi.org/10.1016/j.jseaes.2012 .01.011

Aikman, A.B., Harrison, T.M., and Lin, D. (2008). Evidence for early (> 44 Ma) Himalayan crustal thickening, Tethyan Himalaya, southeastern Tibet. *Earth and Planetary Science Letters. 274,* 14–23. https://doi.org/10.1016/j.epsl.2008.06.038

Aitchison, J.C., Ali, J.R., and Davis, A.M. (2007). When and where did India and Asia collide? *Journal of Geophysical Research: Solid Earth, 112,* B05423. https://doi.org/10.1029/2006JB004706

Beaumont, C., Jamieson, R.A., Nguyen, N.H., and Medvedev, S. (2004). Crustal channel flows: 1. Numerical models with applications to the tectonics of the Himalayan-Tibetan orogen. *Journal of Geophysical Research: Solid Earth, 109*, B06406. https://doi.org/10.1029/2003JB002809

Bird, P. (1978). Initiation of intracontinental subduction in the Himalaya. *Journal of Geophysical Research: Solid Earth 85*, 4975–4987. https://doi.org/10.1029/JB083iB10p04975

Carosi, R., Montomoli, C., Iaccarino, S., and Visona, D. (2019). Structural evolution, meta-morphism and melting in the greater Himalayan sequence in central-western Nepal. In: Treloar, P.J., Searle, M.P. (Eds.), Himalayan Tectonics: A Modern Synthesis. *Geological Society, London, Special Publications, 483*, 305–323. https://doi.org/10.1144 /SP483.3

Carosi, R., Montomoli, C., Iaccarino, S., Massonne, H.J., Rubatto, D., Langone, A., et al. (2016). Middle to late Eocene exhumation of the greater Himalayan sequence in the central Himalayas: Progressive accretion from the Indian plate. *Geological Society of America Bulletin. 128*, 1571–1592. https://doi.org/10.1130/B31471.1

DeCelles, P.G., Gehrels, G.E., Quade, J., and Ojha, T.P. (1998). Eocene-early Miocene foreland basin development and the history of Himalayan thrusting, western and central Nepal. *Tectonics 17*, 741–765. https://doi.org/10.1029/98TC02598

DeCelles, P.G., Kapp, P., Gehrels, G.E., and Ding, L., (2014). Paleocene-Eocene foreland basin evolution in the Himalaya of southern Tibet and Nepal: Implications for the age of initial India-Asia collision. *Tectonics, 33*, 824–849. https://doi.org/10.1002/2014TC003522

DeCelles, P.G., Kapp, P., Quade, J., and Gehrels, G.E. (2011). Oligocene–Miocene Kailas basin, southwestern Tibet: Record of postcollisional upper-plate extension in the Indus-Yarlung suture zone. *Geological Society of America Bulletin, 123*, 1337–1362. https://doi.org/10.1130 /B30258.1

Ding, H., Zhang, Z., Dong, X., Tian, Z., Xiang, H., Mu, H., et al. (2016). Early Eocene (c. 50 Ma) collision of the Indian and Asian continents: Constraints from the North Himalayan metamorphic rocks, southeastern Tibet. *Earth and Planetary Science Letters, 435*, 64–73. https://doi.org/10.1016 /j.epsl.2015.12.006

Garzanti, E. (2019). The Himalayan foreland basin from collision onset to the present: a sedimentary–petrology perspective. In: Treloar, P.J. and Searle, M.P. (Eds.), Himalayan Tectonics: A Modern Synthesis. *Geological Society, London, Special Publications, 483*, 65–122. https://doi.org/10.1144/SP483.17

Hodges, K.V. (2000). Tectonics of the Himalaya and southern Tibet from two perspectives. *Geological Society of America Bulletin, 112*, 324–350. https://doi.org/10.1130/0016-7606(2000)112<324:TOTHAS>2.0.CO;2

Hodges, K.V. and Silverberg, D.S. (1988). Thermal evolution of the greater Himalaya, Garwhal, India. *Tectonics, 7*, 583–600.

Hu, X., Garzanti, E., Wang, J., Huang, W., An, W., and Webb, A. (2016). The timing of India-Asia collision onset – Facts, theories, controversies. *Earth-Science Reviews.160*, 264–299. https://doi.org/1 .1016/j.earscirev.2016.07.014

Huismans, R. and Beaumont, C. (2011). Depth-dependent extension, two-stage breakup and cratonic underplating at rifted margins. *Nature, 473*, 74–78. https://doi.org/10.1038/nature09988

Imayama, T., Takeshita, T., Yi, K., and Fukuyama, M. (2018). Early Oligocene partial melting via biotite dehydration melting and prolonged low-pressure–low-temperature metamorphism of the upper High Himalaya Crystalline Sequence in the far east of Nepal. In: Sharma, R., Villa, I.M., Kumar, S. (Eds.), Crustal Architecture and Evolution of the Himalaya–Karakoram–Tibet Orogen. *Geological Society, London, Special Publications, 481*, 147-173. https://doi.org/10.1144 /SP481.2

Ingalls, M., Rowley, D.B., Currie, B., and Colman, A.S. (2016). Large-scale subduction of continental crust implied by India–Asia mass-balance calculation. *Nature Geoscience., 9*, 848–853. https://doi.org/10.1038 /ngeo2806

Jamieson, R.A., Beaumont, C., Medvedev, S., and Nguyen, M.H. (2004). Crustal channel flows: 2. Numerical models with implications for metamorphism in the Himalayan-Tibetan orogen. *Journal of Geophysical Research: Solid Earth, 109*, B06407. https://doi.org/10.1029/2003JB002811

Ji, W.Q., Wu, F.Y., Chung, S.L., Wang, X.C., Liu, C.Z., Li, Q.L., et al. (2016). Eocene Neo-Tethyan slab breakoff constrained by 45 Ma oceanic island basalt–type magmatism in southern Tibet. *Geology, 44*, 283–286. https://doi.org/10.1130/G37612.1

Kapp, P., Yin, A., Harrison, T.M., and Ding, L. (2005). Cretaceous-Tertiary shortening, basin development, and volcanism in central Tibet. *Geological Society of America Bulletin, 117*, 865–878. https://doi.org/10.1130/B25595.1

Kelly, S., Beaumont, C., and Butler, J.P. (2020). Inherited terrane properties explain enigmatic post-collisional Himalayan-Tibetan evolution. *Geology, 48*, 8–14. https://doi.org/10.1130/G46701.1

Laskowski, A.K., Kapp, P., and Cai, F. (2018). Gangdese culmination model: Oligocene–Miocene duplexing along the India-Asia suture zone, Lazi region, southern Tibet. *Geological Society of America Bulletin, 130*, 1355–1376. https://doi.org/10.1130/B31834.1

Le Fort, P. (1996). Evolution of the Himalaya. In: Yin, A., Harrison, T.M. (Eds.), The Tectonics of Asia. *Cambridge University Press,* New York, 95–106.

Long, S.P., McQuarrie, N., Tobgay, T., Coutand, I., Cooper, F.J., and Reiners, P.W. (2012). Variable shortening rates in the eastern Himalayan thrust belt, Bhutan: Insights from multiple thermochronologic and geochronologic data sets tied to kinematic reconstructions. *Tectonics, 31*, TC5004. https://doi.org/10.1029/2012TC003155

O'Brien, P.J. (2019). Eclogites and other high-pressure rocks in the Himalaya: A review. In: Treloar, P. J. and Searle, M. P. (Eds.), Himalayan Tectonics: A Modern Synthesis, *Geological Society, London, Special Publications*, *483*, 183–213. https://doi.org/10.1144/SP483.13

Orme, D.A. (2019). Burial and exhumation history of the Xigaze forearc basin, Yarlung suture zone, Tibet. *Geoscience Frontiers, 10*, 895–908. https://doi.org/10.1016/j.gsf.2017.11.011

Parsons, A.J., Hosseini, K., Palin, R., and Sigloch, K. (2020). Geological, geophysical and plate kinematic constraints for models of the India-Asia collision and the post-Triassic central Tethys oceans. *Earth-Science Reviews., 208*, 103084. https://doi.org/10.1016/j.earscirev.2020.103084

Ratschbacher, L., Frisch, W., Liu, G., and Chen, C.C. (1994). Distributed deformation in southern and western Tibet during and after the India-Asia collision. *Journal of Geophysical Research: Solid Earth, 99*, 19917–19945. https://doi.org/10.1029/94JB00932

Regis, D., Warren, C.J., Young, D., and Roberts, N.M. (2014). Tectono-metamorphic evolution of the Jomolhari massif: Variations in timing of syn-collisional metamorphism across western Bhutan. *Lithos, 190*, 449–466. https://doi.org/10.1016/j.lithos.2014.01.001

Ryan, P.D. and Dewey, J.F. (2019). The sources of metamorphic heat during collisional orogeny: The Barrovian enigma. *Canadian Journal of Earth Sciences, 56*, 1309–1317. https://doi.org/10.1139/cjes-2018-0182

Searle, M.P. (2019). Timing of subduction initiation, arc formation, ophiolite obduction and India–Asia collision in the Himalaya. In: Treloar, P.J., and Searle, M.P. (Eds.), Himalayan Tectonics: A Modern Synthesis. *Geological Society, London, Special Publications, 483*, 19–37. https://doi.org/10.1144/SP483.8

Sizova, E., Hauzenberger, C., Fritz, H., Faryad, S.W., and Gerya, T. (2019). Late orogenic heating of (ultra)high pressure rocks: Slab rollback vs. slab breakoff. *Geosciences, 9, 499*. https://doi.org/10.3390/geosciences9120499

Smit, M.A., Hacker, B.R., and Lee, J. (2014). Tibetan garnet records early Eocene initiation of thickening in the Himalaya. *Geology, 42*, 591–594. https://doi.org/10.1130/G35524.1

St-Onge, M.R., Searle, M.P., and Wodicka, N. (2006). Trans-Hudson Orogen of North America and Himalaya-Karakoram-Tibetan Orogen of Asia: Structural and thermal characteristics of the lower and upper plates. *Tectonics, 25*, TC4006. https://doi.org/10.1029 /2005TC001907

van Hinsbergen, D.J.J., Lippert, P.C., Li, S., Huang, W., Advokaat, E.L., and Spakman, W. (2019). Reconstructing Greater India: Paleogeographic, kinematic, and geodynamic perspectives. *Tectonophysics, 760*, 69–94. https://doi.org/10.1016/j.tecto.2018.04.006

van Hinsbergen, D.J.J., Steinberger, B., Doubrovine, P.V., and Gassmöller, R. (2011). Acceleration and deceleration of India-Asia convergence since the Cretaceous: Roles of mantle plumes and continental collision. *Journal of Geophysical Research: Solid Earth, 116*, B06101. https://doi.org/10.1029/2010JB008051

Vannay, J.-C. and Hodges, K.V. (1996). Tectonometamorphic evolution of the Himalayan metamorphic core between Annapurna and Dhaulagiri, central Nepal. *Journal of Metamorphic Geology. 14*, 635–656. https://doi.org/10.1046/j.1525-1314.1996.00426.x

Viete, D.R. and Lister, G.S. (2017). On the significance of short-duration regional metamorphism. *Journal of the Geological Society, 174*, 377–392. https://doi.org/10.1144/jgs2016-060

Wang, C., Dai, J., Zhao, X., Li, Y., Graham, S.A., He, D., et al. (2014). Outward-growth of the Tibetan Plateau during the Cenozoic: A review. *Tectonophysics, 621*, 1–43. https://doi.org/10.1016/j.tecto.2014.01.036

Wang, Y.F., Zeng, L., Gao, J., Zhao, L., Gao, L.E., and Shang, Z. (2019). Along-arc variations in isotope and trace element compositions of Paleogene gabbroic rocks in the Gangdese batholith, southern Tibet. *Lithos, 324,* 877–892. https://doi.org/10.1016/j.lithos.2018.11.036

Wang, T., Li, G., Aitchison, J.C., and Sheng, J. (2020). Eocene ostracods from southern Tibet: implications for the disappearance of Neo-Tethys. *Palaeogeography, Palaeoclimatology, Palaeoecology*, *539*, 109488. https://doi.org/10.1016/j.palaeo.2019.109488

Wiesmayr, G. and Grasemann, B. (2002). Eohimalayan fold and thrust belt: Implications for the geodynamic evolution of the NW-Himalaya (India). *Tectonics, 21*, 1–16. https://doi.org/10.1029/2002TC001363

Yin, A., Harrison, T.M., Murphy, M.A., Grove, M., Nie, S., Ryerson, F.J., et al. (1999). Tertiary deformation history of southeastern and southwestern Tibet during the Indo-Asian collision. *Geological Society of America Bulletin, 111*, 1644–1664. https://doi.org/10.1130/0016-7606(1999)111%3C1644:TDHOSA%3E2.3.CO;2

Yin, A. and Harrison, T.M. (2000). Geologic evolution of the Himalayan-Tibetan orogeny. *Annual Review of Earth and Planetary Sciences, 28*, 211–280. https://doi.org/10.1146/annurev.earth.28.1.211

Yin, A. (2006). Cenozoic tectonic evolution of the Himalayan orogen as constrained by along-strike variation of structural geometry, exhumation history, and foreland sedimentation. *Earth-Science Reviews, 76,* 1–131. https://doi.org/10.1016/j.earscirev.2005.05.004

Zeng, L., Gao, L.E., Xie, K., and Liu-Zeng, J. (2011). Mid-Eocene high Sr/Y granites in the Northern Himalayan gneiss domes: Melting thickened lower continental crust. *Earth and Planetary Science Letters, 303*, 251–266. https://doi.org/10.1016/j.epsl.2011.01.005

CHAPTER 5. A MACHINE-LEARNING BASED METHOD FOR DISCRIMINATING TECTONIC ENVIRONMENTS FROM GEOCHEMICAL DATA

5.1 Abstract

Geochemical datasets are important tools for studying mantle-scale tectonic processes, which generally leave little direct evidence behind in the rock record. The recent availability of machine learning tools and access to large geological datasets has opened opportunities for a data-science approach to geochemical interpretations. However, machine learning tools are only useful if they are used to answer geologically relevant questions. In this manuscript I present a machine-learning based method for finding signatures in geochemical data that can serve as candidates for distinct tectonic processes. This is done by finding spatial-temporal clusters of data which share these signatures, which simply reflect an expectation that the processes we seek to infer and understand may also be geographically or temporally localized. The method is outlined in general and then applied to a magmatic dataset from the well-studied Himalayan-Tibetan system. The results show that many common interpretations of the magmatic record derived from traditional geochemical interpretations can be recovered with this method in a quick and semi-automated way, and that this method has the potential to improve upon traditional geochemical methods.

5.2 Introduction

Geochemical analysis of magmatic suites is an important tool for interpreting mantle-scale tectonic processes including subduction, slab break-off, continental lithospheric mantle removal, and crustal thickening, as these processes, which evolve at depth, generally leave little direct evidence in the rock record (Chen and Niu et al., 2017; Guo et al., 2018; Heintz et al., 2009; Klemperer et al., 2013). However, interpretations derived from analyses of magmatic data may be non-unique (e.g., Castillo, 2012; Zheng, 2019). Magmatic suites typically possess significant variability owing to the petrology and

geochemistry of the melt sources, the pressure and temperature conditions of the melt sources, and processes such as fractionation, assimilation, and magma mixing. Geochemical interpretations must therefore attempt to reveal those variations that reflect distinct mantle-tectonic processes from those that do not.

Some constraints concerning geochemical interpretations can be gained by recognizing that the tectonic processes we are attempting to infer, and their associated emplaced magmas, take place in specific geographic regions and during specific intervals of time. Therefore, we expect that if the geochemical characteristics in the magmatic rock record that are used to infer a tectonic process accurately reflect that process, then the rocks sharing those characteristics should also belong to a specific geographic region in space and/or a specific interval of time (i.e., a spatiotemporal cluster).

The goal of the research reported here is to explore a method for finding unrecognized geochemical signatures/characteristics in magmatic rocks which may reflect distinct tectonic processes. This method uses machine learning (ML) to find spatiotemporal clusters of magmatic rocks which are optimally distinguishable (defined later) from each other based on their geochemistry, and then reveal their distinguishing geochemical signatures. The benefit of employing ML is that ML methods can consider many elements at once and overcome cognitive obstacles that often limit visual pattern recognition to bivariant diagrams. This method is not intended to replace traditional geochemical analyses and interpretations, but rather complement them. First, previously unrecognized geochemical features discovered using this method can provide direction for more traditional geochemical analysis. Second, in poorly studied datasets, this method may offer a quick way to find traditional geochemical signatures of relevance (e.g., trace element ratios).

Using ML methods to reveal geochemical signatures/characteristics of known tectonic environments, and thus facilitating similar predictions for poorly understood data, has been explored previously (e.g., Doucet et al., 2022; Lindsay et al., 2021; Perelli et al., 2017; Petrelli and Perugini, 2016; Ueki et al., 2018). In addition, ML methods have been

applied to find spatial patterns of geochemical anomalies in the context of mineral exploration (e.g., Feng et al., 2022; Guan et al., 2022), although the deep-learning approaches used do not reveal the signatures that define these anomalies. To my knowledge, using ML to identify spatiotemporal clusters with distinguishable geochemical signatures has not been explored.

It is worth considering in more detail the question "Why is seeking distinguishable spatiotemporal clusters useful at all?" Using ML methods to predict which of the archetypal tectonic environments your sample most closely resembles may not be particularly useful if the geochemical signatures you are seeking are unique to your system of interest, rather than broadly applicable signatures that reflect already recognized different tectonic environments. Similarly, methods used to study variations specific to your dataset (e.g., cluster analysis or principal component analysis), which focus on the most significant sources of geochemical variation, are not useful if they do not correlate with a feature of interest to your particular study or cannot be easily linked to petrological processes. However, identifying geochemical signatures that do not correspond to those of recognized tectonic environments can help eliminate these as candidates.

For example, if you hypothesize that your system of interest experienced an important change in tectonic processes at some unknown or poorly resolved time, and that this change could be reflected in an unrecognized geochemical signature, then what you seek is a change in geochemistry which correlates with time. Similarly, if rocks possessing distinct geochemical signatures are discovered to also be clustered in space and/or time, it is reasonable to hypothesize that these signatures reflect some tectonic/petrogenic processes corresponding with these spatial regions and time intervals and to seek an interpretation within a tectonic/petrogenic framework. The purpose of the method presented here is to find such clusters and their corresponding geochemical signatures.

This manuscript first outlines the general method, then evaluates it using some hypothetical examples, and finally applies the method in a preliminary way to a magmatic dataset from the Himalayan-Tibetan orogenic system.

5.3 Glossary of Terms

This is a glossary of terms as used in this manuscript. Where descriptions use other glossary terms, they are italicized.

ϕ-values. The Euclidean distance a datum lies in *feature space* from the *discriminating hyperplane*.

Accuracy (*p*). In this manuscript, it is the proportion of correct predictions a model makes (correct predictions/total predictions) when used to predict the classes of a testing-set (where the classes are already known or are temporarily assigned using the method presented here).

Baseline accuracy. The proportion of data belonging to the larger class (p_0). If there is no knowledge of how features can inform classes, the best prediction for class membership is to assume all of the data belong to the larger class, which should achieve the baseline accuracy on average.

Box-Cox Transform. A transformation of data which are not normally distributed to a normal distribution see Appendix D4.1

Class. In the context of machine learning, each sample in a dataset has a class, which may be known (and labeled) or not.

Data Science. A broad interdisciplinary field that uses statistical, computational, and scientific techniques to facilitate the review and analysis of data.

Decision vector. A vector in *feature space*, normal to the *distinguishing hyperplane*. Components of this vector define the variation in *features* that best separate the two *classes*.

Discriminating hyperplane. A *hyperplane* in *feature space* which separates two *classes* of data with the widest margin (distance from the hyperplane to the nearest datum in each class).

Features. In data classification problems, features are data associated with each sample, which can be used to predict/inform the class that sample belongs to. In the context of geochemistry, each major and trace element concentration would represent a feature.

Feature extraction. Techniques that reduce the number of initial *features* of raw data, by identifying or combining relevant features into numerical values which can be used as characteristics for identifying *classes* or extracting meaningful knowledge from the data.

Feature space. A vector space, where the value of each feature is a component. Each sample can be represented as a vector in feature space, where the components of these vectors are the numerical values of each of that sample's features. For example, a geochemical dataset with two measured features, Na_2O and K_2O, each sample in the dataset could be represented as a feature space vector where the MgO and K_2O content of that particular sample are its vector components (e.g., vectors of the form [MgO, K_2O]).

Group proposal scheme. A way of iteratively proposing new *proposed groupings* of data.

Hyperplane. A subspace, which is one dimension less than the space it is embedded in. In 2D, a hyperplane is a line that separates the 2D plane into two halves. In 3D, a hyperplane is a conventional (2D) plane separating the 3D space it is embedded in into two halves. Likewise, in a (N)D *feature space* a hyperplane is a (N-1)D subspace separating an (N)D *feature space* into two halves. See also *discriminating hyperplane.*

Linear support vector machine (SVM). A *supervised machine learning* method that seeks to find a hyperplane (*the discriminating hyperplane*) in *feature space* that separates data based on their *class* membership.

Performance. Supervised machine learning models are typically trained on a randomly chosen subset of the labeled dataset, the training-set, and then tested on the remaining testing-set. The trained model makes predictions about the classes of data in the testing-set based only on the features, and these predictions are compared to the known classes. In the method presented here, datasets are assigned temporary labels during the process of seeking an ideal grouping. The accuracy of the model in predicting the training-set classes can be used to define the model's performance. In this manuscript *scaled accuracy* is used to measure performance where the class sizes are imbalanced in size and *unscaled accuracy* where they are equal in size.

Performance curve. A curve of *performance* plotted against a measurement defining the *proposed groupings*. In this method, an *SVM* model is trained and tested, and its *performance* is measured for a given proposed grouping. This is useful when iteratively *proposed groupings* are defined by a single number (e.g., east or west of a given longitude).

Proposed grouping. A temporary grouping of data into two classes. In the the present manuscript an *SVM* is trained and tested for *performance* using these *classes*. The aim is to discover distinguishable groups.

Regularization parameter (*C*). A parameter controlling the degree to which the SVM model will allow misclassification of training-set data during training. See subsection 5.4.5 and Appendix D4 for further details.

Scaled accuracy (p_s). The improvement in *unscaled accuracy* (proportion of correct predictions) a trained model makes (p), compared to the *baseline accuracy* (the proportion of data belonging to the larger class, p_0), scaled by the available improvement in accuracy above this baseline ($1-p_0$). This is calculated as $p_s = (p-p_0)/(1-p_0)$.

Supervised machine learning. A class of machine learning tools, trained on a labeled dataset. Each sample in the dataset has label-data indicating a *class* this sample belongs to, as well as *feature*-data which may be informative regarding class membership. Supervised learning involves training a model on these data with the goal that the trained model can then predict classes based on the features alone.

Support Vector Machine (SVM). A machine learning model that can be trained on a template of data labeled by *class*, to predict which *class* unlabeled data belong based only on their *features*.

Testing-set. A dataset of labeled data. A trained *SVM model* predicts the *classes* of these data based on their *features*, and these predictions can be compared to the known classes to measure *performance*.

Training-set. A dataset of labeled data used to train a machine learning model (i.e., *SVM*).

Unscaled accuracy (p). proportion of correct predictions to all predictions a trained model makes of a testing-set.

5.4 Outline of the Method

5.4.1 Supervised Learning for Group Identification

Traditionally, supervised learning involves training a model on a labeled dataset, where the labels indicate classes which data belong to. In the context of geochemistry, this could be a dataset of rock samples from known tectonic environments, where each sample has geochemical measurements (generically referred to as features), and where each sample is labeled according to the tectonic environment the sample belongs to (i.e., the class). These data are described as possessing label-data, defining the class they belong to, and feature-data, which (ideally) informs which class these data belong to.

In traditional uses of supervised learning, once the model is trained on the labeled dataset the trained model can then be used to predict the classes of unlabeled data based on their features alone. For example, a supervised learning model could be used to distinguish between magmatic rocks from continental arc settings and other magmatic/tectonic settings based on geochemistry by training the model on a dataset comprising samples which belong to well understood tectonic environments and where each sample is labeled accordingly (e.g., Doucet et. al., 2022; Ueki et al., 2018). If successfully trained, the model could then predict whether a sample from an unknown tectonic environment was from an arc setting using only the geochemistry of the sample (i.e., the feature-data). Figure 5.1 outlines a hypothetical workflow of training an ML model to distinguish between continental arc samples and mid-ocean ridge samples.

Typically, the trained model is tested for accuracy using a subset of the labeled data. The labeled data are randomly subdivided into a training-set and a testing-set (step 1 in Fig 5.1). The model is exclusively trained on the training-set (step 2 in Fig. 5.1), and once trained, can be used to predict the classes of the testing-set data (step 3 in Fig. 5.1), where the classes are known in advance (but not provided to the model). Since the trained model makes predictions based on features alone, the predicted classes of the training-set data can be compared to their labeled classes (i.e., their actual class), and the performance of

the trained model can be evaluated by considering how successful/correct the model's predictions are (step 4 in Fig. 5.1). Once the model is trained, it can be used to predict classes for unlabeled data (set 5 in Fig. 5.1). Details regarding calculating performance are outlined in Subsection 5.4.4, but for this subsection model performance is informally defined as how accurately/correctly a model can predict the classes of a testing-set.

The method presented here also uses supervised learning methods, however with key differences. Unlike traditional supervised learning described above where there is a template of samples belonging to known classes which can be used to train the model, with the method presented here no such template is known in advance. The goal is to find spatiotemporal clusters which are geochemically distinguishable, where neither the distinguishing geochemical signatures, nor the spatiotemporal clusters are known in advance, nor is there a template of samples pocessing these signatures. Instead, all that is known in advance is what criterion constitutes a potentially successful classification according to this method. This can be regarded as a central principle of this method, namely that the discovered classes are spatially and/or temporally grouped together, and that they are distinguishable from each other based on their geochemistry alone. Following this principle, the end-goal of this method is to find the optimally successful classification, namely spatiotemporal groups that are optimally distinguishable based on geochemistry (optimally distinguishable is defined later). The term "cluster" is reserved here for some hypothesized collection of rocks whose geochemistry naturally or genetically reflects some distinct tectonic/petrographic process. The term "grouping" (or optimal grouping) will be used for those classes of rocks discovered by this method, since these may be only approximately equivalent to the natural clusters we seek (Subsection 5.4.6).

To find these classes, samples are temporarily labeled according to a proposed spatiotemporal grouping. For example, in Figure 5.2 (a1) samples are labelled as lying north or south of a given latitude. This grouping serves as a temporary template of labeled data, which can be used to train a ML model. Correspondingly, in Figure 5.2b the samples are labelled (C) west and (D) east of a given longitude. This template is

subdivided into a training and testing-set (e.g., steps a1 in Fig. 5.2a and b1 in Fig. 5.2b), the ML model is trained on the training-set (e.g., steps a2 in Fig. 5.2a and b2 in Fig. 5.2b), and the performance of the model is evaluated using the testing-set (e.g., steps a3 and a4 in Fig. 5.2a and steps b3 and b4 in Fig. 5.2b). If the model performs well (Subsection 5.3.4) meaning it can distinguish the classes of the testing-data accurately (e.g., Fig. 5.2b vs Fig. 5.2a), then this grouping can be regarded as contingently satisfying the criteria for a successful classification since by design these classes form a spatiotemporal grouping and are found to be geochemically distinguishable by the trained ML model.

The goal of this method is to find an optimal grouping, by iteratively proposing spatiotemporal groupings according to a group proposal scheme (Subsection 5.4.6), training, evaluating the trained ML model's performance, and then identifying the grouping corresponding to the best performing model (e.g., Fig. 5.2a vs Fig. 5.2b). Once these groups have been identified, the features important for distinguishing these groups can be extracted from the successful trained model, as discussed below (Subsection 5.4.5). In the simple example presented in Figure 5.2b, the ideal grouping could be found by simply dividing the groups into east/west of a correctly selected longitude. In nature, more complicated arrangements are expected, and methods for exploring more complicated spatiotemporal groupings is discussed in Subsection 5.4.6.

In this manuscript, a linear support vector machine (SVM) is used as the supervised ML technique. However, any supervised ML technique can be used for group identification, and furthermore, once these groups are identified, any ML methods, traditional statistical techniques, and/or traditional geochemical interpretation, can be used to study the groups. SVM was chosen here because it is relatively simple, intuitive, and particularly useful for feature extraction.

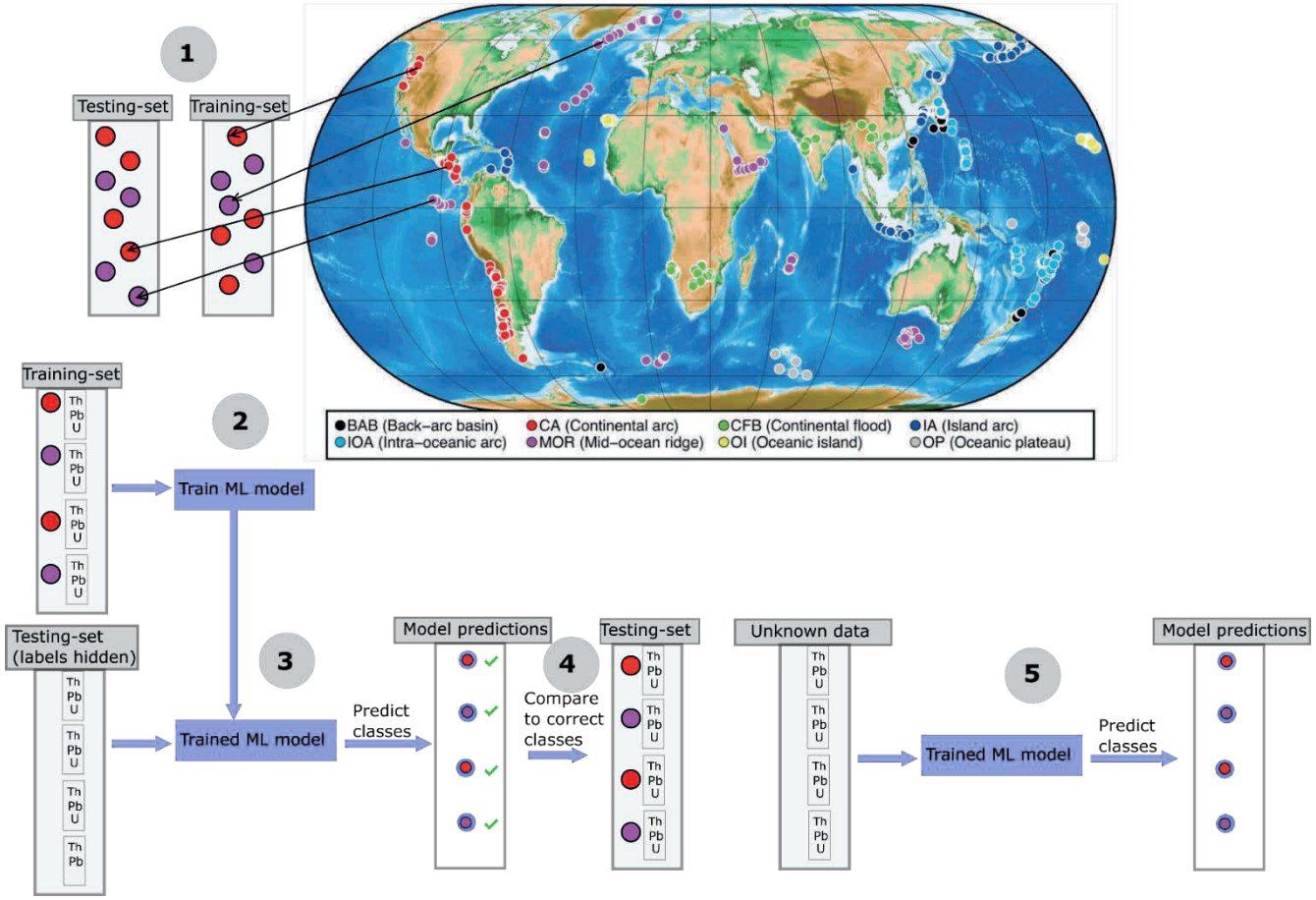

Figure 5.1. Supervised ML model using data from known tectonic environments. Data from known tectonic environments, continental arc rocks (red), and mid-ocean ridge rocks (purple), are used to train a ML model. **1** labeled data divided into training and testing-set; **2** ML model trained on the training-set; **3** trained model used to predict the classes (continental arc vs mid-ocean ridge) of the testing data using geochemistry; **4** those predictions are compared to the known classes, and the performance of the model can be evaluated; **5** trained model can be used to predict classes of unknown data. Map modified from Ueki et al., (2018).

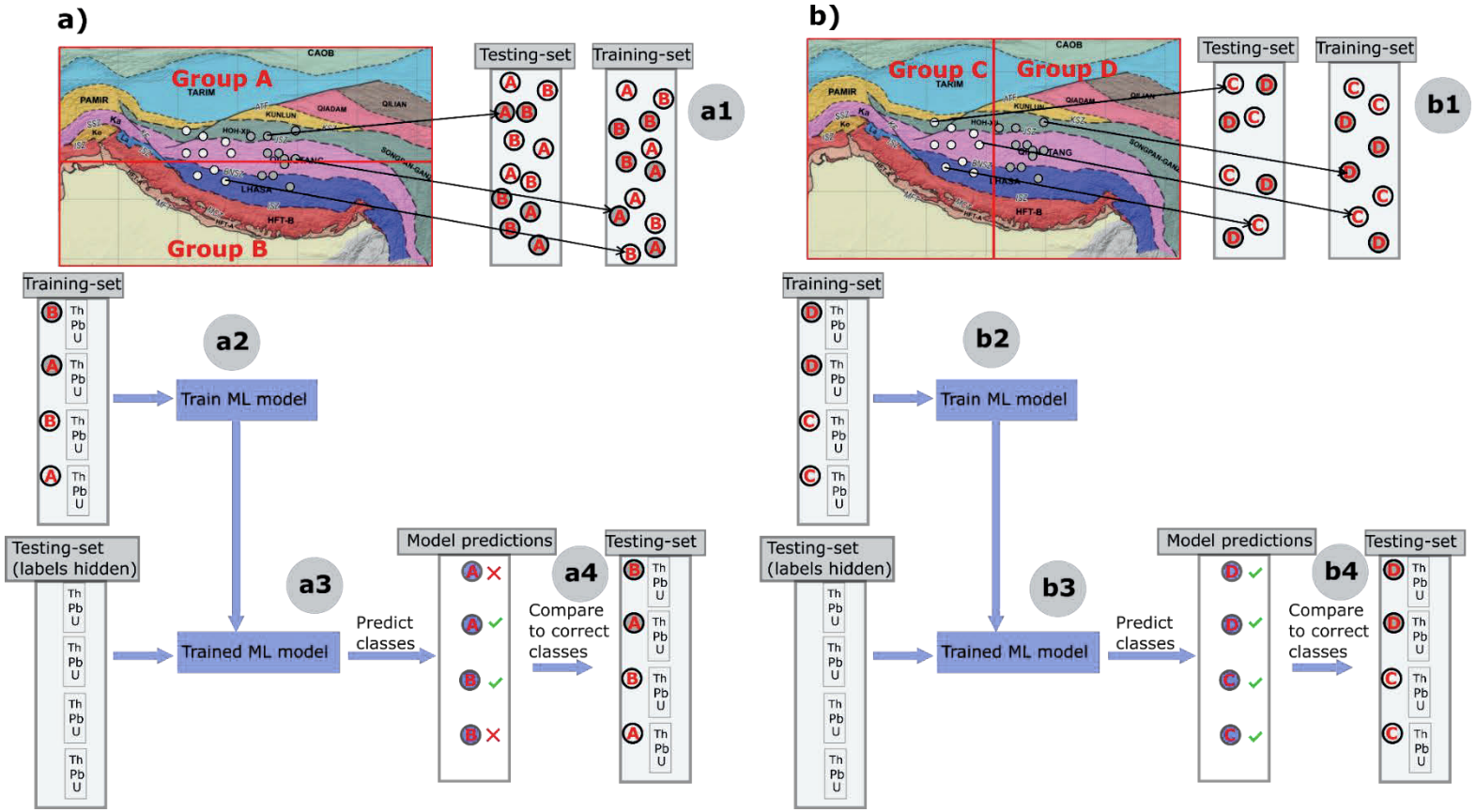

Figure 5.2. Supervised learning applied to data from unknown tectonic environments. **a)** Two geochemically distinguishable classes of data (white vs grey) clustered in space. A proposed grouping (Groups A and B) does not correctly separate the data into the two distinguishable groups. Group A (north) and B (south) have both white and grey classes. The data are subdivided into training/testing-set (**a1**), the ML model is trained (**a2**), and evaluated on the testing-set (**a3**). Here many data are incorrectly classified by the trained model (**a4**), as the proposed grouping does not separate data into geochemically distinguishable groups. **b)** a proposed grouping which does separate the data into the two distinguishable classes (Groups C and D). Steps (**b1**)- (**b3**) are followed as above. Now the model performs well (**b4**), and an ideal grouping has been found. Map modified from Parsons et al., (2020).

5.4.2 Linear Support Vector Machine

SVM is a supervised learning method that considers data as represented by vectors in a "feature space". This feature space is a vector space where, for a given datum, the value of each feature (e.g., the geochemical composition of a rock sample) defines a component in this vector space (e.g., components X_1 and X_2 in Fig. 5.3). In the context of a geochemical dataset, each measured element is a component in the feature space. For each sample in the dataset, the values of each measured element, specific to that sample, are the components of its feature space vector (e.g., p in Fig. 5.3d). Each sample can be represented by such a vector in this feature space. SVM is trained on a labeled dataset (i.e., the training-set) to find a hyperplane in this feature space which separates the training data by their labeled classes. More specifically it seeks to maximize the margins between the classes of the training-set (Fig. 5.3; https://scikit-learn.org/stable/modules/svm.html#svm-classification and references therein). Once trained, the model makes class predictions on unlabeled data by determining on which side of this hyperplane these data belong. More details regarding SVM can be found in Section 5.3 (Glossary of Terms) and Appendix D4.

The benefit of SVM is that the vector normal to this hyperplane (the decision vector; labeled "w" in Figure 5.3c) not only provides information about which features are important for classification, but whether a feature is more or less abundant in each group (Subsection 5.4.5).

In some cases, the training data are not completely separable, meaning no hyperplane exists that can separate data from each class. In these cases, SVM can be trained to find a hyperplane maximizing a "soft margin" in which some data in the training-set are allowed to be misclassified, in order to maximize the margins between the remaining data which are correctly classified. This is necessary in cases where the training data are not completely separable, and potentially beneficial when the training data are separable to avoid overfitting the model. This is because an outlier in the training-set can produce a resulting hyperplane that does not optimally separate the rest of the data. The balance

between maximizing the margins and avoiding misclassified data is controlled by a regularization parameter C (Appendix D4). The effect of regularization is discussed further in Subsection 5.4.5.

Typically, the dataset requires preprocessing prior to training an SVM model, most commonly by removing (subtracting) the mean and normalizing by the standard deviation of each feature. If data, such as trace element data, are not normally distributed, a Box-Cox transformation can be applied to fit the data to a normal distribution (Ueki et al., 2018). Appendix D4 illustrates the effects of these pre-processing transformations.

It is worth considering the two separate ways that data are separated using this method. In section 5.4.1 and Figure 5.2, the data are separated by geography into two groups, and are temporarily labeled as belonging to two classes. In the simple example described in Figure 5.2, the two groups may be defined as east or west of a given longitude. SVM on the other hand, separates labeled data by finding a hyperplane that separates the data in feature space, so that data belonging to each class lie on opposite sides of this hyperplane. The goal of this method is to separate the data into spatial (or spatiotemporal) groups, which can also simultaneously be separated successfully in feature space using SVM.

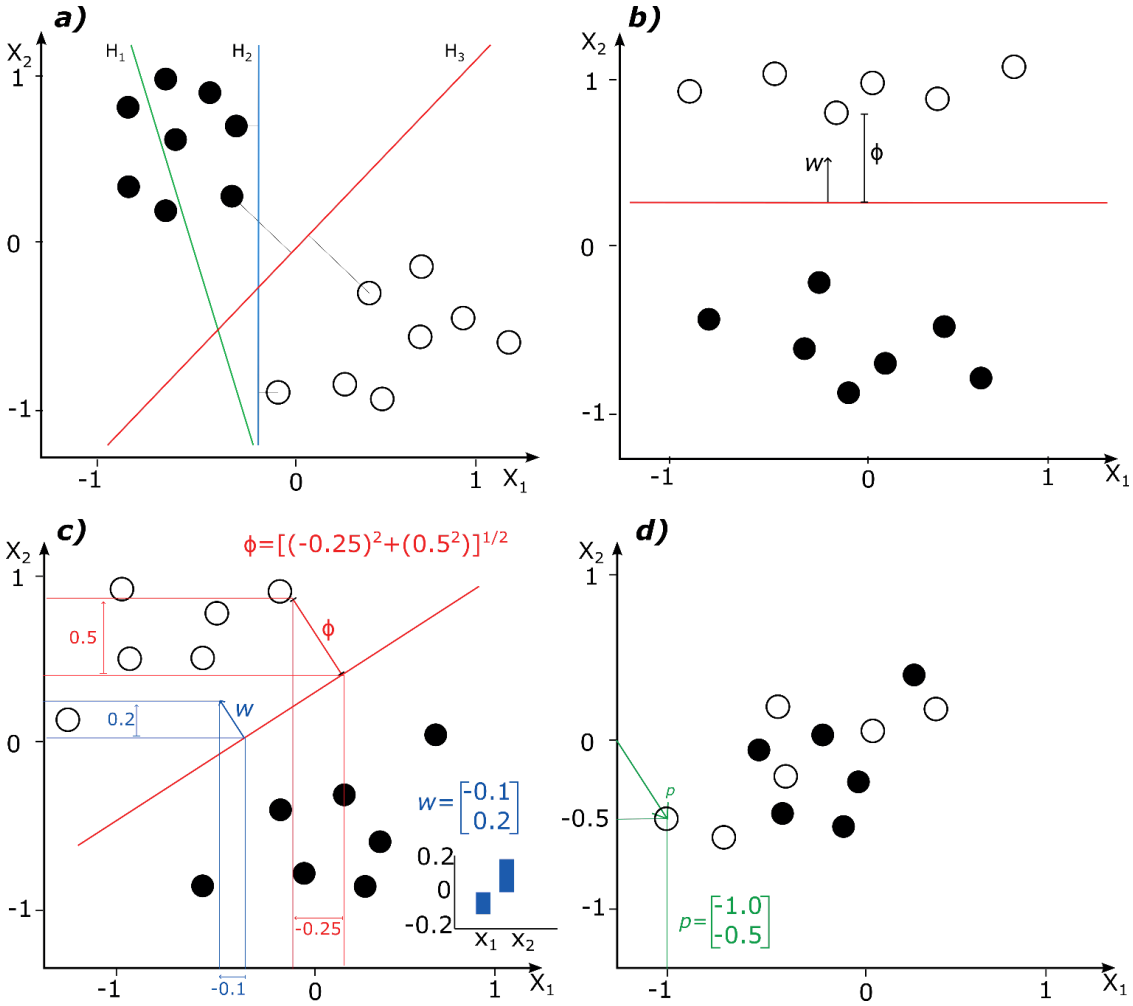

Figure 5.3. Example of SVM with two classes of data (solid and open circles), and two features (parameters X_1 and X_2). **a)** Proposed hyperplanes separating the two classes of data in feature space. "H_1 does not separate the classes, H_2 does but only with a small margin, H_3 separates them with the maximal margin (original caption)." **b)** Two classes of data which are separated along X_2 only. The normal vector (w) points in the direction in feature space which separates the classes. Here X_2 is the only relevant parameter. The parameter ϕ measures the Euclidian distance a particular datum lies in feature space from this hyperplane. In some cases, ϕ can be interpreted to represent how similar data are to a particular class **c)** Here, two classes are separated by increasing X_2 and decreasing X_1 as shown by the vector w, a normal vector to the separating hyperplane, with vector components displayed both numerically and as a bar chart (lower left inset). **d)** Two classes of data which are not separable. Here, there is no obvious way to discriminate these two classes, which may indicate that these data belong to a single indistinguishable class. An example of a datum p is depicted as a vector (graphically in the figure as an arrow) in feature space. This is a vector that points to the datum from the orogen to its coordinates in X_1 and X_2 (Figure and caption modified from Zach Weinberg. Separating hyperplanes (SVG). Citation: https://en.wikipedia.org/wiki/Support_vector_machine#/media/File:Svm_separating_hyperplanes_(SVG).svg)

Separable data are illustrated in Figure 5.4a where hypothetical data clearly form two separable clusters in a simple feature space (X_1 and X_2). These two clusters are easy to recognize visually in this simple 2D feature space, where one cluster represents high X_2 and low X_1 and the other cluster the opposite. These clusters are identified Figure 5.4b where they are colored as grey or white. The grey and white classes are distinguishable based on their features alone. In this example, the grey and white data are also distributed geographically to form two spatial groups as depicted in Figures 5.4c and 5.4d. Figure 5.4c shows a proposed spatial grouping into groups A and B, defined as north or south of a particular latitude. However, the spatial groups A and B do not correspond to the visually identified clusters in feature space (grey and white), nor can groups A and B be separated, even approximately, in feature space because the two spatial groups have significant feature-space overlap, as shown in Figure 5.4e. There is no obvious way to distinguish groups A and B based on features alone. In contrast, Figure 5.4d shows a proposed spatial grouping into groups C and D, defined as east or west of a particular longitude. Here the proposed spatial groups C and D do correspond to the visually identified clusters in feature space, and these data can be successfully separated by a hyperplane in feature space (Fig. 5.4f).

For the illustrative example in Figure 5.4, the grey and white data clusters (Fig. 5.4b) are easy to identify visually in a 2D feature space and are distributed into simple east-west groups, and it is easy to recognize that groups C and D are also simultaneously distinguishable based on features alone. For geochemical datasets, with many measured elements (as features), this may not be possible. Subsection 5.4.4 outlines how to quantify whether an SVM model (or other supervised learning model) can successfully distinguish proposed classes based on geochemistry, and Subsection 5.4.6 explores methods for finding spatial (or spatiotemporal) groups which are not necessarily arranged in such a simple way.

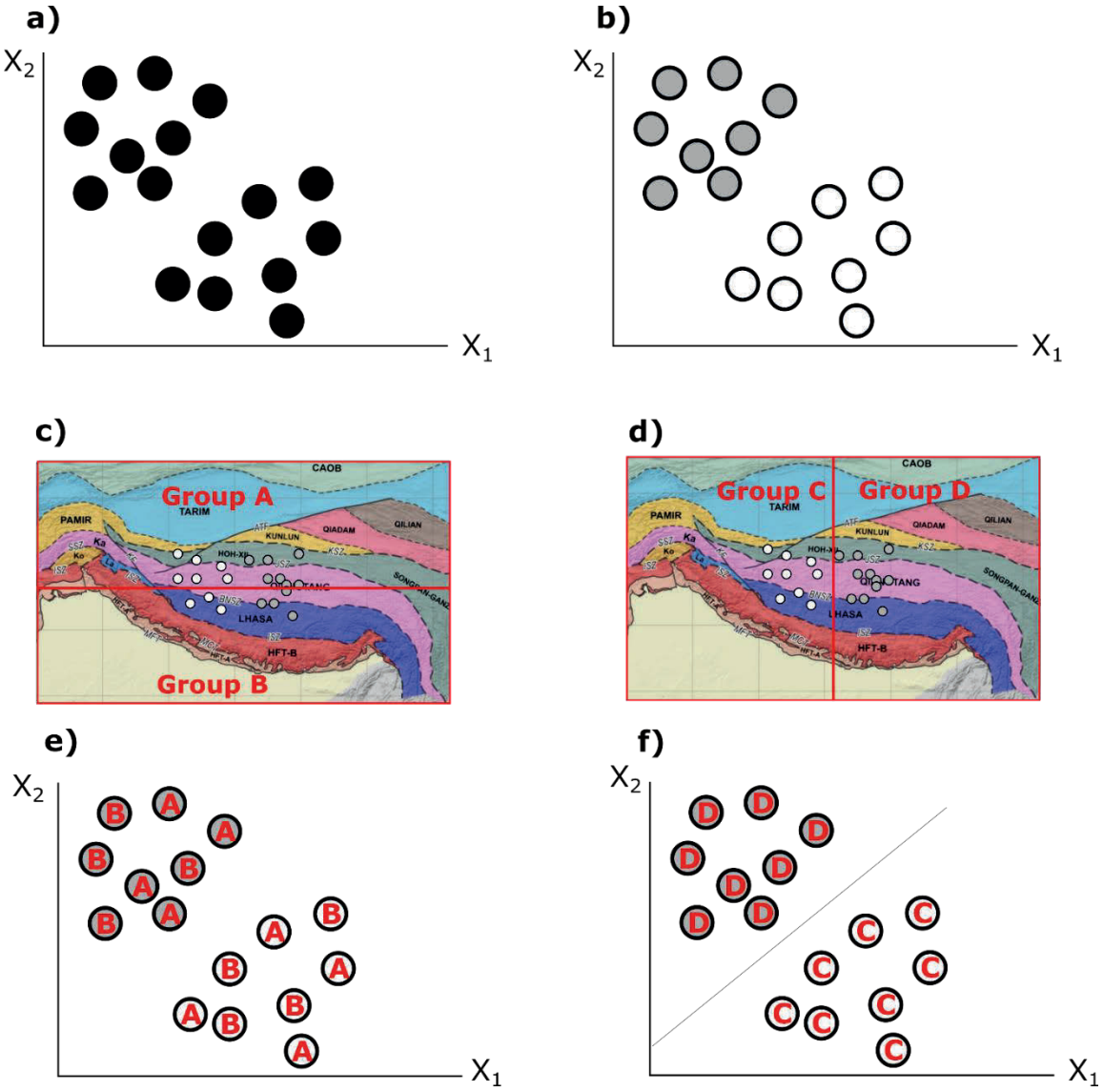

Figure 5.4. a) Two clearly separable groups of data in feature space (e.g., clusters in feature space). X_1 and X_2 could, for example, represent two element concentrations. **b)** These feature-space groups are subsequently identified and colored grey and white. **c)** These data are also separated by latitude into groups A and B, and **d)** by longitude into groups C and D. **e)** Groups A and B are mixed in feature space and not separable, **f)** whereas groups C and D also correspond to white and grey data, which are separable in feature space. Groups C and D separate data into spatial clusters, which can simultaneously be separated in feature space using SVM.

5.4.3 SVM Comparison with Pearce Discrimination Diagrams and Traditional Tectonic Discrimination Diagrams

The method described here bears similarities to Pearce discrimination diagrams – a method familiar to geochemists. Pearce and Cann (1971, 1973) devised a method for

assigning magmatic rocks into tectonic settings using plots of trace elements. They discovered these discriminating elements by using linear discriminant analysis (LDA). LDA finds a parameter space vector which links the means of two labeled clusters of data. Like SVM, it finds a vector in parameter space along which data are expected to vary from one class to the other. Pearce and Cann used LDA to find the most important elements for discriminated data based on tectonic environments, so that a limited number of elements could be plotted and visualized.

Unlike the conventional LDA approach, all the geochemical data available in the labeled dataset are used to train SVM models, and during subsequent predictions for samples from unknown environments. In the context of classifying basalts by tectonic environment Doucet et al. (2022) highlighted the limitations of traditional tectonic discrimination diagrams based on limited numbers of elements, and demonstrated that ML methods can classify basalts more successfully.

5.4.4 Measuring Performance

Evaluating the model performance involves first using the trained model (trained on the randomly chosen training-set) to predict the classes of the testing-set and recording the number of correct/incorrect predictions. In traditional supervised learning the classes are known in advance, whereas with the method presented here, these classes are not known in advance but rather the classes are assigned temporarily based on a proposed spatiotemporal grouping (e.g., groups A/B or C/D in Figs 5.2 and 5.4). This temporary classification is used the same way as with traditional supervised learning for measuring model performance, where all data are assigned the temporary classification (as though this classification was known in advance), and the model is trained on the (temporarily) labeled training-set and used to predict the (temporarily labeled) classes of the testing-set.

There are different ways to measure performance based on the number of correct/incorrect predictions. The simplest measure is to calculate the fraction of correct predictions the model makes of the testing-set, which is defined here as “unscaled accuracy” (p = [number of correctly predicted samples] ÷[total number of samples]).

Unscaled accuracy can be a misleading measure of performance if the two classes are very unequal in size within the labeled dataset. This is because a model which mostly (or always) predicts that data belong to the larger class will perform well according to this measure merely as an artifact of having most data belong to this class. Since the training- and testing-sets are sampled randomly, the imbalance in class size should be approximately equal in both sets.

If two unequally sized classes are indistinguishable based on geochemistry, a hypothetical ML model which simply chooses the larger class every time will offer the maximum accuracy. The expected accuracy of this model is defined as "baseline accuracy" (p_0) and is the proportion of data belonging to the larger class in the labeled dataset (i.e., p_0 = [number of data samples in the larger class]÷[total number of data samples]). The goal of this method is to use the model's performance as a proxy for distinguishability, and the unscaled accuracy of this hypothetical model does not reflect this. Therefore, models which can effectively distinguish between groups based on geochemistry should perform better than this.

If a model achieves unscaled accuracy p, and the baseline accuracy is p_0, the improvement in accuracy above the baseline accuracy is p-p_0. While an improvement in accuracy above the baseline does measure the model's ability to distinguish groups based on geochemistry, a better measure of performance is the improvement in accuracy relative to the available improvements in accuracy above this baseline (i.e., 1-p_0). For example, if the baseline is p_0=0.8, a perfect model with p=1 achieves an accuracy improvement of 0.2, which is the maximum available improvement in accuracy corresponding to this baseline accuracy. A trained model which achieves p=1, where p_0=0.8, is better than one which achieves p=0.8, where p_0=0.6, even though the absolute accuracy improvement is equal. This is because the second model can still be improved significantly, whereas the first cannot. "Scaled accuracy (p_s)", is defined as

$$p_s = \frac{p - p_0}{1 - p_0} \tag{5.1}$$

which measures the proportion of available improvement above the baseline accuracy achieved by the trained model. Scaled accuracy as defined here has a maximum value of 1 when the model achieves perfect accuracy (i.e., when p=1 the scaled accuracy becomes $(1-p_0)/(1-p_0) = 1$) and can be negative when the model performs worse than the baseline (i.e., $p<p_0$). In the cases where the classes are equal in size, such as the examples considered in Subsection 5.3.5 below, the more intuitive unscaled accuracy is used to measure model performance. However, in other examples below where class sizes may be unequal, performance is measured using the scaled accuracy. The differences between these measures are explored in more detail in Section 5.5.

5.4.5 SVM Regularization and Feature Extraction

As noted above, SVM produces a hyperplane in feature space separating two classes and a feature space vector normal to this hyperplane (decision vector). In the context of geochemistry, this vector defines the sources of geochemical variability reflecting the differences between the groups. Each value of each vector component (w in Fig. 5.3c shows an example of this vector for arbitrary features X_1 and X_2) reflects whether this element is typically more or less abundant within each SVM models (See Appendix D4) consider one class to be the "relevant class" and the other the "null class". This distinction is arbitrary, but important for interpreting the decision vectors, as this vector "points" in the direction of the relevant class in feature space. For example, if the strontium component of the decision vector is positive, it means that strontium is more abundant in the relevant class compared to the null class. The values of these vector components can be conveniently visualized as bar charts with the value of each vector component represented graphically (Figure 5.3c inset).

SVM produces a single hyperplane separating one group from another. However, in some cases there are more than two classes. This can be in the context of traditional supervised learning where there is a template of labeled data with more than two classes, or where multiple spatiotemporal groups have been identified using the method described in the present manuscript. In these cases, SVM models are trained to produce a hyperplane separating one group from all the others ("one vs the rest"). However, for the purpose of

feature extraction, it may be informative to train an SVM model separately on only two of the groups so that the resulting decision vector will reflect the feature differences between those two groups alone.

The regularization parameter, C, (Subsections 5.4.2, Appendix D4) controls the degree to which misclassification is allowed during SVM training. This is necessary where the classes are inseparable, but also can be used to prevent overfitting. This parameter is particularly important for interpreting the decision vector. For high values of C the SVM model is sensitive to misclassification of the training data. As a result, outlier data in the training-set can strongly influence the decision vector, and this vector may not reflect the most significant variation between most samples in each class. Conversely, for low values of C the model is less sensitive to misclassification and may not perform as well (see https://towardsdatascience.com/demystifying-support-vector-machines-8453b39f7368).

To illustrate the effect of the regularization parameter, an SVM model was trained on part of a dataset used by Ueki et al. (2018) comprising mid-ocean ridge samples (MOR) and continental arc samples (CA). 114 MOR samples (all their MOR data) and 114 samples randomly chosen from their CA data were used. This dataset was pre-processed as outlined in section 5.4.2, by applying a Box-Cox transform, and then removing the mean and scaling by the standard deviation.

The samples were labeled according to the class (MOR or CA) and randomly divided into a training and testing-set (50% of the data each). An SVM model was trained on the training-set over a range of regularization values (C=10^n for n = {-20, 0}). Since the datasets are equal in size, unscaled accuracy is used to measure model performance. To account for the randomly chosen training and testing-sets, for each value of C an SVM model was trained and tested 50 times after re-sampling the training and testing-sets, and the average unscaled accuracy is reported.

The results are shown in Figure 5.5 where unscaled accuracy of the trained model is plotted against decreasing values of C. Unscaled accuracy decreases modestly between

C=1.0 to C=10^{-5} (from p = 0.97 to p= 0.9), then plateaus until sharply dropping off for values less than 10^{-19}.

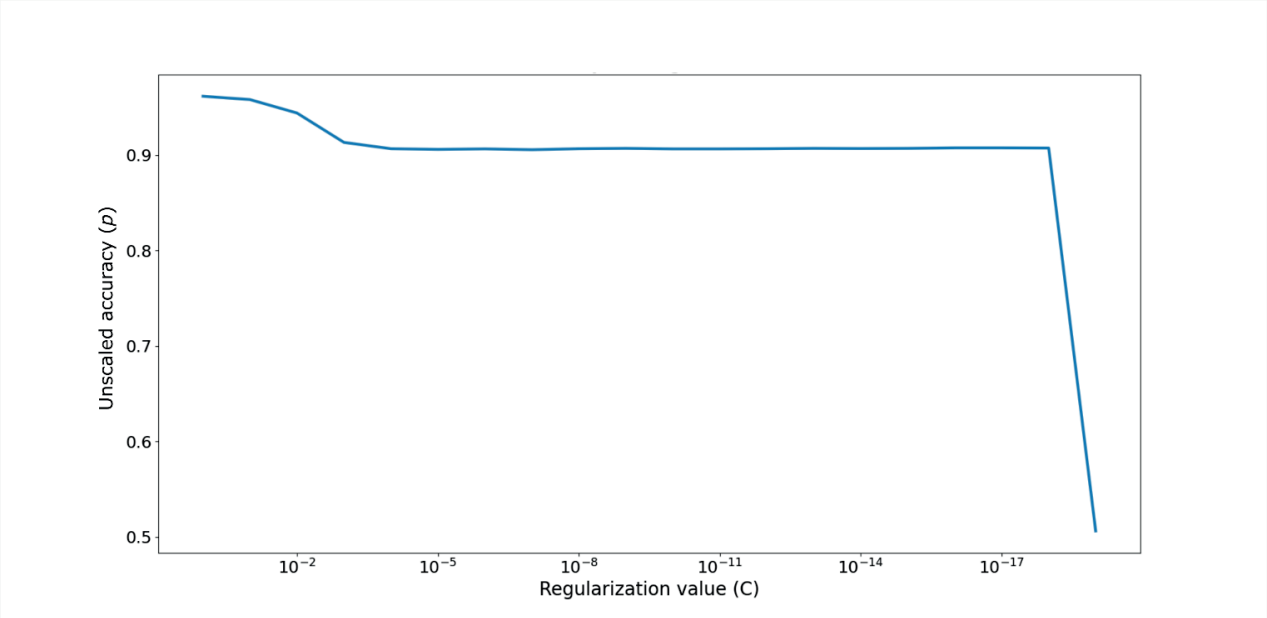

Figure 5.5. Unscaled accuracy with decreasing value of regularization.

To explore the effect regularization has on the resulting decision vector, an SVM model was trained on the entire dataset (rather than a training subset) for a range of values of the regularization parameter, C=10^n, n = {-7, -1}. Figure 5.6 shows the calculated decision vectors for each value of C. Here, the MOR class is the relevant class and the CA the null class, and the elements reported are listed in the order used by Ueki et al. (2018). Major element data are weight percent (wt%) oxides but for clarity are labeled by major element only on Figure 5.6. Trace elements are recorded in parts-per-million (ppm). However, owing to the pre-processing (Subsection 5.4.2, Appendix D4) the decision vector components are unitless. For C=1.0 – 10^{-3}, there is significant variability in the values of the decision vectors as the models are less and less sensitive to outliers. However, between 10^{-3} – 10^{-7} the pattern becomes more consistent.

It should be stressed that the regularization constant, C, does not affect misclassification during testing, but rather only during training by allowing the model to consider hyperplanes that misclassify outlier training-set data. This ensures that the margin

between the hyperplane and the remaining correctly classified data remains wide and prevents overfitting which would otherwise be necessary to accommodate outliers in the training data. However, during testing for model performance, misclassified data are not affected by the choice of *C*. Overfitting can produce a hyperplane and associated decision vector that may correctly classify the training data but may not reflect the feature space variations which characterize the bulk of data in each class. An ideal value of the regularization constant is one that will produce a well performing model, as validated during testing, while still yielding an interpretable decision vector. Ultimately, this will depend on the particular dataset, and typically requires exploring a range of values (Hsu et al., 2003). For the MOR/CA example, the model performs well over a wide range of values of *C* (in the range C=1.0 to C=10^{-19}), but the decision vectors are inconsistent for values of *C* greater than C=10^{-3}.

The decision vector values (using the results for $C = 10^{-4}$), show that MOR samples are lower in the major elements SiO_2, Al_2O_3, Na_2O, K_2O, and higher in TiO_2 Fe_2O_3, MgO, and CaO, relative to CA. For trace elements, MOR rocks are significantly lower in La, Ce, Rb, Ba, Sr, and Th, and enriched in Yb, Lu, and Y, relative to CA. While commonly used element ratios are not included in the features, some are discovered by the model independently. For example, MOR samples are lower in La and Sr and higher in Yb and Y than CA samples, which implies that Sr/Y and La/Yb ratios are lower in MOR samples.

The results are in broad agreement with many traditional discriminating trends associated with continental arc and mid-ocean ridge rocks, with the MOR samples typically having higher TiO_2 content (Pearce and Cann, 1973), lower Zr/Y (Pearce and Norry, 1979) and higher MgO (Pearce et al., 1977).

Similarly, while La, Nb, Ta, and Th content are all lower in MOR samples, La and Th are significantly lower. Conversely, CA rocks are significantly higher in La and Th. While CA rocks are also slightly higher in Nb and Ta, they are significantly higher in La and Th, which is consistent with negative Nb-Ta anomalies commonly associated with subduction related rocks (Baier et al., 2007).

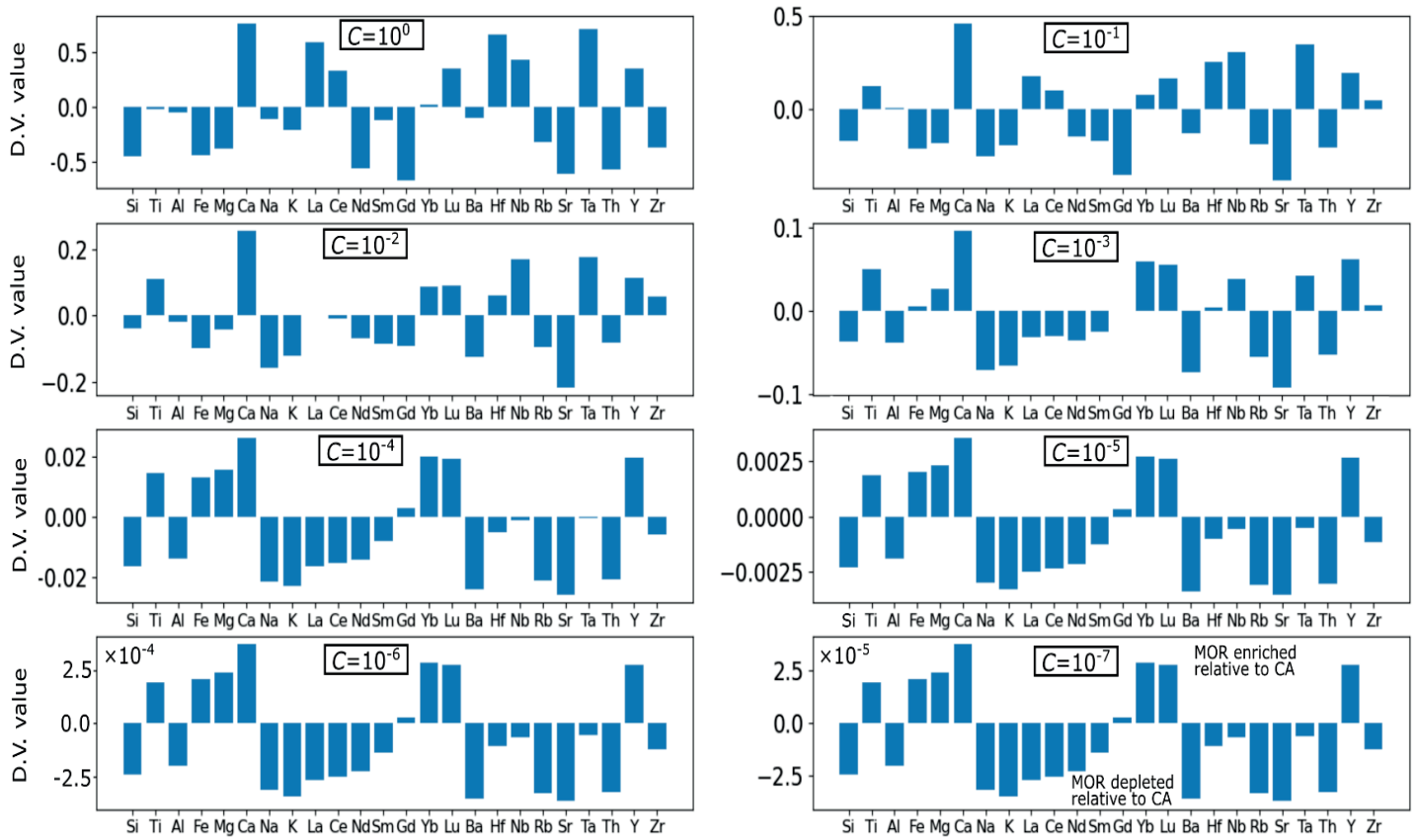

Figure 5.6. Value of the decision vectors (abbreviated as D.V.) for different values of the regularization constant C (ranging from 100 to 10-7). The MOR samples are the relevant class, and CA the null class, meaning that positive values indicate enrichment in the MOR samples relative to the CA samples. Major element data are weight percent oxides, labelled by major element only for clarity. Note that unlike Figure 5.3c where X_1 and X_2 are the only components, each depicted by a single bar, here there are 24 components presented each as a single bar.

The Euclidian distance in feature space that data lie from the separating hyperplane, defined here as ϕ-values (Figure 5.3c), can be calculated for any sample regardless of whether it belongs to the trained dataset.

For example, if an SVM model is trained on two groups from poorly understood geological settings, data from other systems where the tectonic processes are better understood can be compared to those two groups by calculating the ϕ-values of the better understood data and comparing them with the ϕ-values of the two poorly understood groups. The ϕ-value represents those aspects of the geochemistry that differ between the two poorly understood groups. As such, ϕ-values of data from other environments which are similar to a particular class, do not necessarily imply that these data have similar overall geochemistry with that class. Instead, it only implies that those data possess the same geochemical aspects that differentiate the classes. Nevertheless, the ϕ-values of other well-understood datasets may offer guidance for further study. For example, basalts and granites may share the same ϕ-values despite having very different overall geochemistry.

Figure 5.7a displays a histogram of ϕ-values for the MOR (purple) and CA (red) classes used above calculated from the MOR/CA model (i.e., the SVM model trained on these data). This plots frequency of data for a given ϕ-value. Since MOR data are the relevant class, they have positive ϕ-values, meaning that where they lie relative to the separating hyperplane is in the direction of the decision vector. Conversely, CA data lie on the opposite side of the hyperplane and have negative ϕ-values. The small overlap, colored dark purple, reflects data that the trained model has difficulty classifying.

For comparison, 114 samples were randomly chosen from island arc (IA) data, also used in the Ueki et al. (2018) dataset. The preprocessing described above was applied to the combined MOR, CA, and IA dataset. The ϕ-values of these IA data were also calculated from the CA/MOR model (i.e., based on the calculated hyperplane separating MOR and CA).

As shown in Figure 5.7b, IA (blue) data plot more centrally than either CA or MOR data, but skew negative. This indicates that the IA data broadly share the geochemical features of CA data which discriminate them from MOR data. This is perhaps expected given CA and IA data are both from arc environments.

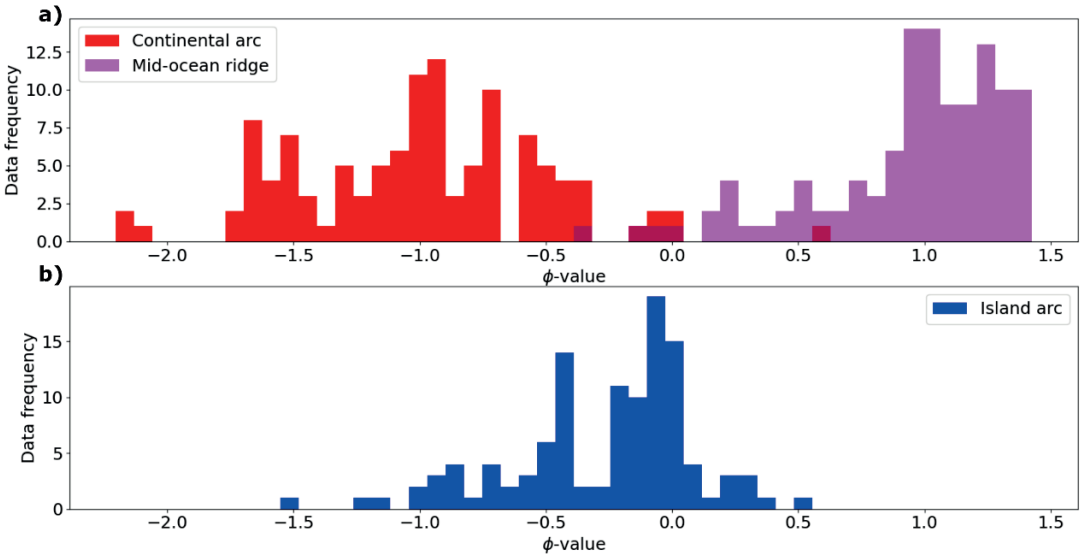

Figure 5.7. a) Histogram of data frequency for ϕ-values of the MOR (purple) and CA (red) classes, with overlap colored dark purple. MOR data (the relevant class) typically have positive ϕ-values, indicating that the distances from the separating hyperplane these data lie are along the direction of the decision vector, whereas CA data plot as negative values, lying in the opposite direction in feature space. **b)** Histogram of data frequency for ϕ-values of the IA data calculated from the CA/MOR model hyperplane. IA plot more centrally then either CA or MOR, however, most IA data have negative ϕ-values. Note that pre-processing of the data changes the standard deviation of each feature to 1 but the values of the features can have a larger range.

5.4.6 Group Proposal Schemes

Longitude-latitude-age group proposal schemes

There are many ways to propose groupings of a dataset by iteration. An appropriate group proposal scheme will likely be informed by the spatial and temporal distribution of the dataset, the geometry of the geological system, initial hypotheses regarding tectonic or geological changes, or other relevant geological observations. Additionally, an initial

group proposal scheme may not be ideal, but can inform further approaches to group proposal improvements.

A particularly simple proposal scheme, which may be appropriate if the system is roughly east/west- or north/south-trending, is presented first. This approach groups the data into longitude-latitude-age blocks. The data are initially separated into two groups which lie east or west of a proposed longitude (e.g., Fig. 5.2). This defines a proposed grouping associated with this choice of longitude. The dataset is then (temporarily) labeled by this proposed grouping, with each group defining a class. The dataset is divided into randomly chosen testing- and training-sets, and the SVM model is trained and tested as described in Subsection 5.4.1. The performance of the trained model is evaluated according to performance measures described in Subsection 5.4.4. Since most proposed groupings will separate the data into groups/classes which are unequal in size, scaled accuracy (p_s) is the appropriate measure of model performance. The longitude defining a grouping is incrementally moved from east to west (spanning the east/west extent of the dataset) and a series of performance measures are collected with each choice of longitudinal grouping. This collection of performance measures is used to generate a performance vs longitudinal grouping curve, or more simply, a performance curve. Peaks in this performance curve are expected where the groups are optimally separated. This is illustrated in Figure 5.8a-b where two classes of distinguishable data are discovered by generating a series of model performance measures (Fig. 5.8b) corresponding to choices of longitudinal grouping (Fig. 5.8a) to produce a performance curve.

In a similar manner to longitude, latitudinal groupings are proposed, the SVM model is trained and tested, and performance measures are calculated for a range of proposed latitudinal groupings spanning the north/south extent of the dataset. This generates a performance curve associated with latitude. Finally, the data are grouped according to proposed age groups (older or younger than a reference age) and a collection of proposed groupings based on age is used to generate an age performance curve in the same manner as for longitude and latitude.

Each of the longitude, latitude, and age performance curves can be generated for the entire dataset, or the performance curves can be generated separately on groups identified by another, previously generated, performance curve. When applied to the Himalaya-Tibetan dataset (Section 5.6) two geographic groups are first identified, and age performance curves are calculated individually for each.

Geographically oblique group proposal schemes

The group proposal scheme described above of generating performance curves for a range of longitude, and latitude is simple, and potentially appropriate for east/west or north/south trending systems. However, this scheme can be informative even when the ideal groupings are not arranged strictly east/west or north/south. For example, Figure 5.8a and b show a hypothetical scenario where two distinguishable classes (represented by open and closed circles) are separated by longitude. In this case, a longitudinal sweep would be expected to produce a performance peak at 90°E (Fig. 5.8b). In the scenario shown in Figure 5.8c, however, the two classes are not separated strictly by longitude. Nevertheless, a subdued peak in the performance curve is expected near 90°E as this initial grouping still separates most data by distinguishable classes. A subsequent performance curve with latitude, would generate subdued peak near ~32°N, illustrated in Figure 5.8f and with inverted axes in Figure 5.8e.

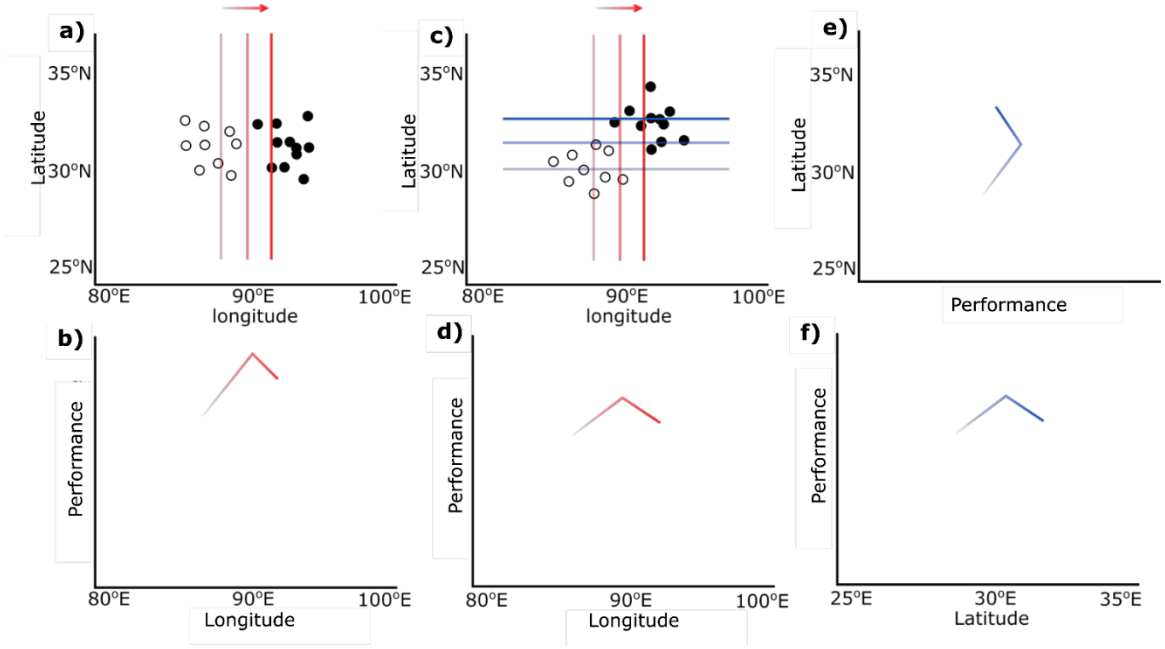

Figure 5.8. Two hypothetical distributions of distinguishable classes, oriented **a)** east/west, and **c)** obliquely to east/west. **b)** The longitudinal performance curve for the east/west scenario is expected to peak at 90°E, whereas the longitudinal performance curve for the oblique data **d)** is expected to show a subdued peak. Red vertical lines indicate proposed groupings based on longitude corresponding to the performance shown below, and blue horizontal lines in **c)** indicate groupings with latitude. **f)** A performance curve for latitudinal groupings, which is also shown in **e)** with inverted axes, showing subdued peak near 32°N.

These hypothetical results could be used to suggest an oblique group proposal scheme as illustrated in Figure 5.9. Here, geographic lines separate the data into ~north-east and south-west groups (Fig. 5.9a). These geographic lines are incremented in a ~north-east direction generating a performance curve with distance in this direction (Fig. 5.9b).

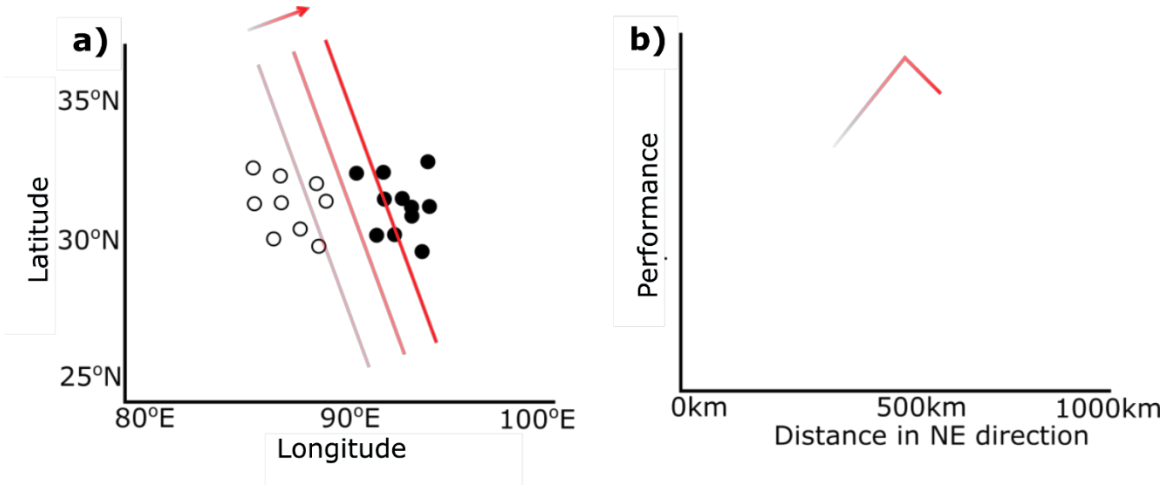

Figure 5.9. A hypothetical oblique group proposal scheme informed by hypothetical results from Figure 5.8**. a)** A series of geographic lines separating the data into groups as with the longitudinal scheme described above. **b)** This is expected to produce a peak at some distance along the direction the geographical line separating the groups is increased.

General spatial group proposal schemes

More general methods for proposing geographic groupings may be required to capture clusters which may not be linear, as shown in Figure 5.10a, but rather some general curve as shown in Figure 5.10b.

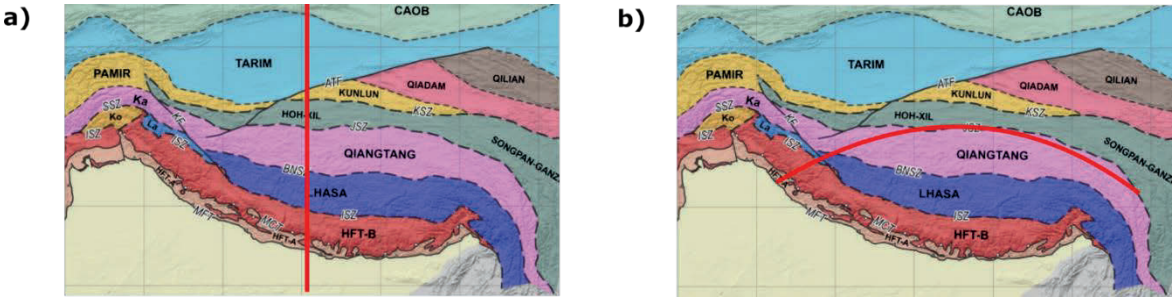

Figure 5.10. Two hypothetical examples of a curve (shown in red) separating data geographically, a) based simply on longitude, and b) a more complicated geometry. Map modified from Parsons et al., 2020.

A method of proposing more general geographical groupings can be conceived by analogy with geological map patterns formed by folded/tilted units intersecting (outcropping) the surface. A simple longitudinal division (Fig. 5.11a) is equivalent to supposing that the samples were arranged on a dipping plane (Fig. 5.11b), with samples lying above a horizontal plane (shown in green) belonging to one group and those below

belonging to the other. Supposing that the samples were arranged on a more general surface (Fig. 5.11d) would give rise to a curved group boundary as shown in Figure 5.11c.

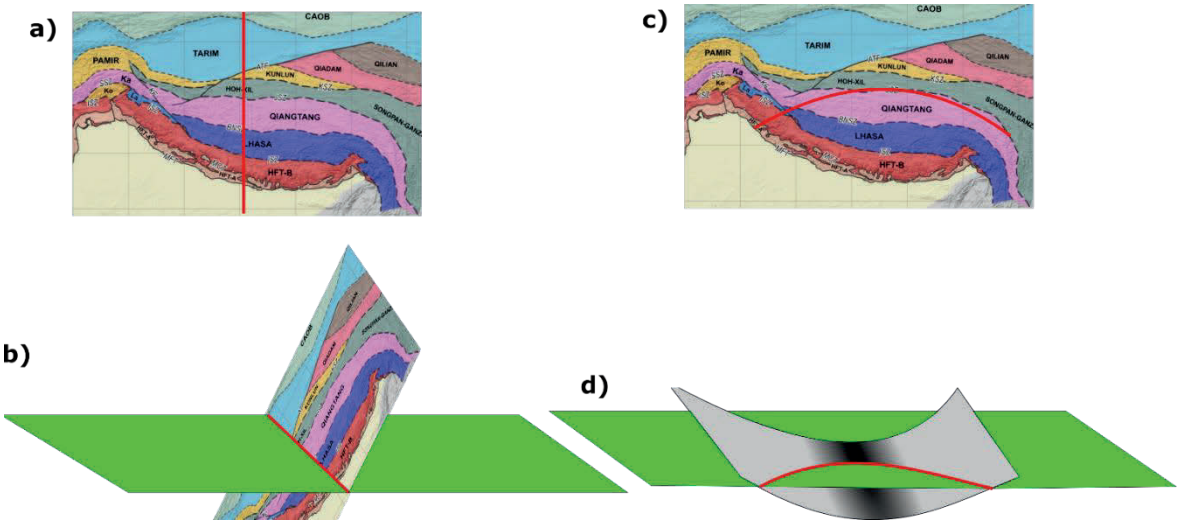

Figure 5.11. Two hypothetical examples of a curve separating data geographically, a) based simply on longitude, which is equivalent to b) a dipping plane intersecting a horizontal green plane, and b) a more complicated geometry, which is equivalent to d) a curved surface intersecting a horizontal plane. Map modified from Parsons et al. 2020.

As with the simpler group proposal schemes, iteratively proposing surfaces may be informed by the geology of the system being studied. However, a general scheme for exploring surfaces is proposed here.

As stated above, for a given surface, the proposed grouping is defined by whether a sample belongs above or below the horizontal plane $z = 0$ (shown in green in Figure 5.11b and 5.11c). Different proposed groupings are then explored by considering different proposed surfaces.

A general (smooth and differentiable) equation of a 2-dimensional surface can be expressed as a series of the form,

5.2

$$z = \sum_{i=0}^{n} \sum_{j=0}^{n} \alpha_{i,j} x^i y^j$$

where z is the height above the plane, x and y are longitude and latitude respectively, and the coefficients $\alpha_{i,j}$ define the surface (note, superscripts represent exponents and subscripts indices; see Appendix D5 for an example of a hypothetical surface). These coefficients can be explored in the same way as with longitudinal/latitudinal groupings. The choice of n determines how many terms the expansion includes, and therefore how many coefficients $\alpha_{i,j}$ need to be explored. For larger values of n the surfaces will, in general, be more locally variable. The values of $\alpha_{i,j}$ can be explored by a global search, which means systematically exploring each combination of $\alpha_{i,j}$ at specified increments over a specified range of values. However, as the value of n increases, this may become computationally difficult, and other methods for exploring values of $\alpha_{i,j}$, such as Monte Carlo methods, may be required. Since higher-order terms in Taylor expansions are generally expected to decrease $\propto \frac{1}{i!j!}$, (owing to the presence of these terms in Taylor expansions) the problem can be made more tractable by decreasing the range of values explored for higher-order terms. For example, choosing $\alpha_{i,j} \in [-\delta_{i,j}, \delta_{i,j}]$, where the values of δ_{i+j} decrease as $i + j$ increases by some chosen amount. This scheme can be expanded to spatiotemporal groupings by exploring 3D hypersurfaces with a time component included in equation 5.2 (i.e., $\alpha_{i,j,k}x^i y^j t^k$).

5.4.7 Summary of the Workflow

The method presented here is intended to be flexible, and adjustments can/should be made based on the initial analysis. The goal is to discover distinguishable groups of data and reveal important signatures which can motivate more in-depth analysis, either with ML tools or traditional geochemical techniques. Figure 5.12 summarizes the workflow for the case of generating a longitudinal grouping.

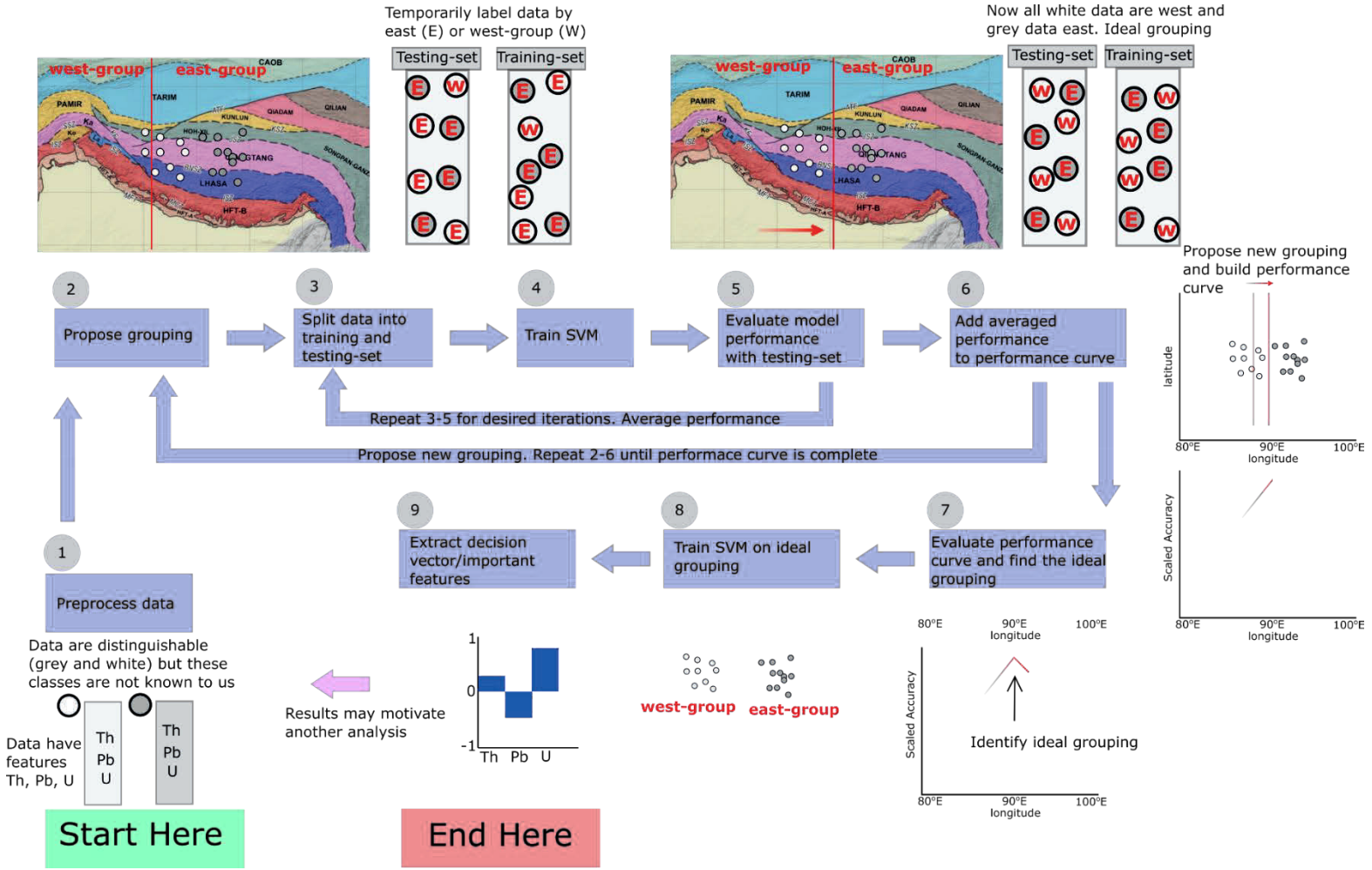

Figure 5.12. Graphical overview of the method workflow used here**.** Starting with data which are geochemically distinguishable (colored white and grey), though it is unknown which samples belong to which class or what their distinguishing signatures are, steps 1-9 build the performance curve for a given group proposal scheme, allowing for these distinguishable groups to be discovered, and their distinguishing signatures revealed. Results may motivate further or different analysis. Map modified from Parsons et al. (2020).

5.5 Evaluating the Method: Group Identification Using Mid-Ocean Ridge and Continental Arc Data

The method outlined above is evaluated using hypothetical spatial clusters of the mid-ocean ridge (MOR) and continental arc (CA) data explored in Subsection 5.4.5. These data were preprocessed as in Subsection 5.4.5.

5.5.1 Longitudinal Group Proposal Scheme

For this example, data are first assigned hypothetical longitudinal locations (not the actual locations of the samples) forming two hypothetical spatial clusters. Longitudes are assigned to each of the MOR and CA data by sampling from a normal distribution, with MOR and CA each sampled from different distributions, as described in more detail below.

Following the method outlined in Subsection 5.4.6, groupings are proposed by separating the data into two groups defined as east or west of a proposed longitude, and an SVM model is trained (on a training-set), tested (on a testing-set) and its performance is evaluated. Since the size of the groups are not generally going to be equal for the proposed longitudes, scaled accuracy (Subsection 5.4.4) is used to measure performance. For each proposed longitudinal grouping, the training and testing-sets are resampled, the model retrained and tested, and an average of 50 performance measurements are reported. Longitudes were proposed from west to east incremented by 2° to produce the performance curves. While the performance is measured by scaled accuracy (p_s), unscaled accuracy (p) and baseline accuracy (p_0) are reported as well to explore the difference between these measures. The value of the regularization parameter was set to $C = 0.001$.

Figure 5.13 shows two clusters of data where the MOR data are assigned longitudes drawn from a normal distribution centered around 30°E, and standard deviation σ=5°, and CA ages are drawn from a normal distribution centered around 65°E and σ=5°. This represents a hypothetical clustering of two distinguishable rock types separated longitudinally, like the scenario in Figure 5.8a and 5.12. The proposed longitudinal

groupings are defined as data east (Group E, shown with green background) or west (Group W, shown with grey background) of a proposed longitude. These proposed longitudinal groupings are evaluated from 26°E to 68°E (incremented every 2°). When a proposed grouping separates MOR data into both the E and W groups, the scaled accuracy is low. This is because the MOR data are randomly assigned longitudes, and therefore there is nothing geochemically distinguishable between MOR data lying east or west of some longitude. This is illustrated in Figure 5.13a where the proposed grouping separates the data into groups east or west of 30°E. As the longitude defining the proposed groupings moves further east, fewer MOR data are included in Group E, and the scaled accuracy increases as the proposed groups become more geochemically distinguishable. At 42°E the proposed longitudinal grouping separates the CA and MOR data entirely into Group E and Group W respectively, and the scaled accuracy reaches a maximum value of $p_s \cong 0.95$ (Fig. 5.13b). Since any proposed longitudinal grouping between 42°E and 50°E also separates the data exactly, the scaled accuracy curve plateaus over this range (Fig. 5.13c), and then begins to decrease for longitudinal groupings further east of 50°E (Fig. 5.13d,e). Figure 5.13f shows an ideal (i.e., actual groupings based on the known CA and MOR groups) data grouping, with Groups E and W colored light red and light purple respectively.

The baseline accuracy (p_0) which is the proportion of samples belonging to the larger group/class, is p_0 0.5 from 42°E to 50°E, where the two groups are separated completely, since the groups are equal in size. The unscaled accuracy also reaches a maximum ($p \cong$ 0.97) during this range, and like the scaled accuracy curve, unscaled accuracy decreases west of 42°E and east of 50°E, albeit less than scaled accuracy. However, for groupings east of 64°E or west of 30°N unscaled accuracy increases to roughly follow the baseline accuracy, as the groups become increasingly more unequal. Since MOR samples (randomly) assigned more eastern or western longitudes are geochemically indistinguishable (likewise with the CA data) these increases in accuracy must reflect the trained ML model preferentially predicting the larger class, rather than an indication that these proposed groupings are geochemically distinguishable. This illustrates the need for scaled accuracy when groups are unequal.

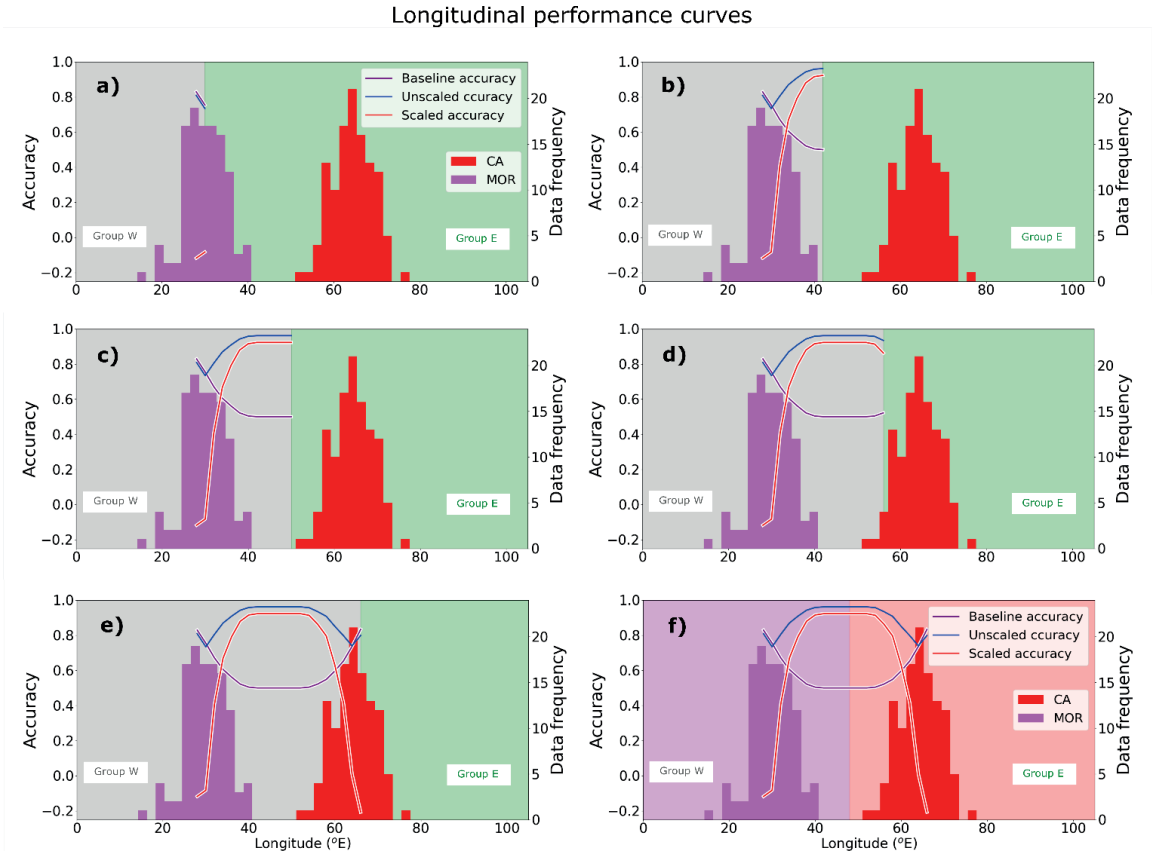

Figure 5.13. Performance curve for CA and MOR data with longitude measured by scaled accuracy (red line); baseline and unscaled accuracy shown as purple and blue lines, respectively, for comparison. The proposed groups, W and E, have grey and green backgrounds respectively. **a)** through **e)** The proposed longitude defining the groups E and W is incremented eastward and the longitudinal performance curve is progressively generated. **f)** Ideal groups colored light purple and light red.

Figure 5.14 shows results from a situation where the MOR and CA clusters are overlapping, with MOR data assigned longitudes drawn from a normal distribution centered around 50°E and standard deviation σ=5°, and CA data assigned longitudes drawn from a normal distribution centered around 60°E, and σ=5°. The result shown in Figure 5.14 could reflect a situation as shown in Figures 5.8c and 5.9, where the longitudes of two clusters overlap. As expected, the model performance does not achieve the peak scaled accuracy shown in Figure 5.13, however, a peak is still reached at 54°E, where the MOR and CA samples are most separated.

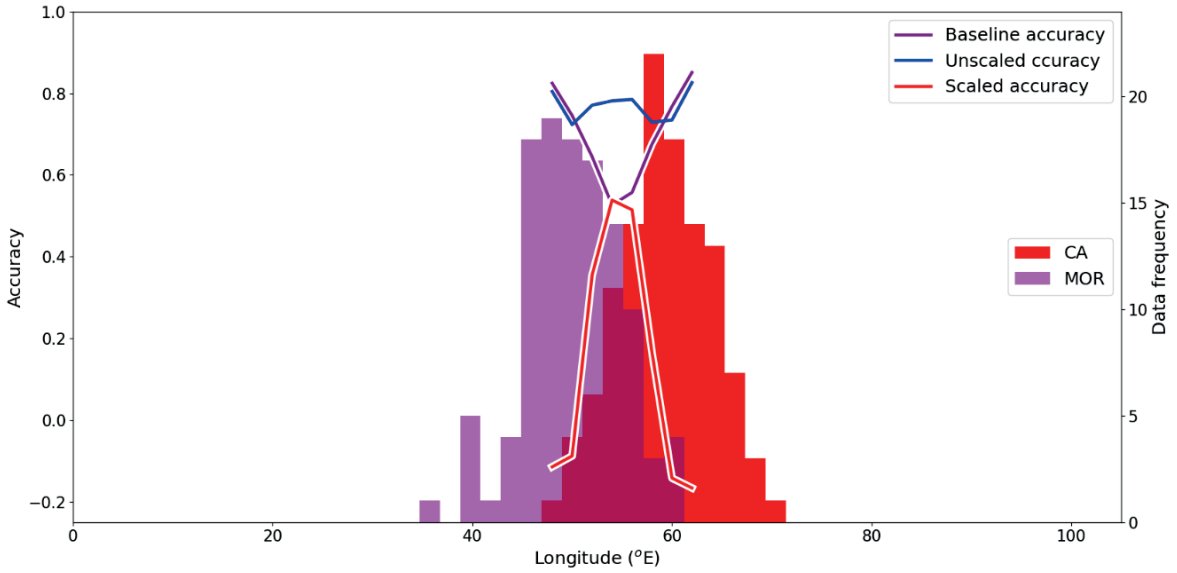

Figure 5.14. Performance curve with longitude where MOR and CA clusters overlap**.** Peak scaled accuracy(red line) is achieved at 54°E, where the data are mostly (but not completely) separated.

In Figure 5.15, the MOR data are assigned hypothetical longitudes, drawn from a normal distribution centered at 55°E, and standard deviation σ=5°. For the CA data a total of 228 samples were drawn from the Ueki et al. (2018) dataset, and assigned longitudes drawn from a normal distribution centered at 60°E and σ=10°. Here the MOR and CA data overlap completely. As expected, the scaled accuracy performance curve is low with $p_s \sim 0$. However, here the unscaled accuracy is nearly identical to the baseline accuracy, indicating the trained model is preferentially choosing the larger class.

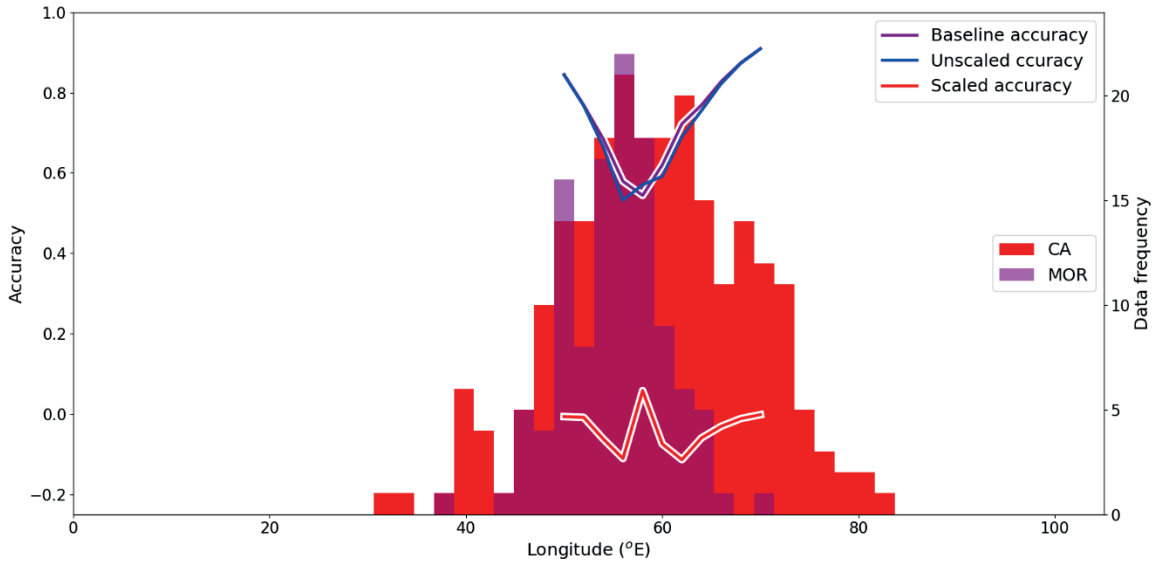

Figure 5.15. Performance curve with longitude where MOR and CA overlap completely**.** Scaled accuracy (red line) is ~0 for the entire performance curve, demonstrating that the two groups are not separable. Unscaled accuracy (blue line) is roughly the same as baseline accuracy (purple line).

5.5.2 General Spatial Group Proposal Scheme

An example of a more general spatial group proposal scheme, as outlined in Subsection 5.4.6, is explored here by assigning hypothetical longitudinal and latitudinal locations to the mid-ocean ridge (MOR) and continental arc (CA) data used in Subsection 5.5.1. The samples were assigned to these locations to form two geographic/spatial clusters. Locations were drawn at random from sample locations in the Tibetan Magmatic Database (Chapman and Kapp, 2017) and used as hypothetical sample locations for the MOR/CA data. This database is a compilation of magmatic rock samples of Tibet and the Himalaya and is explored further in Section 5.5. MOR data were assigned to locations north of the Bangong suture, which demarcates the southern Tibetan Lhasa terrane from the Qiangtang terrane and other terranes to the north. Likewise, CA data were randomly assigned sample locations south of this suture. This ensures that the hypothetical clusters are separated by a realistic geological boundary (shown in Figure 5.16b).

As outlined in Subsection 5.4.6, groupings were explored by proposing surfaces and calculating the height of the surface at each of the sample locations. If the height of the surface is positive (above the plane z = 0) then the sample at that location is assigned to one group (group A), and if negative, the sample is assigned to the other (group B).

Surfaces were proposed according to Equation 5.3

5.3

$$z = \sum_{i=0}^{8} \sum_{j=0}^{8} \alpha_{i,j} x^i \, y^j$$

where z is the height above the plane, x and y are scaled longitude and latitude coordinates respectively, and the coefficients $\alpha_{i,j}$, define the surface (superscripts represent exponents and subscripts indices. See Appendix D5 for further explanation). The x values are defined as $x = (X - 87)/16$, where X is the sample longitude, (the data span 87+/- 16 °E longitudinally). Likewise, $y = (Y - 29.5)/8$. where Y is the sample latitude. This ensures that the coordinate system is centered near the middle of the geographic distribution of the samples, and that the distribution spans ~ -1 to 1 in both x and y coordinates. As with the performance curves above, for each proposed surface, the data are temporarily labeled according to their assigned group (labeled Group A or B), then divided into training and testing-sets, and an SVM model is trained on the training-set and tested for performance on the testing-set. For each proposed grouping (associated with each proposed surface) the scaled accuracy (p_s, Subsection 5.4.4) is used to measure performance (although groupings with >90% of samples belonging to one class were discarded). The values of $\alpha_{i,j}$ for the initial proposed surface were sampled from a normal distribution centered at 0, with standard deviation $\sigma = 1/i!\,j!$. Here, $\boldsymbol{\alpha}$ is defined as the matrix of $\alpha_{i,j}$ coefficients, and $\boldsymbol{\alpha}_n$ as the coefficients of the nth iteration. After each iteration, the updated $\boldsymbol{\alpha}$ was calculated as

5.4

$$\boldsymbol{\alpha}_{n+1} = \begin{cases} \boldsymbol{\alpha}_n p_s + \boldsymbol{\alpha}_r (1 - p_s) & p_s > 0 \\ \boldsymbol{\alpha}_r & p_s < 0 \end{cases}$$

where, $\boldsymbol{\alpha}_{n+1}$ are the updated values of the coefficients for the next proposed surface, and $\boldsymbol{\alpha}_r$ is randomly chosen as described above for the initial surface. This updating scheme mixes the previous choice of $\boldsymbol{\alpha}_n$ with a new randomly chosen one in proportion to how successful the previous choice was. This ensures that values of coefficients are explored preferentially around the neighborhood of those which were successful. The coefficients of the best performing surface and the associated proposed grouping (i.e., corresponding to the maximum p_s) was stored and updated each time a new proposed surface/grouping performs better. Appendix D5 illustrates an example of a choice of $\boldsymbol{\alpha}$ (for n=3) and the associated surface.

Figure 5.16 shows the results of the best performing grouping after 10 000 iterations. Figure 5.16a shows the algorithm's best groups (named Group A and Group B) compared with the actual groups (based on MOR or CA rocks, shown in Figure 5.16b). If Group A is associated with MOR (red dots) and Group B with CA (blue dots) then ~97% of the samples are correctly classified. The averaged scaled accuracy calculated for this grouping was ~0.87. Figure 5.16c shows the values of the decision vector for each element, with blue bars representing the values from the SVM model trained on the correctly labeled data (MOR/CA), and transparent red bars representing the values for the model trained on Group A/B. During group identification, the SVM models were trained using a regularization parameter of C=10^{-2}. However, once the groups were identified, SVM models were separately retrained on both Group A/B and MOR/CA using a value of C=10^{-5}. This value of C was chosen after exploring a range of values, until the decision vectors for A/B and MOR/CA were consistent.

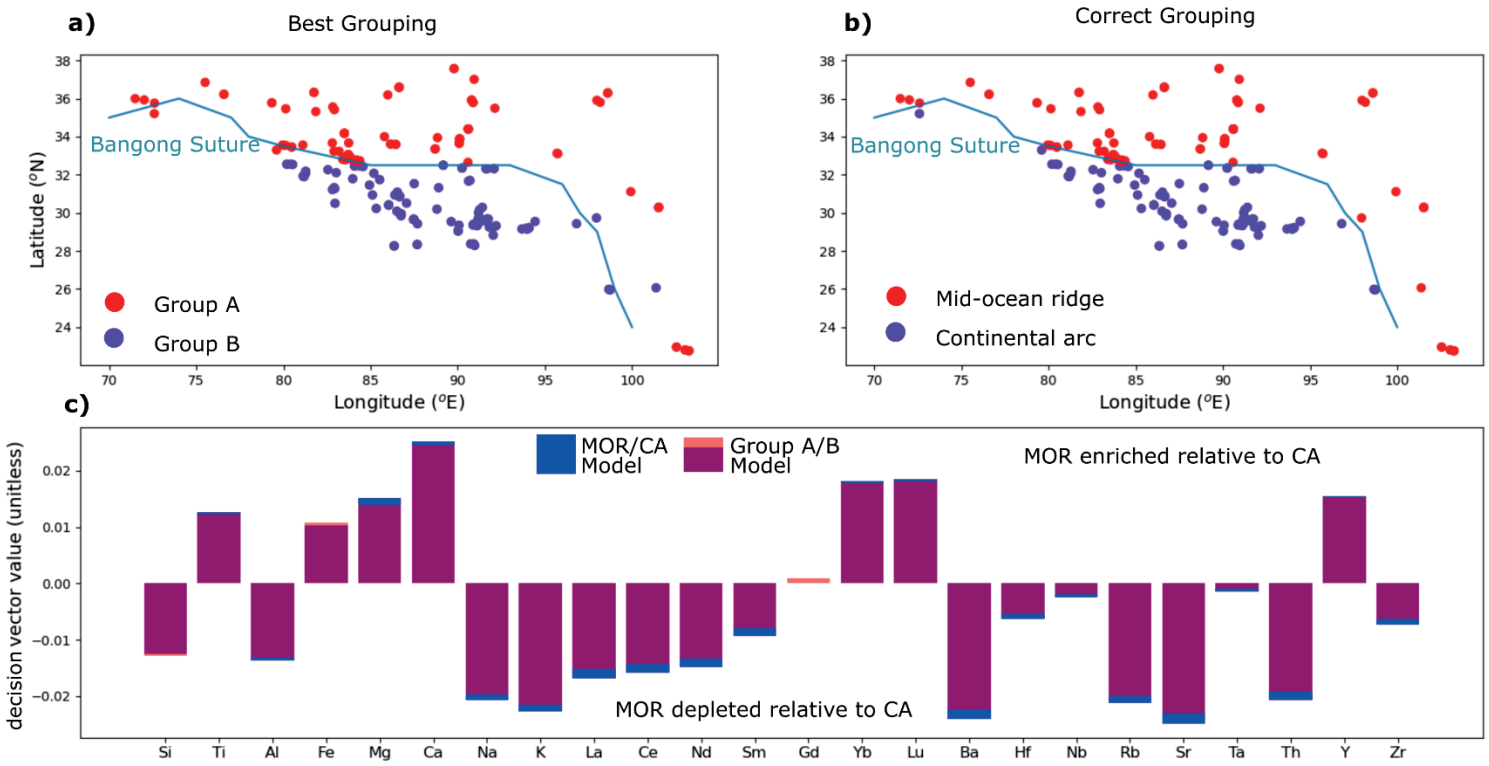

Figure 5.16. Results of the general group proposal scheme. **a)** Groups A and B, the most distinguishable groups discovered by the general group proposal scheme, compared to **b)** the correct mid-ocean ridge (MOR) and continental arc (CA) groups. **c)** Values of the decision vectors for the MOR/CA model in blue and those of the Group A/ B model plotted overtop in transparent red. Overlap is displayed as maroon.

5.6 Applying the method to the Himalayan-Tibetan System

Here the method outlined above is applied to a database of igneous rocks from the Himalayan-Tibetan system compiled from the Tibetan Magmatic Database (Chapman and Kapp, 2017, https://www.jaychapman.org/tibet-magmatism-database.html). See Appendix D3 for data sources.

5.6.1 Himalayan-Tibetan System

The Himalayan-Tibetan (HT) system developed as a consequence of the collision between India and Asia. The Tibetan Plateau comprises a series of ~ east/west oriented elongated terranes (from south to north the Lhasa, Qiangtang, Songpan-Ganze, Kunlun terranes, Fig. 5.3) accreted to Asia by the middle Cretaceous (Yin and Harrison, 2000). Following accretion, the Neotethys oceanic lithosphere subducted northward under Asia, with final closure of the Neotethys and contact of the distal margin of India with Asia between 62–61 Ma (An et al., 2021; Yuan et al., 2021). Following contact and the subsequent ~54 Ma collision between the proximal Indian margin with Asia (Najman et al., 2017), ~4000 km of India-Asia convergence resulted in deformation of both the Indian and Asian lithospheres (Ingalls et al., 2016; van Hinsbergen et al., 2012; Yuan et al., 2021), and likely removal of a significant portion of both Indian and Asian lower lithospheres (Kelly et al., 2020; Kelly and Beaumont, 2021).

There was significant magmatism throughout Tibet both prior to and after the India-Asia collision. The HT magmatic record has been used to infer the nature of the mantle lithosphere behavior. Post-collisional magmatism has been used to infer Neotethys slab break-off at differing times (Zhu et al., 2015 and references therein), flat slab subduction of the Neotethys slab (Kapp et al., 2007) beneath Asia, and removal of lithospheric mantle below the Lhasa (Liu et al., 2014) and/or Qiantang terranes via several different mechanisms (e.g., Chen et al. 2013; Kelly et al., 2020). Given the significance of the magmatic record for interpreting tectonic processes regarding the mantle lithosphere, it is important that those magmatic suites which may reflect these processes and their geochemical characteristics be carefully identified and distinguished where possible.

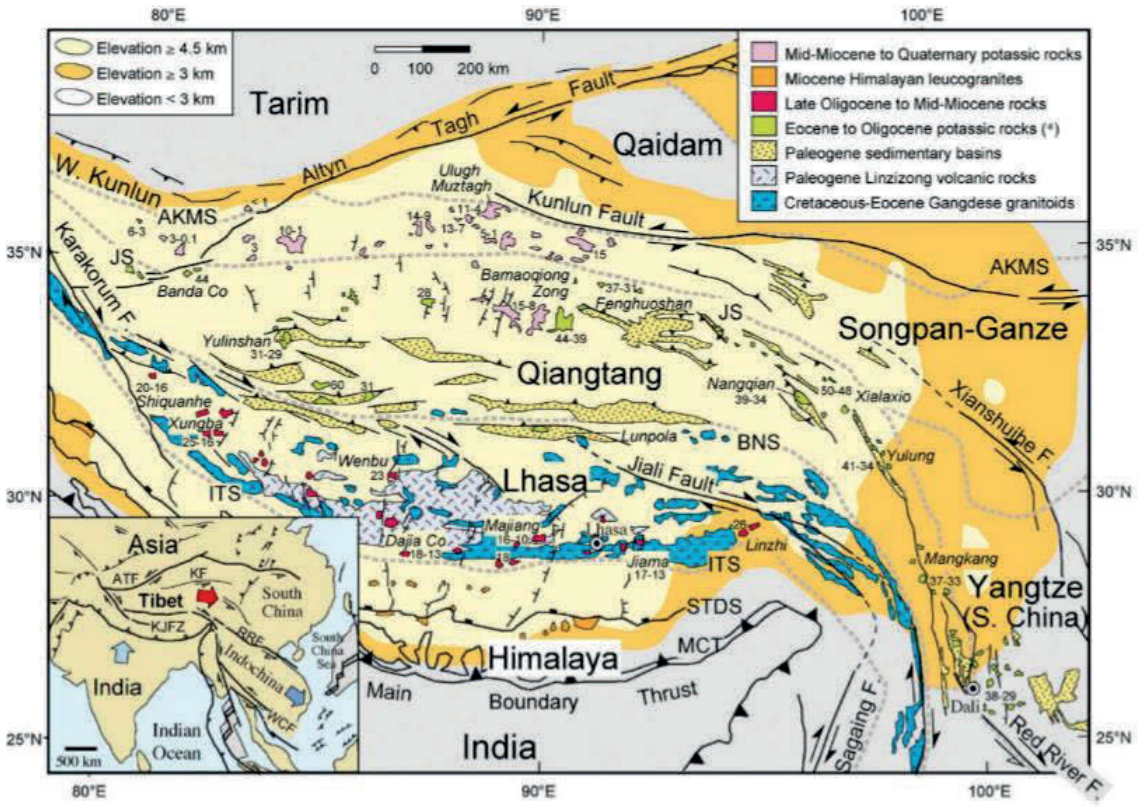

Figure 5.17. Map of the main Himalayan and Tibetan terranes and the distribution of magmatic units (from Chung et al., 2005). BNS = Bangong Suture; ITS = Indus-Yarlung Suture (referred to as Bangong-Nujiang and Indus Tsangpo Sutures in Chung et al., 2005)

5.6.2 Tibetan Magmatic Record

Post-collisional magmatic activity and contemporaneous crustal deformation migrated across the Tibetan plateau with time in a seemingly erratic way (Kapp and DeCelles, 2019). These phases of activity have been interpreted to reflect mantle lithosphere processes (e.g., Chung et al., 2005; Kapp and DeCelles, 2019, Kelly et al., 2020). The Tibetan magmatic record is commonly grouped into five suites (Chung et al., 2005):

1) The predominantly calc-alkaline rocks of the Gangdese arc within the southern Lhasa terrane, which are inferred to record the prolonged (~237–38 Ma) subduction of the Neotethys (Kapp and DeCelles, 2019; Wang, C., et al., 2016; Yin and Harrison, 2000).

2) The Gangdese arc, active during the subduction of the Neotethys oceanic lithosphere, experienced enhanced magmatism between ~65 Ma and 45 Ma (Ma et al., 2022), with a peak flare-up in magmatic intensity about the time of collision of India with Asia (Lee et al., 2009; Zhu et al., 2015, Ma et al., 2022). Linzizong volcanics (predominantly andesitic to rhyolitic), which record an increase in the volume of magmatism within the southern and central Lhasa terrane, commonly interpreted as reflecting Neotethys slab break-off (e.g., Lee et al., 2012; Zhu et al., 2015).

3) Mid-Eocene and Oligocene (~45–25 Ma) Qiangtang ultra(potassic) shoshonitic and/or adakitic magmatism, commonly attributed to removal of Qiangtang lithospheric mantle (e.g., Chen et al., 2013).

4) Miocene (~25–10 Ma) Lhasa terrane adakitic and (ultra)potassic magmatism, which has been interpreted as reflecting late reactivation of Indian subduction (e.g., Guo et al., 2015), or removal of Lhasa continental lithospheric mantle (Kelly et al., 2020, 2022; Liu et al., 2014).

5) Miocene- -Quaternary (since ~18 Ma) potassic magmatism within the Qiangtang, Songpan-Ganze, and Kunlun terranes, which has been attributed to partial melting of hot thickened Tibetan crust. (e.g., Chung et al., 2005; Wang, Q., et al., 2016).

Calc-alkaline rocks (e.g., suites 1 and 2), are commonly interpreted to reflect fluid-induced melting during subduction (Baier et al., 2008) owing to their abundances in modern arc environments, and geochemical signatures including high oxidation and enrichment in Th relative to Ta and Nb. Adakites (e.g., suites 3 and 4) are commonly interpreted as reflecting melting at high pressures (eclogite or granulite facies, e.g., Chung et al., 2005) owning to their high Sr/Y-and La/Yb ratios, depletion in the heavy rare earth elements (HREE), and enrichment in light-REE (LREE), which all suggest garnet in the residuum. Shoshonites and (ultra)potassic rocks (e.g., suites 3-5) are often interpreted to

reflect melting of phlogopite-bearing metasomatized peridotite (e.g., Liu et al., 2014), owing to their enrichment in K_2O, and high K_2O/Na_2O ratios.

Chung et al. (2005) discussed some of the inconsistencies in the definitions and interpretations historically used to characterize these rocks, noting for example that some rocks (suite 3 in northern Tibet) previously termed calc-alkaline are in their opinion shoshonites. Additionally, they pointed out that some groupings of rocks are, in their opinion, arbitrary and misleading. For example, they argue that Miocene to Quaternary magmatic rocks from northern Tibet, previously divided into a "highly potassic" and a "calc-alkaline" group by Yin and Harrison (2000), all plot in the shoshonitic and high-K calc-alkaline field and have indistinguishable trace element characteristics. Hu et al. (2016) reviewed geochemical arguments historically used to constrain the timing of collision based on changes in the Gangdese arc magmatic record. They contended that these arguments are inconsistent and consider them unconvincing and *ad hoc*. For example, they noted that the supposed end of calc-alkaline magmatism at ~40 Ma has been used to constrain the onset of collision by some (e.g., Aitchison et al., 2007), despite evidence of calc-alkaline magmatism persisting until 13 Ma, and that the transition from I-type to S-type granites in the Gandese and Ladakh batholiths has been used to argue for incompatible times of collision ranging from 57 Ma to 47 Ma (e.g., St Onge et al., 2010) to 30 Ma –18 Ma (e.g., White at al., 2012).

These challenges/controversies highlight the importance of identifying those geochemical signatures which best characterize the different phases in the magmatic record, and accurately delineating the spatiotemporal distribution of rocks sharing these signatures. In particular,

a) Given the roughly east/west fabric of the HT system, are there distinguishable geochemical changes associated with ~north/south groupings (or terrane boundaries), or east/west boundaries? What are the most distinguishable temporal changes in geochemistry, and do they correlate with inferred/hypothesized mantle lithosphere processes?

b) Given the traditional focus placed on certain geochemical elements/element ratios listed above, what are the most distinctive characteristics of these suites? Are there other geochemical signatures which better characterize these groups than those traditionally used, and can these signatures offer additional insights into their underlying petrogenesis?

Following the group proposal schemes described in Subsection 5.4.6, identification of geochemically distinguishable groups is first explored using longitudinal, latitudinal, and temporal groupings.

5.6.3 Methodology and Data Preparation

The data used for this study were taken from the Tibetan Magmatic Database (Chapman and Kapp, 2017), comprising >5000 samples (downloaded March 2017). Each of these samples has age data and sample locations (latitude and longitude). The number of elements or isotopes reported varies between the samples, but to use SVM, only data which contain the same measurements (i.e., measurements of the same major and trace elements) can be included. Samples which did not contain complete measurements for each of the selected trace and major elements were excluded. Some trace elements for which measurements were scarce (such as isotopic data) were removed from the analysis to maximize the size of the dataset.

The list of elements included in the analysis (i.e., the features) is shown in Figure 5.21. A total of 2367 samples was used, spanning ~250 Ma to the present. Data from the Tibetan Magmatic Database used in this research are provided in Appendix D3. Figure D.1 in Appendix D1 shows the geographic distribution of samples.

As with the MOR and CA data (Section 5.5), the geochemical data were preprocessed by applying a Box-Cox transformation to the data, followed by removing the mean and normalizing by the standard deviation (Subsection 5.4.2, Appendix D4).

5.6.4 Group Identification

Latitude-longitude grouping

SVM performance curves for longitude and latitude are shown in Figure 5.18. These performance curves were produced using the method outlined in Subsections 5.4.6, and 5.5.1. The red curve shows the scaled accuracy which is used as the performance measure, and for reference, the purple and blue curves show the unscaled accuracy and baseline accuracy, respectively (Subsection 5.4.4). Proposed groupings were evaluated every degree for longitude and half-degree for latitude in calculating performance. For each proposed grouping the process of training and testing is repeated 100 times, and the average accuracies (both scaled and unscaled) are reported. The regularization parameter was set to C=0.001 (Subsection 5.4.5). The frequency of data (grey bars) with longitude/latitude is also plotted to illustrate the effect of unequal class sizes. The general (and expected) trend is that as more data belong to the relevant class (larger class), the unscaled accuracy improves, and at the extremes where nearly all data belong to the relevant (larger class), the unscaled accuracy is nearly one.

The longitudinal performance curve does not reveal any strong peaks in performance (Fig. 18a). While there are some peaks between 75°E and 85° E, the baseline accuracy is so high that these peaks in performance may not be statistically significant. This is because with a particularly high baseline accuracy (i.e., very few data in the smaller class), the available improvement (i.e., 1-p_0) is small and even a small improvement in unscaled accuracy above the baseline accuracy can result in a significant increase in the scaled accuracy. However, the latitude curve performs well at 29.5°N and there is also a very weak peak at ~32°N (Fig. 18b), which drops off significantly for latitudes north of 32°N. This suggests a tentatively optimal grouping into latitudinal-longitudinal blocks would simply be south of ~29.5°N, between 29.5°N and 32°N, and north of 32°N (colored pink, green, and orange, respectively; Fig. 5.18b).

Notably, ~32°N is the approximate location of the Bangong suture zone (BNS Fig. 5.17), separating the Lhasa terrane from the Qiangtang terrane (and more northernly terranes),

and 29.5°N is approximately the latitude of the few samples in the dataset which are located below the Indus-Yarlung suture zone (ITS Fig. 5.17).

The purpose of this method is to discover groups that are candidates for tectonic processes, and the latitude performance curve is only intended to aid in discovering these. Owing to the approximate similarity of the latitudinal peaks with the natural terrane boundaries, rather than group the data into simple latitude-longitude blocks, as initially proposed, the data were separated into two groups: one approximately north of, or on the Qiangtang side of, the approximate location of the Bangong suture, (referred to as the North Group), and one approximately south of, or on the Lhasa side of the Bangong suture (South Group; see Fig. D.2). Data south of the Indus-Yarlung Suture zone were included in the South Group.

Age grouping

Age-performance curves for the North (N) and South (S) groups are shown in Figure 5.19. For the North Group (Fig. 5.19a), the performance curves (scaled accuracy) show an abrupt change in performance at 120, 45, and 22 Ma (from old to young). This suggests that ideal groupings should be older than 120 Ma (N1), between 120 and 45 Ma (N2), between 45 and 22 Ma (N3), and younger than 22 Ma (N4). However, there is a plateau in performance between 120 and 45 which may simply reflect the sparsity of data in this interval (e.g., Figure 5.13c). This is because if there are few data between 120 and 45 Ma (or no data, as an end member), any grouping proposed within this range will separate most/all data into either younger than 45 Ma or older than 120 Ma, which are already distinguishable (see Fig. 5.13). This suggests that N1 and N2 could be grouped together.

The groupings described in this section compare well with the onset of ~45–38 Ma magmatism (N3), and the later Mid-Miocene magmatism in northern Tibet (N4). While the 120 Ma performance change may only represent sparsity in the data, it coincides reasonably well with inferred Lhasa-Qiangtang suturing in the Early Cretaceous (Kapp et al., 2005).

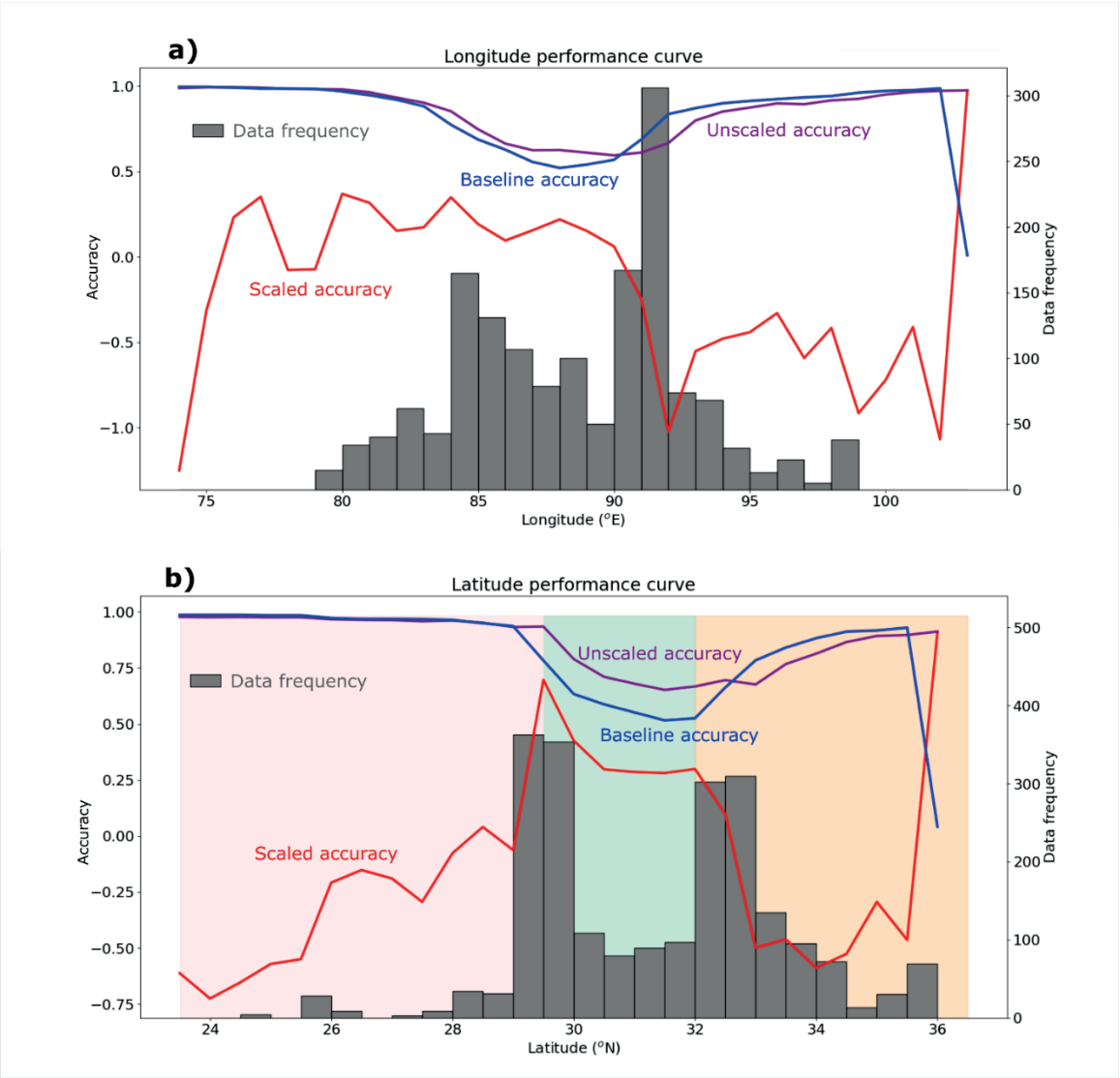

Figure 5.18. Performance curves for the HT dataset for **a)** longitude and **b)** latitude. The performance metric (scaled accuracy) is plotted in red, and for reference the unscaled accuracy (purple) and baseline accuracy (blue) are shown. Accuracy is measured along the left axis. Scaled accuracy is negative where the unscaled accuracy of the SVM model is lower than the baseline accuracy. Data frequency is plotted as grey bars. **a)** bin size = 1°E. **b)** bin size = 0.5°N. For the latitude curve, ideal groupings based on performance peaks are colored pink (south of 29.5°N), green (29.5°N – 32°N), and orange (north of 32°N). As noted in the text above (Section 5.5.4), for further analysis the data were separated spatially based on location above (~north of) and below (~south of) the Bangong suture.

For the South Group (Fig. 5.19b), the scaled accuracy curve increases towards younger ages from ~120 Ma to ~79 Ma, and then continues to increase gradually beginning at ~69 Ma, with a peak/plateau in performance for the interval 45 Ma to 29 Ma, and then

abruptly decreases in performance for ages younger than 29 Ma. This pattern of a gradual increase in performance leveling off in a plateau is similar to the example shown in Figure 5.13. However, unlike Figure 5.13 in which there were no data in the plateau age range, there are samples within the age range of the performance curve plateau for the South Group. Performance decreases gradually for ages older than 45 Ma (suggesting older than 45 Ma as a grouping) and abruptly for ages younger than 29 Ma (suggesting younger than 29 as a grouping). Taken together this suggests three optimal age groupings for data older than 45 Ma (S1), between 29 and 45 Ma (S2), and younger than 29 Ma (S3). The decrease in performance for samples older than 79 Ma could also suggest a distinct change in chemistry, however for the present work these are included in S1. The change in geochemistry starting at 29 Ma coincides well with the onset of late Oligocene-Miocene Lhasa terrane magmatism (Guo et al. 2015). Notably, there is no distinct change in performance near the onset of India-Asia contact (~61-62 Ma) or collision (~54 Ma) (An et al., 2021; Hu et al., 2016).

General spatial group proposal

Data from Groups S2 and S3 were explored further using the spatial group proposal scheme outlined in 5.5.2. In this approach randomly chosen hypothetical surfaces are proposed over the geographic extent of the dataset. In regions where the height of this surface is positive, samples are assigned to one group, and conversely samples are assigned to the other group in regions where the proposed surface is negative (Figs. 5.11 and D.6). This generates a series of more general spatial groupings, rather than the simple east/west or north/south groupings above. For each proposed grouping, an SVM model was trained on a randomly chosen training-set and tested on a testing-set, and the scaled accuracy was calculated. This was repeated for 50 randomly chosen training/testing-sets and the average scaled accuracy was recorded for each proposed surface. After exploring a range of values, the regularization constant was set to C=0.001.

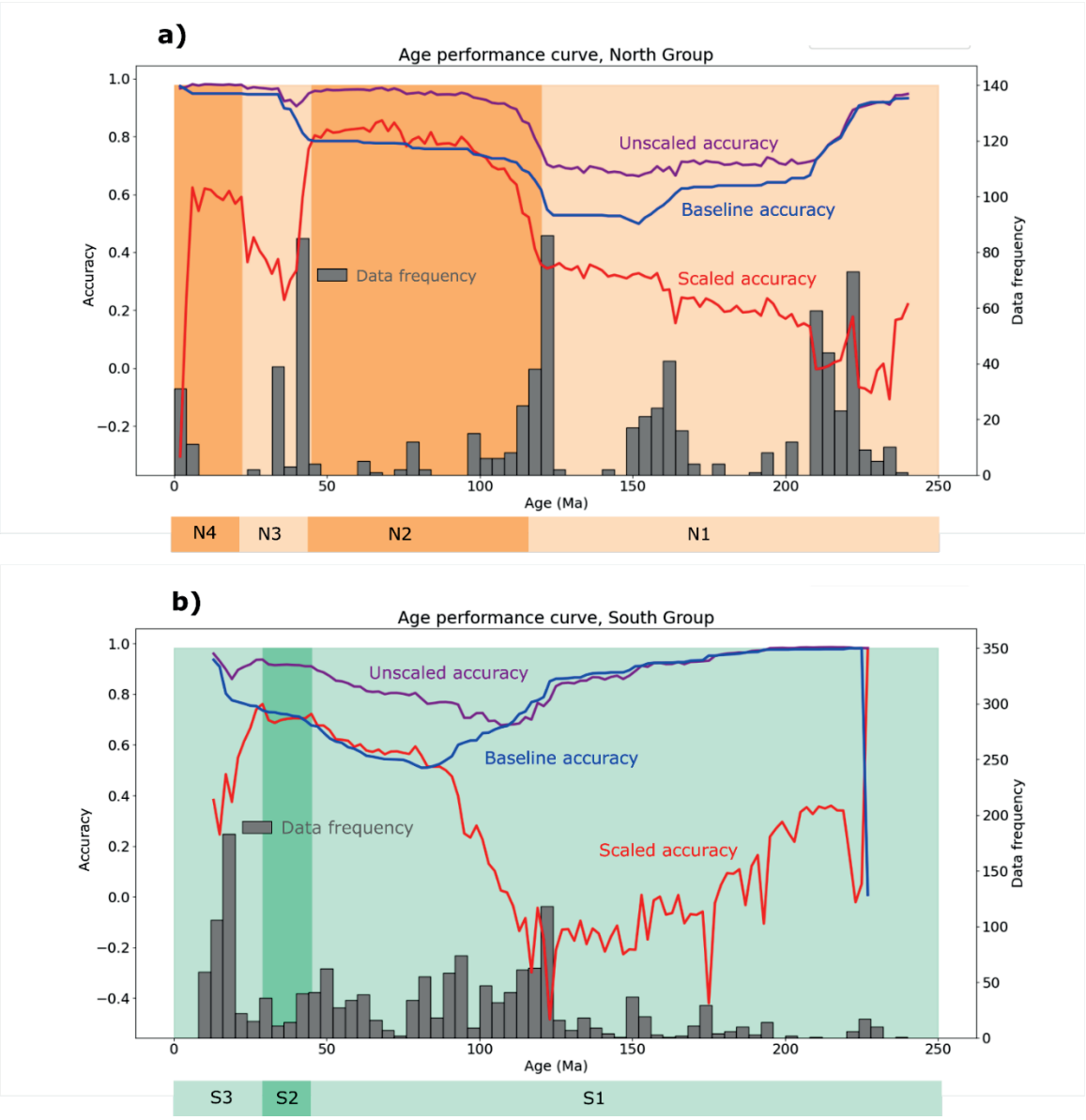

Figure 5.19. Performance curves for a) the North Group and b) the South Group (see 5.5.4 for explanation). The performance metric (scaled accuracy) is plotted in red; unscaled accuracy (purple) and baseline accuracy (blue) are shown for reference. Accuracy is measured along the left axis. Scaled accuracy is negative where the unscaled accuracy of the SVM model is lower than the baseline accuracy. Data frequency (right axis) is plotted as grey bars. For the North Group, ideal groupings based on performance peaks are marked by dark and light orange shades and labeled (below x axis) from oldest to youngest, N1 through N4. For the South Group ideal groupings are marked by dark and light green shades and labeled from oldest to youngest, S1 though S3.

Figure 5.20 shows the algorithm's best performing grouping after 3000 iterations, named Groups S3a and S3b. The scaled accuracy for this grouping was 0.85. This grouping separates the data into approximately southern (S3a) and northern groups (S3b) across a boundary that corresponds well to-the Indus-Yarlung Suture, separating the Himalaya and Lhasa terranes. While the algorithm did not explore temporal groupings, the bulk of the data belonging to S3b are between 25 Ma and 10 Ma, whereas Group S3a includes data from 45 Ma until 10 Ma, comprising data from both Groups S3 and S2.

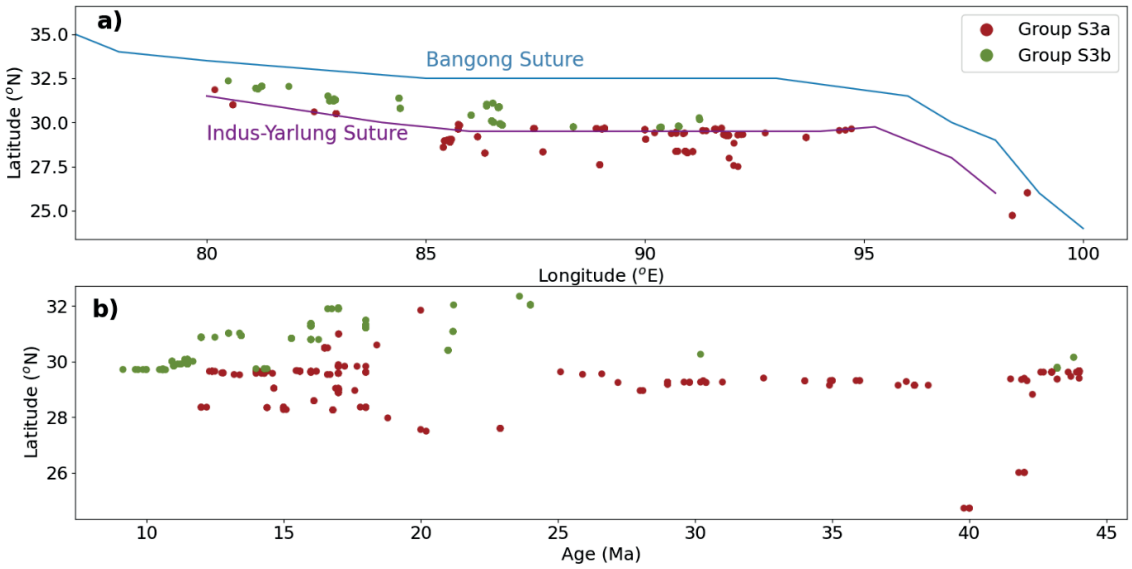

Figure 5.20. The best performing grouping of samples from the south of the Bangong suture and younger than 45 Ma**. a)** The locations of samples from groups S3a (brown) and S3b (olive), and **b)** the ages (and latitudes) of these samples. The boundary between the groups corresponds well to the Indus-Yarlung Suture (shown in purple).

5.6.5 Feature Extraction

Figure 5.21 shows the feature space decision vectors separating some of the identified groups as bar charts. As noted in Subsection 5.4.5, the decision vectors are specific to which groups are being compared. Because of the data preparation the vector is unitless (Subsection 5.4.2, Appendix D4).

Figure 5.21a shows the decision vector separating the combined N1+N2 groups from the combined N3+N4 groups, as shown in Figure 5.19a, with the N1+N2 groups relevant (Subsection 5.3.5). Since N1+N2 (> 45 Ma) are the relevant groups, positive and negative values of the decision vector mean the N1+N2 is richer or poorer in those elements relative to N3+N4 (< 45 Ma). Samples from N1+N2 are richer in HREE and poorer in LREE relative to N3+N4. Samples from N1+N2 are also enriched in Nb, Ta, strongly depleted in Sr and U, and moderately depleted in K, Cr, and Ni relative to N3+N2. Figure 5.22b shows the decision vector separating Group N4 (< 22 Ma) from N3 (22 Ma – 45 Ma), with N3 the relevant group. Samples from N3 are enriched in SiO_2, and the trace elements Ba, Pb, Th and U, and depleted in the major oxides TiO_2, CaO, MgO, P_2O_5, and the trace elements Y, Nb, Ta, the medium REEs (Eu–Dy), and HREE relative to samples from N4.

Figure 5.22a shows the decision vector separating Group S3a+S3b (or equivalently S2+S3) from S1, as shown in Figure 20b, with S1 the relevant group. Samples S3a+S3b (< 45 Ma) are enriched in K_2O, Ni, Rb, Pb, and U and depleted in and the HREE relative to samples from S1 (> 45 Ma). Likewise, Figure 5.22b shows the decision vector separating Group S3a from S3b (see Fig. 5.20), with S3b the relevant group. S3b is enriched K_2O, Ni, Rb, Zr, Nb, Ba, the heavy and medium REEs, Hf, Pb, Th and U, and depleted in Na_2O, relative to S3a.

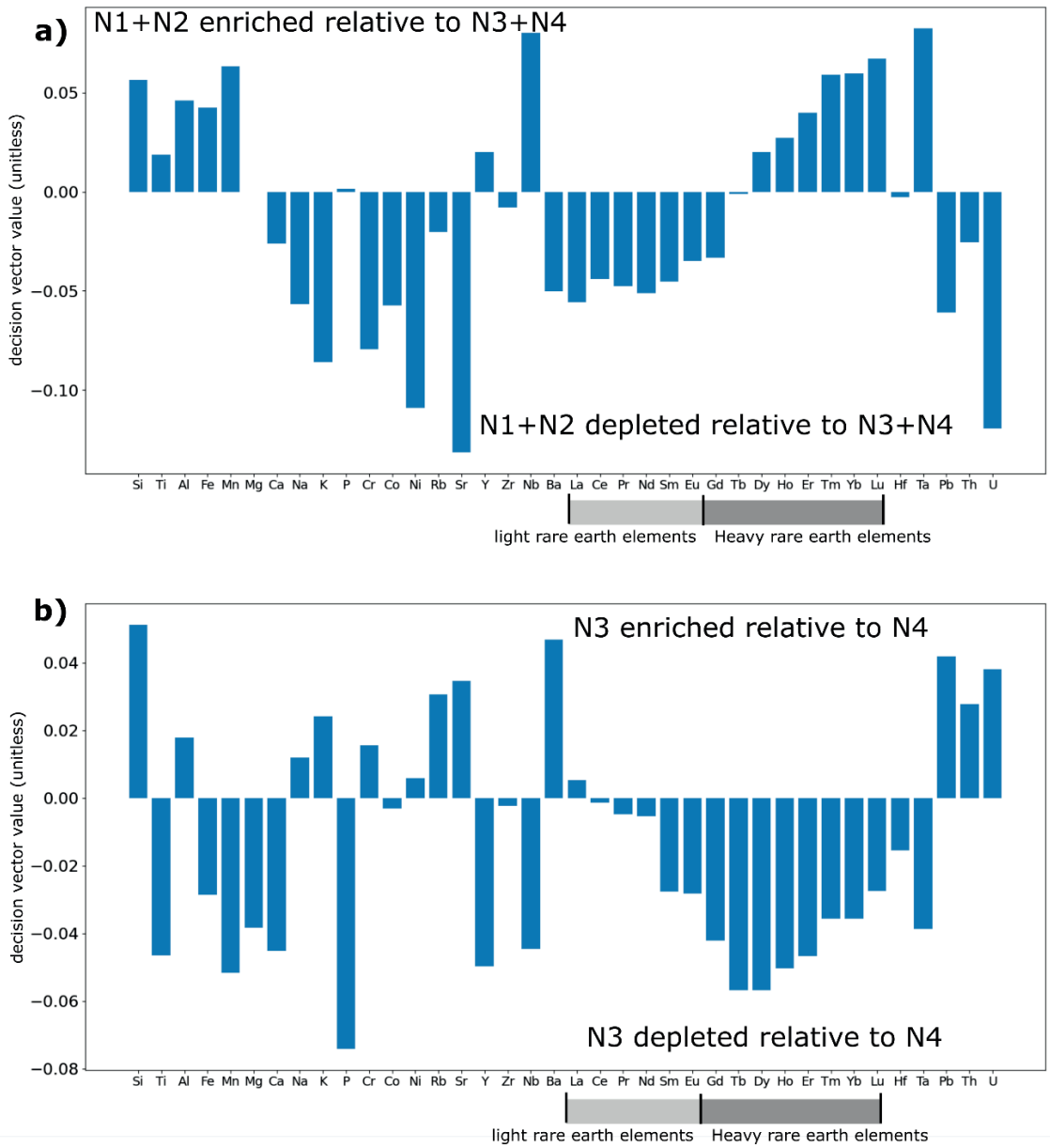

Figure 5.21. Bar chart representation of the unitless decision vector values separating the pre-collisional (N1+N2) and post-collisional (N3+N4) samples (a) and N3 from N4 (b) for each element used in the analysis. Positive values indicate that the element is enriched in the relevant groups (N1+N2 in **a**, and N3 in **b**) compared to the null groups (and converse for negative*).* For the major elements (Si through P) oxide weight percents were reported but only the element is labeled for clarity.

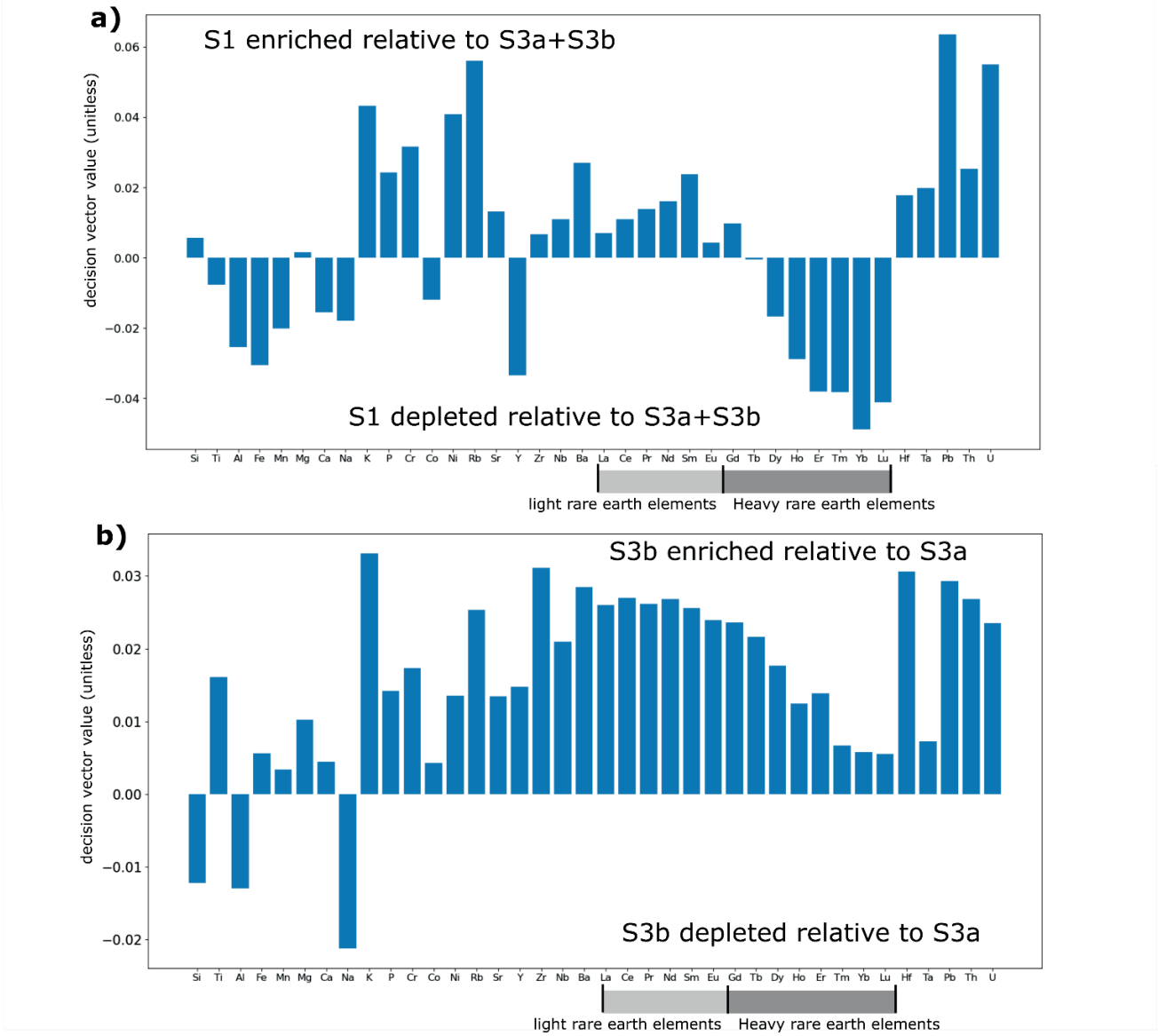

Figure 5.22. Bar chart representation of the unitless decision vector values separating Groups S1 from S3a+S3b (a), and S3a from S3b (b), for each element used in the analysis. Labelling as in Fig. 5.21.

5.6.6 Discussion of HT Groups

While it is not the purpose of this manuscript to study the HT magmatic record in detail, some interpretations can be gathered from these results.

The groups identified by this method coincide well with the magmatic suites discussed in Subsection 5.6.2. In the northern terranes, Groups N1 and N2 (Fig. 5.19a) coincide with the pre-collisional accretionary and active margin history of the Qiangtang terrane, with Group N2 coinciding reasonably well with the inferred timing of Qiangtang terrane accretion. Groups N3 and N4 (Fig. 5.19a) coincide well with the post-collisional onset of magmatism in central Tibet (N3), and the late Miocene-Quaternary magmatism in northern Tibet (N4).

In the Himalaya and Lhasa terrane, the method identifies a temporal grouping separating magmatic rocks before (S1) and after 45 Ma, with the younger rocks further subdivided into a southern group (S3a) which spans from 45 Ma until 10 Ma, and a more northerly group which predominantly spans ~30 Ma - 10 Ma (Fig. 5.20). These groups correspond well with Himalayan rocks (S3b) and Lhasa terrane rocks (S3a). Additionally, the S3b rocks coincide with the apparent southward sweep in magmatism (Kapp et al., 2019) from the Qiangtang terrane to the Lhasa terrane. While some S3a samples are located north of the IYS, no S3b samples are south of it. Although this is speculative, since Indian crust and lithosphere are inferred to have underthrust the Lhasa terrane (Yin and Harrison 2000), those S3a samples north of the IYZ may share a petrological provenance with rocks from the Himalaya.

Notably there is no marked change in the SVM age performance curve coinciding with the onset of contact (~62 Ma) or collision (~54 Ma). Given the historical difficulty in using the Gangdese arc magmatic record to infer the timing of collision (Chung et al., 2005; Hu et al., 2016), these results are perhaps not surprising, and may suggest that there was no abrupt change in Gangdese arc magmatism at the time of or shortly after contact or collision.

Before investigating the relevant features extracted from the SVM models, some of the common geochemical signatures used to characterize the HT magmatic rocks discussed in Subsection 5.6.2 are considered. In Figure 5.23, K_2O, Ta/Th, Sr/Y, and La/Yb values are plotted against sample ages (Fig. 5.23a – d respectively). Samples are colored according

to the identified groups N1+N2 (orange), N3 (cyan), N4 (red), S1 (light green), S3a (olive) and S3b (brown). The post-collisional groups (N3, N4, and S3a, S3b) all show above-average to elevated K_2O and La/Yb ratios relative to the pre-collisional groups, although Group N4 samples have $K_2O<Na_2O$ (Fig. 5.24). This is also consistent with the general pattern of LREE enrichment and HREE depletion of N3+N4 relative to N1+N2 shown by the decision vectors (Fig. 5.21a). Changes in Sr/Y are less pronounced. Samples from Groups S3b and N3 show slight depletion in Ta/Th relative to the other groups. In each case Group S3a shows more variability in these features; however, S3a samples consistently have $K_2O>Na_2O$ (Fig. 24).

For rocks in Groups N3 and S3b, elevated K_2O, K_2O/Na_2O and high La/Yb suggest melt input from phlogopite-bearing mantle, contributing to elevated K_2O concentrations, at depths within the garnet peridotite stability field, since HREE such as Yb preferentially partition into garnet leaving the melt depleted in Yb relative to LREE such as La. This is consistent with interpretations that these rocks reflect melting associated with mantle removal below thickened Qiangtang terrane crust (Chen et al., 2013) and later Lhasa terrane crust (Chung et al., 2005, Liu et al., 2014).

In contrast, some relevant features for distinguishing the groups based on the decision vectors (Figs. 5.21 and 5.22) are shown in Figure 5.25 plotted with sample age. Samples are colored by group as in Figure 5.23. Groups N4 and S3b are enriched and N3 slightly enriched in Sr relative to S1 and N1+N2 (Fig. 5.25a). Groups N4 and S3b are enriched in both Zr (Fig. 5.25b) and P_2O_5 (Fig. 5.25d) relative to the other groups. Groups S3a, S3b and N4 are enriched in Pb relative to the other groups, although the difference is slight (Fig. 5.25c).

Group S3a is similar to the older Lhasa terrane magmatism (S1) for most features explored here, and the similarity persists through most of the post-collisional history of the system. This result likely explains the relatively weak peak at 45 Ma defining these groups. In contrast the more northern S3b rocks, which coincide in time with the apparent southward sweep in magmatism, share many distinguishing features with both earlier N3

samples (elevated K_2O and La/Yb) and later N4 rocks in northern Tibet (elevated P_2O_5 and Zr).

The enriched P_2O_5 content of S3b and N4 is particularly notable and is at least as distinguishing a feature of these rocks as those features shown in Figure 5.23. However, to my knowledge, little research has focused on the significance of P_2O_5 enrichment. P_2O_5 content is partly controlled by the temperature of the melt (Watson and Harrison, 1984; Piccoli and Candela; 2002), with higher P_2O_5 contents expected for higher temperature melts. High lower crustal temperatures (up to ~1000^oC) since ~5 Ma are inferred for the Tibetan crust based on magmatic geochemistry (Wang Q. et al., 2016) and young (~3 Ma) exhumed lower crustal xenoliths (Hacker et al., 2000). If the high P_2O_5 signature is indeed caused by melting at high temperatures, this may imply the Lhasa terrane crust reached these high temperatures by ~30 Ma.

A summary of the most obvious differences between the identified groups is presented below based on the conventional geochemical discriminants considered above and those identified using SVM.

Table 5.1. Comparison of the differences between the identified groups based on some conventional geochemical discriminants and those identified using SVM

Group comparison	Differences based on conventional discriminants	Differences based on SVM identified discriminants
N1+N2 vs N3+N4	N3+N4 slightly enriched in K_2O and higher La/Yb relative to N1+N2	N3+N2 slightly depleted in Sr and higher La/Yb relative to N1+N2.
N4 vs N3	N4 slightly higher Ta/Th ratios relative to N3, although not well discriminated	N4 enriched in P_2O_5 relative to N3
S1 vs S3a+S3b	S3a+S3b slightly higher La/Yb ratios relative to S1, but not well discriminated.	S3a+S3b slightly elevated in Pb relative to S1, also not well discriminated
S3a vs S3b	S3b enriched in K_2O and slightly higher La/Yb ratios and slightly lower Ta/Tb ratios relative to S3a	S3b enriched in Zr relative to S3a

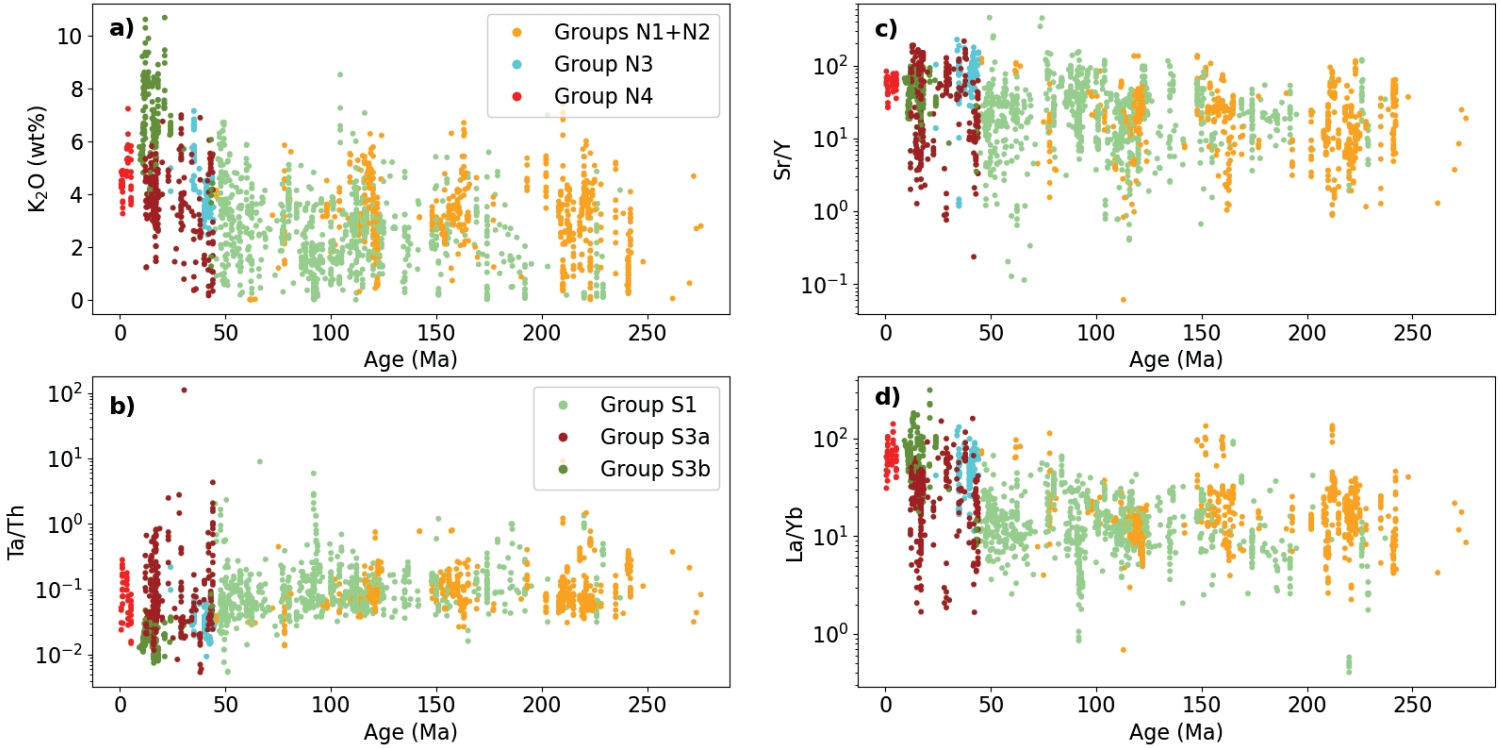

Figure 5.23. Element and element ratios commonly used to characterize the HT magmatic rocks with time, including **a)** K_2O, **b)** Ta/Th, **c)** Sr/Y and **d)** La/Yb. Data are colored according to the groups identified in Subsection 5.5.4. The legend for north groups is inset in **a)** and the south groups inset in **b)**.

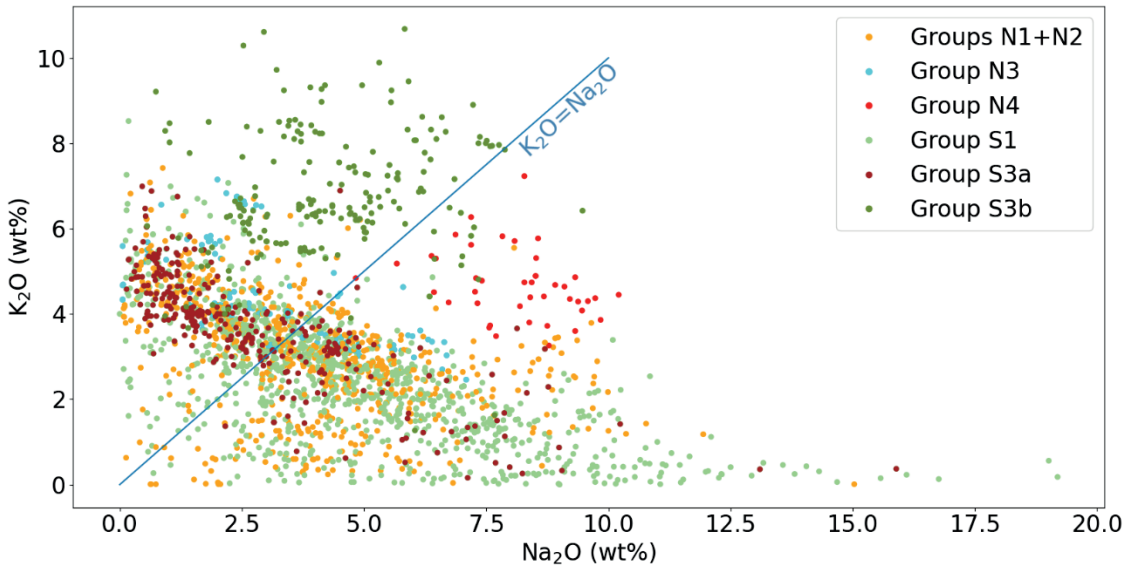

Figure 5.24. K_2O concentrations plotted against N_2O concentrations. Data is colored by group.

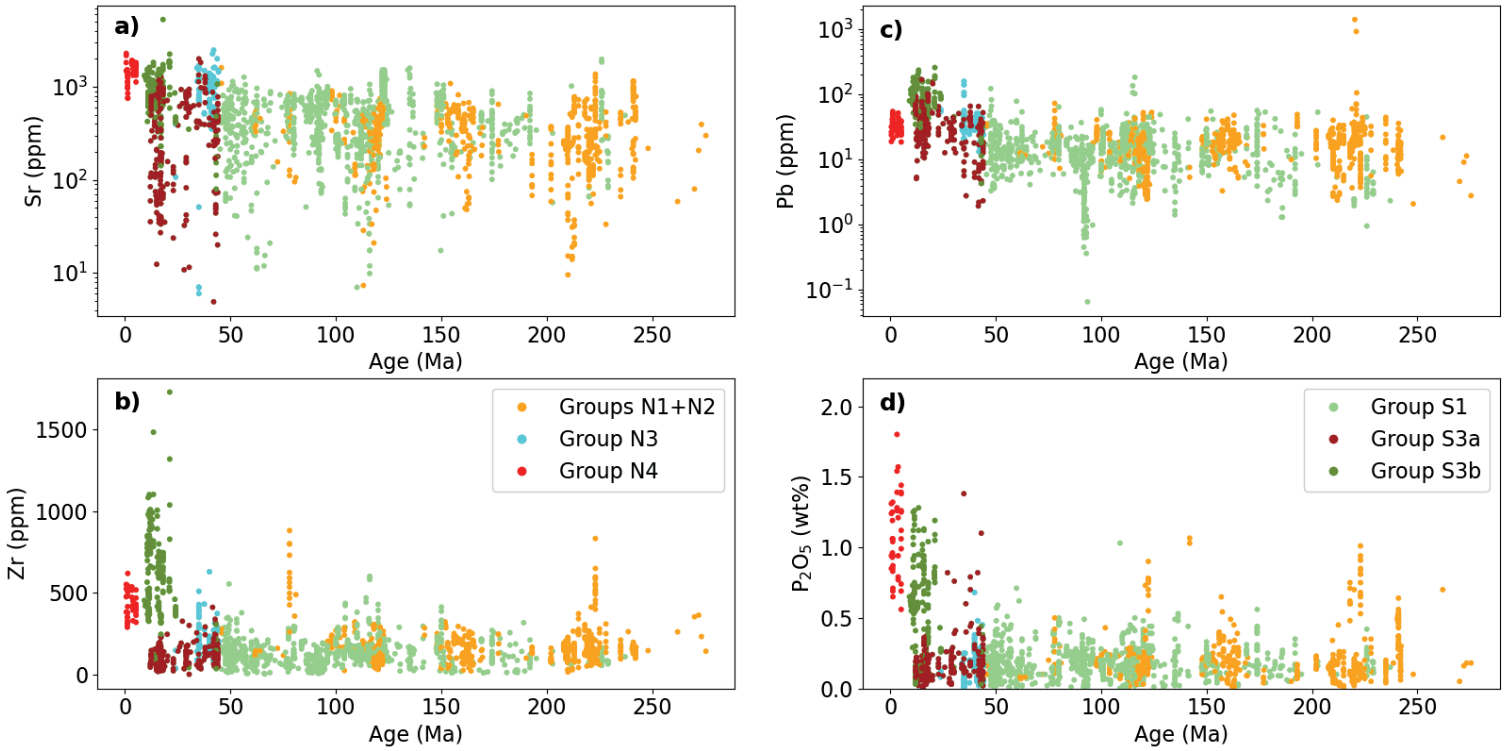

Figure 5.25. Element concentrations identified as important for distinguishing the groups based on the SVM decision vectors (Subsection 5.6.5) plotted with time, including **a)** Sr, **b)** Zr, **c)** Pb and **d)** P_2O_5. Data are colored according to the groups identified in Subsection 5.6.4. The legend for north groups is inset in **b)** and the south groups inset in **d)**.

5.7 Conclusions and Future Research

This manuscript presents a supervised machine learning-based method for finding spatiotemporal groupings of magmatic rocks which are geochemically distinguishable and could reflect distinct tectonic processes. This method is a novel use of ML tools for datasets which does not require an existing template of labeled data from known tectonic environments. This approach may prove useful for geological settings where the tectonic environments/processes remain cryptic by identifying magmatic regions or temporal phases with shared geochemical signatures. This method may be particularly useful for ancient (e.g., Archean) geological settings which may deviate significantly from modern tectonic environments.

The method is shown to identify hypothetical spatial clusters of distinguishable data effectively, namely mid-ocean ridge and continental arc rocks, and identify their distinguishing geochemical signatures. When applied to the Himalayan-Tibetan magmatic record, the method (with additional geological insight regarding terrane boundaries), groups the data into suites which correspond well to those suites commonly identified in the literature (e.g., Chung et al., 2005). The SVM models identify other geochemical signatures (e.g., P_2O_5) that distinguish these suites at least as well as those typically studied in HT literature.

There are several lines of future research to explore regarding this method.

1) SVM requires each sample of the training data to have the same features. For the HT dataset explored in this research, geochemically useful data such as isotopes were excluded to maintain the size of the dataset. Modifying this method to use ML techniques which do not require each sample to have the same features could both expand the datasets and include less frequently measured but geochemically useful measurements in the analysis. This would require researching different ML techniques capable of handling data with different sets of features.

2) The method could be expanded to include data other than whole-rock geochemistry as distinguishing features. More broadly, the method could be applied to seek clusters in any other distinguishable data type (rather than space and time). Some examples could include mineral geochemistry and mineral assemblages in crystalline rocks, or clast lithology/grainsize/age distributions in sediments or sedimentary rocks (e.g. Bengal fan).

3) The exploration of the HT magmatic record done here is preliminary. More detailed spatial group identification, as was done with data south of the Bangong Suture and younger than 45 Ma, could also be explored for the entire dataset. The distinguishing features extracted from the decision vectors should be studied in more detail. In particular, the notable enrichment in P_2O_5, in the Lhasa terrane (S3b) and northern Tibetan rocks (N4) should be explored further.

4) Geochemical data could be filtered to account for the effect of fractional crystallization processes (e.g., Europium anomalies) prior to using the method presented here.

5) A more flexible and user-friendly way of employing this method could be developed to make it more accessible.

Given the recent ease of use and availability of ML tools and large digital datasets, and increasing use of data science, the method outlined here could provide a relatively easy and fast way to analyze new geochemical or other geological data in a novel way. This method (or generalizations of it) may provide insights into, or test hypotheses regarding, important changes in geological data which may otherwise be subtle.

5.8 References for Chapter 5

Aitchison, J.C., McDermid, I.R.C., Ali, J.R., Davis, A.M. and Zyabrev, S.V. (2007). Shoshonites in southern Tibet record Late Jurassic rifting of a Tethyan intraoceanic island arc. *Journal of Geology, 115,* 197-213. https://doi.org/10.1086/510642

An, W., Hu, X., Garzanti, E., Wang, J.G. and Liu, Q. (2021). New precise dating of the India-Asia collision in the Tibetan Himalaya at 61 Ma. *Geophysical Research Letters*, *48*, e2020GL090641. https://doi.org/10.1029/2020GL090641

Baier, J., Audétat, A. and Keppler, H. (2008). The origin of the negative niobium tantalum anomaly in subduction zone magmas. *Earth and Planetary Science Letters, 267*, 290–300. https://doi.org/10.1016/j.epsl.2007.11.032

Castillo, P.R. (2012). Adakite petrogenesis. *Lithos*, *134,* 304–316. https://doi.org/10.1016/j.lithos.2011.09.013

Chapman, J.B., and Kapp, P. (2017). Tibetan magmatism database. *Geochemistry, Geophysics, Geosystems, 18*, 4229–4234. https://doi.org/10.1002/2017GC007217

Chen, M., Niu, F., Tromp, J., Lenardic, A., Lee, C.T.A., Cao, W., and Ribeiro, J. (2017). Lithospheric foundering and underthrusting imaged beneath Tibet. *Nature Communications, 8*. 15659. https://doi.org/10.1038/ncomms15659

Chen, J., Wu, J., Xu, J., Dong, Y., Wang, B., and Kang, Z. (2013). Geochemistry of Eocene high-Mg# adakitic rocks in the northern Qiangtang terrane, central Tibet: Implications for early uplift of the plateau. *Geological Society of America Bulletin, 125*, 1800–1819. https://doi.org/10.1130/B30755.1

Chung, S.-L., Chu, M.-F., Zhang, Y., Xie, Y., Lo, C.-H., Lee, T.-Y., et al. (2005). Tibetan tectonic evolution inferred from spatial and temporal variations in post-collisional magmatism. *Earth-Science Reviews, 68*, 173–196. https://doi.org/10.1016/j.earscirev.2004.05.001

Doucet, L.S., Tetley, M.G., Li, Z.X., Liu, Y. and Gamaleldien, H. (2022). Geochemical fingerprinting of continental and oceanic basalts: A machine learning approach. *Earth-Science Reviews*, *233,* 104192. https://doi.org/10.1016/j.earscirev.2022.104192

Exley, R.A. and Smith, J.V. (1982). The role of apatite in mantle enrichment processes and in the petrogenesis of some alkali basalt suites. *Geochimica et Cosmochimica Acta, 46*, 1375–1384. https://doi.org/10.1016/0016-7037(82)90273-3

Feng, B., Chen, L., Xu, Y. and Zhang, Y. (2022). Comparative study on three autoencoder-based deep learning algorithms for geochemical anomaly identification. *Earth and Space Science, 9*, e2022EA002626. https://doi.org/10.1029/2022EA002626

Gao, S., Rudnick, R.L., Xu, W.L., Yuan, H.L., Liu, Y.S., Walker, R.J., et al. (2008). Recycling deep cratonic lithosphere and generation of intraplate magmatism in the North China Craton. *Earth and Planetary Science Letters, 270,* 41–53. https://doi.org/10.1016/j.epsl.2008.03.008

Guan, Q., Ren, S., Chen, L., Yao, Y., Hu, Y., Wang, R., et al. (2022). Recognizing multivariate geochemical anomalies related to mineralization by using deep unsupervised graph learning. *Natural Resources Research, 31*, 2225–2245. https://doi.org/10.1007/s11053-022-10088-x

Guo, X., Gao, R., Zhao, J., Xu, X., Lu, Z., Klemperer, S.L., and Liu, H. (2018). Deep-seated lithospheric geometry in revealing collapse of the Tibetan Plateau. *Earth-Science Reviews*, *185*, 751–762. https://doi.org/10.1016/j.earscirev.2018.07.013

Guo, Z., Wilson, M., Zhang, M., Cheng, Z., and Zhang, L. (2015). Post-collisional ultrapotassic mafic magmatism in South Tibet: Products of partial melting of pyroxenite in the mantle wedge induced by roll-back and delamination of the subducted Indian continental lithosphere slab. *Journal of Petrology, 56*, 1365–1406. https://doi.org/10.1093/petrology/egv040

Hacker, B.R., Gnos, E., Ratschbacher, L., Grove, M., McWilliams, M., Sobolev, S.V., et al. (2000). Hot and dry deep crustal xenoliths from Tibet. *Science, 287*, 2463–2466. https://doi.org/10.1126/science.287.5462.2463

Harrison, T.M. and Watson, E.B. (1984). The behavior of apatite during crustal anatexis: equilibrium and kinetic considerations. *Geochimica et Cosmochimica Acta, 48*, 1467–1477. https://doi.org/10.1016/0016-7037(84)90403-4

Heintz, M., Kumar, V.P., Gaur, V.K., Priestley, K., Rai, S.S., and Prakasam, K.S. (2009). Anisotropy of the Indian continental lithospheric mantle. *Geophysical Journal International, 179,* 1341–1360. https://doi.org/10.1111/j.1365-246X.2009.04395.x

Hsu, C.W., Chang, C.C., and Lin, C.J. (2003). A practical guide to support vector classification. https://www.datascienceassn.org/sites/default/files/Practical%20Guide%20to%20Support%20Vector%20Classification.pdf

Hu, X., Garzanti, E., Wang, J., Huang, W., An, W., and Webb, A. (2016). The timing of India-Asia collision onset – Facts, theories, controversies. *Earth-Science Reviews, 160*, 264–299. https://doi.org/10.1016/j.earscirev.2016.07.014

Ingalls, M., Rowley, D.B., Currie, B., and Colman, A.S. (2016). Large-scale subduction of continental crust implied by India-Asia mass-balance calculation. *Nature Geoscience, 9*, 848–853. https://doi.org/10.1038/ngeo2806

Kapp, P. and DeCelles, P.G. (2019). Mesozoic–Cenozoic geological evolution of the Himalayan-Tibetan orogen and working tectonic hypotheses. *American Journal of Science, 319,* 159–254. http://dx.doi.org/10.2475/03.2019.01

Kapp, P., DeCelles, P.G., Gehrels, G.E., Heizler, M. and Ding, L. (2007). Geological records of the Lhasa-Qiangtang and Indo-Asian collisions in the Nima area of central Tibet. *Geological Society of America Bulletin, 119*, 91–933. https://doi.org/10.1130/B26033.1

Kelly, S. and Beaumont, C. (2021). Balanced cross-sections and numerical modeling of the lithospheric-scale evolution of the Hindu Kush and Pamir. *Journal of Geophysical Research: Solid Earth*, *126*, e2020JB020678. https://doi.org/10.1029/2020JB020678

Kelly, S., Beaumont, C. and Butler, J.P. (2020). Inherited terrane properties explain enigmatic post-collisional Himalayan-Tibetan evolution. *Geology, 48*, 8–14. https://doi.org/10.1130/G46701.1

Klemperer, S.L., Kennedy, B.M., Sastry, S.R., Makovsky, Y., Harinarayana, T., and Leech, M.L. (2013). Mantle fluids in the Karakoram fault: Helium isotope evidence. *Earth and Planetary Science Letters*, *366*, 59–70. https://doi.org/10.1016/j.epsl.2013.01.013

Kumar D. (2019) Demystifying Support Vector Machines, Towards Data Science. https://towardsdatascience.com/demystifying-support-vector-machines-8453b39f7368

Lee, H.-Y., Chung, S.-L., Ji, J., Qian, Q., Gallet, S., Lo, C.-H., et al. (2012). Geochemical and Sr–Nd isotopic constraints on the genesis of the Cenozoic Linzizong volcanic successions, southern Tibet. *Journal of Asian Earth Sciences, 53*, 96–114. https://doi.org/10.1016/j.jseaes.2011.08.019

Lee, H.-Y., Chung, S.-L., Lo, C.-H., Ji, J., Lee, T.-Y., Qian, Q., and Zhang, Q. (2009). Eocene Neotethyan slab breakoff in southern Tibet inferred from the Linzizong volcanic record. *Tectonophysics*, *477*, 20–35. https://doi.org/10.1016/j.tecto.2009.02.031

Lindsay, J.J., Hughes, H.S., Yeomans, C.M., Andersen, J.C. and McDonald, I. (2021). A machine learning approach for regional geochemical data: Platinum-group element geochemistry vs geodynamic settings of the North Atlantic Igneous Province. *Geoscience Frontiers, 12*, 101098. https://doi.org/10.1016/j.gsf.2020.10.005

Liu, A.L., Wang, Q., Zhu, D.C., Cawood, P.A., Xia, Y., Li, S.M., et al. (2022). Temporal and spatial variations of enriched source components in Linzizong volcanic succession, Tibet, and implications for the India–Asia collision. *Journal of Petrology, 63*, egab103. https://doi.org/10.1093/petrology/egab103

Liu, A.L., Wang, Q., Zhu, D.C., Cawood, P.A., Xia, Y., Li, S.M., et al. (2022). Temporal and spatial variations of enriched source components in Linzizong volcanic succession, Tibet, and implications for the India–Asia collision. *Journal of Petrology, 63*, egab103. https://doi.org/10.1093/petrology/egab103

Liu, D., Zhao, Z., Zhu, D.C., Niu, Y., DePaolo, D.J., Harrison, T.M., et al. (2014). Postcollisional potassic and ultrapotassic rocks in southern Tibet: Mantle and crustal origins in response to India–Asia collision and convergence. *Geochimica et Cosmochimica Acta, 143*, 207–231. https://doi.org/10.1016/j.gca.2014.03.031

Ma, X., Attia, S., Cawood, T., Cao, W., Xu, Z. and Li, H. (2022). Arc tempos of the Gangdese batholith, southern Tibet. *Journal of Geodynamics, 149*, 101897. https://doi.org/10.1016/j.jog.2022.101897

Najman, Y., Jenks, D., Godin, L., Boudagher-Fadel, M., Millar, I., Garzanti, E., et al. (2017). The Tethyan Himalayan detrital record shows that India–Asia terminal collision occurred by 54 Ma in the Western Himalaya. *Earth and Planetary Science Letters, 459*, 301–310. https://doi.org/10.1016/j.epsl.2016.11.036

Parsons, A.J., Hosseini, K., Palin, R.M., and Sigloch, K. (2020). Geological, geophysical and plate kinematic constraints for models of the India-Asia collision and the post-Triassic central Tethys oceans. *Earth-Science Reviews, 208*, 103084. https://doi.org/10.1016/j.earscirev.2020.103084

Pearce, J.A. and Cann, J.R. (1971). Ophiolite origin investigated by discriminant analysis using Ti, Zr and Y. *Earth and Planetary Science Letters, 12*, 339–349. https://doi.org/10.1016/0012-821X(71)90220-2

Pearce, J.A. and Cann, J.R. (1973). Tectonic setting of basic volcanic rocks determined using trace element analyses. *Earth and Planetary Science Letters, 19*, 290–300. https://doi.org/10.1016/0012-821X(73)90129-5

Pearce, J.A. and Norry, M.J. (1979). Petrogenetic implications of Ti, Zr, Y, and Nb variations in volcanic rocks. *Contributions to Mineralogy and Petrology, 69*, 33–47. https://doi.org/10.1007/BF00375192

Pearce, J.A. and Gale, G.H. (1977). Identification of ore-deposition environment from trace-element geochemistry of associated igneous host rocks. In: Gass I. G, (Eds) *Geological Society, London, Special Publications, 7*, 14–24. https://doi.org/10.1144/GSL.SP.1977.007.01.03

Pearce, T.H., Gorman, B.E., and Birkett, T.C. (1977). The relationship between major element chemistry and tectonic environment of basic and intermediate volcanic rocks. *Earth and Planetary Science Letters, 36*, 121–132. https://doi.org/10.1016/0012-821X(77)90193-5

Petrelli, M., Bizzarri, R., Morgavi, D., Baldanza, A., and Perugini, D. (2017). Combining machine learning techniques, microanalyses and large geochemical datasets for tephrochronological studies in complex volcanic areas: New age constraints for the Pleistocene magmatism of central Italy. *Quaternary Geochronology, 40*, 33–44. https://doi.org/10.1016/j.quageo.2016.12.003

Petrelli, M., and Perugini, D. (2016). Solving petrological problems through machine learning: the study case of tectonic discrimination using geochemical and isotopic data. *Contributions to Mineralogy and Petrology, 171*, 1–15. https://doi.org/10.1007/s00410-016-1292-2

Piccoli, P.M. and Candela, P.A. (2002). Apatite in igneous systems. *Reviews in Mineralogy and Geochemistry, 48*, 255–292. https://doi.org/10.2138/rmg.2002.48.6

St-Onge, M.R., Rayner, N. and Searle, M.P. (2010). Zircon age determinations for the Ladakh batholith at Chumathang (Northwest India): Implications for the age of the India–Asia collision in the Ladakh Himalaya. *Tectonophysics, 495*, 171–183. https://doi.org/10.1016/j.tecto.2010.09.010

Ueki, K., Hino, H. and Kuwatani, T. (2018). Geochemical discrimination and characteristics of magmatic tectonic settings: A machine-learning-based approach. *Geochemistry, Geophysics, Geosystems, 19*, 1327–1347. https://doi.org/10.1029/2017GC007401

van Hinsbergen, D.J., Lippert, P.C., Dupont-Nivet, G., McQuarrie, N., Doubrovine, P.V., Spakman, W. and Torsvik, T.H. (2012). Greater India Basin hypothesis and a two-stage Cenozoic collision between India and Asia. *Proceedings of the National Academy of Sciences, 109*, 7659–7664. https://doi.org/10.1073/pnas.1117262109

Wang, C., Ding, L., Zhang, L.Y., Kapp, P., Pullen, A. and Yue, Y.H. (2016). Petrogenesis of Middle–Late Triassic volcanic rocks from the Gangdese belt, southern Lhasa terrane: Implications for early subduction of Neo-Tethyan oceanic lithosphere. *Lithos, 262*, 320–333. https://doi.org/10.1016/j.lithos.2016.07.021

Wang, Q., Hawkesworth, C.J., Wyman, D., Chung, S.-L., Wu, F.-Y., Li, X.-H. et al., (2016). Pliocene-Quaternary crustal melting in central and northern Tibet and insights into crustal flow. *Nature communications, 7*, 11888. https://doi.org/10.1038/ncomms11888

White, L.T., Ahmad, T., Lister, G.S., Ireland, T.R. and Forster, M.A. (2012). Is the switch from I-to S-type magmatism in the Himalayan Orogen indicative of the collision of India and Eurasia? *Australian Journal of Earth Sciences*, *59*, 321–340. https://doi.org/10.1080/08120099.2012.652670

Yin, A., and Harrison, T.M. (2000). Geologic evolution of the Himalayan-Tibetan orogen. *Annual Review of Earth and Planetary Sciences, 28*, 211–280. https://doi/full/10.1146/annurev.earth.28.1.211

Yuan, J., Yang, Z., Deng, C., Krijgsman, W., Hu, X., Li, S. (2021). Rapid drift of the Tethyan Himalaya terrane before two-stage India-Asia collision. *National Science Review, 8*, nwaa173. https://doi.org/10.1093/nsr/nwaa173

Zheng, Y.F. (2019). Subduction zone geochemistry. *Geoscience Frontiers, 10*, 1223–1254. https://doi.org/10.1016/j.gsf.2019.02.003

Zhu, D.C., Wang, Q., Zhao, Z.D., Chung, S.L., Cawood, P.A., Niu, Y., et al. (2015). Magmatic record of India-Asia collision. *Scientific reports, 5*, 14289. https://doi.org/10.1038/srep14289

CHAPTER 6. DISCUSSION

6.1 Mantle-Scale Tectonics of the Himalayan-Tibetan and Pamir-Hindu Kush Systems

The behavior of the continental lithospheric mantle (CLM) during continent-continent orogenesis, while recognized as important to the first-order evolution of these systems (Ghazian and Buiter, 2013; Houseman et al., 1981; Jamieson and Beaumont, 2013; Kay and Kay, 1993; Molnar et al., 1993; Willett et al., 1993), remains poorly understood (Avouac, 2007; Ghazian and Buiter, 2013; Jamieson and Beaumont, 2013; Molnar, 1988; Molnar and Bendick, 2019; Toussaint et al., 2004). This is because direct evidence for these deep processes is typically lacking in the geological record (Chen et al., 2017; Guo et al., 2018; Heintz et al., 2009; Klemperer et al., 2013), or remains unrecognized. In the absence of direct evidence, or a single fingerprinting indirect observation for CLM behavior, a diverse set of indirect observations can provide a strong alternative basis that combines disparate evidence for testing geodynamical models regarding upper mantle-scale processes.

The Himalayan-Tibetan orogenic system, including its western extension, the Hindu Kush and Pamir (HT-HKP), is probably the best example of a modern active large hot orogen in this regard. This is because intensive studies have yielded several apparently disparate observations of this system which are enigmatic and concern the behavior of the lower lithosphere.

Previous geodynamical modelling studies of the HT-HKP system have failed to provide complete explanations for many of these observations, likely because they do not fully consider the role that terrane heterogeneities played in its evolution. The numerical geodynamical model experiments presented here show that terrane heterogeneities, in particular the strengths and densities of the Asian terrane CLMs and the nature of the Indian marginal lithosphere, have a profound influence on the evolution of these systems. These models were designed using geometric arguments based on the timing and location

of India-Asia contact, and the present-day location of terrane boundaries, based on geological and geophysical arguments. The model results presented in Chapters 2-4 show how deformation and removal of CLM, controlled by the inherited terrane properties, provide self-consistent explanations for many of the enigmatic observations of the HT-HKP systems, for example, early post-collisional farfield deformation of the Qiangtang terrane and early Eohimalayan metamorphism. These results are integrated and explored in further detail in the following sections.

Owing to the usefulness of geochemistry for interpreting mantle-scale processes, building on traditional geochemical approaches by using modern machine learning methods can be beneficial for further understanding these deep processes. A machine-learning-based approach is presented with the goal of finding previously unidentified geochemical signatures which may reflect CLM and deeper mantle-scale processes.

6.2 Comparison of Model Processes with Observations from the HT-HKP Systems

There are several phases of CLM deformation and removal which emerge in successful models for the Hindu Kush (MHA), Pamir (MPA) and H-T (MA/MB) parts of the system presented in this thesis, which have important consequences for the evolution of this orogen.

Following India-Asia collision in the models, CLM folding initiates first in the weakest and densest central Asian terrane (representing the Qiangtang terrane for HT section, a composite of the Pamir terranes for the Pamir section, and a northern Hindu Kush terrane for the Hindu Kush section). This CLM folding and delaminating from the crust eventually leads to gravitationally driven sinking of the CLM of these terranes and subsequent detachment/breakoff from the overlying crust. Following CLM and lower crust removal, the mid-crust is exposed to hot upwelling asthenosphere. Focussed deformation and CLM removal within the central Asian terranes explain the initiation of early far field post-contact magmatism and crustal shortening (~45 Ma Qiangtang

magmatism and ~42 Ma Pamir magmatism, e.g., Kapp and DeCelles, 2019; Chapman et al., 2018b respectively). Heating of the base of the lower-middle crust can also lead to diapirism thereby potentially explaining the Pamir gneiss domes. While the folded CLM's are sinking, but remain attached to the adjacent lithosphere, their gravitational pull provides a northward-directed motive force that drives subduction zone widening, leading to hot asthenosphere upwelling into the lower subduction channel, and thereby explaining the heat source for early Eocene Himalayan (Eohimalayan) metamorphism (e.g., Ryan and Dewey, 2019).

Following CLM removal in the central Asian terrane, in both the HK and HT models the attached CLM remaining under southern Asia, now exposed to asthenospheric mantle along its northern edge, begins to delaminate and peel away from the crust from north to south. Peeling delamination exposes the overlying crust to hot upwelling asthenosphere and produces a sweep of crustal deformation and predicted magmatism, which can explain the observed southward jump or sweep in magmatism and a transfer of crustal thickening from the Qiangtang to the Lhasa terrane by 27 Ma (Kapp and DeCelles, 2019).

In the later stages of Pamir and H-T models, following removal of much of the southern Asian CLM, Indian lithosphere underthrusts Asia. As Indian CLM underthrusts Asia, the overlying India crust detaches and accretes, contributing to a growing model Himalaya. The delay in Himalayan growth relative to Asian crustal deformation in the models in part explains the significant asymmetry between the N/S width of the thickened part of Asia (i.e., Tibet/Pamir) and the thickened part of India (i.e., Himalaya). For the HT system, a tectonically quiescent phase between the early Eohimalayan metamorphism and later onset of Neohimalayan Himalayan growth is proposed and attributed to Asia accommodating most of the India-Asia convergence in the interval ~45–30 Ma.

In the Pamir model underthrusting Indian CLM drives delamination of the Alai CLM. Strong Alai crust resists detaching from the peeling Alai CLM, leading to underthrusting of the Alai crust and lower lithosphere beneath the Pamir, resulting in the development of

the northward-facing Pamir orocline and the almost complete burial of the inferred initially wider Alai terrane.

In contrast, north-south orientated thinned Indian marginal lithosphere along its western side led to subduction of Indian lithosphere under Asia beneath the Hindu Kush section, in agreement with seismic imagery (e.g., Kufner et al., 2016). The models imply that thin, cold, marginal Indian crust resisted detaching from the subducting Indian lower lithosphere, leading to underthrusting of the Indian crust beneath Asia rather than its accretion to the Himalaya. This lack of detachment and accretion explains the diminished size of the Indian fold and thrust belt along the Hindu Kush section relative to the Himalaya. These results could have implications for other large orogens containing previously accreted terranes. For example, geodynamical models of large orogens should consider the role that terrane heterogeneity plays in the evolution of orogenic systems and consider how post-collisional subduction zone widening can generate early magmatism and metamorphism in orogenic systems.

6.3 The Asian Shortening Deficit: An Enduring Problem

A notable discrepancy between the models presented in Chapters 2 and 3 and observations is the amount of observed post-collisional shortening within the Asian upper crust. To address this discrepancy, evidence justifying the design of the models is presented and compared with shortening estimates for Asian upper crust. This assessment is presented assuming the simplest model for the collision of India with Asia, namely the subduction of the Neotethys along a single subduction zone beneath the southern Lhasa terrane without subduction zone retreat or a Greater India ocean basin. Since evidence for the amount of shortening in the Hindu Kush is scarce, the focus here is along 74°E for the Pamir and 90°E for the central HT models (MA, MB, MEA).

The interpreted location of the Neotethyan slab, imaged in the lower mantle, is 10°N–20°N along 90°E for the HT section, and between 15°N–27°N along 74°E for the Pamir section (e.g., Parsons et al., 2020; Van der Voo et al., 1999).

Assuming that the subducted Neotethys slab sank vertically following breakoff (e.g., Parsons et al., 2020) and that the location of the trench at terminal subduction of the Neotethys lithosphere was above the inferred present-day location of the seismic anomaly typically inferred to represent the Neotethys slab (e.g., Parsons et al., 2020; Van er Voo et al., 1999), the location of India-Asia contact was between these latitude ranges for each section.

Recent data suggest that the timing of contact was ~61 Ma (An et al., 2021, Hu et al., 2016), and estimates of India-Asia convergence since this time are ~4200 km for the western Indian syntaxis and ~5000 km for the eastern syntaxis (van Hinsbergen et al., 2011), with an approximate mean convergence of ~4600 km.

Paleomagnetic estimates for the location of the southern margin of Asia during the Cretaceous (near, but not necessarily firmly associated with either the time of contact or collision) vary, with some workers (e.g., Tong et al., 2019) placing the central Lhasa terrane (at 92°E present longitude) at ~12.9 °N +/– 1.6°N or 17.4°N +/– 1.3°N depending on the interpretation, and the western Lhasa terrane (at 83°E present longitude) at 16.9°N +/– 1.3°N. However, some recent studies (e.g., Li et al., 2022) have placed the central Lhasa significantly further north (24.8°N +/– 7.1°N). While there is significant uncertainty regarding the location of the southern Asian margin at the time of contact, the lower latitude estimate (12.9 °N) for Lhasa terrane, combined with the locations of the inferred Neotethys slab, are broadly consistent with the design of the numerical models where the location of contact corresponds to latitudes 11°N for the HT models (MA/MB/MEA based on 90°E) and 19°N for the Pamir models (MPA based on 74°E).

Comparing the locations of contact assumed in the models (11°N for the HT section at 90°E and 19°N for the Pamir section at 74°E) with the current locations of the Indus-Yarlung suture zone (IYSZ; 35°N along the Pamir section and 29.3°N along the HT section), implies that the southern margin of Asia that made contact with India was translated north by ~2000 km along the central HT section and 1800 km along the Pamir section, although this does not constrain how this was absorbed within Asia. Additionally,

the location of central Lhasa terrane is estimated to be 17.9°N at ~53 Ma, implying ~550 km of northward Lhasa terrane translation between contact and 53 Ma (Tong et al., 2019). Alternatively, using the upper latitude estimate of 17.4°N for the location of contact implies ~1300 km of northward translation of the southern Lhasa terrane along the central HT section.

Estimates of measured post-50 Ma shortening within Tibet are ~400 km (van Hinsbergen et al., 2011, and references therein), which is likely later than collision or contact (An et al., 2021, Hu et al., 2016). In addition, there is an estimated ~200 +/- 50 km of shortening in the Tien Shan since contact (Avouac et al., 1993) and an estimated ~150 km of north-south shortening associated with ~400–500 km of strike-slip offset on the Altyn-Tagh Fault. This leaves a discrepancy of ~1250 km of convergence not accounted for by measured shortening in central Tibet. However, most shortening estimates only include shortening after 50 Ma, and the 550 km of shortening implied by the 61–53 Ma translation of the southern Asian margin reduces the post-53 Ma shortening deficit to ~700 km. Assuming the lower latitude paleomagnetic estimate (12.9 °N) for the location of contact further reduces the shortening deficit to ~550 km.

Estimates of measured Cenozoic shortening within the Pamir are smaller at ~100 km, although minimal Cenozoic shortening is seemingly contradicted by high-grade Cenozoic metamorphism in exhumed gneiss domes (Chapman et al., 2018a). In addition, it is suggested that the Pamir overthrust the initially wider Alai crust by ~300 km, based on implied offset along the Karakoram fault (Burtman and Molnar, 1993). However, this has been disputed, with some estimating a more modest ~130–190 km offset (Borneman et al., 2015) to a comparatively minor ~52 km offset (Wang et al., 2012). Assuming that the Alai valley was overthrust ~300 km, together with ~200 km of shortening in the Tien Shan, this leaves a shortening deficit in the Pamir of ~1200 km.

There are several factors which may account for the missing upper crustal Asian shortening as measured/estimated structurally in surface and near-surface thin-skinned deformation zones.

1) The simplest explanation is that the missing shortening reflects mapping limitations. Shortening estimates based on surface mapping may underestimate shortening by missing hidden structures such as duplexes and blind thrusts (e.g., Zuza et al., 2016), or underestimate the cumulative shortening from small-scale faults/folds or layer-parallel shortening, which could accommodate 25%–60% of shortening (e.g., Lammie et al., 2020; Marrett and Allmendinger, 1992).

2) While east-west extrusion within Tibet following collision is reasonably well established, if the initial pre-contact geometry of the Asian margin was wedge-shaped, as envisioned by Tong et al. (2019) based on paleomagnetic data, then convergence accommodated by early east-west extrusion of the southern Asian margin could be unrecognized in the rock record. However, at least some of this extrusion may have occurred between 61–53 Ma, and therefore that part would not contribute to reducing the post-53 Ma deficit. Extrusion could be rigid with the entire Tibetan block offset to the east along major strike-slip faults (i.e., the Altyn Tagh fault) or distributed as depicted in Figure 6.1. In the case of distributed extrusion there may be minimal offset on major strike-slip faults.

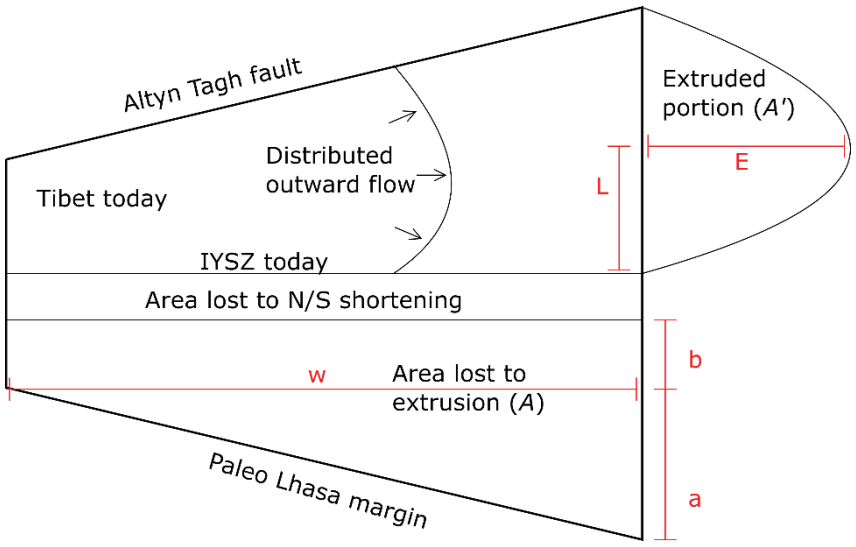

Figure 6.1. A simplified schematic depiction of planform distributed eastward flow of Tibet (not to scale). The planform area of paleo-Tibet lost to N/S convergence is accommodated by distributed flow (as depicted by the arrows) to the east, resulting in an extruded portion. Assuming for simplicity that the shape

of the extruded portion was parabolic and crustal thickness remained constant, then the planform area of paleo-Tibet lost to N/S convergence ($A = \frac{1}{2}aw + bw$) has to balance with the area of the extruded portion ($A' = \frac{2}{3}L^3\alpha$), for some value of α. Balancing these areas sets $\alpha = \frac{3}{2}\frac{w}{L^3}\left(\frac{1}{2}a + b\right)$, which in turn sets the extrusion distance $E = \alpha L^2 = \frac{3}{2}\frac{w}{L}\left(\frac{1}{2}a + b\right)$. If the region lost to convergence (initially occupying area A) had thinner crust (thickness T) , and the extruded portion (occupying A' today) currently has crustal thickness $T' \approx 70\ km$, then the extrusion distance reduces to $E = \frac{T}{T'}\alpha L^2 = \frac{T}{T'}\frac{3}{2}\frac{w}{L}\left(\frac{1}{2}a + b\right)$. If the paleo-Lhasa margin had typical continental crustal thickness at the time of contact (i.e., $T \approx 36\ km$), then $E \approx \frac{1}{2}\alpha L^2 = \frac{3}{4}\frac{w}{L}\left(\frac{1}{2}a + b\right)$.

3) Cryptic shortening, where shortening is accommodated within suture zones, could account for some of the missing shortening. For example, if Lhasa terrane crust was underthrust beneath the Qiangtang terrane with no mappable near-surface thin-skinned detached layer, then unrecognized shortening associated with the Bangong suture zone could account for this discrepancy. While there is some observed post to mid-Cretaceous shortening within the Bangong suture zone (~41 km; e.g, Kapp et al., 2005), there is no direct evidence of shortening within this suture that could entirely account for this post-collisional shortening discrepancy.

4) Unrecognized sutures may exist if oceanic or thinned lithospheric basins opened within Asia before contact and were subsequently closed after contact. Kapp and DeCelles (2019) hypothesized that the Xigaze forearc had previously rifted from Asia. In their hypothesis, the initial ~61 Ma contact (which they assumed to be ~59 Ma based on earlier estimates for the timing of contact) was between India and the rifted Xigaze forearc. Subsequently the hypothesized oceanic basin, separating the rifted forearc from the rest of the Lhasa terrane, closed. Like the hypothesised cryptic shortening above, there is yet no evidence for the hypothetical Xigaze/Lhasa suture.

The model results presented in this thesis are most consistent with a combination of mapping limitations in shortening estimates and unrecognized cryptic shortening.

6.4 Future directions

There is evidence that the Lhasa terrane was shortened prior to contact with India (e.g., Kapp et al., 2007; Murphy et al., 1997). Future models should address the effect that a previously shortened Lhasa terrane would have on the ensuing evolution of the orogen as well as investigate the mechanism of Lhasa terrane shortening during subduction of the Neotethyan ocean. Additionally, these models should explore the hypothesis that Lhasa crust was underthrust beneath the Qiangtang terrane, and whether the resulting cryptic shortening can explain the shortening deficit with Asia.

There are several aspects of the system that cannot be addressed using 2D models. In particular, the oppositely-dipping slabs for the Hindu Kusha and Pamir require the Indian and Asian lithosphere to tear, which cannot be modelled in 2D. Additionally, modelling the east-west extrusion of Tibet cannot be captured with 2D models, except in planform where other important processes such as mantle removal cannot be modelled. Future geodynamical research should explore 3D models, particularly for the western part of the HT-HKP system, with model resolutions capable of capturing crustal-scale processes such as proposed cryptic shortening associated with crustal underthrusting. 3D models with this resolution would likely require computer systems with computational resources not available during the research presented in this thesis.

The machine learning method presented here is preliminary and there are several future directions that could be explored. In particular, the general group proposal scheme was used on the post-collisional Lhasa terrane and Himalayan rocks only. This general proposal scheme should be applied to the entire dataset, and this general group proposal scheme should be further expanded to include age.

Additionally, this machine learning method relies on using a support vector machine which requires each sample to have the same measured geochemical features. Geochemically useful features such as isotopic data were excluded in the present research because these elements are less frequently measured and requiring them to be included

would significantly reduce the size of the dataset. This method should be expanded to be able to include data with incomplete sets of features. This will require researching or developing machine learning methods capable of using incomplete datasets and incorporating them into the method presented here.

Finally, a user-friendly version of the method presented here should be developed to make it more accessible to a wider geological audience.

6.5 References for Discussion Section

An, W., Hu, X., Garzanti, E., Wang, J.G., and Liu, Q. (2021). New precise dating of the India-Asia collision in the Tibetan Himalaya at 61 Ma. *Geophysical Research Letters*, *48*, p.e2020GL090641. https://doi.org/10.1029/2020GL090641

Avouac, J. P. (2007). Dynamic processes in extensional and compressional settings - mountain building: From earthquakes to geological deformation. In: Schubert, G. (Ed.), *Treatise on Geophysics*, *6*, 377–439. Elsevier. https://doi.org/10.1016/B978-044452748-6.00112-7

Avouac, J.-P., Tapponnier, P., Bai, M., You, H., and Wang, G. (1993). Active thrusting and folding along the northern Tien Shan and late Cenozoic rotation of the Tarim relative to Dzungaria and Kazakhstan. *Journal of Geophysical Research: Solid Earth, 98,* 6755–6804. https://doi.org/10.1029/92JB01963

Burtman, V.S. and Molnar, P. (1993). Geological and geophysical evidence for deep subduction of continental crust beneath the Pamir. *Geological Society of America Special Paper, 281,* 1–76. https://doi.org/10.1130/SPE281-p1

Chapman, J.B., Robinson, A.C., Carrapa, B., Villarreal, D., Worthington, J., DeCelles, P.G., et al. (2018a). Cretaceous shortening and exhumation history of the South Pamir terrane. *Lithosphere*, *10,* 494-511.

Chapman, J.B., Scoggin, S.H., Kapp, P., Carrapa, B., Ducea, M.N., Worthington, J., et al. (2018b). Mesozoic to Cenozoic magmatic history of the Pamir. *Earth and Planetary Science Letters*, *482*, 181-192. https://doi.org/10.1016/j.epsl.2017.10.041

Chen, M., Niu, F., Tromp, J., Lenardic, A., Lee, C.T.A., Cao, W., and Ribeiro, J. (2017). Lithospheric foundering and underthrusting imaged beneath Tibet. *Nature Communications, 8,* 15659. https://doi.org/10.1038/ncomms15659

Condie, K.C. (2013). Preservation and recycling of crust during accretionary and collisional phases of Proterozoic orogens: A bumpy road from Nuna to Rodinia. *Geosciences*, *3*, 240–261. https://doi.org/10.3390/geosciences3020240

Ghazian, R.K. and Buiter, S.J. (2013). A numerical investigation of continental collision styles. *Geophysical Journal International*, *193*, 1133–1152. https://doi.org/10.1093/gji/ggt068

Guo, X., Gao, R., Zhao, J., Xu, X., Lu, Z., Klemperer, S.L., and Liu, H. (2018). Deep-seated lithospheric geometry in revealing collapse of the Tibetan Plateau. *Earth-Science Reviews*, *185*, 751–762. https://doi.org/10.1016/j.earscirev.2018.07.013

Heintz, M., Kumar, V.P., Gaur, V.K., Priestley, K., Rai, S.S., and Prakasam, K.S. (2009). Anisotropy of the Indian continental lithospheric mantle. *Geophysical Journal International, 179,* 1341–1360. https://doi.org/10.1111/j.1365-246X.2009.04395.x

Houseman, G.A., McKenzie, D.P., and Molnar, P. (1981). Convective instability of a thickened boundary layer and its relevance for the thermal evolution of continental convergent belts. *Journal of Geophysical Research: Solid Earth*, *86,* 6115–6132. https://doi.org/10.1029/JB086iB07p06115

Hu, X., Garzanti, E., Wang, J., Huang, W., An, W., and Webb, A. (2016). The timing of India-Asia collision onset–Facts, theories, controversies. *Earth-Science Reviews*, *160*, 264-299. https://doi.org/10.1016/j.earscirev.2016.07.014

Jamieson, R.A. and Beaumont, C. (2013). On the origin of orogens. *Geological Society of America Bulletin 125,* 1671–1702. https://doi.org/10.1130/B30855.1

Kapp, P. and DeCelles, P.G. (2019). Mesozoic–Cenozoic geological evolution of the Himalayan-Tibetan orogen and working tectonic hypotheses. *American Journal of Science*, *319*, 159–254. https://doi.org/10.2475/03.2019.01

Kapp, P., DeCelles, P.G., Leier, A.L., Fabijanic, J.M., He, S., Pullen, A., Gehrels, G.E., and Ding, L. (2007). The Gangdese retroarc thrust belt revealed. *GSA today*, *17*, 4-9.

Kay, R.W. and Kay, S.M. (1993). Delamination and delamination magmatism. *Tectonophysics, 219,* 177–189. https://doi.org/10.1016/0040-1951(93)90295-U

Klemperer, S.L., Kennedy, B.M., Sastry, S.R., Makovsky, Y., Harinarayana, T., and Leech, M.L. (2013). Mantle fluids in the Karakoram fault: Helium isotope evidence. *Earth and Planetary Science Letters, 366,* 59–70. https://doi.org/10.1016/j.epsl.2013.01.013

Kufner, S.-K., Schurr, B., Sippl, C., Yuan, X., Ratschbacher, L., and Ischuk, A., et al (2016). Deep India meets deep Asia: Lithospheric indentation, delamination and break-off under Pamir and Hindu Kush (Central Asia). *Earth and Planetary Science Letters, 435,* 171–184. https://doi.org/10.1016/j.epsl.2015.11.046

Lammie, D., McQuarrie, N., and Sak, P.B. (2020). Quantifying shortening across the central Appalachian fold-thrust belt, Virginia and West Virginia, USA: Reconciling grain-, outcrop-, and map-scale shortening. *Geosphere*, *16*, 1276-1292. https://doi.org/10.1130/GES02016.1

Marrett, R. and Allmendinger, R.W. (1992). Amount of extension on "small" faults: An example from the Viking graben. *Geology*, *20*, 47-50. https://doi.org/10.1130/0091-7613(1992)020%3C0047:AOEOSF%3E2.3.CO;2

Molnar, P. (1988). Continental tectonics in the aftermath of plate tectonics. *Nature, 335,* 131–137. https://doi.org/10.1038/335131a0

Molnar, P. and Bendick, R. (2019). Seismic moments of intermediate-depth earthquakes beneath the Hindu Kush: Active stretching of a blob of sinking thickened mantle lithosphere? *Tectonics*, *38*, 1651–1665. https://doi.org/10.1029/2018TC005336

Molnar, P., England, P., and Martinod, J. (1993). Mantle dynamics, uplift of the Tibetan Plateau, and the Indian monsoon. *Reviews of Geophysics, 31,* 357–396. https://doi.org/10.1029/93RG02030

Murphy, M.A., Yin, A., Harrison, T.M., Durr, S.B., Ryerson, F.J., and Kidd, W.S.F. (1997). Did the Indo-Asian collision alone create the Tibetan plateau? *Geology*, *25*, 719-722. https://doi.org/10.1130/0091-7613(1997)025%3C0719:DTIACA%3E2.3.CO;2

Parsons, A.J., Hosseini, K., Palin, R.M., and Sigloch, K. (2020). Geological, geophysical and plate kinematic constraints for models of the India-Asia collision and the post-Triassic central Tethys oceans. *Earth-Science Reviews*, *208*, 103084. https://doi.org/10.1016/j.earscirev.2020.103084

Tong, Y., Yang, Z., Li, J., Pei, J., and Li, J. (2019). New insights into the collision process of India and Eurasia: evidence from the syntectonic-sedimentation-induced inclinational divergence of Cretaceous paleomagnetic data of the Lhasa Terrane. *Earth-Science Reviews*, *190*, 570-588. https://doi.org/10.1016/j.earscirev.2019.02.009

Toussaint, G., Burov, E., and Jolivet, L. (2004). Continental plate collision: Unstable vs. stable slab dynamics. *Geology*, *32*, 33–36. https://doi.org/10.1130/G19883.1

van Hinsbergen, D.J., Steinberger, B., Doubrovine, P.V., and Gassmöller, R. (2011). Acceleration and deceleration of India-Asia convergence since the Cretaceous: Roles of mantle plumes and continental collision. *Journal of Geophysical Research: Solid Earth*, *116*. B06101. https://doi.org/10.1029/2010JB008051

Wang, S., Wang, C., Phillips, R.J., Murphy, M.A., Fang, X., and Yue, Y. (2012). Displacement along the Karakoram fault, NW Himalaya, estimated from LA-ICP-MS U–Pb dating of offset geologic markers. *Earth and Planetary Science Letters*, *337*, 156-163. https://doi.org/10.1016/j.epsl.2012.05.037

Willett, S., Beaumont, C., and Fullsack, P. (1993). Mechanical model for the tectonics of doubly vergent compressional orogens. *Geology, 21,* 371–374. https:/doi.org/10.1130/00917613(1993)021<0371:MMFTTO>2.3.CO;2

Zuza, A.V., Cheng, X., and Yin, A. (2016). Testing models of Tibetan Plateau formation with Cenozoic shortening estimates across the Qilian Shan–Nan Shan thrust belt. *Geosphere*, *12*, 501-532. https://doi.org/10.1130/GES01254.1

CHAPTER 7. CONCLUSIONS

The primary outcomes of this thesis are summarized below.

- Inherited terrane properties, in particular the strengths and densities of the terrane continental lithospheric mantles (CLMs), have profound influences on the evolution of the Himalayan Tibetan (H-T) orogen, including its western extension into the Hindu Kush and Pamir (HK-P). The strength and density of the terrane CLMs can be interpreted as reflecting the degree of dehydration and depletion with respect to the composition of underlying mantle. If the models are correct, deformation and subsequent CLM removal were focused on the weakest Asian terranes (Qiangtang, Pamir and north Hindu Kush terranes), followed by removal of CLM beneath the southern Asian terranes (Lhasa, south Hindu Kush, and Kohistan terranes). After Asian CLM removal, the India lithosphere underthrust Asia. These phases of CLM behavior explain many enigmatic observations and inferences of the H-T and HK-P (HT-HKP) systems, including how magmatism and crustal deformation initiated far from the India-Asian suture and migrated in a seemingly erratic way.

- First-order geometric arguments regarding the location and timing of contact, based on geological and geophysical arguments, can be used to inform hypotheses regarding the mantle-scale evolution of the HT-HKP system, and to provide a framework for the design of geodynamical models.

- Thinned marginal lithosphere along the western edge of the Indian subcontinent could have led to subduction of this western part of the Indian lithosphere, thereby explaining the steeply north-dipping slab imaged beneath the Hindu Kush. In contrast, Indian lithosphere may have been capable of underthrusting beneath Asia, leading to forced delamination of Alai CLM, thereby explaining the shallowly south-dipping slab imaged below the Pamir.

- Strong/cold crust resists detaching from subducting or delaminating CLM, which can lead to underthrusting of this crust beneath the neighboring terranes. For the Hindu Kush, thin and cold Indian crust that was underthrust beneath Asian crust during subduction of Indian lithosphere can explain the reduced size of the Indian fold-and-thrust belt in this region. For the Alai terrane, strong crust underthrust beneath the Pamir during Alai CLM delamination can explain the Pamir orocline. In both cases underthrusting of cold crust at a terrane suture could produce cryptic, unrecognized shortening.

- Gravitationally driven Qiangtang CLM removal could have produced subduction zone widening, leading to upwelling asthenosphere. This is a possible heat source for early (pre-40 Ma) Eohimalayan metamorphism. A tectonically quiescent phase is proposed for the Himalaya during the interval ~45 – 30 Ma, when India-Asia convergence was almost entirely accommodated within Asia. Tectonic quiescence implies that greater total post-contact convergence relative to India is accommodated within Asia, which in turn implies that tectonic quiescence in part explains the relatively narrow width of the thickened part of Indian crust as compared to the thickened part of Asian crust (i.e. Himalaya vs. the Tibetan plateau), contrary to expectations of continuous India-Asia convergence.

- Machine learning techniques applied to geochemical datasets can be used to identify previously unrecognized geochemical signatures reflecting deep mantle-scale processes.

MASTER REFERENCE LIST

Abdrakhmatov, K. Y., Aldazhanov, S. A., Hager, B. H., and Hamburger, M. W. (1996). Relatively recent construction of the Tien Shan inferred from GPS measurements of present-day crustal deformation rates. *Nature, 384*, 450–453. https://doi.org/10.1038/384450a0

Abdulhameed, S., Ratschbacher, L., Jonckheere, R., Gągała, Ł., Enkelmann, E., Käßner, A., et al. (2020). Tajik Basin and southwestern Tian Shan, northwestern India-Asia collision zone: 2. Timing of basin inversion, Tian Shan mountain building, and relation to Pamir-Plateau advance and deep India-Asia indentation. *Tectonics, 39*, e2019TC00587. https://doi.org/10.1029/2019TC005873

Acton, G.D. (1999). Apparent polar wander of India since the Cretaceous with implications for regional tectonics and true polar wander. *Memoir of the Geological Society of India, 44,* 129–175.

Aikman, A.B., Harrison, T.M., and Lin, D. (2008). Evidence for early (> 44 Ma) Himalayan crustal thickening, Tethyan Himalaya, southeastern Tibet. *Earth and Planetary Science Letters, 274,* 14–23. https://doi.org/10.1016/j.epsl.2008.06.038

Aikman, A.B., Harrison, T.M., and Hermann, J. (2012). Age and thermal history of Eo- and Neohimalayan granitoids, eastern Himalaya. *Journal of Asian Earth Sciences, 51*, 85–97. https://doi.org/10.1016/j.jseaes.2012 .01.011

Aitchison, J.C., Ali, J.R., and Davis, A.M. (2007). When and where did India and Asia collide? *Journal of Geophysical Research: Solid Earth, 112,* B05423. https://doi.org/10.1029/2006JB004706

Aitchison, J.C., McDermid, I.R.C., Ali, J.R., Davis, A.M. and Zyabrev, S.V. (2007). Shoshonites in southern Tibet record Late Jurassic rifting of a Tethyan intraoceanic island arc. *Journal of Geology, 115,* 197-213. https://doi.org/10.1086/510642

An, W., Hu, X., Garzanti, E., Wang, J.G., and Liu, Q. (2021). New precise dating of the India-Asia collision in the Tibetan Himalaya at 61 Ma. *Geophysical Research Letters*, *48*, p.e2020GL090641. https://doi.org/10.1029/2020GL090641

An, W., Hu, X., Garzanti, E., Wang, J.G. and Liu, Q. (2021). New precise dating of the India-Asia collision in the Tibetan Himalaya at 61 Ma. *Geophysical Research Letters*, *48*, e2020GL090641. https://doi.org/10.1029/2020GL090641

Andrews, E. R., and Billen, M. I. (2009). Rheologic controls on the dynamics of slab detachment. *Tectonophysics, 464*, 60–69. https://doi.org/10.1016/j.tecto.2007.09.004

Avouac, J. P. (2007). Dynamic processes in extensional and compressional settings - mountain building: From earthquakes to geological deformation. In: Gerald Schubert (Ed.), *Treatise on Geophysics*, *6*, 377–439. Elsevier. https://doi.org/10.1016/B978-044452748-6.00112-7

Avouac, J.-P., Tapponnier, P., Bai, M., You, H., and Wang, G. (1993). Active thrusting and folding along the northern Tien Shan and late Cenozoic rotation of the Tarim relative to Dzungaria and Kazakhstan. *Journal of Geophysical Research: Solid Earth, 98,* 6755–6804. https://doi.org/10.1029/92JB01963

Bai, L., and Zhang, T. (2015). Complex deformation pattern of the Pamir-Hindu Kush region inferred from multi-scale double-difference earthquake relocations. *Tectonophysics, 638*, 177–184. https://doi.org/10.1016/j.tecto.2014.11.006

Baier, J., Audétat, A., and Keppler, H. (2008). The origin of the negative niobium tantalum anomaly in subduction zone magmas. *Earth and Planetary Science Letters, 267*, 290–300. https://doi.org/10.1016/j.epsl.2007.11.032

Beaumont, C., Jamieson, R. A., Butler, J. P., and Warren, C. J. (2009). Crustal structure: A key constraint on the mechanism of ultra-high-pressure rock exhumation. *Earth and Planetary Science Letters, 287,* 116–129. https://doi.org/10.1016/j.epsl.2009.08.001

Beaumont, C., Jamieson, R. A., Nguyen, M. H., and Lee, B. (2001). Himalayan tectonics explained by extrusion of a low-viscosity crustal channel coupled to focused surface denudation. *Nature, 414*, 738-742. https://doi.org/10.1038/414738a

Beaumont, C., Jamieson, R.A., Nguyen, N.H., and Medvedev, S. (2004). Crustal channel flows: 1. Numerical models with applications to the tectonics of the Himalayan-Tibetan orogen. *Journal of Geophysical Research: Solid Earth, 109*, B06406. https://doi.org/10.1029/2003JB002809

Beaumont, C., Nguyen, M. H., Jamieson, R. A., and Ellis, S. (2006). Crustal flow modes in large hot orogens. R. D. Law, M. P. Searle, and L. Godin (Eds.), Channel Flow, Ductile Extrusion and Exhumation in Continental Collision Zones. *Geological Society, London, Special Publications*, 91–145. https://doi.org/10.1144/GSL.SP.2006.268.01.05

Benetti, B., Montomoli, C., Iaccarino, S., Langone, A., and Carosi, R. (2021). Mapping tectono- metamorphic discontinuities in orogenic belts: Implications for mid-crust exhumation in NW Himalaya. *Lithos 392–393*, 106129. https://doi.org/10.1016/j.lithos.2021.106129

Bian, W., Yang, T., Ma, Y., Jin, J., Gao, F., and Zhang, S., (2017). New Early Cretaceous paleomagnetic and geochronological results from the far western Lhasa terrane: Contributions to the Lhasa-Qiangtang collision. *Scientific Reports, 7*, 1–14. https://doi.org/10.1038/ s41598-017-16482-3

Billen, M. I. (2010). Slab dynamics in the transition zone. *Physics of the Earth and Planetary Interiors, 183*, 296–308. https://doi. org/10.1016/j.pepi.2010.05.005.2010

Billington, S., Isacks, B. L., and Barazangi, M. (1977). Spatial distribution and focal mechanisms of mantle earthquakes in the Hindu Kush– Pamir region: A contorted Benioff zone. *Geology, 5*, 699–704. https://doi.org/10.1130/0091-7613(1977)5<699:SDAFMO>2.0.CO;2

Bird, P. (1978). Initiation of intracontinental subduction in the Himalaya. *Journal of Geophysical Research: Solid Earth 85*, 4975–4987. https://doi.org/10.1029/JB083iB10p04975

Bird, P. (1979). Continental delamination and the Colorado Plateau. *Journal of Geophysical Research: Solid Earth*, *84*, 7561–7571. https://doi.org/10.1029/JB084iB13p07561

Borneman, N. L., Hodges, K. V., Soest, M. C., Bohon, W., Wartho, J. A., Cronk, S. S., et al. (2015). Age and structure of the Shyok suture in the Ladakh region of northwestern India: Implications for slip on the Karakoram fault system. *Tectonics, 34*, 2011–2033. https://doi. org/10.1002/2015TC003933

Bouilhol, P., Jagoutz, O., Hanchar, J. M., and Dudas, F. O. (2013). Dating the India–Eurasia collision through arc magmatic records. *Earth and Planetary Science Letters, 366*, 163–175. https://doi.org/10.1016/j.epsl.2013.01.023

Bullen, M. E., Burbank, D. W., Garver, J. I., and Abdrakhmatov, K. Y. (2001). Late Cenozoic tectonic evolution of the northwestern Tien Shan: New age estimates for the initiation of mountain building. *Geological Society of America Bulletin, 113*, 1544–1559. https://doi.org/1 0.1130/0016-7606(2001)113<1544:LCTEOT>2.0.CO;2

Burgess, W.P., Yin, A., Dubey, C.S., Shen, Z.K., and Kelty, T.K. (2012). Holocene shortening across the Main Frontal Thrust zone in the eastern Himalaya. *Earth and Planetary Science Letters*, *357*, 152–167. https://doi-org.ezproxy.library.dal.ca/10.1016/j.epsl.2012.09.040

Burov, E., and Yamato, P. (2008). Continental plate collision, P-T-t-z conditions and unstable vs. stable plate dynamics: Insights from thermo-mechanical modelling. *Lithos, 103*, 178-204. https://doi.org/10.1016/j.lithos.2007.09.014

Burtman, V.S. and Molnar, P. (1993). Geological and geophysical evidence for deep subduction of continental crust beneath the Pamir. *Geological Society of America Special Paper, 281,* 1–76. https://doi.org/10.1130/SPE281-p1

Burtman, V.S. (2000). Cenozoic crustal shortening between the Pamir and Tien Shan and a reconstruction of the Pamir–Tien Shan transition zone for the Cretaceous and Palaeogene. *Tectonophysics, 319*, 69–92. https://doi.org/10.1016/s0040-1951(00)00022-6

Butler, J. P., Beaumont, C., and Jamieson, R. A. (2013). The Alps 1: A working geodynamic model for burial and exhumation of (ultra)high pressure rocks in Alpine-type orogens. *Earth and Planetary Science Letters, 377-378*, 114-131. https://doi.org/10.1016/j.epsl.2013.06.039

Butler, J. P., Beaumont, C., and Jamieson, R. A. (2014). The Alps 2: Controls on crustal subduction and (ultra) high-pressure rock exhumation in Alpine-type orogens. *Journal of Geophysical Research: Solid Earth, 119*, 5987–6022. https://doi.org/10.1002/2013JB010799

Butler, J. P., Beaumont, C., and Jamieson, R. A. (2015). Paradigm lost: Buoyancy thwarted by the strength of the Western Gneiss Region (ultra) high-pressure terrane, Norway. *Lithosphere, 7*, 379–407. https://doi.org/10.1130/L426.1

Capitanio, F.A. and Replumaz, A. (2013). Subduction and slab breakoff controls on Asian indentation tectonics and Himalayan western syntaxis formation. *Geochemistry, Geophysics, Geosystems*, *14*, 3515–3531. https://doi.org/10.1002/ggge.20171

Carosi, R., Montomoli, C., Iaccarino, S., and Visona, D. (2019). Structural evolution, meta-morphism and melting in the greater Himalayan sequence in central-western Nepal. Treloar, P.J., Searle, M.P. (Eds.), Himalayan Tectonics: A Modern Synthesis. *Geological Society, London, Special Publications, 483*, 305–323. https://doi.org/10.1144/SP483.3

Carosi, R., Montomoli, C., Iaccarino, S., Massonne, H.J., Rubatto, D., Langone, A., et al. (2016). Middle to late Eocene exhumation of the greater Himalayan sequence in the central Himalayas: Progressive accretion from the Indian plate. *Geological Society of America Bulletin. 128*, 1571–1592. https://doi.org/10.1130/B31471.1

Carosi, R., Montomoli, C., Rubatto, D., Visonà, D. (2010). Late Oligocene high-temperature shear zones in the core of the Higher Himalayan Crystallines (Lower Dolpo, western Nepal). *Tectonics, 29*, TC4029. https://doi.org/10.1029/2008TC002400

Castillo, P.R. (2012). Adakite petrogenesis. *Lithos*, *134,* 304–316. https://doi.org/10.1016/j.lithos.2011.09.013

Chambers, J., Caddick, M., Argles, T., Horstwood, M., Sherlock, S., Harris, N. (2009). Empirical constraints on extrusion mechanisms from the upper margin of an exhumed high-grade orogenic core, Sutlej valley, NW India. *Tectonophysics 477*, 77–92. https://doi.org/10.1016/j.tecto.2008.10.013

Chapman, J. B., Carrapa, B., Ballato, P., DeCelles, P. G., Worthington, J., Oimahmadov, I., (2017). Intracontinental subduction beneath the Pamir Mountains: Constraints from thermokinematic modeling of shortening in the Tajik fold-and-thrust belt. *Geological Society of America Bulletin, 129*, 1450–1471. https://doi.org/10.1130/B31730.1

Chapman, J.B., and Kapp, P. (2017). Tibetan magmatism database. *Geochemistry, Geophysics, Geosystems, 18*, 4229–4234. https://doi.org/10.1002/2017GC007217

Chapman, J.B., Robinson, A.C., Carrapa, B., Villarreal, D., Worthington, J., DeCelles, P.G., et al. (2018a). Cretaceous shortening and exhumation history of the South Pamir terrane. *Lithosphere*, *10,* 494-511.

Chapman, J. B., Scoggin, S. H., Kapp, P., Carrapa, B., Ducea, M. N., Worthington, J., et al. (2018). Mesozoic to Cenozoic magmatic history of the Pamir. *Earth and Planetary Science Letters, 482*, 181–192. https://doi.org/10.1016/j.epsl.2017.10.041

Chen, J., Wu, J., Xu, J., Dong, Y., Wang, B., and Kang, Z. (2013). Geochemistry of Eocene high-Mg# adakitic rocks in the northern Qiangtang terrane, central Tibet: Implications for early uplift of the plateau. *Geological Society of America Bulletin, 125*, 1800–1819. https://doi.org/10.1130/B30755.1

Chen, J.-L., Wu, J.-B., Xu, J.-F., Dong, Y.-H., Wang, B.-D., and Kang, Z.-Q. (2013), Geochemistry of Eocene high-Mg# adakitic rocks in the northern Qiangtang terrane, central Tibet: Implications for early uplift of the plateau: *Geological Society of America Bulletin, 125*, 1800–1819, https://doi.org/10.1130/B30755.1

Chen, J.-L., Xu, J.-F., Wang, B.-D., and Kang, Z.-Q. (2012), Cenozoic Mg-rich potassic rocks in the Tibetan Plateau: Geochemical variations, heterogeneity of subcontinental lithospheric mantle and tectonic implications: *Journal of Asian Earth Sciences, 53*, 115–130, https://doi.org/10.1016/j.jseaes.2012.03.003

Chen, L., Capitanio, F.A., Liu, L., and Gerya, T.V. (2017). Crustal rheology controls on the Tibetan plateau formation during India-Asia convergence. *Nature Communications*, *8*, 5992. https://doi.org/10.1038/ncomms15992

Chen, L., Liu, L., Capitanio, F.A., Gerya, T.V., and Li, Y. (2020). The role of pre-existing weak zones in the formation of the Himalaya and Tibetan plateau: 3-D thermomechanical modelling. *Geophysical Journal International*, *221*, 1971–1983. https://doi.org/10.1093/gji/ggaa125

Chen, M., Niu, F., Tromp, J., Lenardic, A., Lee, C.- T.A., Cao, W., and Ribeiro, J. (2017), Lithospheric foundering and underthrusting imaged beneath Tibet. *Nature Communications, 8*, 15659. https://doi.org/10.1038/ncomms15659

Chu, M.-F., Chung, S.-L., O'Reilly, S.Y., Pearson, N.J., Wu, F.-Y., Li, X.-H., et al. (2011). India's hidden inputs to Tibetan orogeny revealed by Hf isotopes of Transhimalayan zircons and host rocks: *Earth and Planetary Science Letters, 307*, 479–486. https://doi.org/10.1016/j.epsl.2011.05.020

Chung, S.L., Chu, M. F., Zhang, Y., Xie, Y., Lo, C. H., Lee, T. Y., et al. (2005). Tibetan tectonic evolution inferred from spatial and temporal variations in post-collisional magmatism. *Earth-Science Reviews, 68*. 173–196. https://doi.org/10.1016/j.earscirev.2004.05.001

Chung, S.-L., Liu, D., Ji, J., Chu, M.-F., Lee, H.-Y., Wen, D.-J., et al. (2003). Adakites from continental collision zones: Melting of thickened lower crust beneath southern Tibet: *Geology, 31*, 1021– 1024, https://doi.org/10.1130/G19796.1

Chung, S.-L., Liu, D., Ji, J., Chu, M.-F., Lee, H.-Y., Wen, D.-J., et al. (2003). Adakites from continental collision zones: Melting of thickened lower crust beneath southern Tibet. *Geology*, *31*, 1021–1024. https://doi .org/10.1130/G19796.1

Conrad, C.P. and Molnar, P. (1997). The growth of Rayleigh—Taylor-type instabilities in the lithosphere for various rheological and density structures. *Geophysical Journal International*, *129*, 95-112. https://doi.org/10.1111/j.1365-246X.1997.tb00939.x

Copley, A., Avouac, J.-P., and Wernicke, B. P. (2011). Evidence for mechanical coupling and strong Indian lower crust beneath southern Tibet. *Nature, 472*, 79-81. https://doi.org/10.1038/nature09926

Condie, K.C. (2013). Preservation and recycling of crust during accretionary and collisional phases of Proterozoic orogens: A bumpy road from Nuna to Rodinia. *Geosciences*, *3*, 240–261. https://doi.org/10.3390/geosciences3020240

Cortes, C. and Vapnik, V. (1995). Support-vector networks. *Machine learning, 20,* 273–297.

Coutand, I., Strecker, M. R., Arrowsmith, J. R., Hilley, G., Thiede, R. C., Korjenkov, A., et al. (2002). Late Cenozoic tectonic development of the intramontane Alai Valley, (Pamir-Tien Shan region, central Asia): An example of intracontinental deformation due to the Indo-Eurasia collision. *Tectonics, 21*, 3-1–3-19. https://doi.org/10.1029/2002TC001358

de Sigoyer, J., Guillot, S., Lardeaux, J.M., and Mascle, G. (1997). Glaucophane-bearing eclogites in the Tso Morari dome (eastern Ladakh, NW Himalaya). *European Journal of Mineralogy, 9*, 1073–1083. https://doi.org/10.1127/ejm/9/5/1073

de Sigoyer, J., Chavagnac, V., Blichert-Toft, J., Villa, I.M., Luais, B., Guillot, S., et al. (2000). Dating the Indian continental subduction and collisional thickening in the northwest Himalaya: Multichronology of the Tso Morari eclogites. *Geology 28*, 487–490. https://doi.org/10.1130/0091-7613(2000)28<487:DTICSA>2.0.CO;2

de Sigoyer, J., Guillot, S., and Dick, P. (2004). Exhumation processes of the high-pressure low-temperature Tso Morari dome in a convergent context (eastern Ladakh, NW Himalaya). *Tectonics, 23*, TC3003. https://doi.org/10.1029/2002TC001492

DeCelles, P.G., Gehrels, G.E., Quade, J., and Ojha, T.P. (1998). Eocene-early Miocene foreland basin development and the history of Himalayan thrusting, western and central Nepal. *Tectonics, 17*, 741–765. https://doi.org/10.1029/98TC02598

DeCelles, P.G., Kapp, P., Gehrels, G.E., and Ding, L. (2014). Paleocene-Eocene foreland basin evolution in the Himalaya of southern Tibet and Nepal: Implications for the age of initial India-Asia collision. *Tectonics*, *33*, 824–849. https://doi.org/10.1002/2014TC003522

DeCelles, P.G., Kapp, P., Quade, J., and Gehrels, G.E. (2011). Oligocene–Miocene Kailas basin, southwestern Tibet: record of postcollisional upper-plate extension in the Indus-Yarlung suture zone. *Geological Society of America Bulletin, 123*, 1337–1362. https://doi.org/10.1130 /B30258.1

DeCelles, P.G., Robinson, D.M., and Zandt, G. (2002), Implications of shortening in the Himalayan fold-thrust belt for uplift of the Tibetan Plateau. *Tectonics, 21*, 12-1–12-25, https://doi.org/10.1029/2001TC001322

Dewey, J. F., Shackleton, R. M., Chengfa, C., and Yiyin, S. (1988). The tectonic evolution of the Tibetan Plateau. *Philosophical Transactions of the Royal Society of London – Series A: Mathematical and Physical Sciences, 327*, 379–413. https://doi.org/10.1098/rsta.1988.0135

Ding, H., Kohn, M.J., Zhang, Z. (2021). Long-lived (ca. 22–24 Myr) partial melts in the eastern Himalaya: Petrochronologic constraints and tectonic implications. *Earth and Planetary Science Letters,558*, 116764. https://doi.org/10.1016/j.epsl.2021.116764.

Ding, H., Zhang, Z., Dong, X., Tian, Z., Xiang, H., Mu, H., et al. (2016). Early Eocene (c. 50 Ma) collision of the Indian and Asian continents: Constraints from the North Himalayan metamorphic rocks, southeastern Tibet. *Earth and Planetary Science Letters, 435,* 64–73. https://doi.org/10.1016 /j.epsl.2015.12.006

Ding, H., Zhang, Z., Hu, K., Dong, X., Xiang, H., Mu, H. (2016). P–T–t–D paths of the North Himalayan metamorphic rocks: Implications for the Himalayan orogeny. *Tectonophysics, 683*, 393–404. http://dx.doi.org/10.1016/j.tecto.2016.06.035

Ding, L., Kapp, P., Yue, Y., and Lai, Q. (2007). Postcollisional calc-alkaline lavas and xenoliths from the southern Qiangtang terrane, central Tibet. *Earth and Planetary Science Letters, 254*, 28–38. https://doi.org/10.1016/j.epsl.2006.11.019

Ding, L., Qasim, M., Jadoon, I.A., Khan, M.A., Xu, Q., and Cai, F. (2016). The India–Asia collision in north Pakistan: Insight from the U–Pb detrital zircon provenance of Cenozoic foreland basin. *Earth and Planetary Science Letters, 455,* 49–61. https://doi.org/10.1016/j.epsl.2016.09.003

Dipietro, J. A., Hussain, A., Ahmad, I., and Khan, M. A. (2000). The Main Mantle Thrust in Pakistan: Its character and extent. Asif Khan, M., Treloar, P. J., Searle, M. P., Qasim Jan M. (Eds.), Tectonics of the Nanga Parbat Syntaxis and the Western Himalaya. *Geological Society, London, Special Publications, 170*, 375-393. https://doi.org/10.1144/GSL.SP.2000.170.01.20

Dipietro, J. A., and Pogue, K. R. (2004). Tectonostratigraphic subdivisions of the Himalaya: A view from the west. *Tectonics, 23,* TC5001. https://doi.org/10.1029/2003TC001554

Donaldson, D.G., Webb, A.A.G., Menold, C.A., Kylander-Clark, A.R., and Hacker, B.R. (2013). Petrochronology of Himalayan ultrahigh-pressure eclogite. *Geology*, *41*, 835–838. https://doi.org/10.1130/G33699.1

Doucet, L.S., Tetley, M.G., Li, Z.X., Liu, Y. and Gamaleldien, H. (2022). Geochemical fingerprinting of continental and oceanic basalts: A machine learning approach. *Earth-Science Reviews*, *104192*. https://doi.org/10.1016/j.earscirev.2022.104192

Ducea, M.N., Lutkov, V., Minaev, V.T., Hacker, B., Ratschbacher, L., and Luffi, P. (2003). Building the Pamirs: The view from the underside. *Geology, 31*, 849–852. https://doi.org/10.1130/G19707.1

England, P. and Houseman, G. (1986). Finite strain calculations of continental deformation: 2. Comparison with the India-Asia collision zone. *Journal of Geophysical Research: Solid Earth*, *91*, 3664–3676. https://doi.org/10.1029/JB091iB03p03664

England, P. C., and Houseman, G. A. (1988). The mechanics of the Tibetan Plateau. *Philosophical Transactions of the Royal Society of London – Series A: Mathematical and Physical Sciences, 326*, 301–320. https://doi.org/10.1098/rsta.1988.0089

England, P. C., and Houseman, G. A. (1989). Extension during continental convergence, with application to the Tibetan Plateau. *Journal of Geophysical Research, 94,* 17561–17579. https://doi.org/10.1029/JB094iB12p17561

England, P. and McKenzie, D. (1982). A thin viscous sheet model for continental deformation. *Geophysical Journal International*, *70*, 295–321. https://doi.org/10.1111/j.1365-246X.1982.tb04969.x

England, P., and Molnar, P. (2015). Rheology of the lithosphere beneath the central and western Tien Shan. *Journal of Geophysical Research: Solid Earth, 120*, 3803–3823. https://doi.org/10.1002/2014JB011733

England, P., and Searle, M. (1986). The Cretaceous-Tertiary deformation of the Lhasa block and its implications for crustal thickening in Tibet. *Tectonics 5,* 1-14. https://doi.org/10.1029/TC005i001p00001

Epard, J.-L., and Steck, A. (2008. Structural development of the Tso Morari ultra-high pressure nappe of the Ladakh Himalaya. *Tectonophysics, 451*, 242–264. https://doi.org/10.1016/j.tecto.2007.11.050

Exley, R.A. and Smith, J.V. (1982). The role of apatite in mantle enrichment processes and in the petrogenesis of some alkali basalt suites. *Geochimica et Cosmochimica Acta, 46*, 1375–1384. https://doi.org/10.1016/0016-7037(82)90273-3

Fielding, E., Isacks, B., Barazangi, M., and Duncan, C. (1994). How flat is Tibet? *Geology*, *22*, 63-167. https://doi.org/10.1130/0091-7613(1994)022%3C0163:HFIT%3E2.3.CO;2

Feng, B., Chen, L., Xu, Y. and Zhang, Y. (2022). Comparative study on three autoencoder-based deep learning algorithms for geochemical anomaly identification. *Earth and Space Science, 9*, e2022EA002626. https://doi.org/10.1029/2022EA002626

Fullsack, P. (1995). An arbitrary Lagrangian-Eulerian formulation for creeping flows and its application in tectonic models. *Geophysical Journal International, 120*, 1–23. https://doi.org/10.1111/j.1365-246X.1995.tb05908.x

Gao, S., Rudnick, R.L., Xu, W.L., Yuan, H.L., Liu, Y.S., Walker, R.J., et al. (2008). Recycling deep cratonic lithosphere and generation of intraplate magmatism in the North China Craton. *Earth and Planetary Science Letters, 270,* 41–53. https://doi.org/10.1016/j.epsl.2008.03.008

Gao, L.E., Zeng, L.S., and Xie, K.J. (2012). Eocene high grade metamorphism and crustal anatexis in the North Himalaya Gneiss Domes, Southern Tibet. *Chinese Science Bulletin 57*, 639-650. https://doi: 10.1007/s11434-011-4805-4

Gągała, Ł., Ratschbacher, L., Ringenbach, J.-C., Kufner, S.-K., Schurr, B., Dedow, R., et al. (2020). Tajik Basin and Southwestern Tian Shan, Northwestern India-Asia Collision Zone: 1. Structure, Kinematics, and Salt Tectonics in the Tajik Fold-and-Thrust Belt of the Western Foreland of the Pamir. *Tectonics, 39*, e2019TC005871. https://doi.org/10.1029/2019tc005871

Garzanti, E. (2019). The Himalayan Foreland Basin from collision onset to the present: A sedimentary–petrology perspective, in Treloar, P.J., and Searle, M.P. (Eds.), Himalayan Tectonics: A Modern Synthesis. *Geological Society, London, Special Publications, 483,* https://doi.org/10.1144/SP483.17

Garzanti, E., Radeff, G., and Malusà, M.G. (2018), Slab breakoff: A critical appraisal of a geological theory as applied in space and time. *Earth-Science Reviews, 177*, 303–319, https://doi.org/10.1016/j.earscirev.2017.11.012

Ghazian, R.K. and Buiter, S.J. (2013). A numerical investigation of continental collision styles. *Geophysical Journal International*, *193*, 1133–1152. https://doi.org/10.1093/gji/ggt068

Girard, M. (2001). Metamorphism and tectonics of the transition between non-metamorphic Tethyan Himalaya sediments and the North Himalayan Crystalline Zone (Rupshu area, Ladakh, NW India). *Memoires de Géologie (Lausanne) 35*, 1–100.

Gleason, G. C., and Tullis, J. (1995). A flow law for dislocation creep of quartz aggregates determined with the molten salt cell. *Tectonophysics, 247*, 1-23. https://doi.org/10.1016/0040-1951(95)00011-B

Griffin, W. L., O'Reilly, S. Y., Afonso, J. C., and Begg, G. C. (2009). The composition and evolution of lithospheric mantle: a re-evaluation and its tectonic implications. *Journal of Petrology, 50*, 1185–1204. https://doi.org/10.1093/petrology/egn033

Griffin, W.L., O'reilly, S.Y., Afonso, J.C., and Begg, G.C. (2009). The composition and evolution of lithospheric mantle: a re-evaluation and its tectonic implications. *Journal of Petrology, 50,* 1185–1204. https://doi.org/10.1093/petrology/egn033

Groppo, C., Lombardo, B., Rolfo, F., and Pertusati, P. (2007). Clockwise exhumation path of granulitized eclogites from the Ama Drime range (Eastern Himalayas). *Journal of Metamorphic Geology, 25*, 51–75. https://doi.org/10.1111/j.1525-1314.2006.00678.x.

Groppo, C., Rubatto, D., Rolfo, F., and Lombardo, B. (2010). Early Oligocene partial melting in the Main Central Thrust Zone (Arun valley, eastern Nepal Himalaya). *Lithos 118*, 287–301. https://doi.org/10.1016/j.lithos.2010.05.003

Guan, Q., Ren, S., Chen, L., Yao, Y., Hu, Y., Wang, R., Feng, B., et al. (2022). Recognizing multivariate geochemical anomalies related to mineralization by using deep unsupervised graph learning. *Natural Resources Research, 31*, 2225–2245. https://doi.org/10.1007/s11053-022-10088-x

Guillot, S., and Allemand, P. (2002). Two-dimensional thermal modelling of the early tectonometamorphic evolution in central Himalaya. *Journal of Geodynamics, 34*, 77–98. https://doi.org/10.1016/S0264-3707(02)00016-9

Guillot, S., de Sigoyer, J., Lardeaux, J.M., and Mascle, G. (1997). Eclogitic metasediments from the Tso Morari area (Ladakh, Himalaya): evidence for continental subduction during India–Asian convergence. *Contributions to Mineralogy and Petrology, 128*, 197–212. https://doi.org/10.1007/ s004100050303

Guo, X., Gao, R., Zhao, J., Xu, X., Lu, Z., Klemperer, S.L., and Liu, H. (2018). Deep-seated lithospheric geometry in revealing collapse of the Tibetan Plateau. *Earth-Science Reviews*, *185*, 751–762. https://doi.org/10.1016/j.earscirev.2018.07.013

Guo, Z., Wilson, M., Liu, J., and Mao, Q. (2006). Post-collisional, potassic and ultrapotassic magmatism of the northern Tibetan Plateau: Constraints on characteristics of the mantle source, geodynamic setting and uplift mechanisms. *Journal of Petrology*, *47*, 1177–1220. https://doi.org/10.1093/ petrology/egl007

Guo, Z., Wilson, M., Zhang, M., Cheng, Z., and Zhang, L. (2015). Post-collisional ultrapotassic mafic magmatism in South Tibet: Products of partial melting of pyroxenite in the mantle wedge induced by roll-back and delamination of the subducted Indian continental lithosphere slab. *Journal of Petrology, 56*, 1365–1406. https://doi.org/10.1093/petrology/egv040

Hacker, B.R., Gnos, E., Ratschbacher, L., Grove, M., McWilliams, M., Sobolev, S.V., et al. (2000). Hot and dry deep crustal xenoliths from Tibet: *Science*, *287*, 2463–2466. https://doi.org/10.1126/science.287.5462.2463

Hacker, B.R., Ratschbacher, L., Rutte, D., Stearns, M.A., Malz, N., Stübner, K., et al. (2017). Building the Pamir–Tibet Plateau—Crustal stacking, extensional collapse, and lateral extrusion in the Pamir: 3. Thermobarometry and Petrochronology of Deep Asian Crust. *Tectonics, 36,* 1743–1766. https://doi.org/10.1002/2017TC004488

Harrison, T.M. and Watson, E.B. (1984). The behavior of apatite during crustal anatexis: equilibrium and kinetic considerations. *Geochimica et Cosmochimica Acta, 48*, 1467–1477. https://doi.org/10.1016/0016-7037(84)90403-4

Heermance, R. V., Chen, J., Burbank, D. W., and Wang, C. (2007). Chronology and tectonic controls of Late Tertiary deposition in the southwestern Tian Shan foreland, NW China. *Basin Research, 19*, 599–632. https://doi.org/10.1111/j.1365-2117.2007.00339.x

Heintz, M., Kumar, V.P., Gaur, V.K., Priestley, K., Rai, S.S., and Prakasam, K.S. (2009). Anisotropy of the Indian continental lithospheric mantle. *Geophysical Journal International, 179,* 1341–1360. https://doi.org/10.1111/j.1365-246X.2009.04395.x

Hirth, G., and Kohlstedt, D. L. (1996). Water in the oceanic upper mantle: implications for rheology, melt extraction and the evolution of the lithosphere. *Earth and Planetary Science Letters, 144*, 93–108. https://doi.org/10.1016/0012-821X(96)00154-9

Hodges, K. V. (2000). Tectonics of the Himalaya and southern Tibet from two perspectives. *Geological Society of America Bulletin, 112*, 324–350. https://doi.org/10.1130/0016-7606(2000)112<324:TOTHAS>2.0.CO;2

Hodges, K.V. and Silverberg, D.S. (1988). Thermal evolution of the greater Himalaya, Garwhal, India. *Tectonics, 7*, 583–600. https://doi.org/10.1029/TC007i003p00583

Houseman, G.A., McKenzie, D.P., and Molnar, P. (1981). Convective instability of a thickened boundary layer and its relevance for the thermal evolution of continental convergent belts. *Journal of Geophysical Research: Solid Earth*, *86,* 6115–6132. https://doi.org/10.1029/JB086iB07p06115

Houseman, G. and England, P. (1986). Finite strain calculations of continental deformation: 1. Method and general results for convergent zones. *Journal of Geophysical Research: Solid Earth*, *91*, 3651–3663. https://doi.org/10.1029/JB091iB03p03664

Houseman, G.A. and Molnar, P. (1997). Gravitational (Rayleigh–Taylor) instability of a layer with non-linear viscosity and convective thinning of continental lithosphere. *Geophysical Journal International*, *128*, 125–150. https://doi.org/10.1111/j.1365-246X.1997.tb04075.x

Hsu, C.W., Chang, C.C., and Lin, C.J. (2003). A practical guide to support vector classification. https://www.datascienceassn.org/sites/default/files/Practical%20Guide%20to%20Support%20Vector%20Classification.pdf

Hu, X., Garzanti, E., Moore, T., and Raffi, I. (2015). Direct stratigraphic dating of India-Asia collision onset at the Selandian (middle Pale- ocene, 59 ± 1 Ma). *Geology, 43*, 859–862. https://doi.org/10.1130/G36872.1

Hu, X., Garzanti, E., Wang, J., Huang, W., An, W., and Webb, A. (2016). The timing of India-Asia collision onset - Facts, theories, controversies. *Earth-Science Reviews, 160*, 264–299. https://doi.org/10.1016/j.earscirev.2016.07.014

Huang, W., Lippert, P. C., Zhang, Y., Jackson, M. J., Dekkers, M. J., Li, J., et al. (2017). Remagnetization of carbonate rocks in southern Tibet: Perspectives from rock magnetic and petrographic investigations. *Journal of Geophysical Research: Solid Earth, 122*, 2434–2456. https://doi.org/10.1002/2017JB013987

Huangfu, P., Li, Z.H., Gerya, T., Fan, W., Zhang, K.J., Zhang, H., and Shi, Y. (2018). Multi-terrane structure controls the contrasting lithospheric evolution beneath the western and central–eastern Tibetan plateau. *Nature Communications, 9,* 3780. https://doi.org/10.1038/s41467-018-06233-x

Hubbard, M.S., Spencer, D.A., and West, D.P. (1995). Tectonic exhumation of the Nanga Parbat massif, northern Pakistan. *Earth and Planetary Science Letters, 133*, 213–225. https://doi.org/10.1016/0012- 821X(95)00075-N.

Huismans, R. and Beaumont, C. (2011). Depth-dependent extension, two-stage breakup and cratonic underplating at rifted margins. *Nature, 473*, 74-78. https://doi.org/10.1038/nature09988

Iaccarino, S., Montomoli, C., Carosi, R., Massonne, H.-J., Langone, A., and Visonà, D. (2015). Pressure–temperature–time–deformation path of kyanite-bearing migmatitic paragneiss in the Kali Gandaki valley (Central Nepal): investigation of Late Eocene–Early Oligocene melting processes. *Lithos, 231*, 103–121. http://dx.doi.org/10.1016/j.lithos.2015.06.005

Imayama, T., Takeshita, T., Keewook, Y., Cho, D.-L., Kitajima, K., Tsutsumi, Y., et al. (2012). Two-stage partial melting and contrasting cooling history within the Higher Himalayan Crystalline Sequence in the far eastern Nepal Himalaya. *Lithos, 134–135,* 1–22. https://doi.org/10.1016/j.lithos.2011.12.004

Imayama, T., Takeshita, T., Yi, K., and Fukuyama, M. (2018). Early Oligocene partial melting via biotite dehydration melting and prolonged low-pressure–low-temperature metamorphism of the upper High Himalaya Crystalline Sequence in the far east of Nepal. In: Sharma, R., Villa, I.M., Kumar, S. (Eds.), Crustal Architecture and Evolution of the Himalaya–Karakoram–Tibet Orogen. *Geological Society, London, Special Publications*, *481,* 147-173. https://doi.org/10.1144/SP481.2

Ingalls, M., Rowley, D.B., Currie, B., and Colman, A.S. (2016). Large-scale subduction of continental crust implied by India-Asia mass-balance calculation. *Nature Geoscience, 9,* 848–853. https://doi.org/10.1038/ngeo2806

Jadoon, I. A., and Khurshid, A. (1996). Gravity and tectonic model across the Sulaiman fold belt and the Chaman fault zone in western Pakistan and eastern Afghanistan. *Tectonophysics, 254*, 89–109. https://doi.org/10.1016/0040-1951(95)00078-X

Jamieson, R.A. and Beaumont, C. (2013). On the origin of orogens. *Geological Society of America Bulletin, 125,* 1671–1702. https://doi.org/10.1130/B30855.1

Jamieson, R.A., Beaumont, C., Medvedev, S., and Nguyen, M.H. (2004). Crustal channel flows: 2. Numerical models with implications for metamorphism in the Himalayan-Tibetan orogen. *Journal of Geophysical Research: Solid Earth, 109*, B06407. https://doi.org/10.1029/2003JB002811

Jessup, M.J., Langille, J.M., Diedesch, T.F., and Cottle, J.M. (2019). Gneiss dome formation in the Himalaya and southern Tibet. Treloar, P. J. and Searle, M. P. (Eds.), Himalayan Tectonics: A Modern Synthesis. *Geological Society, London, Special Publications, 483*, 401–422. https://doi.org/10.1144/SP483.15

Ji, W.Q., Wu, F.Y., Chung, S.L., Wang, X.C., Liu, C.Z., Li, Q.L., et al (2016). Eocene Neo-Tethyan slab breakoff constrained by 45 Ma oceanic island basalt–type magmatism in southern Tibet. *Geology*, *44,* 283–286. https://doi.org/10.1130/G37612.1

Jiang, T., Aitchison, J.C., and Wan, X. (2016). The youngest marine deposits preserved in southern Tibet and disappearance of the Tethyan Ocean. *Gondwana Research, 32*, 64–75. https://doi.org/10.1016/j.gr.2015.01.015

Kameyama, M., Yuen, D. A., and Karato, S. I. (1999). Thermal-mechanical effects of low-temperature plasticity (the Peierls mechanism) on the deformation of a viscoelastic shear zone. *Earth and Planetary Science Letters, 168*, 159–172. https://doi.org/10.1016/S0012-821X(99)00040-0

Kaneko, Y., Katayama, I., Yamamoto, H., Misawa, K., Ishikawa, M., Rehman, H.U., et al. (2003). Timing of Himalayan ultrahigh-pressure metamorphism: sinking rate and subduction angle of the Indian continental crust beneath Asia. *Journal of Metamorphic Geology ,21*, 589–599. https://doi.org/10.1046/j.1525-1314.2003.00466.x

Kapp, P. and DeCelles, P.G. (2019). Mesozoic–Cenozoic geological evolution of the Himalayan-Tibetan orogen and working tectonic hypotheses. *American Journal of Science*, *319*, 159–254. https://doi.org/10.2475/03.2019.01

Kapp, P., DeCelles, P.G., Gehrels, G.E., Heizler, M. and Ding, L. (2007). Geological records of the Lhasa-Qiangtang and Indo-Asian collisions in the Nima area of central Tibet. *Geological Society of America Bulletin, 119*, 91–933. https://doi.org/10.1130/B26033.1

Kapp, P., DeCelles, P.G., Leier, A.L., Fabijanic, J.M., He, S., Pullen, A., Gehrels, G.E., and Ding, L. (2007). The Gangdese retroarc thrust belt revealed. *GSA today*, *17*, 4.

Kapp, P., Yin, A., Harrison, T.M., and Ding, L. (2005). Cretaceous-Tertiary shortening, basin development, and volcanism in central Tibet. *Geological Society of America Bulletin., 117*, 865–878. https://doi.org/10.1130/B25595.1

Kapp, P., Yin, A., Manning, C.E., Murphy, M., Harrison, T.M., Spurlin, M., et al. (2000). Blueschist-bearing metamorphic core complexes in the Qiangtang block reveal deep crustal structure of northern Tibet: *Geology, 28,* 19–22. https://doi.org/10.1130/0091-7613(2000)28<19:BMCCIT>2.0.CO;2

Kapp, P., Yin, A., Manning, C.E., Harrison, T.M., Taylor, M.H., and Ding, L. (2003). Tectonic evolution of the early Mesozoic blueschist-bearing Qiangtang metamorphic belt, central Tibet. *Tectonics, 22*, 1043–1054. https://doi.org/10.1029/2002TC001383

Karato, S. and Wu, P. (1993). Rheology of the upper mantle: a synthesis. *Science, 260,* 771–778. https://doi: 10.1126/science.260.5109.771

Katayama, I., and Karato, S. I. (2008). Low-temperature, high-stress deformation of olivine under water-saturated conditions. *Physics of the Earth and Planetary Interiors, 168*, 125-133. https://doi.org/10.1016/j.pepi.2008.05.019

Kay, R.W. and Kay, S.M. (1993). Delamination and delamination magmatism. *Tectonophysics, 219,* 177–189. https://doi.org/10.1016/0040-1951(93)90295-U

Kelly, S., Butler, J.P., and Beaumont, C. (2016). Continental collision with a sandwiched accreted terrane: Insights into Himalayan–Tibetan lithospheric mantle tectonics? *Earth and Planetary Science Letters, 455,* 176–195. https://doi.org/10.1016/j.epsl.2016.08.039

Kelly, S., Beaumont, C. and Butler, J.P. (2020). Inherited terrane properties explain enigmatic post-collisional Himalayan-Tibetan evolution. *Geology, 48*, 8–14. https://doi.org/10.1130/G46701.1

Kelly, S. and Beaumont, C. (2021). Balanced cross-sections and numerical modeling of the lithospheric-scale evolution of the Hindu Kush and Pamir. *Journal of Geophysical Research: Solid Earth*, *126*, e2020JB020678. https://doi.org/10.1029/2020JB020678

Kellett, D.A., Cottle, J.M., and Smit, M. (2014). Eocene deep crust at Ama Drime, Tibet: early evolution of the Himalayan orogeny. *Lithosphere, 6*, 220–229. https://doi.org/10.1130/L350.1

Kellett, D.A., Cottle, J.M., and Larson, K.P. (2019). The South Tibetan Detachment System: history, advances, definition and future directions. Treloar, P. J. and Searle, M. P. (Eds.), Himalayan Tectonics: A Modern Synthesis. *Geological Society, London, Special Publications, 481*, 377-400. https://doi.org/10.1144/SP483.2

Khanal, G. P., Wang, J.-M., Larson, K.P., Wu, F.-Y., Rai, S. M., Wang, J.-G., and Yang, L., (2021). Eocene metamorphism and anatexis in the Kathmandu klippe, central Nepal: implications for early crustal thickening and initial rise of the Himalaya. *Tectonics, 40*, e2020TC006532; https://doi.org/10.1029/2020TC006532

Klemperer, S.L., Kennedy, B.M., Sastry, S.R., Makovsky, Y., Harinarayana, T., and Leech, M.L. (2013). Mantle fluids in the Karakoram fault: Helium isotope evidence. *Earth and Planetary Science Letters*, *366*, 59–70. https://doi.org/10.1016/j.epsl.2013.01.013

Kohn, M.J., and Corrie, S.L. (2011). Preserved Zr-temperatures and U–Pb ages in high-grade metamorphic titanite: evidence for a static hot channel in the Himalayan orogen. *Earth and Planetary Science Letters, 311*,136–143. https://doi.org/10.1016/j.epsl.2011.09.008

Kooijman, E., Smit, M. A., Ratschbacher, L., and Kylander-Clark, A. R. (2017). A view into crustal evolution at mantle depths. *Earth and Planetary Science Letters, 465*, 59–69. https://doi.org/10.1016/j.epsl.2017.02.032

Kosarev, G., Kind, R., Sobolev, S.V., Yuan, X., Hanka, W., and Oreshin, S. (1999). Seismic evidence for a detached Indian lithospheric mantle beneath Tibet. *Science, 283*, 1306–1309, https://doi.org/10.1126/science.283.5406.1306

Koulakov, I. (2011). High-frequency P and S velocity anomalies in the upper mantle beneath Asia from inversion of worldwide traveltime data. *Journal of Geophysical Research, 116*, B04301. https://doi.org/10.1029/2010JB007938

Koulakov, I., Gerya, T., Rastogi, B.K., Jakovlev, A, Medved, I., Kayal, J.R., et al. (2018). Growth of mountain belts in central Asia triggers a new collision zone in central India, *Scientific Reports, 8*, 10710. https://doi.org/10.1038/s41598-018-29105-2

Koulakov, I., and Sobolev, S. V. (2006). A tomographic image of Indian lithosphere break-off beneath the Pamir–Hindukush region. *Geophysical Journal International, 164*, 425–440. https://doi.org/10.1111/j.1365-246X.2005.02841.x

Kouketsu, Y., Hattori, K., Guillot, S., and Rayner, N. (2016). Eocene to Oligocene retrogression and recrystallization of the Stak eclogite in northwest Himalaya. *Lithos, 240–243*, 155–166. https://doi.org/10.1016/j.lithos.2015.10.022

Kufner, S.-K., Schurr, B., Haberland, C., Zhang, Y., Saul, J., Ischuk, A., et al. (2017). Zooming into the Hindu Kush slab break-off: A rare glimpse on the terminal stage of subduction. *Earth and Planetary Science Letters, 461*, 127–140. https://doi.org/10.1016/j.epsl.2016.12.043

Kufner, S.-K., Schurr, B., Sippl, C., Yuan, X., Ratschbacher, L., Ischuk, A., et al. (2016). Deep India meets deep Asia: Lithospheric indentation, delamination and break-off under Pamir and Hindu Kush (Central Asia). *Earth and Planetary Science Letters, 435,* 171–184. https://doi.org/10.1016/j.epsl.2015.11.046

Kumar D. (2019) Demystifying Support Vector Machines, Towards Data Science. https://towardsdatascience.com/demystifying-support-vector-machines-8453b39f7368

Lammie, D., McQuarrie, N., and Sak, P.B. (2020). Quantifying shortening across the central Appalachian fold-thrust belt, Virginia and West Virginia, USA: Reconciling grain-, outcrop-, and map-scale shortening. *Geosphere*, *16*, 1276-1292. https://doi.org/10.1130/GES02016.1

Lanari, P., Riel, N., Guillot, S., Vidal, O., Schwartz, S., Pecher, A., and Hattori, K.H. (2013). Deciphering highpressure metamorphism in collisional context using microprobe mapping methods: application to the Stak eclogitic massif (northwest Himalaya*). Geology 41*, 111–114. https://doi.org/10.1130/G33523.1

Langille, J.M., Jessup, M.J., Cottle, J.M., Lederer, G., and Ahmad, T. (2012). Timing of metamorphism, melting and exhumation of the Leo Pargil dome, northwest India. *Journal of Metamorphic Geology, 30*, 769–791. https://doi.org/10.1111/j.1525-1314.2012.00998.x

Laskowski, A.K., Kapp, P., and Cai, F. (2018). Gangdese culmination model: Oligocene–Miocene duplexing along the India-Asia suture zone, Lazi region, southern Tibet. *Geological Society of America Bulletin, 130*, 1355–1376. https://doi.org/10.1130/B31834.1

Laskowski, A.K., Kapp, P., Ding, L., Campbell, C., and Liu, X.H. (2017). Tectonic evolution of the Yarlung suture zone, Lopu Range region, southern Tibet. *Tectonics, 36*, 108–136. https://doi.org/10.1002/2016TC004334

Le Fort, P., (1996). Evolution of the Himalaya. In: Yin, A., Harrison, T.M. (Eds.), The Tectonics of Asia. *Cambridge University Press*, New York, 95–106

Lee, C.-T. A. (2003). Compositional variation of density and seismic velocities in natural peridotites at STP conditions: Implications for seismic imaging of compositional heterogeneities in the upper mantle. *Journal of Geophysical Research: Solid Earth, 108,* https://doi.org/10.1029/2003JB002413

Lee, H.-Y., Chung, S.-L., Ji, J., Qian, Q., Gallet, S., Lo, C.-H., Lee, T.-Y., and Zhang, Q. (2012). Geochemical and Sr–Nd isotopic constraints on the genesis of the Cenozoic Linzizong volcanic successions, southern Tibet. *Journal of Asian Earth Sciences, 53*, 96–114. https://doi.org/10.1016/j.jseaes.2011.08.019

Lee, H.-Y., Chung, S.-L., Lo, C.-H., Ji, J., Lee, T.-Y., Qian, Q., and Zhang, Q. (2009). Eocene Neotethyan slab breakoff in southern Tibet inferred from the Linzizong volcanic record. *Tectonophysics*, *477*, 20–35. https://doi.org/10.1016/j.tecto.2009.02.031

Lee, J., Hacker, B., and Wang, Y. (2004). Evolution of North Himalayan gneiss domes: structural and metamorphic studies in Mabja Dome, southern Tibet. *Journal of Structural Geology*, *26*, 2297–2316. https://doi.org/10.1016/j.jsg.2004.02.013

Lee, J., and Whitehouse, M.J. (2007). Onset of mid-crustal extensional flow in southern Tibet: Evidence from U/Pb zircon ages. *Geology 35*, 45–48. https://doi.org/10.1130/G22842A.1

Leech, M.L., Singh, T.S., Jain, A.K., Klemperer, S.L., and Manickavasagam, R.M. (2005). The onset of India–Asia continental collision: Early, steep subduction required by the timing of UHP metamorphism in the western Himalaya. *Earth and Planetary Science Letters*, *234*, 83–97. https://doi.org/10.1016/j.epsl.2005.02.038

Li, C., van der Hilst, R.D., Meltzer, A.S., and Engdahl, R.E. (2008), Subduction of the Indian lithosphere beneath the Tibetan Plateau and Burma. *Earth and Planetary Science Letters, 274*, 157–168. https://doi.org/10.1016/j.epsl.2008.07.016

Li, L., Garzione, C.N., Pullen, A., Zhang, P., and Li, Y. (2018). Late Cretaceous–Cenozoic basin evolution and topographic growth of the Hoh Xil Basin, central Tibetan Plateau. *Geological Society of America Bulletin*, *130*, 499–521. https://doi.org/10.1130/B31769.1

Li, Z., Ding, L., Lippert, P. C., Song, P., Yue, Y., and van Hinsbergen, D. J. (2016). Paleomagnetic constraints on the Mesozoic drift of the Lhasa terrane (Tibet) from Gondwana to Eurasia. *Geology, 44*, 727–730. https://doi.org/10.1130/G38030.1

Li, Z. H., Liu, M., and Gerya, T. (2016). Lithosphere delamination in continental collisional orogens: A systematic numerical study. *Journal of Geophysical Research: Solid Earth, 121*, 5186–5211. https://doi.org/10.1002/2016JB013106

Liao, J., and Gerya, T. (2017). Partitioning of crustal shortening during continental collision: 2-D thermomechanical modeling. *Journal of Geophysical Research Solid Earth, 122*, 592 606. https://doi.org/10.1002/2016JB013398

Lindsay, J.J., Hughes, H.S., Yeomans, C.M., Andersen, J.C. and McDonald, I. (2021). A machine learning approach for regional geochemical data: Platinum-group element geochemistry vs geodynamic settings of the North Atlantic Igneous Province. *Geoscience Frontiers, 12*, 101098. https://doi.org/10.1016/j.gsf.2020.10.005

Lippitsch, R., Kissling, E., and Ansorge, J. (2003). Upper mantle structure beneath the Alpine orogen from high-resolution teleseismic tomography. *Journal of Geophysical Research, 108*, 2376. https://doi.org/10.1029/2002JB002016

Lister, G., Kennett, B., Richards, S., and Forster, M. (2008). Boudinage of a stretching slablet implicated in earthquakes beneath the Hindu Kush. *Nature Geoscience, 1,* 196–201. https://doi.org/10.1038/ngeo132

Liu, A.L., Wang, Q., Zhu, D.C., Cawood, P.A., Xia, Y., Li, S.M., et al. (2022). Temporal and spatial variations of enriched source components in Linzizong volcanic succession, Tibet, and implications for the India–Asia collision. *Journal of Petrology, 63*, egab103. https://doi.org/10.1093/petrology/egab103

Liu, D., et al. (2014). Postcollisional potassic and ultrapotassic rocks in southern Tibet: Mantle and crustal origins in response to India–Asia collision and convergence. *Geochimica et Cosmochimica Acta*, *143*, 207–231. https://doi.org/10.1016/j.gca.2014.03.031

Liu, D., Zhao, Z., Zhu, D.C., Niu, Y., DePaolo, D.J., Harrison, T.M., et al. (2014). Postcollisional potassic and ultrapotassic rocks in southern Tibet: Mantle and crustal origins in response to India–Asia collision and convergence. *Geochimica et Cosmochimica Acta 143*, 207–231. https://doi.org/10.1016/j.gca.2014.03.031

Liu, D., Zhao, Z., DePaolo, D.J., Zhu, D.-C., Meng, F.- Y., Shi, Q., and Wang, Q. (2017), Potassic volcanic rocks and adakitic intrusions in southern Tibet: Insights into mantle-crust interaction and mass transfer from Indian plate: Lithos, v. 268, p. 48– 64, https://doi.org/10.1016/j.lithos.2016.10.034

Lombardo, B., and Rolfo, F., (2000). Two contrasting eclogite types in the Himalayas: implications for the Himalayan orogeny. *Journal of Geodynamics,* 30, 37–60. https://doi.org/10.1016/S0264-3707(99)00026-5

Long, S.P., McQuarrie, N., Tobgay, T., Coutand, I., Cooper, F.J., Reiners, P.W., et al. (2012). Variable shortening rates in the eastern Himalayan thrust belt, Bhutan: Insights from multiple thermochronologic and geochronologic data sets tied to kinematic reconstructions. *Tectonics*, *31,* TC5004. https://doi.org/10.1029/2012TC003155

Ma, L., Wang, Q., Li, Z.-X., Wyman, D.A., Yang, J.-H., Jiang, Z.-Q., et al. (2017), Subduction of Indian continent beneath southern Tibet in the latest Eocene (~35 Ma): Insights from the Quguosha gabbros in southern Lhasa block. *Gondwana Research, 41*, 77–92, https://doi.org/10.1016/j.gr.2016.02.005

Ma, X., Attia, S., Cawood, T., Cao, W., Xu, Z. and Li, H. (2022). Arc tempos of the Gangdese batholith, southern Tibet. *Journal of Geodynamics, 149*, 101897. https://doi.org/10.1016/j.jog.2022.101897

Mackwell, S. J., Zimmerman, M. E., and Kohlstedt, D. L. (1998). High-temperature deformation of dry diabase with application to tectonics on Venus. *Journal of Geophysical Research, 103*, 975-984. https://doi.org/10.1029/97JB02671

Marrett, R. and Allmendinger, R.W. (1992). Amount of extension on "small" faults: An example from the Viking graben. *Geology*, *20*, 47-50. https://doi.org/10.1130/0091-7613(1992)020%3C0047:AOEOSF%3E2.3.CO;2

Martin, A.J. (2017). A review of Himalayan stratigraphy, magmatism, and structure. *Gondwana Research, 49*, 42–80. https://doi.org/10.1016/j.gr.2017.04.031

Massonne, H. J., and Fockenberg, T. (2012). Melting of metasedimentary rocks at ultrahigh pressure - Insights from experiments and thermodynamic calculations. *Lithosphere, 4,* 269–285. https://doi.org/10.1130/L185.1

Mckenzie, D. A. N., and Bickle, M. J. (1988). The volume and composition of melt generated by extension of the lithosphere. *Journal of Petrology, 29*, 625–679. https://doi.org/10.1093/petrology/29.3.625

Mechie, J., Yuan, X., Schurr, B., Schneider, F., Sippl, C., Ratschbacher, L., et al. (2012). Crustal and uppermost mantle velocity structure along a profile across the Pamir and southern Tien Shan as derived from project TIPAGE wide-angle seismic data. *Geophysical Journal International, 188*, 385–407. https://doi.org/10.1111/j.1365-246X.2011.05278.x

Mei, S., Suzuki, A. M., Kohlstedt, D. L., Dixon, N. A., and Durham, W. B. (2010). Experimental constraints on the strength of the lithospheric mantle. *Journal of Geophysical Research, 115*, B08204. https://doi.org/10.1029/2009JB006873

Molnar, P. (1988). Continental tectonics in the aftermath of plate tectonics. *Nature, 335,* 131–137. https://doi.org/10.1038/335131a0

Molnar, P. and Bendick, R. (2019). Seismic moments of intermediate-depth earthquakes beneath the Hindu Kush: Active stretching of a blob of sinking thickened mantle lithosphere? *Tectonics*, *38*, 1651–1665. https://doi.org/10.1029/2018TC005336

Molnar, P., England, P., and Martinod, J. (1993). Mantle dynamics, uplift of the Tibetan Plateau, and the Indian monsoon. *Reviews of Geophysics, 31,* 357–396. https://doi.org/10.1029/93RG02030

Murphy, M.A., Yin, A., Harrison, T.M., Durr, S.B., Ryerson, F.J., and Kidd, W.S.F. (1997). Did the Indo-Asian collision alone create the Tibetan plateau? *Geology*, *25*, 719-722. https://doi.org/10.1130/0091-7613(1997)025%3C0719:DTIACA%3E2.3.CO;2

Najman, Y., Appel, E., Boudagher-Fadel, M., Bown, P., Carter, A., Garzanti, E., et al. (2010). Timing of India-Asia collision: geological, biostratigraphic, and palaeomagnetic constraints. *Journal of Geophysical Research: Solid Earth, 115*, B12416. http://dx.doi.org/10.1029/2010JB007673

Najman, Y., Jenks, D., Godin, L., Boudagher-Fadel, M., Millar, I., Garzanti, E., et al. (2017). The Tethyan Himalayan detrital record shows that India–Asia terminal collision occurred by 54 Ma in the Western Himalaya. *Earth and Planetary Science Letters, 459*, 301–310. https://doi.org/10.1016/j.epsl.2016.11.036

Negredo, A. M., Replumaz, A., Villaseñor, A., and Guillot, S. (2007). Modeling the evolution of continental subduction processes in the Pa- mir-Hindu Kush region. *Earth and Planetary Science Letters, 259*, 212–225. https://doi.org/10.1016/j.epsl.2007.04.043

Neil, E.A. and Houseman, G.A. (1997). Geodynamics of the Tarim Basin and the Tian Shan in central Asia. *Tectonics*, *16*, 571–584. https://doi.org/10.1029/97TC01413

Nomade, S., Renne, P.R., Mo, X., Zhao, Z., and Zhou, S. (2004). Miocene volcanism in the Lhasa block, Tibet: Spatial trends and geodynamic implications. *Earth and Planetary Science Letters, 221*, 227–243, https://doi.org/10.1016/S0012-821X(04)00072-X

Nunn, C., Roecker, S.W., Tilmann, F.J., Priestley, K.F., Heyburn, R., Sandvol, E.A., et al. (2014). Imaging the lithosphere beneath NE Tibet: eleseismic P and S body wave tomography incorporating surface wave starting models. *Geophysical Journal International, 196,* 1724–1741. https://doi.org/10.1093/gji/ggt476

O'Brien, P. J. (2019). Eclogites and other high-pressure rocks in the Himalaya: a review. In: Treloar, P.J., Searle, M.P. (Eds.), Himalayan Tectonics: A Modern Synthesis *Geological Society, London, Special Publications, 483,* 183–213. https://doi.org/10.1144/SP483.13

O'Brien, P.J., Zotov, N., Law, R., Khan, M.A., and Jan, M.Q. (2001). Coesite in Himalayan eclogite and implications for models of India–Asia collision. *Geology, 29*, 435–438. https://doi.org/10.1130/0091-7613(2001)029<0435:CIHEAI>2.0.CO;2.

Orme, D.A. (2019). Burial and exhumation history of the Xigaze forearc basin, Yarlung suture zone, Tibet. *Geoscience Frontiers, 10,* 895–908. https://doi.org/10.1016/j.gsf.2017.11.011

Ou, Q., Wang, Q., Wyman, D.A., Zhang, H.-X., Yang, J.-H., Zeng, J.-P., et al. (2017). Eocene adakitic porphyries in the central-northern Qiangtang Block, central Tibet: Partial melting of thickened lower crust and implications for initial surface uplifting of the plateau. *Journal of Geophysical Research: Solid Earth*, *122*, 1025–1053. https://doi.org/10.1002/2016JB013259

Owens, T.J. and Zandt, G. (1997). Implications of crustal property variations for models of Tibetan plateau evolution. *Nature, 387,* 37–43. https://doi.org/10.1038/387037a0

Palin, R.M., Reuber, G.S., White, R.W., Kaus, B.J.P., and Weller, O.M. (2017). Subduction metamorphism in the Himalayan ultrahigh-pressure Tso Morari massif: an integrated geodynamic and petrological modelling approach. *Earth and Planetary Science Letters, 467*, 108–119. https://doi.org/10.1016/j.epsl.2017.03.029

Pang, Y., Zhang, H., Gerya, T.V., Liao, J., Cheng, H., Shi, Y. (2018). The mechanism and dynamics of N-S rifting in Southern Tibet: Insight from 3-D thermomechanical modeling. *Journal of Geophysical Research; Solid Earth, 23*, 859-877. https://doi.org/10.1002/2017JB014011

Parrish, R.R., Gough, S.J., Searle, M.P., and Waters, D.J. (2006). Plate velocity exhumation of ultrahigh-pressure eclogites in the Pakistan Himalaya. *Geology, 34*, 989–992. https://doi.org/10.1130/G22796A.1

Parsons, A.J., Hosseini, K., Palin, R.M., and Sigloch, K. (2020). Geological, geophysical and plate kinematic constraints for models of the India-Asia collision and the post-Triassic central Tethys oceans. *Earth-Science Reviews, 208*, 103084. *https://doi.org/10.1016/j.earscirev.2020.103084*

Pearce, J.A. and Cann, J.R. (1971). Ophiolite origin investigated by discriminant analysis using Ti, Zr and Y. *Earth and Planetary Science Letters, 12*, 339–349. https://doi.org/10.1016/0012-821X(71)90220-2

Pearce, J.A. and Cann, J.R. (1973). Tectonic setting of basic volcanic rocks determined using trace element analyses. *Earth and Planetary Science Letters, 19*, 290–300. https://doi.org/10.1016/0012-821X(73)90129-5

Pearce, J.A. and Norry, M.J. (1979). Petrogenetic implications of Ti, Zr, Y, and Nb variations in volcanic rocks. *Contributions to Mineralogy and Petrology, 69*, 33–47. https://doi.org/10.1007/BF00375192

Pearce, J.A. and Gale, G.H. (1977). Identification of ore-deposition environment from trace-element geochemistry of associated igneous host rocks. In: Gass I. G, (Eds) *Geological Society, London, Special Publications, 7*, 14–24. https://doi.org/10.1144/GSL.SP.1977.007.01.03

Pearce, T.H., Gorman, B.E., and Birkett, T.C. (1977). The relationship between major element chemistry and tectonic environment of basic and intermediate volcanic rocks. *Earth and Planetary Science Letters, 36*, 121–132. https://doi.org/10.1016/0012-821X(77)90193-5

Pegler, G., and Das, S. (1998). An enhanced image of the Pamir-Hindu Kush seismic zone from relocated earthquake hypocenters. *Geophysical Journal International, 134*, 573–595. https://doi.org/10.1046/j.1365-246x.1998.00582.x

Petrelli, M., Bizzarri, R., Morgavi, D., Baldanza, A., and Perugini, D. (2017). Combining machine learning techniques, microanalyses and large geochemical datasets for tephrochronological studies in complex volcanic areas: New age constraints for the Pleistocene magmatism of central Italy. *Quaternary Geochronology, 40*, 33–44. https://doi.org/10.1016/j.quageo.2016.12.003

Petrelli, M., and Perugini, D. (2016). Solving petrological problems through machine learning: the study case of tectonic discrimination using geochemical and isotopic data. *Contributions to Mineralogy and Petrology, 171*, 1–15. https://doi.org/10.1007/s00410-016-1292-2

Piccoli, P.M. and Candela, P.A. (2002). Apatite in igneous systems. *Reviews in Mineralogy and Geochemistry, 48*, 255–292. https://doi.org/10.2138/rmg.2002.48.6

Pognante, U., Benna, P., and Lefort, P. (1993). High pressure metamorphism in the High Himalayan Crystallines of the Stak valley, northeastern Nanga Parbat-Haramosh syntaxis, Pakistan Himalaya. *Geological Society, London, Special Publications, 74*, 161–172. https://doi.org/10.1144/GSL.SP.1993.074.01.12

Pullen, A., Kapp, P., Gehrels, G.E., Ding, L., and Zhang, Q. (2011). Metamorphic rocks in central Tibet: Lateral variations and implications for crustal structure. *Geological Society of America Bulletin, 123*, 585–600. https://doi.org/10.1130/B30154.1

Pusok, A. E., and Kaus, B. J. P. (2015). Development of topography in 3-D continental-collision models. *Geochemistry, Geophysics, Geosystems, 16*, 1378-1400. https://doi.org/10.1002/2015GC005732

Qasim, M., Ding, L., Khan, M. A., Jadoon, I. A., Haneef, M., Baral, U., et al. (2018). Tectonic implications of detrital zircon ages from lesser Himalayan Mesozoic-Cenozoic strata, Pakistan. *Geochemistry, Geophysics, Geosystems, 19*, 1636–1659. https://doi.org/10.1002/2017GC006895

Ratschbacher, L., Frisch, W., Liu, G., and Chen, C.C. (1994). Distributed deformation in southern and western Tibet during and after the India-Asia collision. Journal of Geophysical Research: Solid Earth, 99, 19917–19945. https://doi.org/10.1029/94JB00932

Regis, D., Warren, C.J., Young, D., and Roberts, N.M. (2014). Tectono-metamorphic evolution of the Jomolhari massif: variations in timing of syn-collisional metamorphism across western Bhutan. *Lithos, 190*, 449–466. https://doi.org/10.1016/j.lithos.2014.01.001

Rehman, H. U., Seno, T., Yamamoto, H., and Khan, T. (2011). Timing of collision of the Kohistan-Ladakh Arc with India and Asia: Debate. *Island Arc, 20*, 308–328. https://doi.org/10.1111/j.1440-1738.2011.00774.x

Replumaz, A., Capitanio, F.A., Guillot, S., Negredo, A.M., and Villaseñor, A. (2014). The coupling of Indian subduction and Asian continental tectonics. *Gondwana Research, 26,* 608–626. https://doi.org/10.1016/j.gr.2014.04.003

Replumaz, A., Guillot, S., Villaseñor, A., and Negredo, A.M. (2013). Amount of Asian lithospheric mantle subducted during the India/Asia collision. *Gondwana Research, 24*, 936–945, https://doi.org/10.1016/j.gr.2012.07.019

Robinson, A.C., Yin, A., Manning, C.E., Harrison, T.M., Zhang, S.H., and Wang, X.F. (2007). Cenozoic evolution of the eastern Pamir: implications for strain-accommodation mechanisms at the western end of the Himalayan–Tibetan orogen. *Geological Society of America Bulletin*, *119*, 882–896. https://doi.org/10.1130/B25981.1

Robyr, M., and Lanari, P. (2020). Kinematic, metamorphic, and age constraints on the Miyar Thrust Zone: Implications for the Eohimalayan history of the High Himalayan Crystalline of NW India. *Tectonics, 39*, e2020TC006379. https://doi.org/10.1029/2020TC006379

Rosenberg, C. L., and Handy, M. R. (2005). Experimental deformation of partially melted granite revisited: implications for the continental crust. *Journal of Metamorphic Geology, 23,* 19-28. https://doi.org/10.1111/j.1525-1314.2005.00555.x

Rowley, D. B. (1996). Age of initiation of collision between India and Asia: A review of stratigraphic data. *Earth and Planetary Science Letters, 145*, 1–13. https://doi.org/10.1016/S0012-821X(96)00201-4

Ryan, P.D. and Dewey, J.F. (2019). The sources of metamorphic heat during collisional orogeny: the Barrovian enigma. *Canadian Journal of Earth Sciences*, *56*, 1309–1317. https://doi.org/10.1139/cjes-2018-0182

Schmidt, J., Hacker, B. R., Ratschbacher, L., Stübner, K., Stearns, M., Kylander-Clark, A., et al. (2011). Cenozoic deep crust in the Pamir. *Earth and Planetary Science Letters, 312*, 411–421. https://doi.org/10.1016/j.epsl.2011.10.034

Schneider, F. M., Yuan, X., Schurr, B., Mechie, J., Sippl, C., and Kufner, S.-K, et al. (2019). The crust in the Pamir: Insights from receiver functions. *Journal of Geophysical Research: Solid Earth*, *124*, 9313-9331. https://doi.org/10.1029/2019JB017765

Schwab, M., Ratschbacher, L., Siebel, W., McWilliams, M., Minaev, V., Lutkov, V., et al. (2004). Assembly of the Pamirs: Age and origin of magmatic belts from the southern Tien Shan to the southern Pamirs and their relation to Tibet. *Tectonics*, *23,* TC4002. https://doi.org/10.1029/2003TC001583

Searle, M.P. (2019). Timing of subduction initiation, arc formation, ophiolite obduction and India–Asia collision in the Himalaya. In: Treloar, P.J., Searle, M.P. (Eds.), Himalayan Tectonics: A Modern Synthesis. *Geological Society, London, Special Publications, 483*, 19–37. https://doi.org/10.1144/SP483.8

Searle, M. P., and Treloar, P. J. (2019). Introduction to Himalayan tectonics: A modern synthesis. Treloar, P. J. and Searle, M. P. (Eds.), Himalayan tectonics: A modern synthesis. *Geological Society, London, Special Publications, 483,* 1–17. https://doi.org/10.1144/SP483-2019-20

Shrestha, S., Larson, K.P., Martin, A.J., Guilmette, C., Smit, M.A., and Cottle, J.M. (2020). The Greater Himalayan thrust belt: insight into the assembly of the exhumed Himalayan metamorphic core, Modi Khola valley, central Nepal. *Tectonics, 39*, e2020TC006252. https://doi.org/10.1029/2020TC006252

Sippl, C., Schurr, B., Tympel, J., Angiboust, S., Mechie, J., Yuan, X., et al. (2013). Deep burial of Asian continental crust beneath the Pamir imaged with local earthquake tomography. *Earth and Planetary Science Letters, 384,* 165–177. https://doi.org/10.1016/j.epsl.2013.10.013

Sippl, C., Schurr, B., Yuan, X., Mechie, J., Schneider, F. M., Gadoev, M., et al. (2013). Geometry of the Pamir-Hindu Kush interme- diate-depth earthquake zone from local seismic data. *Journal of Geophysical Research: Solid Earth, 118*, 1438–1457. https://doi.org/10.1002/jgrb.50128

Sizova, E., Hauzenberger, C., Fritz, H., Faryad, S.W., and Gerya, T. (2019). Late orogenic heating of (ultra)high pressure rocks: Slab rollback vs. slab breakoff. *Geosciences, 9*, 499. https://doi.org/10.3390/geosciences9120499

Smit, M.A., Hacker, B.R., and Lee, J. (2014). Tibetan garnet records early Eocene initiation of thickening in the Himalaya. *Geology, 42*, 591–594. https://doi.org/10.1130/G35524.1

Smit, M. A., Ratschbacher, L., Kooijman, E., and Stearns, M. A. (2014). Early evolution of the Pamir deep crust from Lu-Hf and U-Pb geo-chronology and garnet thermometry. *Geology, 42*, 1047–1050. https://doi.org/10.1130/G35878.1

Smith, H.A., Chamberlain, C.P., and Zeitler, P.K. (1994). Timing and duration of Himalayan metamorphism within the Indian Plate, Northwest Himalaya, Pakistan. *The Journal of Geology, 102,* 493–508. https://doi.org/10.1086/629694

Spicer, R.A., Su, T., Valdes, P.J., Farnsworth, A., Wu, F.X., Shi, G., et al. (2021). Why 'the uplift of the Tibetan Plateau' is a myth. *National Science Review*, *8*, nwaa091. https://doi.org/10.1093/nsr/nwaa091

Spicer, R.A., Su, T., Valdes, P.J., Farnsworth, A., Wu, F.X., Shi, G. et al. (2021). The topographic evolution of the Tibetan Region as revealed by palaeontology. *Palaeobiodiversity and Palaeoenvironments*, *101*, 213-243. https://doi.org/10.1007/s12549-020-00452-1

Spurlin, M.S., Yin, A., Horton, B.K., Zhou, J., and Wang, J. (2005). Structural evolution of the Yushu-Nangqian region and its relationship to syncollisional igneous activity, east-central Tibet. *Geological Society of America Bulletin*, *117*, 1293–1317. https://doi.org/10.1130/B25572.1

St-Onge, M.R., Rayner, N., Palin, R.M., Searle, M.P., and Waters, D.J. (2013). Integrated pressure– temperature–time constraints for the Tso Morari dome (Northwest India): implications for the burial and exhumation path of UHP units in the western Himalaya. *Journal of Metamorphic Geology, 31*, 469–504. https://doi.org/10.1111/jmg.12030

St-Onge, M.R., Rayner, N. and Searle, M.P. (2010). Zircon age determinations for the Ladakh batholith at Chumathang (Northwest India): implications for the age of the India–Asia collision in the Ladakh Himalaya. *Tectonophysics, 495*, 171–183. https://doi.org/10.1016/j.tecto.2010.09.010

St-Onge, M.R., Searle, M.P., and Wodicka, N. (2006). Trans-Hudson Orogen of North America and Himalaya-Karakoram-Tibetan Orogen of Asia: structural and thermal characteristics of the lower and upper plates. *Tectonics, 25*, TC4006. https://doi.org/10.1029 /2005TC001907

Staisch, L.M., Niemi, N.A., Hong, C., Clark, M.K., Rowley, D.B., and Currie, B. (2014). Cretaceous- Eocene depositional age for the Fenghuoshan Group, Hoh Xil Basin: Implications for the tectonic evolution of the northern Tibet Plateau. *Tectonics*, *33*, 281–301, https://doi.org/10.1002/2013TC003367

Staisch, L.M., Niemi, N.A., Clark, M.K., and Chang, H. (2016). Eocene to late Oligocene history of crustal shortening within the Hoh Xil Basin and implications for the uplift history of the northern Tibetan plateau. *Tectonics*, *35*, 862–895. https://doi.org/10.1002/2015TC003972

Štípská, P., Závada, P., Collett, S., Kylander-Clark, A.R.C., Hacker, B.R., Tabaud, A.-S., and Racek, M. (2020). Eocene migmatite formation and diachronous burial revealed by petrochronology in NW Himalaya, Zanskar. *Journal of Metamorphic Geology, 38*, 655–691. https://doi.org/10.1111/ jmg.12534

Stübner, K., Grujic, D., Parrish, R.R., Roberts, N.M.W., Kronz, A., Wooden, J., and Ahmad, T. (2014). Monazite geochronology unravels the timing of crustal thickening in NW Himalaya. *Lithos 210–211*, 111–128. http://dx.doi.org/10.1016/j.lithos.2014.09.024

Stübner, K., Ratschbacher, L., Weise, C., Chow, J., Hofmann, J., Khan, J., et al. (2013). The giant Shakhdara migmatitic gneiss dome, Pamir, India-Asia collision zone: 2. Timing of dome formation. *Tectonics, 32,* 1404–1431. https://doi.org/10.1002/tect.20059

Sun, J., and Jiang, M. (2013). Eocene seawater retreat from the southwest Tarim Basin and implications for early Cenozoic tectonic evolution in the Pamir Plateau. *Tectonophysics, 588*, 27–38. https://doi.org/10.1016/j.tecto.2012.11.031

Sundell, K.E., Laskowski, A.K., Howlett, C., Kapp, P., Ducea, M., Chapman, J.B. and Ding, L. (2023). Episodic Late Cretaceous to Neogene crustal thickness variation in southern Tibet. *Terra Nova*, *36,* 45-52. https://doi.org/10.1111/ter.12689

Tapponnier, P., Peltzer, G., Le Dain, A.Y., Armijo, R., and Cobbold, P. (1982). Propagating extrusion tectonics in Asia: New insights from simple experiments with plasticine. *Geology*, *10*, 611–616. https://doi.org/10.1130/0091-7613(1982)10%3C611:PETIAN%3E2.0.CO;2

Tilmann, F., and Ni, J., and INDEPTH III Seismic Team. (2003). Seismic imaging of the downwelling Indian lithosphere beneath central Tibet. *Science, 300,* 1424–1427, https://doi.org/10.1126/science.1082777

Tong, Y., Yang, Z., Li, J., Pei, J., and Li, J. (2019). New insights into the collision process of India and Eurasia: evidence from the syntectonic-sedimentation-induced inclinational divergence of Cretaceous paleomagnetic data of the Lhasa Terrane. *Earth-Science Reviews*, *190*, 570-588. https://doi.org/10.1016/j.earscirev.2019.02.009

Tong, Y., Yang, Z., Mao, C., Pei, J., Pu, Z., and Xu, Y. (2017). Paleomagnetism of Eocene red-beds in the eastern part of the Qiangtang Terrane and its implications for uplift and southward crustal extrusion in the southeastern edge of the Tibetan Plateau. *Earth and Planetary Science Letters*, *475*, 1–14. https://doi.org/10.1016/ j.epsl.2017.07.026

Toussaint, G., Burov, E., and Jolivet, L. (2004). Continental plate collision: Unstable vs. stable slab dynamics. *Geology*, *32*, 33–36. https://doi.org/10.1130/G19883.1

Turcotte, D.L. and Schubert, G. (2002). *Geodynamics (2nd ed)*. *Cambridge University press. Cambridge*. 492–499.

Turner, S., Hawkesworth, C., Liu, J., Rogers, N., Kelley, S., and van Calsteren, P. (1993). Timing of Tibetan uplift constrained by analysis of volcanic rocks: *Nature, 364,* 50–54, https://doi.org/10.1038/364050a0

Turner, S., Arnaud, N., Liu, J., Rogers, N., Hawkesworth, C., Harris, N., et al. (1996), Post-collision, shoshonitic volcanism on the Tibetan plateau: Implications for convective thinning of the lithosphere and the source of ocean island basalts. *Journal of Petrology, 37,* 45–71, https://doi.org/10.1093/petrology/37.1.45

Ueki, K., Hino, H. and Kuwatani, T. (2018). Geochemical discrimination and characteristics of magmatic tectonic settings: A machine-learning-based approach. *Geochemistry, Geophysics, Geosystems, 19*, 1327–1347. https://doi.org/10.1029/2017GC007401

Van der Voo, R., Spakman, W., and Bijwaard, H. (1999). Tethyan subducted slabs under India. *Earth and Planetary Science Letters, 171*, 7–20. https://doi.org/10.1016/S0012-821X(99)00131-4

van Hinsbergen, D.J., Lippert, P.C., Dupont-Nivet, G., McQuarrie, N., Doubrovine, P.V., Spakman, W. and Torsvik, T.H. (2012). Greater India Basin hypothesis and a two-stage Cenozoic collision between India and Asia. *Proceedings of the National Academy of Sciences, 109*, 7659–7664. https://doi.org/10.1073/pnas.1117262109

van Hinsbergen, D.J.J., Lippert, P.C., Li, S., Huang, W., Advokaat, E.L., and Spakman, W. (2019). Reconstructing Greater India: Paleogeographic, kinematic, and geodynamic perspectives. *Tectonophysics, 760*, 69–94. https://doi.org/10.1016/j.tecto.2018.04.006

van Hinsbergen, D.J.J., Steinberger, B., Doubrovine, P.V., and Gassmöller, R. (2011). Acceleration and deceleration of India-Asia convergence since the Cretaceous: Roles of mantle plumes and continental collision. *Journal of Geophysical Research: Solid Earth*, *116,* B06101. https://doi.org/10.1029/2010JB008051

Vannay, J.-C. and Hodges, K.V. (1996). Tectonometamorphic evolution of the Himalayan metamorphic core between Annapurna and Dhaulagiri, central Nepal. *Journal of Metamorphic Geology, 14*, 635–656. https://doi.org/10.1046/j.1525-1314.1996.00426.x

Viete, D.R. and Lister, G.S. (2017). On the significance of short-duration regional metamorphism. *Journal of the Geological Society, 174*, 377–392. https://doi.org/10.1144/jgs2016-060

Wang, C., Dai, J., Zhao, X., Li, Y., Graham, S.A., He, D., et al. (2014). Outward-growth of the Tibetan Plateau during the Cenozoic: A review. *Tectonophysics*, *621*, 1–43. https://doi.org/10.1016/j.tecto.2014.01.036

Wang, C., Ding, L., Zhang, L.Y., Kapp, P., Pullen, A., and Yue, Y.H. (2016). Petrogenesis of Middle–Late Triassic volcanic rocks from the Gangdese belt, southern Lhasa terrane: Implications for early subduction of Neo-Tethyan oceanic lithosphere. *Lithos*, *262*, 320–333. https://doi.org/10.1016/j.lithos.2016.07.021

Wang J-M., Wu, F-Y., Rubatto, D., Liu, K., Zhang, J-J., and Liu, X-C. (2018). Early Miocene rapid exhumation in southern Tibet: insights from P-T-t-D-magmatism path of Yardoi dome. *Lithos, 304–307,* 38–56. https://doi.org/10.1016/j.lithos.2018.02.003

Wang, J-M., Zhang, J-J., Liu, K., Zhang, B., Wang, X-X., Rai, S., and Scheltens, M. (2016). Spatial and temporal evolution of tectonometamorphic discontinuities in the central Himalaya: Constraints from P–T paths and geochronology. *Tectonophysics, 679*, 41–60. http://dx.doi.org/ 10.1016/j.tecto.2016.04.035

Wang, Q., Hawkesworth, C.J., Wyman, D., Chung, S.-L., Wu, F.-Y., Li, X.-H., Li, et al., (2016). Pliocene-Quaternary crustal melting in central and northern Tibet and insights into crustal flow. *Nature Communications*, 7, 11888. https://doi.org/10.1038/ncomms11888

Wang, S., Wang, C., Phillips, R.J., Murphy, M.A., Fang, X., and Yue, Y. (2012). Displacement along the Karakoram fault, NW Himalaya, estimated from LA-ICP-MS U–Pb dating of offset geologic markers. *Earth and Planetary Science Letters*, *337*, 156-163. https://doi.org/10.1016/j.epsl.2012.05.037

Wang, T., Li, G., Aitchison, J.C., and Sheng, J. (2020). Eocene ostracods from southern Tibet: implications for the disappearance of Neo-Tethys. *Palaeogeography, Palaeoclimatology, Palaeoecology, 539*, 109488. https://doi.org/10.1016/j.palaeo.2019.109488

Wang, Y. F., Zeng, L., Gao, J., Zhao, L., Gao, L. E., and Shang, Z. (2019). Along-arc variations in isotope and trace element compositions of Paleogene gabbroic rocks in the Gangdese batholith, southern Tibet. *Lithos*, *324*, 877-892. https://doi.org/10.1016/j.lithos.2018.11.036

Warren, C. J., Beaumont, C., and Jamieson, R. A. (2008). Modeling tectonic styles and ultra-high pressure (UHP) rock exhumation during the transition from oceanic subduction to continental collision. *Earth and Planetary Science Letters, 267*, 129–145. https://doi.org/10.1016/j. epsl.2007.11.025

White, L.T., Ahmad, T., Lister, G.S., Ireland, T.R. and Forster, M.A. (2012). Is the switch from I-to S-type magmatism in the Himalayan Orogen indicative of the collision of India and Eurasia? *Australian Journal of Earth Sciences*, *59*, 321–340. https://doi.org/10.1080/08120099.2012.652670

White, R., and McKenzie, D. (1989). Magmatism at rift zones: the generation of volcanic continental margins and flood basalts. *Journal of Geophysical Research, 94*, 7685–7729. https://doi.org/10.1029/JB094iB06p07685

Wiesmayr, G. and Grasemann, B. (2002). Eohimalayan fold and thrust belt: Implications for the geodynamic evolution of the NW-Himalaya (India). *Tectonics*, *21*, 8–1. https://doi.org/10.1029/2002TC001363

Wilke, F.D.H., O'Brien, P.J., Altenberger, U., Konrad-Schmolke, M., and Khan, M.A., (2010). Multistage history in different eclogite types from the Pakistan Himalaya and implications for exhumation processes. *Lithos ,114*, 70–85.

Willett, S., Beaumont, C., and Fullsack, P. (1993). Mechanical model for the tectonics of doubly vergent compressional orogens. *Geology, 21,* 371–374. https:/doi.org/10.1130/00917613(1993)021<0371:MMFTTO>2.3.CO;2

Worthington, J.R., Ratschbacher, L., Stübner, K., Khan, J., Malz, N., Schneider, S., et al. (2020). The Alichur dome, South Pamir, western India–Asia collisional zone: Detailing the Neogene Shakhdara–Alichur syn-collisional gneiss-dome complex and connection to lithospheric processes. *Tectonics*, *39,* https://doi.org/10.1029/2019TC005735

Yi, Z., Huang, B., Chen, J., Chen, L., and Wang, H. (2011). Paleomagnetism of early Paleogene marine sediments in southern Tibet, China: Implications to onset of the India–Asia collision and size of Greater India. *Earth and Planetary Science Letters*, *309*, 153–165. https://doi.org/10.1016/j.epsl.2011.07.001

Yin, A. (2006). Cenozoic tectonic evolution of the Himalayan orogen as constrained by along-strike variation of structural geometry, exhumation history, and foreland sedimentation. *Earth-Science Reviews, 76*, 1–131. https://doi.org/10.1016/j.earscirev.2005.05.004

Yin, A. and Harrison, T.M. (2000). Geologic evolution of the Himalayan-Tibetan orogen. *Annual Review of Earth Planetary Sciences, 28,* 211–280. https://doi.org/10.1146/annurev.earth.28.1.211

Yin, A., Harrison, T.M., Murphy, M.A., Grove, M., Nie, S., Ryerson, F.J., et al. (1999). Tertiary deformation history of southeastern and southwestern Tibet during the Indo-Asian collision. *Geological Society of America: Bulletin, 111*, 1644–1664

Yuan, J., Yang, Z., Deng, C., Krijgsman, W., Hu, X., Li, S., et al. (2021). Rapid drift of the Tethyan Himalaya terrane before two-stage India-Asia collision. *National Science Review*, *8*, nwaa173. https://doi.org/10.1093/nsr/nwaa173

Zeng, L., Gao, L-E., Tang, S., Hou, K., Guo, C., and Hu, G. (2015). Eocene magmatism in the Tethyan Himalaya, southern Tibet. Mukherjee S., Carosi, R., van der Beek, P. A., Mukherjee, B. K., and Robinson, D.M. (Eds.) Tectonics of the Himalaya*. Geological Society, London, Special Publications, 412*, 287–316. https://doi.org/10.1144/SP412.8

Zeng, L., Gao, L.E., Xie, K., and Liu-Zeng, J. (2011). Mid-Eocene high Sr/Y granites in the Northern Himalayan gneiss domes: Melting thickened lower continental crust. *Earth and Planetary Science Letters*, *303*, 251–266. https://doi.org/10.1016/j.epsl.2011.01.005

Zheng, Y.F. (2019). Subduction zone geochemistry. *Geoscience Frontiers, 10*, 1223–1254. https://doi.org/10.1016/j.gsf.2019.02.003

Zheng, Y.-F., Xia, Q.-X., Chen, R.-X., and Gao, X.-Y. (2011). Partial melting, fluid supercriticality, and element mobility in ultrahigh-pressure metamorphic rocks during continental collision. *Earth-Science Reviews, 107*, 342-374. https://doi.org/10.1016/j.earscirev.2011.04.004

Zhu, D.C., Wang, Q., Zhao, Z.D., Chung, S.L., Cawood, P.A., Niu, Y., et al. (2015). Magmatic record of India-Asia collision. *Scientific reports, 5*, 14289. https://doi.org/10.1038/srep14289

Zhu, D., Wang, Q., and Zhao, Z. (2017). Constraining quantitatively the timing and process of continent-continent collision using magmatic record: Method and examples. *Science China Earth Sciences, 60,* 1040–1056. https://doi.org/10.1007/s11430-016-9041-x

Zhu, D.-C., Wang, Q., Chung, S.-L., Cawood, P.A., and Zhao, Z.-D. (2019). Gangdese magmatism in southern Tibet and India–Asia convergence since 120 Ma. Treloar, P.J., and Searle, M.P. (Eds.), Himalayan Tectonics: A Modern Synthesis. *Geological Society, London, Special Publications, 483*. https://doi.org/10.1144/SP483.14

Zhu, D.-C., Wang, Q., Zhao, Z.-D., Chung, S.-L., Cawood, P.A., Niu, Y., et al. (2015). Magmatic record of India-Asia collision. *Scientific Reports*, *5*, 14289. https://doi.org/10.1038/srep14289

Zhu, D.-C., Zhao, Z.-D., Niu, Y., Mo, X.-X., Chung, S.-L., Hou, Z.-Q., et al. (2011. The Lhasa Terrane: Record of a microcontinent and its histories of drift and growth: *Earth and Planetary Science Letters, 301*, 241–255. https://doi.org/10.1016/j.epsl.2010.11.005

Zhu, G., Gerya, T. V., Honda, S., Tackley, P. J. and Yuen, D. A. (2011). Influences of the buoyancy of partially molten rock on three-dimension- al plume patterns and melt productivity above retreating slabs. *Physics of the Earth and Planetary Interiors, 185*, 112–121. https://doi.org/10.1016/j.pepi.2011.02.005

Zuza, A.V., Cheng, X., and Yin, A. (2016). Testing models of Tibetan Plateau formation with Cenozoic shortening estimates across the Qilian Shan–Nan Shan thrust belt. *Geosphere*, *12*, 501-532. https://doi.org/10.1130/GES01254.1

APPENDIX A
CHAPTER 2 APPENDICES

Supporting Information for

Balanced Cross-sections and Numerical Modelling of the Lithospheric-scale Evolution of the Hindu Kush and Pamir

S. Kelly and C. Beaumont

Introduction

The Supporting Information is a description of the methods used in the numerical models, a table describing the assumptions used to construct the balanced cross-sections (Table A1), and a table describing the parameters used in models MHA and MPA (Table A2).

Additional Supporting Information files include animations for MPA and MHA (Animation MHA and Animation MPA) in Kelly et al. (2021)

1. **Modeling methods**

1.1. The SOPALE Nested software

We use two-dimensional thermal-mechanical models computed using the software SOPALE Nested (Beaumont et al., 2009; Butler et al., 2014; Fullsack, 1995) t o investigate the dynamics of continent- continent collisional orogens at the upper-mantle and part lower-mantle-scale. The models are designed based on simplified lithospheric scale sections for each of the Hindu Kush and Pamir regions representing oceanic subduction followed by continent-continent (India-Asia) collision (Figures 2.3, 2.4 and 2.6). The methodology remains similar to our recent work (Beaumont et

al., 2009; Butler et al., 2014, Kelly et al., 2016; 2020) and therefore, where appropriate, we quote directly from these previous publications. The models are computed by solving the equations for incompressible creeping (Stokes) flows (equations A.1 and A.2) and energy (equation A.3) subject to mechanical and thermal boundary conditions:

$$\frac{\partial \sigma_{i,j}}{\partial x_i} + \frac{\partial P}{\partial x_j} + \rho g = 0 \quad i,j = 1,2 \tag{A.1}$$

$$\frac{\partial v_i}{\partial x_i} = 0 \qquad i = 1,2 \tag{A.2}$$

$$\rho(T) c_p \left(\frac{\partial T}{\partial t} + v_i \frac{\partial T}{\partial x_i}\right) = \frac{\partial}{\partial x_i}\left(K(T)\frac{\partial T}{\partial x_i}\right) + A_R + A_{SH} + v_2 \alpha g T \rho(T) \quad i = 1,2 \tag{A.3}$$

where $\sigma_{i,j}$ is the deviatoric stress tensor, x_i ($i = 1, 2$) s patial coordinates, P pressure (mean stress), ρ density, g gravitational acceleration, v_i ($i = 1, 2$) a component of velocity, c_p specific heat, T temperature, t time, K thermal conductivity, A_R crustal radiogenic heat production per unit volume, A_{SH} shear heating, and α volumetric thermal expansion. Coupling of the mechanical and thermal solutions is achieved through the advection of radioactive crust, shear heating, thermal activation of viscous flow, and buoyancy forces arising from metamorphic phase changes and thermal expansion.

The models use a sub-grid approach in which a higher-resolution computational domain is ‘nested’ within a larger, lower-resolution domain. The velocity and thermal solution is first obtained for the full domain. This solution is then interpolated onto the boundaries of the nested domain encompassing the vicinity of the subduction zone and the accreted terranes (Figure 2.6a). Coupling of the domains is maintained by using a single cloud of Lagrangian tracking particles, which is passed between the two solutions, with the particles within the nested domain always obeying the higher resolution solution.

1.2. Model geometry and boundary conditions

The model domain is 4000 km wide by 1200 km deep. The initial configurations of the simplified models for each of the H (Hindu Kush) and P (Pamir) model types are shown in Figure 2.6. We label each of the model regions with an acronym derived from the natural setting. This is designed to distinguish models from observations but allow easy comparison.

For the P-type models (Figure 2.6a) the starting geometry comprises (left to right) 'I' a continent (India) and its rifted margin IR, 'NT' a 1000-km-wide ocean (Neotethys), and a composite retrocontinent, overlying upper mantle to depth of 660 km and then lower mantle to 1200 km. The retrocontinent comprises (from left to right); 'K' a 500 km wide terrane (Kohistan Arc), 'P' a 1000 km composite terrane (composite Pamir), 'A' a 600 km wide terrane (Alai), 'TS' a 700 km wide terrane (Tien Shan), and 'AI' a strong lithosphere region representing undeformed interior Asia to the north. The Greater India rifted margin is represented by a 1000 km wide depth-dependent extension geometrical margin (Huismans & Beaumont, 2011), 'IR'(Figure 2.6a,b). The models are simple in that we adopt uniform layering for all continental regions (Table A2), comprising 24 km thick continental upper/mid crust, 12 km thick lower crust, and 84 km thick continental lithospheric mantle (CLM) (i.e., extending to a depth of 120 km). The CLMs of the retrolithosphere terranes are variably chemically depleted which determines their density (Table A2), but the prolithosphere CLM has a constant depletion leading to a compositional density that is 50 kg/m^3 less dense than the sublithospheric mantle. In preliminary models it was established that prolithosphere CLM with higher density does not result in advancing S-point subduction and therefore fails a crucial basic requirement of models designed to investigate the Hindu Kush and Pamir regions. The oceanic lithosphere comprises, 2 km sediment, 6 km oceanic crust and 92 km oceanic mantle lithosphere, in which the upper 50 km is chemically depleted and 30 kg/m^3 less dense than the lower lithosphere and sublithospheric mantle.

For the H-type models (Figure 2.6c), the starting geometry comprises (from left to right) 'FI' a fringe Indian continent (west India rifted margin) and its rifted margin 'IR', 'NT' a 1000 km wide ocean (Neotethys), 'SH' a 400 km wide terrane (south Hindu Kush), 'NH'

a 1000 km wide terrane (north Hindu Kush), 'TB' a 600 km wide terrane (Tajik Basin, equivalent to the Alai terrane in the Pamir models), 'T' a 1100 km wide terrane (Tien Shan), and 'AI' a strong lithosphere region representing interior Asia to the north. The subdivision of the Hindu Kush into SH and NH terranes allows us to explore possible lateral (N/S) variations in the properties of this composite terrane. The FI, fringe-

Indian continent, comprises a 22 km thick upper crust, an 8 km thick lower crust (total 30 km), and a 70 km thick lithospheric mantle inherited from the rifting of the west India fringe margin. This lithosphere has been further thickened by accretion of cooling sublithospheric mantle and the thickness increment is determined by the steady-state initial thermal structure of the model.

The northern rifted continental margin of the Indian fringe continent (the Greater India continental margin) consists of a 1000 km wide depth-dependent margin. This region is also assumed to have been underplated by decompressed and cooling sublithospheric mantle and is therefore depleted by 30 kg/m^3 at depths less than 60 km. The geometry of the lithospheric layers for the oceanic and retrolithosphere are the same as those of P-type models. However, the widths of the accreted terranes differ, as noted above. All of these widths were derived from the initial widths of the restored balanced cross sections (Figures 2.3 and 2.4). In both H and P model types, the lower mantle/upper mantle boundary is at 660 km. Subduction is initiated using a weak zone, that spans both the crust and lithospheric mantle, and is embedded between ocean and respectively K and HK terranes in the P- and H-type models (Figure 2.6). Other geometrical properties are given in Table A2.

The velocity boundary conditions applied to the models comprise a time-varying left boundary lithospheric convergence velocity $V_p(t)$, (14 cm/a) during oceanic subduction, through contact and collision, and reducing to 3.6 cm/a by 0 Ma, (Figure 6d) and a stationary right boundary lithospheric velocity, V_r = 0 cm/a. The time variation of $V_p(t)$ approximates that of convergence in the H-T orogen following Ingalls et al. (2016). T he main reason for choosing the variable velocity is that it allows model and natural

timescales to be the same, thereby making comparisons much easier. Model time is expressed in millions of years measured backward from the present (Ma) a ssuming contact at 56 Ma. Small sublithospheric boundary fluxes are used to 'pump' material out of the sides of the model to conserve volume and maintain isostatic equilibrium. The sides of the model domain have no vertical slip boundary conditions and the base has a horizontal free slip condition. The top of the model is a free surface. Thermal boundary conditions include a basal heat flux of 21 mW/m^2, a 0˚C surface, and insulated side boundaries. The initial temperature regime corresponds to 2D thermal steady state.

1.3. Mechanical and thermal material properties

The flow laws and material properties are similar to those used in Beaumont et al. (2001), Butler et al. (2013), and Kelly et al. (2016; 2020). For a more detailed justification for the choice of flow laws and the scaling of these flow laws see Butler et al. (2014). As mentioned above the parameters of the reference model are considered typical of continental and oceanic lithospheric materials (Beaumont et al., 2006, and refs. therein). Model materials deform by either frictional-plastic (brittle) or viscous (ductile) flow that includes additional strain-softening/strain-weakening mechanisms. Brittle deformation is modeled using the frictional-plastic Drucker–Prager yield criterion, σ_y:

$$J'^{1/2}_2 = \sigma_y = P\sin\phi_{eff} + C\cos\phi_{eff} \quad \text{(A.4)}$$

where J'_2 is the second invariant of the deviatoric stress, P dynamical pressure (mean stress), and C cohesion. The effective angle of internal friction, ϕ_{eff}, is defined to include the effects of pore fluid pressure P_f,

$$P\sin\phi_{eff} = (P - P_f)\sin\phi$$

For dry frictional sliding conditions (approximating Byerlee's law), $\phi = 30°$ when the pore fluid pressure, $P_f = 0$. For all model materials except the weak zone and sediments, ϕ_{eff}=15°, approximating hydrostatic or slightly higher fluid pressures for typical crustal densities.

Ductile deformation is modeled using power-law flow, for which the effective viscosity is:

$$\eta_{eff}^{v} = \frac{f}{W_s} A^{-1/n} \dot{I}_2^{\prime(1-n)/2n} exp\left(\frac{Q+PV^*}{nR\ T_K}\right) \quad (A.5)$$

where f is a viscosity scaling factor, W_s a strain-weakening factor, A the pre-exponential factor, converted to the tensor invariant form, $\dot{I}'_2$ the second invariant of the deviatoric strain rate, n the stress exponent, Q molar activation energy, P pressure, V^* the molar activation volume for power-law creep, T_K absolute temperature, and R the universal gas constant. For simplicity, we base the model materials on a small set of laboratory-determined flow laws, wet quartzite (WQ) (G leason and Tullis, 1995), dry Maryland diabase (DMD) (Mackwell et al., 1998), and wet olivine (WOL) (Karato and Wu, 1993) (Table A2).We also include a high-stress, low-temperature deformation mechanism that modifies the viscous power-law flow (equation A.5) for olivine-based materials and approximates exponential or Peierls law creep for water-saturated (Katayama & Karato, 2008) and anhydrous (dry) (Mei et al., 2010) conditions. The method approximates experimental results (e.g., Katayama & Karato, 2008, their Figure 7, converted to geological conditions in Figure 10) by reducing the deviatoric stress and effective viscosity by a constant scaling factor when the deviatoric stress is above a threshold value (Table A2). This scaling only reduces the deviatoric stress to the threshold value, the Peierls threshold stress σp, not below it. We chose this simple approximation (e.g., Andrews and Billen, 2009) because the control parameters for Peierls flow law are only known approximately (Kameyama et al., 1999; Katayama and Karato, 2008) and vary significantly from wet to dry olivine (Katayama and Karato, 2008), making the use of this flow law subject to large uncertainties. Models in which σ_p varies from 100 to 350 MPa were used to test the sensitivity of slab break off to σ_p.

Crustal materials and the lithospheric mantle soften/weaken in the frictional-plastic and viscous regimes, respectively. Frictional-plastic materials strain-soften through a linear decrease in their effective angle of internal friction, ϕ_{eff}, with accumulated strain: $\phi_{eff} = \phi_{eff}(\epsilon)$. $\epsilon = I'^{1/2}$ the square root of the second invariant of deviatoric strain, with ϵ(strain) used for simplicity. Viscous strain-weakening occurs through a linear decrease in effective viscosity by the factor W_s over a specified ϵ range. For all models, crustal materials weaken by W_s = 3 over the range ϵ = 5–10. Strain-weakening (and softening) as implemented in our models depends on the resolution of the computational grid (2 × 2 km in the nested region). Given that natural shear zones form at finer scales, equivalent natural strain weakening/softening occurs at smaller offsets across shear zones because the shear zones are narrower than the typical 6 km in these models. It follows that the models weaken/soften more slowly than ones would with higher resolution. By implication, higher resolution models will give equivalent results with proportionally larger values of the minimum ϕ_{eff}, and smaller values of W_S. The values used here should therefore be interpreted as minimum and maximum values, respectively. Each crustal unit comprises an upper/middle crust with ϕ_{eff} (hereafter simply ϕ) = 15–2° (except where noted), and a scaled wet quartzite (WQ × 1) flow law (Gleason and Tullis, 1995), overlying a lower crust with ϕ = 15–2° (where ϕ = 2° is fully strain-softened) and a dry Maryland diabase (DMD × 0.1) flow law, scaled to represent intermediate granulite (Mackwell et al., 1998). The underlying lithospheric mantle, has ϕ = 15–2° and a scaled wet olivine flow law (WOL; Karato and Wu, 1993) scaled to represent a somewhat depleted/dehydrated lithosphere, and overlies sublithospheric upper mantle (WOL × 2) that extends to 660 km. The I and AI continental lithospheric mantle has WOL × 5 and the *f* values for the accreted terranes CLMs vary among the model experiments. Owing to considerable uncertainty in the rheology of the lower mantle (Billen, 2010), we assume that the lower mantle has a constant/uniform viscosity of 1×10^{21} Pa s. The 660-km-deep upper to lower mantle boundary corresponds to a dynamical phase change boundary across which density increases by ~8%, and the viscosity changes from power-law creep to constant linear viscosity.

Sediment and upper/mid continental crust undergo melt weakening in the same temperature and pressure dependent manner as in Butler et al. (2015). The viscosity decreases linearly from the calculated power-law value to a fixed linear value of 10^{19}

Pa s from the pressure-dependent dry solidus to the solidus temperature plus 50ºC. The dry solidus is defined by P-T line segments joining the points (680°C, 0 GPa), (900°C, 2.8 GPa), and (1437°C, 15 GPa) (Zheng et al., 2011). This is designed to represent the viscosity reduction that results from the presence of minor partial melting with a melt fraction of ~ 4 –7% (Rosenberg & Handy, 2005).

In addition, upper/middle crust coesite-eclogite materials which reach pressures and temperatures 100°C above the dry solidus (Butler et al., 2015) undergo an increase in power-law viscosity (f = 1.25 to 10), and these materials may subsequently revert to high-pressure eclogite densities, but do not further retrograde to normal crustal density. This is designed to model, in a simple way, the formation of restite after extraction of a small amount of melt at these pressures and temperatures (Massonne and Fockenberg, 2012).

The continents have uniform crustal radioactive heat production (A_R) for the upper/mid, and lower continental crust of 2.0 and 0.4 μW/m^3, respectively. Coupled with the thermal boundary conditions, basal heat flux 21 mW/m^2 and no-flux side boundaries, the resulting initial steady state surface heat flow and Moho temperatures on the continents are 74 mW/m^2 and ~650˚C, but less for the Indian fringe continent. The base lithosphere temperature throughout the model is ~1370°C. Material thermal expansivity (α) and conductivity (K) are temperature dependent, with their values varying linearly from K_1 to K_2 over the temperature range T_1 to T_2, (Table A2). Other thermal properties are given in Table A2.

1.4. Density, volume and mass conservation during phase transitions

Crustal materials undergo reversible pressure- and temperature-dependent density changes corresponding to the eclogite and coesite-eclogite phase transitions following Warren et al. (2008) (Table A2). Mantle materials undergo a reversible phase change at the upper-lower mantle boundary (~660 km depth) corresponding to the transformation of olivine to perovskite. The latter transformation is determined by a reaction with a Clapeyron slope of –2.0 MPa/K and results in a density increase (proportional for all mantle materials) of ~8% (for a discussion of these parameters, see Billen, 2010). Crustal materials undergo equivalent phase changes at the upper-lower mantle boundary. For simplicity, the models do not include the transformation of olivine to ringwoodite in the mantle transition zone (~440–660 km).

During these phase changes the incompressibility equation is modified to that of mass conservation: $\partial \rho / \partial t = -\partial (\rho v_i) / \partial x_i$. This accounts for the volume change and its effect on the buoyancy and velocity field. The volume change is calculated numerically by applying additional normal, compressive/dilatational forces to finite elements at the time they are subject to phase-related density changes. The value of the excess pressure is $P = \Delta \rho / \beta_v \rho$, where βv is the viscous bulk modulus of the material, and $\Delta \rho / \rho$ is the fractional change in density corresponding to the phase change. The excess pressure compresses material locally and only during the model time steps when the phase changes occur, thereby ensuring mass conservation. The fractional volume change accompanying a phase change is small in these models and its effect on the velocity field is minor because it only applies at the time of the phase change. However, failure to ensure mass conservation would have a long-term effect on the model because the buoyancy forces will be over- or under-estimated by the cumulative fractional error in the material volume.

1.5. Surface Processes

The models have an upper free surface, and the model topography is a product of the model calculation without any imposed constraints except for water loading where the

surface is below sea level. Surface uplift and subsidence are mostly the result of crustal thickening and downward flexure near the subduction zone, and the density changes associated with the phase changes have relatively little influence on the topography. Slope-dependent surface erosion, a proxy for fluvial and glacial erosion, acts on the current local subaerial topography. It varies according to local slope of the model surface, where it is defined by a maximum erosion rate *E(x)* that operates on a slope of 45° and is scaled down linearly to the local slope of the surface. The erosion rate is also modulated by a spatial climate function (Figure 2.6c) designed to reproduce humid (moderate erosion) conditions on the left-facing orogenic front and arid (low erosion) conditions over the interior plateau region. The climate function tracks the development and movement of the orogen. Maximum erosion rates are ~ 0.5 mm/year on the orogenic front.

Table A1: Assumptions used in balanced sections

Assumption	Value	Variable	Basis	References
1. Timing of contact	Hindu Kush and Pamir: 56 Ma	-	Timing of first arrival of Asian detritus on the distal Indian margin	Hu et al. [2015]
2. Location of suture and S-point at contact	Hindu Kush and Pamir: ~19°N	S_i	Location of the imaged Neotethys slab in lower mantle; paleomagnetic constraints	Negredo et al. [2007]; Replumaz et al. [2014]; Kufner et al. [2016]; Ingalls et al. [2016]; Zhu et al., [2017]
3. Current location of suture	Hindu Kush: ~34°N Pamir: ~35°N	S_f	Geological mapping.	Dipietro et al. [2000]
4. Current location of S-point	Hindu Kush: ~36°N Pamir: ~38.5°N	Sp_f	Seismic imaging	Negredo et al. [2007]; Replumaz et al. [2014]; Kufner et al. [2016]
5. Relative India-Asia convergence since contact	Hindu Kush and Pamir: 3150 km	C	Plate circuit motions	Ingalls et al. [2016]
6. Shortening accommodated by Asian crust	Hindu Kush: ~1700 km Pamir: ~1800 km	L_a	$S_f - S_i$ (difference in initial and final suture locations)	-
7. Length of removed Asian lower lithosphere (assuming no internal shortening)	Hindu Kush: ~1900 km Pamir: ~1750 km	R_a	Hindu Kush: $Sp_f - S_i$ Pamir: ($Sp_f - Si$) minus the ~400 km of dipping slab imaged in the mantle	Negredo et al. [2007]; Replumaz et al. [2014]; Kufner et al. [2016]
8. Length of removed Indian lower lithosphere (assuming no internal shortening)	Hindu Kush: ~1250 km Pamir: ~1000 km	R_i	Hindu Kush: C-($Sp_f - S_i$) minus the ~600 km of dipping slab imaged in the mantle Pamir: $C - (Sp_f - S_i)$	Negredo et al. [2007]; Replumaz et al. [2014]; Kufner et al. [2016]
9. Shortening in Alai Valley/Tajik Basin	Hindu Kush (Tajik): ~350 km Pamir (Alai): ~500 km	L_b	Assumption that the Tajik/Alai/Tarim terranes were similar in north to south widths	Burtman & Molnar [1993]; Chapman et al. [2017]
10. Shortening in the Tien Shan	Hindu Kush and Pamir: ~200 km	L_t	Isostasy modeling	Avouac et al. [1993]
11. Shortening in the Hindu Kush and Pamir mountain belts	Hindu Kush: ~1400 km Pamir: ~1500 km	L_p	$L_a - (L_b + L_t)$	-
12. Thickness of upper crust under the Pamir and Hindu Kush mountain belts	Hindu Kush ~60 km Pamir: ~68 km	T	Pamir: Seismic imaging Hindu Kush: gravitational anomaly modelling. (assuming that the lower crust is normal ~12 km thickness; i.e., Moho depth minus 12 km)	Mechie et al. [2012]; Jadoon and Khurshid [1996]
13. Current width (N/S) of the Hindu Kush and Pamir ranges along HK and P sections	Hindu Kush: ~250 km Pamir: ~500 km	W_f	Geological mapping	e.g., Chapman et al. [2018] and references therein.
14. Width (N/S) of Hindu Kush and Pamir ranges prior to collision	Hindu Kush: ~1400 km Pamir: ~1500 km	W_i	$W_i + L_p$	-

Assumption	Value	Variable	Basis	References
15. Width (N/S) of normal thickness Asian upper crust removed by erosion	Hindu Kush: ~800 km Pamir: ~100 km	E_a	Hindu Kush: $[(24\ km \times W_i) - (T \times W_f)]/24\ km$ Assuming that the Hindu Kush and Pamir ranges had normal thickness upper crust (~24 km) prior to collision, and lower crust was removed	-
16. Shortening accommodated by Indian crust	Hindu Kush: 1450 km Pamir: 1350 km	L_i	$C - L_a$	-
17. Shortening observed in Indian crust	Hindu Kush: ?? Pamir: ~300 km	O_i	Structural mapping	Dipietro & Pogue [2014]

Table A2: Model parameters used in MPA and MHA

	Units	Oceanic Sediment	PC upper crust (P and H models)	RC upper crust	PC lower crust (P and H models)	RC lower crust	Oceanic crust	PC continental lithospheric mantle	RC continental lithospheric mantle	Oceanic lithospheric mantle	Sub-lithospheric upper mantle	Lower mantle
Thickness (max)	km	2	24/22 fringe crust	24	12/8 fringe crust	12	6	84	84	92	To 660 km depth	660 to 1200 km depth
Reference density (0°C)	kg/m^3	2700	2700 (both)[a]	2700	2900 (both)[a]	2900	2950	3320	Varies, see Fig. 6	3370[b]	3370	3630
Reference density HP (0°C)[c]	kg/m^3	2800	2950 (both)[a]	2950	3300 (both)[a]	3300	3400	No change[d]	No change[d]	No change[d]	No change[d]	No change[d]
Reference density UHP (0°C)[c]	kg/m^3	2900	3200 (both)[a]	3200	No change[d] (both)[a]	No change[d]	No change[d]	Changes to 3580 below 660 km depth	Increases from reference density by 260 below 660 km depth	Changes to 3630 below 660 km depth	Changes to 3630 below 660 km depth	No change[d]
Effective angle of internal friction (φ_{eff})	deg	8–2[e]	15–2[e] (both)[a]	15–2[e]	15–2[e] (both)[a]	15–2[e]	15–2[e]	15–2[e]	15–2[e]	15–2[e]	15–2[e]	15–2[e]
Cohesion	MPa	2	2 (both)[a]	2	2 (both)[a]	2	0	0	0	0	0	0
Flow law	-	WQ	WQ (both)[a]	WQ	DMD (both)[a]	DMD	DMD	WOL	WOL	WOL	WOL	Constant viscosity 1×10^{21} Pa s
Viscosity scaling factor (f)	-	1	1.25 (both)[a]	Varies, see Fig. 6	0.1 (both)[a]	0.1	0.1	5	Varies, see Fig. 6	2	2	-
Strain weakening factor (W_s)	-	3	3 (both)[a]	3	3 (both)[a]	3	3	1	1	1	1	-
n	-	4	4 (both)[a]	4	4.7 (both)[a]	4.7	4.7	3	3	3	3	-
A^f	1/Pa^{n}s	8.57×10^{-28}	8.57×10^{-28} (both)[a]	8.57×10^{-28}	5.78×10^{-27} (both)[a]	5.78×10^{-27}	5.78×10^{-27}	1.76×10^{-14}	1.76×10^{-14}	1.76×10^{-14}	1.76×10^{-14}	-
Q	kJ/mol	223	223 (both)[a]	223	485 (both)[a]	485	485	430	430	430	430	-
V^*	m^3/mol	0	0 (both)[a]	0	0 (both)[a]	0	0	11×10^{-6}	11×10^{-6}	11×10^{-6}	11×10^{-6}	-
Peierls stress	Mpa	-	-	-	-	-	-	100	350	150	-	-
Peierls weakening factor	-	-	-	-	-	-	-	1×10^{-5}	1×10^{-5}	1×10^{-5}		-

	Units	Oceanic sediment	PC upper crust	RC upper crust	Lower crust (PC and RC)	Oceanic crust	PC continental lithospheric mantle	RC continental lithospheric mantle	Oceanic lithospheric mantle	Sub-lithospheric upper mantle	Lower mantle
Specific heat	m^2/s^2K	750	750	750	750	750	1250	1250 (all)	1250	1250	1250
Thermal conductivity	W/mK	2.25	2.25	2.25	2.25	2.25	5–2.4[g]	5–2.4 (all)[g]	5–2.4[g]	2.4–52.5[g,h]	2.4–52.5[g,h]
Thermal diffusivity	m^2/s	1×10^{-6}	1×10^{-6}	1×10^{-6}	1×10^{-6}	1×10^{-6}	$1.3–0.64\times10^{-6}$ [e]	$1.3–0.64\times10^{-6}$ [g]	$1.3–0.64\times10^{-6}$ [g]	$0.64–14\times10^{-6}$ [g]	$0.64–14\times10^{-6}$ [g]
Thermal expansion coefficient	1/K	3×10^{-5}	3×10^{-5}	3×10^{-5}	3×10^{-5}	3×10^{-5}	$3.2–3.9\times10^{-5}$ [i]	$3.2–3.9\times10^{-5}$ [i]	$3.2–3.9\times10^{-5}$ [i]	$3.2–3.9\times10^{-5}$ [i]	$3.2–3.9\times10^{-5}$ [i]
Radioactive heat production	$\mu W/m^3$	1	2	2	0.4	0	0	0	0	0	0

[a] Applies to both pro- and retro- lithosphere.

[b] Oceanic lithospheric mantle is depleted by 30 kg/m^3 above a depth of 60 km.

[c] High-pressure (HP) and ultrahigh-pressure (UHP) densities.

[d] No change to HP or UHP densities.

[e] Includes the effect of strain softening. φ_{eff} varies from 15° to 2°, or 8° to 2°, as the accumulated effective strain increases from 0.5 to 1.5.

[f] Experimental pre-exponential factor has been converted from laboratory value to a corresponding one written in terms of the second invariants of deviatoric stress and strain rate. This is required to ensure that the flow law is coordinate invariant.

[g] Thermal conductivity and diffusivity for lithospheric mantles vary linearly over the temperature range 273–1050 K.

[h] Enhanced thermal conductivity and diffusivity required to maintain adiabatic temperature gradient of 0.4 K/km.

[i] Thermal expansion coefficient increases linearly over the temperature range 500–2000 K.

APPENDIX B
CHAPTER 3 APPENDICES

GSA Data Repository 2020002

Supplementary information to "Inherited terrane properties explain enigmatic post-collisional Himalayan-Tibetan evolution"

Sean Kelly *[1], Christopher Beaumont[2], and Jared P. Butler[2,3]
[1]Earth Science and [2]Oceanography Departments, Dalhousie University, Halifax, NS, Canada, B3H 4R2
[3] Now at Geological Survey of Newfoundland and LabradorSt. John's, NL, Canada, A1B 4J6

TESTABLE PREDICTIONS

Testable Predictions and Relationships Derived from Models MA and MB

We derive the following testable predictions and relationships from MA and MB model results and comparison with observations. They are listed in chronological order. Times listed in Ma are approximate.

1) At 90°E contact between distal margins of Asia and Greater India was at ~11°N.
2) The rifted margin of Greater India was ~1000 km wide based on sedimentary contact, and was subducted northward between 58 and 52 Ma, leading to full continent–continent collision at 52 Ma. The width may have been less if the apron of sediment on the Greater Indian margin extended significantly onto Neotethys oceanic lithosphere.
3) Slab breakoff at 52 Ma was in the Greater India margin, and was followed by UHP exhumation at 50 Ma. Slab breakoff may explain the 51 Ma peak

Gangdese arc magmatic flare up.

4) Lithospheric decoupling and widening of the subduction channel followed UHP exhumation. It allowed asthenospheric upwelling causing decompression melting and heating of overlying Tethyan Himalayan crust. This heating can explain Eo-Himalayan crustal magmatism and metamorphism.
5) Asthenospheric upwelling in, and adjacent to, the subduction channel at ~50 Ma may also be responsible for the Gangdese magmatic flare up.
6) After slab break-off, Indian lithosphere primarily indented Asia resulting in little growth of the Himalayan by accretion from India during the interval ~50–25 Ma.
7) Initial Indian indentation is accommodated primarily by shortening and delamination of the Qiangtang CLM. This leads to rapid northward translation of both the IYS suture and the Lhasa terrane.
8) Delamination of the Qiangtang CLM at ~44 Ma causes Qiangtang magmatism. The style and timing of delamination may vary resulting in diachroneity and differences in the amount of Qiangtang magmatism along strike.
9) Closure of the opening in the subduction channel at ~36 Ma explains termination of 50–38 Ma low-volume Linzizong magmatism.
10) Northward subduction of Lhasa terrane CLM follows Qiangtang CLM delamination. The style may be intracontinental subduction (MB) or double subduction followed by detachment and retreat (MA), while the overlying crust translates northward.
11) Progressive removal of Lhasa CLM and exposure of overlying crust to upwelling asthenosphere explains the 27–22 Ma southward sweep or jump of magmatism from the Qiangtang to south Lhasa terranes.
12) South Lhasa crust remains exposed to upwelled asthenosphere from 20–10 Ma, which leads to additional magmatism and significant heating of the lower/middle Lhasa crust.
13) Removal of Lhasa (± Songpan-Ganzi) CLM allows the initiation of Indian CLM underthrusting beneath the Lhasa crust at ~20 Ma. This underthrusting is responsible for renewed detachment and accretion of Indian crust and

reactivation of thrusting in the vicinity of the IYS suture and on the Himalayan Main Central Thrust.

14) Indian CLM underthrusts Lhasa crust and contacts Songpan-Ganzi by ~10 Ma CLM causing south Lhasa magmatism to cease.
15) Onset of north Tibetan magmatism is partly explained by radioactive crustal incubation heating which spans ~ 20 Myr after crustal shortening and thickening.
16) Underthrust Indian CLM entrains the Kunlun CLM followed by delamination and curl-back of the combined CLM lump. Recent 3 Ma magmatism and hot xenoliths in Qiangtang crust can be explained by asthenospheric upwelling following delamination of this CLM lump.
17) Underthrusting of Indian CLM since 23–20 Ma amounts to ~500 km, in agreement with 400–670 km estimates of coeval shortening in the Himalaya.
18) Significant removal of Asian CLM by either subduction or delamination leads to loss of attached Asian lower crust. Although this missing lower crust may be replaced by Indian lower crust or magmatic underplating, regions of thin lower crust may remain under the Tibetan plateau.
19) Convergence of the IYS suture on stable Asia is much greater than current geological estimates of the shortening of Tibetan terranes if the 90°E contact between distal margins of Asia and Greater India was at ~11°N at 58 Ma.

Implications of Models MA and MB for Mantle Tomography Images

While the models show general agreement with some tomographic images, uncertainties remain about the current state of the mantle under India and Tibet. We list predictions derived from MA and MB concerning the locations and nature of seismic tomographic anomalies.

1) At 90°E, the combined Neotethys and Indian margin slab is located at ~11°N. This corresponds to anomaly NT from Replumaz et al. (2013).
2) Delaminated Qiangtang CLM is located at ~27°N along 90°E. This

corresponds to the tomographic anomaly AS from Replumaz et al. (2013) at 1000 km depth, 90°E.

3) Delaminated Lhasa CLM is also located at ~27°N along 90°E, albeit at shallower depth than the Qiangtang CLM. This corresponds to the 90°E tomographic anomaly 'IN' at 600 km depth and 25–28°N, above the AS anomaly. This is predicted to be Lhasa CLM, not Indian.
4) Entrained Indian/Kunlun CLM curls back to produce thick regions of CLM below the Lhasa terrane.
5) In other regions, no equivalent curled CLM lump is imaged and the slow velocity region to the north is missing. In these regions the delamination and curl back of the CLM lump is yet to happen.

Testable Predictions Reference

Replumaz, A., Guillot, S., Villaseñor, A., and Negredo, A.M. (2013). Amount of Asian lithospheric mantle subducted during the India/Asia collision. *Gondwana Research, 24*, 936–945. https://doi.org/10.1016/j.gr.2012.07.019

Recent Numerical Modelling Papers that Address Aspects of the Evolution of the Himalayan-Tibetan Orogen

Burov and Yamato (2008) addresses the problem of deviations from lithostatic pressure in accreted and subsequently exhumed metamorphic rocks by numerical thermal-mechanical modeling of lithospheric simple shear (subduction), pure shear (collision), folding and Rayleigh- Taylor instabilities. Variations in Moho temperature and convergence velocity are tested. Their results indicate near normal pressures in the subduction channel but large-scale zones of tectonic overpressure outside the channel. However, these do not affect the exhumed rocks. The results support the interpretation that UHP rocks are exhumed from deep in the lithosphere. The same mechanism is seen in models MA and MB.

Burov, E., and Yamato, P. (2008). Continental plate collision, P-T-t-z conditions and unstable vs. stable plate dynamics: Insights from thermo-mechanical modelling. *Lithos, 103*, 178-204. https://doi.org/10.1016/j.lithos.2007.09.014

Chen et al. (2017) uses 3D numerical models to examine the effects of crustal rheology on the formation of the Himalayan-Tibetan orogenic system. They show that deformation and plateau development focuses in weaker crust far into the interior of the upper (Asian) plate, whereas stronger crust suppresses plateau formation. It is concluded that crustal strength heterogeneity controls lithospheric deformation of the Asian continental crust. We agree that crustal heterogeneity may play a role but Chen et al. (2017) present little about the behavior of the mantle lithosphere so that its role in convective removal, delamination and other styles of deformation, and associated magmatism, is not addressed. We suggest that lithospheric mantle heterogeneity is the main determinant of Himalayan-Tibetan orogenesis.

Chen, L., Capitanio, F.A., Liu, L., and Gerya, T.V. (2017). Crustal rheology controls on the Tibetan plateau formation during India-Asia convergence. *Nature Communications*, *8*, 5992. https://doi.org/10.1038/ncomms15992

Copley et al. (2011) model active stress and faulting in the Tibetan plateau crust to show that the difference between strike-slip faulting in the northern plateau and normal faulting in southern Tibet requires mechanical coupling between the upper crust in southern Tibet and the underthrusting Indian crust. They conclude such coupling is inconsistent with active channel flow beneath southern Tibet. Only three end-member models are considered, so it is not clear whether a ~ 25 km thick mid-crustal channel region with a viscosity of 10^{19} Pa s would transmit sufficient shear stress to give normal faulting in the model in southern Tibet. Nor is the possible effect of 'patchy' weak mid-crust investigated. Models MA and MB develop hot weak regions in the thick mid-crust beneath the plateau region which undergo limited channel flow. The system remains coupled to the degree that underthrusting of the Indian lower crust and mantle lithosphere continues to advect overlying Asian crust to the north.

Copley, A., Avouac, J.-P., and Wernicke, B. P. (2011). Evidence for mechanical coupling and strong Indian lower crust beneath southern Tibet. *Nature, 472*, 79-81. https://doi.org/10.1038/nature09926

Koulakov et al. (2018) uses 2D thermomechanical numerical modelling to support the interpretation that earthquakes in India, far from the active plate boundary, correspond to the initiation of deformation which has been transferred from high mountain areas to a weak zone in the Indian lithosphere. The model results are relevant to our study in that the effects of thick and thin lithospheric regions are investigated. The model results show systematic migration of deformation from the weak to strong domains, which tend to underthrust the weak regions.

However, their progressive development of the H-T orogen contrasts with Models MA and MB.

Koulakov, I., Gerya, T., Rastogi, B.K., Jakovlev, A, Medved, I., Kayal, J.R., et al. (2018). Growth of mountain belts in central Asia triggers a new collision zone in central India. *Scientific Reports, 8*, 10710. https://doi.org/10.1038/s41598-018-29105-2

Li, Z.H., Liu, M., and Gerya, T. (2016). Lithosphere delamination in continental collisional orogens: A systematic numerical study. *Journal of Geophysical Research, 121*, 5186-5211. https://doi.org/10.1002/2016JB013106. This paper is referenced and discussed in the main text.

Liao and Gerya (2017) uses 2D thermomechanical numerical modelling to investigate the effects of upper crustal strength, Moho temperature and convergence rate on partitioning of deformation between lower and upper plates during continental collision. Their results favor upper plate deformation when the lower plate has a strong upper crust, there is a high Moho temperature, and a slow convergence rate. These results are generally comparable to ours. We, like Kelly et al. (2016) find that a strong lower plate

mantle, moderate Moho temperatures and even rapid convergence result in upper plate (Asian) deformation when models contain relatively weak Asian terranes.

Liao, J., and Gerya, T. (2017). Partitioning of crustal shortening during continental collision: 2-D thermomechanical modeling. *Journal of Geophysical Research Solid Earth, 122*, 592 -06. https://doi.org/10.1002/2016JB013398

Kelly, S., Butler, J. P., and Beaumont, C. (2016). Continental collision with a sandwiched accreted terrane: Insights into Himalayan–Tibetan lithospheric mantle tectonics? *Earth and Planetary Science Letters, 455*, 176–195. https://doi.org/10.1016/j.epsl.2016.08.039. This paper is referenced and discussed in the main text.

Pang et al. (2018) uses 3D thermomechanical numerical models to investigate N-S trending rifts in the Tibetan plateau. The models have velocity boundary conditions that cause N-S shortening and E-W extension. Models with a weak mid- to lower crust reproduce the N-S rifts, whereas stronger lower crust produces strike-slip faulting. Taken at face value these results appear to be the opposite of those reported by Copley et al. (2011) (see above). However, the Pang et al. (2018) modelling does involve our complexity number 12 (Fig. 1 caption) which cannot be addressed with 2D cross-sectional models.

Pang, Y., Zhang, H., Gerya, T.V., Liao, J., Cheng, H., Shi, Y. (2018). The mechanism and dynamics of N-S rifting in Southern Tibet: Insight from 3-D thermomechanical modeling. *Journal of Geophysical Research; Solid Earth, 23*, 859-877. https://doi.org/10.1002/2017JB014011

Pusok and Kaus (2015) investigates the roles of subduction, collision and indentation on convergent margin lithospheric dynamics leading to the formation of plateaus in the upper plate. The results show that slab-pull alone does not form plateaus. There needs to be additional compressional lithospheric tectonic forces bolstered by strong retaining lithospheric blocks (e.g. Tarim terrane). Scaling analysis is used to identify four regimes

of surface expression during continental collision, in which the Himalayan-Tibetan orogeny belongs to regime iv.

Pusok, A. E., and Kaus, B. J. P. (2015). Development of topography in 3-D continental-collision models. *Geochemistry, Geophysics, Geosystems, 16*, 1378-1400. https://doi.org/10.1002/2015GC005732

Methods

Overview of SOPALE Nested Code

The numerical geodynamical models were computed using the 2D ALE thermomechanical finite-element (FE) software SOPALE-nested (Fullsack, 1995; Beaumont et al., 2009; Butler et al., 2014). Models are designed based on a simple geometry representing oceanic subduction followed by continent-continent collision in which one continent contains five already accreted terranes (Fig. 2). The methodology remains similar to our recent work (Beaumont et al., 2009; Butler et al., 2014; Kelly et al., 2016).

The models are computed by solving the equations for incompressible creeping (Stokes) flows (Eqs. M.1 and M.2) and energy balance (Eq. M.3) on an Eulerian grid subject to mechanical and thermal boundary conditions:

$$\text{(M.1)}\quad \frac{\partial \sigma_{ij}}{\partial x_i} - \frac{\partial P}{\partial x_j} + \rho g = 0, \quad i,j = 1,2$$

$$\text{(M.2)}\quad \frac{\partial v_i}{\partial x_i} = 0, \quad i = 1,2$$

$$\text{(M.3)}\quad \rho(T) c_p \left(\frac{\partial T}{\partial t} + v_i \frac{\partial T}{\partial x_i}\right) = \frac{\partial}{\partial x_i} K(T) \frac{\partial T}{\partial x_i} + A_R + A_{SH} + v_2 \alpha g T \rho(T), \quad i = 1,2,$$

where σ_{ij} is the deviatoric stress tensor, x_i spatial coordinates, P pressure (mean stress), ρ density, g gravitational acceleration, v_i a component of velocity, c_p specific heat, T temperature, t time, K thermal conductivity, A_R crustal radioactive heat production per unit volume, A_{SH} shear heating, and α volumetric thermal expansion. Coupling of the

mechanical and thermal solutions is achieved through the advection of radioactive crust, shear heating, thermal activation of viscous flow, and buoyancy forces arising from metamorphic phase changes and thermal expansion.

The models use a sub-grid approach in which a higher-resolution Eulerian computational domain is 'nested' within a larger, lower-resolution Eulerian domain. The velocity and thermal solution is first obtained for the full domain. This solution is then interpolated onto the boundaries of the nested domain encompassing the vicinity of the subduction zone and the accreted terranes. The computation is then repeated on the higher resolution grid. Coupling of the grids is maintained by using a single Lagrangian grid and cloud of tracking particles, which is passed between the two solutions, with the particles within the nested domain always obeying the higher resolution solution. The Lagrangian grid and particles are advected by the incremental displacement field each time step and they progressively accumulate the total model displacement and deformation and advection of the temperature field.

Model Geometry and Boundary Conditions

The Eulerian model grid is 4000 km wide by 1200 km deep. The initial configuration of the Lagrangian model (Fig. 3.2) is 11350 km wide by 1200 km deep. This means that much of the Lagrangian grid is outside of the Eulerian computational grid but is progressively translated into the Eulerian grid by the boundary velocities. We also make use of the ALE (Arbitrary Lagrangian-Eulerian) nature of SOPALE which allows the Lagrangian grid to be translated with respect to the Eulerian grid by an externally imposed uniform velocity. This 'panning' process is used to move the retro-part of the Lagrangian grid into the Eulerian grid as deformation propagates through the retrolithosphere. This ensures that any part of the model that is currently deforming is within the Eulerian computational grid.

The starting geometry of the H-T system (Fig. 3.2a; Table DR1) is a simplification of the natural equivalent but contains the main components of the system, particularly estimated pre- collisional widths and properties of the previously accreted retrocontinent

terranes and the Indian side of the system. The width of the retrocontinent is restored based on assumed Neotethys (NT) breakoff at 11°N at 90°E. This implies an increase in width of the retrocontinent of ~ 2200 km with respect to the current configuration, which is achieved by proportional increases in the lengths of the terranes south of the Tarim terrane. This approach is simple and avoids biasing the model geometry by observed estimates of the shortening of the individual terranes. We do not include prior deformation of the Asian terranes which remains poorly understood, although there was certainly some deformation. Each lithospheric region is labelled with an abbreviation derived from the natural setting, thereby distinguishing models from observations but allowing easy comparison. Model properties (Fig. 3.2; Table DR1) are described in more detail below.

Differences in the depletion density (i.e., decrease in density with respect to sublithospheric mantle) of continental lithospheric mantle (CLM) may be interpreted to measure varying amounts of chemical depletion (e.g., as reflected in the Mg#). We explore retrolithosphere CLMs with variable depletion densities (Table DR1). The prolithosphere CLM has a constant depletion density of 50 kg/m^3. Models with significantly higher density (e.g., a depletion density of 40 kg/m^3 or less) fail to produce indentation or advancing subduction, a crucial requirement for H-T orogenesis.

Subduction is initiated by a weak seed embedded between the NT oceanic lithosphere and the L-terrane which spans the entire lithosphere. Models have stress-free boundary conditions at the upper surface, and respectively free-slip and no-slip boundary conditions at the base and sides of the model. Total convergence of 4000 km over 58 Myr is based on mean convergence from Ingalls et al. (2017). The left lithospheric velocity boundary condition varies from V_p = 15–4.5 cm/yr (Fig. 3.2) to reproduce the slowing convergence rate of the Indian plate after collision. The right lithospheric boundary condition has V_r = 0 until the last 15 Myr of convergence, when it increases to 1 cm/yr, thereby allowing for 150 km of late convergence in the Tien Shan, which is outside of the model domain and not computed. Small sublithospheric boundary fluxes

are used to 'pump' material out of the sides of the model to conserve volume and maintain isostatic equilibrium.

The continents have laterally uniform crustal radioactive heat production (A_R) for the upper/middle, and lower continental crust of 2.0 and 0.4 μW/m^3, respectively. Coupled with the thermal boundary conditions, basal heat flux 21 mW/m^2, and no-flux side boundaries, the resulting initial steady state surface heat flow and Moho temperatures on the continents are 74 mW/m^2 and ~650°C. The steady state initial base-lithosphere temperature is ~1370°C everywhere in the model. Material thermal expansivity (α) and conductivity (K) are temperature-dependent, with values varying linearly (e.g., from K_1 to K_2) over a range of temperatures (e.g., T_1 to T_2), as described in Table DR1. Other thermal properties are given in Table DR1.

Material Properties

The flow laws and material properties are similar to those used in Beaumont et al. (2001) and Butler et al. (2013). For a more detailed justification for the choice of flow laws and the scaling of these flow laws see Butler et al. (2014). The parameters of the models are considered typical of continental and oceanic lithospheric materials (Beaumont et al., 2006, and refs. therein).

Model materials deform by either frictional-plastic (brittle) or viscous (ductile) flow that includes additional strain-softening/strain-weakening mechanisms. Brittle deformation is modeled using the frictional-plastic Drucker-Prager yield criterion, σ_y:

$$\text{(M.4)} \quad \sigma_y = (J_2')^{1/2} = P\sin\phi_{\text{eff}} + C\cos\phi_{\text{eff}}$$

where J_2' is the second invariant of the deviatoric stress, P dynamical pressure (mean stress), and C cohesion. The effective angle of internal friction, ϕ_{eff} is defined to include the effects of near- hydrostatic pore fluid pressure. The friction angle of all materials, except oceanic sediment, is decreased linearly from $\phi_{\text{eff}} = 15°$ (initial friction

angle) to 2° (strain-softened value) as the effective strain increases from 0.5 to 1.5 (Table DR1). Oceanic sediment has ϕ_{eff} = 8–2°.

Ductile deformation is modeled using power-law flow, for which the effective viscosity is:

$$\text{(M.5)} \quad \eta_{\text{eff}}^{v} = \frac{f}{W_s} A^{-1/n} I_2'^{(1-n/2n)} exp\left(\frac{Q+PV}{nRT_K}\right)$$

where f is a viscosity scaling factor, W_s a strain-weakening factor, A the pre-exponential factor converted to the tensor invariant form, the second invariant of the deviatoric strain rate, n the stress exponent, Q activation energy, P pressure, V the activation volume for power-law creep, T_K absolute temperature, and R the universal gas constant. The scaling factor f allows us to model stronger and weaker materials than the laboratory-derived flow law in a predictable way. This scaling may be interpreted as dehydrated or hydrated rock types, or slightly different compositions.

For simplicity, we base the model materials on a small set of laboratory-determined flow laws. Continental upper/middle-crust and sediment rheologies are based on a wet quartzite flow- law (WQ×*f,* Gleason and Tullis, 1995), lower-crustal and oceanic crustal rheologies are based on a dry Maryland diabase flow law (DMD× f, where f = 0.1, Mackwell et al., 1998), and mantle rheologies are based on a wet olivine flow-law (WOL×*f,* Karato and Wu, 1993) (Table DR1).

Crustal materials viscously strain-weaken according to W_s, the strain-weakening factor (equation M.5), which varies linearly from 1 to 3 as the effective strain increases from 5 to 10.

When stress levels are high in the lithospheric mantle they are subject to a high stress limit, the Peierls stress (Katayama and Karato, 2008) by rescaling the effective viscosity by the Peierls weakening factor so that the stress is close to, but not less than, the Peierls threshold stress, σ_p (Table DR1). This is an approximation to the rapid decrease in

effective viscosity that materials experience under an exponential flow law beyond the Peierls threshold stress.

Each crustal unit comprises an upper/middle crust with ϕ_{eff} (hereafter simply ϕ) = 15–2° (except where noted), and a scaled wet quartzite (WQ×*f*) flow law (Gleason and Tullis, 1995), overlying a lower crust with ϕ = 15–2° (where ϕ = 2° is fully strain-softened) and a dry Maryland diabase (DMD×0.1) flow law (Mackwell et al., 1998), scaled to represent intermediate granulite. The continents and accreted terranes have WQ×1 upper crusts, except for I-crust which has WQ×1.25. The underlying CLM has ϕ = 15–2° and scaled wet olivine flow laws (WOL× *f*; Karato and Wu, 1993) and overlies sublithospheric upper mantle (WOL×2) that extends to 660 km. For the pro-continent (I) and retro-continent (T), the CLM has WOL× 5, corresponding to cratonic properties. The *f*-scaling of the CLM of the accreted terranes varies among the model experiments (Fig. 3.2d), with the values for the MA model shown in Figure 3.2a. Owing to considerable uncertainty concerning the rheology of the lower mantle (Billen, 2010), we assume that the lower mantle has a uniform and constant viscosity of 1×10^{21} Pa s.

Sediment and upper/middle continental crust undergo melt-weakening in a similar temperature- and pressure-dependent manner as in Butler et al. (2015). The viscosity decreases linearly (representing the effect of a small, 4–7 per cent, partial melt) from the calculated power- law value to a fixed linear value of 10^{19} Pa s over the range from the pressure-dependent dry solidus to the solidus temperature plus 50°C. The dry solidus is defined by P-T line segments joining the points (680°C, 0 GPa), (900°C, 2.8 GPa), and (1437°C, 15 GPa) (Zheng et al. 2011). This fixed 10^{19} Pa s viscosity is maintained at higher temperatures except for coesite-eclogite which develops restite properties if it exceeds P-T conditions defined by the line joining points (1000°C, 2.87 GPa) and (1700°C, 12.67 GPa). Overall, melt weakening is a secondary effect which enhances the decoupling between the mid- and lower crust and leads to channel flow in the retrolithosphere.

Density, Volume and Mass Conservation During Phase Transitions

Crustal materials undergo reversible pressure- and temperature-dependent density changes corresponding to the eclogite and coesite-eclogite phase transitions following Warren et al. (2008) (see Table DR1 for density changes). In addition, sediment and upper/middle crust coesite-eclogite materials that achieve restite conditions (Butler et al., 2015) undergo an increase in f to 10 in the power-law viscosity to represent the formation of dry restite after melt extraction (Massonne and Fockenberg, 2012). Restite may subsequently revert to high-pressure eclogite densities, but does not further retrograde to reference crustal density.

Mantle materials undergo a reversible phase change at the upper-lower mantle boundary (~660 km depth) corresponding to the transformation of olivine to perovskite. The latter transformation is determined by a reaction with a Clapeyron slope of -2.0 MPa/K and results in a density increase (proportional for all mantle materials) of ~8% (for a discussion of these parameters, see Billen, 2010). Crustal materials undergo equivalent phase changes at the upper-lower mantle boundary. For simplicity, the models do not include the transformation of olivine to ringwoodite in the mantle transition zone (~440–660 km).

During these phase changes the incompressibility equation is modified to that of mass conservation: $\partial \rho / \partial t = -\partial (\rho v_i) / \partial x_i$. This accounts for the volume change and its effect on the buoyancy and velocity field. The volume change is calculated numerically by applying additional normal, compressive/dilatational forces to finite elements at the time they are subject to phase-related density changes. The value of the excess/reduced pressure is $\Delta P = \Delta \rho / \beta_v \rho$, where β_v is the viscous bulk modulus of the material, and $\Delta\rho / \rho$ is the fractional change in density corresponding to the phase change. The excess/reduced pressure compresses/dilates material locally and only during the model time steps when the phase changes occur, thereby ensuring mass conservation. The fractional volume change accompanying a phase change is small in these models and its effect on the velocity field is minor because it only applies at the time of the phase change. However, failure to ensure mass conservation would have a

long-term effect on the model because the buoyancy forces will be over- or under-estimated by the fractional error in the material volume.

Surface Processes

The models have an upper free surface and the model topography is a product of the model calculation without any imposed constraints except for water loading where the surface is below sea level. Slope-dependent surface erosion acts on the local subaerial topography (Fig. 3.2). It varies according to local slope of the model surface, where it is defined by a maximum erosion rate E*(x)* that operates on a slope of 45° and is scaled down linearly to the local slope of the surface. The erosion rate is also modulated by a spatial climate function (Fig. 3.2) designed to reproduce wet (moderate erosion) conditions on the left-facing orogenic front and dry (lower erosion) conditions over the interior plateau region. The climate function tracks the development and movement of the orogen. Maximum erosion rates are ~ 0.5 cm/yr on the orogenic front.

Methods References

Beaumont, C., Jamieson, R.A., Butler, J.P., and Warren, C.J. (2009), Crustal structure: A key constraint on the mechanism of ultra-high-pressure rock exhumation. *Earth and Planetary Science Letters, 287*, 116–129. https://doi.org/10.1016/j.epsl.2009.08.001

Beaumont, C., Nguyen, M.H., Jamieson, R.A. and Ellis, S. (2006), Crustal flow modes in large hot orogens. In: Law, R.D., Searle, M.P., and Godin, L., (Eds.), Channel Flow, Ductile Extrusion, and Exhumation of Lower-Midcrust in Continental Collision Zones: *Geological Society, London, Special Publication, 268*, 91–145. https://doi.org/10.1144/GSL.SP.2006.268.01.05

Beaumont, C., Jamieson, R.A., Nguyen, M.H., and Lee, B. (2001). Himalayan tectonics explained by extrusion of a low-viscosity crustal channel coupled to focused surface denudation. *Nature, 414*, 738–742. https://doi.org/10.1038/414738a

Billen, M. I. (2010). Slab dynamics in the transition zone. *Physics of the Earth and Planetary Interiors, 183,* 296–308. https://doi. org/10.1016/j.pepi.2010.05.005.2010

Butler, J. P., Beaumont, C., and Jamieson, R. A. (2015). Paradigm lost: Buoyancy thwarted by the strength of the Western Gneiss Region (ultra) high-pressure terrane, Norway. *Lithosphere, 7*, 379–407. https://doi.org/10.1130/L426.1

Butler, J. P., Beaumont, C., and Jamieson, R. A. (2014). The Alps 2: Controls on crustal subduction and (ultra) high-pressure rock exhumation in Alpine-type orogens. *Journal of Geophysical Research: Solid Earth, 119*, 5987–6022. https://doi.org/10.1002/2013JB010799

Butler, J. P., Beaumont, C., and Jamieson, R. A. (2013). The Alps 1: A working geodynamic model for burial and exhumation of (ultra)high pressure rocks in Alpine-type orogens. *Earth and Planetary Science Letters, 377-378*, 114-131 https://doi.org/10.1016/j.epsl.2013.06.039.

Fullsack, P. (1995). An arbitrary Lagrangian-Eulerian formulation for creeping flows and its application in tectonic models. *Geophysical Journal International, 120*, 1–23. https://doi.org/10.1111/j.1365-246X.1995.tb05908.x

Gleason, G. C., and Tullis, J. (1995). A flow law for dislocation creep of quartz aggregates determined with the molten salt cell. *Tectonophysics, 247*, 1-23. https://doi.org/10.1016/0040-1951(95)00011-B

Ingalls, M., Rowley, D.B., Currie, B., and Colman, A.S. (2016). Large-scale subduction of continental crust implied by India-Asia mass-balance calculation. *Nature Geoscience, 9*, 848–853. https://doi.org/10.1038/ngeo2806

Karato, S. and Wu, P. (1993). Rheology of the upper mantle: A synthesis. *Science, 260*, 771–778. https://doi: 10.1126/science.260.5109.771

Katayama, I., and Karato, S. I. (2008). Low-temperature, high-stress deformation of olivine under water-saturated conditions. *Physics of the Earth and Planetary Interiors, 168*, 125-133. https://doi.org/10.1016/j.pepi.2008.05.019

Kelly, S., Butler, J.P., and Beaumont, C. (2016). Continental collision with a sandwiched accreted terrane: Insights into Himalayan–Tibetan lithospheric mantle tectonics? *Earth and Planetary Science Letters, 455*, 176–195. https://doi.org/10.1016/j.epsl.2016.08.039

Mackwell, S. J., Zimmerman, M. E., and Kohlstedt, D. L. (1998). High-temperature deformation of dry diabase with application to tectonics on Venus. *Journal of Geophysical Research, 103*, 975-984. https://doi.org/10.1029/97JB02671

Massonne, H. J., and Fockenberg, T. (2012). Melting of metasedimentary rocks at ultrahigh pressure - Insights from experiments and thermodynamic calculations. *Lithosphere, 4,* 269–285. https://doi.org/10.1130/L185.1

Warren, C. J., Beaumont, C., and Jamieson, R. A. (2008). Modeling tectonic styles and ultra-high pressure (UHP) rock exhumation during the transition from oceanic subduction to continental collision. *Earth and Planetary Science Letters, 267*, 129–145. https://doi.org/10.1016/j. epsl.2007.11.025

Zheng, Y.-F., Xia, Q.-X., Chen, R.-X., and Gao, X.-Y. (2011). Partial melting, fluid supercriticality, and element mobility in ultrahigh-pressure metamorphic rocks during continental collision. *Earth-Science Reviews, 107*, 342-374. https://doi.org/10.1016/j.earscirev.2011.04.004

Table DR1: Model Mechanical and Thermal parameters.

The Table lists reference (constant) properties for oceanic, and pro- and retro- model regions (labelled P and R). The densities and *f*-scaling factors are for the reference properties. The density for pro-CLM, 3320 kg m^{-3}, corresponds to a depletion density of 50 kg m^{-3} with respect to sublithospheric upper mantle. These properties are varied for the retrolithospheric terranes in the model experiments as shown in Figure 3.2 where densities are given in terms of depletion density.

	Units	Oceanic Cover	Upper crust (PC and RC)	lower crust (PC and RC)	Oceanic crust	Continental lithospheric mantle (PC and RC)	Oceanic lithospheric mantle	Sub-lithospheric upper mantle	Lower mantle
Thickness (max)	km	2	24	12	6	84	92	To 660 km depth	660 to 1200 km depth
Reference density (0°C)	kg m^{-3}	2700	2700	2900	2950	Varies, see Fig. 2	3370†	3370	3630
Reference density HP (0°C)§	kg m^{-3}	2800	2950	3300	3400	No change	No change	No change	No change
Reference density UHP (0°C) §	kg m^{-3}	2900	3200	No change	No change	Increases from reference density by 260 below 660 km depth	Changes to 3630 below 660 km depth	Changes to 3630 below 660 km depth	No change
Effective angle of internal friction (φ_{eff})	deg	8-2#	15-2#	15-2#	15-2#	15-2#	15-2#	15-2#	15-2#
Cohesion	MPa	2	2	2	0	0	0	0	0
Flow law	-	WQ	WQ	DMD	DMD	WOL	WOL	WOL	Constant viscosity 1×10^{21} Pa s
Viscosity scaling factor (f)	-	1	Varies, see Fig. 2	0.1	0.1	Varies, see Fig. 2	2	2	-
Strain weakening factor (W_s)	-	3	3	3	3	1	1	1	-
n	-	4	4	4.7	4.7	3	3	3	-
A††	Pa^{-n} s^{-1}	8.57×10^{-28}	8.57×10^{-28}	5.78×10^{-27}	5.78×10^{-27}	1.76×10^{-14}	1.76×10^{-14}	1.76×10^{-14}	-
Q	kJ mol^{-1}	223	223	485	485	430	430	430	-
V^*	m^3 mol^{-1}	0	0	0	0	11×10^{-6}	11×10^{-6}	0	-
Peierls stress	MPa	-	-	-	-	100 (PC), 350 (RC)	150	-	-
Peierls weakening factor	-	-	-	-	-	1×10^{-5}	1×10^{-5}	-	-
Specific heat	m^2 s^{-2} K^{-1}	750	750	750	750	1250	1250	1250	1250
Thermal conductivity	W m^{-1} K^{-1}	2.25	2.25	2.25	2.25	5-2.4§§	5-2.4§§	2.4-52.5§§,##	2.4-52.5§§,##
Thermal diffusivity	m^2 s^{-1}	1×10^{-6}	1×10^{-6}	1×10^{-6}	1×10^{-6}	$1.3\text{-}0.64\times10^{-6}$ §§	$1.3\text{-}0.64\times10^{-6}$ §§	$0.64\text{-}14\times10^{-6}$ §§	$0.64\text{-}14\times10^{-6}$ †††
Thermal expansion coefficient	K^{-1}	3×10^{-5}	3×10^{-5}	3×10^{-5}	3×10^{-5}	$3.2\text{-}3.9\times10^{-5}$ †††	$3.2\text{-}3.9\times10^{-5}$ †††	$3.2\text{-}3.9\times10^{-5}$ †††	$3.2\text{-}3.9\times10^{-5}$ †††
Radioactive heat production	μW m^{-3}	1	2	0.4	0	0	0	0	0

† Oceanic lithospheric mantle is depleted by 15 kg m^{-3} above a depth of 60 km.

§ High-pressure (HP) and ultrahigh-pressure (UHP) densities.

Includes the effect of strain softening. ϕ_{eff} varies from 15 to 2, or 8 to 2, as the accumulated effective strain increases from 0.5 to 1.5.

†† Experimental pre-exponential factor has been converted from laboratory value to a corresponding one written in terms of the second invariants of deviatoric stress and strain rate. This is required to ensure that the flow law is coordinate invariant.

§§ Thermal conductivity and diffusivity for lithospheric mantles vary linearly over the temperature range 273–1050 K.

Enhanced thermal conductivity and diffusivity required to maintain adiabatic temperature gradient of 0.4 K km^{-1}.

††† Thermal expansion coefficient increases linearly over the temperature range 500–2000 K.

Supplementary Figures

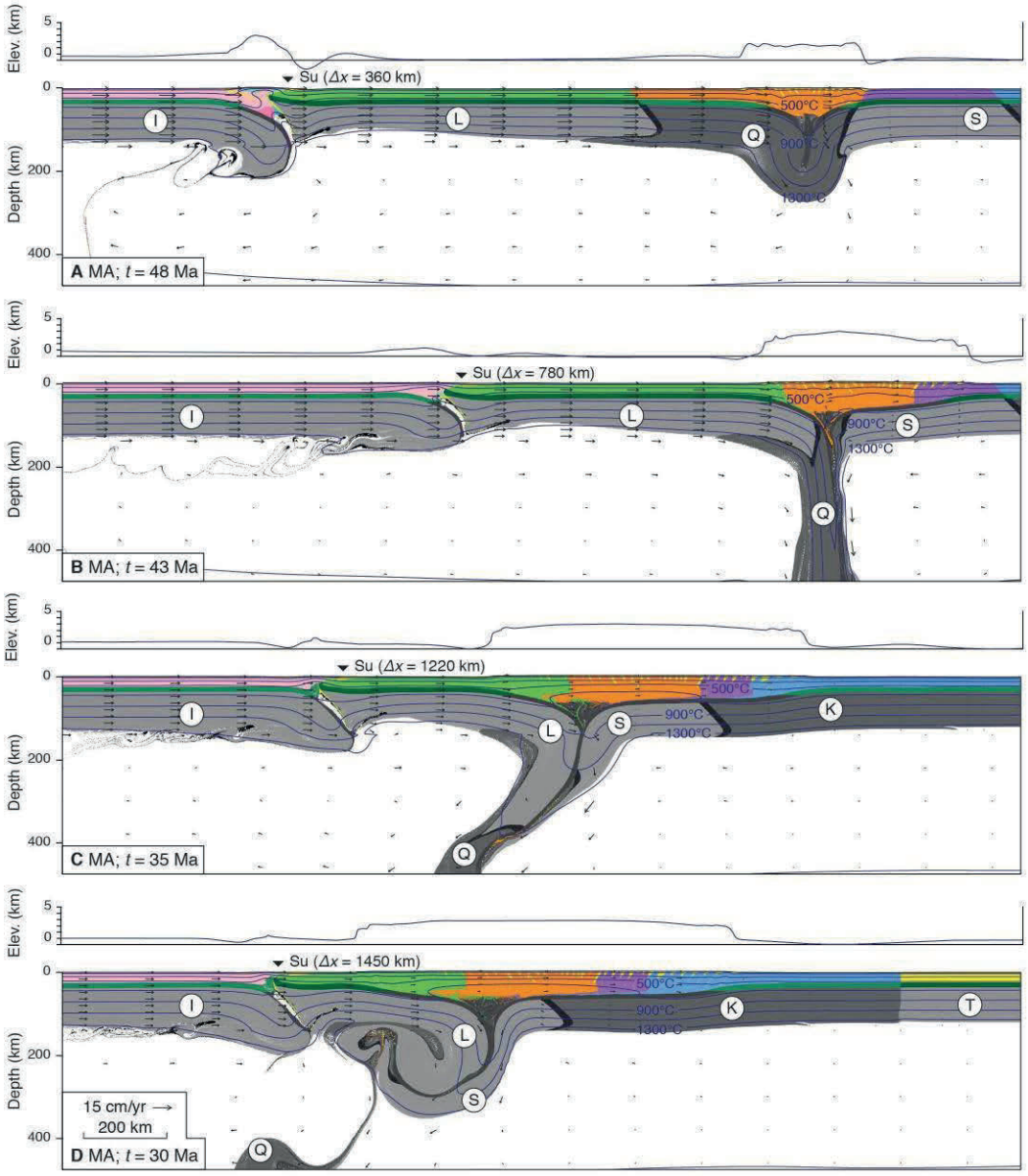

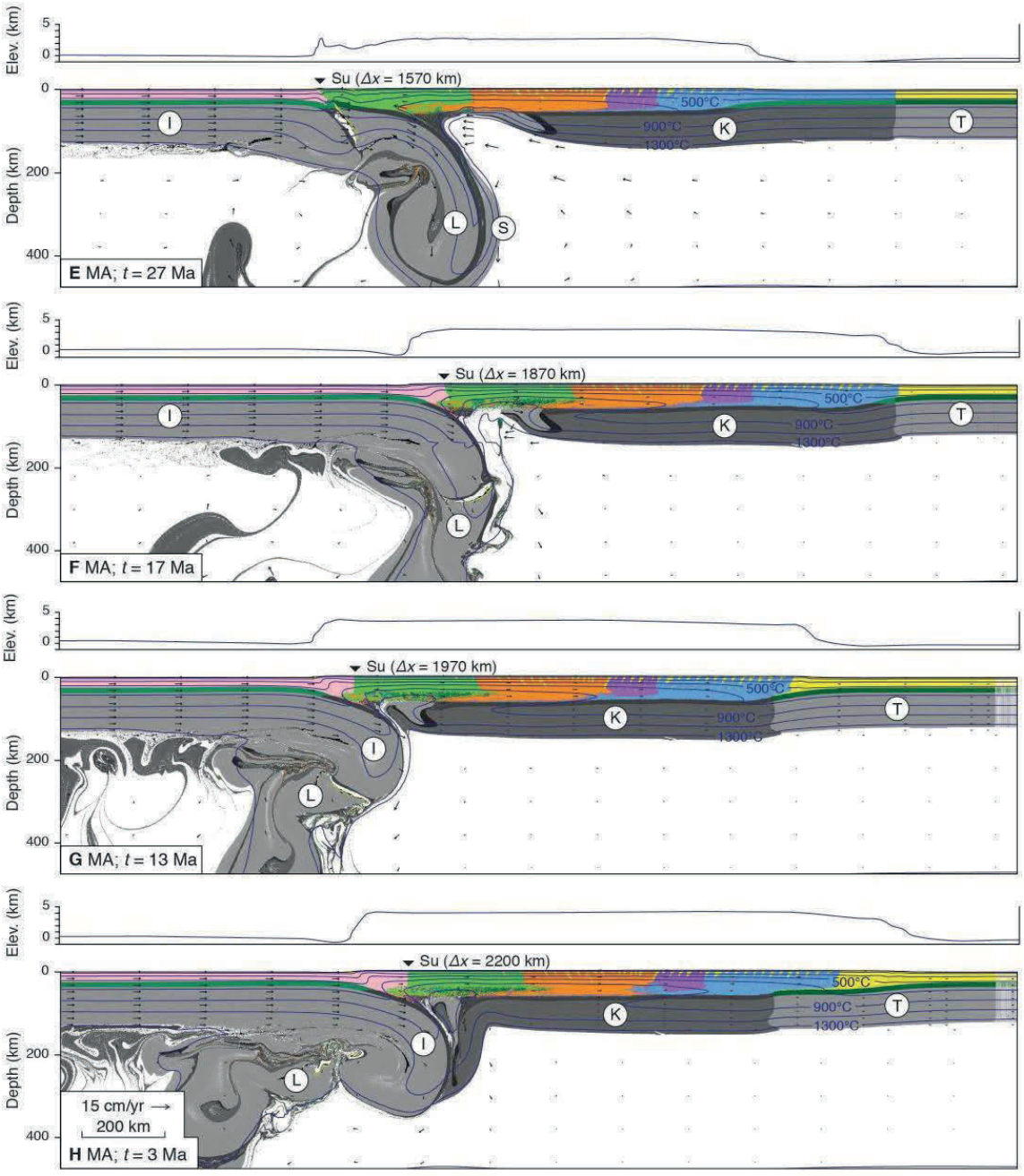

Figure DR1. Evolution of Model MA showing early plateau development in the Q-terrane and subsequent north and south expansion. See Video DR1 in Kelly et al. (2020) for complete annotated evolution. Δx =…..km is the northward translation of the model IYS suture, Su, since slab breakoff. Note panels are shown in a model window that moves to the right as the model evolves.

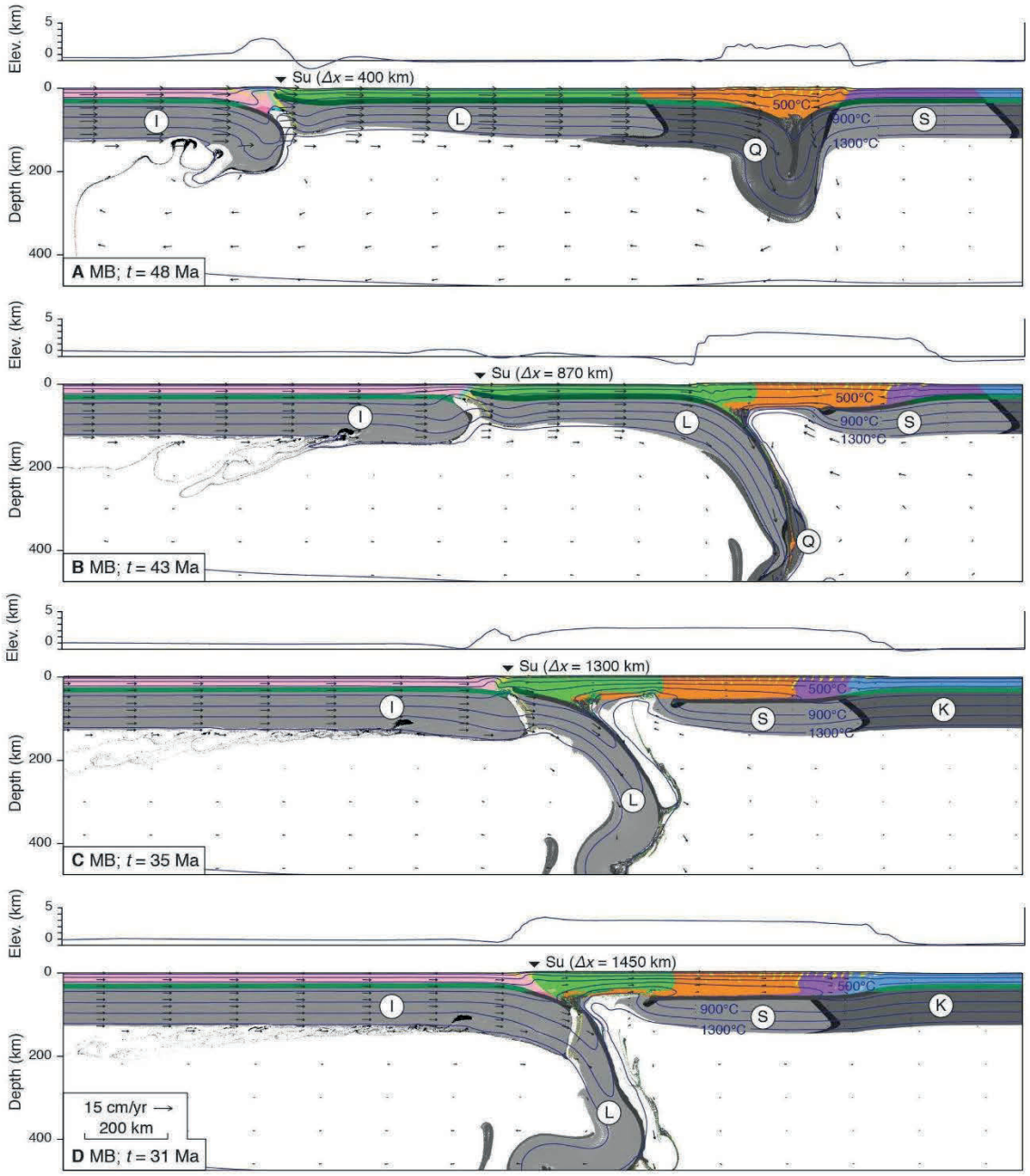
Elev. (km)
5
0
Su (Δx = 400 km)
0
Depth (km)
200
400
I
L
Q
S
500°C
900°C
1300°C
A MB; t = 48 Ma
Su (Δx = 870 km)
I
L
Q
S
500°C
900°C
1300°C
B MB; t = 43 Ma
Su (Δx = 1300 km)
I
L
S
K
500°C
900°C
1300°C
C MB; t = 35 Ma
Su (Δx = 1450 km)
I
L
S
K
500°C
900°C
1300°C
15 cm/yr
200 km
D MB; t = 31 Ma

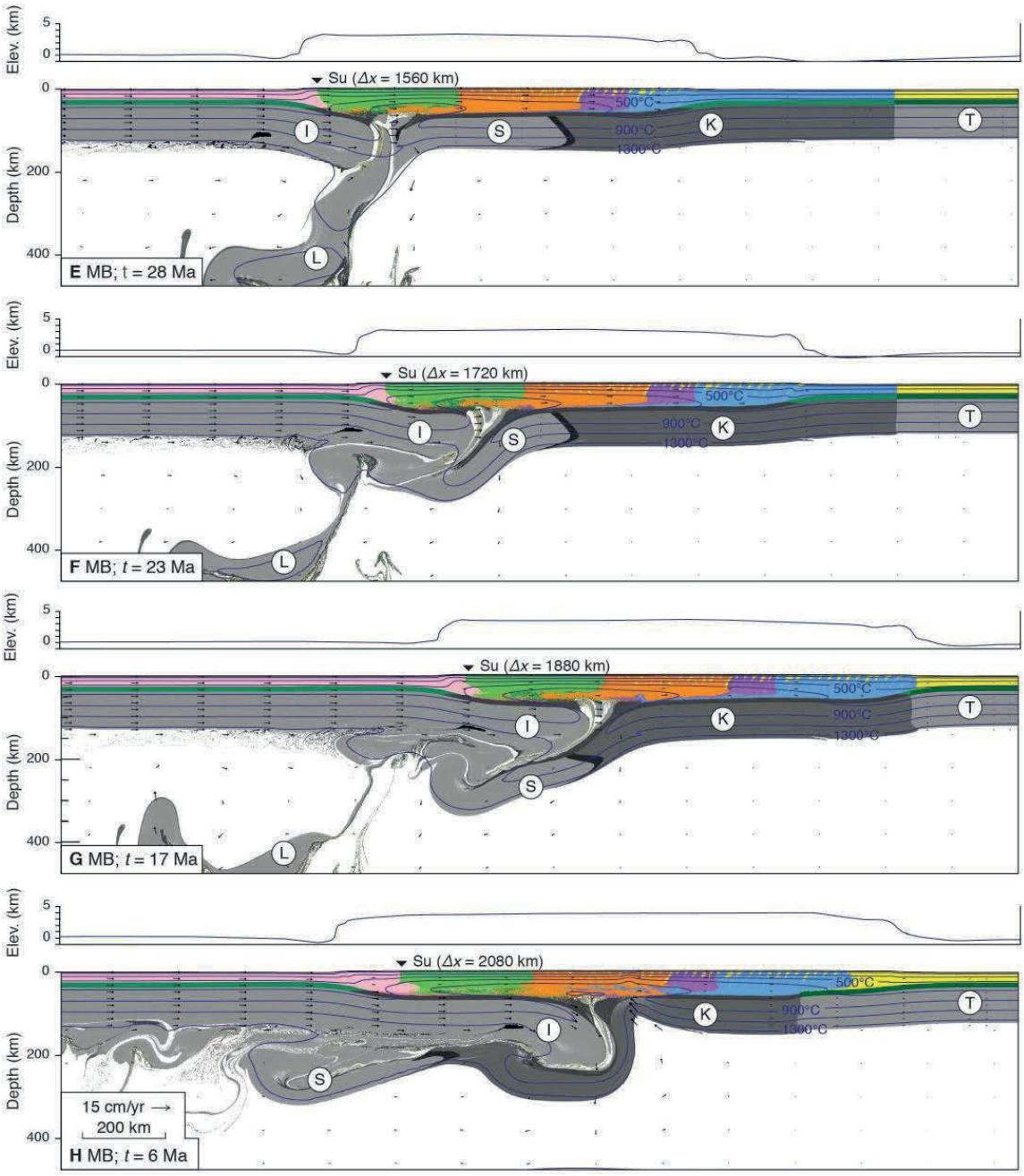

Figure DR2. Evolution of Model MB showing early plateau development in the Q-terrane and subsequent north and south expansion. See Video DR2 in Kelly et al. (2020) for complete annotated evolution. Δx =…..km is the northward translation of the model IYS suture, Su, since slab breakoff. Note panels are shown in a model window that moves to the right as the model evolves.

APPENDIX C
CHAPTER 4 APPENDICES

Supporting Information For

Eohimalayan Metamorphism and Subsequent Tectonic Quiescence Explained

Kelly S., Beaumont, C. and Jamieson, R. A.

Appendix C1. Observations Requiring Explanation

Here we list key observations from the Early (~58-45 Ma) and Late Eohimalayan (~45-30 Ma) Himalayan-Tibetan (H-T) evolution which require explanation (Section 4.2, Fig. C.1). The focus is on the vicinity of 90°E, with additional information from elsewhere along the Himalayan arc where it contributes to defining the problem.

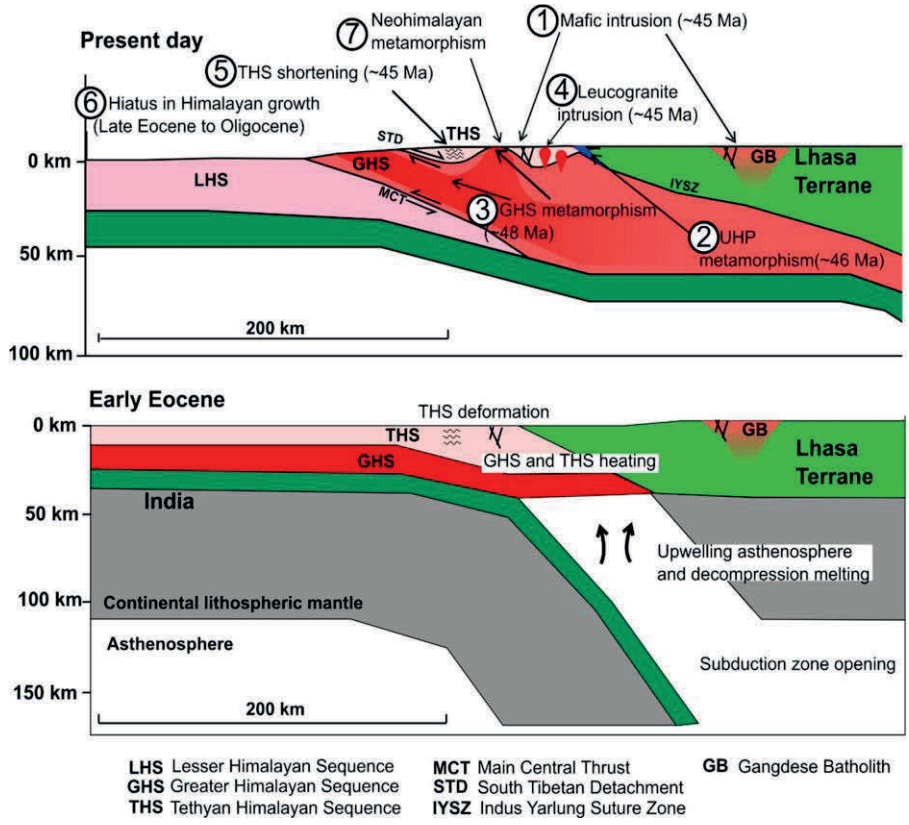

Figure C.1. Generalized present-day cross-section of the Himalaya at ~90°E (see Fig. 4.1e for location), showing the key Eohimalayan observations requiring explanation (1-7, see text for details). The figure shows the current configuration. The Early Eocene (Eohimalayan) configuration would have been very different, with an inferred much smaller orogen, less crustal accretion and thickening, and no, or just nascent, features like the MCT, GHS and STD.

1) Early Eohimalayan sublithospheric magmas: Early Eohimalayan diorites, gabbros, and basaltic dykes in southern and southeastern Tibet, with ages ranging from 57-45 Ma, suggest that sublithospheric magmas intruded Tibetan crust soon after initial India-Asia contact. Gabbroic rocks with no crustal contamination were intruded into the Tethyan Himalayan (TH) rocks in the Gyangze region (~90°E) at ~45±1.4 Ma (Ji et al., 2016) and the eastern Gangdese batholith (between 90 and 94°E) at ~50 Ma (Wang et al., 2019). On the basis of their oceanic island basalt compositions and depleted Sr-Nd isotopes the source of the Gyangze gabbros is best explained by decompression melting of enriched asthenosphere (Ji et al., 2016).

2) *Eohimalayan (ultra-)high-pressure (UHP) metamorphism:* Tethyan Himalayan mid-crustal rocks adjacent to the Indus-Yarlung-Tsangpo suture in the Kaghan Valley (~73°E) and at Tso Morari (~78°E) reached UHP metamorphic conditions of ~2.7-3.6 GPa and <770°C at ~48-46 Ma (Fig. A.2, O'Brien et al., 2001; Parrish et al., 2006; Donaldson et al., 2013; St-Onge et al., 2013; Palin et al., 2017; O'Brien, 2019). These rocks were exhumed to mid-crustal levels and overprinted by amphibolite-facies metamorphism at ~45-40 Ma (Epard and Steck, 2008). At Kaghan, the amphibolite-facies overprint indicates heating to 650–720°C at 1.0–1.2 GPa (Lombardo and Rolfo, 2000; Kaneko et al., 2003; Parrish et al., 2006; Wilke et al., 2010) prior to cooling at 42-39 Ma (e.g., Smith et al., 1994; Hubbard et al., 1995). At two locations in the Tso Morari nappes, P-T conditions of 590 ± 90°C at 0.8 ± 0.3 GPa at 48 ± 2 Ma (de Sigoyer et al., 1997, 2000, 2004; Guillot et al., 1997) and 650 ± 50°C, 0.9 ± 0.1 GPa (Girard, 2001) were recorded by amphibolite-facies assemblages. In the western Himalaya, the HP Stak eclogite recorded P_{max} and $T@P_{max}$ conditions of ~2.5 GPa and 750°C at ~51.5 Ma, followed by decompression and reheating at ~1.2 GPa by 32 Ma (Pognante et al., 1993; Lanari et al., 2013; Kouketsu et al., 2016). In the central Himalaya, HP rocks record peak P-T conditions of 1.5-2.0 GPa and 600-700°C at 40-35 Ma (e.g., Groppo et al., 2007, 2010; Kellett et al., 2014; Laskowski et al., 2017), with exhumation after 30 Ma. While the (U)HP metamorphism itself does not require a special explanation, the reheating is not readily explained by existing models.

3) *Eohimalayan Barrovian (MP-MT) metamorphism*: While evidence for two distinct phases of metamorphism in the GHS has long been recognized (e.g., Hodges and Silverberg, 1988), until recently the timing and duration of the early phase have been difficult to resolve. Data from southeastern Tibet (Fig. C2) show that prograde metamorphism (550°C at 0.7 GPa; Lee et al., 2004) was underway in the Mabja dome (~88°E) by 54 Ma (Smit et al., 2014), with peak conditions of 600-700°C reached by ~35 Ma (Lee and Whitehouse, 2007). Peak P-T conditions of 650-700°C at 0.7-0.9 GPa were reached as early as 48-45 Ma in the Yardoi dome (~92°E; Gao et al., 2012; Ding et al., 2016). Further south, peak

conditions of ca 730°C at 1 GPa were reached in the upper GHS at Cona (~92°E) by 40 Ma (Ding et al., 2021), while data from migmatitic rocks in the Ghunsa region (~88°E; Imayama et al., 2012, 2018) suggest peak conditions of~800°C at ≥ 1 GPa, with some decompression before 33 Ma. In the central and western Himalaya (Fig. C.2) metamorphic ages in the range 50-40 Ma have been interpreted in terms of similar prograde and peak metamorphic conditions (650-750°C, 0.8-1.2 GPa; e.g., Chambers et al., 2009; Kohn and Corrie, 2011; Langille et al., 2012; Stübner et al., 2014; Iaccarino et al., 2015; Carosi et al., 2019; Shresta et al., 2020; Robyr and Lanari, 2020; Benetti et al., 2021; Khanal et al., 2021), with data from the Kalopani Shear Zone (Carosi et al., 2016) and the Gumburanjun dome (Stipska et al., 2020) indicating that exhumation was locally underway by ~40 Ma.

Taken together, these data suggest that widespread MP-MT (Barrovian) metamorphism affected the upper Greater Himalayan Sequence (GHS) and its presumed equivalents further to the north at or before ~35 Ma. Peak metamorphic temperatures of 650-750°C were reached by 40-35 Ma, and sustained at approximately constant or somewhat decreasing pressure until the onset of Neohimalayan metamorphism and exhumation after 30 Ma. The heat source for the Eohimalayan metamorphism remains enigmatic (e.g., Guillot and Allemand, 2002).

4) *Eohimalayan crustal magmatism:* Eohimalayan granitic intrusions ranging from 45-35 Ma, with inferred crustal sources, have been documented in some north Himalayan gneiss domes (e.g., Aikman et al., 2008; Zeng et al., 2011; Regis et al. 2014). Leucogranites were intruded into the Tethyan Himalayan Sequence as early as ~45 Ma (Zeng et al., 2015) in the Yardoi dome (~92°E) and by ~36 Ma (Regis et al., 2014) in the Jomolhari massif (~89°E). In the latter case, the magmas were interpreted to be from a GHS source (Regis et al., 2014), indicating that high- temperature GHS rocks were positioned beneath the TH at ~36 Ma. Within the Yardoi dome, 43.5± 1.3 Ma metamorphism and partial melting of garnet amphibolite at inferred elevated pressures suggest melting of thickened

lower crust (Zeng et al., 2011). In combination with migmatites associated with some Eohimalayan metamorphic rocks (e.g., Imayama et al., 2018), these observations imply that Tethyan Himalayan crust was hot enough to melt by the mid- Eocene.

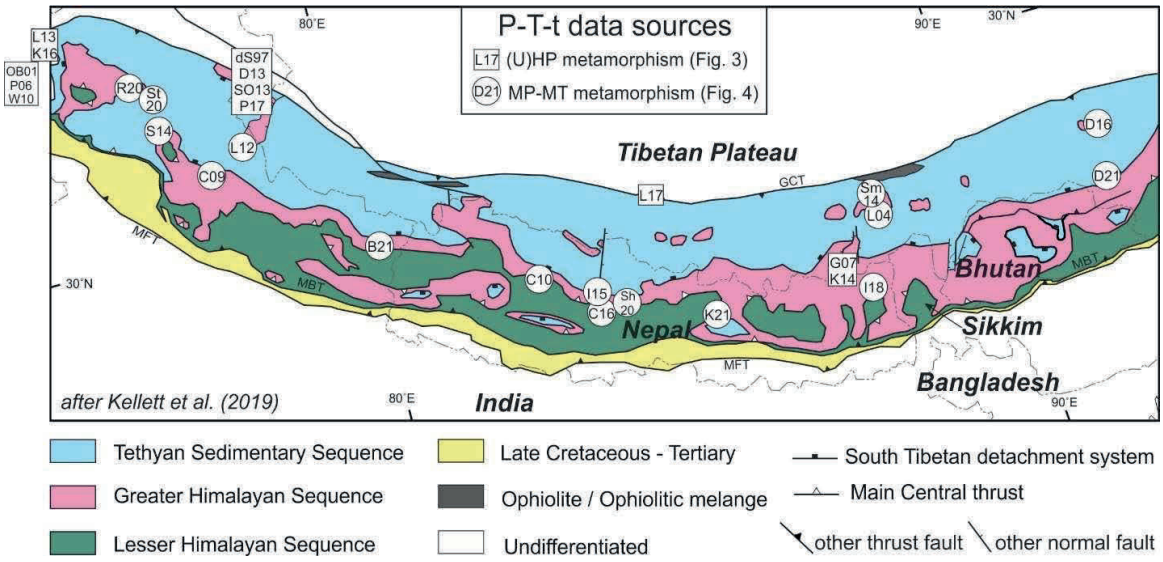

Figure C.2. Locations of P-T-t data compiled in Figures 4.3 and 4.4 (main text). MFT = Main Frontal thrust; MBT = Main Boundary thrust. Rectangles: data from (U)HP metamorphic rocks, from the following sources. Kaghan (west of map area): OB01 = O'Brien et al. (2001), P06 = Parrish et al. (2006), W10 = Wilkes et al. (2010); Stak (just west of map area): L13 = Lanari et al. (2013), K16 = Kouketsu et al. (2016); Tso Morari: dS97 = deSigoyer et al. (1997, 2000, 2004), D13 = Donaldson et al. (2013), SO13 = St-Onge et al. (2013), P17 = Palin et al. (2017); Lopu: L17 = Laskowski et al. (2017); Ama Drime: G07 = Groppo et al. (2007), K14 = Kellett et al. (2017). Circles: data from MP-MT (Barrovian) metamorphic rocks, from the following sources. Western Himalaya (78-82°E): Sutlej - C09 = Chambers et al. (2009); Leo Pargil – L12= Langille et al. (2012); Central Himachal - S14 = Stübner et al. (2014); Garwhal - B21 = Benetti et al. (2021); Gianbul - R20 = Robyr & Lanari (2020); Gumburanjun - St20 = Stipska et al. (2020); Central Himalaya (82-88°E): Kathmandu klippe - K21 = Khanal et al. (2021); Kali Gandaki - I15 = Iaccarino et al. (2015), C16 = Carosi et al. (2016); Dolpo - C10 = Carosi et al. (2010); Modi Khola - Sh20 = Shrestha et al. (2020); Eastern Himalaya (88-92°E): Ghunsa - I18= Imayama et al. (2018); Cona - D21 = Ding et al. (2021); Mabja dome - Sm14 = Smit et al. (2014), L04 = Lee et al. (2004); Yardoi dome - D16 = Ding et al. (2016). Base map provided by Dawn Kellett (Kellett et al., 2019).

5) Eohimalayan deformation: The India-Asia collision was progressive (Najman et al., 2010, 2017; DeCelles et al., 2014; Hu et al., 2016), starting with initial contact of distal margins at ~59±1 Ma, with full-thickness Indian crust involved in the

collision by ~54 Ma. Tethyan Himalayan (TH) rocks were deformed and thickened by at least ~45 Ma based on ages of TH fabrics (Wiesmayr and Grasemann, 2002) and undeformed granitoids cutting deformed TH rocks (e.g., Aikman et al., 2008). Paleocene-Eocene deposition of inferred TH-derived sediments into the Indian foreland basin at Sangdanlin (~85°E) in south-central Tibet (DeCelles et al., 2014) indicates that uplift and erosion of TH rocks was underway at this time.

6) Tectonic quiescence: Aikman et al. (2008, 2012) inferred a quiescent interval in the development of the eastern Himalaya from the Middle Eocene to Miocene based on two separate episodes of amphibolite-grade metamorphism and monazite growth (~40 Ma and 15 Ma) in the Yala-Xiangbo dome and Dala igneous complex (92°E). In addition, metamorphic crystallization ages from the Kali Gandaki valley (84°E) require that GHS rocks resided in the hot middle crust (710-720°C at 1.0-1.1 GPa) from 36 to 28 Ma following Eohimalayan prograde metamorphism (Iaccarino et al., 2015). Eclogite-facies rocks from the Ama Drime massif (87.5°E) record Late Eocene burial of Indian crust to at least ~60 km followed by >20 Myr residence in the lower- middle crust before Neohimalayan (<13 Ma) granulite and amphibolite facies metamorphic overprinting (Kellet et al., 2014). However, data from these and other Eohimalayan metamorphic sequences do not require further burial beneath the Himalaya after ca 40-35 Ma. Later Neohimalayan decompression and cooling (25-15 Ma) were accompanied by pervasive deformation.

Furthermore, reconstructions of the development and southward advance of the Himalayan thrust belt and foreland basin (e.g., Fig. 12 of DeCelles et al., 2014) suggest limited shortening of Indian crust in the intervals 45-40 Ma and 40-25 Ma, much less than the estimated India-Asia convergence of ~2000 km. A remnant marine seaway existed south of the Indus-Yarlung- Tsangpo suture, possibly until as late as ~38 Ma (Jiang et al., 2016; Wang et al., 2020), suggesting little to no underthrusting of Indian lithosphere. Limited advance of the thrust belt is also consistent with the widespread un/dis-conformity (Garzanti, 2019)

attributed to erosion of, or no deposition on, the foreland flexural bulge. That this inferred flexural bulge was near- stationary within India is additional evidence of limited underthrusting of Indian lithosphere beneath the Himalaya (Aitchison et al., 2007).

In summary, evidence from Eohimalyan metamorphic sequences for early heating and sustained high temperatures in Tethyan Himalayan rocks, combined with stratigraphic and structural evidence that there was little or no advance of the Himalayan thrust front toward itsforeland, is consistent with ~40-28 Ma tectonic quiescence accompanied by sustained high temperatures between the Eohimalayan and Neohimalayan tectonic episodes.

7) Neohimalayan metamorphism: Neohimalayan metamorphism, anataxis, and deformation in the GHS are well documented (e.g., Iaccarino et al., 2015; Carosi et al., 2016; Ding et al., 2016; Wang et al., 2018; Jessup et al., 2019; summaries by Wang et al., 2016; Carosi et al., 2019, and references therein). Data demonstrate diachronous evolution of the GHS ductile nappe stack, with the upper GHS below and close to the South Tibetan Detachment System (STDS) buried, metamorphosed, and locally exhumed earlier than lower GHS structural levels close to the Main Central Thrust zone. The later Neohimalayan evolution, starting at ≤30 Ma and continuing throughout the Miocene, is distinct from the Early Eohimalayan prograde metamorphism and Late Eohimalayan heating and melt generation.

Supplementary References: Observations and P-T-t Data Sources

Aikman, A.B., Harrison, T.M., and Lin, D. (2008). Evidence for early (> 44 Ma) Himalayan crustal thickening, Tethyan Himalaya, southeastern Tibet. *Earth and Planetary Science Letters 274,* 14–23. https://doi.org/10.1016/j.epsl.2008.06.038

Aikman, A.B., Harrison, T.M., and Hermann, J. (2012). Age and thermal history of Eo- and Neohimalayan granitoids, eastern Himalaya. *Journal of Asian Earth Sciences, 51*, 85–97. https://doi.org/10.1016/j.jseaes.2012 .01.011

Aitchison, J.C., Ali, J.R., and Davis, A.M. (2007). When and where did India and Asia collide? *Journal of Geophysical Research: Solid Earth, 112*, B05423. https://doi.org/10.1029/2006JB004706

Benetti, B., Montomoli, C., Iaccarino, S., Langone, A., and Carosi, R. (2021). Mapping tectono- metamorphic discontinuities in orogenic belts: implications for mid-crust exhumation in NW Himalaya. *Lithos 392–393*, 106129. https://doi.org/10.1016/j.lithos.2021.106129

Carosi, R., Montomoli, C., Rubatto, D., and Visonà, D. (2010). Late Oligocene high-temperature shear zones in the core of the Higher Himalayan Crystallines (Lower Dolpo, western Nepal). *Tectonics, 29*, TC4029. https://doi.org/10.1029/2008TC002400

Carosi, R., Montomoli, C., Iaccarino, S., Massonne, H.J., Rubatto, D., Langone, A., et al. (2016). Middle to late Eocene exhumation of the greater Himalayan sequence in the central Himalayas: progressive accretion from the Indian plate. *Geological Society of America: Bulletin, 128*, 1571–1592. https://doi.org/10.1130/B31471.1

Carosi, R., Montomoli, C., Iaccarino, S., and Visona, D. (2019). Structural evolution, meta-morphism and melting in the greater Himalayan sequence in central-western Nepal. Treloar, P.J., Searle, M.P. (Eds.), Himalayan Tectonics: A Modern Synthesis. *Geological Society of London Special Publication, 483*, 305–323. https://doi.org/10.1144/SP483.3

Chambers, J., Caddick, M., Argles, T., Horstwood, M., Sherlock, S., and Harris, N. (2009). Empirical constraints on extrusion mechanisms from the upper margin of an exhumed high-grade orogenic core, Sutlej valley, NW India. *Tectonophysics 477*, 77–92. https://doi.org/10.1016/j.tecto.2008.10.013

de Sigoyer, J., Guillot, S., Lardeaux, J.M., and Mascle, G. (1997). Glaucophane-bearing eclogites in the Tso Morari dome (eastern Ladakh, NW Himalaya). *European Journal of Mineralogy*, 1073–1083. https://doi.org/10.1127/ejm/9/5/1073

de Sigoyer, J., Chavagnac, V., Blichert-Toft, J., Villa, I.M., Luais, B., Guillot, S., et al. (2000). Dating the Indian continental subduction and collisional thickening in the northwest Himalaya: Multichronology of the Tso Morari eclogites. *Geology 28*, 487–490. https://doi.org/10.1130/0091-7613(2000)28<487:DTICSA>2.0.CO;2

de Sigoyer, J., Guillot, S., and Dick, P. (2004). Exhumation processes of the high-pressure low-temperature Tso Morari dome in a convergent context (eastern Ladakh, NW Himalaya). *Tectonics, 23*, TC3003. https://doi.org/10.1029/2002TC001492

DeCelles, P.G., Kapp, P., Gehrels, G.E., and Ding, L. (2014). Paleocene-Eocene foreland basin evolution in the Himalaya of southern Tibet and Nepal: Implications for the age of initial India-Asia collision. *Tectonics*, *33*, 824–849. https://doi.org/10.1002/2014TC003522

Ding, H., Zhang, Z., Hu, K., Dong, X., Xiang, H., and Mu, H. (2016). P–T–t–D paths of the North Himalayan metamorphic rocks: Implications for the Himalayan orogeny. *Tectonophysics, 683*, 393–404. http://dx.doi.org/10.1016/j.tecto.2016.06.035

Ding, H., Kohn, M.J., and Zhang, Z. (2021). Long-lived (ca. 22–24 Myr) partial melts in the eastern Himalaya: Petrochronologic constraints and tectonic implications. *Earth and Planetary Science Letters, 558*, 116764. https://doi.org/10.1016/j.epsl.2021.116764

Donaldson, D.G., Webb, A.A.G., Menold, C.A., Kylander-Clark, A.R., and Hacker, B.R. (2013). Petrochronology of Himalayan ultrahigh-pressure eclogite. *Geology*, *41*, 835–838. https://doi.org/10.1130/G33699.1

Epard, J.-L., and Steck, A. (2008). Structural development of the Tso Morari ultra-high pressure nappe of the Ladakh Himalaya. *Tectonophysics, 451*, 242–264. https://doi.org/10.1016/j.tecto.2007.11.050

Gao, L.E., Zeng, L.S., and Xie, K.J. (2012). Eocene high grade metamorphism and crustal anatexis in the North Himalaya Gneiss Domes, Southern Tibet. *Chinese Science Bulletin, 57*, 639-650. https://doi: 10.1007/s11434-011-4805-4

Garzanti, E. (2019). The Himalayan Foreland Basin from collision onset to the present: A sedimentary–petrology perspective. Treloar, P.J., and Searle, M.P. (Eds.), Himalayan Tectonics: A Modern Synthesis. *Geological Society, London, Special Publications, 483,* https://doi.org/10.1144/SP483.17

Girard, M. (2001). Metamorphism and tectonics of the transition between non-metamorphic Tethyan Himalaya sediments and the North Himalayan Crystalline Zone (Rupshu area, Ladakh, NW India). *Memoires de Géologie (Lausanne) 35*, 1–100.

Groppo, C., Lombardo, B., Rolfo, F., and Pertusati, P. (2007). Clockwise exhumation path of granulitized eclogites from the Ama Drime range (Eastern Himalayas). *Journal of Metamorphic Geology*, 51–75. https://doi.org/10.1111/j.1525-1314.2006.00678.x

Groppo, C., Rubatto, D., Rolfo, F., and Lombardo, B. (2010). Early Oligocene partial melting in the Main Central Thrust Zone (Arun valley, eastern Nepal Himalaya). *Lithos 118*, 287–301. https://doi.org/10.1016/j.lithos.2010.05.003

Guillot, S., and Allemand, P. (2002). Two-dimensional thermal modelling of the early tectonometamorphic evolution in central Himalaya. *Journal of Geodynamics. 34*, 77–98. https://doi.org/ 10.1016/S0264-3707(02)00016-9

Guillot, S., de Sigoyer, J., Lardeaux, J.M., and Mascle, G. (1997). Eclogitic metasediments from the Tso Morari area (Ladakh, Himalaya): evidence for continental subduction during India–Asian convergence. *Contributions to Mineralogy and Petrology, 128*, 197–212. https://doi.org/10.1007/ s004100050303

Hodges, K.V., and Silverberg, D.S. (1988). Thermal evolution of the greater Himalaya, Garwhal, India. *Tectonics, 7*, 583–600. https://doi.org/10.1029/TC007i003p00583

Hu, X., Garzanti, E., Wang, J., Huang, W., An, W., and Webb, A. (2016). The timing of India-Asia collision onset–Facts, theories, controversies. *Earth-Science Reviews, 160*, 264–299. https://doi.org/10.1016/j.earscirev.2016.07.014

Hubbard, M.S., Spencer, D.A., and West, D.P. (1995). Tectonic exhumation of the Nanga Parbat massif, northern Pakistan. *Earth and Planetary Science Letters, 133*, 213–225. https://doi.org/10.1016/0012- 821X(95)00075-N

Iaccarino, S., Montomoli, C., Carosi, R., Massonne, H.-J., Langone, A., and Visonà, D. (2015). Pressure–temperature–time–deformation path of kyanite-bearing migmatitic paragneiss in the Kali Gandaki valley (Central Nepal): Investigation of Late Eocene–Early Oligocene melting processes. *Lithos, 231*, 103–121. http://dx.doi.org/10.1016/j.lithos.2015.06.005

Imayama, T., Takeshita, T., Keewook, Y., Cho, D.-L., Kitajima, K., Tsutsumi, Y., et al. (2012). Two-stage partial melting and contrasting cooling history within the Higher Himalayan Crystalline Sequence in the far eastern Nepal Himalaya. *Lithos, 134–135*, 1–22. https://doi.org/10.1016/j.lithos.2011.12.004

Imayama, T., Takeshita, T., Yi, K., and Fukuyama, M. (2018). Early Oligocene partial melting via biotite dehydration melting and prolonged low-pressure–low-temperature metamorphism of the upper High Himalaya Crystalline Sequence in the far east of Nepal. In: Sharma, R., Villa, I. M., and Kumar, S. (Eds.), Crustal Architecture and Evolution of the Himalaya–Karakoram–Tibet Orogen. *Geological Society, London, Special Publications, 481*, 147-173. https://doi.org/10.1144/SP481.2

Jessup, M.J., Langille, J.M., Diedesch, T.F., and Cottle, J.M. (2019). Gneiss dome formation in the Himalaya and southern Tibet. In: Treloar, P. J. and Searle, M. P. (Eds.), Himalayan Tectonics: A Modern Synthesis. *Geological Society, London, Special Publications, 483*, 401–422. https://doi.org/10.1144/SP483.15

Ji, W.Q., Wu, F.Y., Chung, S.L., Wang, X.C., Liu, C.Z., Li, Q.L., et al (2016). Eocene Neo-Tethyan slab breakoff constrained by 45 Ma oceanic island basalt–type magmatism in southern Tibet. *Geology*, *44,* 283–286. https://doi.org/10.1130/G37612.1

Jiang, T., Aitchison, J.C., and Wan, X. (2016). The youngest marine deposits preserved in southern Tibet and disappearance of the Tethyan Ocean. *Gondwana Research, 32*, 64–75. https://doi.org/10.1016/j.gr.2015.01.015

Kaneko, Y., Katayama, I., Yamamoto, H., Misawa, K., Ishikawa, M., Rehman, H.U., et al. (2003). Timing of Himalayan ultrahigh-pressure metamorphism: sinking rate and subduction angle of the Indian continental crust beneath Asia. *Journal of Metamorphic Geology ,21*, 589–599. https://doi.org/10.1046/j.1525-1314.2003.00466.x

Kellett, D.A., Cottle, J.M., and Smit, M. (2014). Eocene deep crust at Ama Drime, Tibet: early evolution of the Himalayan orogeny. *Lithosphere, 6*, 220–229. https://doi.org/10.1130/L350.1

Kellett, D.A., Cottle, J.M., and Larson, K.P. (2019). The South Tibetan Detachment System: history, advances, definition and future directions. In: Treloar, P. J. and Searle, M. P. (Eds.), Himalayan Tectonics: A Modern Synthesis. *Geological Society, London, Special Publications, 481*, 377-400. https://doi.org/10.1144/SP483.2

Khanal, G. P., Wang, J.-M., Larson, K.P., Wu, F.-Y., Rai, S. M., Wang, J.-G., and Yang, L. (2021). Eocene metamorphism and anatexis in the Kathmandu klippe, central Nepal: implications for early crustal thickening and initial rise of the Himalaya. *Tectonics, 40*, e2020TC006532; https://doi.org/10.1029/2020TC006532

Kohn, M.J., and Corrie, S.L. (2011). Preserved Zr-temperatures and U–Pb ages in high-grade metamorphic titanite: evidence for a static hot channel in the Himalayan orogen. *Earth and Planetary Science Letters, 311*,136–143. https://doi.org/10.1016/j.epsl.2011.09.008

Kouketsu, Y., Hattori, K., Guillot, S., and Rayner, N. (2016). Eocene to Oligocene retrogression and recrystallization of the Stak eclogite in northwest Himalaya*. Lithos, 240–243*, 155–166. https://doi.org/10.1016/j.lithos.2015.10.022

Lanari, P., Riel, N., Guillot, S., Vidal, O., Schwartz, S., Pecher, A., and Hattori, K.H. (2013). Deciphering highpressure metamorphism in collisional context using microprobe mapping methods: application to the Stak eclogitic massif (northwest Himalaya*). Geology 41*, 111–114. https://doi.org/10.1130/G33523.1

Langille, J.M., Jessup, M.J., Cottle, J.M., Lederer, G., and Ahmad, T. (2012). Timing of metamorphism, melting and exhumation of the Leo Pargil dome, northwest India. *Journal of Metamorphic Geology, 30*, 769–791. https://doi.org/10.1111/j.1525-1314.2012.00998.x

Laskowski, A.K., Kapp, P., Ding, L., Campbell, C., and Liu, X.H. (2017). Tectonic evolution of the Yarlung suture zone, Lopu Range region, southern Tibet. *Tectonics, 36*, 108–136. https://doi.org/10.1002/2016TC004334

Lee, J., Hacker, B., and Wang, Y. (2004). Evolution of North Himalayan gneiss domes: structural and metamorphic studies in Mabja Dome, southern Tibet. *Journal of Structural Geology*, *26*, 2297–2316. https://doi.org/10.1016/j.jsg.2004.02.013

Lee, J., and Whitehouse, M.J. (2007). Onset of mid-crustal extensional flow in southern Tibet: Evidence from U/Pb zircon ages. *Geology 35*, 45–48. https://doi.org/10.1130/G22842A.1

Lombardo, B., and Rolfo, F., (2000). Two contrasting eclogite types in the Himalayas: Implications for the Himalayan orogeny. *Journal of Geodynamics,* 30, 37–60. https://doi.org/10.1016/S0264-3707(99)00026-5

Najman, Y., Appel, E., Boudagher-Fadel, M., Bown, P., Carter, A., Garzanti, E., et al. (2010). Timing of India-Asia collision: geological, biostratigraphic, and palaeomagnetic constraints. *Journal of Geophysical Research: Solid Earth, 115,* B12416. http://dx.doi.org/10.1029/2010JB007673

Najman, Y., Jenks, D., Godin, L., Boudagher-Fadel, M., Millar, I., Garzanti, E., et al. (2017). The Tethyan Himalayan detrital record shows that India–Asia terminal collision occurred by 54 Ma in the Western Himalaya. *Earth and Planetary Science Letters, 459*, 301–310. https://doi.org/10.1016/j.epsl.2016.11.036

O'Brien, P.J. (2019). Eclogites and other high-pressure rocks in the Himalaya: A review. In: P. J. Teloar, and M. P. Searle (Eds.), Himalayan Tectonics: A Modern Synthesis, *Geological Society, London, Special Publications*, *483*, 183–213. https://doi.org/10.1144/SP483.13

O'Brien, P.J., Zotov, N., Law, R., Khan, M.A., and Jan, M.Q. (2001). Coesite in Himalayan eclogite and implications for models of India–Asia collision. *Geology, 29*, 435–438. https://doi.org/10.1130/0091-7613(2001)029<0435:CIHEAI>2.0.CO;2.

Palin, R.M., Reuber, G.S., White, R.W., Kaus, B.J.P., and Weller, O.M. (2017). Subduction metamorphism in the Himalayan ultrahigh-pressure Tso Morari massif: An integrated geodynamic and petrological modelling approach. *Earth and Planetary Science Letters, 467*, 108–119. https://doi.org/10.1016/j.epsl.2017.03.029

Parrish, R.R., Gough, S.J., Searle, M.P., and Waters, D.J. (2006). Plate velocity exhumation of ultrahigh-pressure eclogites in the Pakistan Himalaya. *Geology, 34*, 989–992. https://doi.org/10.1130/G22796A.1

Pognante, U., Benna, P., and Lefort, P. (1993). High pressure metamorphism in the High Himalayan Crystallines of the Stak valley, northeastern Nanga Parbat-Haramosh syntaxis, Pakistan Himalaya. *Geological Society, London, Special Publications, 74*, 161–172. https://doi.org/10.1144/GSL.SP.1993.074.01.12

Regis, D., Warren, C.J., Young, D., and Roberts, N.M. (2014). Tectono-metamorphic evolution of the Jomolhari massif: Variations in timing of syn-collisional metamorphism across western Bhutan. *Lithos, 190*, 449–466. https://doi.org/10.1016/j.lithos.2014.01.001

Robyr, M., and Lanari, P. (2020). Kinematic, metamorphic, and age constraints on the Miyar Thrust Zone: Implications for the Eohimalayan history of the High Himalayan Crystalline of NW India. *Tectonics, 39*, e2020TC006379. https://doi.org/10.1029/2020TC006379

Shrestha, S., Larson, K.P., Martin, A.J., Guilmette, C., Smit, M.A., and Cottle, J.M. (2020). The Greater Himalayan thrust belt: insight into the assembly of the exhumed Himalayan metamorphic core, Modi Khola valley, central Nepal. *Tectonics, 39*, e2020TC006252. https://doi.org/10.1029/2020TC006252

Smit, M.A., Hacker, B.R., and Lee, J. (2014). Tibetan garnet records early Eocene initiation of thickening in the Himalaya. *Geology, 42*, 591–594. https://doi.org/10.1130/G35524.1

Smith, H.A., Chamberlain, C.P., and Zeitler, P.K. (1994). Timing and duration of Himalayan metamorphism within the Indian Plate, Northwest Himalaya, Pakistan. *The Journal of Geology, 102,* 493–508. https://doi.org/10.1086/629694

St-Onge, M.R., Rayner, N., Palin, R.M., Searle, M.P., and Waters, D.J. (2013). Integrated pressure– temperature–time constraints for the Tso Morari dome (Northwest India): Implications for the burial and exhumation path of UHP units in the western Himalaya. *Journal of Metamorphic Geology, 31*, 469–504. https://doi.org/10.1111/jmg.12030

Štípská, P., Závada, P., Collett, S., Kylander-Clark, A.R.C., Hacker, B.R., Tabaud, A.-S., and Racek, M. (2020). Eocene migmatite formation and diachronous burial revealed by petrochronology in NW Himalaya, Zanskar. *Journal of Metamorphic Geology, 38*, 655–691. https://doi.org/10.1111/ jmg.12534

Stübner, K., Grujic, D., Parrish, R.R., Roberts, N.M.W., Kronz, A., Wooden, J., and Ahmad, T. (2014). Monazite geochronology unravels the timing of crustal thickening in NW Himalaya. *Lithos 210–211*, 111–128. http://dx.doi.org/10.1016/j.lithos.2014.09.024

Wang J-M., Wu, F-Y., Rubatto, D., Liu, K., Zhang, J-J., and Liu, X-C. (2018). Early Miocene rapid exhumation in southern Tibet: Insights from P-T-t-D-magmatism path of Yardoi dome. *Lithos, 304–307,* 38–56. https://doi.org/10.1016/j.lithos.2018.02.003

Wang, J-M., Zhang, J-J., Liu, K., Zhang, B., Wang, X-X., Rai, S., and Scheltens, M. (2016). Spatial and temporal evolution of tectonometamorphic discontinuities in the central Himalaya: Constraints from P–T paths and geochronology. *Tectonophysics, 679*, 41–60. http://dx.doi.org/ 10.1016/j.tecto.2016.04.035

Wang, T., Li, G., Aitchison, J.C., and Sheng, J. (2020). Eocene ostracods from southern Tibet: implications for the disappearance of Neo-Tethys. *Palaeogeography, Palaeoclimatology, Palaeoecology, 539*, 109488. https://doi.org/10.1016/j.palaeo.2019.109488

Wang, Y. F., Zeng, L., Gao, J., Zhao, L., Gao, L. E., and Shang, Z. (2019). Along-arc variations in isotope and trace element compositions of Paleogene gabbroic rocks in the Gangdese batholith, southern Tibet. *Lithos*, *324*, 877-892. https://doi.org/10.1016/j.lithos.2018.11.036

Wiesmayr, G. and Grasemann, B. (2002). Eohimalayan fold and thrust belt: Implications for the geodynamic evolution of the NW-Himalaya (India). *Tectonics*, *21*, 8–1. https://doi.org/10.1029/2002TC001363

Wilke, F.D.H., O'Brien, P.J., Altenberger, U., Konrad-Schmolke, M., and Khan, M.A., (2010). Multistage history in different eclogite types from the Pakistan Himalaya and implications for exhumation processes. *Lithos ,114*, 70–85.

Zeng, L., Gao, L-E., Tang, S., Hou, K., Guo, C., and Hu, G. (2015). Eocene magmatism in the Tethyan Himalaya, southern Tibet. In: Mukherjee S., Carosi, R., van der Beek, P. A., Mukherjee, B. K., and Robinson, D.M. (Eds.) Tectonics of the Himalaya. *Geological Society, London, Special Publications, 412*, 287–316. https://doi.org/10.1144/SP412.8

Zeng, L., Gao, L.E., Xie, K., and Liu-Zeng, J. (2011). Mid-Eocene high Sr/Y granites in the Northern Himalayan gneiss domes: Melting thickened lower continental crust. *Earth and Planetary Science Letters*, *303*, 251–266. https://doi.org/10.1016/j.epsl.2011.01.005

Appendix C2. Modelling Methods

C2a. Abbreviated Methods

The methods are similar to those in Kelly et al. (2020) and the models discussed are variations on models MA and MB (Kelly et al., 2020) with additional tracking of model particles for pressure-temperature-time (P-T-t) evolution.

Our mantle-scale 2-D finite element model computations used SOPALE-nested software (http://geodynamics.oceanography.dal.ca/sopale_nested.html) which calculates frictional-plastic and creeping viscous flows and the evolving temperature and pressure fields. The initial configuration of the models (Fig. 4.1) represents the restored natural system at ~90°E, particularly the Asian accreted terranes. Regions (Fig 4.1a) are labeled with an abbreviation corresponding to the natural feature they represent.

Continental lithospheric mantles (CLMs) of the terranes are characterized by d and f (Fig 4.1). Depletion density, d, measures the effect of chemical depletion (e.g., as in the Mg# = 100 × Mg/(Mg + Fe)) of the CLM density with respect to the density of the sub-lithospheric mantle. The viscosity scaling factor, f, measures the dehydration effect on CLM viscosity and ranges from $f = 2$ (hydrated) to $f \geq 5$ (dehydrated). Viscous flow laws are based on laboratory measurements of wet quartzite, dry Maryland diabase, and wet olivine, and include strain softening and weakening (Appendix C2b). The left lithospheric (prolithospheric) boundary velocity, $Vp(t)$, varies with time (t) between 15 and 4.5 cm/yr (Fig 4.1b), reproducing slowing of the Indian plate, while the right (retrolithospheric) boundary has $Vr(t) = 0$, except in the last 15 Myr. Sublithospheric side-boundary velocities ensure that the model is volumetrically and isostatically balanced. Convergence totals 4000 km over 58-0 Ma and 2800 km over the 58-30 Ma that we present here. The reduced convergence appropriate for the western H-T orogen is discussed in Appendix C2b.

Sediment, generated and deposited by the model, and middle and upper continental crust undergo viscosity reduction corresponding to melt-weakening by 4-7% melt

(Appendix C2b.3). Crustal materials undergo reversible density changes corresponding to eclogite and coesite- eclogite phase changes (Table 4.1), Appendix C2b.4). Reversible phase changes at the 660 km depth boundary correspond to the olivine-perovskite transformation.

The models have a free upper surface. Slope-dependent erosion acts on the local topography and is modulated by a climate function representing the wet-to-arid transition across the orogen (Fig. 4.1c). Maximum erosion rates are limited to 0.1 cm/yr (MEA, MEC, MED) and 0.5 cm/yr (MEB).

The initial model configuration (Fig 4.1a), is the same as that in Kelly et al. (2020). Q (Qiangtang) delamination in the models (the key driver for both the timing and amount of subduction channel opening) is largely controlled by the density and strength (*d* and *f)* of its CLM and the CLM of the adjacent L (Lhasa) terrane (i.e., Archimedes number; Kelly et al., 2016). We therefore test a template of models (Fig 4.1d) and explore both variations of the *d* and *f* values of the L- and Q-CLMs and maximum erosion rates. The models shown were chosen because they demonstrate different timings and intensities of Q-CLM delamination and subduction channel opening.

An initial wider parameter search (Kelly et al., 2020) allowed us to focus on 4 models. All of these models are geometrically the same as that shown in Figure 4.1a but have variations in the depletion densities and viscosities of the L (Lhasa) and Q (Qiangtang) CLMs (Fig. 4.1) (Appendix C2b). The main text (Section 4.4) focuses on a successful model, MEA, complemented by other models that illustrate the effects of variations in model properties (Sections 4.6 and 4.7).

C2b. Detailed Methods

C2b.1. Overview of the SOPALE-nested code

The numerical geodynamical models were computed using the 2D ALE thermomechanical finite-element (FE) software SOPALE-nested (Fullsack, 1995;

Beaumont et al., 2009; Butler et al. 2014). Models are designed based on a simple geometry representing oceanic subduction followed by continent-continent collision in which one continent contains five already accreted terranes (Fig. 4.1a). The methodology remains similar to our recent work (Beaumont et al., 2009; Butler et al., 2014; Kelly et al., 2020).

The models are computed by solving the equations for incompressible creeping (Stokes) flows (Eqs. C2b.1 and C2b.2) and energy balance (Eq. C2b.3) on an Eulerian grid subject to mechanical and thermal boundary conditions:

$$\frac{\partial \sigma_{ij}}{\partial x_i} - \frac{\partial P}{\partial x_j} + \rho g = 0, \quad i, j = 1,2 \tag{C2b.1}$$

$$\frac{\partial v_i}{\partial x_i} = 0, \quad i = 1,2 \tag{C2b.2}$$

$$\rho(T) c_p \left(\frac{\partial T}{\partial t} + v_i \frac{\partial T}{\partial x_i} \right) = \frac{\partial}{\partial x_i} K(T) \frac{\partial T}{\partial x_i} + A_R + A_{SH} + v_2 \alpha g T \rho(T), \quad i = 1,2, \tag{C2b.3}$$

where σ_{ij} is the deviatoric stress tensor, x_i spatial coordinates, P pressure (mean stress), ρ density, g gravitational acceleration, v_i a component of velocity, c_p specific heat, T temperature, t time, K thermal conductivity, A_R crustal radioactive heat production per unit volume, A_{SH} shear heating, and α volumetric thermal expansion. Coupling of the mechanical and thermal solutions is achieved through the advection of radioactive crust, shear heating, thermal activation of viscous flow, and buoyancy forces arising from metamorphic phase changes and thermal expansion.

The models use a sub-grid approach in which a higher-resolution Eulerian computational domain is 'nested' within a larger, lower-resolution Eulerian domain. The velocity and thermal solutions are first obtained for the full domain. These solutions are then interpolated onto the boundaries of the nested domain encompassing the vicinity of the subduction zone and the accreted terranes. The computation is then repeated on the higher resolution grid. Coupling of the grids is maintained by using a

single Lagrangian grid and cloud of tracking particles, which is passed between the two solutions, with the particles within the nested domain always obeying the higher resolution solution. The Lagrangian grid and particles are advected by the incremental displacement field each time step and they progressively accumulate the total model displacement, and deformation and evolution of the temperature field.

C2b.2. Model Geometry and Boundary Conditions

The Eulerian model grid is 4000 km wide by 1200 km deep. The initial configuration of the Lagrangian model (Fig. 4.1a) is 11350 km wide by 1200 km deep. This means that much of the non-deforming Lagrangian grid is outside of the Eulerian computational grid but is progressively translated into the Eulerian grid by the boundary velocities. We also make use of the ALE (Arbitrary Lagrangian-Eulerian) nature of SOPALE which allows the Lagrangian grid to be translated with respect to the Eulerian grid by an externally imposed velocity. This 'panning' process is used to move the retro-part of the Lagrangian grid into the Eulerian grid as deformation propagates through the retrolithosphere. This ensures that any part of the model that is currently deforming lies within the Eulerian computational grid.

The starting geometry of the H-T system (Fig. 4.1a; Table 4.1) is a simplification of the natural equivalent but contains the main components of the system, particularly estimated pre- collisional widths and properties of the previously accreted retrocontinent terranes and the Indian side of the system. The width of the retrocontinent is restored based on assumed Neotethys (NT) breakoff at 11°N at 90°E (Fig 4.1e). This implies an increase in width of the retrocontinent of ~ 2200 km with respect to the current configuration, which is achieved by proportional increases in the lengths of the terranes south of the Tarim terrane. This approach is simple and avoids biasing the model geometry by estimates of the shortening of the individual terranes based on observations. Each lithospheric region is labeled with an abbreviation derived from the natural setting, thereby distinguishing models from observations but allowing easy comparison. Model properties (Fig. 4.1a; Table 4.1) are described in more detail below.

The design of MEA-MED is the same except for differences in the *f* and *d* factors (viscosity scaling factor and depletion density, respectively) of the L- and Q-CLMs (continental lithospheric mantle) (see below). The models were also designed to be very similar to models MA and MB (Kelly et al., 2020) so that MA provides the evolution of MEA after 30 Ma, the Neohimalayan part of the model story. The model design includes lateral variations among the properties of the Asian terranes, which makes it fairly complex, but is otherwise generic with no specific tailoring to other more local properties of the H-T system. The models do not contain a volcanic arc at the time of collision, corresponding to the Gangdese arc, and there is no spatial variation in the geometry of the retrolithosphere terranes designed to take into account precursor shortening and crustal thickening, although there was certainly some deformation. How these additional properties modify the evolution of the models is taken into account in the next set of models. Preliminary results indicate that the L-terrane, with weak hot lithosphere but thick crust in the arc region, can transmit the collisional force to the Q-CLM and initiate folding and delamination after first shortening and thickening the L-crust north of the model volcanic arc.

This behavior is in agreement with England and Searle (1986) who showed that the buoyancy of thick weak Lhasa lithosphere allows the transmission of the collision force to the rest of Tibet.

Differences in the depletion density, *d,* (i.e decrease in density with respect to sublithospheric mantle) of continental lithospheric mantle (CLM) may be interpreted to measure varying amounts of chemical depletion (e.g. as reflected in the Mg#, e.g., Lee, 2003). We explore retrolithosphere CLMs with variable depletion densities (Table 4.1). The prolithosphere CLM has a constant depletion density of 50 kg/m^3. Models with significantly higher density (e.g. a depletion density of 40 kg/m^3 or less) fail to produce indentation or advancing subduction, a crucial requirement for H-T orogenesis.

Subduction is initiated conditions at the base and sides of the Eulerian model. Total convergence of 4000 km over 58 Myr is based on mean convergence from Ingalls et al.

(2017). Model results are presented up to 30 Ma, in which there is a total of 2800 km of convergence. The left lithospheric velocity boundary condition varies from V_p = 15 - 4.5 cm/yr (Fig. 4.1b) to reproduce the slowing convergence rate of the Indian plate after collision. The right lithospheric boundary condition has V_r = 0 until the last 15 Myr of convergence, when it increases to 1 cm/yr, thereby allowing for 150 km of late convergence in the Tien Shan, which is outside of the model domain and not computed. Small sublithospheric boundary fluxes are used to 'pump' material out of the sides of the model to conserve volume and maintain isostatic equilibrium.

The continents have laterally uniform crustal radioactive heat production (A_R) for the upper/middle, and lower continental crust of 2.0 and 0.4 μW/m^3, respectively. Coupled with the thermal boundary conditions, basal heat flux 21 mW/m^2, and no-flux side boundaries, the resulting initial steady state surface heat flow and Moho temperatures on the continents are 74 mW/m^2 and ~650°C. The steady state initial base-lithosphere temperature is ~1370°C everywhere in the model. Material thermal expansivity (α) and conductivity (K) are temperature- dependent, with values varying linearly (e.g., from K_1 to K_2) over a range of temperatures (e.g., T_1 to T_2), as described in Table 4.1. Other thermal properties are given in Table 4.1.

As noted above, MEA-MED geometries are based on restorations for 90°E such that the initial southern limit of Asia is at 11°N and the total convergence of India on Asia to 0 Ma would be 4000 km, of which 2800 km by 30 Ma is shown in this paper. This convergence is significantly larger than that for the western Himalaya which raises the question whether the models apply there. Kelly and Beaumont (2021) investigated similar models for the Hindu Kush and Pamir in which convergence rates and total convergence were tuned for this region (Kelly and Beaumont, 2021, Fig. 6) In the Pamir case the transect is very close to the UHP regions of the western Himalaya. The Pamir model evolves in a similar way to MEA, presented here, with only small differences in the by a weak seed embedded between the NT oceanic lithosphere and the L-terrane which spans the entire lithosphere. Models have stress-free boundary conditions at the upper surface, and respectively free-slip and no-slip boundary time of

mantle delamination of the P-CLM (Q-CLM equivalent). We are therefore confident that differences in the initial widths of the Asian terranes and the convergence rates and amounts do not have major effects on the main the results of the models. The essential model behavior illustrated in Figure 4.8 remains valid for the western Himalaya.

C2b.3. Material Properties

The flow laws and material properties are similar to those used in Beaumont et al. (2001) and Butler et al. (2013). For a more detailed justification for the choice of flow laws and the scaling of these flow laws see Butler et al. (2014). The parameters of the models are considered typical of continental and oceanic lithospheric materials (Beaumont et al., 2006, and references therein).

Model materials deform by either frictional-plastic (brittle) or viscous (ductile) flow that includes additional strain-softening/strain-weakening mechanisms. Brittle deformation is modeled using the frictional-plastic Drucker-Prager yield criterion, σ_y:

$$\sigma_y = (J_2')^{1/2} = P\sin\phi_{\text{eff}} + C\cos\phi_{\text{eff}} \quad \text{(C2b.4)}$$

where J_2' is the second invariant of the deviatoric stress, P dynamical pressure (mean stress), and C cohesion. The effective angle of internal friction, ϕ_{eff}, is defined to include the effects of near-hydrostatic pore fluid pressure. The friction angle of all materials, except oceanic sediment, is decreased linearly from $\phi_{\text{eff}} = 15°$ (initial friction angle) to 2° (strain-softened value) as the effective strain increases from 0.5 to 1.5 (Table 4.1). Oceanic sediment has $\phi_{\text{eff}} = 8 - 2°$.

Ductile deformation is modeled using power-law flow, for which the effective viscosity is:

$$\eta_{\text{eff}}^{v} = \frac{f}{W_s} A^{-1/n} \dot{I}_2'^{(1-n/2n)} exp\left(\frac{Q+P}{nRT_K}\right) \quad \text{(C2b.5)}$$

where f is a viscosity scaling factor, W_S a strain-weakening factor, A the pre-exponential factor converted to the tensor invariant form, $\dot{I}_2'$ the second invariant of the deviatoric

strain rate, n the stress exponent, Q activation energy, P pressure, V the activation volume for power-law creep, T_K absolute temperature, and R the universal gas constant. The scaling factor f allows us to model stronger and weaker materials than the laboratory-derived flow law in a predictable way. This scaling may be interpreted as dehydrated or hydrated rock types, or slightly different compositions.

For simplicity, we base the model materials on a small set of laboratory-determined flow laws. Continental upper/middle-crust and sediment rheologies are based on a wet quartzite flow- law (WQ×*f,* Gleason and Tullis, 1995), lower-crustal and oceanic crustal rheologies are based on a dry Maryland diabase flow law (DMD× *f*, where $f = 0.1$, Mackwell et al., 1998), and mantle rheologies are based on a wet olivine flow-law (WOL×*f,* Karato and Wu, 1993) (Table 4.1). Crustal materials viscously strain-weaken according to W_S, the strain-weakening factor (equation c2b.5), which varies linearly from 1 to 3 as the effective strain increases from 5 to 10.

When stress levels are high in the lithospheric mantle they are subject to a high stress limit, the Peierls stress (Katayama and Karato, 2008) by rescaling the effective viscosity by the Peierls weakening factor so that the stress is close to, but not less than, the Peierls threshold stress, σ_p (Table 4.1). This is an approximation to the rapid decrease in effective viscosity that materials experience under an exponential flow law beyond the Peierls threshold stress.

Each crustal unit comprises an upper/middle crust with ϕ_{eff} (hereafter simply ϕ) = 15–2° (except where noted), and a scaled wet quartzite (WQ×*f*) flow law (Gleason and Tullis, 1995), overlying a lower crust with ϕ = 15–2° (where ϕ = 2° is fully strain-softened) and a dry Maryland diabase (DMD×0.1) flow law (Mackwell et al., 1998), scaled to represent intermediate granulite. The continents and accreted terranes have WQ×1 upper crusts, except for I-crust which has WQ×1.25. The underlying CLM has ϕ = 15–2° and scaled wet olivine flow laws (WOL× *f*; Karato and Wu, 1993) and overlies sublithospheric upper mantle (WOL×2) that extends to 660 km. For the pro-continent (I) and retro-continent (T), the CLM has WOL× 5, corresponding to cratonic properties.

The *f*-scaling of the CLM of the accreted terranes varies among the model experiments (Fig. 4.1d), with the values for the MEA model shown in Figure 4.1a. Owing to considerable uncertainty concerning the rheology of the lower mantle (Billen, 2010), we assume that the lower mantle has a uniform and constant viscosity of 1×10^{21} Pa s.

Sediment and upper/middle continental crust undergo melt-weakening in a similar temperature- and pressure-dependent manner as in Butler et al. (2015). The viscosity decreases linearly (representing the effect of minor, 4–7%, partial melt) from the calculated power-law value to a fixed linear value of 10^{19} Pa s over the range from the pressure-dependent dry solidus to the solidus temperature plus 50°C. The dry solidus is defined by P-T line segments joining the points (680°C, 0 GPa), (900°C, 2.8 GPa), and (1437°C, 15 GPa) (Zheng et al. 2011). This fixed 10^{19} Pa s viscosity is maintained at higher temperatures except for coesite-eclogite which develops restite properties if it exceeds P-T conditions defined by the line joining points (963°C, 2.85 GPa) and (1700°C, 12.67 GPa). Melt weakening is an effect that enhances the decoupling between the mid- and lower crust and leads to channel flow in the retrolithosphere.

C2b.4 Density, Volume and Mass Conservation During Phase Transitions

Crustal materials undergo reversible pressure- and temperature-dependent density changes corresponding to the eclogite and coesite-eclogite phase transitions following Warren et al. (2008) (see Table 4.1 for density changes). In addition, sediment and upper/middle crust coesite- eclogite materials that achieve restite conditions (Butler et al., 2015) undergo an increase in *f* to 10 in the power-law viscosity to represent the formation of dry restite after melt extraction (Massonne and Fockenberg, 2012). Restite may subsequently revert to high-pressure eclogite densities but does not further retrograde to reference crustal density.

Mantle materials undergo a reversible phase change at the upper-lower mantle boundary (~660 km depth) corresponding to the transformation of olivine to perovskite. The latter transformation is determined by a reaction with a Clapeyron slope of -2.0 MPa/K and results in a density increase (proportional for all mantle materials) of ~8% (for a

discussion of these parameters, see Billen, 2010). Crustal materials undergo equivalent phase changes at the upper- lower mantle boundary. For simplicity, the models do not include the transformation of olivine to ringwoodite in the mantle transition zone (~440–660 km).

During these phase changes the incompressibility equation is modified to that of mass conservation: $\partial \rho / \partial t = -\partial (\rho v_i) / \partial x_i$. This accounts for the volume change and its effect on the buoyancy and velocity field. The volume change is calculated numerically by applying additional normal, compressive/dilatational forces to finite elements at the time they are subject to phase-related density changes. The value of the excess/reduced pressure is $\Delta P = \Delta \rho / \beta_v \rho$, where β_v is the viscous bulk modulus of the material, and $\Delta\rho / \rho$ is the fractional change in density corresponding to the phase change. The excess/reduced pressure compresses/dilates material locally and only during the model time steps when the phase changes occur, thereby ensuring mass conservation. The fractional volume change accompanying a phase change is small in these models and its effect on the velocity field is minor because it only applies at the time of the phase change. However, failure to ensure mass conservation would have a long-term effect on the model because the buoyancy forces will be over- or under-estimated by the fractional error in the material volume.

C2b.5 Surface Processes

The models have an upper free surface and the model topography is a product of the model calculation without any imposed constraints except for water loading where the surface is below sea level. Slope-dependent surface erosion acts on the local subaerial topography (Fig. 4.1c). It varies according to local slope of the model surface, where it is defined by a maximum erosion rate E*(x)* that operates on a slope of 45° and is scaled down linearly to the local slope of the surface. The erosion rate is also modulated by a spatial climate function (Fig 4.1c) designed to reproduce wet (moderate erosion) conditions on the left-facing orogenic front and dry (lower erosion) conditions over the interior plateau region. The climate function tracks the development and movement of

the orogen. Maximum erosion rates are ~0.1 cm/yr on the orogenic front, except Model MEB, where the maximum erosion rate is 0.5 cm/yr.

The model erosion should be regarded as generic, but does vary with local surface slope and climate conditions ('wet' Himalayan southern front, 'arid' plateau). Models with maximum erosion rates of 0.1 and 0.5 cm/yr were tested. Erosion has not been tuned to take into account variations along the Himalayan arc because the models span 58-30 Ma and it is doubtful that west to east spatial variations in erosion rates are well known for this time interval.

C2b.6 Tracked particles

Model-calculated pressures and temperatures (P-T) of tracked Lagrangian particles, located in the Indian margin upper and lower crust, are recorded with time. The tracked particles are uniformly spaced with depth (~1.3 km) in vertical columns spaced 10-20 km apart. In total 7 columns of particles, arranged within the most proximal part of the Indian margin (Fig. 4.1a), are tracked with P-T conditions recorded every 0.5 Myr.

Supplementary References: Methods C2a and C2b

Beaumont, C., Jamieson, R.A., Butler, J.P., and Warren, C.J. (2009). Crustal structure: A key constraint on the mechanism of ultra-high-pressure rock exhumation. *Earth and Planetary Science Letters, 287,* 116–129. https://doi.org/10.1016/j.epsl.2009.08.001

Beaumont, C., Jamieson, R. A., Nguyen, M. H., and Lee, B. (2001). Himalayan tectonics explained by extrusion of a low-viscosity crustal channel coupled to focused surface denudation. *Nature, 414*, 738-742. https://doi.org/10.1038/414738a

Beaumont, C., Nguyen, M. H., Jamieson, R. A., and Ellis, S. (2006). Crustal flow modes in large hot orogens. In: R. D. Law, M. P. Searle, and L. Godin (Eds.), Channel Flow, Ductile Extrusion and Exhumation in Continental Collision Zones. *Geological Society, London, Special Publications*, 91–145. https://doi.org/10.1144/GSL.SP.2006.268.01.05

Billen, M. I. (2010). Slab dynamics in the transition zone. *Physics of the Earth and Planetary Interiors, 183*, 296–308. https://doi. org/10.1016/j.pepi.2010.05.005.2010

Butler, J. P., Beaumont, C., and Jamieson, R. A. (2013). The Alps 1: A working geodynamic model for burial and exhumation of (ultra)high pressure rocks in Alpine-type orogens. *Earth and Planetary Science Letters, 377-378*, 114-131. https://doi.org/10.1016/j.epsl.2013.06.039

Butler, J. P., Beaumont, C., and Jamieson, R. A. (2014). The Alps 2: Controls on crustal subduction and (ultra) high-pressure rock exhumation in Alpine-type orogens. *Journal of Geophysical Research: Solid Earth, 119*, 5987–6022. https://doi.org/10.1002/2013JB010799

Butler, J. P., Beaumont, C., and Jamieson, R. A. (2015). Paradigm lost: Buoyancy thwarted by the strength of the Western Gneiss Region (ultra) high-pressure terrane, Norway. *Lithosphere, 7*, 379–407. https://doi.org/10.1130/L426.1

England, P., and Searle, M. (1986). The Cretaceous-Tertiary deformation of the Lhasa block and its implications for crustal thickening in Tibet. *Tectonics 5,* 1-14. https://doi.org/10.1029/TC005i001p00001

Fullsack, P. (1995). An arbitrary Lagrangian-Eulerian formulation for creeping flows and its application in tectonic models. *Geophysical Journal International, 120*, 1–23. https://doi.org/10.1111/j.1365-246X.1995.tb05908.x

Gleason, G. C., and Tullis, J. (1995). A flow law for dislocation creep of quartz aggregates determined with the molten salt cell. *Tectonophysics, 247*, 1-23. https://doi.org/10.1016/0040-1951(95)00011-B

Ingalls, M., Rowley, D.B., Currie, B., and Colman, A.S. (2016). Large-scale subduction of continental crust implied by India-Asia mass-balance calculation. *Nature Geoscience, 9,* 848–853. https://doi.org/10.1038/ngeo2806

Karato, S. and Wu, P. (1993). Rheology of the upper mantle: A synthesis. *Science, 260,* 771–778. https://doi: 10.1126/science.260.5109.771

Katayama, I., and Karato, S. I. (2008). Low-temperature, high-stress deformation of olivine under water-saturated conditions. *Physics of the Earth and Planetary Interiors, 168*, 125-133. https://doi.org/10.1016/j.pepi.2008.05.019

Kelly, S., Butler, J.P., and Beaumont, C. (2016). Continental collision with a sandwiched accreted terrane: Insights into Himalayan–Tibetan lithospheric mantle tectonics? *Earth and Planetary Science Letters, 455,* 176–195. https://doi.org/10.1016/j.epsl.2016.08.039

Kelly, S., Beaumont, C. and Butler, J.P. (2020). Inherited terrane properties explain enigmatic post-collisional Himalayan-Tibetan evolution. *Geology, 48*, 8–14. https://doi.org/10.1130/G46701.1

Kelly, S. and Beaumont, C. (2021). Balanced cross-sections and numerical modeling of the lithospheric-scale evolution of the Hindu Kush and Pamir. *Journal of Geophysical Research: Solid Earth*, *126*, e2020JB020678. https://doi.org/10.1029/2020JB020678

Lee, C.-T. A. (2003). Compositional variation of density and seismic velocities in natural peridotites at STP conditions: Implications for seismic imaging of compositional heterogeneities in the upper mantle. *Journal of Geophysical Research: Solid Earth, 108,* https://doi.org/10.1029/2003JB002413

Mackwell, S. J., Zimmerman, M. E., and Kohlstedt, D. L. (1998). High-temperature deformation of dry diabase with application to tectonics on Venus. *Journal of Geophysical Research, 103*, 975-984. https://doi.org/10.1029/97JB02671

Massonne, H. J., and Fockenberg, T. (2012). Melting of metasedimentary rocks at ultrahigh pressure - Insights from experiments and thermodynamic calculations. *Lithosphere, 4,* 269–285. https://doi.org/10.1130/L185.1

Warren, C. J., Beaumont, C., and Jamieson, R. A. (2008). Modeling tectonic styles and ultra-high pressure (UHP) rock exhumation during the transition from oceanic subduction to continental collision. *Earth and Planetary Science Letters, 267*, 129–145. https://doi.org/10.1016/j. epsl.2007.11.025

Zheng, Y.-F., Xia, Q.-X., Chen, R.-X., and Gao, X.-Y. (2011). Partial melting, fluid supercriticality, and element mobility in ultrahigh-pressure metamorphic rocks during continental collision. *Earth-Science Reviews, 107*, 342-374. https://doi.org/10.1016/j.earscirev.2011.04.004

Appendix C3. The Effect of Late Eohimalayan Crustal Radioactive Heating: Comparison of MEA and MEA'

We have computed a version of MEA, termed MEA', in which there is no radioactive heating in the IR- and I-crusts between 44 Ma and 30 Ma (Fig. C.3), as opposed to the 2 x and 0.4 x 10^{-6} W, respectively, in the upper/mid-crust and lower crust in MEA. The purpose is to show how much crustal radioactive heating was contributed to the model Himalayan orogen between the end of the Early Eohimalayan metamorphism, which we judge in the models to be at ~44 Ma, and the onset of renewed convergence and Neohimalayan metamorphism (~30 Ma). We interpret the difference in crustal temperatures between MEA (with crustal radioactive heating) and MEA' (with no radioactive heating) as the contribution made by radioactive heating during his time interval. This allows us to distinguish the heat sources for Early and Late Eohimalayan metamorphism.

An exact comparison of MEA and MEA' is not possible because the cooling in MEA' that results from removing the radioactive heating also influences the model evolution,

making the crust stronger (higher viscosity). This leads to somewhat greater crustal thickening and a narrower orogen (Fig. C.3). Therefore, the geometries of MEA and MEA' are not the same.

However, it can be seen from comparing MEA and MEA' isotherms in the part of the crust that has not been deformed (Fig. C.3, left boundaries of panels a *vs.* e) that cooling in MEA' between 44 and 30 Ma is ~ 140°C (540°C to 400°C) at the base of the mid-crust, 24 km depth, whereas the equivalent temperature in MEA (Fig. C.3d) remains at 540°C, as expected.

In the thicker region of the model Himalayan crust, where the temperature in both models at a depth of 24 km is 700°C at 44 Ma (Fig. C.3a), the temperature is only ~400°C at 30 Ma in MEA' (Fig C.3e), i.e., 300°C cooler. Part of this cooling is apparent, the result of crustal thickening and the downward advection of the isotherms. However, the temperature of the deepest part of the black maker horizon in the model, an actual material location (Fig. C.3a), is ~680°C at 44 Ma and ~520°C at 30 Ma in MEA' (Fig. C.3e), 160°C cooler.

If we now make the inverse comparison, radioactive heating in MEA between 44 and 30 Ma heats the base of the undeformed mid-crust by 140°C, and by 160°C somewhat deeper in the interior of the orogen. We therefore conclude that direct conductive heating from upwelling in the subduction channel provides a thermal pulse that heats this region rapidly to ~ 700°C, leading to MP-MT Early Eohimalayan metamorphism that lasts until ~44 Ma in MEA. In the Late Eohimalayan interval, 44-30 Ma, after the heat pulse begins to wane, the orogen mid-crustal temperature in MEA is maintained by crustal radioactive self-heating until the onset of Neohimalayan crustal thickening and metamorphism (~30 Ma). Without the radioactive heating the mid-crust would cool by ~140-160°C. Therefore, the persistence of the MT-MP metamorphism throughout Late Eohimalayan tectonic quiescence is attributed to crustal radioactive heating.

The message is the same as that for cooking in an electric oven. The rate of initial heating must be high to bring the oven to the desired cooking temperature rapidly, analogous to the Early Eohimalayan MP-MT interval when the temperature of the mid-crust increased from 540°C to 700°C. A significantly lower rate of heating is all that is required to maintain the temperature during the cooking time, analogous to the Late Eohimalayan ~700°C MP-MT interval. This result also implies that the temperature of the base of the Himalayan mid-crust was maintained at ~700°C until the onset of Neohimalayan orogenesis.

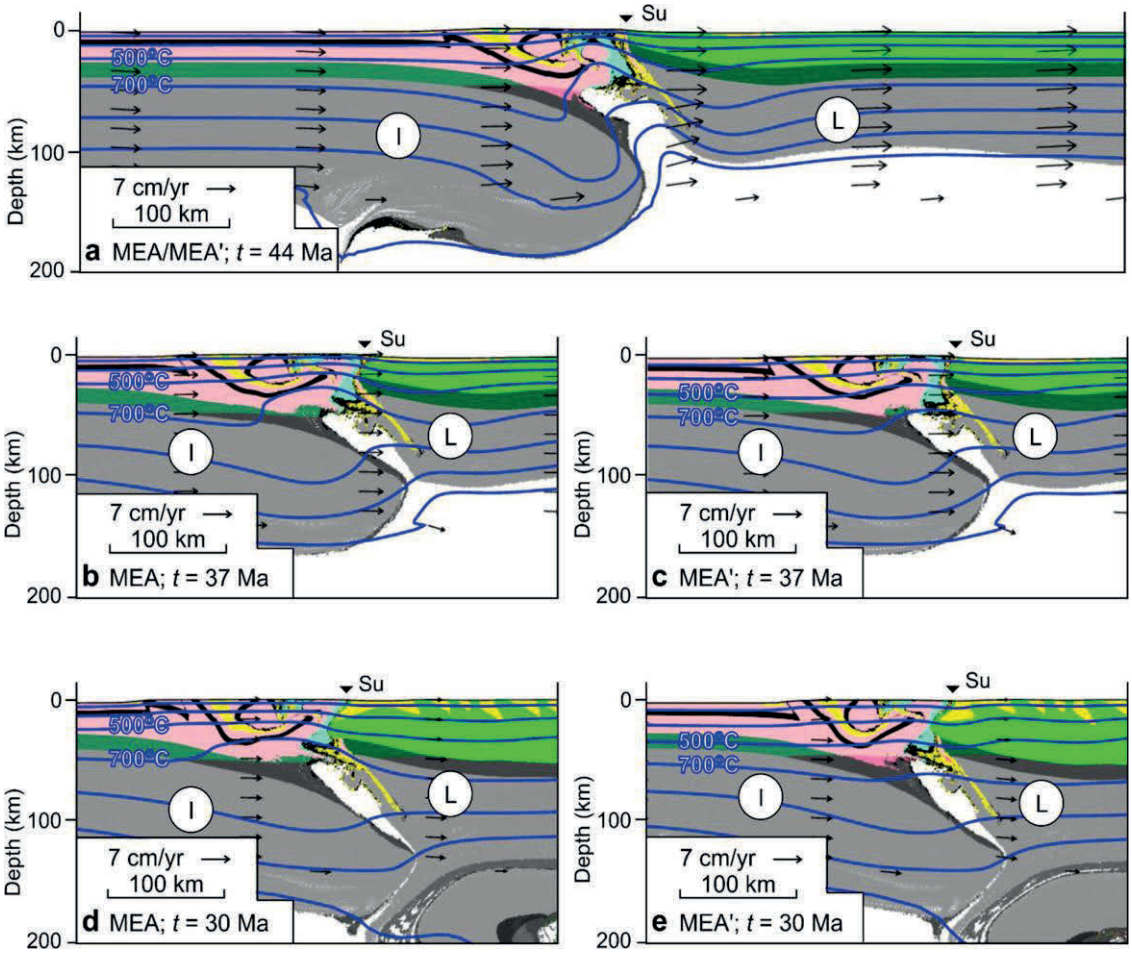

Figure C.3. Model MEA (left) compared with Model MEA' (right), which lacks crustal radioactive heating. a) Model MEA/MEA' at 44 Ma; at this time the models are essentially identical, with the 700°C isotherm elevated to middle crust above opened subduction channel. b) MEA at 37 Ma; 700°C isotherm remains in middle crust. c) MEA' at 37 Ma; 700°C isotherm has relaxed to base of lower crust. d) MEA at 30 Ma; 700°C isotherm remains at mid-crustal depth even though subduction channel has largely closed. e) MEA' at 30 Ma; 700°C isotherm has relaxed to upper mantle depths.

APPENDIX D

CHAPTER 5 APPENDICES

Supporting Information for

A Machine-Learning Based Method for Discriminating Tectonic Environments from Geochemical Data

Kelly, S.

Appendix D1 Additional Figures

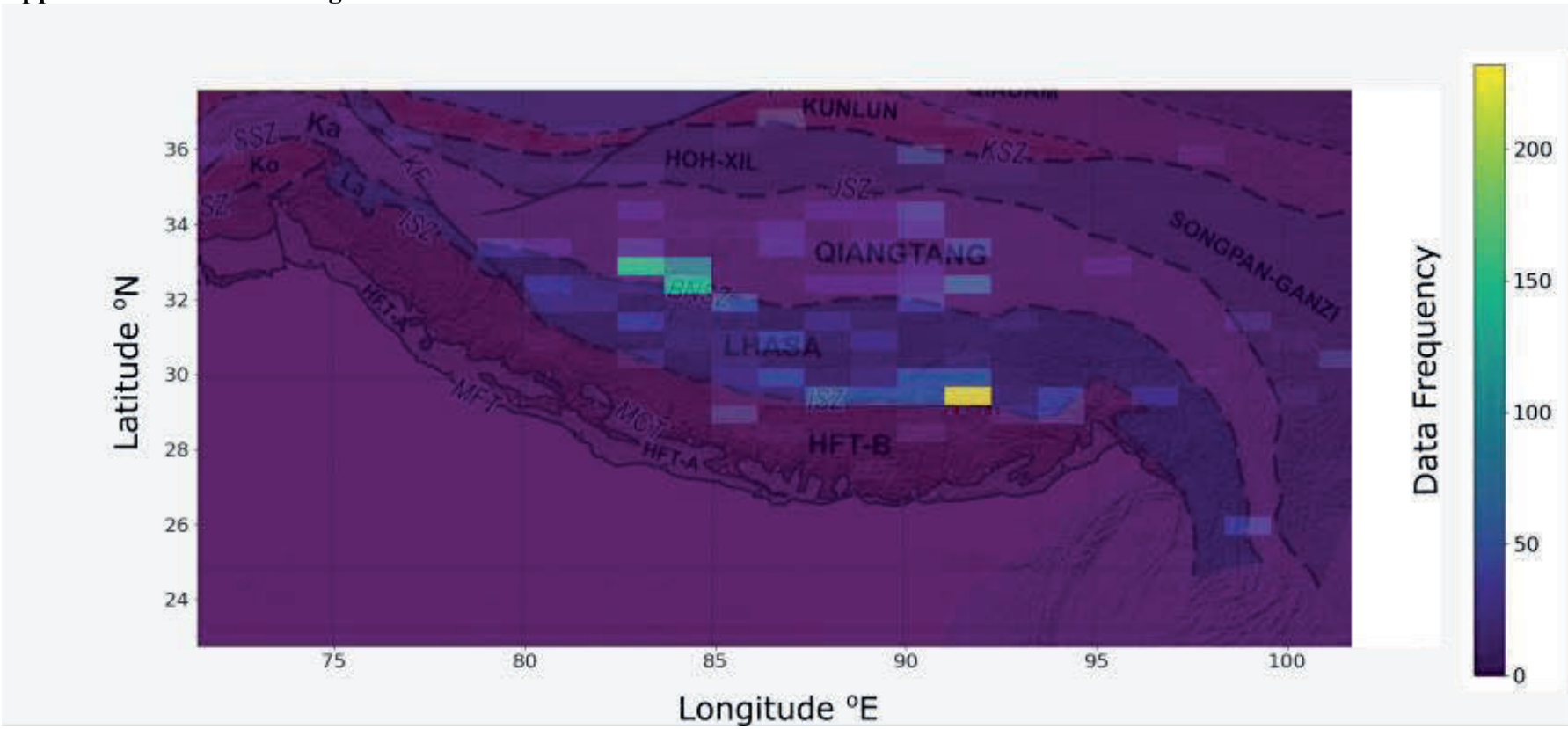

Figure D.1 Data frequency of Tibetan data used in ML analysis overlaying terrane map of the India-Asia orogen (modified from Parsons et al., 2020).

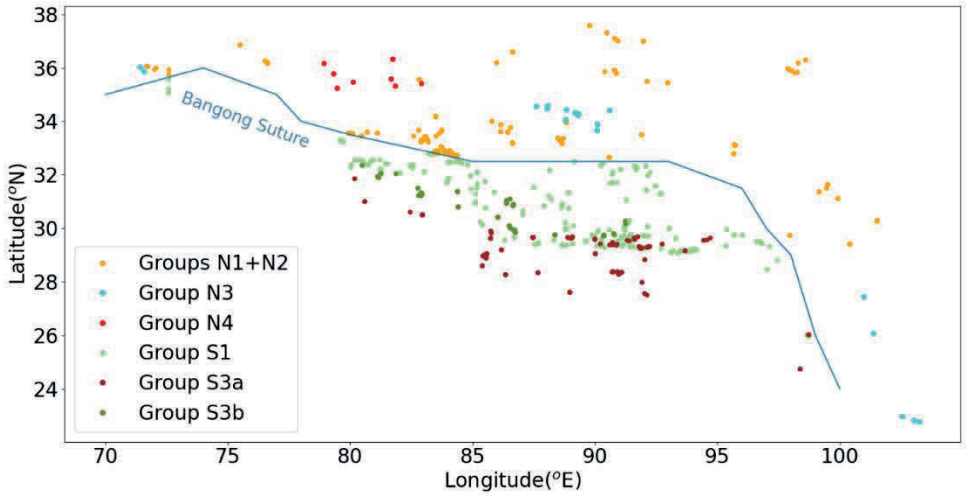

Figure D.2 Tibetan data colored by group and the approximate location of the Bangong suture used to separate the North (N1 – N4) and South groups (S1, S3a, S3b). See section 5.6.4.

Appendix D2 Software

The ML analysis was completed using python scripts employing the "scikit learn" machine learning library (http://scikit-learn.org/stable/), as well as other commonly used python libraries for scientific computing and plotting (e.g., NumPy, pandas, Matplotlib). The scripts used in this research are available at https://github.com/Sean-Kelly-Dal/Geo_example

Appendix D3 Data Sources

Data and references used from the Tibetan Magmatic Database and from the mid-ocean ridge, continental arc and island arc data sets (from Ueki et al., 2018) can be found on Dalspace in the following Excel files, respectively.

Tibetan_Magmatic_Data.xlsx

MOR_CA_IA_Ueki_2018.xlsx

Appendix D4 Methods

D4.1 Support Vector Machine

A Linear support vector machine is trained on a labeled dataset, where each sample has label-data (labeling the class data belong to) and feature-data. In the method presented here, data are assigned a temporary assigned a class based on a proposed spatiotemporal grouping and labelled according to these temporary classes. The method seeks to find a hyperplane that separates the two classes in feature space and maximizes the margins between the hyperplane and the closest members in each class. For convenience, Figure 5.3 is copied below as Figure D.3.

As noted above, the data typically require pre-processing before training an SVM model, the most common being to remove the mean and normalize by the standard deviation of each feature of data (Ueki, et. al., 2018). Specifically, the normalized data are calculated as,

D4.1

$$z_{k,i} = \frac{x_{k,i} - \mu_k}{\sigma_k}$$

Where $x_{k,i}$ are the unprocessed data, with features indexed by k and samples by i, μ_k is the mean of the kth feature and $\sigma_k$is the standard deviation of the kth feature.

If the data are not normally distributed, which is typically the case with trace element data, a Box-Cox transformation can be applied first (Ueki et. al., 2018). This is defined as the following:

D4.2

$$\bar{x}_{k,i} = \begin{cases} \dfrac{x_{k,i}^{\lambda} - 1}{\lambda} & \lambda \neq 0 \\ \ln\left(x_{k,i}\right) & \lambda = 0 \end{cases}$$

Where $\bar{x}_{k,i}$ is the transformed data, and λ is chosen so that the log-likelihood function of the resulting distribution of $\bar{x}_{k,i}$ is maximized. Figure D.4, shows a histogram of strontium data from the Ueki et al. (2018) MOR dataset used in Subsections 5.4.4 and Section 5.5. The untransformed data is skewed and contains high Sr outliers (Fig. D.4a). After the Box-Cox transformation, the data are more normally distributed (Fig. D.4b). The resulting normally distributed data is again transformed by removing the mean and normalizing by the standard deviation (Fig. D.4c). The final distribution (Fig. D.4c) has a mean of zero, a standard deviation of one, and is now unitless.

Defining $\boldsymbol{x}_i$ as the preprocessed feature space vector of the i[th] sample, $\boldsymbol{x}$ a generic feature space vector, $\boldsymbol{w}$ a vector normal to the hyperplane we seek, and b an offset parameter, the hyperplane is defined by the following:

D4.3
$$\boldsymbol{w} \cdot \boldsymbol{x} + b = 0$$

Noting that the value of $\boldsymbol{w} \cdot \boldsymbol{x_i} + b$ will either be positive or negative depending on which side of the hyperplane $\boldsymbol{x}_i$ lies on. The vector $\boldsymbol{w}$ defines the orientation of the hyperplane and the parameter b controls its offset from the feature space origin. Defining a decision function $\boldsymbol{y}_i(\boldsymbol{w} \cdot \boldsymbol{x}_i + b)$ as positive if the point $\boldsymbol{x_i}$ lies on the correct side of the hyperplane corresponding to its label, negative otherwise, and greater than one for data lying outside the margin, then $\boldsymbol{w}$, b are found by the following optimization problem (Cortes and Vapnik, 1995; https://towardsdatascience.com/demystifying-support-vector-machines-8453b39f7368).

D4.4
$$\min_{\boldsymbol{w},b,\zeta}\left(\frac{1}{2}\|\boldsymbol{w}\|^2 + C\sum_{i=0}^{n}\zeta_i\right)$$
$$subject\ to: \boldsymbol{y}_i(\boldsymbol{w} \cdot \boldsymbol{x}_i + b) \geq 1 - \zeta_i\,, \quad \zeta_i \geq 0$$

Where the parameters ζ_i are known as slack parameters and C is a regularization parameter, and n is the number of data which are misclassified by the hyperplane. If the

slack parameters are not included (i.e., no misclassified data), the first condition maximizes the margins between data from each class and the hyperplane, while the second condition is that the hyperplane must be chosen so that the data are separated completely, since as defined above, $\boldsymbol{y}_i(\boldsymbol{w} \cdot \boldsymbol{x}_i + b)$ is greater than 1 for data lying on the correct side of the hyperplane margins.

However, SVM problems may not be perfectly solvable, such that no hyperplane exists to completely separate the data (non-separable). The slack parameters make the problem solvable by merely penalizing misclassified data. If some data were instead within the margin, or on the incorrect side of the hyperplane, these data would fail the condition $y_i(\boldsymbol{w} \cdot \boldsymbol{x}_i + b) \geq 1$. Introducing a slack parameter for these data allows this condition to be relaxed. However, since any data can be allowed to be misclassified by introducing an appropriate slack parameter, the sum of chosen slack parameters is included in the minimization problem, which penalizes these slack parameters. This penalization is controlled by C, with larger values of C more heavily penalizing slack parameters in the minimization problem. This penalization balances maximizing the width of the margin with minimizing the number of misclassified data.

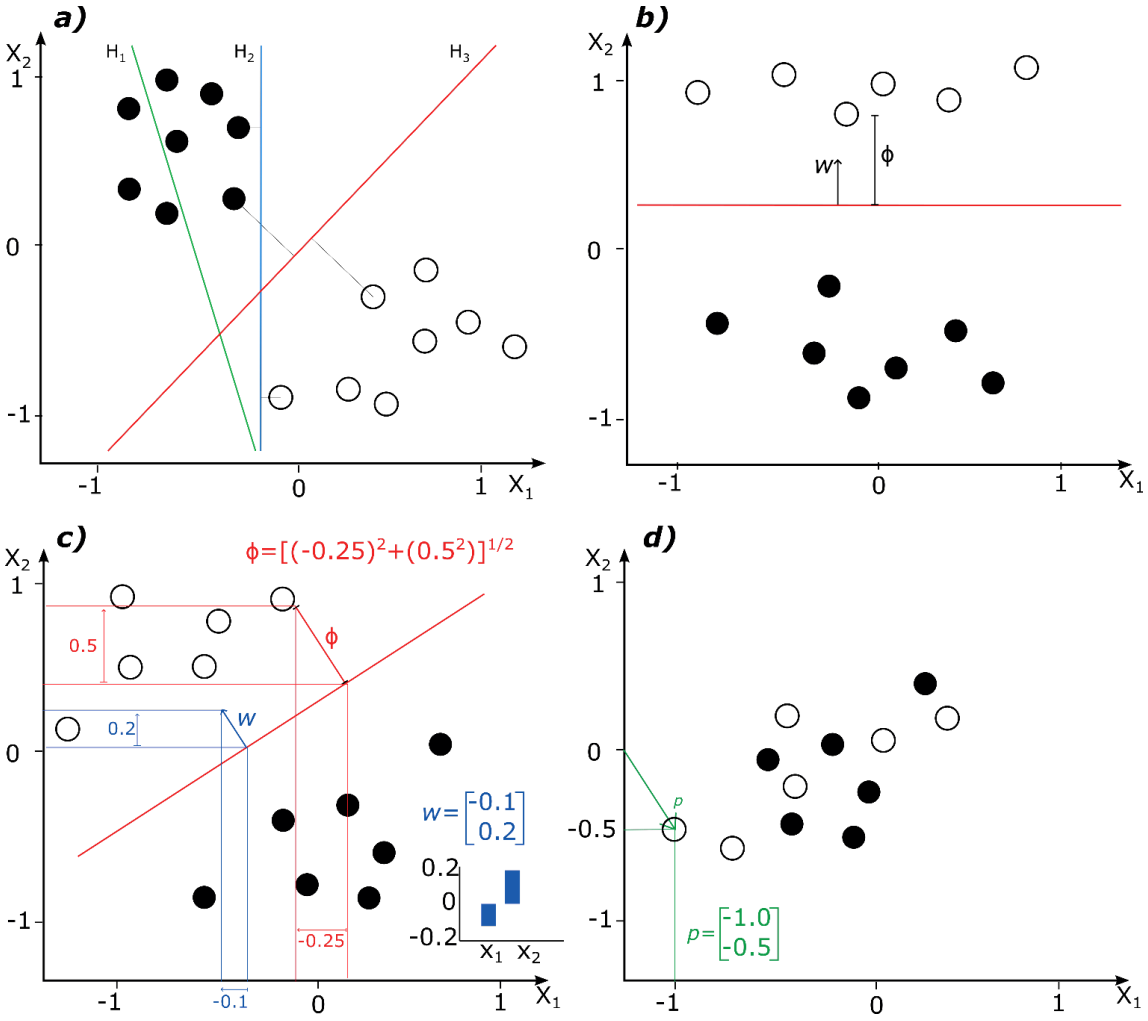

Figure D.3 Example of SVM with two classes of data (solid and open circles), and two features (parameters X_1 and X_2). **a)** Proposed hyperplanes separating the two classes of data in feature space. "H_1 does not separate the classes, H_2 does but only with a small margin, H_3 separates them with the maximal margin (original caption)." **b)** Two classes of data which are separated along X_2 only. The normal vector (w) points in the direction in feature space which separates the classes. Here X_2 is the only relevant parameter. The parameter ϕ measures the Euclidian distance a particular datum lies in feature space from this hyperplane. In some cases, ϕ can be interpreted to represent how similar data are to a particular class **c)** Here, two classes are separated by increasing X_2 and decreasing X_1 as shown by the vector w, a normal vector to the separating hyperplane, with vector components displayed both numerically and as a bar chart (lower left inset). **d)** Two classes of data which are not separable. Here, there is no obvious way to discriminate these two classes, which may indicate that these data belong to a single indistinguishable class. An example of a datum p, is depicted as a vector in feature space. (Figure and caption modified from Zach Weinberg. Separating hyperplanes (SVG). Citation: https://en.wikipedia.org/wiki/Support_vector_machine#/media/File:Svm_separating_hyperplanes_(SVG).svg)

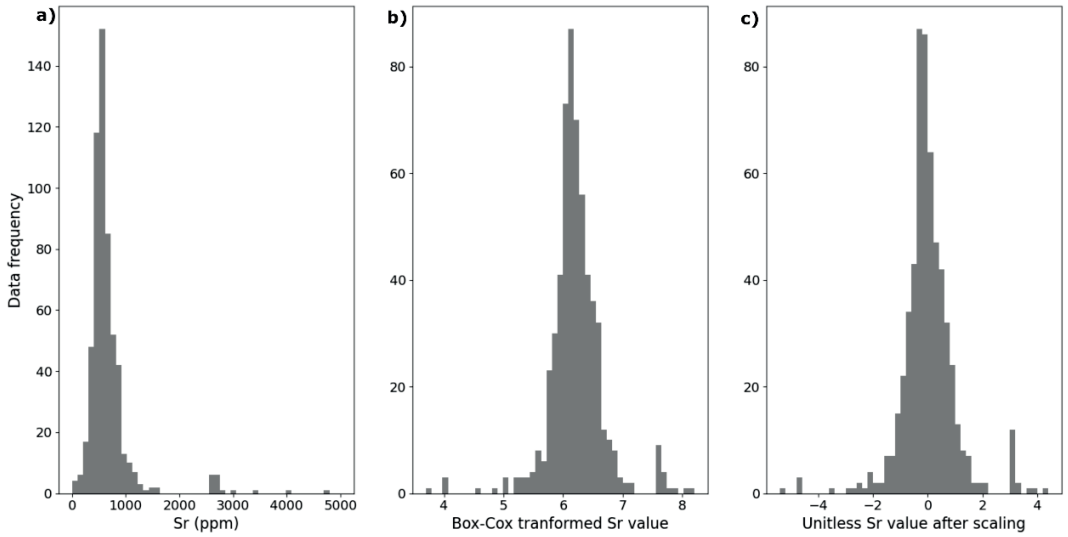

Figure D.4. Illustration of the effects of a data preparation for Sr data from the Ueki et al. (2018) MOR data. **a**) Histogram of Sr values from this dataset before processing. These data are not normally distributed. **b**) Sr data after applying a Box-Cox transformation which approximately fits the data to a normal distribution. **c**) The mean is subtracted from the resulting Box-Cox transformed data and then the data are divided by the standard deviation resulting in an approximately normally distributed dataset with zero mean and unit standard deviation.

D4.2 References

Cortes, C. and Vapnik, V. (1995). Support-vector networks. *Machine learning, 20,* 273–297.

Kumar D., (2019) Demystifying Support Vector Machines, Towards Data Science, https://towardsdatascience.com/demystifying-support-vector-machines-8453b39f7368

Ueki, K., Hino, H. and Kuwatani, T. (2018). Geochemical discrimination and characteristics of magmatic tectonic settings: A machine-learning-based approach. *Geochemistry, Geophysics, Geosystems, 19*, 1327–1347.

Appendix D5 Example of a Proposed Surface.

To illustrate the proposed surfaces used in 5.5.2, an example of equation,

D5.1
$$z = \sum_{i=0}^{3}\sum_{j=0}^{3} \alpha_{i,j} x^i \, y^j$$

is explored below. Values of $\alpha_{i,j}$ were sampled from a normal distribution centered at 0, with standard deviation $\sigma = 1/i!\,j!$, yielding:

$$\alpha_{i.j} = \begin{pmatrix} 0.63438989 & 0.57745825 & -0.46352053 \\ -1.3450354 & -0.33638668 & -0.07410117 \\ -0.0163604 & 0.08127852 & -0.02856442 \end{pmatrix}$$

Expanding Equation D5.1 yields the following equation for this surface.

D5.2
$$z(x,y) \approx 0.63 - 1.35x + 0.58y - 0.02x^2 - 0.34xy - 0.46y^2 + 0.08x^2y - 0.07xy^2 - 0.03x^2y^2$$

Figure D5.1 shows the values of the surface over the range [-1,1], and Figure D.6 shows regions where this surface is negative (purple) or positive (yellow). Samples within the positive region would be assigned one class and samples lying within the negative region would be assigned the other.

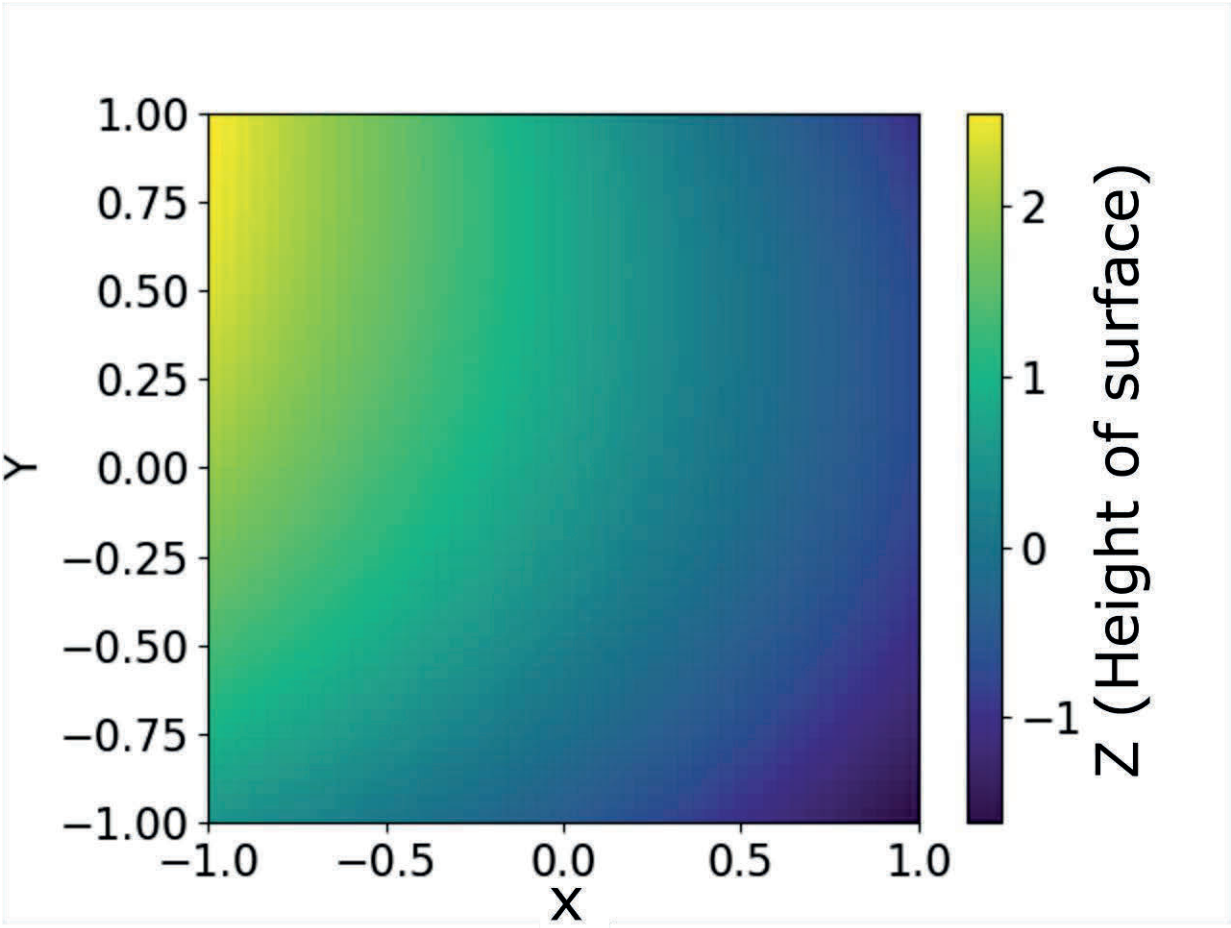

Figure D.5. The values of the height of the surface in Equation 5.E2 over the range [-1,1] for x and y. Note that the values of z are unitless.

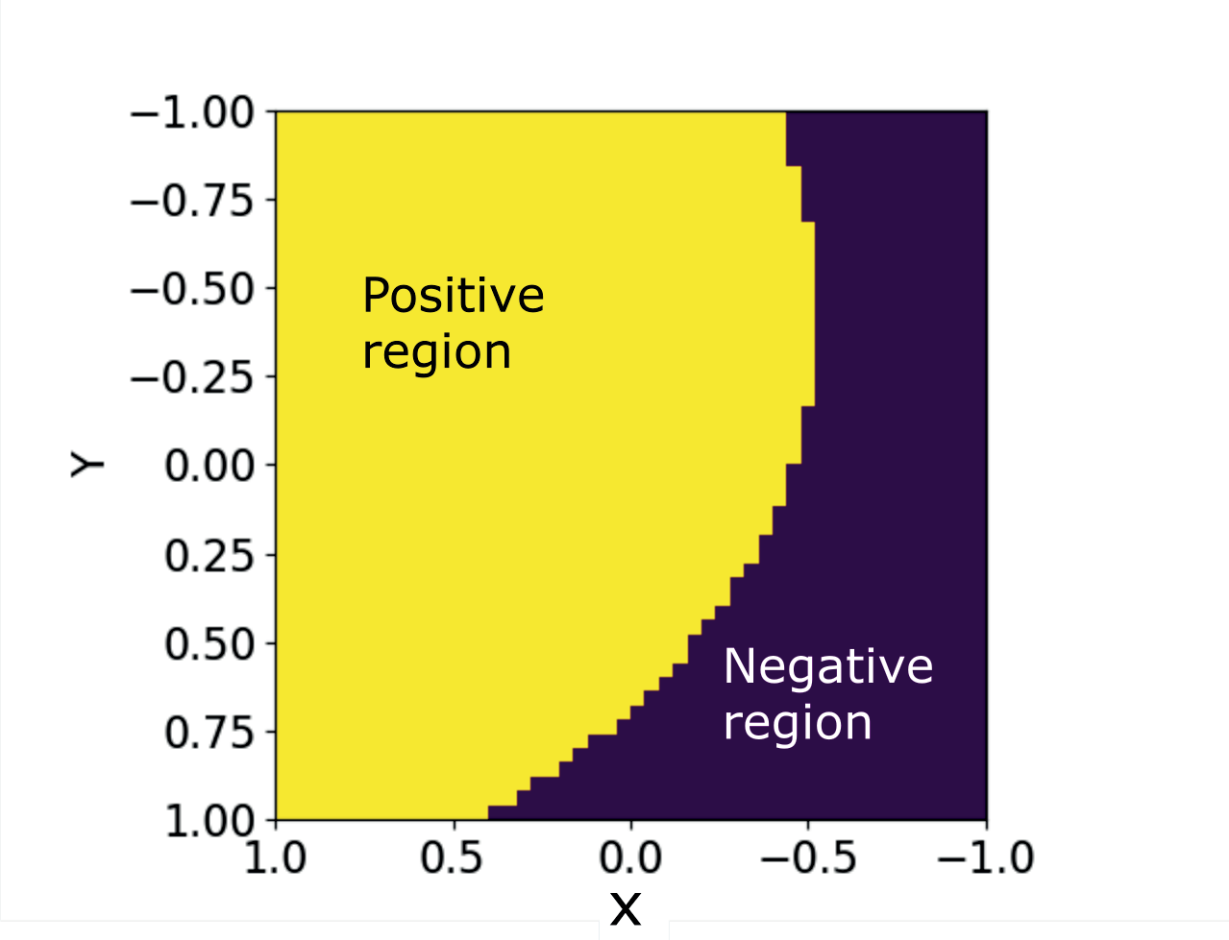

Figure D.6. Regions where the surface height in Equation 5.E2 is positive (yellow) or negative (purple).

APPENDIX E
PERMISSIONS

RE: Copyright permissions

Publications <publications@agu.org>
Thu 2023-08-17 10:04 AM
To:Sean Kelly <sn454421@dal.ca>

Dear Sean,

Articles can be included in their entirety in doctoral theses and dissertations without specific permission. Please be sure to include all relevant citation information.

Congratulations on nearing the end of such a long process! We wish you all the best in your future endeavors.

Best wishes,

Kevin Jewett

From: Sean Kelly <sn454421@dal.ca>
Sent: Wednesday, August 16, 2023 5:56 PM
To: Publications <publications@agu.org>
Subject: Copyright permissions

To whom it may concern

I am requesting permission to include our paper Balanced cross-sections and numerical modeling of the lithospheric-scale evolution of the Hindu Kush and Pamir, published in the Journal of Geophysical Research: Solid Earth, in my PhD Thesis.

I have attached a form to be billed out by the appropriate person and returned to me. Alternatively, if you could provide contact detail for the appropriate person, I can forward the attached form to them directly.

Thank you,
Sean Kelly

August 21, 2023

Copyright Permissions
GSA
PO Box 9140
Boulder, CO, 80301-9140

I am preparing my PhD thesis for submission to the Faculty of Graduate Studies at Dalhousie University, Halifax, Nova Scotia, Canada. I am seeking your permission to include a manuscript version of the following paper(s) as a chapter in the thesis:

Inherited terrane properties explain enigmatic post-collisional Himalayan-Tibetan evolution

By S. Kelly, C. Beaumont, and J.P. Butler

Geology, 48(1), 8–14, 2020

Dalhousie graduate theses are collected and stored online by Dalhousie University and Library and Archives of Canada. I am seeking your permission for the material described above to be stored online in Dalhousie University's institutional repository and in Library and Archives of Canada (LAC)'s Theses Canada Collection.

Full publication details and a copy of this permission letter will be included in the thesis.

Yours sincerely,

Sean Kelly

Permission is granted for:

a) the inclusion of the material described above in your thesis.

b) for the material described above to be included in the copy of your thesis that is sent to the Library and Archives of Canada inclusion in Theses Canada.

c) For the material described above to be included in the copy of your thesis that is sent to Dalhousie University's institutional repository.

Name: April Leo Title: Senior Managing Editor, Books

Signature: Date: 8/21/23

Re: Copyright Permissions [230817-004141]

Permissions Helpdesk <permissionshelpdesk@elsevier.com>
Fri 2023-08-18 2:15 PM
To:Sean Kelly <sn454421@dal.ca>

Dear Sean Kelly

We hereby grant you permission to reprint the material below at no charge in your thesis subject to the following conditions:

RE: Eohimalayan metamorphism and subsequent tectonic quiescence explained, Earth and Planetary Science Letters, Volume 584, 2022, Kelly et al.

1. If any part of the material to be used (for example, figures) has appeared in our publication with credit or acknowledgment to another source, permission must also be sought from that source. If such permission is not obtained then that material may not be included in your publication/copies.

2. Suitable acknowledgment to the source must be made, either as a footnote or in a reference list at the end of your publication, as follows:

"This article was published in Publication title, Vol number, Author(s), Title of article, Page Nos, Copyright Elsevier (or appropriate Society name) (Year)."

3. Your thesis may be submitted to your institution in either print or electronic form.

4. Reproduction of this material is confined to the purpose for which permission is hereby given.

5. This permission is granted for non-exclusive world English rights only. For other languages please reapply separately for each one required. Permission excludes use in an electronic form other than submission. Should you have a specific electronic project in mind please reapply for permission.

6. As long as the article is embedded in your thesis, you can post/share your thesis in the University repository.

7. Should your thesis be published commercially, please reapply for permission.

8. Posting of the full article/ chapter online is not permitted. You may post an abstract with a link to the Elsevier website [http://www.elsevier.com%2C/]www.elsevier.com, or to the article on ScienceDirect if it is available on that platform.

Kind regards,

Roopa Lingayath
Senior Copyrights Specialist
ELSEVIER | HCM - Health Content Management